The 1st National Conference on Green Energy

(NCGE'2023)

December 02, 2023, University of Boumerdes, Algeria

Conference Proceedings

ISBN: 978-9969-9733-4-1

Dépôt légal: 9969-2023

The 1st National Conference on Green Energy (NCGE'2023)

December 2, 2023, University of Boumerdes

PROCEEDINGS BOOK

Editors:

Yassine YAKHELEF

Fares NAFA

Mohamed KAOUANE

Meziane HAMEL

Samia BELKACEM

Abdelmalek MOUATSI

Abdelhakim DAOUI

Noureddine MESSAOUDI

ISBN:978-9969-9733-4-1
Dépôt légal: 9969-2023

Conference website: https://ncge2023.univ-boumerdes.dz

The 1st National Conference on Green Energy (NCGE'2023)

December 2, 2023, University of Boumerdes

Conference Honorary Chairs

Pr. Mustepha YAHI, Rector of University of Boumerdes, Algeria

Pr. Mohamed SAIDI, Dean of the Faculty of Technology, University of Boumerdes, Algeria

Conference General Chair

Dr. Yassine YAKHELEF, University of Boumerdes, Algeria

Conference General Co-Chair

Dr. Fares NAFA, University of Boumerdes, Algeria

The 1st National Conference on Green Energy (NCGE'2023)

December 2, 2023, University of Boumerdes

Organization Board

Dr. Yassine Yakhelef
Dr. Fares Nafa
Dr. Meziane Hamel
Dr. Karima Dichou
Dr. Mohamed Kaouane
Mr. Abdelkarim Soukhal
Dr. Abdelmalek Mouatsi
Dr. Noureddine Messaoudi
Dr. Samia Belkacem
Dr. Nidhal Cherrat
Mrs. Radhia Haroun
Mr. Hocine Kamel

Scientific Board

Pr. Djamal Aouzellag, University of Bejaia
Pr. Nassima Mziou, University of Boumerdes
Pr. Kaci Ghedamsi, University of Bejaia..
Pr. Mounir Khiat, University of Oran.
Pr. Abdelhalim Benachenhou, University of Mostaganem.
Pr. Abdellah Kouzou, University of Djelfa.
Pr. Messaoud Boulouh, University of Guelma.
Pr. Abdemalek Kouadri, University of Boumerdes
Dr. Ahcene Bouzida, University of Bouira.
Dr. Nidhal Cherrat, Univ. Boumerdes
Pr. Sihem Kechida, University of Guelma.
Dr. Yacine Bensafia, University of Bouira
Pr. Sid-Ali Fellag, University of Boumerdes
Dr. Meziane Fares, CDER, Alger.
Pr. Madjid Hachemi, University of Boumerdes
Pr. Latéfa Ghomri, University of Tlemcen
Pr. Mustapha Zaouia, University of Tizi Ouzou
Dr. Fares Bouriachi, University of USTHB, Alger.
Dr. Youcef Djeriri, University of Sidi-Bel Abbès
Dr. Salah Hanafi, University of Sidi-Bel-Abbès
Pr. Mostefa Brahami, University of Sidi-Bel-Abbès
Pr. Idriss Benlaloui, University of Batna 2
Dr. Rachid Abdessamed, University of Batna 2
Dr. Samia Belkacem, University of Boumerdes
Pr. Abdelmadjid Recioui, University of Boumerdes
Pr. Hamid Bentarzi, University of Boumerdes
Pr. Youcef Boutoura, University of Tizi Ouzou
Pr. Khatir Khattab, University of M'sila
Pr. Aimad Ahriche, University of Boumerdes
Dr. Moussa Hamadache, University of Boumerdes.
Dr. Karima Dichou, University of Boumerdes
Dr. Fatma Zouhra Dekhandji, University of Boumerdes
Dr. Abdelkarim Ammar, University of Boumerdes.
Dr. Slimane Souag, University of Mostaganem.
Pr. Abdellatif Zerga, University of Tlemcen.
Dr. Bilal Tolbi, University of Sidi-Bel-Abbès.
Pr. Mohand Lagha, University of Blida1.
Pr. Farid Hamoudi, University of Bejaia.
Pr. Hocine Labar, University of Annaba.
Pr. Lazhar Rahmani, University of Setif.
Pr. Aissa Khaldoun, University of Boumerdes.
Pr. Sofiane Mendaci, University of Guelma.
Pr. Hamoud Radjeai, University of Setif.
Pr. Youcef Soufi, University of Tebessa.
Dr. Mohamed Kaouane, University of Boumerdes
Pr. Ahmed Hafaifa, University of Djelfa
Dr. Haroun Aouzellag, University of Bejaia
Dr. Ali Dali, CDER, Alger.
Dr. Nour El Houda Gabour, University of Boumerdes
Dr. Leila Ghomri, University of Mostaganem.
Dr. Chouaib Chattah, University of Skikda
Pr. Farouk Chellali, University of Djelfa
Dr. Abdelhakim Idir, University of M'sila
Dr. Meziane Hamel, University of Boumerdes
Dr. Ratiba Fellag, CDTA
Dr. Aimad Boudouda, University of Boumerdes
Dr. Abderrezak Aibeche, University of Boumerdes
Dr. Ilyes Nouicer, CDER, Alger
Dr. Lalia Miloudi, University of Boumerdes
Dr. Samah Riache, University of Boumerdes

Table of Contents

Yamina BENHADDA, Mokhtaria DERKAOUI, Kheira MENDAZ, Design of Wind Turbine Blade Using Finite Element Method 1

Mohammed ZEBACH, Abderrahmane HEMMANI, Hamid KHACHAB, Mohammed BABA, An experimental and modeling study of a 100-watt photovoltaic panel, including series and parallel resistances influences.......... 6

Zahira BOUGUERRA, The Effect of Extrenal and Internal Parametre Variations on Photovoltaic Characteristics 10

Amar BENMOUSSA, Barkahoum LAROUCI, Ahmed BELASRI, Plasma homogenous DBD in Ar-NH3 mixtures for photovoltaic celllule: A parametric study 16

Mohamed Abdelghani BENZIADA, Mohamed OUAIL, Comparative study of the different topologies of the Z-source inverter using simple boost control 21

Kelthoum SAADALLAH, Chifaa AD, Mebrouk DJEDID, Mokhtar BENALIA, Potential use of biomass waste for crystal dye removal: Isotherm , thermodynamic and mechanism of adsorption 26

Hamza ASSIA, Abdelhamid ZABOURI, Houari BOULOUIHA MERABET, Mouloud DENAI, Estimate Battery Degradation Using Kalman Filter 31

Dyhia KAIS, Hakim DENOUN, Zoulikha TEBRI, Mohamed Lamine HAMIDA, Sabrina MOHAND SAIDI, Arezki FEKIK, Performance evaluation of two MPPT algorithms for a photovoltaic system using Buck converter based battery-charging controller 35

Amar BERKACHE, Belkhir NORA, Investigating Turbulence Modeling's Influence on Darrieus Vertical Axis Wind Turbine Aerodynamics 40

Said ZERGANE, Amar BERKACHE, Effect of the Atmospheric Boundary Layer on a Wind Turbine 44

Mohamed Abdelghani BENZIADA, Mohamed OUAIL, Comparison between Traditional and Z-Source Inverters for photovoltaic system using MPPT control method 46

Assam BENBAHA, Boubekeur AZOUI, Fatiha YETTOU, Amor GAMA, An Experimental Study To Evaluate the Thermal Performance of a Box-Type Solar Cooker With Sensible Thermal Energy Storage 51

Naouel CHELIL, Mohammed SAHNOUN, First principles calculation of shift current bulk photovoltaic effect in polar sulfosalt Ag5SbS4 for solar cells 56

Haroune AOUZELLAG, Meziane HAMEL, Fuzzy Logic Based Energy Management for Electric UAV 63

Wiam HERKAT, Yassine YAKHELEF, Closed loop inner current control of Grid Connected MMC based microgrid solar system in dq Frame 69

Amira AGGOUNE, Farid BERREZZEK, Khaled KHELIL, Robustness evaluation of the finite-control-set model predictive control for DFIG based wind turbine system 74

Bachir ALLAM, Assala ZEHOUANI, Taieb NEHARI, Mohammed HADJADJ, Energy performance of phase change materials integrated into brick wall for cooling load management in residential buildings on a sunny day in Bechar, Algeria 79

Nadir BENALIA, Idriss BENLALOUI, Rachad MOUMNI, Kouider LAROUSSI, Tarek BOUTABBA, Amor FEZZANI, Improving Efficiency and Reliability in Wireless Energy Transfer Systems via Electromagnetic Analysis 85

Mokhtaria DERKAOUI, Yamina BENHADDA, Integrated On-Chip Inductor Design for Photovoltaic DC-DC Converter 90

Mohamed Lamine FRIKH, Fractional and Integer Orders PI Controllers Application to Wind Power Systems.... 96

Kheira MENDAZ, Yamina BENHADDA, Mohamed FLITTI, Neural Input Output Linearization Control of DFIG based Wind Turbine 102

Omar FEZAZI, Ahmed Nour El Islam AYAD, Integrating Photovoltaic Panels into Electric Drive Motors for Environmentally-Friendly Electric Vehicles 107

Hichem ITOUCHENE, Fayssal AMRANE, Zoubir BOUDRIES, Idris ISSAADI, Design and Implementation of Field-Oriented Control (FOC) in Wind Energy Conversion Systems Based on DFIGs Using Back-to-Back Converters.......... 112

Hichem ITOUCHENE, Fayssal AMRANE, Zoubir BOUDRIES, Kaddour ABDOUNE, Analysis and Simulation of Conventional Sliding Mode Control for Wind Turbines based on a Doubly Fed Induction Generators ……….….118

Hocine KAMEL, Yassine YAKHELEF, Optimal Tuning of Fractional Order PID Controller Applied to Renewable Energy Systems: A Review ……………………………………………………………………………………………………..123

Chettah Chouaib, Mouatsi Abdelmalek, Study of optimal fuzzy MPPT controller of a photovoltaic system…..127

Mohamed Lamine FRIKH, Two-Mass Wind Turbine Speed Control Using Computational Tuning Methods …. 131

Louiza AIT MOULOUD, Aissa KHELDOUN, Oussama MERABET, Hamza BELMADANI, Assessment of hybrid bidirectional deep learning models for short term global horizontal irradiance forecasting …………….. 135

Oualid DJOUDI, Sofia LALOUNI BELAID, Salah TAMALOUZT, Direct reactive power control of DFIG with fixed switching frequency for grid-connected wind turbine …………………………………………………………….. 140

Moutaz Bellah BENTRAD, Tahar BAHI, Adel BOULASSEL, Power Tracking Optimization of Conventional MPPTs using Artificial Neural Network Hybrid algorithm ……………………………………………………………………………… 145

Salah Anis KRIM, Fateh KRIM, Hamza AFGHOUL, Enhancing PV System Maximum Power Point Tracking (MPPT) with KGMO and Fast Terminal Sliding Mode-GWO ……………………………………………………………………………… 151

Oussama MERABET, Aissa KHELDOUN, Mohamed BOUCHAHDANE, Louiza AIT MOULOUD, Hamza BELMADANI, Intissar HATTABI, An adaptive microgrid protection coordination scheme based on dual settings DOCRs ……… 157

Meryem LAGOUNE, Samia LATRECHE, Badreddine BABES, Mabrouk KHEMLICHE, Implementation of an artificial neural network MPPT method based on Perturb&Observe algorithm for Photovoltaic system ……… 162

Aicha MOULAY, Tarak BENSLIMANE, Othmane AABDELKHALEK, Partial Shading Detection Using Neural Network Methods ……… 167

Fatima Zohra BELAIMECHE, Comparative Study Between Three Types of Controllers (PI,SMC,BS) For MPPT Of Wind Turbine …… 172

Khoukha BOUGUERRA, Samia LATRECHE, Faiçal KHARCHOUCHE, Mabrouk KHEMLICHE, Controle of PV system by fuzzy logic based on MPPT using P&O algrithms …………………………………………………………………… 178

Amel SMAILI, El Ghalia BOUDISSA, M'hamed BOUNEKHLA, Intelligent Maximum Power Point Tracking of Photovoltaic Solar Systems using Fuzzy Logic control ……………………………………………………………………… 183

Elouahab BOUGUENNA, Walid MERROUCHE, Bilal TAGHEZOUIT, Development of a smart controller for a stand-alone photovoltaic system with Battery State of Health monitoring ……………………………………………… 188

Mohammed Tahar Habib KAIB, Yassine YAKHELEF, Abdelhalim LOUIFI, Abdelmalek KOUADRI, Abderazak BENSMAIL, Mohamed Faouzi HARKAT, Kernel Principal Components Analysis Improvement Based on Variogram Data Selection for Fault Detection ……………………………………………………………………………………… 195

Mohamed Seddik MAHGOUN, A Maximum Power Point Tracking Technique of Photovoltaic System Based on the Synergetic Control method ……………………………………………………………………………………………………….. 199

Oussama BELAROUSSI, Abdelkarim AMMAR, Ahmed LECHELAH, Maximum Power Point Tracking of Solar Water Pumping Systems Using Fuzzy Logic Algorithm …………………………………………………………………………… 204

Nassir DEGHFEL, Abd Essalam BADOUD, An Improved Robust of Twisting Sliding Mode Control Based Maximum Power Point Tracking For Solar PV Systems ………………………………………………………………………….209

Mohamed Seddik MAHGOUN, Standalone Wind Energy Conversion System Control Using New Maximum Power Point Tracking Technique ……213

Badis LEKOUAGHET, Sid-Ahmed TOUIL, Photovoltaic Model Parameters Estimation via the Fully Informed Search Algorithm …….220

Design of Wind Turbine Blade Using Finite Element Method

Benhadda Yamina
Department of Electrical Engineering
University of Science and Technology
Oran, Algeria
yamina.benhadda@univ-usto.dz

Derkaoui Mokhtaria
National Institute of Telecommunication
Oran, Algeria
mderkaoui@inttic.dz

Kheira Mendaz
Department of Electrical Engineering
University of Centre Belhadj Bouchaib
Ain Temouchent, Algeria
kheiramendez@gmail.com

Abstract—**In the dynamic landscape of energy development, the urgent need to enhance energy efficiency and extend the operational lifespan of wind turbines has become paramount. A profound comprehension of wind turbine behavior under diverse load conditions is a critical pursuit. This research paper presents an innovative approach to investigate and analyze the stresses and deformations exhibited by wind turbine blades, both in steady-state and eigenfrequency conditions.**

The study delves into various load scenarios, encompassing gravitational forces and centrifugal loads, to scrutinize the performance of a Horizontal-Axis Wind Turbine blade. To construct the blade, three distinct materials—Carbon-epoxy, Glass-vinylester, and PVC foam—were meticulously selected, highlighting their role in shaping the blade's structural characteristics. Leveraging Comsol 6.0, a 3D model of the wind turbine blade was meticulously crafted. The finite element analysis software, also Comsol 6.0, based on the finite element method, was employed to unravel the intricate stress distribution and deformation patterns that emerge within the blade under the influence of wind forces. The model, spanning 61.5 meters, with a layer thickness of 0.28 mm, and comprising 19 airfoil sections, serves as the canvas for this analysis. The wind turbine blade was scrutinized at maximum rated power and a rotational velocity of 15 rpm. The resultant Von Mises stress within the blade soared to 3.07 10^8 N/m². Areas of pronounced stress concentration emerged proximate to the blade's root and at the juncture between circular and airfoil cross sections. Additional insights were gleaned through computations of tip displacement, maximum stress values, and through-thickness stress distribution, affording a comprehensive understanding across various load cases. Among the materials, Glass-vinylester and PVC foam exhibited minimal stress levels, underscoring their resilience in diverse conditions. In contrast, Carbon-epoxy displayed the highest stress levels. By scrutinizing deformation and mode shapes, the research further elucidates the blade's behavior. Importantly, the marginal maximum displacement of about 7.2 10^{-5} meters attests to the robustness of the blade in withstanding the forces of wind flow.

Keywords-* *wind turbine blade; finite element method; Von Mises stress; deformation; mode shapes

I. INTRODUCTION

Renewable energy sources, including solar, wind, hydropower, and geothermal, offer a sustainable solution to the global energy challenge. Unlike conventional sources like coal, natural gas, oil, and uranium, which deplete natural reserves and emit harmful gases upon combustion, renewable energy exhibits two key attributes: an infinite supply and minimal carbon emissions. Wind energy, a prominent member of the clean energy category, possesses the potential to address Earth's resource scarcity when harnessed efficiently [1-5].

Central to wind turbine performance, blades undergo deformation due to the influence of wind loads [6-13]. Given their pivotal role, monitoring large deformations is imperative to ensure structural integrity and safety. Employing the Comsol Multiphysics 6.0 software [14], this study delves into the deformation and stress distribution analysis of wind turbine blades. Finite Element Analysis (FEA) stands as a fundamental tool for scrutinizing the stresses at play, notably the impact of gravity and centrifugal forces. As a preliminary endeavor, the study discretizes the object of interest, employing mesh structures that align with the intricate geometry.

The research embraces two distinct analytical avenues: stationary analysis, unveiling responses to varied loads, and eigenfrequency analysis, probing dynamic behavior. The blade's composition features Carbon-epoxy, Glass-vinylester, PVC foam, and a specialized additional layer. The architecture of turbine blades encompasses both skin and spars components, each characterized by distinct airfoil shapes across diverse segments. These elements, influenced by structural forces and centrifugal effects from rotation, collectively shape the blade's performance.

The results illuminate significant stress concentrations near the blade's root and the transition between circular and airfoil cross sections, with the maximum Von Mises stress recorded at 3.07 10^8 N/m². Delving deeper, analyses reveal tip displacements, maximum stress values, and through-thickness stress distributions across various load cases. It is noteworthy that Glass-vinylester and PVC foam exhibited minimal stress levels, while Carbon-epoxy experienced the highest stresses. Furthermore, the study embarks on understanding blade deformation and mode shapes. Remarkably, despite external forces, the blade exhibits limited displacement about 7.21 10^{-5} meters underscoring its robustness against wind forces.

II. STRUCTUREL OF WIND TURBINE BLADES

The example at hand illuminates the intricacies of analyzing a composite wind turbine blade, ingeniously composed of a fusion of carbon-epoxy, glass-vinylester, and

PVC foam. The blade's architecture is envisioned as a sandwich structure, where the resilient PVC foam core acts as a buffer between the carbon-epoxy and glass-vinylester layers. Figure 1 serves as a visual cornerstone, encapsulating a three-dimensional model of the blade, stretching an impressive 61.5 meters in length. This specific blade design aligns with the NREL 5MW wind turbine model, harnessing advanced engineering principles. The blade's intricate structure encompasses 19 distinctive segments, each meticulously tailored with a unique airfoil shape to optimize performance across diverse operational conditions.

The wind turbine blade comprises two crucial components:

• **Skin**: This outer layer encompasses the curved boundaries of the blade and carries a substantial portion of the overall loading.

• **Spar**: To enhance both bending and torsional stiffness, the blade is fortified with spars. These internal vertical elements contribute significantly to the blade's structural integrity.

Together, the skin and spars work in tandem to optimize the blade's overall efficiency and performance, enabling it to harness wind energy effectively.

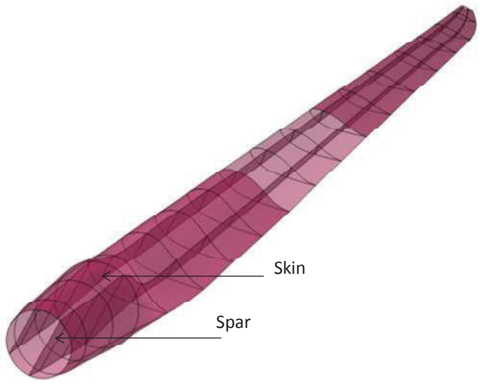

(a)

(b)

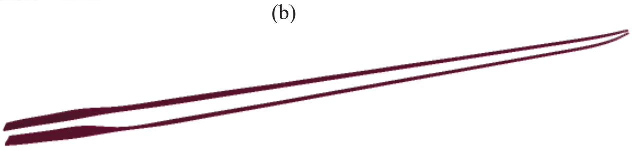

(c)

Figure 1. 3D model of the blade, (a) blade, (b) skin, (c) spar

Figure 2 provides a visual representation of the arrangement of airfoils employed in the turbine blade design. The utilization of NACA series airfoils holds prominence in crafting the geometry of these blades. Originally tailored for aircraft, a substantial subset of NACA airfoils has been seamlessly adapted for wind turbine applications [15].

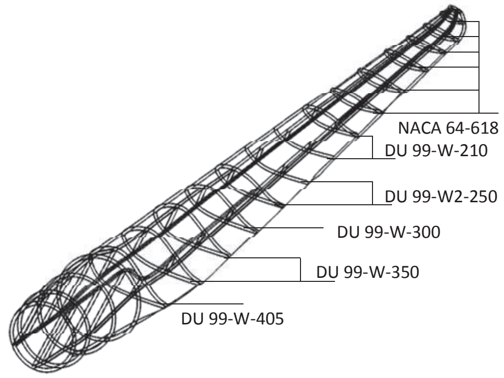

Figure 2. Arrangement of airfoils

Figure 3 visually portrays the applied loads on the wind turbine blade. This depiction highlights the distribution of the two distinct types of loads gravity load and centrifugal load across the blade's structure. The gravity load is specifically applied to one half of the blade. This load, stemming from gravitational forces, contributes to the overall structural stress and deformation experienced by the blade during operation. In contrast, the centrifugal load is concentrated at the blade's end, where rotation is most pronounced. As the blade spins, this load represents the centrifugal forces generated by its rotational motion. This load distribution recognizes the spatial variation in forces along the blade's length, emphasizing the significance of accounting for these dynamic influences in the structural analysis.

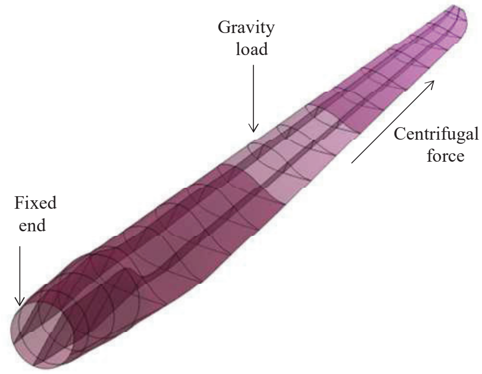

Figure 3. Load on wind turbine blade

Gravity load are calculated by [16]:

$$a_f = \rho g \quad (1)$$

ρ : density of material; g : gravity acceleration.

Centrifugal load are calculated by :

$$a_f = a_{cen} \quad (2)$$

$$a_{cen} = \Omega \times (\Omega \times r_p) \quad (3)$$

$$r_p = -r_{bp} \quad (4)$$

r_{bp} : Leigh of root.

To ensure precise representation and accurate simulation, a physics-controlled mesh with a fine element size is meticulously chosen. The resultant mesh configuration, depicted in Figure 4, reflects the culmination of this meticulous meshing process. In this endeavor, the meshing technique centers around rectangular elements, chosen for their capability to effectively capture the intricate details and dynamic behaviors inherent in the system.

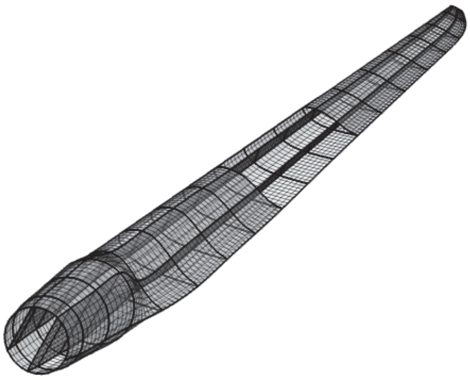

Figure 4. Mapping the mesh for wind turbine blade discretization

The outermost layer of this sandwich structure is crafted from a carbon-epoxy laminate, comprising 10 individual layers. Each of these layers measures 0.28 mm in thickness and is aligned at an angle of 0 degrees relative to the laminate coordinate system's first axis. The density attributed to each lamina within this carbon-epoxy layer is set at 1560 kg/m³. Moving inward, the subsequent layer within the sandwich structure consists of a glass-vinylester laminate. For this layer, each individual lamina is assigned a density of 1890 kg/m³. The composition of this laminate encompasses 40 layers, each boasting a uniform thickness of 0.28 mm. This meticulous arrangement contributes to the overall structural robustness and integrity of the blade. At the heart of the sandwich structure lies the central core, composed of PVC Foam with a substantial thickness of 15 cm. The density of this core material is designated as 200 kg/m³. Importantly, this foam material exhibits specific properties that significantly influence the overall behavior of the blade. These properties include a Young's modulus of 250 MPa, a shear modulus of 92.6 MPa, and a Poisson's ratio of 0.35

III. Results and Discussion

The von Mises yield criterion serves as a pivotal concept in the realm of material science and engineering, particularly in assessing the structural integrity of materials. It is rooted in the von Mises stress, a metric employed to gauge whether a ductile material is poised to yield or fracture. Specifically, the von Mises stress signifies the point at which a ductile material initiates yielding, a phenomenon that transpires when the von Mises stress surpasses a critical value known as the yield strength. Within the context of the wind turbine blade analysis, Figure 5 encapsulates the stress distribution throughout the blade structure. Regions of heightened stress become evident, primarily congregating near the base of the blade and at the juncture between circular and airfoil cross sections. Noteworthy is the observation that the highest Von Mises stress across the entire structure ascends to 3.07 10^8 N/m², whereas the least Von Mises stress is documented at 0 N/m².

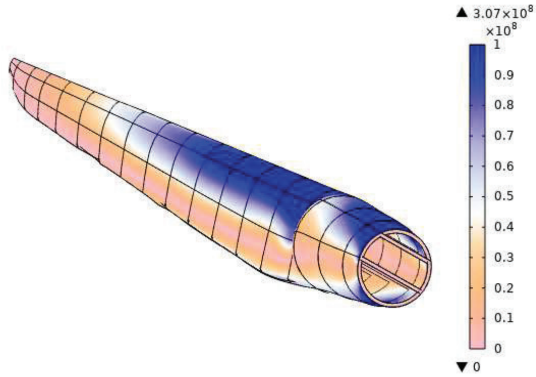

Figure 5. Distribution of Von Mises stress in blade

Figure 6 illustrates the through-thickness changes in Von Mises stress at a specific location on the wind turbine blade, considering various load cases. Stress values exhibit differences both among different laminates and within plies within those laminates. Notably, the highest stress concentrations are observed in the carbon-epoxy material composing the outermost layer of the sandwich structure.

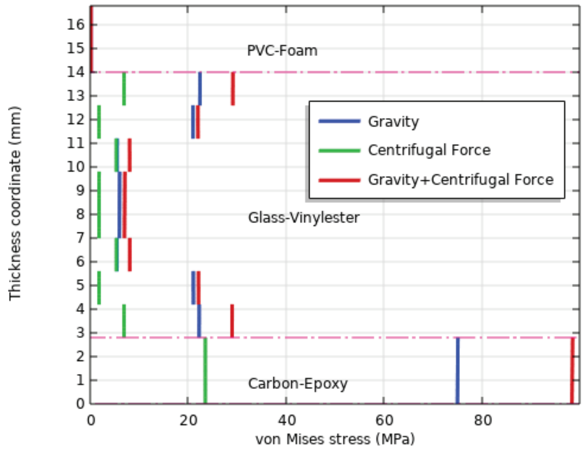

Figure 6. Through-thickness variation of Von Mises stress for different load cases

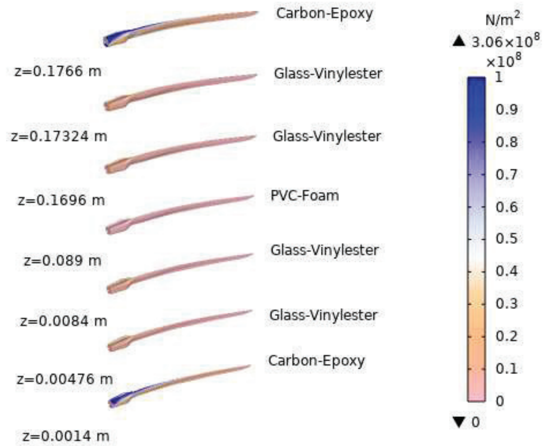

Figure 7. Von Mises stress distribution in the layers materials

Figure 7 serves as a visual depiction of the Von Mises stress distribution within the distinct materials, Carbon-epoxy, Glass-vinylester, and PVC foam comprising the wind turbine

Identify applicable sponsor/s here. If no sponsors, delete this text box. (sponsors) blade structure. The Von Mises stress within Glass-vinylester and PVC foam is observed to be 0 N/m², indicating minimal stress-induced deformation or damage within these materials. In contrast, the Von Mises stress within the Carbon-epoxy material reaches a substantial value of 3.07 10^8 N/m². Figure 8 presents distinct mode shapes of the blade and highlights the impact of the centrifugal force on these mode shapes, particularly when the blade is at rest and not undergoing rotation. This illustration provides valuable insights into how the structural dynamics of the blade are affected by centrifugal loading, even in static conditions. Throughout this analysis, it is observed that the root mean square (RMS) value of 0.5 1/s is associated with the mode shapes. The first eight eigenfrequencies are as follows: mode 1: 1.2456 Hz, mode 2: 2.6061 Hz, mode 3: 4.3624 Hz, mode 4: 4.9535 Hz, mode 5: 7.824 Hz, mode 6: 9.7181 Hz, mode 7: 9.8244 Hz, and mode 8: 11.268 Hz. Significantly, it's noted that as eigenfrequencies increase, the deformation of the blade decreases. At the blade's tip, a total deformation of 7.21 mm is recorded. This analysis effectively highlights the dynamic interplay between eigenfrequencies, deformation, and the impact of centrifugal forces on the blade's structural behavior. Despite the complex forces at play, the wind turbine blade displays a remarkably limited maximum displacement, measuring approximately 7.2 10^{-5} meters. This observation underscores the inherent strength of the blade's structural composition, which effectively shields it from the impact of wind flow and associated dynamic loads.

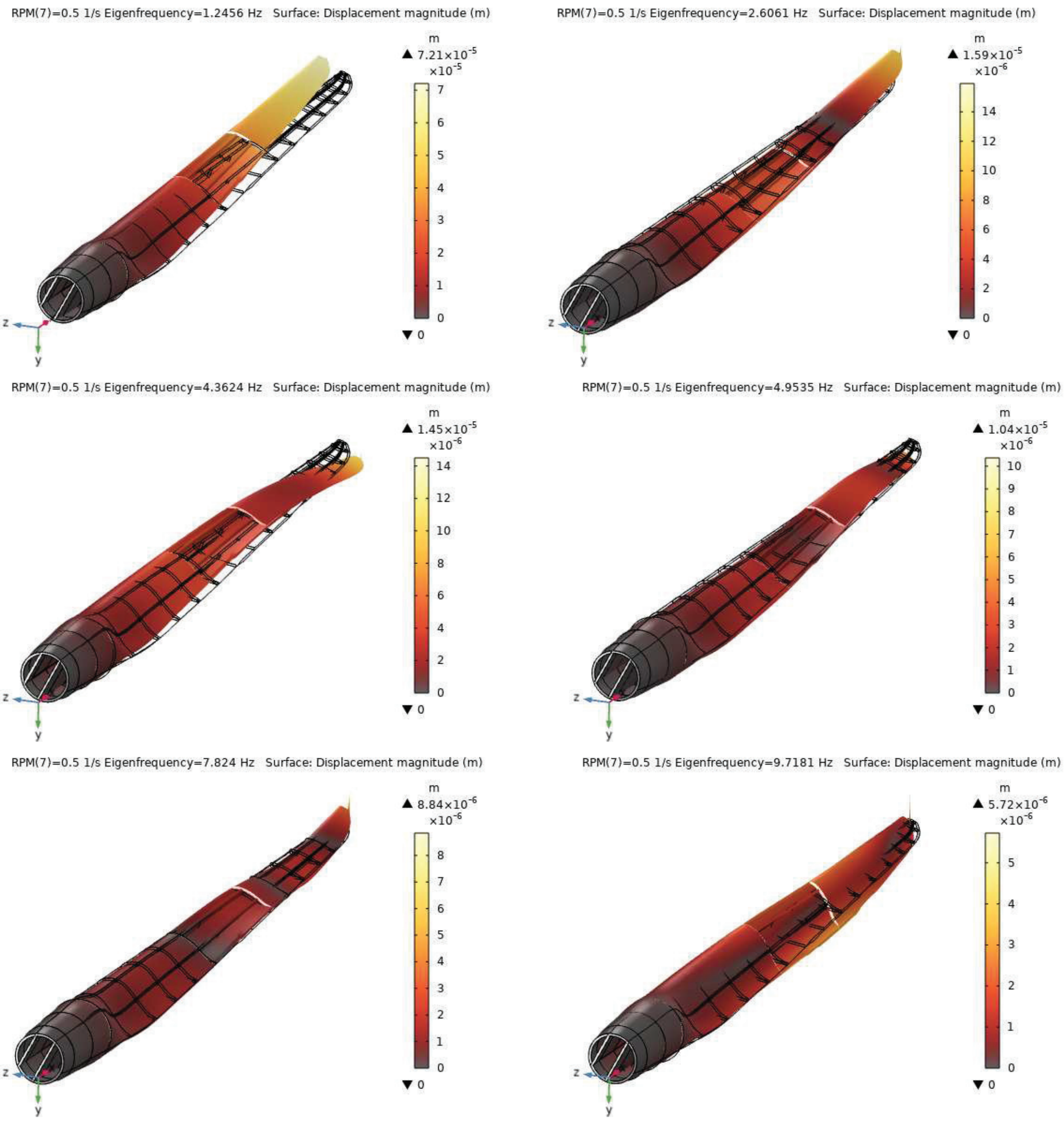

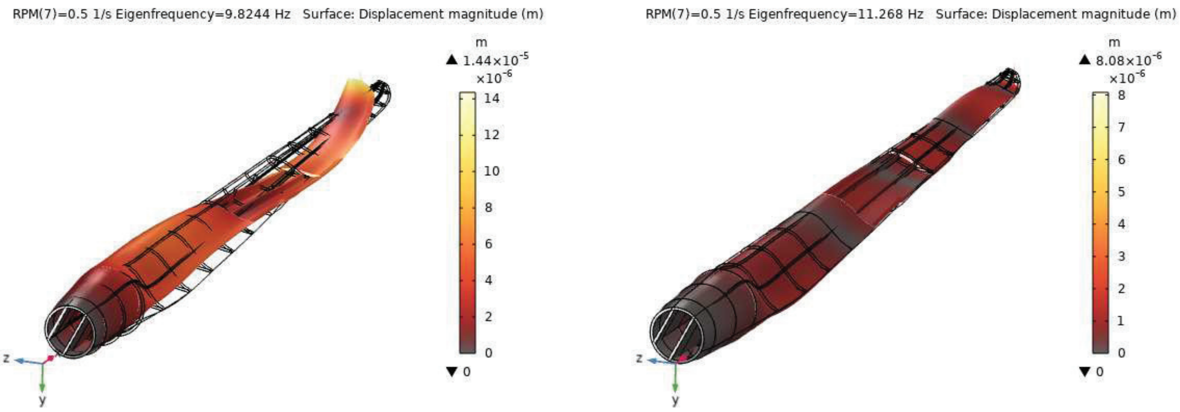

Figure 8. Primary eight blades modal

IV. CONCLUSION

In summary, this study has delved into the intricate analysis of stress distribution and deformation within a wind turbine blade subjected to a variety of loads, utilizing the finite element analysis software Comsol 6.0. The findings provide insights into the behavior of a wind turbine blade crafted from a composite structure composed of Carbon-epoxy, Glass-vinylester, and PVC foam. The results are presented across varying angular positions, offering a comprehensive understanding of the blade's response under diverse loading conditions. The numerical simulations conducted shed light on crucial performance metrics. The computed von Mises stress and deformation profiles underscore the mechanical resilience of the blade. The maximum Von Mises stress registers at an impressive 3.07 10^8 N/m², juxtaposed with a minimum stress of 0 N/m². Notably, areas of elevated stress manifest near the blade's root and at the intersection of circular and airfoil cross sections. These observations are significant, as they inform design enhancements and material optimization. Furthermore, the minimal displacement exhibited by the blade stands as a testament to its structural strength in countering wind-induced forces. The proximity of maximum stress to the rigid blade end indicates that the blade's design efficiently manages these forces. Crucially, the ample yield strength of the composite materials—Carbon-epoxy, Glass-vinylester, and PVC foam—ensures that the blade operates with a substantial safety margin, reinforcing its robustness against potential failure.

The model developed through this study provides a valuable tool for selecting optimal materials for wind turbine blades under varying loading conditions. The findings contribute to the broader endeavor of refining wind turbine technology, ultimately enhancing efficiency, reliability, and sustainability. By underscoring the strength of the blade's design and materials, this study fortifies the blade's ability to endure diverse operational challenges, thereby bolstering the overall performance of wind energy systems in the pursuit of a greener and more sustainable energy landscape.

REFERENCES

[1] J. M. Jonkman, Dynamics of Offshore Floating Wind Turbines—Model Development and Verification, Wind Energ. 2009; 12:459–492.

[2] K. Coxa, A. Echtermeyer, Structural design and analysis of a 10MW wind turbine blade, Energy Procedia 24, 2012, 194 – 201.

[3] Z. Feng, M. Liang, Fault diagnosis of wind turbine planetary gearbox under nonstationary conditions via adaptive optimal kernel timeefrequency analysis, Renewable Energy 66, 2014, 468-477.

[4] M. Asareha, W. Schonberga, and J. Volz, Fragility, Analysis of a 5-MW NREL Wind Turbine Considering Aero-Elastic and Seismic Interaction Using Finite Element Method, 2016 published by Elsevier.

[5] E. I. Katsanosa, A. A.e Sanzb, C. T. Georgakisc, S. Thöns, Multi-hazard response analysis of a 5MW offshore wind turbine, Procedia Engineering 199, 2017, 3206–3211.

[6] M.-K. Yeh and C.-H. Wang, Stress analysis of composite wind turbine blade by finite element method, Materials Science and Engineering 241, 2017, 012015.

[7] A. S. Verma, N. P. Vedvik, Z. Gao, Numerical assessment of wind turbine blade damage due to contact/impact with tower during installation, Conf. Series: Materials Science and Engineering 276 (2017) 012025.

[8] B. D. Tandle, L. Sunil, YC S. Yadav, Stress and vibration analyses of the wind turbine blade (A NREL 5MW), Journal of Mechanical Engineering Research and Developments (JMERD).

[9] Ö. ÖĞÜÇLÜ, Structural Design and Stress Analysis of a Helical Vertical Axis Wind Turbine Blade, Sakarya University Journal of Science 24(6), 1151-1161, 2020.

[10] T. Guo, X. Guo, Z. Gao, S. Li, X. Zheng, X. Gao,R. Li, T. Wang, Y. Li, D. Li, Nacelle and tower effect on a stand-alone wind turbine energy output−A discussion on field measurements of a small wind turbine, Applied Energy 303, 2021, 117590.

[11] X. Fu and M. Sheng, Research on Structural Failure Analysis and Strengthening Design of Offshore Wind Turbine Blades, J. Mar. Sci. Eng. 2022, 10, 1661.

[12] S. Yao, M. Chetan, D T. Griffith, A. S. E. Mendoza, M. S. Selig, D. Martin, S. Kianbakht, K. Johnson and E. Loth, Aero-structural design and optimization of 50 MW wind turbine with over 250-m blades, Wind Engineering 2022, Vol. 46(1) 273–295.

[13] S. Ø. Rokvam, N. P. Vedvik, L. Savio and A. Echtermeyer, Designing Composite Adaptive Propeller Blades with Passive Bend–Twist Deformation for Periodic-Load Variations Using Multiple Design Concepts, Polymers 2023, 15, 2749.

[14] COMSOL, COMSOL Multiphysics User's Guide, 2021.

[15] S. Cantarelli, D. Francia, A. Liverani, L. Frizziero, Design for Additive Manufacturing of a Horizontal Axis Wind Turbine , Proceedings of the International Conference on Industrial Engineering and Operations Management Rome, Italy, August 2-5, 2021.

[16] Fakada D. Gurmesa, Johnson A. Santhosh, Biniyam A. Abebe, Demeke G. Waskhume1 Firew T. Kassaye1 and Yahiya A. Kedir, A fatigue and stress distribution analysis of horizontal axis wind turbine blade, Asia-Pacific Journal of Science and Technology, Vol 27. No 03, 2021.

An experimental and modeling study of a 100-watt photovoltaic panel, including series and parallel resistances influences

1st Mohammed Zebach
Laboratory of Development Renewables Energies & Their Application in Saharan Areas (LDREAS)
University of Tahri Mohammed Bechar, Algeria
zebach.mohammed@univ-bechar.dz

2nd Abderrahmane Hemmani
Laboratory of Development Renewables Energies & Their Application in Saharan Areas (LDREAS)
University of Tahri Mohammed Bechar, Algeria
hemmani.abderrahmane@univ-bechar.dz

3rd Hamid Khachab
Laboratory of Development Renewables Energies & Their Application in Saharan Areas (LDREAS)
University of Tahri Mohammed Bechar, Algeria
khachab_hamid_2000@univ-bechar.dz

4th Mohammed BABA
Smart Grids & Renewable Energies Laboratory (SGRE)
University of Tahri Mohammed Bechar, Algeria
baba.mouhamed@univ-bechar.dz

***Abstract*— This paper presents an experimental study and a modeling method for a 100-watt photovoltaic solar panel. The main objective is to determine the experimental and modeling parameters for the I-V (current-voltage) and P-V (power-voltage) equations by fitting the curve to three key points: open circuit, maximum power, and short circuit. These three points are listed and sourced from a commercial photovoltaic panel's technical data sheet, the method finds the best I-V and P-V equations for the single-diode photovoltaic (PV) model including the effect of the series and parallel resistances and ensures that the maximum power of the model matches with maximum power of the real panel. The main content extracting the experimental data from the real photovoltaic panel used under real climatic conditions in real-time, this data is remodeled using MATLAB software to find the best I-V and P-V characteristics, appending effects of the series, and parallel resistances.**

Keywords—modeling Photovoltaic, MPP, PV model, Energy

I. INTRODUCTION

Fast-growing global energy demand and global growth. Pollution as well as the decreasing conventional energy resources a need for affordable and sustainable clean energy. Supplies. There are not many resources that can meet the power demand of the tera-watts (TW) scale by 2050. Solar energy is considered a compelling alternative at can meet the demand of 15 TW with a huge amount of solar energy to spare [1]. Renewables are growing in importance thanks to advances in grid technologies and the need for sustainable clean energy. Different sources of renewable energy, such as wind turbines, biomass gasification units, solar modules, fuel cells, etc., are used as distributed energy resources to implement microgrids and smart grids. Amongst all alternative energy sources, photovoltaic solar panels are more promising and are widely used as an efficient energy source [2]. To take advantage of the benefits of the application of photovoltaic systems, research activities are undertaken to further enhance their performance, cost, efficiency, integration, and reliability. Over the past several years PV simulation models have been developed to analyze their integration into the existing power system or to study their performance as standalone systems. Traditional methods of mathematical simulation the modeling of PV arrays in the literature currently available, and simulation [3][4]. These modeling methods allow for the construction of PV circuit models using physical elements like a diode, resistor, etc. To improve solar conversion technology and gain more benefits, this area has attained great attention, due to which it has been possible to install Grid-connected PV systems and several stand-alone PV systems [5][6].

II. EXPERIMENTAL STUDY

In real climatic conditions, we perform our experimental characterization to find the experimental curves by drawing experimental curves I(V) and P(V) using the PV analyzer instrument. The photovoltaic module technical sheet brings the following information: the open-circuit voltage Voc, the short-circuit current Isc, the voltage at the maximum power point Vmp, the current at the maximum power point Imp, and the maximum experimental peak output power Pmax,e. This information is always provided with standard test conditions (STC) of temperature T and solar irradiation G. Some manufacturers provide I(V) curves for several irradiation and temperature conditions. These curves make easier the adjustment and the validation of the desired mathematical I(V) equation. This is all the information one can get from the data sheets of a photovoltaic module.

TABLE I

PARAMETERS OF THE PV SOLAR MODULE AT REAL CLIMATIC CONDITIONS $\mathrm{T} = 25.8^{\circ}\mathrm{C}, 1.5\mathrm{AM}, \mathrm{G} = 678\ \mathrm{W/m^2}$.

I_{mp}	4.035 A
V_{mp}	15.82 V
$P_{max,e}$	63.85 W
I_{sc}	4.483 A
V_{oc}	21.03 V
N_s	36

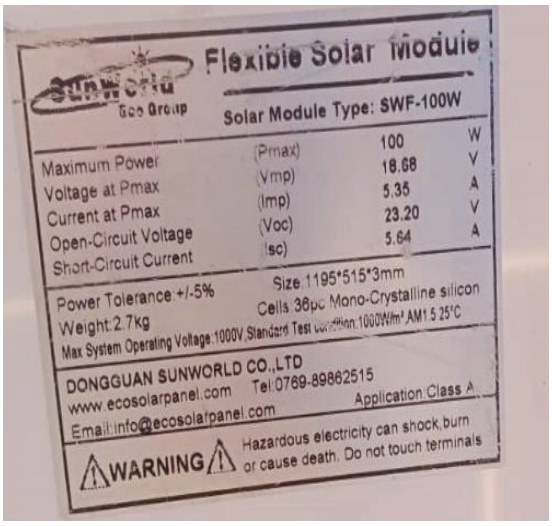

Fig. 1. Parameters of the PV solar module at standard test (STC) $\mathrm{T} = 25^{\circ}\mathrm{C}, 1.5\mathrm{AM}, \mathrm{G} = 1000\ \mathrm{W/m^2}$.

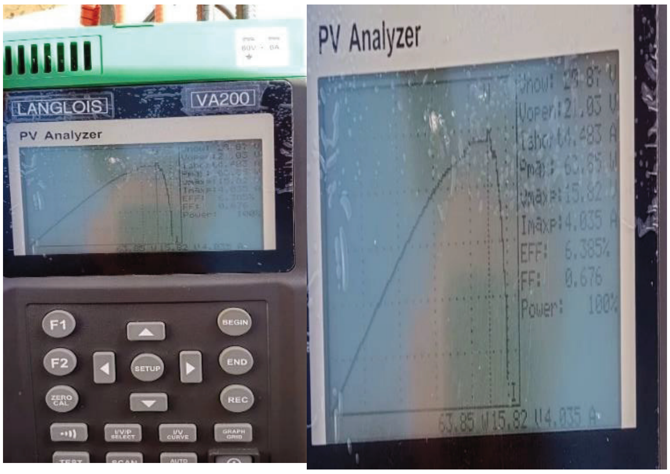

Fig.2. PV Analyzer shows Parameters of the PV solar module at real climatic conditions

Figure 03 shows the variation of irradiation in the duration of the 24-hour experiment with disturbance due to the climatic conditions affecting radiation (sunrise, sunset, clouds...). Figure 04 shows the variation of Temperature in the duration of the 24-hour experiment.

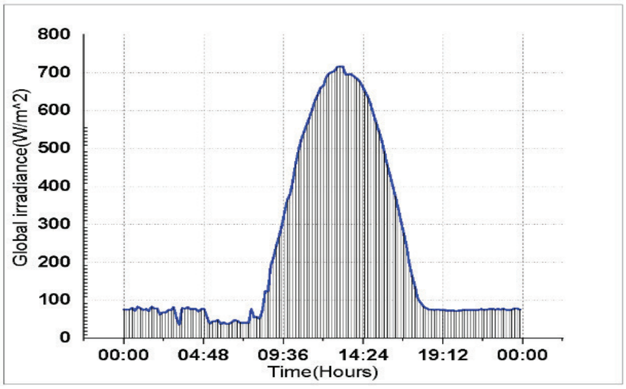

Fig.3. irradiation variation

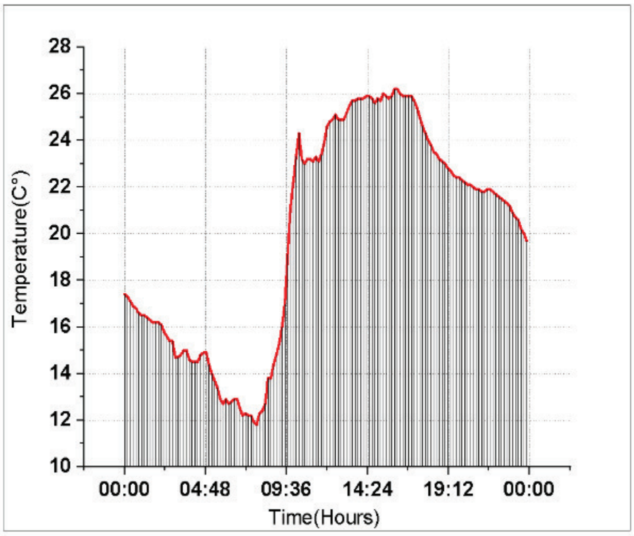

Fig.4. Temperature variation

III. MODELING THE PHOTOVOLTAIC MODULE

A. Modeling the photovoltaic module

The basic equation of the elementary photovoltaic module does not represent the I(V) characteristic of a practical photovoltaic module. A practical module is composed of several connected photovoltaic cells and the observation of the characteristics at the terminals of the photovoltaic array requires the inclusion of additional parameters to the basic equation.

$$I = I_{pv}N_{par} - I_0 N_{par}\left[exp\left(\frac{V+R_s\left(\frac{N_s}{N_p}\right)I}{V_t a N_s}\right) - 1\right] - \frac{V+R_s\left(\frac{N_s}{N_p}\right)I}{R_p\left(\frac{N_s}{N_p}\right)} \quad (1)$$

where I_{pv} and I_0 are the photovoltaic and saturation currents the array an $Vt = N_s kT/q$ is the thermal voltage of the PV Module with Ns cells connected in series. Cells connected in parallel increase the current and cells connected in series provide greater output voltages. If the module is composed of Np parallel connections of cells the photovoltaic and saturation current may be expressed as: $Ipv = Ipv, cell\,.Np$ and $I_0 = I_0, cell.Np$.

In equation (1) Rs is the equivalent series resistance of the PV module and Rp is the equivalent parallel resistance.

B. Adjusting the Model

Two parameters remain unknown in equation (1), as R_s and R_p. A few authors have proposed ways to mathematically determine these resistances. While a mathematical formula may be useful for determining these unknown parameters, any expression for R_s and R_p will always rely on experimental data. Some authors propose varying R_s in an iterative process, incrementing R_s until the $I(V)$ curve visually fits the experimental data and then vary R_p in the same fashion. It is a fairly poor and inaccurate method of adjustment, mainly because R_s and R_p may not be adjusted separately if a good $I(V)$ model is desired. This paper proposes a method for adjusting R_s and R_p based on the fact that there is an only pair $\{R_s, R_p\}$ that warranties that $P_{\text{max,e,m}} = P_{\text{max,m}} = P_{\text{max,e}} = V_{\text{mp}}.I_{\text{mp}}$ at the $(V_{\text{mp}}, I_{\text{mp}})$ point of the $I(V)$ curve, i.e., the maximum power calculated by the $I(V)$ model of equation (1) $(P_{\text{max,m}})$ is equal to the maximum experimental power from the datasheet $(P_{\text{max,e}})$ at the MPP. Conventional modeling methods found in the literature take care of the $I(V)$ curve but forget that the $P(V)$ (power versus voltage) curve must match the experimental data too.

The relation between R_s and R_p, the only unknowns of equation (1), may be found by making $P_{\text{max,m}} = P_{\text{max,e}}$ and solving the resulting equation for R_s, as shown.

$$P_{\text{max,m}} = V_{\text{mp}} \left\{ I_{\text{pv}} - I_0 \left[\exp\left(\frac{q}{kT} \frac{V_{\text{mp}} + R_s I_{\text{mp}}}{a N_s} \right) - 1 \right] - \frac{V_{\text{mp}} + R_s I_{\text{mp}}}{R_p} \right\} = P_{\text{max,e}} \quad (2)$$

$$R_p = \frac{V_{\text{mp}} (V_{\text{mp}} + I_{\text{mp}} R_s)}{\left\{ V_{\text{mp}} I_{\text{pv}} - V_{\text{mp}} I_0 \exp\left[\frac{(V_{\text{mp}} + I_{\text{mp}} R_s)}{N_s a} \frac{q}{kT} \right] + V_{\text{mp}} I_0 - P_{\text{m,e}} \right\}} \quad (3)$$

IV. ITERATIVE SOLUTION OF RS AND RP

The objective is to find the value of Rs (and hence Rp) that makes the peak of the mathematical curve P(V) agree with the experimental peak power at the (Vmp, Imp) point. This requires several iterations until Pmax,m = Pmax,e.

In the iterative process, Rs must be slowly incremented starting from Rs = 0. Adjusting the P(V) curve to match the experimental data requires finding the curve for several values of Rs and Rp. Actually, plotting the curve is not necessary, as only the peak power value is required. Figures. 5 and 6 illustrate how this iterative process works. In Figure 5, as Rs increases, the P(V) curve moves to the left, and the peak power (Pmax,m) goes toward the experimental MPP.

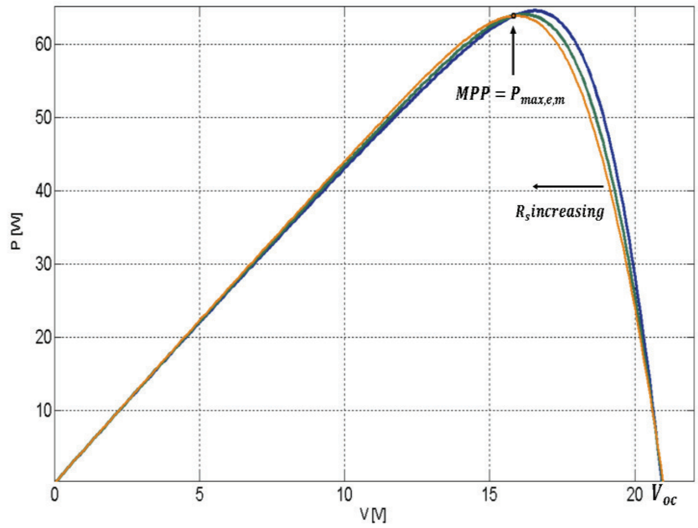

Fig.5. P(V) curves plotted for different values of Rs and Rp .

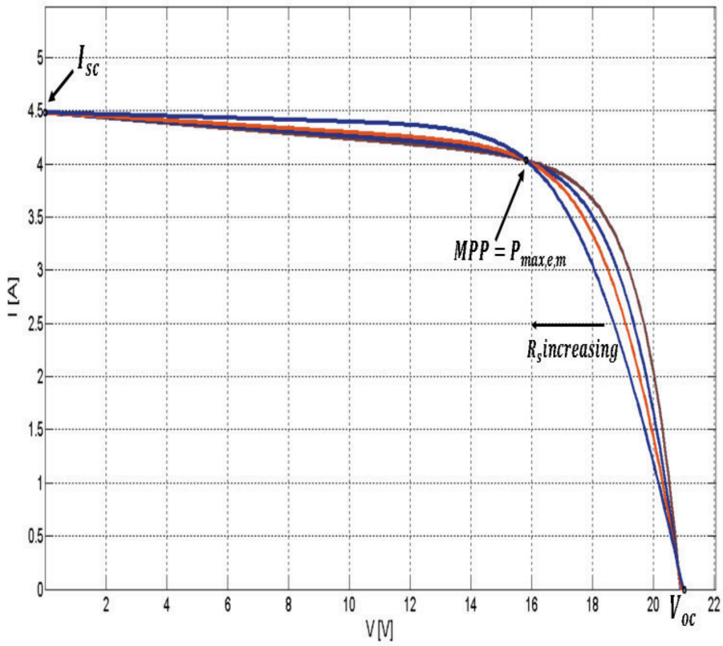

Fig.6. I(V) curves plotted for different values of Rs and Rp .

Plotting the $P(V)$ and $I(V)$ curves require solving equation (1) for $I \in [0, I_{sc}]$ and $V \in [0, V_{oc}]$. Equation (1) does not have a direct solution because $I = f(V, I)$ and $V = f(I, V)$. This transcendental equation must be solved by a numerical method and this imposes no difficulty. The $I(V)$ points are easily obtained by numerically solving $g(V, I) = I - f(V, I)$ for a set of V values and obtaining the corresponding set of I points. Obtaining the P(V) points is straightforward.

Figures. 7 and 8 show the *I (V)* and *P (V)* curves of the our PV module was adjusted with the proposed method. The model curves exactly match with the experimental data at the three remarkable points provided by the technical data: short circuit, maximum power, and open circuit. The adjusted parameters and model constants are listed in table **II**.

TABLE II
PARAMETERS OF THE ADJUSTED MODEL OF PV MODULE AT REAL CLIMATIC CONDITIONS.

I_{mp}	4.035 A
V_{mp}	15.82 V
$P_{max,e}$	63.85 W
$P_{max,m}$	63.83337 W
I_{sc}	4.483 A
V_{oc}	21.03 V
R_s	0.52 Ω
R_p	141.7 Ω
N_s	36

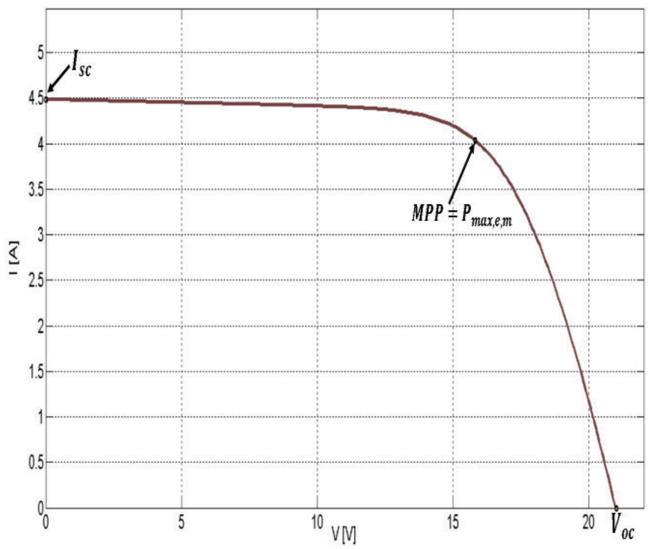

Fig.7.I(V) curve adjusted at $T = 25.8°C, 1.5AM, G = 678\ W/m^2$.

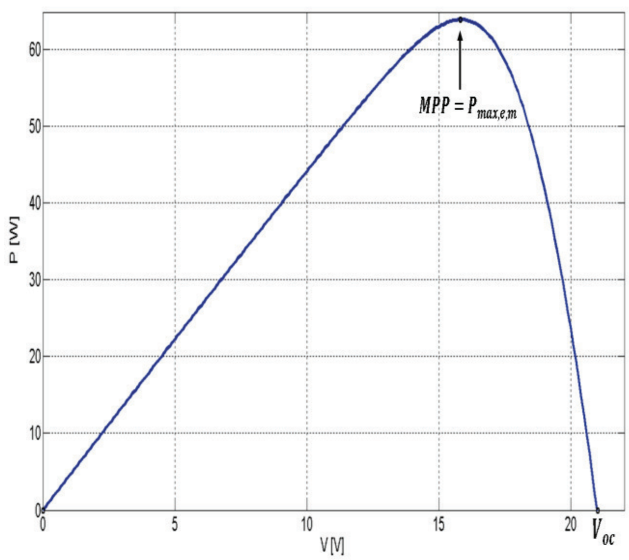

Fig.8. P(V) curve adjusted at $T = 25.8°C, 1.5AM, G = 678\ W/m^2$.

V. CONCLUSION

This paper examined the development of a mathematical modeling method for the PV module. The objective of the method is to fit the mathematical I(V) equation to the experimental remarkable points of the I(V) and P(V) curves of the practical module. The method obtains the parameters of the I(V) equation by using the following nominal information from the module technical data sheet: open circuit voltage, short-circuit current, and maximum output power. Moreover, in these models, Rs and Rp parameters are one wishes to correctly adjust the model so that the maximum power of the model is equal to the maximum power of the practical PV panel.

ACKNOWLEDGMENT

The authors thank The Algerian research direction DGRSDT, Laboratory of Renewable Energies and their Applications in Saharan areas (LDREAS), The Smart Grids and Renewable Energies Laboratory (SGRE) for supporting this research.

REFERENCES

[1] M. Atowar Rahman, “Performance analysis of WSe2-based bifacial solar cells with different electron transport and hole transport materials by SCAPS-1D,” Heliyon, vol. 8, no. 6, Jun. 2022, doi: 10.1016/j.heliyon.2022.e09800.

[2] Purohit, I., & Purohit, P. (2010). Techno-economic evaluation of concentrating solar power generation in India. Energy Policy, 38(6). https://doi.org/10.1016/j.enpol.2010.01.041

[3] Altas, I. H., & Sharaf, A. M. (2007). A photovoltaic array simulation model for matlab-simulink GUI environment. 2007 International Conference on Clean Electrical Power, ICCEP ’07. https://doi.org/10.1109/ICCEP.2007.384234

[4] Cao, J. (2011). Analysis and Implementation of Grid-Connected Solar PV with Harmonic Compensation.

[5] F. I. and H. C. Koch-Ciobotaru, L. Mihet-Popa, P. of 7th I. Bindner, “Simulation Model developed for a Small-Scale PVSystem in a Distribution Network,” I. S. on A. Computational, T.-R. Intelligence and Informatics-SACI 2012, . 2009. Labouret, A., M. Villoz, « Energie solaire photovoltaique. Ed Dunod », livre.

[6] Koch-Ciobotaru, C., Mihet-Popa, L., Isleifsson, F., & Bindner, H. (2012). Simulation model developed for a small-scale PV system in distribution networks. SACI 2012 - 7th IEEE International Symposium on Applied Computational Intelligence and Informatics, Proceedings. https://doi.org/10.1109/saci.2012.6250027

The Effect of Extrenal and Internal Parametre Variations on Photovoltaic Characteristics

Bouguerra zahira
Faculty of science and technology
University of Mohamed El Bachir El Ibrahimi
Bordj bou arreridj, Algeria
bouguerra.zahira@yahoo.com

Abstract— **The conversion of sunlight into electricity utilizes the characteristics of semiconductors that make up the PV cell. However, the PV cell efficiency can be changed from an area to another depending on the available irradiation density and temperature. This paper aims to study the effect of different factors variation affecting the performances of PV module; external metrological conditions as irradiation and temperature, internal electrical parameters as diode ideality, series and shut resistances. In order to study their impacts on PV panel efficiency, it is necessary to analysis its behavior and performances using current-voltage (I-V) and power-voltage (P-V) characteristics under the variation of these different parameters. For that, a simple model approach is utilized which includes a photo-current source, a single diode, a series and shunt resistances. Using MATLAB simulation, the electrical performances of a crystalline silicon PV module (200W) are tested under external and internal parameters variation in order to adequately evaluate their impacts on PV efficiency. The chosen model showed the strong dependence on metrological conditions (temperature and irradiation) and the great influence of series and shunt resistances on PV cell performances.**

Keywords—PV cell, Electrical parameter, current-voltage (I-V), power, voltage (P-V).

I. INTRODUCTION

The growth of human population has resulted in significant increase in energy demand [1]. The traditional energy sources have dangerous impacts on environment equilibrium and human health such as CO2 emission, pollution, weather change......etc which forces the world to use renewable energies to guarantee a suitable future offering many advantages over conventional power generation system, safe and reliable for the environment, high efficiency, abundant presence…. In recent years, the development of renewable energy has gained worldwide attention [2]. The power generation from solar photovoltaic (PV) has gradually increased all over the world in recent years [3]. This is mainly due to its simplicity of installation in residential and industrial places with its high compatibility with the electrical grid and in addition, it has many other advantages such as being non-polluting, noise-free and low maintenance.

The estimated energy received from the sun to the earth in hour is 4.310^{11} GJ. The most part of this energy is found in Middle East, North Africa, Mexico, Australia and India. North Africa has an enormous average solar irradiance which can produce a huge potential for solar electricity (figure 1). In this area, Algeria benefits the high density of irradiance of around 3000 hours per year. For the transformation of this energy into electricity, a certain system is implemented consisting of PV panels, power converters, cables, filter and certain control as maximum power point tracking which can maximize the output power of photovoltaic system. The maximization of the PV power always remains a major challenge [4]. At any surrounding condition, the maximum power can be extracted from the PV panel at a particular voltage (V_{mpp}), and a particular current (I_{mpp}) [5]. This point (V_{mpp}, I_{mpp}) is called maximum power point (MPP), where the PV cell generates the maximum power. PV systems are highly exposed to shadows, dust, metrological and electrical parameters variation, etc., which makes seeking high efficiency very difficult.

Choosing the adequate model that can perfectly present the PV characteristics is an important step in evaluating the behavior of the PV panel under different factors affecting its efficiency. For that different models are utilized as one diode model ([6], [7]), two diode model ([8], [9], [10]) and three diode model ([11]).

This work aims to study the influence of different factors affecting the efficiency of PV array, especially the internal and external parameters using the model of a single diode. Therefore, the article is structured as following; in the first section, the introduction is presented. In the second part, the different factors affecting the PV efficiency are discussed. After that, the modeling of PV array is detailed to show the effect of the internal and external parameters in the last section. Finally, the conclusion is presented.

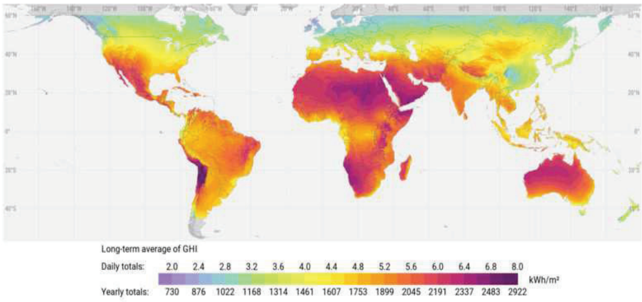

Fig. 1 Annual word irradiation

II. DIFFRENT FACTORS AFFECTING PV SYSTEM EFFICIENCY

The PV system efficiency is affected by many factors such as PV technology, tilt angle orientation, shading effect, dust accumulation, internal parameters variations and environmental conditions (sunlight and temperature density). Figure 2 presents these major factors affecting the PV performances.

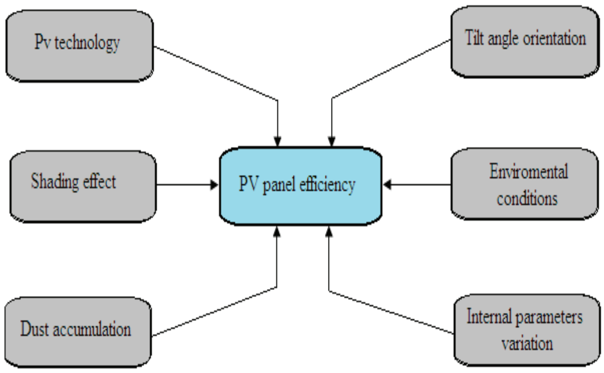

Fig. 2 Factors affecting PV panel efficiency

A. *PV Technology*

The crystal photocell (C-Si) is the most common technology on the market. However, thin film technology makes the photovoltaic cell more flexible and durable to be more adaptable to any area of any shape. Moreover, this kind is less affected by high temperature compared to C-Si panels. This film technology includes amorphous silicon (A-Si), CIGS (Copper Indium Gallium Selenide)/ CIS (Copper, Indium and Selenium), CdTe (Cadmium Telluride)/ CdS (Cadmium Sulfide).

Fig. 3 PV panel technologies

Table. 1 solar cell types and panel efficiency [12]

Material	C-Si		Thin films		
Sub-material	Single crystal	Polycrystal	a-Si	CdTe/Cds	CIS-CIGS
percentage	20%	16%	11.3%	18.30%	22.8%

B. *PV Shading*

PV panels should be installed in areas exposed to direct sunlight without any shading as this can cause dangerous damage to PV panels. Shade may be created by various structures, such as clouds, trees, building, poles…etc. The shaded cells act as a resistive semiconductor load. Thus, the excess current flowing through this shaded cell heats it, which leads to a hot spot.

Fig. 4 shading effect in PV installation

C. *Dust accumulation*

Dust is very small dry pieces of soil, sand or other substances that form a thin layer on the surface of the PV module blocking partially or completely sunlight from passing through the PV panel. When dust accumulates non-uniformly on the surface of PV module, it can create hot spots in the photovoltaic panels. The reduction in solar efficiency due to dust on PV panel is approximately 40% [13].

Fig. 5 dust accumulation effect on PV panel

D. *Tilt angle orientation*

In general, this angle of inclination increases with latitude, so the further places from the equator, the higher the angle of inclination must be. The orientation of solar panels is also an important factor in achieving an optimal production. In the northern hemisphere, the panels should face south, while north is preferable for the southern hemisphere.

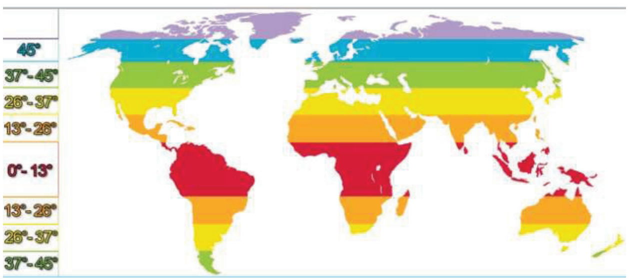

Fig. 6 Tilt angle inclination

E. Internal and external parameters variation

The efficiency of PV panel is affected principally by the sunlight and temperature intensity. In addition, the internal parameters have an important effect in the characteristics of PV panel. Therefore in this part, we will detail theirs impacts on PV panel performances.

III. PV SYSTEM MODELING

The PV model utilized is shown in figure 10, it consists of a generator current in parallel of single diode, a shunt resistance and series resistance. In real cells, power is dissipated through a series resistance R_s created due to the ohmic contact in the front surface and shunt resistance R_{sh} due to leakage current [6]. The real circuit of PV cell is demonstrated schematically in figures (10)

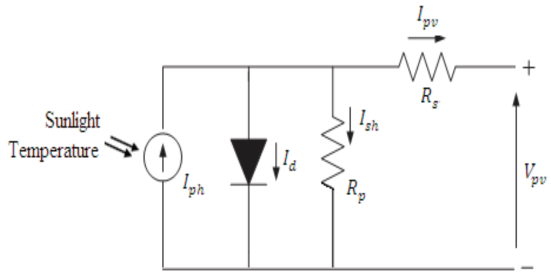

Fig. 7 Solar cell

When sunlight is incident on the PV cell, a certain current is generated [17]:

$$I_{pv} = I_{ph}N_p - I_oN_p\left[exp\left(\frac{V+R_sI}{nkTN_s}\right) - 1\right] - \frac{V+R_sI}{R_{sh}N_s} \qquad (1)$$

The photo-current depends lineally to irradiance density as detailed in equation (2):

$$I_{ph} = [I_{sc} + K_i(T - T_{ref})]\frac{G}{G_{ref}} \qquad (2)$$

The saturation current is depended on temperature as detailed in this function [18]:

$$\begin{cases} I_o = \frac{I_{sc,n}+K_i\Delta T}{\exp\left((V_{oc,n}+K_v\Delta T)/aV_t\right)-1} \\ I_{o,n} = \frac{I_{sc,Tref}}{\left(\exp\left(\frac{qV_{oc,ref}}{nKT}\right)-1\right)} \end{cases} \qquad (3)$$

The output power is given in this equation [19]:

$$P_{PV} = P_{PVpeak}\frac{G}{G_{ref}}(1 + K_T(T - T_{ref})) \qquad (4)$$

Where: I_{ph}: photo-current, I_o: saturation current of the diode, q electron charge ($q=1.60210^{-19}$C), K is the boltzmann constant ($K=1.3854^{-23}$J/K), n is the ideality factor(1<n>2), R_s series resistance, R_{sh} shunt resistance, N_s number of cells in series, N_p number of cells in series, V_t the thermal voltage of an array. E_g is the bandgap energy of the semiconductor. K_i short-circuit current temperature coefficient. P_{PVpeak} is the PV power at standard condition, K_T is temperature coefficient of PV cell (K_T=-3.7*10-3[1/C°] for mono and polycrystalline silicon).

IV. SIMULATION RESULTS

To show the effects of internal and external factors in PV performances, the simulation model detailed in the following figure is simulated using MATLAB/simulink. The solar KC200GT module is utilized which has (Pmax is 200W, V_{mp} is 26.3V, Voc is 32.9V, I_{mp} equals 7.61A, I_{sc} equals 8.1A with 54 cells in series)

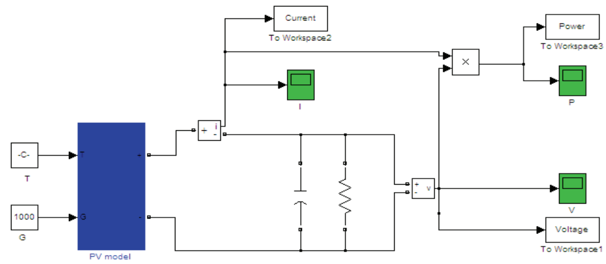

Fig. 8 Simulation model of PV system

A. Internal parameter effect

In this section the effect of internal parameters (ideality diode, series and shunt resistances) is analyzed.

- *Series resistance variation*

The influence of series resistance is shown in the following figures for different values (Rs= 0.2, 05, 09 and 2Ω). The variations of R_s influence significantly the output power of PV array without any variation in V_{mpp} and I_{sc}. Its impact in the slope of curve is very clear, at high value (2Ω) the slope of PV curves (I(V)) and P(V)) is completely changed.

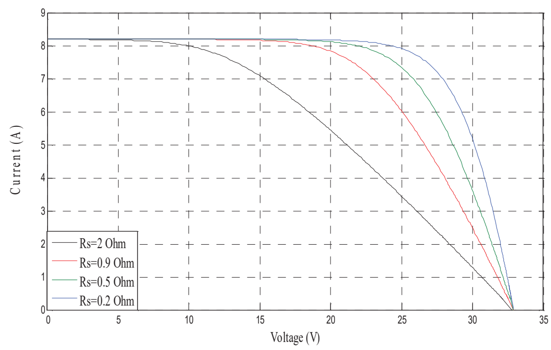

Fig. 13 I-V characteristics under series resistance variation

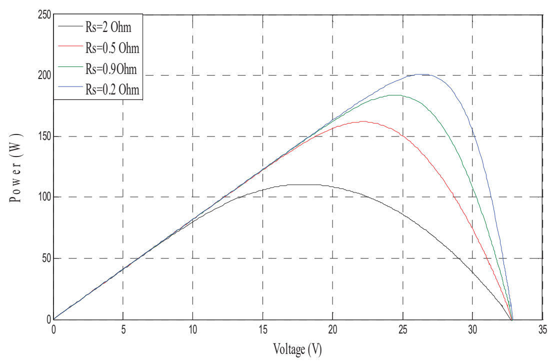

Fig. 14 P-V characteristics under series resistance variation

Table.2 PV Module results for varying series resistance

Series resistance(Ω)	0.2	0.5	0.9	2
P_{mpp}(W)	200.98	183.837	161.85	110.65
V_{oc}(V)	33.62	33.65	33.68	33.7
I_{cc}(A)	8.208	8.206	8.202	8.19

- *Shunt resistance variation*

The figures below show the effect of shunt resistance variation in the PV characteristic for different values (5, 8, 15, 950Ω). The low shunt resistances (5, 8, 15Ω) cause power loses, reducing also the I_{sc} and V_{oc} values.

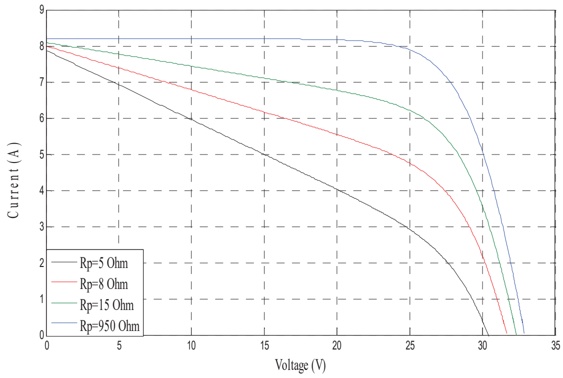

Fig. 9 I-V characteristics under parallel resistance variation

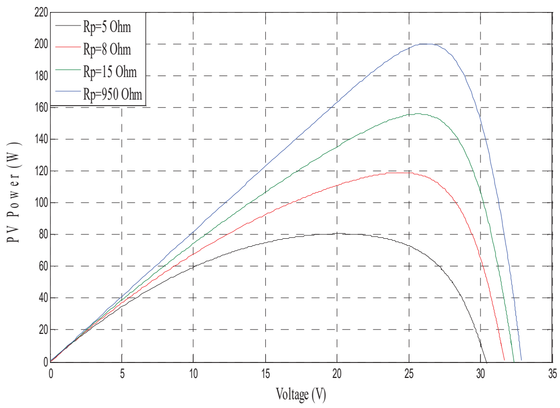

Fig. 10 I-V characteristics under parallel resistance variation

Table. 3 PV Module results for varying series resistance

shunt resistance(Ω)	5	8	15	950
P_{mpp}(W)	80.25	119	155.75	199.996
V_{oc}(V)	30.5	31.23	31.78	31.97
I_{cc}(A)	7.85	7.98	8.078	8.208

- *Ideality diode*

The figures bellows present the PV graphs for different values of diode ideality (1, 1.3, 1.6 and 2). The increase of diode ideality decreases the maximum power point.

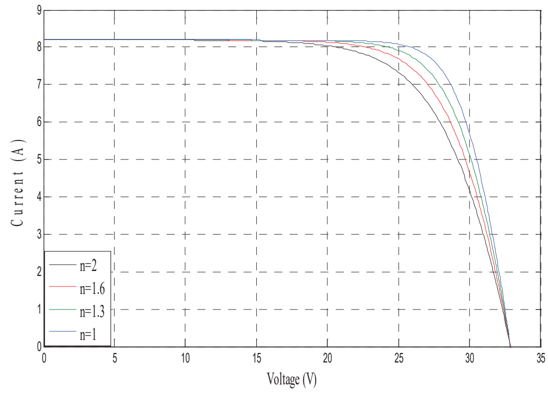

Fig. 11 I-V characteristics under ideality diode variation

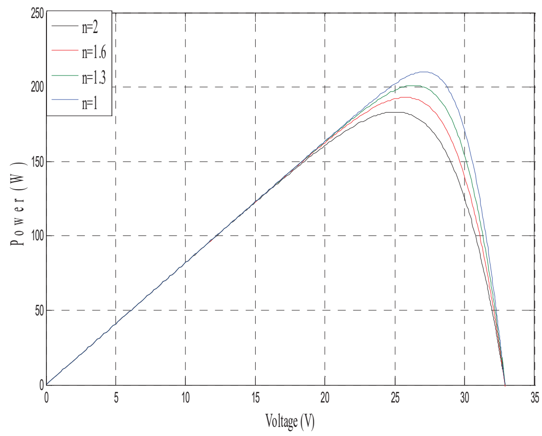

Fig. 12 P-V characteristics under ideality diode variation

Table. 4 PV Module results for varying diode ideality

Diode ideality	1	1.3	1.6	2
	210.2	200.8	193.05	183.4
V_{oc}(V)	33.2	33.2	33.2	33.2
I_{cc}(A)	8.2074	8.2074	8.2074	8.2037

B. External parameters

As shown in the equations that detailed the mathematical model of PV cell, the most important factors influencing PV performances are the temperature and irradiance density, therefore the study of their effects is detailed in this first section.

- *Temperature effect*

The characteristics of PV cell under temperature variation are shown in figure 16 for several values (0, 15, 25, 35, 45°C) while solar irradiation is kept at 1000W/m^2. The current slightly increases with temperature because the photons absorption is enhanced with increasing temperature. While the voltage drops because of the exponential increase of I_{sc}. As a result, the output power deceases.

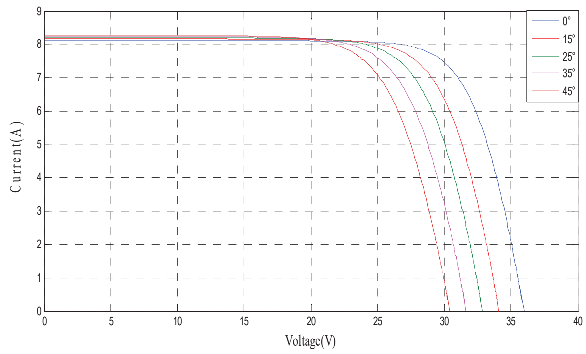

Fig. 13 P-V characteristics under temperature variation

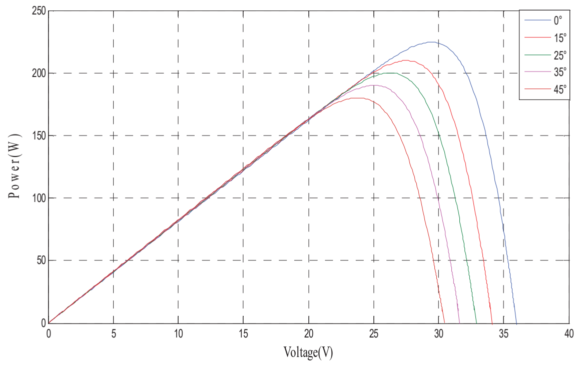

Fig. 14 I-V characteristics under temperature variation

Table. 5 PV module results for varying temperature

Temerature (°C)	0	15	25	35	45
P_{mpp}(W)	224.6	209.86	200	190.16	180
V_{oc}(V)	35.27	34.15	33.1	31.86	30.2
I_{cc}(A)	8.128	8.176	8.208	8.239	8.27

- *Irradiance effect*

The influence of irradiation on PV curves is shown in the following figure for several values (400, 600, 800, 1000W/m^2) while temperature is kept at 25°C. The current changes frictionally with the variation of the sunlight density while the voltage changes only slightly. The power increases when the irradiance increases.

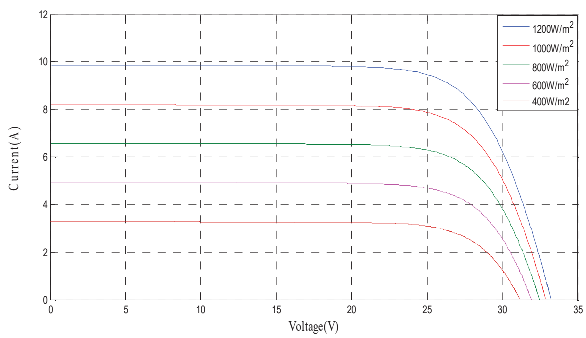

Fig. 15 I-V characteristics under irradiance variation

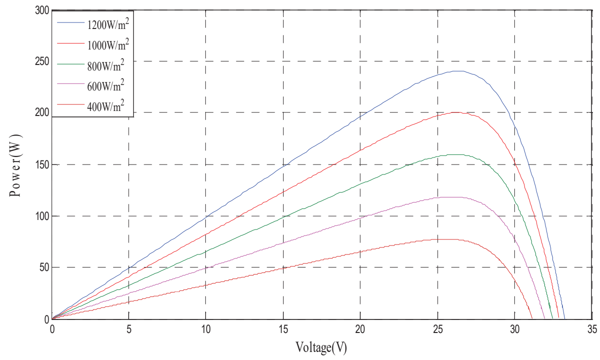

Fig. 16 P-V characteristics under irradiance variation

Table. 6 PV Module results for varying sunlight density

Irradiance (W/m^2)	400	600	800	1000	1200
P_{mpp}(W)	76.65	118.41	159.35	200	240
V_{oc}(V)	33.27	33.19	33.01	32.41	31.8
I_{cc} (A)	3.2807	4.9229	6.559	8.2	9.848

- *Shading effect*

Figure17 shows the series-connected PV array operated at a normal condition and with partial shading. In the first case, the three modules have identical sunlight density (1000W/m^2). In the second case, the three modules are exposed to different irradiation (1000, 600 and 200W/m^2), respectively. The effect of shading is very clear which exhibits multiple peaks in PV curves unlike normal conditions with a significant decrease in the output power compared to the generator works in normal condition. In this case of partial shading, the pay-pass diodes play an important role to prevent the shaded cells to consume the current generated by unshaded cells.

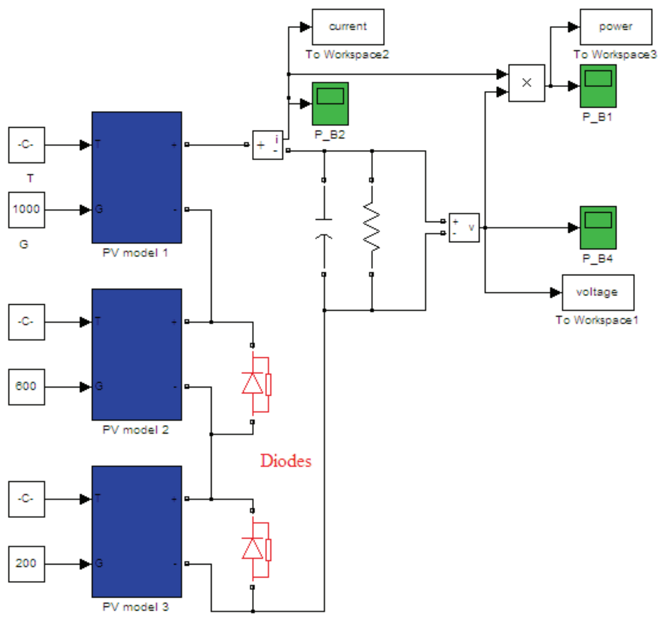

Fig. 17 Three PV model under shading effect

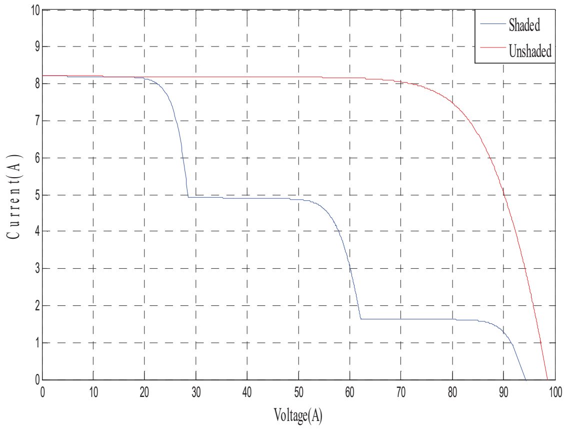

Fig. 24 I-V characteristics under shading

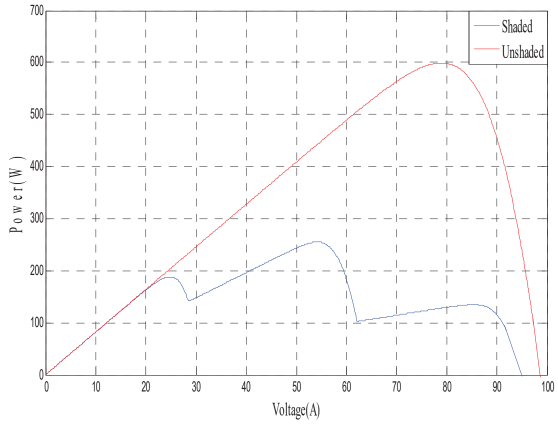

Fig. 25 P-V characteristics under shading

Conclusion

The performance of the PV panel is affected by various factors, internal and external parameters that make the study of their effects important to improve the total productivity of the PV system. Therefore, the first part discussed these parameters and their affect on PV panels. In the second part, the modeling of PV panel using single diode is presented with simulation results presentation of the effect of these factors on PV characteristics. The results prove the high dependence of PV performance not only on metrological conditions (temperature and irradiance), but also on internal conditions (series and shunt resistances, diode ideality); The PV power depends strongly on sunlight density, when the high temperature deceases it too. The shedding provoking by closing obstacles or by dust accumulation degrades the PV panel and can provoke many damages (hot-spot). A small variation of the series resistance largely affects the PV output power, so its value is kept very small, unlike the parallel resistance which should be large.

References

[1] B. Subudhi, R. Pradhan, A New Adaptive Maximum Power Point Controller for a Photovoltaic System, IEEE Transactions on sustainable energy, vol. 10,no. 4, pp. 1625–1632, 2019.

[2] P. K. Sahu, S. Jena, B. C. Babu, Power management and bus voltage control of a battery backup-based stand-alone PV system, Electrical Engineering. vol. 104, pp. 97–110, 2022.

[3] M. K. Sharma, D. Kumar, S. Dhundhara, D. Gaur, and Y. P. Verma, Optimal Tilt Angle Determination for PV Panels Using Real Time Data Acquisition, Global Challenges, vol. 4, 2020

[4] S. Motahhir, A. Ghzizal, S. Sebti, A. Derouich, Modeling of Photovoltaic System with Modified Incremental Conductance Algorithm for Fast Changes of Irradiance, International Journal of Photoenergy, vol. 13, pp. 1–13, 2018.

[5] Y. Chaibi, A. Allouhi, M. Salhi and A. El-jouni, Annual performance analysis of different maximum power point tracking techniques used in photovoltaic systems, Protection and Control of Modern Power Systems, vol. 4, no. 15, 2019.

[6] A. S. Al-Ezzi and M. N. M. Ansari, Photovoltaic Solar Cells: A Review, Appl. Syst. Innov, vol. 5, pp. 67, 2022.

[7] L. Zaghba , M. Khennane , A. Borni, A. Fezzani, Investigation of the major internal and external factors that affect photovoltaic modules energy production and systems performance, Journal of Renewable Energies, vol. 24, pp. 121–151, 2021.

[8] N. Barth, R. Jovanovic, S. Ahzi, M. A. Khaleel, PV panel single and double diode models: optimization of the parameters and temperature dependence, Solar Energy Materials & Solar Cells, vol. 148, no. 2, pp. 87–98, 2015.

[9] A. J. Nascimento, M. C. Cavalcanti, F. Bradaschia, E. A. Silva, L. Michels, and L. P. Pietta, Parameter estimation technique for double-diode model of photovoltaic modules, in 2017 Brazilian Power Electronics Conference (COBEP), pp. 1–6, 2017.

[10] P. Singh, N. M. Ravindra, Analysis of series and shunt resistance in silicon solar cells using single and double exponential models, Emerging Materials Research, vol. 1, no. 1, pp. 33–38, 2011.

[11] A. Harrag, Y. Daili, Three-diodes PV model parameters extraction using PSO algorithm, Revue des Energies Renouvelables, vol. 22, no. 1, pp. 85–91, 2019.

[12] https://www.cleanenergyreviews.info/blog/most-efficient-solar-panels

[13] A. Hussain, A. Batra, and R. Pachauri, An experimental study on effect of dust on power loss in solar photovoltaic module, Renewables: Wind, Water, and Solar, vol. 4, no. 1, pp. 1–13, 2017.

[14] A. Aslam, N. Ahmed, S. A. Qureshi, M. Assadi and N. Ahmed, Advances in Solar PV Systems; A Comprehensive Review of PV Performance, Influencing Factors, and Mitigation Techniques, Energies, vol. 15, no. 20, pp. 7595, 2022.

[15] F. Sedaghati, A. Nahavandi, M. A. Badamchizadeh, S. Ghaemi and M. A. Fallah, PV Maximum Power-Point Tracking by Using Artificial Neural Network, Mathematical Problems in Engineering, 2012.

[16] G. Walker, evaluating MPPT converter topologies using a MATLAB PV model, Journal of electrical and electronics engineering, vol. 21, no. 1, pp. 49–56, 2001.

[17] Z. Bouguerra, A. Benfdila, Comparative study of individual and hybrid renewable energy systems (photovoltaic, wind energy and hybridization), controlled by fuzzy logic control, Journal of Engineering Science and Technology Review. 2021, vol. 14, no. 5, pp.180–186.

[18] M. R. Villalva, J. R. Gazoli, E. R. Filho, Comprehensive Approach to Modeling and Simulation of Photovoltaic Arrays, IEEE transactions on power electronics, vol. 24, no. 5, pp. 1198–1208, 2009.

[19] N. E. Morsy, M. A. Attia, A. Y. Abdelaziz, N. Kanwar, Optimization of the PI controller to improve the dynamic performance of grid-connected photovoltaic system, 8th International Conference on Power Systems (ICPS), India, 2019

Plasma homogenous DBD in Ar-NH_3 mixtures for photovoltaic celllule: A parametric study

Amar Benmoussa
Laboratoire de Physique des Plasmas, Matériaux Conducteurs et leurs Applications, Université des Sciences et de la Technologie d'Oran El-Mnaour B.P.1505, 31000, Oran, Algérie.
Ecole Supérieure en Génie Electrique et Energétique (ESG2E), Oran, Algérie.

Barkahoum Larouci
Université Yahia Farés, Faculté de Technologie, Médéa, Algérie.

Laboratoire de Physique des Plasmas, Matériaux Conducteurs et leurs Applications, Université des Sciences et de la Technologie d'Oran El-Mnaour B.P.1505, 31000, Oran, Algérie.

Ahmed Belasri
Laboratoire de Physique des Plasmas, Matériaux Conducteurs et leurs Applications, Université des Sciences et de la Technologie d'Oran El-Mnaour B.P.1505, 31000, Oran, Algérie.

Abstract— **The plasmas electrical characteristics and kinetics of dielectrics barriers discharge are investigated for operating conditions typical to homogenous DBDs in Ar-NH_3 mixture at atmospheric pressure. The main goal of the present work is to simulate a homogenous dielectrics barriers discharge at atmospheric pressure for SiNx photovoltaic cellule deposition. An overview of kinetic scheme in Ar-NH_3 mixture taking into account all possible energies transfers into the gas mixture was done to study the electrical and kinetic characteristics of DBD discharge. The time variations of charged particles, atomic and molecular excited species, also the current densities, the voltage, and deposited power in the DBD are calculated by a kinetic zerodimensional model. A parametric study of the influence of some discharge parameters such as the applied voltage, the total pressure, the dielectric capacitance, as well as the NH_3 concentration in the mixture is essential to see the effect of these parameters on discharge efficiency.**

Keywords- Plasma modelling; DBDs; Ar-NH3 gas mixture.

I. INTRODUCTION

Plasma generated by a dielectrics barriers discharge at atmospheric pressure has been recently received much attention over the last ten years [1-7]. However, homogenous DBD working with gas mixture are used in many applications fields such as biomedicine, materials technology, and environmental applications [8-11]. For surface treatment application [12-15], only homogenous DBDs can be used to obtain a stable diffuse discharge in gas mixture at atmospheric pressure under certain specific conditions of discharge such as the applied voltage, and properties of external electrical circuit. According to the literature, a homogenous DBD is investigated in many different gas mixtures [16-21], especially for thin film deposition. The most of efforts devoted to this subject are used the diffuse DBD of ArNH3 mixture in order to increase the efficiency of deposition processes of Si3-N4 films from suitable monomer [22-24]. However, the DBD of argon/ammonia mixture can be covers the entire of surface discharge with low voltage and excitation frequency [25]. Recent theoretical and experimental works are focused on the study of discharge conditions parameters effect on electrical and chemical characteristics of atmospheric pressure glow discharge (APGD) [16, 26-28].

Vallade et al [29] analyzed the chemical properties of glow dielectric barrier discharges DBDs in Ar/NH_3/SiH_4 gas mixture to make thin films. A 50 kHz discharge excitation power was varied by increasing voltage and modulating excitation. Their results show that the modulation can be decreases the energy needed to establish the plasma chemistry and consequently the control of thin film properties. In Ref [30], an experimental measurement was carried out to investigate the production of dense thin film with a RF-DBD and analyze the influence of discharge mode on silica-film properties. The authors were found that the using a sinusoidal radio-frequency voltage instead of a low-frequency can increases the power delivered to the homogenous discharge. Zenghui et al [31] have investigated the influence of ammonia admixture on argon discharge properties. They found that a small amount of NH_3 can lead to APGD due to the Penning ionization of NH_3 molecules by metastable argon.

In this paper, we present a computer modeling of homogenous DBD in Ar/NH_3/SiH_4 at atmospheric pressure. In the kinetic scheme of gas mixture all types of energy transfers into the discharge are considered in the homogenous model. The influence of some discharge parameters on charged and excited particles densities and VUV photon generation in the DBDs is presented and discussed.

II. DISCHARGE MODEL

The schematic of the DBD configuration studied in the present work is presented in Figure1. The applied sinusoidal voltage through the discharge is summarized as follows:

$$V_{ap}(t) = V_D(t) + V_g(t) \quad (1)$$

Where: VD (t) and Vg (t) are the voltage across the dielectric and the positive column, respectively. The homogenous model considered in the frame of this work is similar to that described in Refs [32, 33]. The zero-dimensional model is based on the Boltzmann equation and the plasma chemistry which coupled to the electrical circuit. We note that the transport coefficients depending on the reduced electric field are precalculated and tabulated by solving the steady-state homogenous electron Boltzmann equation in Ar-NH_3 using Bolsig+ software [34].

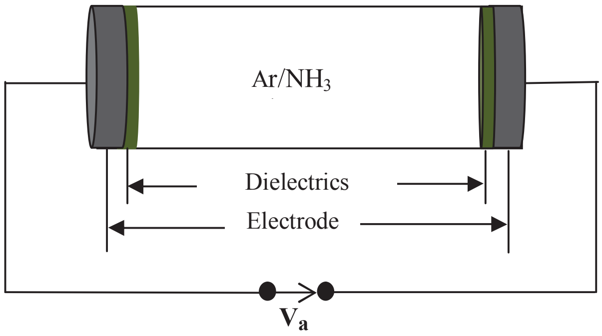

Figure 1. Schematic of DBD configuration.

III. RESULTS AND DISCUSSION

An important investigation on the homogenous DBD in Ar-NH_3 concerns the influence of the sinusoidal applied voltage on the discharge behavior. The operating conditions of Ar-NH_3 DBD using in this work are considered as follows: the gas pressure (p) is taken equal to 760 Torr. The gap length (d) is 0.1 cm, the discharge active area A=10 cm^2, the dielectric capacitance (Cd) is equal to 0.18 nF. The gas temperature (T) of both electrodes is equal to 300 °k, the peak value of applied voltage (Vs) vary from 400 to 800 V, and the frequency (f) is fixed to 50 kHz.

A. Applied voltage effect

The physical discharge properties could be changed by varying the sinusoidal applied voltage (V_s) or changing the ballast resistance (R) of external circuit. In Figure 2, we show the time variations of excited molecules densities of Ar_2^* (Figure 2(a)), Ar^* (Figure 2(b)), and NH_3^* (Figure 2(c)) for different values of sinusoidal applied voltages. Note that theses excited molecules reach peaks of about 7.7×10^7 , 7.8×10^8 , and 9.8×10^{10} cm^{-3}, respectively, during each single current pulse. The increase in the applied voltage induces an increasing in the production of metastables by electron excitation of argon.

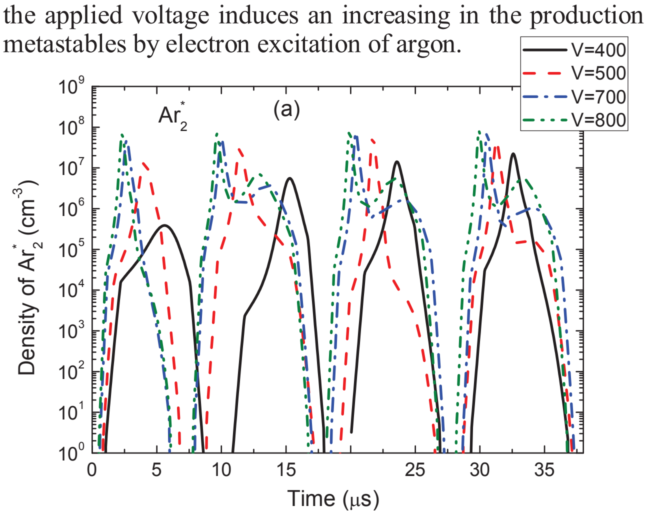

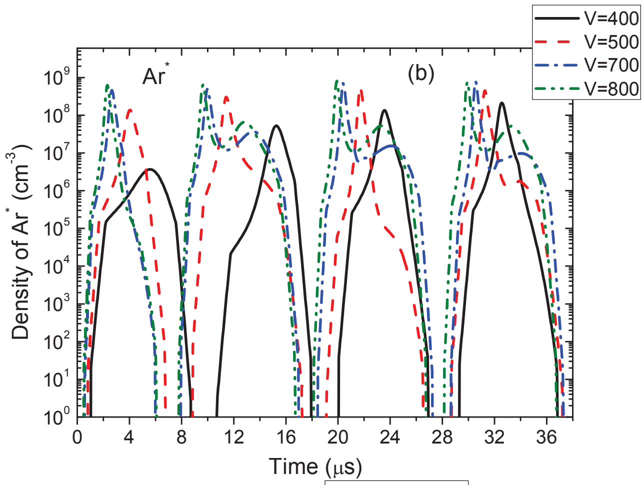

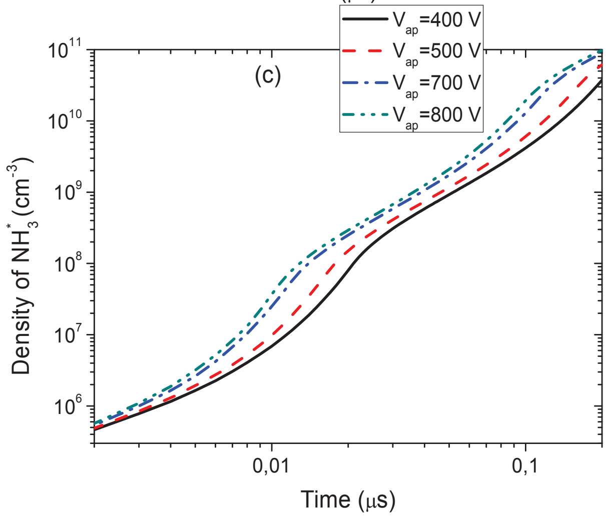

Figure 2. Ions density for different sinusoidal applied voltages for: (a) Ar_2*, (b) Ar* , and (c) NH_3* .

In Figure 3, we have calculated the waveform of deposited power density in the discharge DBD under different applied voltages. The magnitude of deposited power peaks increase with the rise of applied voltage. The peaks values of the deposited power are 4.28, 3.66, 2.58, and 0.63 W.cm-3 at 800, 700, 500, and 400 V, respectively. We also investigate the effect of applied voltage on the density of hν (120 nm), in Figure 4. It seems clearly that the generations of 120 nm photons increase with the large values of applied voltage amplitude, which induce an increasing in the production of metastable by electron excitation of argon.

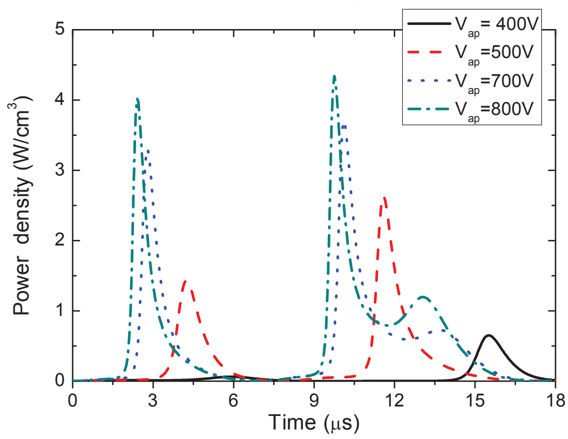

Figure 3. Power density deposited in the discharge for different voltage values

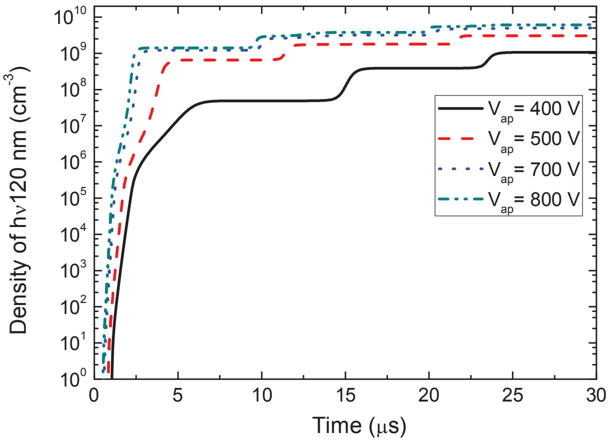

Figure 4.Time variations of the photon hν (120 nm) density for different values of applied voltage

B. *Dielectric capacitance effect*

The consequences of the dielectric capacitance on voltage and current discharge, for different values of C_{diel}=10, 18, 28, and 38 pF/cm$_2$ are presented in Figure 5. In Fig. 5(a)-(d), the indexes I, V_a, V_p, and V_d refer to the current discharge, the applied voltage, the voltage across the plasma, and the voltage across the dielectrics, respectively. It found that for a larger dielectric capacitance, the current required to charge the dielectric becomes also larger. For the values of dielectric capacitance 10, 18, 28, and 38 pF/cm^2, the peak values of the current are 8.65, 13.17, 17.56, and 21 (mA), respectively. The influence of the dielectric capacitance on the photon hν (120 nm) emission and deposited power in the DBDs is analyzed as shown in Figure 6. For large values of dielectric capacitance the energy deposited in the DBD becomes important; and the deposited power in the DBD and 120 nm photon fluxes were affected significantly.

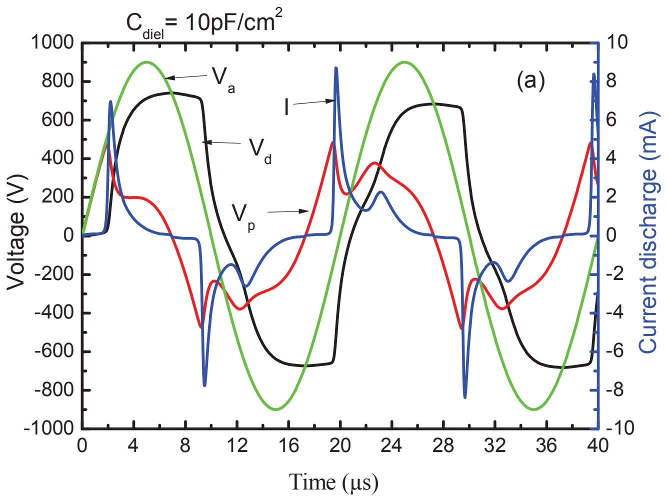

C. *NH_3 concentration in Ar- NH_3 gas mixture effect*

In order to see the influence of the ammonia concentration in the Ar- NH_3 gas mixture on the 120 nm photons emission, we presented in the Figure 6 the time variation of 120 nm density, for different values of concentration ammonia (100, 133, 200, 300 ppm) at fixed pressure of 760 Torr. It seems clearly that the generation of hν (120 nm) increases with the decrease in NH_3 mole fraction in the mixture. This Figure indicates that for low NH_3 concentrations an important fraction of power deposited in the DBD goes into producing ionization due to the high values of discharge current.

The waveforms of Ar^+ and NH_3^+ densities are also plotted in Figures 7(a) and 7(b), respectively. The magnitude of Ar^+ and NH_3^+ densities increase with an increasing in ammonia concentration. The peak of the density reaches values of 7.5×10^4 cm^{-3} for Ar^+ and 3.1×10^{10} cm^{-3} for NH_3^+ at 300 ppm.

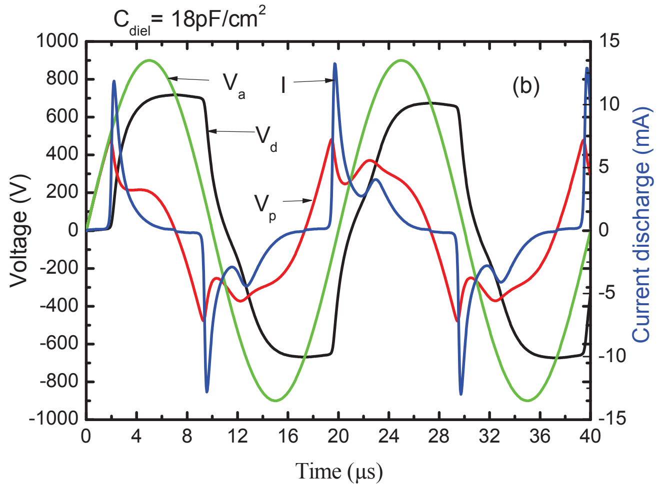

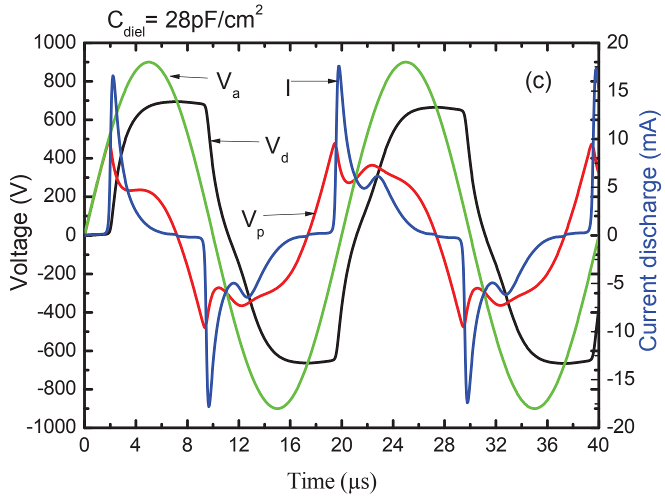

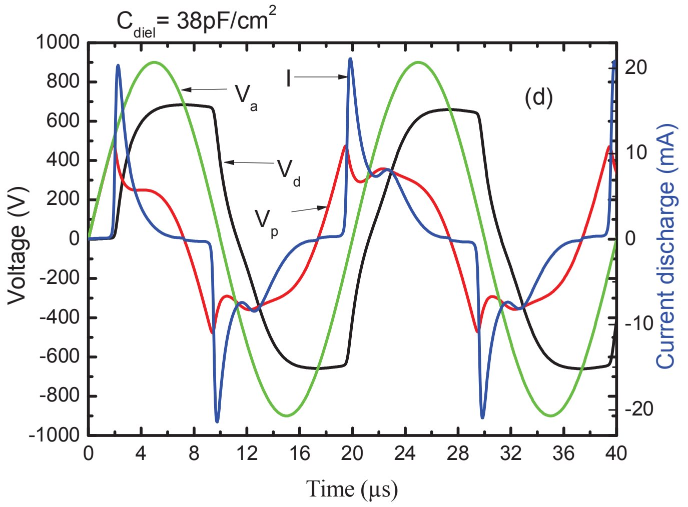

Figure 5. Waveforms of voltages and current discharge for different values of dielectric capacitance: (a) C_{diel}=10 pF/cm^2 , (b) C_{diel}=18 pF/ cm^2 , (c) C_{diel} =28 pF/ cm^2 , and (d) C_{diel} =38 pF/ cm^2 .

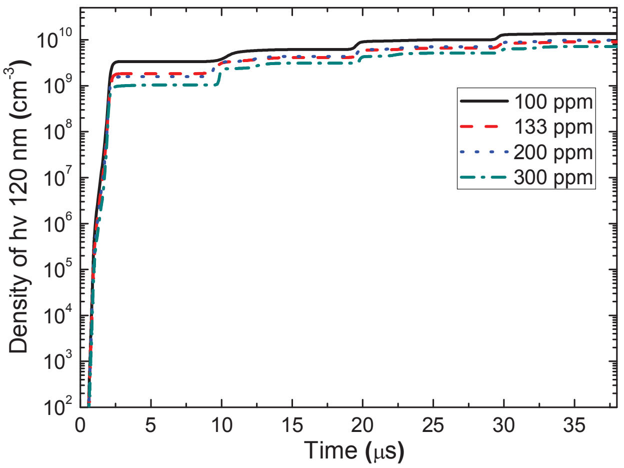

Figure 6. Time evolution of photon hν (120 nm) density in the DBDs for different values of dielectric capacitance: C_{diel}=10, 18, 28, and 38 pF/cm^2

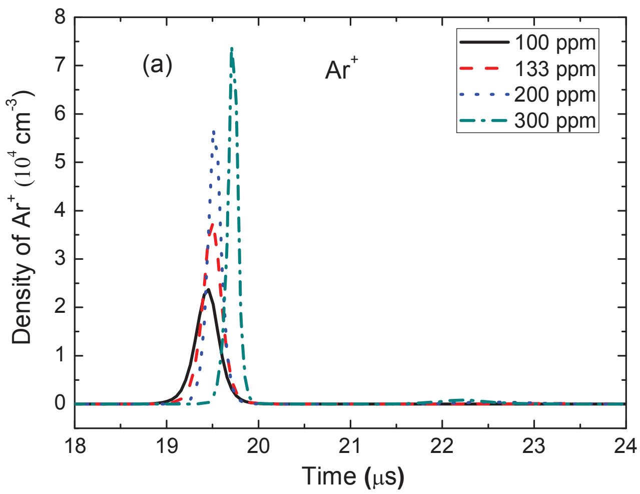

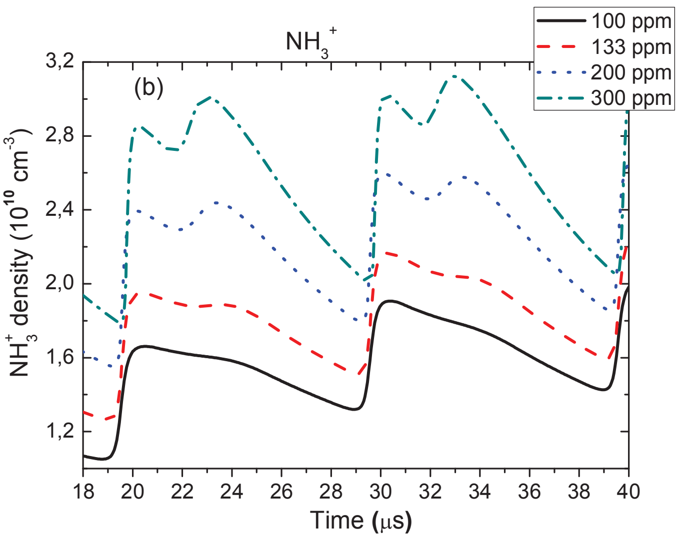

Figure 7. Time variation of: (a) Ar^+ density, (b) NH_3^+ density for different values of NH_3 concentration: 100, 133, 200, and 300 ppm.

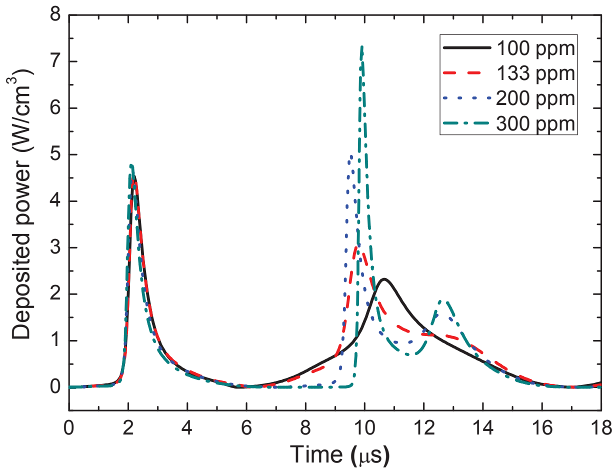

Figure 8. Time variation of power density for different values of NH_3 concentration: 100, 133, 200, and 300 ppm.

In Figures 8, we plotted the temporal evolution of deposited power density in Ar-NH_3 DBD for many values of NH_3 concentrations. We note that the power deposition in the plasma reaches a maximum value at low Ar concentrations in NH_3. This result shows that the NH_3 gas breakdown for 300 ppm occurs quickly that for 100 ppm.

IV. Conclusion

In this paper, a theoretical study of Ar-NH_3 homogenous dielectrics barriers discharge DBDs was carried out for typical operating conditions found in the literature. The results obtained in the frame of this work were based on a homogenous model including the electrical module and the chemical kinetic module, with the aim of best understanding the discharge behavior of Ar-NH_3 gas mixture. This model predicts the optimal operating conditions and describes the electrical and chemical characteristics of Ar-NH_3 homogenous DBDs. The parametric study reveals that the temporal variations of current, voltage across the discharge, charged and excited species concentrations are strongly influenced by variation of some discharge parameters such as the applied voltage, the dielectric capacitance, the concentration of NH_3 in the mixture, the gas pressure. For higher applied voltage and higher gas pressure, the charged and excited species will be increasing. The large values of dielectric capacitance lead also to a significant increase in charged particles, and 120 nm photon generation. Finally, the findings of this work suggest that the choice of the optimal values of discharge parameters in the DBD can play an important role in order to obtain ideal homogenous discharge.

REFERENCES

[1] A. Chirokov, A. Gutsol, and A. Fridman, "Atmospheric pressure plasma of dielectric barrier discharges", Pure Appl. Chem., Vol. 77, No. 2, pp. 487–495, 2005.

[2] Y. B. Golubovskii, V. A. Maiorov, and J. F. Behnke, "Numerical modeling of a DBD in glow mode at atmospheric pressure" J. Phys. D: Appl. Phys., vol. 37, pp.1346–1356, 2004.

[3] U. Kogelschatz, B. Eliasson, and W. Egli," From ozone generators to flat television screens: history and future potential of dielectric-barrier discharges", Pure Appl. Chem. Vol.71, No. 10, pp.1819–1828, 1999.

[4] U. Kogelschatz, "Ultraviolet excimer radiation from nonequilibrium gas discharges and its application in photophysics, photochemistry and photobiology", J. Opt. Technol. Vol.79, No.8, pp. 484–493, August, 2012.

[5] A. Benmoussa, A. Belasri, and Z. Harrache, "Numerical investigation of gas heating effect in dielectric barrier discharge for Ne-Xe excilamp", Current Applied Physics, vol. 17, pp. 479–483, January, 2017.

[6] A. Benmoussa, B. Larouci, and A. Belasri, "A simple Study of Joule Heating Effect in Argon DBD Reactor", High Temperature Material Processes, vol. 27, no.2, pp.1–9, 2023.

[7] X. Yuan, J. Shin, and L.L. Raja, "One-dimensional simulations of multi pulse phenomena in dielectric-barrier atmospheric-pressure glow discharges", Vacuum, vol. 80, pp. 1199–1205, 2006..

[8] A. Eid, K. Takashima, A. Mizuno, "Experimental and. Simulation Investigations of DBD Plasma Reactor at Normal. Environmental Conditions", IEEE Trans. Industry Appl. Vol.50, No.6, pp. 4221–4227, November, 2014.

[9] J. Y. Kim, S-O. Kim, Y. Wei, and J. Li, "A flexible cold microplasma jet using biocompatible dielectric tubes for cancer therapy", Appl. Phys. Lett, Vol.96, 203701, May 2010.

[10] P. Rajasekaran, P. Mertmann, N. Bibinov, D. Wandke, W. Viol, and P. Awakowicz, "Filamentary and Homogeneous Modes of Dielectric Barrier Discharge (DBD) in Air: Investigation through Plasma Characterization and Simulation of Surface Irradiation" Plasma Process. Polym. Vol.7, pp.665-675, 665–675, 2010.

[11] J. Tang, S. Li, W. Zhao, Y. Wang, and Y. Duan, "Development of a stable dielectric-barrier discharge enhanced laminar plasma jet generated at atmospheric pressure", Appl. Phys. Lett. Vol.100 253505, June 2012.

[12] G. Borcia1, C.A. Anderson, and N. M. D. Brown, 'Dielectric barrier discharge for surface treatment: application to selected polymers in film and fibre form', Plasma Sources Sci. Technol. Vol.12, pp. 335-344, May 2003.

[13] F. Massines and G. Gouda, 'A comparison of polypropylene-surface treatment by filamentary, homogeneous and glow discharges in helium at atmospheric pressure' J. Phys. D: Appl. Phys. Vol.31, pp. 3411–3420, september1998.

[14] F. Massines, C. Mayoux, R. Messaoudi, A. Rabehi, and P. Ségur, in Proceedings of the Tenth International Conference on Gas Discharges and Their Applications, edited by W. T. Williams (University College of Swansea, U.K., 1992), Vol. II, p. 730.

[15] H.-E. Wagner, R. Brandenburg, K.V. Kozlov, A. Sonnenfeld, P. Michel, and J.F. Behnke, "The barrier discharge: basic properties and applications to surface treatment" , Vacuum , vol.71, pp. 417-436, November 2003.

[16] Z. Li, Z. Zhao, and X. Li, 'Numerical model of an Ar/NH3 atmospheric pressure direct current discharge in parallel plate geometry, J. Appl. Phys. Vol. 19, 033510, March 2012.

[17] P. Kloc, H-E. Wagner, D. Trunec, Z. Navrâtil, and G. Fedoseev, "An investigation of dielectric barrier discharge in Ar and Ar/NH3 mixture using cross-correlation spectroscopy", J. Phys. D: Appl. Phys. Vol. 43, 345205, August 2010.

[18] A. Fateev, F. Leipold, Y. Kusano, B. Stenum, E. Tsakadze, and H. Bindslev, "Plasma Chemistry in an Atmospheric Pressure Ar/NH3 Dielectric Barrier Discharge" Plasma Process. Polym. Vol.2, pp. 193–200, Februray 2005.

[19] D. Lee, J. M. Park, S. H. Hong, and Y. Kim, "Numerical Simulation on Mode Transition of Atmospheric Dielectric Barrier Discharge in Helium–Oxygen Mixture" IEEE Trans. Plasma Sci. vol.33, pp.949– 957, April 2005.

[20] C. Yao, S. Chen, S. Wang, Z. Chang, A. Sun, H. Mu, and G-J. Zhang, 'Characteristics of Atmospheric Ar/NH3 DBD and its Comparison with He/N2 DBD', J. Phys. D: Appl. Phys. Vol. 51, 225201, 2018.

[21] C. Meyer, S. Müller, B. G-Lopez, and J. Franzke, " Impact of homogeneous and filamentary discharge modes on the efficiency of dielectric barrier discharge ionization mass spectrometry ", Anal Bioanal Chem. Vol. 405, pp. 4729– 4735, 2013.

[22] R. Bazinette, R. Subileau, J. Paillol, and F. Massines, 'Identification of the different diffuse dielectric barrier discharges obtained between 50 kHz to 9 MHz in Ar/NH3 at atmospheric pressure', Plasma Sources Sci. Technol, vol. 23, 035008, 2014.

[23] F. Massines, C. S-Bournet, F. Fanelli, N. Naudé , and N. Gherardi, 'Atmospheric Pressure Low Temperature Direct Plasma Technology: Status and Challenges for Thin Film Deposition' Plasma Process. Polym. DOI: 10.1002/ppap.201200029, August 2012.

[24] F. Massines, J. Silva, J-F. Lelièvre, R. Bazinette, J. Vallade, P. Lecouvreur, and S. Pouliquen, 'Hydrogenated Silicon Nitride SiNx:H Deposited by Dielectric Barrier Discharge for Photovoltaics', Plasma Process. Polym. Vol. 13, pp. 170–183, December 2015.

[25] Y. B. Golubovskii, V. A. Maiorov, J. Behnke, and J. F. Behnke, "Modelling of the homogeneous barrier discharge in helium at atmospheric pressure", J. Phys. D: Appl. Phys. Vol. 36, pp. 39-49, 2003.

[26] Z-S. Chang, C-W. Yao, S-L. Chen, and G-J. Zhang, "Electrical and optical properties of Ar/NH3 atmospheric pressure plasma jet", Phys. Plasmas, Vol. 23, 093503, 2016.

[27] J. Vallade, and F. Massines, "Fourier-transformed infrared absorption spectroscopy: a tool to characterize the chemical composition of Ar–NH3–SiH4 dielectric barrier discharge", J. Phys. D: Appl. Phys., vol. 46, 464007, Octobre 2013.

[28] F. Zhi, L. Xiao, C. Lingling, Q. Yuchang, and E. KUFFELF, "Study on the Microsecond Pulse Homogeneous Dielectric Barrier Discharges in Atmospheric Air and Its Influencing Factors", Plasma Sci. Technol, vol.13, pp. 676-681, 2011.

[29] J. Vallade, R. Bazinette, L. Gaudy, and F. Massines, 'Effect of glow DBD modulation on gas and thin film chemical composition: case of Ar/SiH4/NH3 mixture', J. Phys. D: Appl. Phys., vol. 47, No. 22, 224006, 2014.

[30] R. Bazinette, J. Paillol, J-F. Lelièvre, and F. Massines, "Atmospheric Pressure Radio-Frequency DBD Deposition of Dense Silicon Dioxide Thin Film", Plasma Process. Polym. DOI: 10.1002/p pap.201600038, July 2016.

[31] Z. Zenghui, Z. Guanjun, S. Xianjun, C. Zhengshi, and G. Chunhui, 'nvestigation of atmospheric pressure dielectric barrier glow discharge in argon/ammonia mixture' High Voltage Engineering. 39, pp.2254–2259, September 2013.

[32] A. Belasri, Z. Harrache, Phys Plasmas, 'Electrical and kinetical aspects of homogeneous dielectric-barrier discharge in xenon for excimer lamps', vol. 17,123501, December 2010.

[33] A. Belasri, Z. Harrache, "Electrical approach of homogenous high pressure Ne/Xe/HCl dielectric barrier discharge for XeCl (308 nm) lamp", Plasma Chem Plasma Process, vol. 31, pp.787-798, 2011.

[34] BOLSIG+ KINEMA Software, P.O. Box 1147, 236 N. Washington St., Monument, CO 80132, USA, http://www.siglo-kinema.com.

Comparative study of the different topologies of the Z-source inverter using simple boost control

Benziada Mohamed Abdelghani[1]
Process Control Laboratory National Polytechnic school
Algiers, Algeria
abdelghani.benziada@gmail.com

Ouail Mohamed[2]
Electrical Engineering Laboratory University of Chlef
Chlef, Algeria
mohamed.ouail152@gmail .com

Abstract— **The main purpose of this paper is to study the different topologies of Z-source inverter in photovoltaic systems. We presented several topologies of Z-source inverter used for photovoltaic systems using the simple boost control. These include the two levels Z-source inverter, the two level embedded Z-source inverter and the two level dc link embedded Z-source inverter. The MATLAB simulation results may indicate the advantages and disadvantages of each of the converters.**

Keywords- Z-source; DC/DC inverter; P&O; MPPT; Shoot-through; boosting method.

I. INTRODUCTION

The global electricity consumption observed in recent decades is strongly linked to the development of industry, transport and the means of communication. Today, a large portion of electricity generation is generated from non-renewable resources such as coal, natural gas, oil and uranium. The price of the latter is rising and global warming is increasingly severe because of environmental pollution.

As a result, countries are now looking for alternative energy sources to partially replace fossil fuels. As a result, countries are now looking for alternative energy sources to partially replace fossil fuels. Photovoltaic systems provide promising ways to produce clean electricity, meet growing energy demand and mitigate global warming. An important advantage of PV systems is the use of abundant and free energy from the sun, and being environmentally safe and renewable.

A power adaptation between the source and the load is important for better operation and to ensure system reliability. With the development of specific power electronics for photovoltaic applications, many innovative conversion systems have been developed, including inverters with input adaptation stages. Indeed, these devices make it possible to adapt and optimize photovoltaic production through DC-DC power converters inserted between the photovoltaic modules and the inverter input.

Although these converters are widely used, they are not devoid of disadvantages: congestion of the power conditioning system, increase of the construction cost of the SCP, and reduction of efficiency.

Fang Z. Peng [1], to solve the problems mentioned earlier, proposed a new structure in 2002; it is the Z-source inverter.

Previous studies by many researchers have been carried out to study the influence of Z-source inverters on the photovoltaic systems and numerous works have been published to this effect [2-6].

In this paper, a comparative study between the different topologies will be held, by simulating ZSI in MATLAB/Simulink using simple boost control.

II. DIFFERENT TOPOLOGIES OF THE ZSI

A. Two level ZSI

A two level Z-source inverter is shown in Fig. 1, with six switches that can buck/boost the input dc voltage fed into the Z-source network consisting of equal values of L & C through a series diode. The simple boost PWM is used to control the six switches of the inverter.

Here a filter circuit would be added, if required between the source and impedance network to supply a smooth dc power to the network so as to obtain better characteristics of the system or before the load [7].

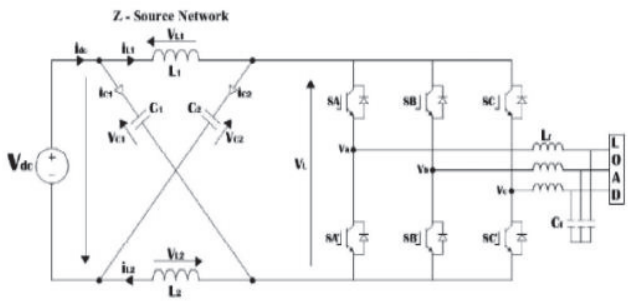

Figure 1. Two level Z-source inverter [7].

B. Two level embedded ZSI

A two level embedded Z-source inverter as shown in Fig. 2. The isolated sources can simply be obtained by rerouting the existing PV panels or cell units already needed in producing the required voltage and current ratings.

Even if one of the sources fails to feed power to the system at times of interruptions or fault conditions, continuous operation is possible by feeding power from the other source [7].

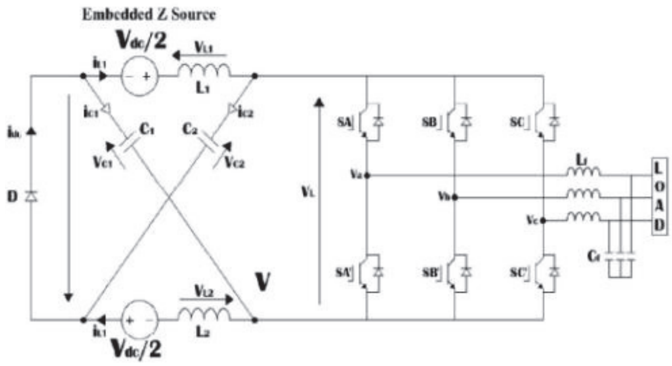

Figure 2. Two level embedded Z-source inverter [7].

C. *Two level dc link Embedded ZSI*

The dc sources are now embedded within the inverter dc link as shown in Fig. 3, known as dc link embedded Z-source inverter [7].

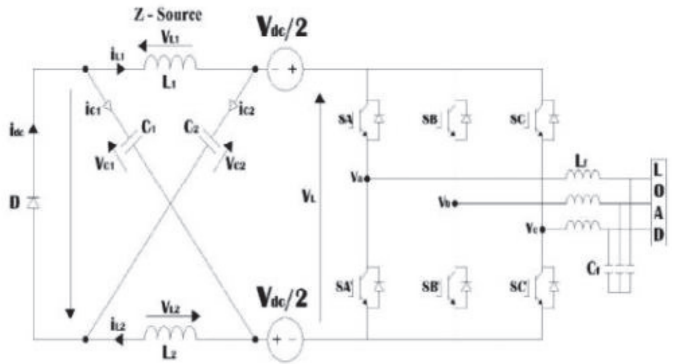

Figure 3. Two level dc link embedded Z-source inverter [7].

III. SIMPLE BOOST CONTROL FOR ZSI

The Simple Boost control is simple and easy to implement. However, the Shoot-Through cyclic ratio obtained D decreases with the increase of the modulation rate M.

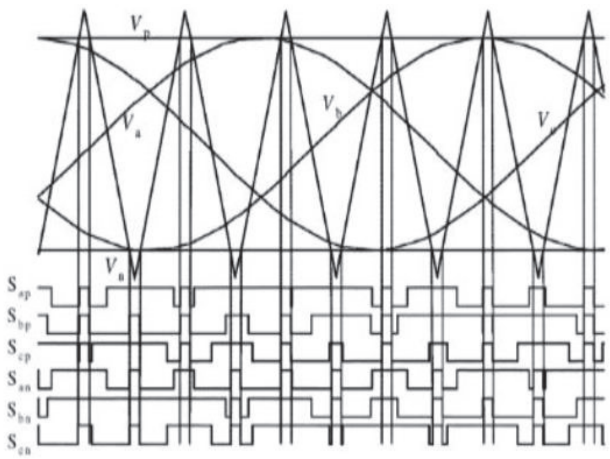

Figure 4. Simple boost control waveform [8].

The maximum Shoot-Through cyclic ratio of the Simple Boost control is limited to 1-M for a particular operation, reaching zero for a modulation rate equal to 1 [8]. Therefore, the operation with a high modulation rate for the Simple Boost control, leads to a low output voltage. In order to generate an output voltage that requires a high voltage gain, a low modulation rate must be used [8].

In fact, this control strategy inserts the Shoot-Through in all the null states of traditional PWM during a switching period, which keeps the six active states unchanged as in conventional carrier PWM [8].

IV. SIMULATION RESULTS

A comparative study between the different topologies will be held, by simulating ZSI using simple boost control. These different topologies have been simulated in MATLAB/Simulink. Tables (I) and (II) summarizes the selected system parameters for the simulation.

TABLE I. OPEN LOOP SIMULATION DATA

Vdc (V)	L (mH)	C (mF)	fref (Hz)	fp (Hz)	Vp	M	B	Rch (Ω)
100	1.5	1	50	5000	0.7	0.7	2.5	200

TABLE II. FILTER CHARACTERISTICS

Lf (mH)	Cf (mF)	fcut (Hz)
3	0.5	130

A. *Two level ZSI*

We illustrate the architecture of the system studied in the figure 5.

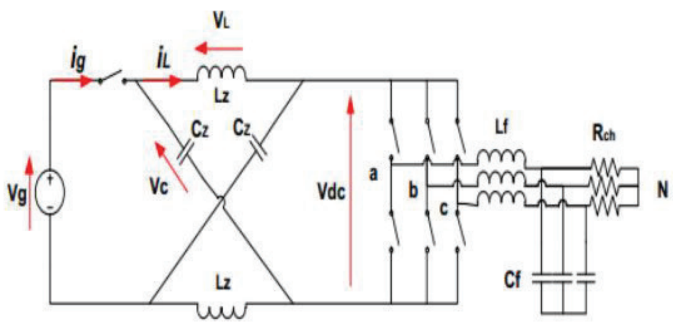

Figure 5. Two levels Z-source inverter architecture [9].

Fig. 6 shows the modulation, the attack signals for the six switches and the ST signals of the simple boost control process. The simulation results of the single boost control of the energy conversion system are shown in figures (7) to (12). These results were obtained by imposing the max value D=0.3, which gives a simple voltage to the inverter output of the maximum value, calculated as follows:

$$V_{ch} = M * B * \frac{V_g}{2} = 0.7 * 2.5 * \frac{100}{2} = 87.5\ V$$

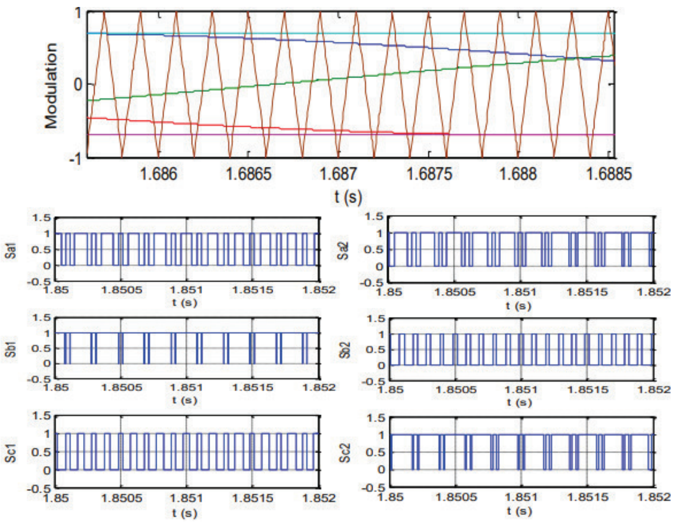

Figure 6. Pulse-width modulation (PWM) control method.

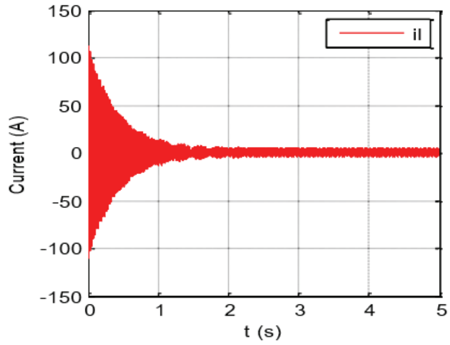

Figure 7. Current passing through inductance.

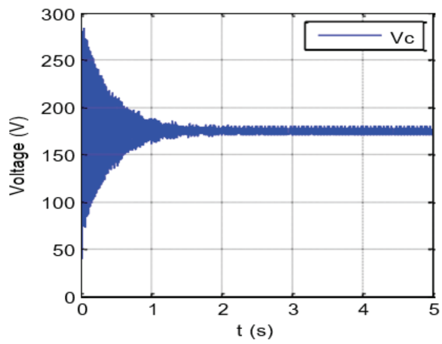

Figure 8. Voltage at capacitor terminals.

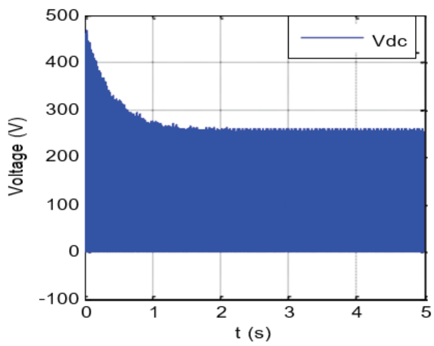

Figure 9. Continuous bus voltage.

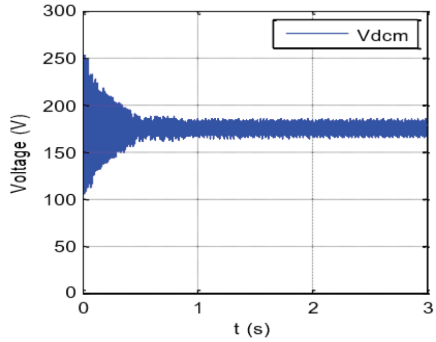

Figure 10. Continuous bus average voltage.

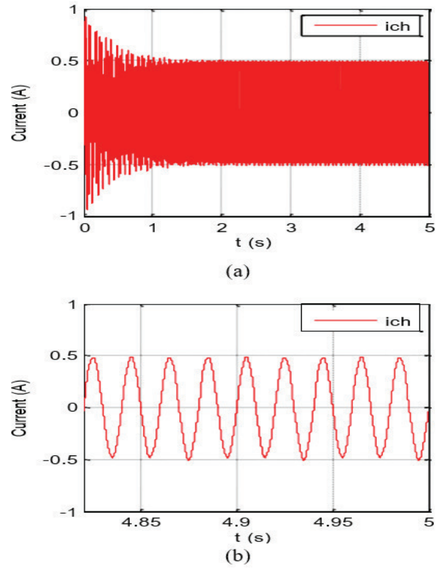

Figure 11. Charge current and zoom.

In Fig. 11, line currents have a maximum value of 0.44A, which can be calculated as follows:

$$I = \frac{V}{Z} = \frac{87.5}{200} = 0.44\ A$$

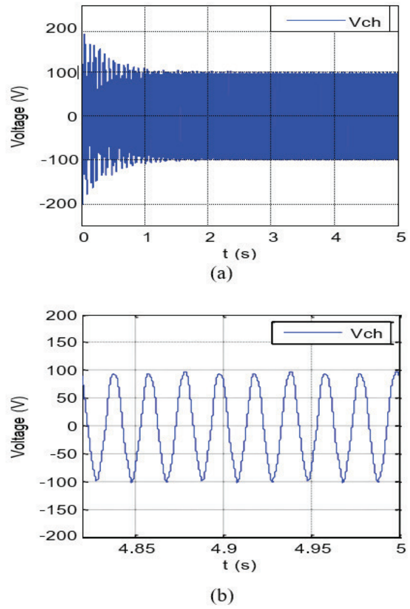

Figure 12. Charge voltage and zoom.

B. *Two level embedded ZSI*

We illustrate the architecture of the system studied in the figure 13. The simulation results are shown in figures (14) to (18).

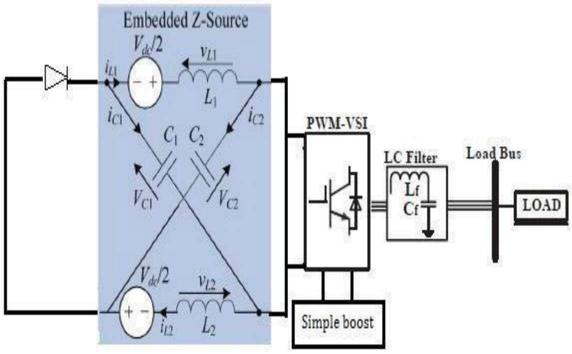

Figure 13. Two level embedded ZSI architecture [7].

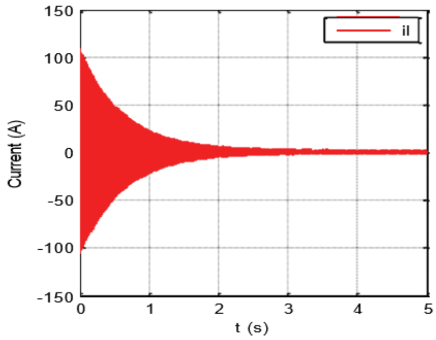

Figure 14. Current passing through inductance.

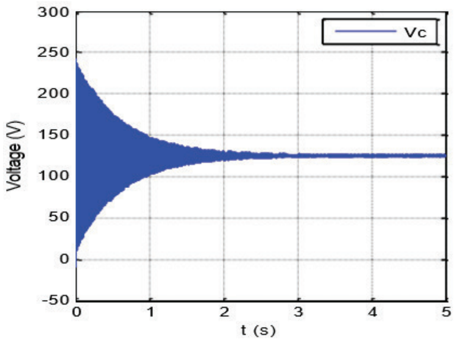

Figure 15. Voltage at capacitor terminals.

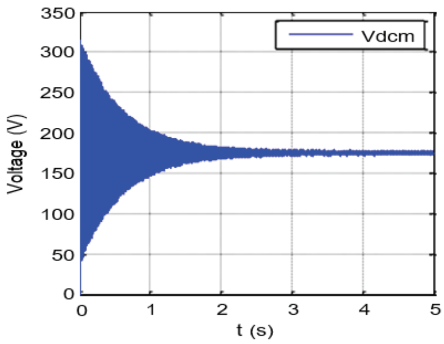

Figure 16. Continuous bus average voltage.

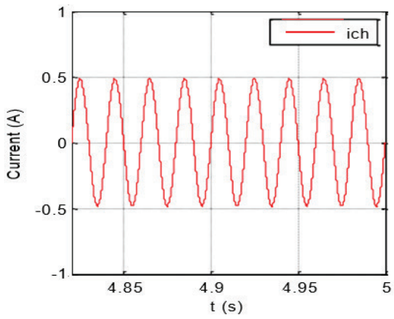

Figure 17. Charge current.

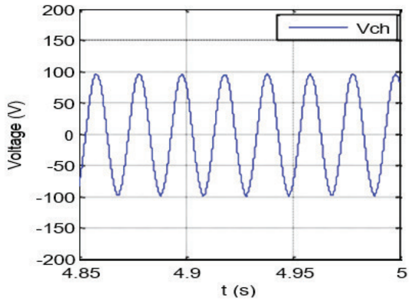

Figure 18. Charge voltage.

From this results, we can observe that the embedded Z-source inverter has better voltage boosting capability with smooth waveform compared with the two level Z-source inverter.

C. *Two level dc link Embedded ZSI*

We illustrate the architecture of the system studied in the figure 19. The simulation results are shown in figures (20) to (23).

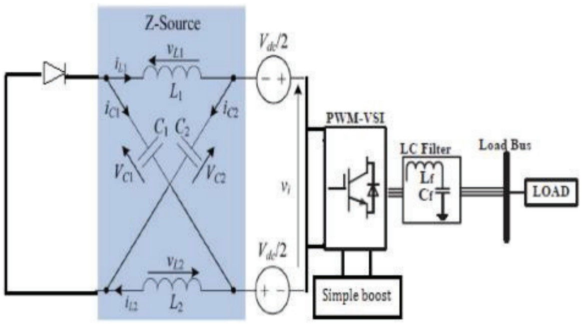

Figure 19. Charge voltage.

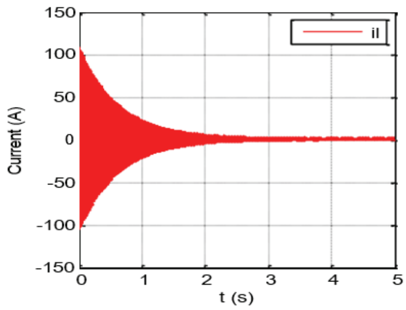

Figure 20. Current passing through inductance.

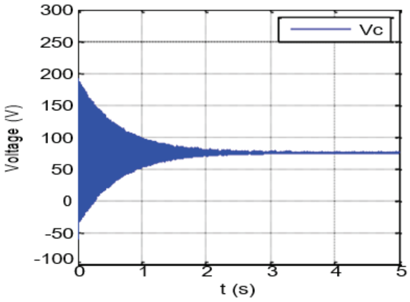

Figure 21. Voltage at capacitor terminals.

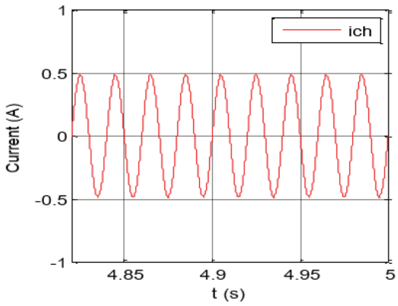

Figure 22. Charge current.

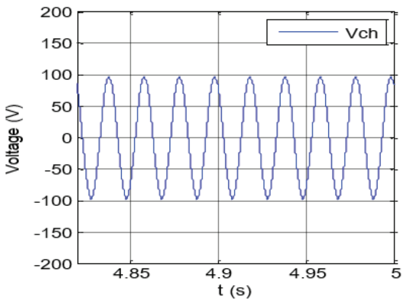

Figure 23. Charge voltage.

The simulations conducted revealed the following:

- The embedded Z-source inverter has better voltage boosting capability with smooth waveform compared with other two level topologies.
- Choice of L inductance and C capacity is important the possibility of Z-source inverter over-voltage.
- The Z-source inverter can receive inputs of different values from the given PV installation and produce the same output with less total harmonic distortion.
- Recent topologies of Z-source inverters handled two or more sources independently and sends energy to the load, even if one source fails.

V. CONCLUSION

In this paper, we simulated three topologies of the two Z-source inverters, which are the two levels ZSI, the two level embedded ZSI and the two level dc link embedded ZSI to discuss the difference between the three inverters and extract the advantages and disadvantages of each of the three.

REFERENCES

[1] F. Z. peng, "Z-source inverter," IEEE Transactions on Industry Applications , vol. 39, no. 2, pp. 504-510, 2003.

[2] D. Sera, R. Teodorescu, and P. Rodriguez, "PV panel model based on datasheet values", IN Proc. IEEE Int. Symp. Ind. Electron. (ISIE), pp. 2392-2396, 2007.

[3] H. Patel, and V. Agarwal, "MATLAB-based Modeling to Study the Effects of Partial Shading on PV Array characteristics", IEEE Transactions on Energy Conversion, Vol. 23, No. 1, pp. 302-310, 2008.

[4] M. G. Villalva, J. R. Gazoli and E. R. Filho, "Comprehensive Approach to Modeling and Simulation of Photovoltaic Arrays", IEEE Transactions on Power Electronics, Vol. 24, No. 5, pp. 1198- 1208, 2009.

[5] A. Chatterjee, A. Keyhani and D. Kapoor, "Identification of Photovoltaic Source Models", IEEE Transactions on Energy Conversion, Vol. 26, No. 3, pp. 883- 889, 2011.

[6] E. V. Paraskevadaki, S. A. Papathanassiou, "Evaluation of MPP Voltage and Power of mc-Si PV Modules in Partial Shading Conditions", IEEE Transactions on Energy Conversion, Vol. 26, No. 3, pp. 923-932, 2011.

[7] P. C. Loh, F. Gao and F. Blaabjerg, "Embedded EZ-Source Inverters", IEEE Transactions on Industry Applications,Vol. 46, No. 1, pp.256-267, 2010.

[8] J. Li, J. Liu, and Z. Liu, "Loss Oriented Evaluation and Comparison of Z-Source Inverters Using Different Pulse Width Modulation Strategies", IEEE Applied Power Electronics Conference and Exposition, pp. 851 - 856, 2009.

[9] C. Ibtissam, B. Asma, H. F. Zahra, B. Ouarda and B. El-Madjid, "Comparative study between diffirent control strategy of the z-source inverter," 2017 5th International Conference on Electrical Engineering - Boumerdes (ICEE-B), Boumerdes, Algeria, 2017, pp. 1-6, doi: 10.1109/ICEE-B.2017.8192064

Potential use of biomass waste for crystal dye removal: Isotherm , thermodynamic and mechanism of adsorption

Kelthoum SAADALLAH, Chifaa AD, Mebrouk DJEDID, Mokhtar BENALIA
Dept. Process engineering, Laghouat University
Laboratory of process engineering
Laghouat, Algeria
K.saadallah@lagh-univ.dz

Abstract— **Biomass, which originates from organic matter such as trees, plants, and agricultural residues, exhibits advantageous attributes including affordability, abundant supply, cost-effectiveness, and high efficacy. These qualities render biomass a feasible choice for the purification of water contaminated with dyes through the process of adsorption. Consequently, biomass is regarded as a sustainable energy source with potential for future utilization. The aim of this study was to examine the efficacy of pea peels material (PP) as a cost-effective and environmentally friendly alternative adsorbent for the removal of crystal violet (CV) dye from aqueous solutions. Several physicochemical parameters, including contact time, concentration, adsorbent dosage, pH, and temperature, were investigated to determine their effect on batch-mode adsorption. A wide range of CV concentrations (15-150 mg/L), pH values (2-10) and temperatures (25-45°C) were examined. Langmuir and Freundlich isotherm models were used to analyze adsorption data. The research concludes that the Freundlich isotherm model describes experimental data precisely. The Freundlich constant (n) indicate that adsorption is favorable. The thermodynamic study has shown that the positive value of the exchanged standard enthalpy (ΔH = 28.055 kJ/mol) calculated using the Van't Hoff equation indicates that the adsorption process is endothermic, At various temperatures, negative standard enthalpy values (ΔG) spanning from -12.54 to -11,55 KJ/mol confirms the spontaneity of CV dye adsorption. The study demonstrates that pea peels (PP) can serve as a promising, cost-effective adsorbent and sustainable energy source for the efficient removal of Crystal Violet from aqueous solution.**

Keywords*- *pea peels; aqueous solution; Crystal Violet; adsorption; isotherm; thermodynamic.

I. INTRODUCTION

Water pollution has become a major environmental challenge in the 21st century, devastatingly affecting the environment and human health. Various industries, including chemicals, textiles, tanneries, food, and pharmaceuticals, are the primary contributors to water pollution. These industries release waste containing harmful substances like hydrocarbons, phenolic compounds, heavy metals, pesticides, and dyes [1, 2]. Among these pollutants, dyes significantly threaten human and environmental health. Dyes are coloring substances that possess toxicological properties and have been identified as potential carcinogens. [3]. Crystal violet, a cationic dye, belongs to the triarylmethane dye class and is extensively used as a coloring agent in various industries, such as textile, paper, leather, additives, ink, and cosmetics. Additionally, it is used in analytical chemistry and biochemistry as a pH indicator. However, the substance possesses toxic properties that can irritate the eyes, skin, and digestive tract, leading to long-term damage to the cornea and conjunctiva. In severe cases, it can cause respiratory and kidney failure and even lifelong blindness. Discharging wastewater containing crystal violet into aquatic ecosystems can lead to environmental degradation as the dye gets reduced to form leuco moiety, specifically leucocrystal violet [4-6]. However, several physicochemical and biological methods exist for decolorizing dye-laden effluents. Adsorption stands out as the most efficient technology capable of removing a more significant amount of color from polluted water when the appropriate adsorbent is chosen [7- 9]. Adsorption offers several advantages, including ease of operation, low energy requirements, insensitivity to toxic pollutants, and high efficiency. Additionally, it can remove a wide range of dyes without generating secondary pollutants [10-12]. Selecting an appropriate adsorbent is a crucial step in the adsorption process. Extensive research has been conducted to investigate various materials for dye adsorption, and in recent years, natural and agricultural materials have emerged as promising options for the adsorptive removal of pollutants from the liquid phase. Researchers have been exploring affordable and efficient alternatives to activated carbon, and peel-based materials like banana peel, hydnocarpus pentandra, pineapple peel, and mandarin peel have shown a capacity of dye removal of the order of 85–90% [13]. The present research aims to explore the adsorptive removal of crystal violet dye onto pea peel material. The study additionally incorporates the utilization of isotherm and thermodynamic modeling techniques to analyze the process being investigated.

I. TECHNICAL SPECIFICATIONS

Adsorption isotherms, also known as equilibrium data, are necessary to analyze and design adsorption systems. These isotherm models shed light on the mechanics of adsorption and surface characteristics. This study investigated the adsorption capacity of an agricultural waste (pea peels) for eliminating crystal violet from an aqueous solution by applying the experimental data on Langmuir and Freundlich isotherm models. In addition, this study includes the determination of the thermodynamic parameters of change in enthalpy, entropy, and Gibbs free energy.

A. Langmuir specification

Langmuir isotherm is valid for monolayer adsorption on a homogenous adsorbent surface with a finite number of identical sites assuming no interaction between adsorbate molecules.

The linear form of the Langmuir isotherm [6] is given by: Equation (1).

$$\frac{1}{q_e} = \frac{1}{q_{\max}.K_L}\frac{1}{C_e} + \frac{1}{q_{\max}} \quad (1)$$

Where qe is the equilibrium amount of dye adsorbed on the surface of adsorbent (mg/g); Ce is the equilibrium dye concentration in solution (mg/L); qmax is the monolayer capacity of the adsorbent (mg/g); KL is the Langmuir constant. .

B. Freundlich specification

The Freundlich isotherm, on the other hand, is an empirical equation based on the premise that the heat of adsorption is distributed uniformly over a heterogeneous surface. The well-known logarithmic form of the Freundlich isotherm is given by the equation below [14].Equation (2) is a linear form of Freundlich isotherm model:

$$\ln q_e = \ln K_f + \frac{1}{n}\ln C_e \quad (2)$$

Where, C*e* (mg/ L) is dye concentration at equilibrium; qe (mg/g), is dye adsorption capacity at equilibrium; KF (L/mg), Freundlich constant related to the adsorption energy and n (L/g) is Freundlich constant [3].

C. Thermodynamic parameters

Gibbs free energy, enthalpy, and entropy are three thermodynamic metrics that can be used to determine the type of adsorption and feasibility of process. A straight line is produced when we plot lnKc against 1/T. Where T is the temperature in kelvin, and R is the universal gas constant, which has the value of 8.314 J/ mol K [15, 16].Relation between thermodynamic parameters is given by the following "Equations (3-4)"

$$\Delta G = \Delta H - T\Delta S \quad (3)$$

$$\ln Keq = -\frac{\Delta H}{RT} + \frac{\Delta S}{R} \quad (4)$$

III. EXPERIMENTAL METHOD

A. Adsorbent preparation

In this study, pea peels were procured from a local market in Laghouat city and underwent a thorough washing process using both tap water and distilled water to eliminate contaminants. The sample was then air-dried for several days then dried in a desiccator at 105 °C for 24 hours to eliminate residual moisture. The dried pea peels (PP) were ground using an electric grinder for 15 minutes to reduce particle within the range of 0.5 to 2 mm , hence increasing the specific surface area. A sieve technique was subsequently employed to obtain a uniform particle size for the milled material. The obtained material was then stored in a vacuum-sealed container for a subsequent adsorptive experiment.

B. Adsorbate preparation

In this investigation, the cationic dye selected was Crystal Violet (CV), which has a chemical formula of $C_{25}N_3H_{30}Cl$ and a molar mass of 407.979 g/mol. . To prepare the dye solutions, a stock solution of Crystal Violet was first prepared by dissolving 1 gram of the dye in 1000 milliliters of distilled water, resulting in a concentration of 1000 milligrams per liter. The dye solutions were then prepared by diluting the stock solution with distilled water, yielding 15-150 mg/L **.**

C. Adsorption experiment

To investigate the adsorption capacity of untreated pea peels in removing Crystal Violet from an aqueous solution, batch adsorption studies were carried out using a thermostatic orbital water shaker (Nuve ST 30). In each experiment, 0.6 g of PP was added to 50 mL of a colored solution with a concentration range of 15-150 mg/L and temperature range of 25-45 °C. The flasks were agitated at 150 rpm until equilibrium was achieved after 60 minutes, and the adsorbent was then filtered out. The concentration of the dye was determined using a UV/VIS spectrophotometer at a specific wavelength of 664 nm. The experimental procedure was repeated three times for each run to ensure precision. The amount of adsorption at time t, qt (mg/g), was calculated by using Equation (5). Before conducting the measurements, the solutions were appropriately diluted to achieve absorbance values within the range of 0-1. The amount of adsorption at time t, qt (mg/g), was calculated by [3]: "Equation (5).

$$q_t = \frac{(C_0 - C_{res}) \times V}{m} \quad (5)$$

Where C_0 is the initial dye concentration (mg/L); Cres is the residual dye concentration at any time (mg/L), V is volume of solution (L); m is the mass of the adsorbent (g); At equilibrium, C_{res} is equal to C_{eq} and q is equal to q_{eq}.

IV. ATTAINED RESULTS

A. *Equilibrium Modelling Application*

An isotherm model is required to mathematically depict the equilibrium relationship between the dye concentration in solution and the quantity of dye adsorbed by an adsorbent. This study has been undertaken on two key models, specifically the Langmuir model and Freundlich isotherm models.

1) *Langmuir isotherm*

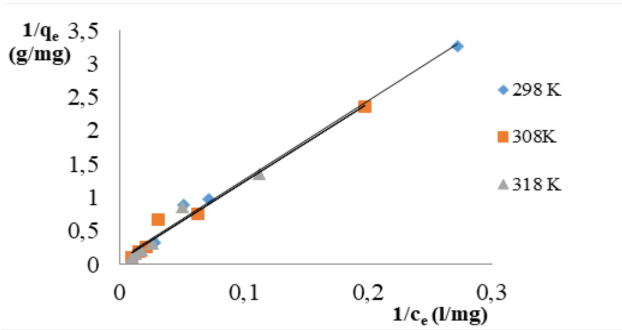

Figure 1. Langmuir isotherm for CV adsorption onto pea peels powder

2) *Freundlich isotherm*

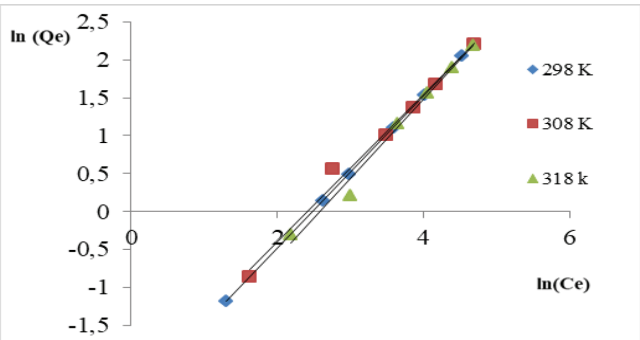

Figure 2. Freundlich isotherm for adsorption of CV onto pea peels powder

Table 1 presents the results obtained from the adsorption studies. It is clear from the data that the Freundlich model exhibits a significantly higher coefficient of determination (R2) value range of 0.9861 to 1 compared to the Langmuir isotherm. This finding indicates that the collected data aligns more closely with the Freundlich adsorption model, suggesting that the adsorption of CV on PP follows a multilayer adsorption mechanism. Moreover, the Freundlich constant (n) serves as an indicator of the viability of the adsorption process. This result is consistent with the literature [17, 18, 19], where the adsorption of CV was found not to follow Langmuir isotherm.

TABLE 1. MODELLING PARAMETERS FOR THE LANGMUIR AND FREUNDLICH ADSORPTION PROCESS.

Model	**Langmuir model**			**Freundlich model**		
T (K)	**KL(l/mg)**	**QL(mg/g)**	**R2**	**n**	**KF(l/mg)**	**R2**
298	*0,0063*	*13,4589*	*0,9911*	*1*	*0,0833*	*1*
308	*0,0056*	*15,2672*	*0,9805*	*1,0318*	*0,0970*	*0,9898*
318	*0,0022*	*37,3134*	*0,9586*	*0,9558*	*0,0669*	*0,9861*

The results noted above were attained under the following conditions: (pH of the solution, adsorbent dosage: 0.6g, initial concentrations 15-150 mg/L, V=50ml ,agitation rate: 150 rpm)

B. *Thermodynamic study*

The experiment aimed to investigate the thermodynamic behavior of CV adsorption using pea peels (PP). Using Equations (3) and (4), the researchers calculated the changes in Gibb's free energy (G), entropy (S), and enthalpy (H) and presented them in Table 2. The enthalpy of adsorption (ΔH) was calculated to be +28.05 kJ mol−1, indicating that the adsorption process is endothermic. This suggests increased temperature promotes contact between CV molecules and the PP surface The enthalpy change observed in the 10–40 kJ mol−1 range corresponds to physisorption, while the 40–1000 kJ mol−1 range indicates the chemisorption process [20]. The enthalpy change (ΔH) observed in this investigation falls within the range associated with the physisorption phenomenon. The change in entropy, ΔS, was +0.537 kJ mol−1 K−1, indicating an increase in disorderliness at the interface between the solid (PP) and liquid (CV) phases during adsorption. This increase in entropy suggests the potential fragmentation of dye molecules following adsorption. The presence of fragmentations inside the suspension can persist and contribute to an overall rise in entropy [21]. Using the values of ΔH and ΔS, the researchers also calculated the values of ΔG, organized in Table 2. The Gibbs free energy values (ΔG) were negative, indicating that the adsorption process is spontaneous and becomes increasingly favorable as thetemperaturerises[22].

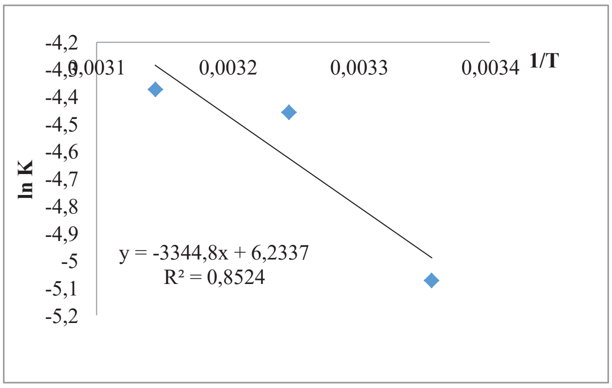

Figure 3. Plot of lnK versus 1/T for adsorption of aqueous crystal violet onto pea peels with varying temperature.

TABLE 2: DATA FOR ESTIMATING THE THERMODYNAMIC PARAMETERS FOR ADSORPTION OF CRYSTAL VIOLET ON PEA PEELS.

T (K)	ΔG (KJ/mol)	ΔS (KJ/mol.K)	ΔH(KJ /mol)
298	-12.548	0.537	28.055
308	-11.406		
318	11,554		

V. CONCLUSION

The present study aimed to evaluate the adsorption of crystal violet from aqueous solution using pea peels in a batch experiment. The results of the isothermal and thermodynamic analyses indicate that the Freundlich isotherm model provides the most accurate description of the experimental data. This suggests that the adsorption of CV on PP can be attributed to a multilayer adsorption mechanism. The thermodynamic study suggests that the system exhibits spontaneity and is characterised by an endothermic process involving physical interactions between the adsorbent and adsorbate. The study's findings indicate that the use of pea skins powder, which is a both low cost and readily accessible, exhibit significant as sustainable adsorbent for successfully eliminating crystal violet dye from aqueous solutions.

REFERENCES

[1] Al Rubai, H. F., Hassan, A. K., Sultan, M. S., & Abood, W. M. "Kinetics of Adsorption of Reactive Red 120 Using Bentonite Modified by CTAB and Study the Effect of Salts,"*Nature Environment and Pollution Technology*, *vol 20,*1,2021, pp.281-289.

[2] Shakoor, S., & Nasar, A." Adsorptive treatment of hazardou methylene blue dye from artificiallycontaminated water using cucumis sativus peel waste as a low-cost adsorbent", *Groundwater for Sustainable Development*, *vol 5*, 2021, pp 152-159.

[3] Batool, M., Javed, T., Wasim, M., Zafar, S., & Din, M. I. "Exploring the usability of Cedrus deodara sawdust for decontamination of wastewater containing crystal violet dye", *Desalination and Water Treatment*,vol *224*, 2021, pp433-448.

[4] A. Mittal, J. Mittal, A. Malviya, D. Kaur, V.K. Gupta. "Adsorption of hazardous dye crystal violet from waste water by waste materials", J. Colloid Interface Sci, vol 343,2010, pp 463–473.

[5] A.L. Prasad, T. Santhi. "Adsorption of hazardous cationic dyes from aqueous solution onto Acacia nilotica leaves as an eco-friendly adsorbent", Sustainable Environ. Res, vol 22, 2012, pp 113–122.

[6] S. Senthilkumar, P. Kalaamani, C.V. Subburaam. "Liquid phase adsorption of crystal violet onto activated carbons derived from male flowers of coconut tree", J. Hazard. Mater.,vol 136 ,2006,pp 800–808.

[7] Qi, J., Li, X., Zheng, H., Li, P., & Wang, H. " Simultaneous removal of methylene blue and copper (II) ions by photoelectron catalytic oxidation using stannic oxide modified iron (III) oxide composite electrodes", *Journal of Hazardous materialsv*, *vol293*, 2015, pp105-111.

[8] Asfaram, A., Ghaedi, M., Ghezelbash, G. R., Dil, E. A., Tyagi, I., Agarwal, S., & Gupta, V. K." Biosorption of malachite green by novel biosorbent Yarrowia lipolytica isf7: application of response surface methodology", *Journal of Molecular Liquids*, *vol 214*, 2016, pp 249-258.

[9] Yagub, M. T., Sen, T. K., Afroze, S., & Ang, H. M. (2014). "Dye and its removal from aqueous solution by adsorption: a review", *Advances in Colloid and Interface Science*,vol *209*, 2014, pp 172-184.

[10] Kyzas, G. Z., & Matis, K. A. "Nanoadsorbents for pollutants removal: a review",*Journal of Molecular Liquids*, *vol203*, 2015, pp159-168.

[11] Ngulube, T., Gumbo, J. R., Masindi, V., & Maity, A. "An update on synthetic dyes adsorption onto clay based minerals: A state-of-art review", *Journal of environmental management*, *vol191*, 2017, pp35-57.

[12] Rad, L. R., & Anbia, M. "Zeolite-based composites for the adsorption of toxic matters from water: A review", *Journal of environmental chemical engineering*, *vol 9*(5), 2017, pp106088.

[13] Mahajan, Prashant G., and Dipika Jaspal. "Application of Peel-Based Biomaterials in Textile Wastewater." *Textile Wastewater Treatment: Sustainable Bio-nano Materials and Macromolecules, s*ingapore: Springer Nature Singapore, vol 2,2022, pp55-70.

[14] Shakoor, S., & Nasar, A."Adsorptive treatment of hazardous methylene blue dye from artificially contaminated water using cucumis sativus peel waste as a low-cost adsorbent", *Groundwater for Sustainable Development*, *vol 5*, 2017, pp152-159.

[15] Liu, X., & Lee, D.-J. "Thermodynamic parameters for adsorption equilibrium of heavy metals and dyes from wastewaters", *Bioresource Technology*, *vol160*, 2014, pp24-31.

[16] Ouass, A., Kadiri, L., Essaadaoui, Y., Belakhmima, R. A., Cherkaoui, M., Lebkiri, A., & El Housseine, R. " Removal of trivalent chromium ions from aqueous solutions by Sodium polyacrylate beads", *Mediterranean Journal* ,2018.

[17] Chandrasekaran Muthukumaran, Vaiyazhipalayam MurugaiyanSivakumar, Marimuthu Thirumarimurugan, "Adsorption isotherms and kinetic studies of crystal violet dye removal from aqueous solution using surfactant modified magnetic nanoadsorbent", Journal of the Taiwan Institute of Chemical Engineers, Vol 63, 2016, pp354-362.

[18] Khan, T.A., Rahman, R. & Khan, E.A."Decolorization of bismarck brown R and crystal violet in liquid phase using modified pea peels: non-linear isotherm and kinetics modeling", *Model. Earth Syst. Environ.*, vol **2**, 2016, pp 141.

[19] D Permatasari, Buhani, M Rilyanti Suhars. " Adsorption Kinetic and Isotherm of Solution Pair of Methylene Blue and Crystal Violet by Algae-Silica-Magnetite Hybrid Adsorbent on

Porphyridium sp. Algae " Journal of Physics: Conference Series, vol 1751, 2021.

[20] McCash EM. In: Surface Chemistry, Oxford University Press, pp 54–56. https://books.google.com/books/about/Surface_Chemistry.html?id=QdJyQgAACAAJ, 2001.

[21] Messina PV, Schulz PC. "Adsorption of reactive dyes on titania–silica mesoporous materials", J Colloid Interface Sci , vol 299(1),2006, pp305–320.

[22] Li J, Huang Y, Liu Z, Zhang J, Liu X, Luo H, Ma Y, Xu X, Lu Y, Lin J, Zou J, Tang C. "Chemical activation of boron nitride fbers for improved cationic dye removal performance", Mater Chem , vol 3(15),2015, pp8185–8193.

Estimate Battery Degradation Using Kalman Filter

ASSIA Hamza
Dept. Electrical Engineering
National Polytechnic School of Oran
Oran, Algeria
hamza.assia@enp-oran.dz

ZABOURI Abdelhamid
Dept. Electrical Engineering
National Polytechnic School of Oran
Oran, Algeria
abdelhamid.zabouri@enp-oran.dz

BOULOUIHA MERABET Houari
Dept. Electrical Engineering
National Polytechnic School of Oran
Oran, Algeria
houari.merabet-boulouiha@enp-oran.dz

DENAI Mouloud
School of Physics, Engineering and
Computer Science
University of Hertfordshire
London, United Kingdom
m.denai@herts.ac.uk

***Abstract*—This paper presents a novel Kalman filter-based method for estimation of battery degradation. Accurate assessment of battery health is vital for diverse applications like electric vehicles and renewable energy systems. Our approach integrates a dynamic battery degradation model with the Kalman filter to provide responsive degradation estimates. By continually updating the model using live battery data, the method effectively tracks changes in battery health. Extensive testing across various battery types validates its superiority over traditional techniques. This research contributes a practical framework for degradation assessment, enhancing decision-making for maintenance and system performance. The proposed approach holds promise for extending battery lifespan and improving overall system efficiency through accurate degradation estimation.**

Keywords—Battery, Kalman filter, Degradation.

I. Introduction

The rising demand for efficient and sustainable energy storage solutions has accentuated the critical need for accurate assessment of battery health across various industries. Batteries play an integral role in powering a wide spectrum of applications, spanning from portable electronic devices to electric vehicles and renewable energy systems.

However, battery degradation is a complex and multifaceted phenomenon that has become increasingly important with the widespread adoption of lithium-ion batteries in various applications, including consumer electronics, electric vehicles, and energy storage systems. Degradation mechanisms describe the physical and chemical changes that occur within the battery cell, leading to a decrease in its performance and capacity over time. Understanding these mechanisms is crucial for designing experiments or models for investigating battery degradation and developing strategies to mitigate it [1,2].

Battery degradation can be caused by a variety of factors, including temperature, cycling, depth of discharge, and age. High temperatures can accelerate the degradation of the battery, leading to a decrease in its capacity and performance. Conversely, low temperatures can also affect the battery's performance, reducing its ability to deliver power. Repeated charging and discharging cycles can cause the battery to degrade over time, leading to a decrease in its capacity and performance. Discharging the battery to a low level can also lead to degradation, reducing its capacity and performance over time. As the battery ages, its performance and capacity naturally degrade, leading to a decrease in its overall lifespan [3,4]. The mechanisms of battery degradation are complex and multifaceted, involving physical and chemical changes that occur within the battery cell. Some of the most common mechanisms of battery degradation include loss of conductivity, loss of active material, loss of lithium supply, and lithium plating. Over time, the battery's internal resistance increases, leading to a decrease in its conductivity and performance [5]. The active material within the battery can degrade over time, leading to a decrease in its capacity and performance. Side reactions within the battery can consume some of the available lithium, leading to a decrease in its capacity and performance. Under certain conditions, lithium ions can plate onto the battery's anode, leading to a decrease in its capacity and performance. There are several methods for measuring and modeling battery degradation, including capacity fade, electrochemical impedance spectroscopy (EIS), cycle life testing, and mathematical modeling. Measuring the battery's capacity over time can provide insights into its degradation and performance [6]. EIS can be used to measure the battery's internal resistance and conductivity, providing insights into its degradation. Cycling the battery through repeated charge and discharge cycles can provide insights into its degradation and performance. Mathematical models can be used to simulate the battery's behavior and predict its degradation over time. There are several strategies for prolonging battery life and mitigating degradation, including temperature control, depth of discharge control, charging control, and battery management systems. Maintaining the battery at a moderate temperature can help to reduce its degradation and prolong its lifespan. Limiting the battery's depth of discharge can help to reduce its degradation and prolong its lifespan. Using the correct charging protocol can help to reduce the battery's degradation and prolong its lifespan. Implementing a battery management system can help to monitor the battery's performance and mitigate its degradation over time [7].

Addressing these challenges, this paper introduces an innovative approach that harnesses the power of the Kalman filter to estimate battery degradation. The Kalman filter, a widely employed recursive estimation technique, excels in amalgamating real-time measurements with predictive degradation models, culminating in agile and responsive degradation estimates. By seamlessly integrating a dynamic battery degradation model with the Kalman filter, we establish a robust framework that delivers accurate and dynamically adjustable degradation estimates over time.

II. MODELING OF BATTERY

Contemplate a battery model characterized by the subsequent equivalent circuit [8],

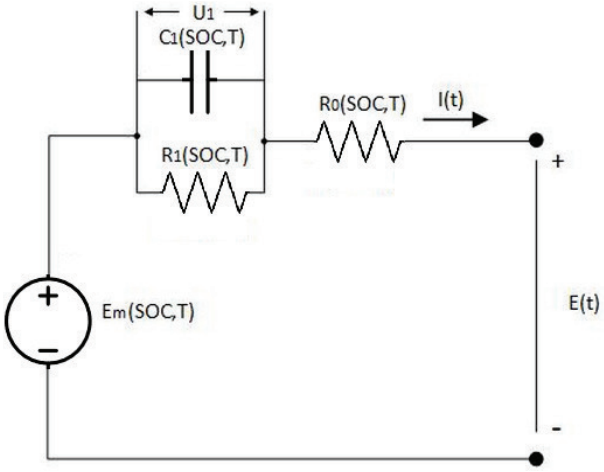

Figure 1 Equivalent circuit for a battery.

The configuration includes a voltage source E_m, a resistor arranged in series R_0, and a solitary RC unit comprising elements R_1 and C_1. The battery undergoes cycles of both charging and discharging. Within this illustration, the focus lies on gauging the battery model's state of charge (SOC), achieved through the utilization of measured currents, voltages, and battery temperature.

The equation describing the measurement is as follows,

$$E = E_m(soc, T_b) - U_1 - IR_0(soc, T_b) + V \quad (1)$$

Here, E symbolizes the recorded output voltage, R_0(SOC, T_b) represents the series resistor, $E_m = E_m$(SOC, T_b) stands for the electromotive force originating from the voltage source, and denotes V the presence of measurement noise.

The equations governing the state transition for the battery model are as follows [9],

$$\frac{d}{dt}\begin{pmatrix} SOC \\ U_1 \end{pmatrix} = \begin{pmatrix} 0 \\ -\frac{1}{R_1(soc,T_b)*C_1(soc,T_b)}U_1 \end{pmatrix} + \begin{pmatrix} -\frac{1}{3600*C_q} \\ \frac{1}{C_1(soc,T_b)} \end{pmatrix} I + W \quad (2)$$

The expressions and pertain to the thermal (R_1(SOC, T_b) and C_1(SOC, T_b)) and state-of-charge-sensitive resistor and capacitor within the RC block. Additionally, symbolizes the voltage across the capacitor, while represents the input current. Furthermore, denotes the battery temperature, stands for the battery capacity measured in ampere-hours (Ah), and accounts for the presence of process noise.

III. DESINING KALMAN FILTER FOR DEGRADATION

We gauge the battery model's state of charge (SOC) by analyzing recorded currents, voltages, and battery temperature. The underlying assumption considers the battery as a nonlinear entity, leading us to employ the Unscented Kalman Filter for SOC estimation. However, the battery's capacity undergoes degradation after each discharge-charge cycle, consequently leading to less precise SOC estimations.

To address this, we introduce an event-based linear Kalman filter. This filter comes into play during the battery's shift between charging and discharging states, facilitating the estimation of battery capacity. The derived capacity estimate serves as a pivotal indicator for the battery's overall health status.

A. Estimate State of Charge (SOC)

In the case of a generic nonlinear system $\dot{x} = f(x, u)$, discretization of the system can be represented as follows,

$$\dot{x}_T = x_T + f(x_T, u_T)T_s \quad (3)$$

The state vectors for the nonlinear battery system are as follows,

$$x_T = \begin{pmatrix} SOC_T \\ U_{1T} \end{pmatrix} \quad (4)$$

The estimated SOC is given by,

$$\begin{pmatrix} SOC_{T+1} \\ U_{1_{T+1}} \end{pmatrix} = \begin{pmatrix} SOC_T \\ U_{1_T} \end{pmatrix} + \begin{pmatrix} -\frac{1}{3600*C_q}I \\ -\frac{1}{C_1(SOC_T,T_b)R_1(SOC_T,T_b)}U_1 + \frac{1}{C_1(SOC_T,T_b)}I \end{pmatrix} T_s + W_T \quad (5)$$

Thus, the process noise W is:

$$W = \begin{bmatrix} (max(|dSOC|))^2 & 0 \\ 0 & (max(|dSOC|))^2 \end{bmatrix} \quad (6)$$

B. Estimate Battery Degradation

The representation of battery degradation involves a reduction in capacity. In this instance, the battery's capacity is configured to diminish by 1 Ah following each discharge-charge cycle, demonstrating the impact of degradation. Given the uncertainty surrounding the degradation rate of capacity, the state equation of is configured as a random walk due to the absence of advance knowledge.

$$C_{q_{k+1}} = C_{q_{k+1}} + W_{C_q} \quad (7)$$

Here, k represents the count of discharge-charge cycles, and W_{Cq} denotes the process noise.

The equation depicting the measurement for Cq is as follows,

$$C_{q_k}^{Measured} = C_{q_k} + V_{C_q} = \frac{\int_{t_{k-1}}^{t_k} Idt}{(\Delta SOC)_{Nominal}} \quad (8)$$

In this context, V_{C_q} accounts for the presence of measurement noise.

The state transition and measurement equations governing battery degradation can be formulated in the subsequent state-space configuration,

$$\begin{cases} C_{q_{k+1}} = A_{C_q}C_{q_k} + W_{C_q} \\ C_{q_k}^{Measured} = C_{C_q}C_{q_k} + V_{C_q} \end{cases} \quad (9)$$

For the integration of an event-based Kalman Filter, the activation of the state equation occurs exclusively when the event takes place. In simpler terms, the state equation also operates on an event-based basis. In the case of a linear system $x_{t+1} = Ax_t + Bu_t + \omega_t$, configure the state equation as follows [10],

$$x_{t+1} = \begin{cases} Ax_t + Bu_t + \omega_t, & t = t_{enable} \\ x_t, & t \neq t_{enable} \end{cases} \tag{10}$$

where

$$A : \begin{cases} A_{C_q}, & t = t_{enable} \\ 1, & t \neq t_{enable} \end{cases}$$

$$B : \begin{cases} C_{C_q}, & t = t_{enable} \\ 1, & t \neq t_{enable} \end{cases}$$

$$\omega_t : W_{C_q}$$

IV. SIMULATION RESULTS

The simulation is done using MATLAB-Simulink 2017b results are shown in follows figures.

Observing the simulation results in figure 2, it's evident that charging and discharging currents directly impact battery degradation. Higher currents typically contribute to accelerated degradation, as demonstrated by the decline in estimated capacity.

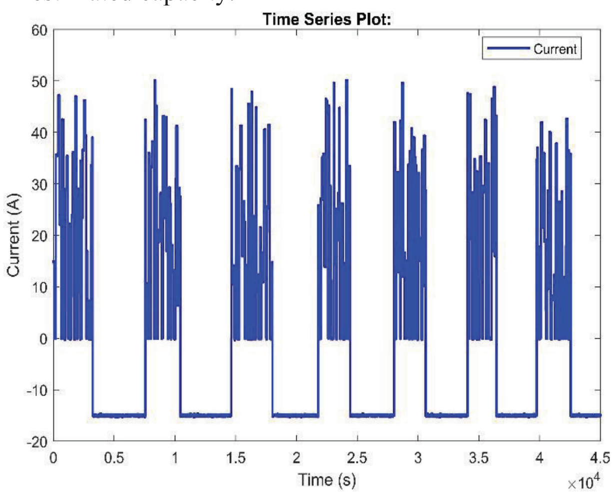

Figure 2 Current of battery durring charge and discharge states.

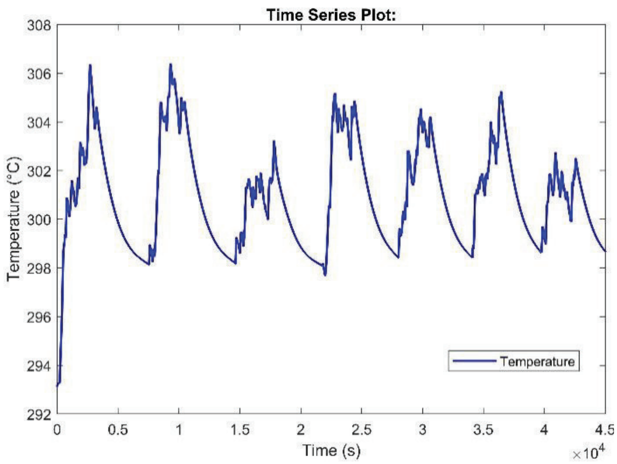

Figure 3 Temperature of battery durring charge and discharge states.

The enabling signal's shown in figure 4 role in the estimation process is evident in the simulation results. The event-based activation of the Kalman Filter state equation during transitions between charging and discharging contributes to accurate capacity estimation. The enabling signal ensures that the estimation adapts to the changing battery behavior, resulting in more precise degradation tracking.

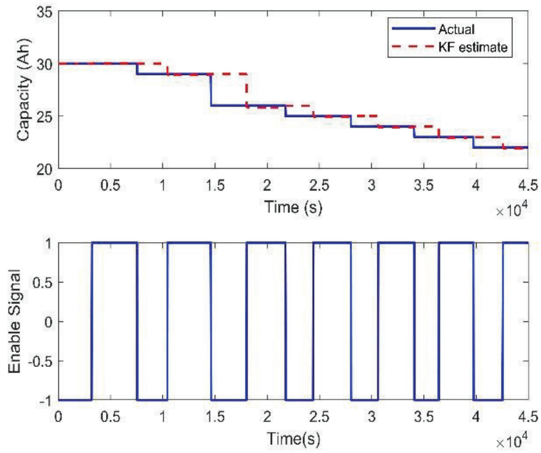

Figure 4 Measured and estimated capacity with enabling signal.

Comparing actual and estimated battery capacities provides a comprehensive view of the method's performance. The simulation demonstrates that the method effectively captures capacity degradation due to discharge-charge cycles. The estimated capacity aligns well with actual values, confirming the method's capacity prediction accuracy.

Comparing actual and estimated State of Charge (SOC) values in figure 5 underscores the method's reliability. The close alignment between actual and estimated SOC throughout the simulation signifies the model's adaptability to changing conditions and validates its predictive capabilities.

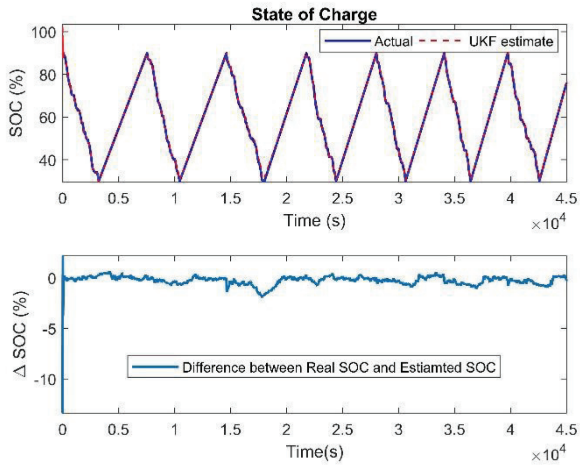

Figure 5 Actual and estimated state of charging battery.

Delta SOC, representing the discrepancy between actual and estimated SOC, provides valuable insights. Smaller delta SOC values indicate accurate estimation, especially under varying load and environmental conditions. Larger delta SOC values may arise in instances where the battery's behavior deviates from the model's assumptions, offering opportunities for further refinement.

V. Conclusion

In conclusion, the simulation results collectively validate the proposed approach's efficacy in estimating battery degradation. The assessment of charging and discharging currents, temperature variations, SOC values, delta SOC, enabling signal, and capacity reinforces the method's robustness and precision. These findings hold significant promise for optimizing battery performance, extending operational life, and bolstering overall system efficiency.

References

[1] García-Miguel, P.L.C.; Alonso-Martínez, J.; Arnaltes Gómez, S.; García Plaza, M.; Asensio, A.P. A Review on the Degradation Implementation for the Operation of Battery Energy Storage Systems. Batteries 2022, 8, 110. https://doi.org/10.3390/batteries8090110.

[2] Kemeny, M.; Ondrejka, P.; Mikolasek, M. Comprehensive Degradation Analysis of NCA Li-Ion Batteries via Methods of Electrochemical Characterisation for Various Stress-Inducing Scenarios. Batteries 2023, 9, 33. https://doi.org/10.3390/batteries9010033.

[3] de la Vega, J.; Riba, J.-R.; Ortega-Redondo, J.A. Mathematical Modeling of Battery Degradation Based on Direct Measurements and Signal Processing Methods. Appl. Sci. 2023, 13, 4938. https://doi.org/10.3390/app13084938

[4] Yao, L.; Xu, S.; Tang, A.; Zhou, F.; Hou, J.; Xiao, Y.; Fu, Z. A Review of Lithium-Ion Battery State of Health Estimation and Prediction Methods. World Electr. Veh. J. 2021, 12, 113. https://doi.org/10.3390/wevj12030113

[5] Xing, W.W.; Shah, A.A.; Shah, N.; Wu, Y.; Xu, Q.; Rodchanarowan, A.; Leung, P.; Zhu, X.; Liao, Q. Data-Driven Prediction of Li-Ion Battery Degradation Using Predicted Features. Processes 2023, 11, 678. https://doi.org/10.3390/pr11030678

[6] Shchurov, N.I.; Dedov, S.I.; Malozyomov, B.V.; Shtang, A.A.; Martyushev, N.V.; Klyuev, R.V.; Andriashin, S.N. Degradation of Lithium-Ion Batteries in an Electric Transport Complex. Energies 2021, 14, 8072. https://doi.org/10.3390/en14238072.

[7] Fanoro, M.; Božanić, M.; Sinha, S. A Review of the Impact of Battery Degradation on Energy Management Systems with a Special Emphasis on Electric Vehicles. Energies 2022, 15, 5889. https://doi.org/10.3390/en15165889

[8] R. R. Thakkar, ‘Electrical Equivalent Circuit Models of Lithium-ion Battery’, Management and Applications of Energy Storage Devices. IntechOpen, Mar. 30, 2022. doi: 10.5772/intechopen.99851.

[9] Huria, Tarun, et al. "High fidelity electrical model with thermal dependence for characterization and simulation of high power lithium battery cells." Electric Vehicle Conference (IEVC), 2012 IEEE International. IEEE, 2012.

[10] Wan, Eric A., and Rudolph Van Der Merwe. "The unscented Kalman filter for nonlinear estimation." Adaptive Systems for Signal Processing, Communications, and Control Symposium 2000. AS-SPCC. The IEEE 2000. Ieee, 2000.

The 1st National Conference on Green Energy (NCGE' 2023)
December 02, 2023, Boumerdes, Algeria.

Performance evaluation of two MPPT algorithms for a photovoltaic system using Buck converter based battery-charging controller

Kais Dyhia, Denoun Hakim, Tebri Zoulikha, Hamida Mohamed Lamine, Mohand Saidi Sabrina
Electrical Engineering Advanced Technology Laboratory (LATAGE)
Mouloud Mammeri University, Tizi Ouzou, Algeria
dyhiakais@yahoo.com, akim_danoun2002dz@yahoo.fr, zouli263@gmail.com, ml_hamida@yahoo.com, Sabrina.mohandsaidi@ummto.dz

Fekik Arezki
Department of Electrical Engineering
Akli Mohand Oulhadj University, Bouria, Algeria
arezkitdk@yahoo.fr

Abstract—**This paper presents a comparative study of various maximum power point tracking (MPPT) methods for a photovoltaic (PV) system. In this study, our system comprises a PV panel, a Buck converter and a battery. Two different MPPT methods namely perturb and observation (P&O), and Fuzzy Logic control (FLC), were applied to extract the maximum power of PV panel and optimize the performance of the solar battery charger. These techniques were tested under different solar irradiation and temperature levels to confirm the efficacy of each one.**

Keywords- PV panel; Perturb and Observation (P&O); Fuzzy Logic control (FLC), Maximum Power Point Tracking (MPPT); Buck converter; Battery charging

I. Introduction

In recent years, the depletion of fossil fuels, increasing energy demands, and growing concerns over pollution have prompted extensive research into renewable energy sources [1]. In this context, photovoltaic energy stands out as one of the significant renewable energy sources due to its effectiveness and potential for cost reduction, and offering a solution to our energy production challenge [2], [3]. These systems offer advantages such as being a clean energy sources, reliant on natural sunlight, and capable of generation electrical energy anywhere sunlight is available [4]. However, PV systems also come with certain drawback where the voltage and current of PV panels exhibit nonlinearity, and they are influenced by environmental factors such as temperature and irradiance [3].

This paper presents the implementation of a battery charging system using a buck converter, which is specifically suitable for scenarios in which the battery voltage is lower than the PV module voltage. Furthermore, the buck converter's purpose is to regulate the power flow from the PV panels to the battery, necessitation the implementation of an MPPT control algorithm to extract the peak power of the PV panel using two different method; Perturb and Observation (P&O), and Fuzzy Logic control (FLC) [1], [5].

The MPPT algorithms extract voltage and current information from the polarity of PV panels and adjust the duty cycle of PWM (Pulse Width Modulation) signals applied to the switches (MOSFET, IGBT…) in a DC-DC converter. This regulation of the duty cycle helps in controlling the voltage and current of the converter to optimize the overall performance of the system and then charging the battery [6].

II. Proposed System

The system under consideration consists of four primary components: PV array, a battery, a DC-DC buck converter and a solar charge controller MPPT [2]. The overall configuration is illustrated in fig 1.

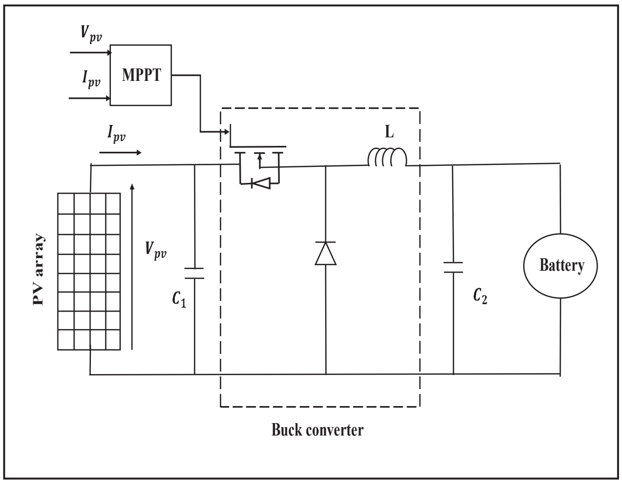

Figure 1. PV system based battery charging circuit.

A. PV panel

The PV panels operate based on the photovoltaic effect of a semiconductor PN junction. When exposed to light, they generate a direct current (DC). The magnitude of the generated current is directly related to the intensity of solar irradiance [7].

The PV cell's equivalent circuit, as depicted in fig 2, comprises two resistances and a diode. The parallel resistance R_p represents losses resulting from small leakage current flowing through a parallel path, and the series resistance R_s accounts for losses in the metal grid and current collection bus. The diode represents a cross current associated with the PN junction of the semiconductor device [8].

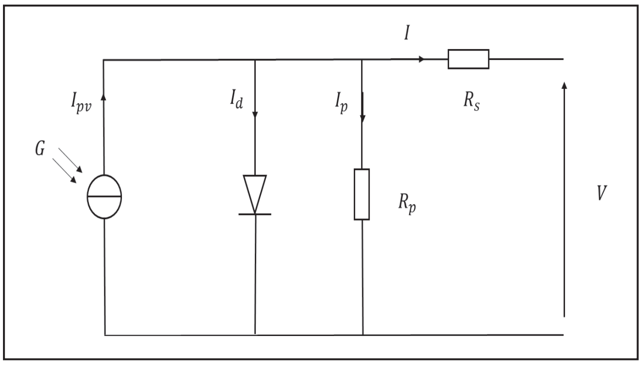

Figure 2. Electric circuit of PV cell.

The following sequence of equations will calculate the final usable current of the PV cell [7].

$$I = I_{ph} - I_d - I_P \tag{1}$$

The individual current components are given in Equations (2,3) and (4):

$$I_{ph} = \left(I_{scn} + K_i\left(T - T_n\right)\right)\frac{G}{G_n} \tag{2}$$

$$I_d = I_{sat}\left(\exp\left(\frac{V + R_S}{V_T}\right) - 1\right) \tag{3}$$

$$I_p = \frac{V + R_s I}{R_P} \tag{4}$$

Where:

$$I_{sat} = \frac{I_{scn} + K_i\left(T - T_n\right)}{\exp\left(\left(V_{OC} + K_v\left(T - T_n\right)\right)/V_T\right) - 1} \tag{5}$$

$$V_T = \frac{\alpha K T}{q} \tag{6}$$

Where T_n is the standard operating temperature (25 °C or 298 K), G_n is the standard irradiation (1000 W/m^2), I_{scn} is the short circuit current output at standard temperature and irradiation, K_i is the temperature coefficient of the short circuit current variation from standard temperature, K_v coefficient of open circuit voltage and T and G are the ambient temperature and irradiation, V is the voltage across the diode, q is the electron charge (1.602 × 10−19 C), K is the Boltzmann constant (1.3805 × 10−23 J/K), V_T is called the thermal voltage, V_{OC} is the open circuit voltage of the PV cell.

B. Buck converter

The buck converter is known as the voltage step down and current step up converter [2]. In this configuration, the conversion ratio, noted by $M = V_{out}/V_{in}$, varies with the duty cycle of the switch.

C. Battery

The battery used in the suggested system was a lead-acid cell battery, rating of 12V voltage and having a charging capacity of 100Ah [2], [7].

D. MPPT controller

Typically, solar panels can only convert a small quantity of the total solar irradiance into electrical energy. Therefore, the performance of a specific solar panel can be enhanced using MPPT [2].

MPPT is an algorithm included in the controllers to extract the maximum power from the solar panel and transmit this power from the PV panel to the load. This control principle involves the automatic adjustment of the duty cycle α. Among the existing methods, we have chosen to study two techniques [3].

a. (P&O) method

The perturbation and observation (P&O) method is widely used approach in MPPT research due to its simplicity and minimal requirements. It only relies on voltage and current measurements of the photovoltaic panel. This method can effectively detect the Maximum Power Point (MPP) even under varying illumination and temperature conditions. As its name suggests, this technique operates by perturbing the voltage and observing the resulting impact on the output power of the photovoltaic panel [2], [5].

The operating voltage of the PV panel is perturbed in a specific direction. If the power drawn from the PV increases, it indicates that, the operating point has moved closer to the MPP. Consequently, the operating voltage must be further perturbed in the same direction. On the other hand, if the power drawn from the PV decreases, it implies that the operating point has moved away from the MPP. Thus, the direction of the operating voltage perturbation must be reversed [1], [9]. The flowchart of this method is depicted in figure below [10].

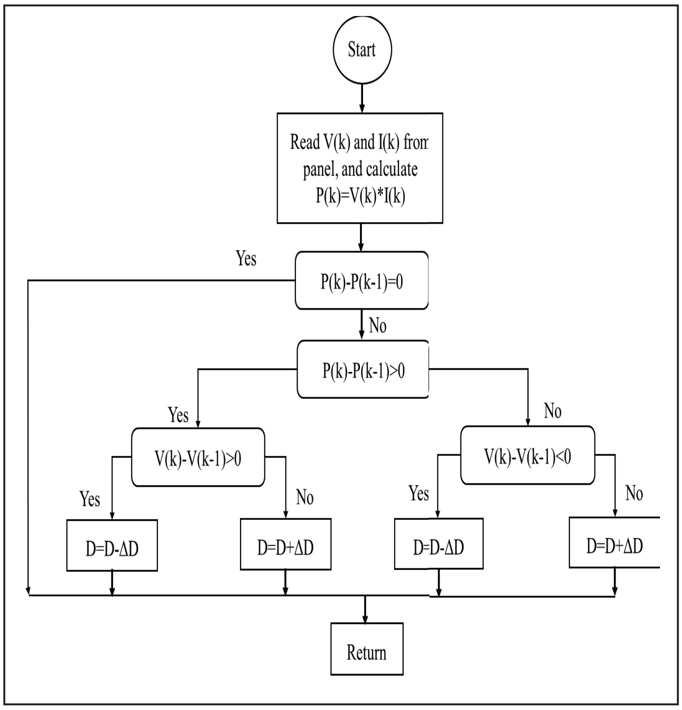

Figure 3. Flowchart of P & O method.

b. FL control

Lately, fuzzy logic control has gained popularity in MPPT systems. This control method does not demand precise knowledge of the exact mathematical model of the system [8]. It is particularly suitable for handling nonlinear systems [9]. The most popular controller inputs are error (*e*) and the rate of change of the error (Δ*e*). The following equations give us the values of (e) and (Δe) [10-12].

$$e(k)=\frac{\Delta P_{pv}}{\Delta V_{pv}}=\frac{P_{pv}(k)-P_{pv}(k-1)}{V_{pv}(k)-V_{pv}(k-1)} \tag{9}$$

$$\Delta e(k)=e(k)-e(k-1) \tag{10}$$

$P_{pv}(k)$ represents the power, and $V_{pv}(k)$ denotes the voltages of the PV panels, while $P_{pv}(k-1)$ and $V_{pv}(k-1)$ correspond to the previous values, and k represents the sampling time.

When there is a positive change in both power ($P_{pv}(k) > P_{pv}(k-1)$) and voltage ($V_{pv}(k) > V_{pv}(k-1)$), increasing the voltage will lead towards the MPP. The same principle applies when there is a negative change in both power voltage ($P_{pv}(k) < P_{pv}(k-1)$ and $V_{pv}(k) < V_{pv}(k-1)$). On the other hand, if there is a positive change in power but negative change in voltage ($P_{pv}(k) > P_{pv}(k-1)$ and $V_{pv}(k) < V_{pv}(k-1)$), decreasing the voltage is required to reach the MPP. Similarly when there is a negative change in power but a positive change in voltage ($P_{pv}(k) < P_{pv}(k-1)$ and $V_{pv}(k) > V_{pv}(k-1)$), decreasing the voltage is required to reach the MPP [3], [6].

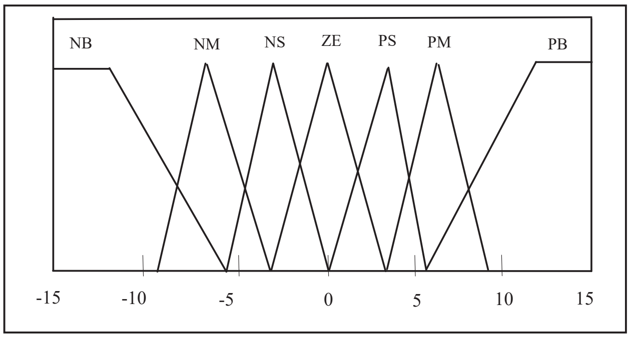

(a)

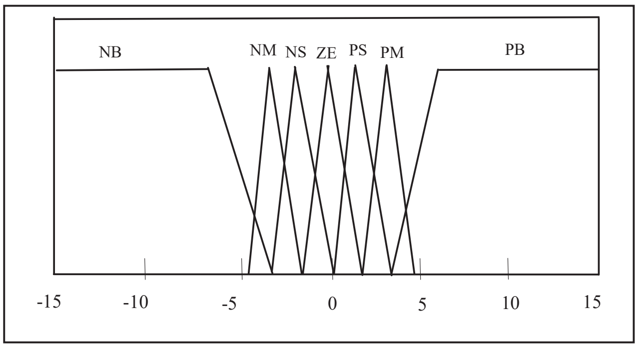

(b)

Figure 4. (a) The inputs of FLC (e) and (Δe), (b) The output of FLC.

TABLE I. RULES OF THE FUZZY LOGIC CONTROLLER

e / *Δe*	NB	NM	NS	ZE	PS	PM	PB
NB	NB	NB	NB	NB	NM	NS	ZE
NM	NB	NB	NB	NM	NS	ZE	PS
NS	NB	NB	NS	NS	ZE	PS	PM
ZE	NB	NM	NS	ZE	PS	PM	PB
PS	NM	NM	ZE	PS	PM	PB	PB
PM	NS	ZE	PS	PM	PB	PB	PB
PB	ZE	PS	PM	PB	PB	PB	PB

III. SIMULATION RESULTS

The complete setup of the system has been modeled and simulated using MATLAB/Simulink software. In order to operate the PV system at its maximum power point (MPP), two MPPT techniques has been employed.

Numerical values for simulation.
Dc-Dc buck converter:
C_1=1000µF, R_L=1e-4Ω , L=100e-4H , C_2=100µF , F=100KHz
PV module (G = 1000 W/m^2 and Tc= 25°C):
P_{max}= 214. 812 W , V_{max}= 46.8V , I_{max}= 4.59A

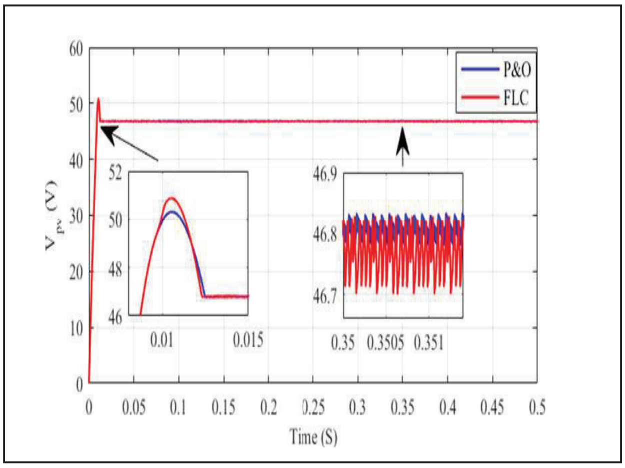

Figure 5. The PV voltage with P&O, FL MPPT algorithms.

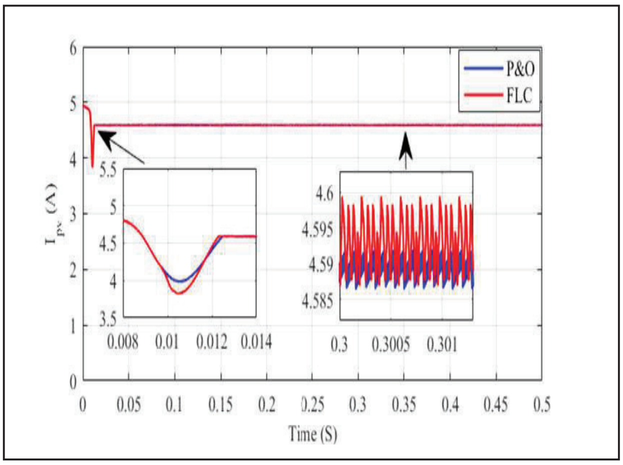

Figure 6. The PV current with P&O, FL MPPT algorithms.

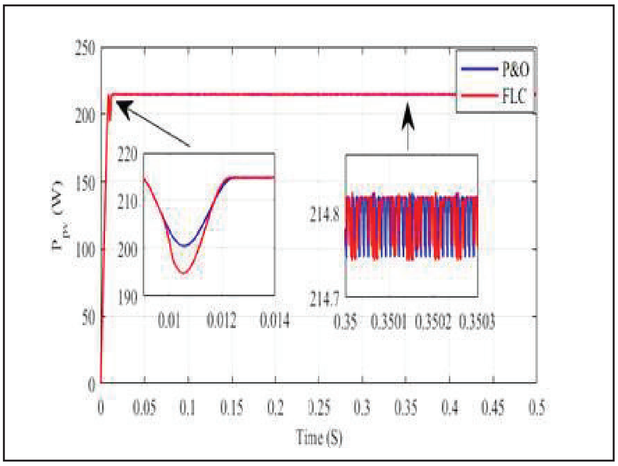

Figure 7. The PV power with P&O, FL MPPT algorithms.

The initial test consists of confirming the effectiveness of the two distinct methods in tracking the maximum power point under standard conditions: temperature of 25°C and solar irradiance of 1000 W/m^2.
Fig 5, 6, and fig 7 present PV voltage, PV current and PV power, respectively. They illustrate the results of the power tracked by the two controllers. Observations highlight the efficiency of both the P&O and FL methods in accurately tracking the MPP. Upon comparing the two controller, it becomes apparent that the FL exhibits a better response time than P&O, though accompanied by increased oscillations.

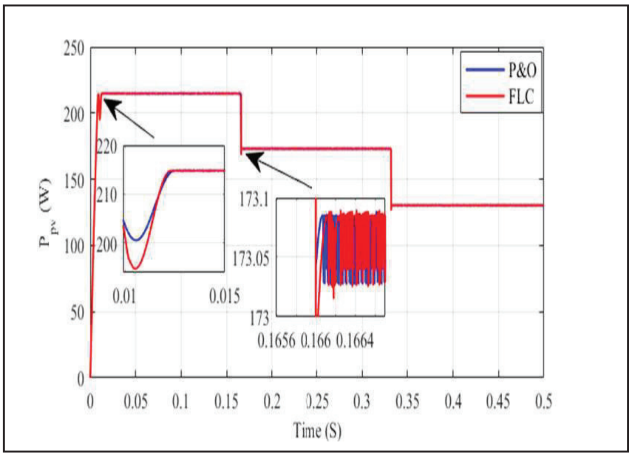

Figure 8. PV Power curves generated by P&O and FL algorithms at different solar irradiation.

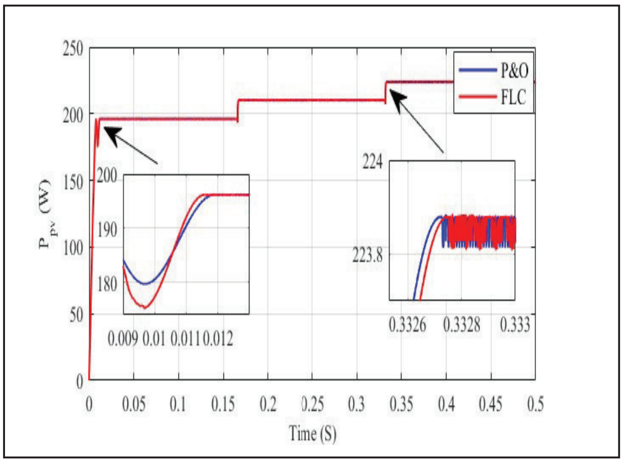

Figure 9. PV Power curves generated by P&O and FL algorithms at different temperature level.

Based on fig 8 and 9, the MPPT generated using the FLC has shown effective functionality under various atmosphere conditions. This method appears to exhibit an enhancement over the P&O, indeed, it displays better performance during rapid changes in meteorological conditions.

CONCLUSION

The aim of this research was to optimize the duty cycle of the buck converter in order to achieve the maximum power output from a photovoltaic (PV) generator and effectively charge a battery, regardless of varying solar irradiation and temperature conditions. The simulation outcomes demonstrate that both P&O algorithm and FL approach lead to the achievement of this objective. However, the Fuzzy Logic shows a good behavior and better performances compared to the other method.

REFERENCES

[1] M. Khan, M. Ahmad, S. A .Farooqui, A. Wajid, and F. Khan, " Performance evaluation of a PMDC motor with battery storage control and MPPT based solar photovoltaic system," International Journal of Power Electronics and Drive Systems, vol. 13, no. 3, pp. 1704, 2022.

[2] P. K. Atri, P. S. Modi, and N. S. Gujar, "Comparison of different MPPT control strategies for solar charge controller," IEEE International Conference on Power Electronics & IoT Applications in Renewable Energy and its Control (PARC). pp. 65-69, February 2020.

[3] H. Abbes, H. Abid, K. Loukil, A. Toumi, and M. Abid ," Etude comparative de cinq algorithmes de commande MPPT pour un système photovoltaïque," Journal of Renewable Energies, vol. 17, no. 3, pp. 435-445. 2014.

[4] A. Belkaid, I. Colak, K. Kayisli, and R. Bayindir, " Design and implementation of a cuk converter controlled by a direct duty cycle INC-MPPT in PV battery system, " International Journal of Smart Grid-ijSmartGrid, vol. 3, no. 1, pp. 19-25, 2019.

[5] B. S. Manju, R. Ramaprabha, and B. L. Mathur, "Modelling and control of standalone solar photovoltaic charging system," IEEE International Conference on Emerging Trends in Electrical and Computer Technology. pp. 78-81, March 2011.

[6] U. Yilmaz, A. Kircay, and S. Borekci,"PV system fuzzy logic MPPT method and PI control as a charge controller," Renewable and Sustainable Energy Reviews, vol. 81, pp. 994-1001, 2018.

[7] S. Chakraborty, M. M. Hasan, I. Worighi, O.Hegazy, and M. A. Razzak, "Performance evaluation of a PID-controlled synchronous buck converter based battery charging controller for solar-powered lighting system in a fishing trawler," Energies, vol. 11, no. 10, pp. 2722, 2018.

[8] S. Samal, P. K. Barik, and S. K. Sahu," Extraction of maximum power from a solar PV system using fuzzy controller based MPPT technique," IEEE Technologies for Smart-City Energy Security and Power (ICSESP), pp. 1-6, March 2018.

[9] H. S. Allah, R. M. Mounir, and K. A. Milod, " Comparison of Fuzzy Logic and P&O MPPT Techniques for solar Photovoltaic system," In The 2nd International Workshop on Signal Processing Applied to Rotating Machinery Diagnostics, SIGPROMD'2018, pp. 1-11. Djelfa, Algeria, 2018

[10] L.Abderezak, B. Aissa, and S. Hamza, " Comparative study of three MPPT algorithms for a photovoltaic system control," IEEE World Congress on Information Technology and Computer Applications (WCITCA), pp. 1-5, June 2015.

[11] B. Meryem, " Photovoltaic power control using fuzzy logic and fuzzy logic type 2 MPPT algorithms and buck converter," Advances in Technology Innovation, vol. 4. no. 3, pp.125, 2019.

[12] C. S. Shieh," Fuzzy PWM based on Genetic Algorithm for battery charging," Applied Soft Computing, vol. 21, pp. 607-616, 2014.

The 1st National Conference on Green Energy (NCGE' 2023)
December 02, 2023, Boumerdes, Algeria.

Investigating Turbulence Modeling's Influence on Darrieus Vertical Axis Wind Turbine Aerodynamics

BERKACHE Amar
Mechanical engineering department
Laboratory of Materials and Structural Mechanics (LMMS),
University of m'sila Msila, Algeria
amar.berkache@univ-msila.dz

NORA Belkhir
Mechanical engineering department
FIMA Laboratory
university of Khemis Miliana
Khemis Miliana Algeria
b.noura@univ-dbkm.dz

Abstract— **This study investigates turbulence model impact on aerodynamic performance of Darrieus-H vertical axis wind turbines utilizing symmetric NACA0021 airfoils. Two turbulence models, k-ω SST and DESS-A, were employed for simulations. Comparative analysis reveals that Delayed Eddy simulations (DES) more accurately predict power coefficients, aligning closely with experimental data from literature, in contrast to k-ω shear stress transport model. The study underscores Delayed Detached Eddy Simulation's reliability in assessing vertical axis wind turbine aerodynamics. These findings emphasize the significance of turbulence modeling in enhancing the precision of performance predictions for such turbines, offering valuable insights for efficient wind energy utilization.**

Keywords – vawt rotor h; sst k-ω; Darieus, naca0021; power coefficient

I. INTRODUCTION

Over the past decades, the global energy landscape has predominantly relied on fossil fuels for electricity generation, a practice that has significantly contributed to the escalating crisis of global warming. Adding to this concern, fossil fuel reserves are finite, emphasizing the urgency of transitioning towards sustainable energy sources. This pressing need compels nations worldwide to adopt effective strategies aimed at energy conservation and the reduction of CO_2 emissions. As a potential remedy to this predicament, renewable energy sources have emerged as a promising solution. Within the realm of renewables, wind energy shines as a particularly viable option. Its potential is astounding, with the capacity to meet energy demands twenty times over. Wind energy is harnessed through two principal technologies: horizontal axis wind turbines (HAWTs) and vertical axis wind turbines (VAWTs). However, HAWTs have faced limitations in terms of structural design and production efficiency. The enhancements needed for VAWTs often come at a high investment cost, rendering them less competitive when compared to other energy sources. Nevertheless, VAWTs boast several advantages, including their low operational noise, adaptability to various environments, and reduced start-up torque requirements. As a result, the focus of this study centers on the potential of vertical axis wind turbines. Among the methodologies employed to predict the performance of such turbines, Computational Fluid Dynamics (CFD) stands out. CFD technology has become integral to the comprehensive analysis of turbine mechanics. Researchers have extensively explored the impact of different turbulence models on wind turbine aerodynamics. For instance, Peng Bo and colleagues conducted a numerical study on an S825 profile wind turbine using a k-ω turbulence model. Their observations indicated improved turbulent viscosity and reduced stall areas when the blade operated under conditions of significant separation. Mertens investigated H-rotor Darrieus turbines subjected to deflective flow using CFD simulations. The outcomes demonstrated that power coefficients increase when the H-rotor operates in deflective flow. Other researchers applied RANS models, such as k-ω SST, and DES with S-A turbulence models to simulate intricate flow patterns around wind turbines. Amidst the intertwined challenges of energy sustainability and climate change mitigation, vertical axis wind turbines emerge as a critical focal point. The synergy between turbulence modeling and CFD simulations offers deeper insights into the aerodynamic performance of these turbines, paving the way for more efficient and ecologically sound energy solutions.

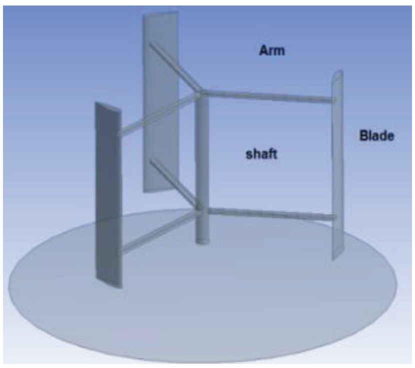

Figure 1. Darrieus Wind turbine

This study addresses the H-rotor Darrieus turbine using a two-dimensional model. Computational Fluid Dynamics (CFD) serves as the computational tool for assessing the turbine's overall behavior. Through numerical unsteady calculations, the aerodynamic performance of the vertical axis wind turbine is examined, considering the impact of diverse turbulence models. The primary goal is to identify the optimal turbulence model that best suits the simulation and accurately represents the turbine's dynamics.

II. NUMERICAL SIMULATION METHOD

The turbulence model of SST k-ω, also known as the Menter shear stress transport turbulence model, it was introduced in 1994 by Menter. It is a two-equation turbulence model that uses k-ω in the inner boundary layer region and shifts to k-ε in the free shear flow to improve predictions of adverse pressure gradients [7].

A. Aerodynamic Structure of Turbine

The Figure.1 shows the Darrieus wind turbine. The H-rotor consists of straight blades with a bearing surface cross section profile. The strut and support arms serve as structural support.

Figure.2 shows the directions of lift and drag and their normal and tangential components, When fluid flows over the surface of a body, a surface force acts on it, Lift is the component of that force which is perpendicular to the direction of oncoming flow. In contrasts to the lift force, the drag is the component of the surface force parallel to the flow direction. In aerodynamics, the lift and drag forces are commonly carried to analyze the aerodynamic characteristics of airfoil.

The tangential and normal force can be expressed by the following expression

$$F_T = L \sin\alpha - D \cos\alpha \quad (1)$$

$$F_N = L \cos\alpha + D \sin\alpha \quad (2)$$

The overall power (P) and it coefficient is defined by:

$$P = Q \cdot \omega \quad (3)$$

$$C_P = P/0.5\rho A U^3 \quad (4)$$

B. The Domain and the grids Computational

the rotor styded her is the Darrieus H type of three blades straight, airfoil of NACA0021, the

length of chord is C=0.265m, the radius of installation is 1m, , wind velocity is 8m/s and -6^0 pitch angle is taken as the reference case for comparison. , In this 2D numerical study the

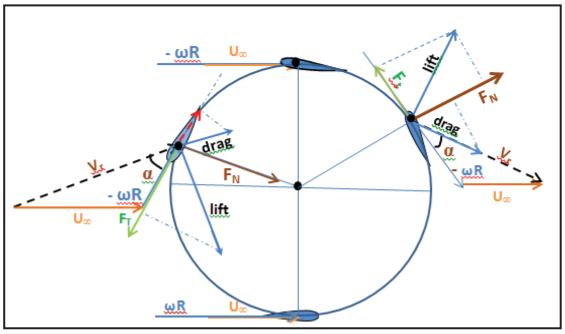

Figure 2. Distribution of the forces and velocities on Darrieus rotor airfoil

effects of supporting arms and the shaft were neglected. The geometrical parameter values of the domain of the solution 2D, is 60 R by 30 R. The figure. 3 shows the computational domain of the VAWT.

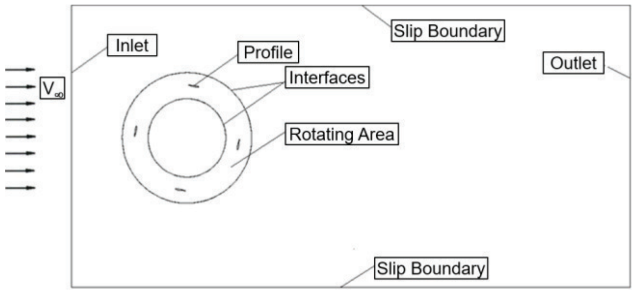

Figure 3. computational domain of the VAWT

These dimensions are chosen based on numerical studies on the effects of the numerical far fields as indicated in the bibliography, Marco Raciti and al [8] boundaries. In order to allow a full development of the wake, the outlet boundary conditions respectively 20R upwind and 38 R downwind with respect to rotor test section for a wind tunnel CFD simulation. The geometrical parameters of the rotor are identical to the experimental data of Qing'on li et al [9].

The computational grids are divided at fixed part and sliding part, the fixed domain is divided into nine parts (split with edge) to use the structured and unstructured mesh, this technique it allows us to reduce the computation time

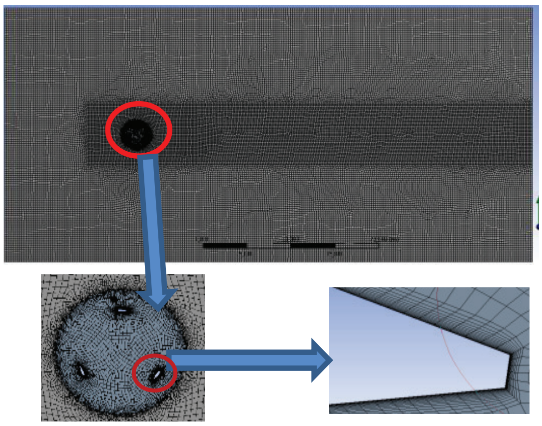

Figure 4. grids of computational domain and grids around the blade

The local structured meshes around the blades are refined for accurate and efficient resolution as show in the fig .4. The grids are coarse in the far-field zone of the rotor of the wind turbine, while the grids are medium in the region close to the rotational zone of the rotor.

III. RESULTS AND DISCUSSION

In order to investigate the effect of the turbulence models on the performances aerodynamic of the wind turbine, Figure 5,6,7 shows the field of the pressure, velocity magnitude and vorticity magnitude generated by the turbulence model DDES with Splarat Almaras and k-ω SST at the speed ratio values 1.75 which is chosen arbitrarily.

The best viewing field is that provide by turbulent model DES S-A, especially far downstream rotor.

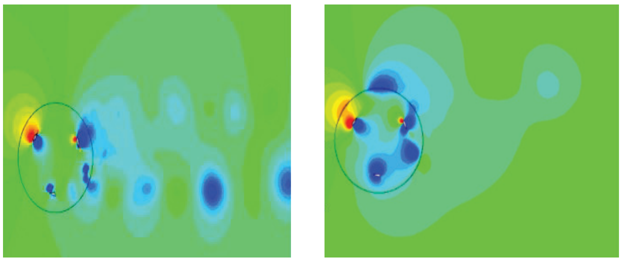

a) DES-Splarat Almaras at TSR=1.75 b) k-ω SST at TSR=1.75

Figure5. Pressure field of wind turbine

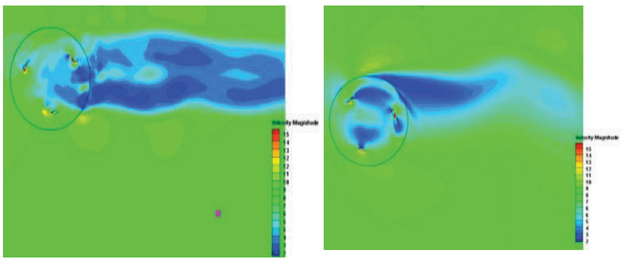

e) DES-splarat almaras f) k-ω SST at TSR=1.75

Figure.6. Velocity magnitude field of wind turbine

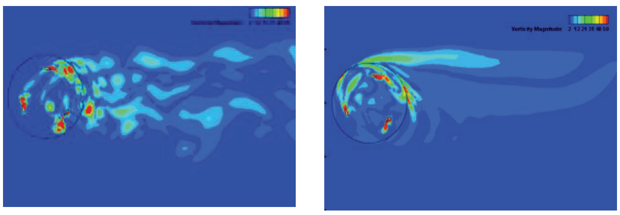

a) DES-Splarat Almaras at TSR=1.75 b) k-ω SST at TSR=1.75

Figre7. Vorticity magnitude field of wind turbine

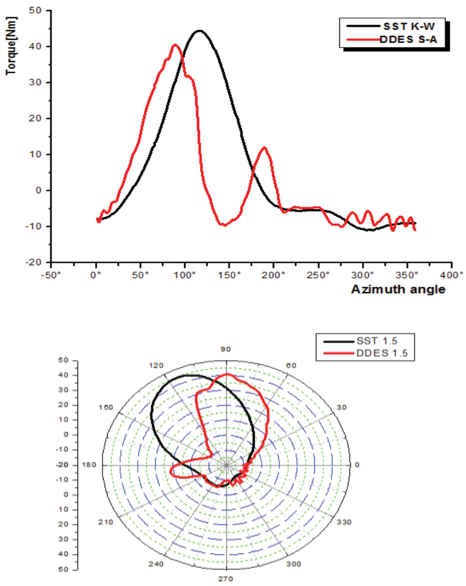

Figure 8. Curve of instantaneous torque for the single blade with two turbulence models At TSR=1.5

A. *Simulation and comparison of the instantaneous torque*

Figure.8 shows the instantaneous torque for the one blade of the wind turbine versus azimuth angle, it is clearly that the torque is depended to the turbulence models and the tip speed ratio, the turbulence model DDES with Splarat Almaras gives an instantaneous torque unstable at low speed ratio, When the blade is moving in the upstream region, the torque values increase until reach its maximum around azimuth angle less to 90° ,on the contrary the torque values decrease and becomes small and smooth in the downstream region , the reason for this tendency is mainly considered to be the influence of angle of attack [5]. In addition to the wake effect in the downstream region as shown in fig. 5,6,7. the turbulence model SST k-ω gives a stable instantaneous torque during rotor rotation.

B. *comparison of the power coefficient*

In this section, for the purpose of the research, we want to demonstrate the effect of two turbulence models on the simulation result, the turbulence models DES S-A and SST K-w are studied, and then we compare them with the experimental result found by qing [9] as shows in figure.9 above. The maximum power coefficient of model SST k-ω equal 0.30 while the DDES S-A gives a maximum power coefficient estimated at 0.25, this coefficient is closer to the coefficient of experimental result found by qing et al [9], this difference between the power coefficients is due to the simplification performed on the wind turbine, where we neglected the effect of the shaft, the arms and the friction of the rotating structures body ,in order to gain the time and reduce the grid size during the simulation .

C. *Conclusion*

The DDES S-A and k-ω SST turbulence models were applied to simulate aerodynamic airfoil of NACA0021, in order to obtain the aerodynamic performance of the wind turbine blade profile. When the simulated aerodynamic performances have been compared with the experimental value of the aerodynamic profile, The power coefficients

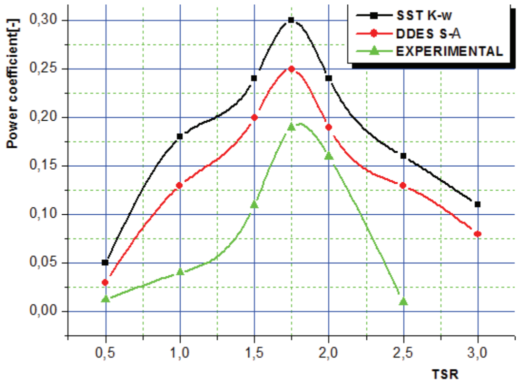

Figure 9. Power coefficient of the wind turbine

obtained through the two turbulence models (DDES S-A and k-ω SST) were compared against experimental data, the comparison of power coefficients shows a good agreement, especially for DDES S-A. despite the fact that the DDES S-A result deviates from the experimental data in the 20% range, the power coefficient of SST deviates by more than 50%. A single model of turbulence sufficient to provide good simulation results with some simulation errors that have been mentioned previously.

For an aerodynamic simulation of the turbine, better use the two turbulence models, using the turbulence model K-W SST to capture the flow field inside the rotor and use the turbulence model DDES S-A to better visualize the wake behind the rotor.

[1] Jianyang Zhu, Hailin et al (2015) 'Self- starting aerodynamics analysis of vertical axis wind turbine' Vol. 7(12) 1–12

[2] G. martinat, M. braza (2008) Turbulence_modelling of the flow past a pitching NACA0012 airfoil at 10^5 and 10^6 Reynolds numbers' journal of fluids and structures. 241 294-1303

[3] PENG Bo, YAN Hao 2015 Modification of k-ω Turbulence Model for Predicting Airfoil Aerodynamic Performance .24, No.3 221–228

[4] Mertens, S., Van Kuik, G., Van Bussel, G. (2003). Performance of an H-Darrieus in the skewed flow on a roof. *Journal of Solar Energy Engineering*, *125*(4),433–440.

[5] Ping Ma, Meishen Li, Jonathan Jilesen (2014) A comparison of coarse-resolution numerical simulation with experimental measurements of wind turbine aerodynamic ......performance Procedia Engineering 79 17 –27

[6] Ece Sagol,1 Marcelo Reggio (2012). Assessment of Two-Equation Turbulence..Models and Validation of the Performance.Characteristics of an Experimental Wind Turbine by CFD Volume 2012, Article ID.428671

[7] Hao Wang, Jiaojiao Ding (2014) Aerodynamic .simulation of wind turbine blade airfoil with different turbulence models College of ......Energy and Mechanical Engineering, ...Shanghai University of Electric Power, ...Shanghai, China email whouco@163.com

[8] Marco RacitiCastelli, ET Al (2012) Effect of. Blade Number on a Straight-Bladed ......Vertical-Axis Darrieus Wind Turbine, International Journal of Mechanical, Aerospace, Industrial Mechatronic and. Manufacturing Engineering Vol:6, No:1,

[9] Li, Qing'an, Takao Maeda, Et Al (2015) effect ….of number of blades an aerodynamic force ......on a straight- blade vertical axis wind ......turbine Energy, vol. 90, issue P1, 784-795

Effect of the Atmospheric Boundary Layer on a Wind Turbine

Said Zergane
Mechanical department
University of M'sila
M'sila, Algeria
said.zergane@univ-msila.dz

Amar Berkache
Mechanical department
University of M'sila
M'sila, Algeria
amar.berkache@univ-msila.dz

Abstract— To produce electricity from the wind, horizontal axis turbines exceeding 80 m in height are often used. Entirely immersed in the atmospheric boundary layer, these wind turbines undergo the same changes as the speed of the wind in a wind farm. In this context comes our study for the effect of the atmospheric boundary layer on the energy production for a single wind turbine, then generalize it to all the wind turbines of the farm. Using the logarithmic profile of wind speed in the atmospheric boundary layer, data from two types of wind turbines; NREL-V and ENERCON-E2 are introduced in a computer program for the calculation of the developed power. The results obtained are compared and discussed.

Keywords-component; Wind turbine, atmospheric boundary layer, wind energy, wind park, wind speed profile

I. Introduction

Energy from the wind is renewable energy, clean, inexhaustible, sustainable and does not emit radioactive or toxic waste, By the construction of wind farms in windy sites, it has become one of the most promising sources for the production of electricity and to meet the increased demand for energy consumption. with the other forms of renewable energy, it can be an alternative to fossil energy, such as oil and natural gas in the decades to come.

The characteristic curve of each wind turbine is based on a uniform, unidirectional wind speed on the rotor. However, in reality in the atmospheric boundary layer, the wind has a different profile, it depends on the height Z. Near the ground, the presence of obstacles, the roughness of the ground, turbulence….[1] significantly influence the quality of the wind speed, the further you are from the ground, the more stable the wind becomes. In this objective we present a study which aims to elucidate the effect of the atmospheric boundary layer on the energy produced by a wind turbine. This study is based on the introduction of geometric data and characteristic curves representing the power produced by two types of wind turbines, one small; NREL-V 17 m high and the other large; 85 m ENERCON E-2 in a calculation computer program. The results obtained from the power developed by each wind turbine are analyzed and compared.

II. Geometric data and characteristic

Figures 1 and 2 illustrate the characteristic curves of the power developed by each of the two wind turbines used in this study; NREL-V [3] and ENERCON E2 [4] respectively

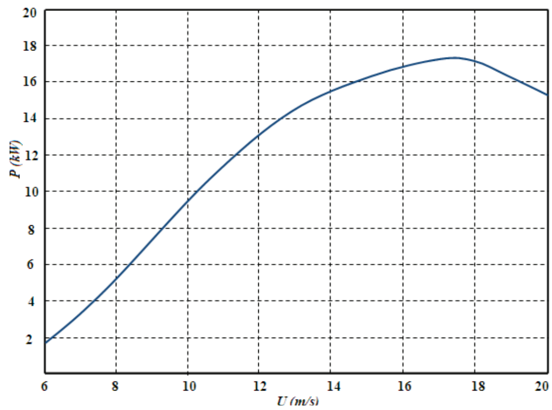

Fig. 1 Power characteristic curve of the NREL-V turbine

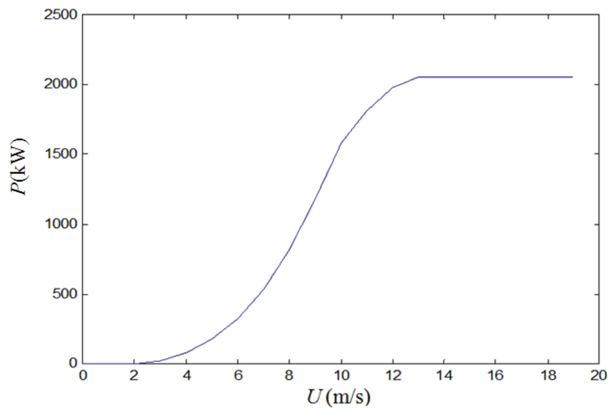

Fig. 2 Power characteristic curve of the ENERCON E2 Turbine

III. ATMOSPHERIC BOUNDARY LAYER

In the atmospheric boundary layer (ABL), the model of the wind speed, uniform and unidirectional, seems insufficient to accurately calculate the power developed by a wind turbine. In reality, in ABL the wind speed has an exponential as follows: [5]

$$\frac{U}{U_{ref}} = \left(\frac{Z}{Z_{ref}}\right)^{\alpha} \qquad (1)$$

IV. ATMOSPHERIC BOUNDARY LAYER

It is clear that In the atmospheric boundary layer wind profile depends on the reference speed $Z_{ref,}$ the reference height Z_{ref} and the designed height Z. therefore, the power of a single turbine is strongly related to the same parameters. To calculate this power, we propose described as follows:

- The actuator disc is divided into surface elements ΔS_i
- Each surface element corresponds to a velocity $U_i(Z)$
- Using the power curve of the two wind turbines NREL-V and ENERCON E2 we calculate the power ΔP_i which corresponds to each surface element ΔP_i (see figure 3)
- The total power P of a single wind turbine is only the sum of the elemental powers as follows:

$$P = \sum_{i=1}^{n} \Delta P_i \qquad (2)$$

Table 1 power produced of NREL- V wind turbine

N	2	3	4	5	6	8	10	12
P(kW)	1.91	1.93	1.95	1.98	1.99	2.00	2.01	2.01

Table 2 power produced of ENERCON E2 wind turbine

N	2	7	10	20	100	150	200
P(kW)	621.7	621.9	622.0	622.1	622.2	622.3	622.3

By varying the number of discretization N (number of elementary surfaces), we have two results obtained from the power produced by the two wind turbines; NREL-V and ENERCON E2 in atmospheric boundary layer. The following observations can be deduced:

- The discretization of the actuator disc of the NRELL-V turbine has no effect from the number N = 5, because the power stabilizes around 2 kW.
- The ENERCON E2 turbine has a higher height than NRELL-V and the wind speed seems more uniform and constant, therefore the atmospheric boundary layer has no effect on the power produced.

V. CONCLUSION

The work presented is a new method for calculating the power of two types of wind turbines in the atmospheric boundary layer. the introduction of the wind speed profile in a program developed under Matlab with the disrcitization of the actuator disc into surface elements of each wind turbine, this method has allowed us to quantify the power produced more precisely, and to show that a A large wind turbine is less affected by the atmospheric boundary layer than a small wind turbine, because the wind speed profile at high altitude is far from the effects of terrain obstacles and ground roughness, it becomes significantly uniform.

REFERENCES

[1] S. ZERGANE, A. SMAILI. Effect of turbulence on the energy production of the wind farm. In: Advances in Green Energy and Materials Technology. Springer, Singapore, 2021. p. 393-400.

[2] S. Frandsen, Turbulence and turbulence generated structural loading in wind turbine clusters, Risø National Laboratory, Roskilde,Denmark. 2007

[3] S. Zergane, A. Smaïli. "Optimisation de la micro-localisation des aérogénérateurs dans un parc éolien." Revue des énergies renouvelables 14.4 (2011). 727-732

[4] https://fr.wind-turbine-models.com/turbines/550-enercon-e-82-e2-2.300.

[5] Liu, Boming, et al. "The relationship between the atmospheric boundary layer and the temperature inversion layer and their aerosol capture capabilities." Recherche atmosphérique 271 (2022): 106121.

[6] Vahidi, Dara et Fernando Porté-Agel. "Un modèle basé sur la physique pour l'expansion du sillage des éoliennes dans la couche limite atmosphérique." Tourillon de mécanique des fluides 943 (2022).

Comparison between Traditional and Z-Source Inverters for photovoltaic system using MPPT control method

Benziada Mohamed Abdelghani[1]
Process Control Laboratory National Polytechnic school
Algiers, Algeria
abdelghani.benziada@gmail.com

Ouail Mohamed[2]
Electrical Engineering Laboratory University of Chlef
Chlef, Algeria
mohamed.ouail152@gmail .com

Abstract—**The main purpose of this paper is to study and control the Z-source converter suitable for photovoltaic systems. We applying the P & O algorithm for maximizing the power MPPT. We looked at the development of a mathematical model of the Z-source converter. Thereafter, the control of these converters was synthesized through the state "Shoot-Through" and methods of boosting and integration of the shoot-through state to the conventional PWM were exposed to control the Z-source inverter. Finally, we compared the Z-source inverter with that of the conventional system, based on simulation results.**

Keywords- Z-source; DC/DC inverter; P&O; MPPT; Shoot-through; boosting method.

I. INTRODUCTION

The use of the photovoltaic source requires an adaptation stage, that optimize the transfer energy for the different application such as DC/DC converter, DC/AC inverter. Several topologies were proposed in the literature to fulfill the industry needs [1].

In power conversion systems, the traditional inverter can provide only buck output voltage and its maximum output voltage cannot exceed the dc-link voltage. In two-level inverters, the upper and the lower power switch of each phase leg cannot be turned on at the same time.

Otherwise, shoot-through would occur and the power semiconductor switching devices will be destroyed. To overcome such limitations, several recent research studies proposed different improved inverter topologies. One of them is the Z-source inverter proposed by Peng [2].

The Z-source inverter uses an impedance network (Z network), to replace the traditional dc link. It employs an impedance network, that consists of split-inductors L_1 and L_2 and capacitors C_1 and C_2 connected in an X shape. It couples the inverter to the dc source, load, or another converter.

Therefore, the dc source can be a battery, a diode rectifier, thyristor converter, fuel cell, an inductor, a capacitor, or a combination of those. Compared to the conventional two-level three-phase inverter which has six active vectors and two zero vectors, the commutation cell of the two-level three-phase Z-source inverter bridge has one extra state, called the shoot-through state. This state can be generated when both switches of any one phase leg are gated on. This state can be generated in seven different ways: shoot-through via any one phase leg, combinations of any two-phase leg, and all three-phase legs.

The Z-source inverter advantageously uses the shoot-through states to buck and boost the dc bus voltage to the desired output voltage. The equivalent circuit and the model of the Z-source inverter have been studied in [2].

The Z-source inverter is recently integrated into a wide range of applications: in electrical and hybrid vehicles [1,3,4], in renewable power generation systems such as photovoltaic system [5,6], wind turbine systems [7]. Furthermore, the Z-source inverter is used as a multilevel inverter in [8].

In this paper, a comparative study between the traditional and Z-source inverter will be held, by simulating in MATLAB/Simulink

II. TRADITIONAL INVERTER

We use in this study a Boost converter which is represented by the figure opposite [9]:

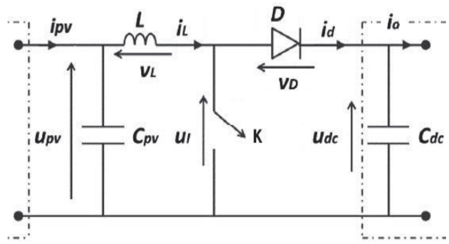

Figure 1. Boost converter.

There are two operating intervals of the DC/DC converter:

- Interval [0, αTs]: When the K switch is closed, the diode is polarized in reverse, the continuous bus is isolated from the source, which supplies the energy to the inductance L.

By applying Kirchhoff's law to this circuit we obtain the following equations:

$$\begin{cases} i_{C_{pv}}(t) = C_{pv}\,\frac{dU_{pv}(t)}{dt} = i_{pv}(t) - i_L(t) \\ i_{C_{dc}}(t) = C_{dc}\,\frac{dU_{dc}(t)}{dt} = -i_0(t) \\ V_L(t) = L\,\frac{di_L(t)}{dt} = U_{pv}(t) \end{cases} \quad (1)$$

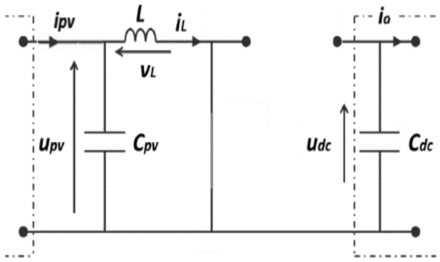

Figure 2. First Boost converter conduction mode.

- Interval [αTs, Ts]: When switch K is open, the continuous bus receives energy from source and inductance L. The circuit is represented by the figure below:

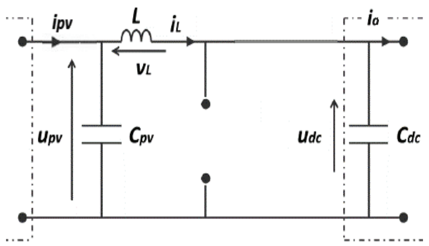

Figure 3. Second Boost Converter Conduction Mode.

The equation model in this configuration is:

$$\begin{cases} i_{C_{pv}}(t) = C_{pv}\frac{dU_{pv}(t)}{dt} = i_{pv}(t) - i_L(t) \\ i_{C_{dc}}(t) = C_{dc}\frac{dU_{dc}(t)}{dt} = i_L(t) - i_0(t) \\ V_L(t) = L\frac{di_L(t)}{dt} = U_{pv}(t) - U_{dc}(t) \end{cases} \quad (2)$$

The continuous speed is obtained by eliminating the derivatives of the dynamic variables and replacing these signals with their average values. The system becomes:

$$\begin{cases} (1-\alpha)(I_{pv} - I_L) + \alpha(I_{pv} - I_L) = 0 \\ (1-\alpha)(I_L - I_0) - \alpha I_0 = 0 \\ \alpha U_{pv} + (1-\alpha)(U_{pv} - U_{dc}) = 0 \end{cases} \quad (3)$$

The conversion ratio, which represents the ratio of the output voltage to the input voltage:

$$M(\alpha) = \frac{U_{dc}}{U_{pv}} = \frac{1}{1-\alpha} \quad (4)$$

With this last expression, we can see that the output voltage is always higher than the input voltage (the cyclic ratio varying between 0 and 1).

III. Z-SOURCE INVERTER

An equivalent DC load is considered instead of the AC portion of the circuit to simplify the study. We have two main states:

- Shoot-Through: ZS circuit is short circuit (S_1=0 and S_2=1).
- Active state: the ZS impedances network sees the load through the inverter (S_1=1 and S_2=0).

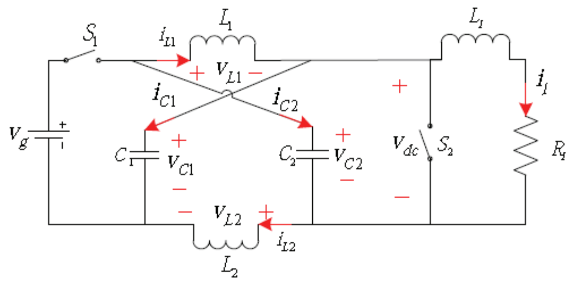

Figure 4. Simplified diagram of the ZS converter.

The following assumptions are made:

$$\begin{cases} L_1 = L_2 = L \\ C_1 = C_2 = C \end{cases} \quad (5)$$

So we'll have a symmetrical circuit:

$$\begin{cases} V_{C1} = V_{C2} = V_C \\ i_{L1} = i_{L2} = i_L \end{cases} \quad (6)$$

With:

- V_g, V_C, V_L and V_{dc} represent the voltages of the DC source, capacitor, inductance and ZSC output respectively.
- i_l, i_g, i_L, i_C: are the charge and source currents and the currents passing through the inductance and capacitor respectively.

There are four states to present, they depend on the S_1 and S_2 switch configurations.

A. Status 1: Shoot-Through

S_1=0 and S_2=1 therefore: the ZS circuit is in short circuit.

The load voltage is zero (V_{dc}=0): there is no energy transfer. The duration of the Shoot-Through state is T_0, and the switching period is T.

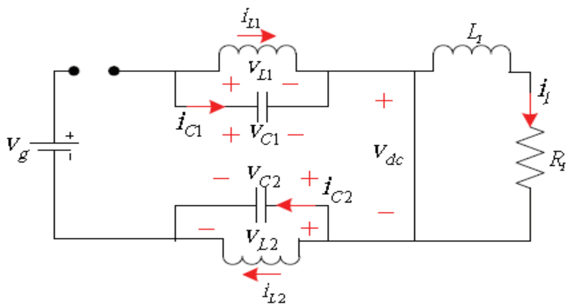

Figure 5. Shoot-Through status.

We see that $V_c = V_L$, so:

$$\begin{cases} \frac{dv_c}{dt} = -\frac{i_L}{C} \\ \frac{di_L}{dt} = \frac{v_c}{L} \\ v_{dc} = 0 \\ i_g = 0 \end{cases} \quad (7)$$

B. *Status 2: Active Status*

S_1=1 and S_2=0, the duration of this state is (T - T_0): there is a transfer of energy.

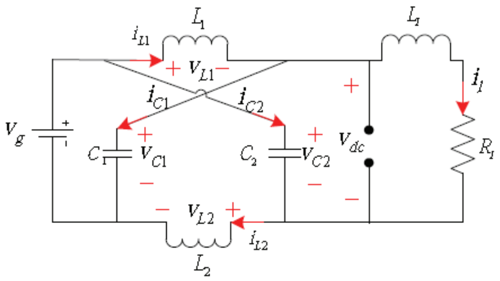

Figure 6. Active status.

$V_L = V_g - V_c$ and $i_g = i_L + i_c = i_L + C\frac{dV_c}{dt}$

We find:

$$\begin{cases} \frac{dv_c}{dt} = \frac{i_g - i_L}{C} \\ \frac{di_L}{dt} = \frac{v_g - v_c}{L} \\ v_{dc} = v_c - v_L = 2v_c - v_g \\ i_g = i_L + i_C \end{cases} \quad (8)$$

C. *Status 3 : Status zero*

When S_1=0 and S_2=0: $i_L = -i_c$

$$\begin{cases} \frac{dv_c}{dt} = -\frac{i_L}{C} \\ \frac{di_L}{dt} = \frac{v_c - v_{dc}}{L} \\ v_{dc} = v_c - v_L \\ i_g = 0 \end{cases} \quad (9)$$

D. *Status 4*

When S_1=1 et S_2=1:

$V_L = V_C \; et \; i_g = i_L + i_C = i_L + C\frac{dV_c}{dt}$

Hence:

$$\begin{cases} \frac{dv_c}{dt} = \frac{i_g - i_L}{C} \\ \frac{di_L}{dt} = \frac{v_c}{L} \\ v_{dc} = 0 \\ i_g = i_L + i_C \end{cases} \quad (10)$$

To summarize all the states, we will have the following equations:

$$\begin{cases} \frac{dv_c}{dt} = \frac{S_1 i_g - i_L}{C} \\ \frac{di_L}{dt} = S_1\frac{v_c}{L} + \bar{S}_1\left[S_2\frac{v_c}{L} + \bar{S}_2\frac{v_c - v_{dc}}{L}\right] \\ v_{dc} = \bar{S}_2(v_c - v_L) \\ i_g = \; S_1(i_L + i_C) \end{cases} \quad (11)$$

Such as $\bar{S}_1 = 1 - S_1 \; et \; \bar{S}_2 = 1 - S_2$.

E. *Boost Factor B*

In steady state, it is known that the average voltage value during a switching period at the inductance level is zero, so:

$$V_L = \frac{1}{T}\left[\int_0^{T_0} v_c dt + \int_{T_0}^{T}(v_g - v_c)dt\right] = 0 \quad (12)$$

$$V_C = \frac{1 - \frac{T_0}{T}}{1 - \frac{2T_0}{T}} V_g$$

We pose $D = \frac{T_0}{T}$, is the cyclic ratio, we obtain:

$$V_C = \frac{1-D}{1-2D} V_g \quad (13)$$

On the other hand, the maximum voltage of the steady state continuous bus is written:

$$V_{dcn} = 2V_C - V_g \quad (14)$$

We thus obtain the relationship between the input voltage and the maximum voltage of the continuous bus:

$$V_{dcn} = \frac{1}{1-2D} V_g = BV_g \quad (15)$$

Where's $B = \frac{1}{1-2D}$ the boost factor.

Figure 7 shows the variation of the modulation factor as a function of the cyclic ratio.

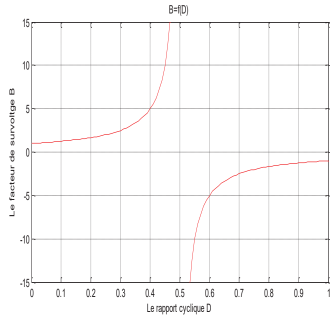

Figure 7. Variation of the modulation factor as a function of the cyclic ratio.

IV. MPPT METHOD

Given the changing climatic conditions of the environment. Specific control laws exist to bring our renewable energy conversion devices to function at the maximum of their characteristics without prior knowledge of these operating points or the moments or reasons for this change. This type of command is often referred to in the literature as the Maximum Power Point Search (MPPT) [9].

A. Disturbance and Observation Method (P&O)

This is the method most used in practice because of the simplicity of its algorithm, and therefore the ease of its implementation [9].

Figure 8 shows the output power of a photovoltaic panel as a function of voltage (Ppv - Upv) at a fixed irradiation and constant temperature. Suppose the module is running at a point that is far from the PPM Maximum Power Point. In this algorithm the PV panel voltage is disturbed with a small increment, the resulting power change ΔP is observed [25]:

- If ΔP is positive, then it means we are approaching the PPM. Thus, other disturbances in the same direction will move the operating point to the PPM.
- If ΔP is negative, the operating point is moved away from the PPM, and the direction of the disturbance must be reversed to advance to the PPM.

Figure 9 shows the P&O algorithm flow chart.

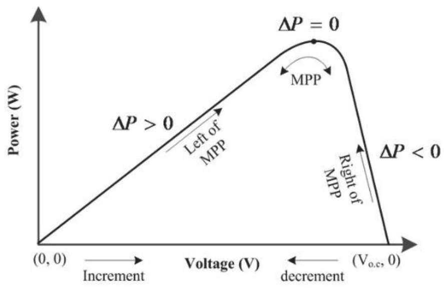

Figure 8. Output power of a photovoltaic panel as a function of voltage.

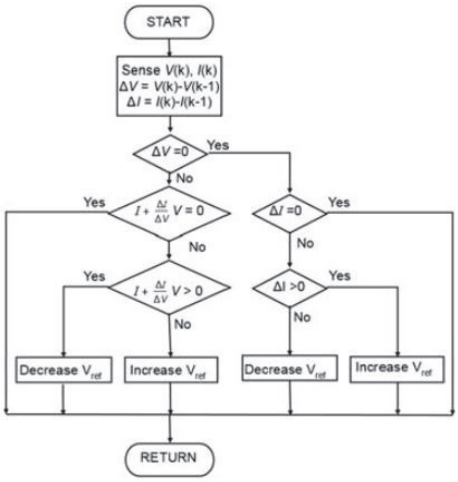

Figure 9. P&O algorithm flow chart.

V. SIMPLE BOOST CONTROL

The Simple Boost control is simple and easy to implement. However, the Shoot-Through cyclic ratio obtained D decreases with the increase of the modulation rate M. The maximum Shoot-Through cyclic ratio of the Simple Boost control is limited to 1-M for a particular operation, reaching zero for a modulation rate equal to 1 [9].

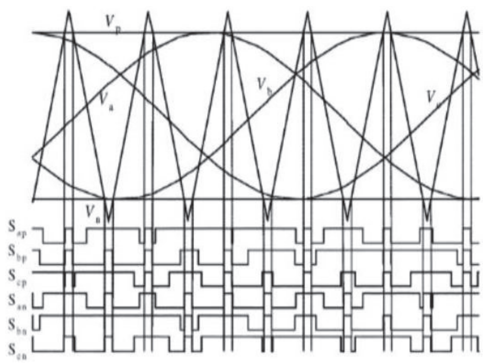

Figure 10. Simple boost control waveform.

Therefore, the operation with a high modulation rate for the Simple Boost control, leads to a low output voltage. In order to generate an output voltage that requires a high voltage gain, a low modulation rate must be used [9].

In fact, this control strategy inserts the Shoot-Through in all the null states of traditional PWM during a switching period, which keeps the six active states unchanged as in conventional carrier PWM [9].

VI. SIMULATION RESULTS

A comparative study between the two inverters will be held, by simulating ZSI using simple boost control. These different systems have been simulated in MATLAB/Simulink. Tables (I) to (III) summarizes the selected system parameters for the simulation.

TABLE I. CONVENTIONAL SYSTEM SIMULATION DATA

L (mH)	C (mF)	fref (Hz)	fp (Hz)
20	5	50	2000

TABLE II. Z-SOURCE SYSTEM SIMULATION DATA

L (mH)	C (mF)	fref (Hz)	fp (Hz)
0.5	1	50	2000

TABLE III. FILTER CHARACTERISTICS

Lf (mH)	Cf (mF)	fcut (Hz)
3	1	92

A. *Traditional system*

The simulation results are shown in figures (11) to (14).

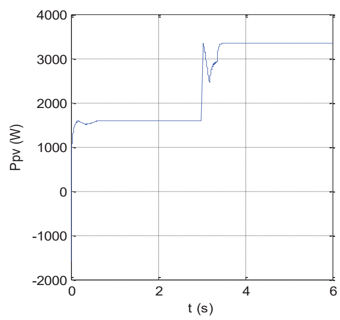

Figure 11. Power of PV Panel.

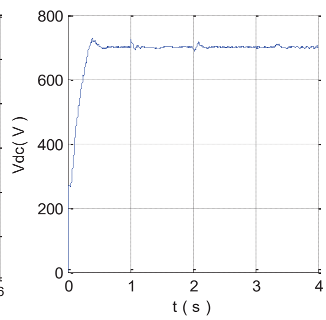

Figure 12. Continuous bus voltage

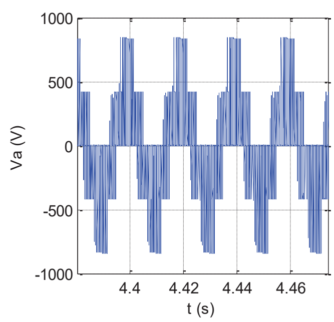

Figure 13. The simple charge voltage.

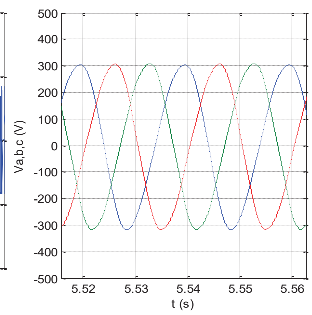

Figure 14. The 3 filtred charge voltage

B. Z-source system

The simulation results are shown in figures (15) to (18).

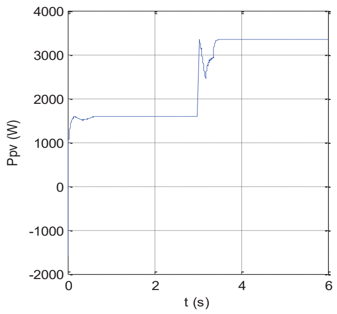

Figure 15. Power of PV Panel.

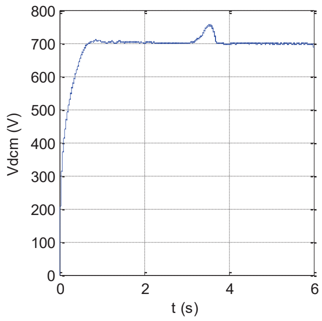

Figure 16. Continuous bus voltage

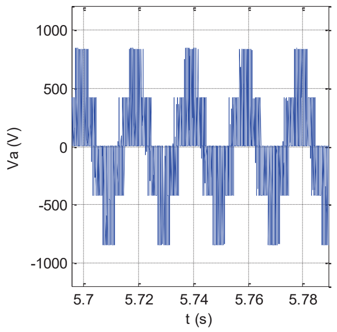

Figure 17. The simple charge voltage.

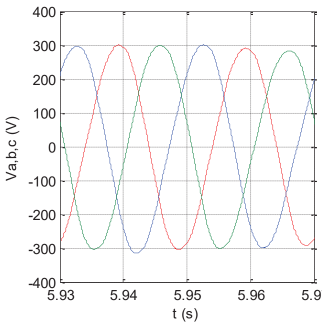

Figure 18. The 3 filtred charge voltage

C. Comparison between the two systems

The implementation of the Simple Boost control is interesting in terms of results, with a structure comparable with that of the Z-source converter, the first observation is that of the invariance of the quantities of the power of the PV panel and the load.

This system can follow the maximum power of a photovoltaic panel, it requires a slightly high switching frequency, comparing with the conventional system, not to have a bad influence on the inverter output voltage. Using the Z-source topology allows you to boost the inverter input DC voltage without using a Boost converter, reducing the number of switches and the complexity of the system.

Z-source inverter offers several advantages over traditional inverter, including:

- **Output voltage flexibility:** The Z-source inverter allows you to change the output voltage by adjusting the pulse width modulation (PWM) without having to modify the circuit components. This provides greater flexibility in applications requiring variable output voltage.
- **Surge Management Capability:** The Z-circuit of the Z-source inverter is used to manage surges generated by inductive loads or power supply voltage variations. It provides better surge protection, reducing the risk of damage to inverter components and connected loads.
- **Harmonics Reduction:** The Z-source inverter can reduce current and voltage harmonics, helping to improve the quality of energy delivered to connected loads.
- **Fault tolerance:** Due to its Z-topology, the Z-source inverter is more tolerant to component failures than traditional inverter. It may continue to function even if one or more circuit components fail.

VII. CONCLUSION

The work presented in this paper is an attempt to arrive at an optimal solar photovoltaic system configuration and the most appropriate converter topologies. we modeled the Traditional and Z-source inverters and simulated them to better understand the dynamics and operation of the system. We have introduced the Shoot-Through state that does not exist in conventional inverters. A comparison between the Traditional and Z-source inverters is made.

REFERENCES

[1] Chaib. I., "The integration of Z-source inverters in an intelligent network “Smart Grid", PhD Thesis, Ecole Nationale Polytechnique, Algeria, 2022.

[2] Peng. F. Z., "Z-Source inverter", IEEE Transactions on Industry Applications, Vol. 39, No. 2, pp. 504-510, 2003.

[3] T. Na, Q. Zhang, S. Dong, H. J. Raherimihaja, G. Chuai, and J. Wang, "A Soft-Switched Modulation for a Single-Phase Quasi-Z-Source Integrated Charger in Electric Vehicle Application," IEEE Transactions on Power Electronics, 2019.

[4] H. Peng, J. Wang, W. Shen, D. Shi, and Y. Huang, "Compound control for energy management of the hybrid ultracapacitor-battery electric drive systems," Energy, vol. 175, pp. 309-319, 2019.

[5] C. Ibtissam, EL MADJID, Berkouk, PAUL, Gaubert Jaun., "Study of Fuzzy Logic controller based MPPT and the P&O for the Z-source inverter integrated in PV system," In : 2018 International Conference on Electrical Sciences and Technologies in Maghreb (CISTEM). IEEE, 2018, pp. p.1-6, 2018.

[6] A. Lashab, D. Sera, and J. M. Guerrero, "A low-computational high-performance model predictive control of single phase battery assisted Quasi Z-source PV inverters," in 2019 10th International Conference on Power Electronics and ECCE Asia (ICPE 2019- ECCE Asia), 2019, pp. 1873-1878.

[7] M. M. Bajestan, H. Madadi, and M. A. Shamsinejad, "Control of a new stand-alone wind turbine-based variable speed permanent magnet synchronous generator using quasi-Z-source inverter," Electric Power Systems Research, vol. 177, p. 106010, 2019.

[8] R. Guisso, A. Andrade, H. Hey, and M. d. S. Martins, "Grid-tied single source quasi-Z-source cascaded multilevel inverter for PV applications," Electronics Letters, vol. 55, pp. 342-343, 2019.

[9] M.A.Benziada, M..Ouail, " Utilisation de convertisseur Z-source dans un système photovoltaique ", Enginnering Thesis, Ecole Nationale Polytechnique, Algeria, 2015.

An Experimental Study To Evaluate the Thermal Performance of a Box-Type Solar Cooker With Sensible Thermal Energy Storage

Assam Benbaha
Laboratoire de Recherche LEB, Département d'Electrotechnique, Université Mostefa Ben Boulaïd, Boukhlouf Med ElHadi, Batna 2, Algérie
issambenbaha@gmail.com

Boubekeur Azoui
Laboratoire de Recherche LEB, Département d'Electrotechnique, Université Mostefa Ben Boulaïd, Boukhlouf Med ElHadi, Batna 2, Algérie
azoui_b@yahoo.com

Fatiha Yettou
Unité de Recherche Appliquée en Energies Renouvelables, URAER, Centre de Développement des Energies Renouvelables, CDER, 47133, Ghardaïa, Algeria
yettou.t @gmail.com

Amor Gama
Unité de Recherche Appliquée en Energies Renouvelables, URAER, Centre de Développement des Energies Renouvelables, CDER, 47133, Ghardaïa, Algeri
gama.amor@gmail.com

Abstract— **This study presents a comprehensive evaluation and testing of a box-type solar cooker that incorporates sensible heat storage. Sunflower oil-filled copper tubes were strategically positioned horizontally beneath the absorber to facilitate effective heat storage. The experiments were carried out under various conditions, both with and without a load, to gather extensive data. In the absence of a load, the solar cooker, exposed to solar radiation intensity of 864W/m², yielded remarkable results. The oil and absorbent plate reached temperatures of 117°C and 121.8°C, respectively. Furthermore, the system demonstrated its ability to sustain a temperature above 40°C for a duration of 200 minutes, ensuring reliable heat retention. Under load conditions, with 1.5 kg of water and solar radiation of 736 W/m², the solar cooker continued to exhibit outstanding performance. The absorbent plate, oil, and water recorded maximum temperatures of 103°C, 96°C, and 86°C, respectively. Notably, the system successfully maintained the water temperature above 40°C for an impressive duration of 420 minutes, showcasing its capability for long-term heat storage. These findings validate the exceptional effectiveness of our solar box cooker in maintaining optimal heat levels, which in turn ensures the preservation of food temperatures during late dinners. The successful integration of sensible heat storage in our system provides a reliable and dependable solution for achieving prolonged heat retention and underscores its potential for practical applications.**

Keywords- Solar radiation, Box type solar cooker, Experimental tests, Thermal performances, Cooking power, Sensible heat storage.

I. INTRODUCTION

Solar energy has been used in many ways as one of the main sources of alternative energy over the years. In order to boost its acceptance, some of its drawbacks, including initial cost, storage, and efficiency, have been addressed. Solar thermal energy has been used for a variety of tasks, including drying, cooking, frying, baking, producing electricity, heating water, and warming homes. The availability of solar thermal energy at times of low or no solar radiation is the main constraint of these applications [1,2]. The solar thermal energy storage (STES) system, which absorbs and stores heat during the day and releases it at night, is one way to get around this restriction [1]. The efficiency of the solar cooker relies on factors such as the amount of energy input, size, and heat losses [1]. It primarily comprises three essential components: the heat storage material (HSM), the heat transfer mechanism, and the containment system [3]. Commonly utilized HSMs include sensible, latent, and thermochemical ones. Even though they have the largest storage density, thermochemical HSMs [4] are not practical for low-temperature applications.

In sensible HSMs, heat is stored by increasing a material's temperature in order to take use of the material's heat capacity as well as the temperature shift that occurs while charging and discharging. The quantity of heat energy stored relies on the specific heat of the medium, the temperature change, and the amount of storage material [5], and heat discharge at a faster flow rate is a sign of higher heat usage [4]. The primary drawback of this type of HSM is its low heat storage density, which is inversely correlated with its HSM content. The issue of having a suitable STES for low-temperature applications is to assure an efficient and quick use of the stored heat. This can only be done by using various computational and experimental methodologies to study the behavior of the STES and the appropriate HSM. Some of the sensible heat materials used for low-temperature applications include basaltic rock [1], sand [6], bricks [7], and biomass [8].

While PCM (phase change material) offers clear advantages in enhancing the thermal performance of solar box cookers, it is often economically challenging for low-income families in developing nations to access these materials. As a result, to improve the efficiency of solar cookers and enable cooking during nighttime hours, users often resort to sensible thermal energy storage [9]. Saxena and Karakilcik [10] use inexpensive materials for practical thermal energy storage to experimentally explore the thermal performance of a solar box cooker. Under the climatic conditions of India, an ideal mixture of granular carbon and sand is created and used for long-term heat storage. The system's overall energy efficiency is found to be 37.1%, and it is discovered to be operating under non-sunny conditions. In the design, construction, and testing of a parabolic dish-type solar cooker conducted by Agrawal and Yadav [11], four different sensible thermal energy storage materials were utilized: sand, stone pebbles, iron grits, and iron balls. These materials were chosen due to their availability, affordability, and non-toxic nature. The study revealed that each material achieved varying maximum temperatures, with sand reaching 104.1 °C, stone pebbles reaching 108.2 °C, iron grits reaching 116.7 °C, and iron balls reaching 99.7 °C. Furthermore, the corresponding stored energy values for these materials were found to be 628.7 kJ, 843.3 kJ, 467.7 kJ, and 670.4 kJ, respectively. These findings demonstrate that these materials possess desirable temperature levels and offer substantial stored energy, making them suitable for nocturnal cooking purposes.

When it comes to thermal storage in solar cookers, two common types are sensible heat storage and latent heat storage. Sensible heat storage involves storing heat energy in a material by raising its temperature, while latent heat storage involves storing heat energy by utilizing the phase change of a material, such as from solid to liquid or liquid to gas. Sensible heat storage has the advantage of simplicity and cost-effectiveness. It typically utilizes materials with high specific heat capacities, such as water or rocks, to absorb and store heat. These materials can efficiently retain heat over a longer duration and release it gradually, allowing for sustained cooking even during cloudy periods or after sunset.

This study examines the performance of a box-type solar cooker by utilizing sunflower oil as a sensible heat storage material. The sunflower oil is specifically placed within copper tubes that are installed underneath the absorbent plate of the cooker. This arrangement allows for efficient heat transfer and retention, enabling optimal utilization of the sunflower oil's thermal properties in the solar cooking process. Margins, column widths, line spacing, and type styles are built-in; examples of the type styles are provided throughout this document and are identified in italic type, within parentheses, following the example. Some components, such as multi-leveled equations, graphics, and tables are not prescribed, although the various table text styles are provided. The formatter will need to create these components, incorporating the applicable criteria that follow.

II. PERFORMANCE EVALUATION OF BOX-TYPE SOLAR COOKER

To evaluate the performance of a box-type solar cooker, some parameters must be checked. First number of merit F1, second number of merit F2, cooking power P and thermal efficiency η [12-13].

A. First Figure Of Merit

The first figure of merit is determined by the no-load test. It is the ratio of the optical efficiency to the total heat loss coefficient [13]:

$$F_1 = \frac{\eta_o}{U_L} = \frac{T_{ps} - T_{as}}{I_s} \tag{1}$$

Where:

T_{ps} Absorber plate temperature (°C);

T_{as} Ambient temperature (°C);

Is Solar radiation on horizontal surface (W/m²).

Box-type solar cookers are classified according to the Indian Standard IS 13429 (2000) into grades A and B. where in grade A; The first figure of merit F1 must not be less than 0.12, classified in class B; F2 must not be less than 0.11.

B. Second Figure Of Merit

The first figure emphasizes the advantage that the heat loss factor of the cooker is low, however, there must be a good heat transfer between the water and the cooking pot. Therefore, the second figure of merit F2 must be calculated to evaluate the heat exchange efficiency factor, F́' and the optical efficiency, η0 of the cooker. The second figure of merit is calculated by the following expression [13]:

$$F_2 = \frac{F_1 (mc_p)_w}{A_{sc}\tau} \ln \frac{1 - \frac{1}{F_1}\left(\frac{T_{wi} - \overline{T}_a}{\overline{I}_s}\right)}{1 - \frac{1}{F_1}\left(\frac{T_{wf} - \overline{T}_a}{\overline{I}_s}\right)} \tag{2}$$

Where:

m is the mass of water (kg), c_p is the specific heat capacity of water (J/kg.°C) A_i is the intercepted area of the cooker (m²), Δ_t is the time interval (s), T_{wi} Initial water temperature, T_{wf} final water temperature, T_a is the average ambient temperature (°C) , I_s is the average solar radiation (W/m²).

III. MATERIALS AND METHODOLOGY

The solar box cooker comprises an inner box that is thermally insulated, with mirrors lining its inner walls. It also includes a simple glazing lid and a booster reflector. The dimensions of the cooker are 460 mm x 380 mm x 115 mm x 430 mm. Inside the cooking chamber, there is a black-coated aluminium absorbent plate designed to capture and absorb the sunlight. A black aluminium cooking pot is placed on top of the absorbent plate, and heat is transferred from the plate to the pot through direct contact. To increase the temperature inside the cooker, a booster mirror measuring 555 mm x 380 mm is used. To achieve quick cooking response with the Solar Box Cooker (SBC), a strategic placement of copper tubes filled with sunflower oil was implemented beneath the absorption plate of the cooker, as depicted in Figure 1. This arrangement was intended to harness the remarkable heat transfer properties of sunflower oil, ensuring efficient cooking. Sunflower oil was specifically chosen as the sensible heat storage material.

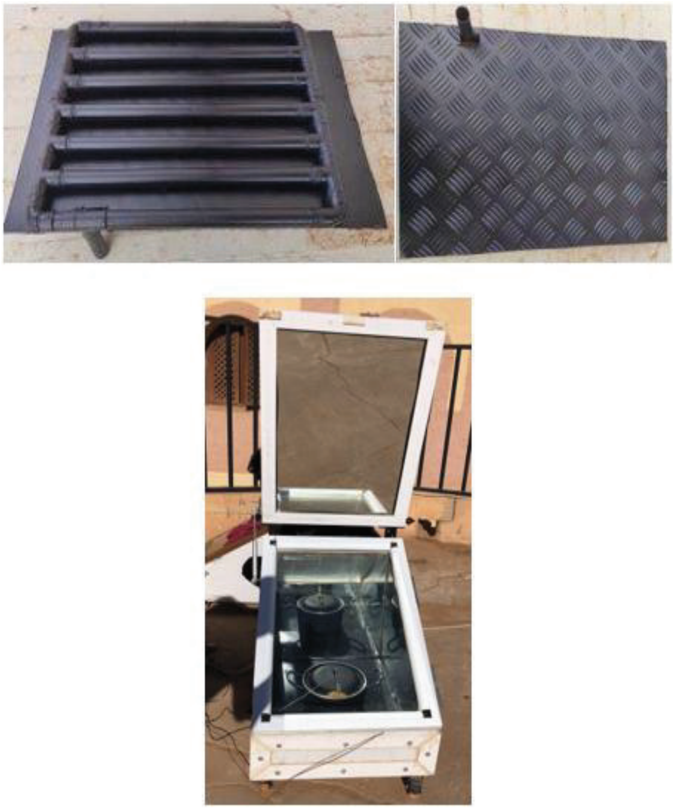

Figure 1. Photograph showcasing a box-type solar cooker with sensible heat storage

IV. EXPERIMENT AND MEASUREMENT

The performance evaluation took place at the Applied Research Unit in Renewable Energies of the Renewable Energy Development Center, located in Ghardaia, Algeria. The tests were conducted in June 2023, adhering strictly to the international standard for box cooker testing. Various parameters such as ambient temperature, wind speed, solar irradiation on a horizontal surface, absorbent plate heat, oil temperature (for heat storage), and water temperature in the cooking pot were consistently measured throughout the duration of the experiment. Furthermore, an AGILENT 34972A data acquisition unit is employed to connect sensors that monitor climatic parameters, including ambient temperature, solar radiation, and wind velocity. This data acquisition unit is then connected to a microcomputer via a USB port, enabling data transfer and analysis. During the experimental investigation, a range of instruments was utilized to gather the required data for assessing the performance of the cooker. These instruments are presented in Table 1, showcasing the tools employed in the data collection process.

TABLE I. DESCRIPTION OF THE EQUIPMENT USED DURING THE TEST.

Names of the measurement devices	**Measurement Range**	**Suspicion**
Pyranometer	0–1361 W/m²	±3 W/m²
Anemometer	0.6–20 m/s	±0.2 m/s
Micro computer	-	-
K-type differential thermocouple	-180°C to 1250°C	±1.2%
AGILENT 34972A	-	0-1%

V. RESULTS AND DISCUSSION

A. Test Without Water

To evaluate the performance of our solar cooking system and assess the efficiency of the new storage technology, a no-load experiment was performed. This experiment aimed to measure the temperature profiles of both the absorbent plate and the oil contained within the copper tubes. By conducting this experiment, we could gather valuable data regarding the thermal behavior and heat transfer capabilities of the system, providing insights into its overall effectiveness.

Figure 2 presents the typical results obtained on a sunny day, displaying the radiation intensity, ambient temperature, and various temperatures recorded within the cooker. These results show:

- During the test day, the maximum solar radiation recorded reached 864W/m².
- The absorbent plate reached a maximum temperature of 121.8°C, while the temperature of the oil (storage) peaked at 117°C.
- The absorbent plate and sunflower oil were maintained at a temperature exceeding 40°C for a duration of 200 minutes.

This sustained elevated temperature demonstrates the efficient heat retention and storage capabilities of the system over an extended period of time.

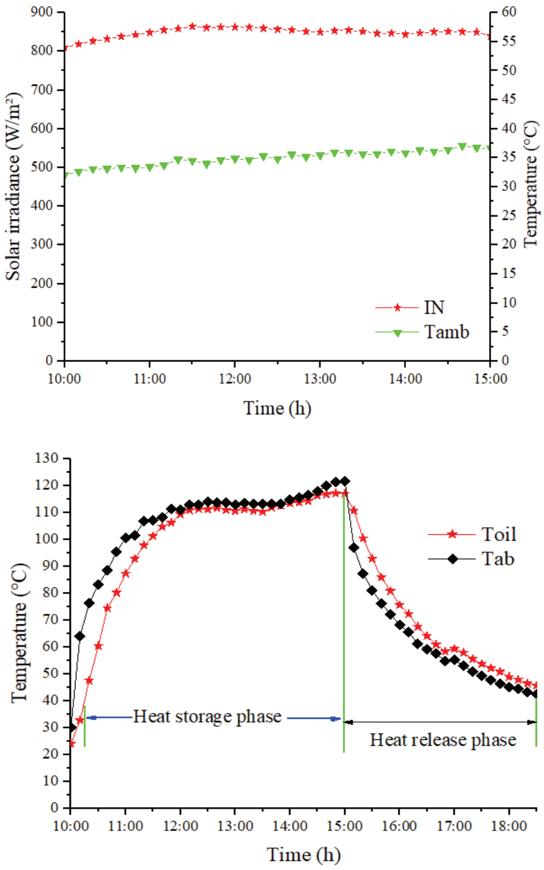

Figure 2. Variation of global solar radiation and ambient temperature, and temperature of the oil and absorbent plate during the experiment. June 2023.

B. *Test With Water*

A loading test is conducted to verify the efficient transfer of heat from the absorbent plate to the contents of the container. This test ensures that the system effectively delivers and maintains the desired temperature within the cooking vessel or container, enabling optimal heating and cooking performance.

Fig. 3 presents the typical results obtained on a sunny day, displaying the radiation intensity, ambient temperature, and various temperatures recorded within the cooker. These results show:

- The maximum solar radiation and ambient temperature during the test day are 736W/m² and 33.49°C respectively.
- The temperature of the absorbent plate, oil (storage), and water reached their maximum values at 103°C, 96°C, and 86°C, respectively.
- The water remains at a temperature above 40°C for a duration of 420 minutes.

Based on these results, our system has proven to be highly effective in long-term heat storage, making it a reliable solution for maintaining food temperature during a late dinner.

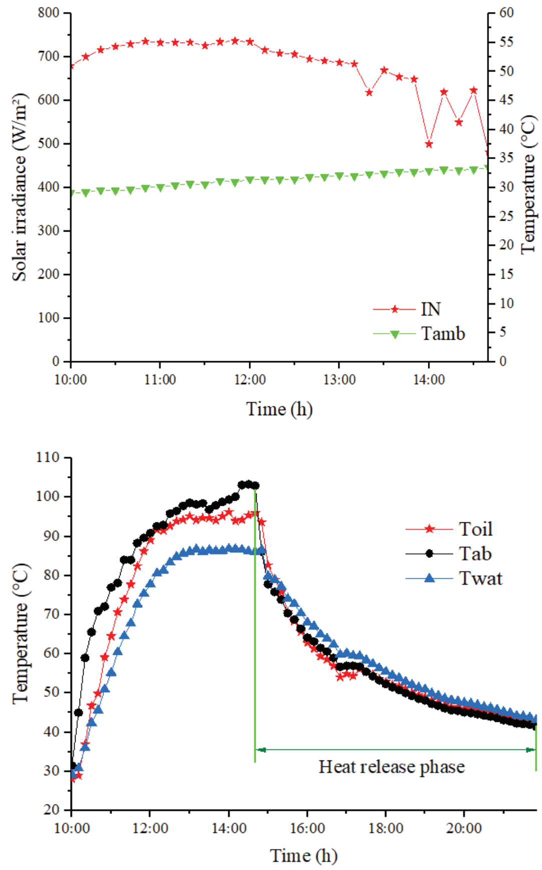

Figure 3. Variation of global solar radiation and ambient temperature, and temperature of the oil, absorbent plate, and water during the experiment. June 2023.

VI. CONCLUSION

In conclusion, the study focused on exploring the viability of heat storage in a solar cooker and its potential for practical application. Through rigorous experimentation and analysis, it was found that the solar cooker effectively stored heat, enabling it to maintain high temperatures for extended periods. This breakthrough holds significant promise for cooking enthusiasts and individuals in regions with limited access to conventional energy sources.

The results indicate that the solar cooker's heat retention capabilities, exemplified by the absorbent plate, oil storage, and water temperature measurements, are impressive. The maximum temperatures achieved 103°C for the absorbent plate, 96°C for the oil storage, and 86°C for the water demonstrate its ability to sustain high temperatures for cooking various types of food. Moreover, the system showcased exceptional performance by maintaining water temperature above 40°C for a remarkable duration of 420 minutes. This achievement signifies the solar cooker's potential for extended cooking periods, making it suitable for late dinners or instances where the food needs to be kept warm for an extended time. The findings of this research provide a solid foundation for further exploration and improvement of heat storage mechanisms in solar cookers.

References

[1] D. Phueakphum, K. Fuenkajorn, A rock fills based solar thermal energy storage system for housing, ScienceAsia, 36, 2010, 237–243.

[2] B. O. Adetifa and A. K. Aremu, Computational and experimental study of solar thermal energy store for low-temperature application. Journal of Energy Storage, 2018, 20, 427-438.

[3] S. Kuravi, J. Trahan, D.Y. Goswami, M.M. Rahman and E.K. Stefanakos, Thermal energy storage technologies and systems for concentrating solar power plants, Prog. Energy Combust. Sci. 39, 2013, 285–319.

[4] A.H. Abedin and M.A. Rosen, A critical review of thermochemical energy storage systems, Open Renew. Energy J. 4, 2011, 42–46.

[5] S.D. Sharma, H. Kitano and K. Sagara, Phase change materials for low temperature solar thermal applications, Res. Rep. Fac. Eng. Mie Univ. 29, 2004, 31–64.

[6] MEDP, The Hawkeye Solar Cooker. Class Project. Iowa, UI University of Iowa College of Engineering, 2011.

[7] R. Rahul, A. Tiwari and S. Chakravarty, Team Anshuk - Solar Cooker. [Online] Climate Healers Availableat:www.engineeringforchange.org/uploads/activity/22/22/448/1325007307434/SudarshanChakrvarthy.pdf [Accessed 23June 2014]

[8] G. Anirban, K. Jan, G. Stefan and S. Llewellyn, Estimation of biomass heat storage using thermal infrared imagery: application to a walnut orchard, Bound.-Layer Meteorol.137, 2010, 333–342.

[9] M. Augspurger and H.S. Udaykumar, Transient multi-day simulations of thermal storage and heat extraction for a finned solar thermal storage device. Sol. Energy 151, 2017, 48–60.

[10] A. Saxena and M. Karakilcik, Performance evaluation of a solar cooker with low cost heat storage material. Int. J. Sustain. Green Energy 6 (4), 2017, 57–63.

[11] H. Agrawal and A. Yadav, Design and experimental testing of solar cooker with sensible heat storage. J. Energy Res. Environ. Technol. 2, 2015, 200–204.

[12] Indian Standard (IS 13429), 2000. Bureau of Indian Standards (BIS) IS 13429.

[13] S.C. Mullick , T.C. Kandpal and A.K. Saxena . ‘’Thermal test procedure for box-type solar cooker,’’.1987.

First principles calculation of shift current bulk photovoltaic effect in polar sulfosalt Ag_5SbS_4 for solar cells

Naouel Chelil[1*]
[1]Laboratoire de Physique Quantique de la Modélisation Mathématique (LPQ3M),
Mascara, Algeria.
n.chelil@univ-masacare.dz

Mohammed.Sahnoun[1]
[1]Laboratoire de Physique Quantique de la Modélisation Mathématique (LPQ3M),
Mascara, Algeria.

Abstract— ***Ferroelectric materials for photovoltaics have sparked great interest because of their switchable photoelectric responses and above-bandgap photovoltages that violate conventional photovoltaic theory. However, their relatively low photocurrent and power conversion efficiency limit their potential application in solar cells. To improve performance, conventional strategies focus mainly on narrowing the bandgap to better match the solar spectrum, leaving the fundamental connection between polar order and photovoltaic effect largely overlooked. By unravelling the relationship between the responses of ferroelectric materials to solar radiation and their local structure and electrical polarization, we show here by first principles that a significant bulk photovoltaic effect (BPVE) is achieved in the naturally occurring mineral stephanite (Ag5SbS4) with a narrow band gap of around 1.51 eV, which agrees well with previous experimental results. Therefore, the ferroelectric properties have been studied. The calculated results show that this system has a strong electrical polarization of 41.56 µC/cm2. Furthermore, a large absorption coefficient for visible light is predicted, leading to a promising photovoltaic effect with a maximum light-to-electricity conversion efficiency of up to 27 %.***

Keywords-component; *bulk photovoltaic effect, stephanite, electric polarization, and absorption coefficient.*

I. Introduction

The bulk photovoltaic effect (BPVE) refers to the generation of a consistent photocurrent and photovoltage above the bandgap in a uniform, single-phase material lacking inversion symmetry. The mechanism driving BPVE significantly diverges from the conventional photovoltaic mechanism based on p-n junctions observed in heterogeneous materials. In recent times, there has been a renewed interest in exploring ferroelectric materials for the conversion of solar energy. This renewed enthusiasm is triggered by the discovery of photovoltages above the bandgap in ferroelectrics. To make efficient use of this large photovoltage in ferroelectric materials, we identified a candidate material from a data set of 193 naturally occurring multi-component minerals [1] that has attracted researchers' interest, is Stephanite (Ag_5SbS_4), which is known for its intriguing properties and possible applications in various fields [2-3]. The first synthesis and electrical properties of stephanite were reported by Butsko et al. [4]. They record a resistivity of about 9 Ω cm at 110 °C. As well as, stephanite has been documented to have a bandgap of 1.62 eV [5], and a recent study on a natural sample of stephanite measured a bandgap of 1.67 eV and p-type conductivity [6]. The theoretical findings of Ag_5SbS_4 were also published by Suzanne et al., [7] who studied its optoelectronic and ferroelectric properties. However, to our knowledge, the photovoltaic properties of Ag_5SbS_4 have not been investigated yet, especially the bulk photovoltaic effect (BPVE) that is universal to all materials lacking inversion symmetry. Therefore, in the current work, the FP-LAPW method based on density functional theory and the modern theory of polarization based on the Berry phase approach were used to calculate the optical and ferroelectric properties of Ag_5SbS_4, respectively. Subsequently, utilizing the derived computed results, we delved into the examination of photoresponse and photovoltaic characteristics employing the Spectroscopic Limited Maximum Efficiency (SLME) model. Within this framework, we evaluated both the power conversion efficiency and the photocurrent density–voltage (J–V) characteristics. We will illustrate that the ferroelectric phase of Ag_5SbS_4 is capable of manifesting promising nonlinear optical responses. This observed phenomenon could potentially underlie the high photovoltaic efficiency observed in forthcoming solar cell technologies.

II. COMPUTATIONAL DETAILS

For the computation of Ag_5SbS_4 material's physical properties, the Full Potential Linear Augmented Plane Wave (FP-LAPW) method within the framework of the DFT was employed, utilizing the WIEN2k code [8]. The Perdew-Burke-Ernzerhof (PBE) generalized gradient approximation (GGA) was used to describe the exchange correlation energy. To enhance accuracy, the modified Becke-Johnson approximation (mBJ) functional [9] was adopted. This modification addresses the common underestimation of band gaps by the standard DFT functional (GGA), particularly regarding optical and electronic property calculations. In the FP-LAPW calculations, convergence of energy eigenvalues was achieved using a plane wave with a cutoff of Kmax×RMT = 8. Additionally, potentials and wave functions within interstitial regions were expanded using spherical harmonics. Here, in plane wave propagation, Kmax signifies the highest K-vector magnitude, while the smallest muffin-tin (MT) sphere radius is denoted by RMT.

III. RESULTS AND DISCUSSIONS

A. structural stability of Stephanite (Ag5SbS4)

Stephanite, denoted by the chemical formula Ag_5SbS_4, organizes itself within the orthorhombic crystal lattice, specifically adopting the $Cmc2_1$ space group configuration (as illustrated in Figure 1 (b)). This structural arrangement involves the alignment of SbS_3 trigonal pyramids into layers along the z-axis, interconnected by silver (Ag) atoms. These Ag atoms form geometric configurations that are both triangular and nearly tetrahedral in relation to sulfur (S) atoms. Notably, this arrangement alternates between pyramids occupied by antimony and those that remain vacant. Within the compound, there are two short Sb-S bond lengths, measuring 2.47 Å, in addition to a single extended distance of 2.52 Å. Silver atoms exhibit a tetrahedral coordination pattern with the SbS_3 groups. The arrangement of the structure reveals three distinct AgS_4 tetrahedra types, each marked by varying Ag-S distances. A remarkable highlight of this arrangement is the significant occurrence of shared edges interconnecting the Ag tetrahedral.

First, a volume optimization was performed to predict the most favorable configuration (shown in Figure 1(a)). The resulting calculated equilibrium lattice constants were determined to be a = 7.7853 Å, b = 12.526 Å and c = 9.1221 Å. Remarkably, these values agree with previous calculations that gave a = 7.830 Å, b = 12.450 Å and c = 8.54 Å [7], as well as with the experimentally observed dimensions of a = 7.830 Å, b = 12.450 Å and c = 8.54 Å [10].

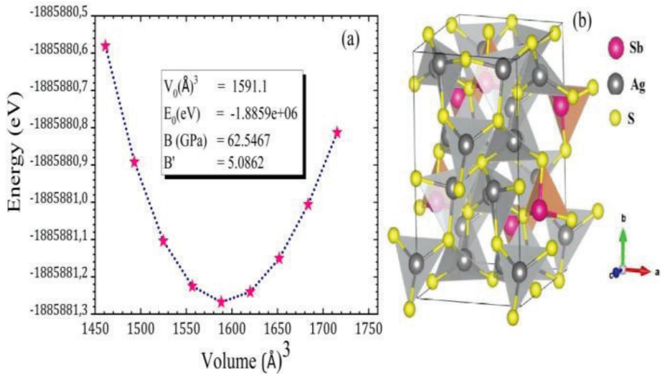

Figure 1. (a) Calculated the total energy against the cell volume, (b) Illustrations of the crystal structure of stephanite.

B. Electronic properties

To delve into the electronic characteristics of this compound, one initiates the exploration with the computed band structure across symmetry directions, namely Γ, X, S, R, A, Z, Γ, Y, X, and A. Furthermore, partial density of states (PDOSs) for the Stephanite (Ag_5SbS_4) material is depicted in Figure 2. It's worth noting that the energy zero reference was established at the summit of the valence band. Prominently, our predictions unveil a direct band gap, measuring 1.51 eV, situated at the Γ point within the Brillouin zone. This outcome finds good accord with the values reported in experimental literature [11, 12]. The dispersive nature of the conduction band minimum (CBM) at the band edge (fig. 2(a)) suggests the possibility of significant carrier mobility.

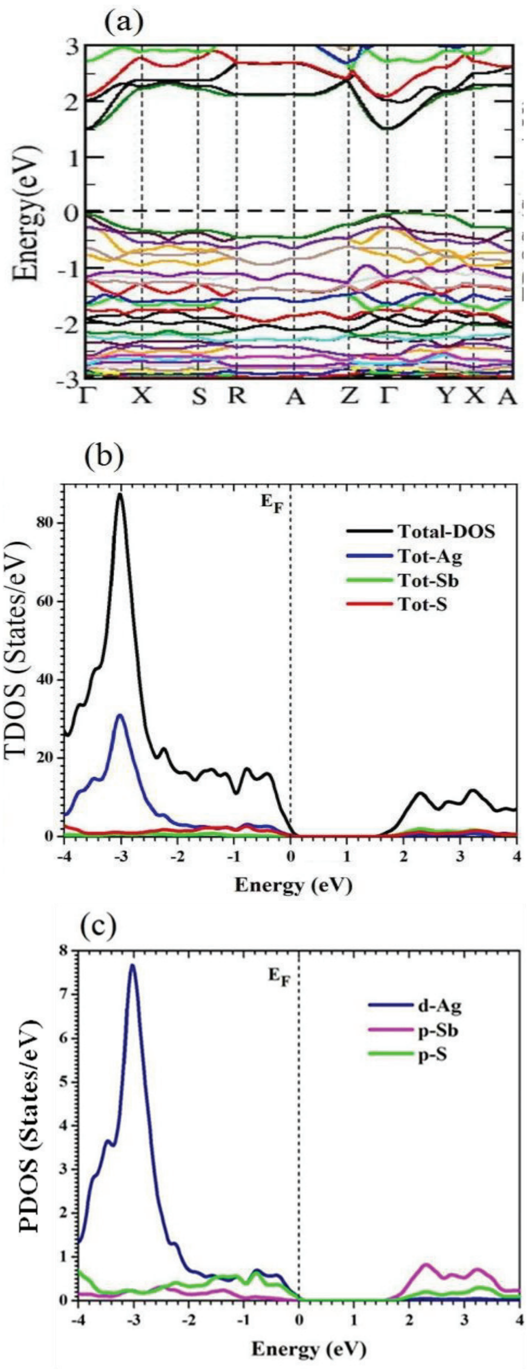

Figure 2. (a) Electron structure and both (b) the total DOS and (c) atomic projected DOS for Ag_5SbS_4.

The density of states associated with the electronic structure of stephanite, as illustrated in Figures 2 (b) and (c), unveils insightful details. It becomes apparent that the valence band (VBM) primarily originates from an anti-bonding hybridization interaction between Ag d-states and neighboring S p-states. While Sb p-states seem to make a marginal contribution to the VBM, they hold relatively minor influence. On the contrary, the formation of the conduction band predominantly stems from bands linked to the lower energy states of Sb 5p.

C. Optical properties

As elucidated in the previous subsection, Ag_5SbS_4 boasts a nearly optimal bandgap of 1.51 eV, situated within the lower threshold of visible light. This bandgap proves well-suited for solar light absorption, given the photon energy range of visible light. Furthermore, the inherent polar arrangement may offer advantageous prospects for the separation of photogenerated electron-hole pairs, a trait anticipated in ferroelectric materials [13-16].

In order to complete the comprehension of its optical properties, it becomes paramount to establish the dielectric function [17]. This function is represented as

$\varepsilon(\omega) = \varepsilon_1(\omega) + i\varepsilon_2(\omega)$, where the real component ($\varepsilon_1(\omega)$) is expressed as follows:

$$\varepsilon_1(\omega) = 1 + \frac{2}{\pi} P \int_0^{\infty} \frac{\omega' \varepsilon_2(\omega')}{\omega'^2 - \omega^2} d\omega' \tag{1}$$

On the other hand, imaginary part $\varepsilon_2(\omega)$, may also calculate using the momentum tensors between the occupied and unoccupied wave functions [18, 19].

$$\varepsilon_2(\omega) = \frac{2e^2\pi}{\Omega \varepsilon_0} \sum_{K,V,C} \left|\langle \psi_k^c | \hat{U} \cdot \vec{r} | \psi_k^v \rangle\right|^2 \delta\left(E_K^C - E_K^V\right. \tag{2}$$

Here, ω signifies the light frequency. Ψ_K^C and Ψ_K^V denote the conduction and valance band wave function at k, respectively, *e* is the electronic charge, Ω represents the unit cell volume, and U indicates the unit vector along the polarization of the incident electric field. The delta function ensures energy and momentum conservation during a transition between occupied and unoccupied electronic states through the emission or absorption of photon energy, E. E_K^C and E_K^V denote the energy of electrons at a certain k-vector in the conduction and valence bands, respectively. The rest of the optical parameters are calculated using the expressions given elsewhere [20].

Figs. 3 (a) and (b) illustrate the real $\varepsilon_1(\omega)$ and imaginary $\varepsilon_2(\omega)$ parts of the calculated dielectric function for Stepahnite. Our computations reveal distinct peaks in $\varepsilon_2(\omega)$ at around 2.8, 4.1 and 6.9eV, signifying interband transitions from valence to conduction band states. From Figure 3(a), we deduce the average static dielectric function $\varepsilon_1(0)$, yielding a value of 6.91.

Ag_5SbS_4 displays a broad absorption spectrum up to photon energy of 1.51 eV, accompanied by a substantial optical absorption coefficient (around $14*10^5$ cm^{-1} within the photon energy range below 8 eV). This remarkable absorption coefficient over a wide range of photon energy endows Ag_5SbS_4 the advantageous capability of efficiently absorbing incident light, while maintaining the absorber layer thickness small. The anisotropy of the dielectric constant results naturally from the anisotropy of the crystal. As a result, anisotropy is also present in the absorption, which depends on the dielectric constant.

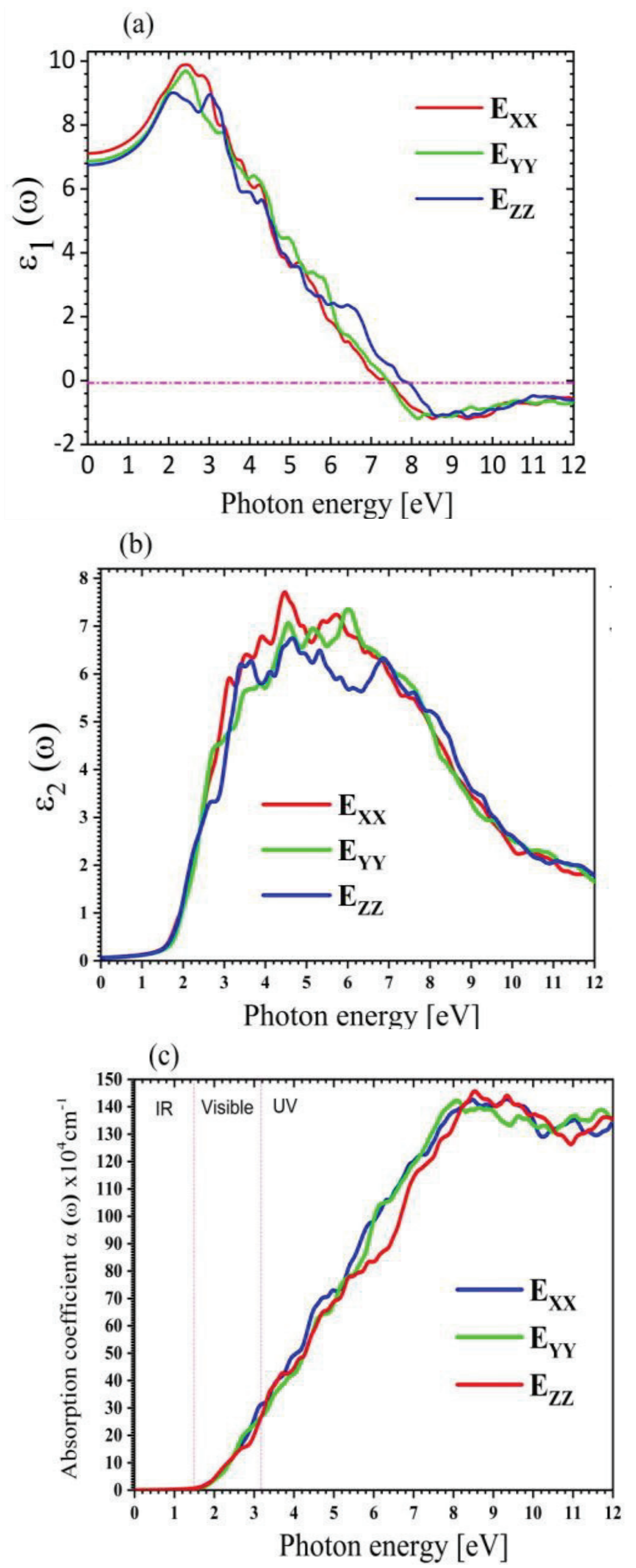

Figure 3. Optical properties calculated using Tb-mBJ exchange method. The calculated dielectric spectra: (a-b) real and imaginary parts. (c) The calculated absorption coefficient α(ω) of Ag_5SbS_4.

D. ferroelectric properties

Stephanite adopts the space group configuration of $Cmc2_1$ (#36). This group lacks polarization along the x-axis because a mirror plane is present in the yz-plane. Additionally, polarization is limited to the z-direction when there is a helical axis along it [10]. In this section, we have calculated the magnitude of spontaneous polarization using modern theory of the polarization based on the Berry phase formalism [21]. Our analysis reveals that the strength of Ps for stephanite stands at 41.56 µC/cm², exceeding the computed value (of 31.9 $\mu C.cm^{-2}$) from first principles [7]. This calculated Ps is substantial and comparable to that of conventional ferroelectric materials including: $BaTiO_3$ and $PbTiO_3$. In particular, our structure shows that there is no polarization along the x and y axes. The moving of silver ions through the crystal lattice, where these changes contribute to their ferroelectric features, causes spontaneous polarization (Ps) to arise along the z-axis in Ag_5SbS_4.

E. Spectroscopic Limited Maximum Efficiency Results and Their Correlation to Absorption Strength

A strong optical absorption above a suitable Eg is a necessary condition for realizing highly efficient, thin-film PV performance [22]. Having clearly established the bandgap in the present material, we then evaluated its performance as an active layer in PV cells using a spectroscopically limited maximum efficiency model (SLME) [23]. The estimated current density-voltage (J−V) curve of a single p-n junction based Stephanite solar cell is used to determine the solar to electric power conversion efficiency (PCE), η. The PCE of a solar cell is the ratio of power output from the solar cell (P_{out}^{max}) to the power input from the Sun (Pin)

$$\eta = P_{out}^{max} / P_{in} \qquad (3)$$

Where P_{out}^{max} is given in terms of the V_{OC} (the voltage from the J−V curve of the solar cell at J = 0) and the short-circuit current density, J_{SC}, (the current density on the J−V curve at V= 0).

Fig. 4 illustrates the thickness-dependent efficiency (η) and performance characteristics of the active (absorber) layer in the proposed sulfosalt stephanite. The curve underlines the significant impact of absorber layer thickness (L) on efficiency, whose maximum limit can reach 25 % for a thickness of 80 µm, with accompanying values of J_{SC} = 34.16 $mA.cm^{-2}$, V_{OC} = 1.22 V and a fill factor (FF) of 0.89.
This result is surprising since the SQ limit is widely regarded as the theoretical maximum efficiency of a single junction absorber layer, and the SLME is based on the same detailed balance approach as the SQ limit. Due to the design of the SLME, the calculated efficiency returns to the SQ limit for $L\to\infty$, since for an infinitely thick absorption layer the absorptivity becomes a step function.

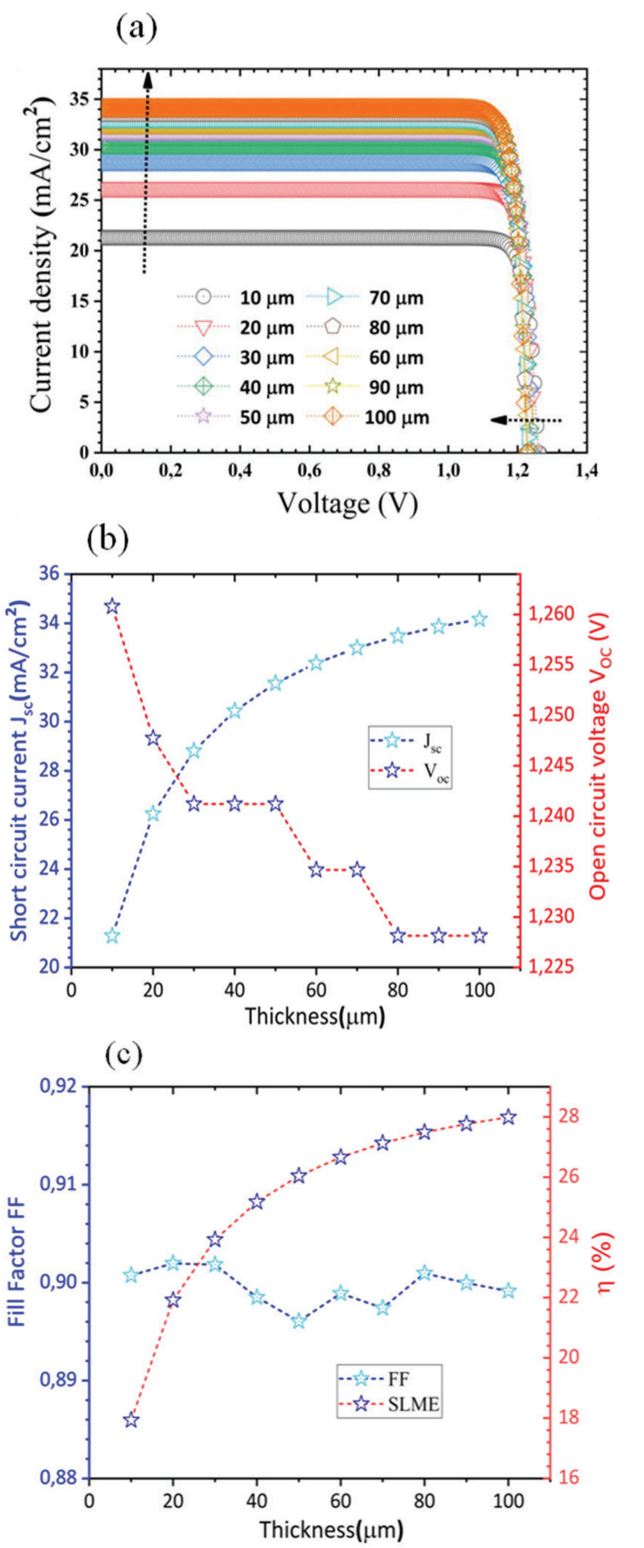

Figure 4. (a) J-V characteristic, (b) photovoltaic performances and (c) calculated maximum photovoltaic energy conversion efficiency for the stephanite Ag_5SbS_4 as a function of absorber layer thickness.

Compared to the estimated efficiencies of other photovoltaic materials such as $AgInTe_2$ (27.6%), $CH3NH_3PbI_3$ (30%), and $CuBiS_2$ (22%) [24-25] (evaluated using the same methodology), the demonstrated efficiencies remain remarkable. The increased J_{SC} is attributed to increased light absorption and a possible reduction in the photocharge recombination rate, both of which are due to the lower (direct) bandgap. In this regard, Ag_5SbS_4 is proving to be a promising photovoltaic material with significant efficiency potential.

F. Bulk photovoltaic effect (Nonlinear photocurrent)

Under uniform steady illumination on homogeneous crystals lacking inversion symmetries, a steady-state direct current (DC) is generated as a result of a second-order nonlinear optical response of the crystal, leading to phenomenon such as the bulk photovoltaic effect (BPVE) [26-31]. The direction of these direct currents has been found to depend on the light polarization, movement of electrons upon excitation, and photon energies [32].

A monochromatic electric field is in the form, $E^b(t)=E^b(\omega)e^{i\omega t}+E^b(-\omega)e^{-i\omega t}$ and the shift current can be expressed in terms of a third rank tensor, $\sigma^{abc}(0;\omega,-\omega)$ as

$$J^a_{\text{shift}}(\omega) \cong C\sum_b \sigma^{abc}(0;\omega,-\omega)E^b(\omega)E^c(-\omega) \tag{4}$$

The shift-current tensor is given by

$$\sigma^{abc} = C\int \frac{dk^D}{(2\pi)^D}\sum_{n,m} f_{n,m} I^{abc}_{nm} \times \delta(\omega_{nm}-\omega)$$

Where $r_{mn}{}^a$ is the velocity matrix element and $r_{mn}{}^a$; a is the generalized derivative, defined as

$$r^a_{mn;b} = \frac{\partial r^a_{mn}}{\partial k^b} - i(A^b_{nn} - A^b_{mm})r^a_{nm}, \text{ and } A^a_{nm}$$

The Berry connection [33], with a and b denoting Cartesian directions. The Fermi–Dirac occupation numbers are $f_{nm} = f_n - f_m$, while the band energy difference is defined as $\hbar\omega_{nm} = \hbar\omega_n - \hbar\omega_m$.

For linearly polarized incident light, a = b, thus, eq 5 is proportional to the shift “vector” $R_{nm}{}^{ab}$, defined as

$$r^a_{mn;b} = \frac{\partial r^a_{mn}}{\partial k^b} - i(A^b_{nn} - A^b_{mm})r^a_{nm}, \text{ and } A^a_{nm}$$

The point group $Cmc2_1$ to which the stephanite belongs, allows five tensorial components of $\sigma^{abc}(0;\omega,-\omega)$ to be nonzero, namely σ^{xzX}, σ^{yzY}, σ^{xxZ}, σ^{yyZ}, and σ^{zzZ}.

Fig.5 represents the nonzero components of the shift-current spectrum as a function of photon energies for Ag_5SbS_4.

All shift current responses are zero below the bandgap, and they all achieve a maximum absolute value of about 30 µA V^{-2} above the band edge in the visible spectrum, which is highly desired for efficient solar energy conversion. The dominat current response is $\sigma^{zzZ}(0,\omega,-\omega)$ that reaches −217.6 $\mu A/V^2$ at an incident photon energy of 3.32 eV (Fig. 5) where the negative sign indicates the current along –Z opposite to the direction of the spontaneous polarization. This is much larger than the other components (σ^{xzX}, σ^{yzY}, σ^{xxZ}, and σ^{yyZ}). The large SCs are related to the composition of the highest VB and the lowest CB of this material, with the *d* orbitals making a large contribution and the *p* orbitals making a small contribution. Note that this value surpasses the SC photoconductivity calculated in many other two-dimensional (2D) materials, such as MoS_2 [34], GeS [35], and α-NP [36]. The characteristics of representative photovoltaic materials are collected in Table I, where the last two entries correspond to low-dimensional materials; while their peak photo-conductivities surpass that of Ag_5SbS_4.

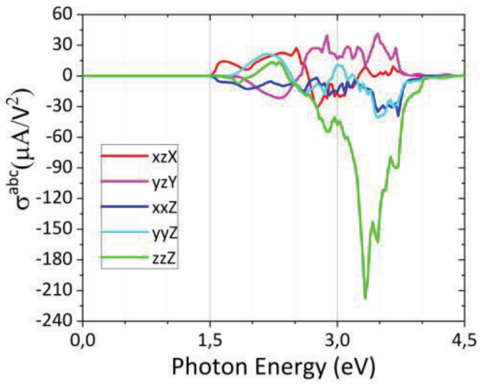

Figure 5. Calculated shift current tensor elements for the stephanite Ag_5SbS_4.

TABLE I. Peak shift photoconductivities, peak frequencies, and employed XC functionals, for a collection of bulk and lowdimensional photovoltaic materials. Here GGA denotes generalized gradient approximation and LDA local-density approximation.

Material	σ^{abc} (μAV^{-2})	E(eV)	XC functional
Ag_5SbS_4	~30	~2.5	Tb-mBJ
	-60, -217.6	2.8, 3.32	
BC2N-A_2 [a]	50	1.3	GGA
$PbTiO_3$, $BaTiO_3$ [b]	50, 30	6.0, 6.5	GGA
GaAs [c]	40	5.5	LDA+scissors
$LiAsSe_2$, $NaAsSe_2$ [d]	13, 15	2.0, 3.1	GGA+scissors
$BiFeO_3$ [e]	0.8	3.5	GGA+U
RhBiS, IrBiSe [f]	80, 40	1.3, 2.1	GGA
CaAlSiH [g]	6	1.3	GGA
2D GeS, GeSe [h]	160, 200	2.8, 2.0	GGA+scissors
1D polymers [i]	60–180	0.6–0.8	GGA

[a] *Ref.* [37], [b] *Ref.* [38], [c] *Ref.* [39], [d] *Ref.* [40], [e] *Ref.* [41], [f] *Ref.* [42], [g] *Ref.* [43], [h] *Ref.* [44], [i] *Ref.* [45].

G. Conclusions

In summary, we report the electronic structures and optical properties of the naturally-occurring mineral with polar structure (Ag_5SbS_4) through the first principle calculations. It was found to have strong ferroelectric polarization. Furthermore, a large visible light absorption coefficient is predicted, leading to a promising photovoltaic effect with a maximum light-to-electricity conversion efficiency of up to 27 %. We also calculate the shift current in this material to understand the implication of polarizations on BPVE. A larger shift current of 217 $\mu A/V^2$ at a photon energy of 3.32 eV is obtained along the direction of out-of-plane polarization under the illumination of zz polarized light whereas a negligible shift current is obtained along the direction of in-plane polarization under xx(yy)-polarized light. This is related to the real spatial transition of the valence electron occupied by Ag-d and the conduction electron occupied by Sb-p. However, the peak of shift current response lies well outside the visible spectrum in the ultraviolet range. The peak of shift current response in the visible spectrum is highly desired for efficient solar energy conversion. This study would be crucial for understanding the BPVE in Ag_5SbS_4. Therefore, further implementation is required to tune the displacement current response to visible light.

ACKNOWLEDGMENT (HEADING 5)

We thank Professor Sahnoun Mohammed for sharing his idea with me and helping me to prepare this work.

REFERENCES

[1] R. L. Bonewitz, Rocks and Minerals, Dorling Kindersley, Ltd, 2012

[2] Wallace, S. K., Svane, K. L., Huhn, W. P., Zhu, T., Mitzi, D. B., Blum, V., & Walsh, A. (2017). Candidate photoferroic absorber materials for thin-film solar cells from naturally occurring minerals: enargite, stephanite, and bournonite. Sustainable Energy & Fuels, 1(6), 1339-1350.

[3] Setter, N., Damjanovic, D., Eng, L., Fox, G., Gevorgian, S., Hong, S., ... & Streiffer, S. (2006). Ferroelectric thin films: Review of materials, properties, and applications. Journal of applied physics, 100(5).

[4] N. I. Butsko, I. D. Zhezhnich and M. M. Pidorya, Russ. Phys. J., 1973, 16, 223–224

[5] H. Dittrich, A. Stadler, D. Topa, H.-J. Schimper and A. Basch, Phys. Status Solidi A, 2009, 206, 1034–1041

[6] B. Durant and B. A. Parkinson, 2016 IEEE 43rd Photovoltaic Specialists Conference (PVSC), 2016

[7] Wallace, S. K., Svane, K. L., Huhn, W. P., Zhu, T., Mitzi, D. B., Blum, V., & Walsh, A. (2017). Candidate photoferroic absorber materials for thin-film solar cells from naturally occurring minerals: enargite, stephanite, and bournonite. Sustainable Energy & Fuels, 1(6), 1339-1350.

[8] Blaha, P., Schwarz, K., Madsen, G. K., Kvasnicka, D., & Luitz, J. (2001). wien2k. An augmented plane wave+ local orbitals program for calculating crystal properties, 60(1).

[9] Tran, F., & Blaha, P. (2009). Accurate band gaps of semiconductors and insulators with a semilocal exchange-correlation potential. Physical review letters, 102(22), 226401.

[10] Butsko, N. I., Zhezhnich, I. D., & Pidorya, M. M. (1973). Some physical properties of stephanite in the phase transition region. Soviet Physics Journal, 16, 223-224.

[11] B. Durant and B. A. Parkinson, 2016 IEEE 43rd Photovoltaic Specialists Conference (PVSC), 2016.

[12] H. Dittrich, A. Stadler, D. Topa, H.-J. Schimper and A. Basch, Phys. Status Solidi A, 2009, 206, 1034–1041

[13] K. T. Butler, J. M. Frosta, and A. Walsh, Energy Environ. Sci. 8, 838 (2015).

[14] Y. Yuan, T. J. Reece, P. Sharma, S. Poddar, S. Ducharme, A.Gruverman, Y. Yang, and J. Huang, Nature Mater. 10, 296 (2011).

[15] R. Nechache, C. Harnagea, S. Li, L. Cardenas, W. Huang, J. Chakrabartty, and F. Rosei, Nature Photon. 9, 61 (2015).

[16] X. Huang, T. R. Paudel, S. Dong, and E. Y. Tsymbal, Phys. Rev. B 92, 125201 (2015).

[17] Mubarak, A. A. The first-principle study of the electronic, optical thermoelectric properties of XTiO3 (X = Ca, Sr, Ba) compounds. Int. J. Mod. Phys. B 30, 1650141 (2016).

[18] Draxl, C. A. & Sofo, J. O. Linear optical properties of solids within the full-potential linearized augmented plane wave method. Comput. Phys. Commun. 175, 1–14 (2006).

[19] Smith, N. V. Photoelectron energy spectra the band structures of the noble metals. Phys. Rev. B 3, 1862–1878 (1971).

[20] Hadi, M. A., Vovk, R. V. & Chroneos, A. Physical properties of the recently discovered Zr2(Al1−x Bix)C MAX phases. J. Mater. Sci. Mater. Electron. 27, 11925–11933 (2016).

[21] Spaldin, N. A. (2012). A beginner's guide to the modern theory of polarization. Journal of Solid State Chemistry, 195, 2-10.

[22] L. Yu , S. Lany , R. K. Kykyneshi , V. Jieratum , B. Pelatt , E. Altschul , H. A. S. Platt , J. F. Wager , D.A. Keszler , A. Zunger , Adv. Energy. Mater. 2011 , 1 , 748.

[23] Yu, L., & Zunger, A. (2012). Identification of potential photovoltaic absorbers based on first-principles spectroscopic screening of materials. Physical review letters, 108(6), 068701.

[24] Yu, L., Kokenyesi, R. S., Keszler, D. A., & Zunger, A. (2013). Inverse design of high absorption thin-film photovoltaic materials. Advanced Energy Materials, 3(1), 43-48.

[25] Yin, W. J., Shi, T., & Yan, Y. (2014). Unique properties of halide perovskites as possible origins of the superior solar cell performance. Advanced materials, 26(27), 4653-4658.

[26] von Baltz, R.; Kraut, W. Theory of the Bulk Photovoltaic Effect in Pure Crystals. Phys. Rev. B 1981, 23, 5590.

[27] Fridkin, V. M. Bulk Photovoltaic Effect in Noncentrosymmetric Crystals. Crystallogr. Rep. 2001, 46, 654– 658.

[28] Boyd, R. W. Chapter 2-Wave-equation Description of Nonlinear Optical Interactions. Nonlinear Opt. 2008, 69– 133.

[29] Ivchenko, E. L.; Pikus, G. E. Localized Electron States and Excitons in Heterostructures. In Superlattices and Other Heterostructures; Springer: Berlin, Heidelberg, 1997; pp 125– 161.

[30] Chynoweth, A. G. Surface Space-Charge Layers in Barium Titanate. Phys. Rev. 1956, 102, 705.

[31] Rangel, T.; Fregoso, B. M.; Mendoza, B. S.; Morimoto, T.; Moore, J. E.; Neaton, J. B. Large Bulk Photovoltaic Effect and Spontaneous Polarization of Single-Layer Monochalcogenides. Phys. Rev. Lett. 2017, 119, 067402.

[32] Panday, S. R.; Barraza-Lopez, S.; Rangel, T.; Fregoso, B. M. Injection Current in Ferroelectric Group-IV Monochalcogenide Monolayers. Phys. Rev. B 2019, 100, 195305.

[33] G. Pizzi , V. Vitale , R. Arita , S. Blügel , F. Freimuth , G. Géranton , M. Gibertini , D. Gresch , C. Johnson , T. Koretsune and J. Ibañez-Azpiroz , J. Phys.: Condens. Matter, 2020, 32 , 165902

[34] H. Xu, H. Wang, J. Zhou, and J. Li, Pure spin photocurrent in non-centrosymmetric crystals: Bulk spin photovoltaic effect, Nat. Commun. 12, 4330 (2021).

[35] X. Mu, Y. Pan, and J. Zhou, Pure bulk orbital and spin photocurrent in two-dimensional ferroelectric materials, npj Comput. Mater. 7, 61 (2021).

[36] N. T. Kaner, Y. Wei, T. Ying, X. Xu, W. Li, A. Raza, X. Li, J. Yang, Y. Y. Jiang, and W. Q. Tian, Giant shift photovoltaic current in group V-V binary nanosheets, Adv. Theory Simul. 5, 2100472 (2022).

[40] Ibañez-Azpiroz, J., Souza, I., & de Juan, F. (2020). Directional shift current in mirror-symmetric BC 2 N. Physical Review Research, 2(1), 013263.

[41] S. M. Young and A. M. Rappe, First Principles Calculation of the Shift Current Photovoltaic Effect in Ferroelectrics, Phys. Rev. Lett. 109, 116601 (2012).

[42] F. Nastos and J. E. Sipe, Optical rectification and shift currents in GaAs and GaP response: Below and above the band gap, Phys. Rev. B 74, 035201 (2006).

[43] J. A Brehm, S. M Young, F. Zheng, and A. M Rappe, Firstprinciplescalculationofthebulkphotovoltaiceffectinthepolar compounds LiAsS2, LiAsSe 2, and NaAsSe2, J. Chem. Phys. 141, 204704 (2014).

[44] S. M. Young, F. Zheng, and A. M. Rappe, First-Principles Calculation of the Bulk Photovoltaic Effect in Bismuth Ferrite, Phys. Rev. Lett. 109, 236601 (2012).

[45] Y. Zhang, F. de Juan, A. G. Grushin, C. Felser, and Y. Sun, Strong bulk photovoltaic effect in chiral crystals in the visible spectrum, Phys. Rev. B100, 245206 (2019).

[46] J.A.Brehm,Predictedbulkphotovoltaiceffectinhydrogenated Zintl compounds, J. Mater. Chem. C 6, 1470 (2018).

[47] T. Rangel, B. M. Fregoso, B. S. Mendoza, T. Morimoto, J. E. Moore, and J. B. Neaton, Large Bulk Photovoltaic Effect and Spontaneous Polarization of Single-Layer Monochalcogenides, Phys. Rev. Lett. 119, 067402 (2017).

[48] S. Liu, F. Zheng, and A. M. Rappe, Giant bulk photovoltaic effect in vinylene-linked hybrid heterocyclic polymer, J. Phys. Chem. C 121, 6500 (2017).

Fuzzy Logic Based Energy Management for Electric UAV

Haroune Aouzellag
Département de génie électrique,
Faculté de Technologie, Université de Béjaia, UAMB
06000 Béjaia, Algeria
haroune.aouzellag@univ-bejaia.dz

Meziane Hamel
Département d'ingénierie des systèmes électriques
Faculté de Technologie, université de Boumerdes
35000 Boumerdes, Algeria

Abstract—**this paper presents an energy management strategy for an unmanned aerial vehicle (UAV) based on fuzzy logic control (FLC). The FLC is an online technique to optimize the energy flows between different sources in aim to minimize fuel consumption and maintain the state of charge of storage sources. The UAV has a fuel cell (FC), photovoltaic panels (PV) and ultra capacitor (UC) as sources and these sources are chosen to increase the system's energy autonomy for long-endurance missions. The UAV's electrical and mechanical elements are modeled using MATLAB/Simulink and SimPower Systems packages. The state-flow control system of MATLAB is utilized to implement the strategy.**

Keywords-Energy management; ultra capacitor; battery; fuel cell; vehicle; equivalent consumption minimization.

I. Introduction

Compared with the conventional UAV that uses fossil energy, the uses of renewable energy sources in such as application, takes many advantages in terms of emission, efficiency, stealth and noise. For short-distance application, only a suitable battery pack can meet all power requirements and support a flight mission of tens of minutes. For longue distance application, several research projects are proposing structures based on renewable energies. However, the proposed solutions remain insufficient in the face of the endurance of fossil fuels due to their very high energy density. The solution to the endurance problem for clean UAVs is a combination of onboard renewable energy sources.

The use of multiple energy sources in the same system requires the installation of energy management techniques to control the flow of energy between the sources and the traction system.

II. Model of the UAV

The power system of the UAV is expected to guaranty high energy density and high power density.

A. Model of the UAV

In this sub-section, the mathematical models of different UAV components as shown in Fig. 1 are presented.

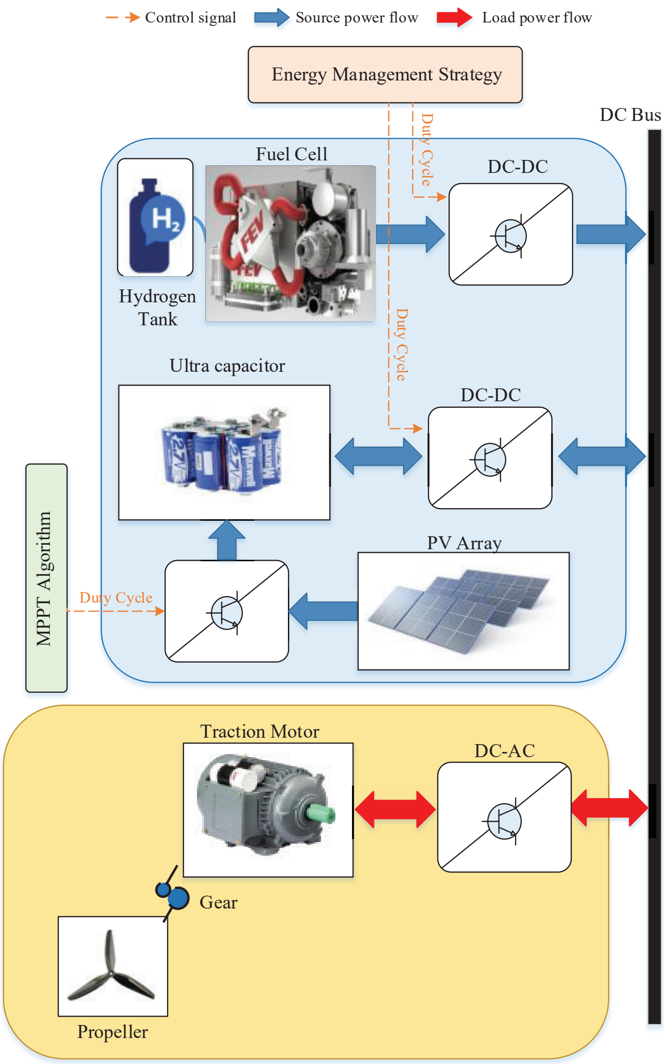

Figure 1. Electric UAV model

1) Dynamic model of the UAV

The dynamic model of the UAV can be described by the following equations system [1-2]:

$$\begin{cases} m\,\dot{V} = T\cos\alpha - D - m\,g\sin\gamma \\ m\,V\,\dot{\gamma} = T\sin\alpha + L - m\,g\cos\gamma \\ \dot{y} = V\sin\gamma \\ \dot{x} = V\cos\gamma \end{cases} \quad (1)$$

The drag (D) and lift force (L) are expressed as following:

$$D = \frac{1}{2}\rho\,V^2\,S\,C_D \quad (2)$$

$$C_D = C_{D0} + k\,C_L^2 \quad (3)$$

$$k = \frac{1}{e\,\pi\,A\,R} \quad (4)$$

$$e = 1.78\,(1 - 0.045\,A\,R^{0.68}) - 0.64 \quad (5)$$

$$L = \frac{1}{2}\rho\,V^2\,S\,C_L \quad (6)$$

where V is the linear speed of the UAV, ρ air density, S surface area of the wing, C_L and C_D lift and drag coefficients.

The power consumed by a moving object is the product of the torque (T) on the drive shaft and the speed of movement (V). If we take into account the efficiency of the propeller, we have the following formula:

$$P_{dem} = \frac{T\,V}{\eta_{prop}} \quad (7)$$

$$T = D \quad (8)$$

2) *Fuel cell model*

The specific parameters calculation of the PEMFC are as follow [3-4]:

$$V_{fc} = N_{fc}\,(E_{nernst} - V_{act} - V_{ohm} - V_{con}) \quad (9)$$

where V_{fc} is the FC output voltage, obtained from the theoretical voltage E_{nernst}, which is subject to various voltage drops.

The Nernst voltage E_{nernst} that can be expressed as follow:

$$E_{nernst} = 1.229 + 0.85\times10^{-3}(T - 298.15) + 4.3085\times10^{-5}T\left[\ln\left(P_{H_2}\right) + \tfrac{1}{2}\ln\left(P_{O_2}\right)\right] \quad (10)$$

The gas pressure is assumed to be constant and only the electrical dynamics are taken into account in this study.

The resistive losses can be calculated as follows:

$$V_{ohm} = R_{fc}I_{fc} \quad (11)$$

The activation losses are deduced from the relationship between I_{fc} and the current density I_0. They are given by the Tafel relation as follows:

$$\boldsymbol{V_{act} = A\ln\left(\frac{I_{fc}}{I_0}\right)} \quad (12)$$

The concentration polarization losses are defined as:

$$\boldsymbol{V_{con} = \frac{R\,T}{z\,F}\ln\left(1 - \frac{I_{fc}}{I_{lim}}\right)} \quad (13)$$

TABLE I. PEMFC PARAMETERS

Parameter	*Value*	*Unit*
Maximal Stack power	22.5	kW
Nominal Stack Power	18.3	kW
Nernst Voltage	1.28	V
Nominal Airflow rate	1698	Lpm
Nominal fuel supply pressure	H2: 2.1, O2: 2	bar
Nominal efficiency	55	%
Operating temperature	95	℃

A FC of 18.3 kW is used with 22.5 kW maximal power, as mentioned in Tab. 1, to guarantee the maximum power that can be requested by the propeller and to cover the various losses.

To reduce the fuel consumption, the FC system should be operated efficiently. Fuel cell theoretical efficiency is defined as the ratio between FC output power and the power of hydrogen consumed as follow:

$$\eta_{LHV} = \frac{P_{fc}}{P_{H_2}} \quad (14)$$

The efficiency of the FC system is the product of the theoretical efficiency and the efficiency of the auxiliary systems.

$$\eta_{fcs} = \eta_{LHV}\times\eta_{aux} = \frac{V_{fc}}{1.254}\left(\frac{P_{fc} - P_{aux}}{P_{fc}}\right) \quad (15)$$

The hydrogen mass consumption rate can be defined by fuel cell power as the following equation [12]:

$$m_{H_2} = \int_0^t \frac{P_{fc}(t)}{\eta_{fcs}\,\rho_{H_2}}\,dt \quad (16)$$

As we can see in equation (9), the hydrogen consumption is inversely proportional to the FC system efficiency.

B. Model of the ultra capacitor

The UC model of MATLAB is used, which is modeled as an equivalent circuit model based on Stern model, where the voltage is obtained by the following equation [5]:

$$U_{uc} = \frac{N_s\, Q\, d}{N_p\, N_c\, \varepsilon\, \varepsilon_0\, S_{uc}} + \frac{N_C N_s 2RT_{uc}}{F} \operatorname{arsinh}^{-1}\left(\frac{Q}{N_p\, N_s^2\, S_{uc}\sqrt{8\, R\, T\, \varepsilon\, \varepsilon_0\, C}}\right) \quad (17)$$

The implemented model is considered as a variable voltage given by Eq. (7), in series with an internal resistance R_{uc} as shown in figure 3. The output voltage is calculated by taking into account the losses by the Joule effect.

$$V_{uc} = U_{uc} - R_{uc} I_{uc} \quad (18)$$

The state of charge in percent can be calculated by the following expression:

$$SOC = (1 - \frac{\int i_{uc}\, dt}{CU_{uc,max}}).100 \quad (19)$$

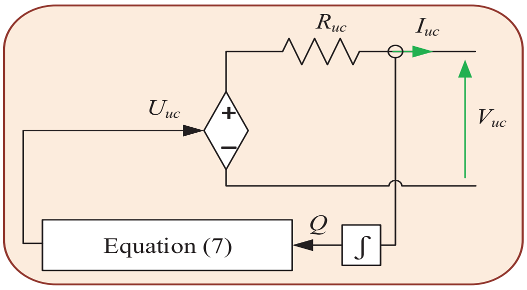

Figure 2. Simulation model of UC

C. Photovoltaic model

Exposing a photovoltaic cell to light flux generates a voltage between the p-n junctions. The equivalent model showed in Fig. X describes how a photovoltaic panel works.

The output current (I_{PV}) of the PV module can be expressed as [6]:

$$\begin{cases} I_{PV} = I_{pv} - I_d \\ I_d = I_0\left[\exp\left(\dfrac{V_{PV} + R_s I_{PV}}{a\, V_T}\right) - 1\right] \end{cases} \quad (20)$$

where Ipv is the equivalent photocurrent, I_0 is the reverse saturation current, a is the factor coefficient, VT is the thermal voltage related to temperature, Rs is the equivalent series resistance.

The expression of the open circuit voltage (Voc) and the short circuit current can be described as:

$$\begin{cases} V_{oc} = a\, V_T \ln\left(\dfrac{I_{pv}}{I_0}\right) \\ I_{pv} = \dfrac{G}{G_{ref}}\left[I_{sc,ref} + k(T_{cell} - T_{cell,ref})\right] \end{cases} \quad (21)$$

where Tcell represents the cell temperature, G is the irradiance, k is the current temperature coeffcient, Gref = 1000 W/m^2 and Isc,ref (standard short-circuit current) in Tcell,ref = 25 ◦C.

The panels are connected to a boost DC/DC converter, which is controlled by an MPPT algorithm as presented in [14].

D. DC/DC converters modeling

The DC/DC converters associated to the FC and the Battery are realized using the power electronics elements of the Sim-Power system library and placed as shown in Fig. 4. Both converters have the boost structure, with an additional switch for the battery converter to ensure current flow in both directions. The UC is used as a DC bus to decouple the propulsion system from the energy sources. This decoupling filters out power peaks and guarantees stable power to the energy sources.

The switches (K_1 and K_{21}) are controlled by the control signals (u_1 and u_2) and current inversion in UC converter is guaranteed by the K_{22} switch associated with the u'$_2$ control signal.

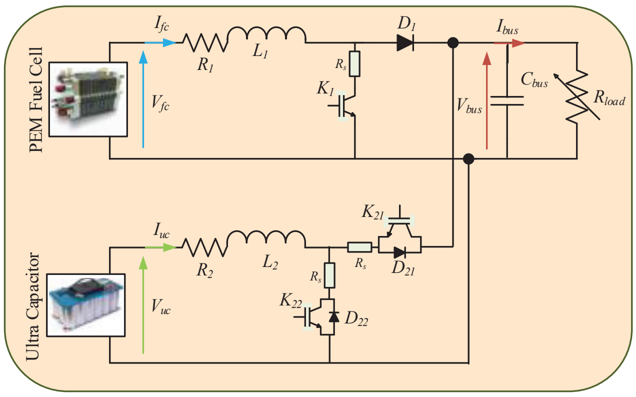

Figure 3. Sources and associated converters

The mathematical model of the converters presented in Fig. 4, in boost mode, is given by the following equations system [6-7]:

$$\begin{cases} L_1 \dfrac{di_{L_1}}{dt} = V_{fc} - (R_1 + R_s)i_{L_1} - (1 - u_1)V_{bus} \\ L_2 \dfrac{di_{L_2}}{dt} = V_{uc} - (1 - u_2)V_{bus} - [R_2 + R_s]i_{L_2} \\ C_{bus}\dfrac{dv_{bus}}{dt} = (1 - u_2)i_{uc} + (1 - u_1)i_{fc} \end{cases} \quad (22)$$

Tab. 2 shows the FC and UC converters parameters.

TABLE II. DC/DC CONVERTERS PARAMETERS

Parameter	***Value***	***Unit***
R_{L1}	0.1	Ω
R_{L2}	0.1	Ω
R_s	15	mΩ
L_1	6.4	mH
L_2	3	mH
C_{bus}	560	µF

III. PROPOSED ENERGY MANAGEMENT STRATEGY

The power management of the flow of energy in the UAV is designed as shown in Fig. 4.

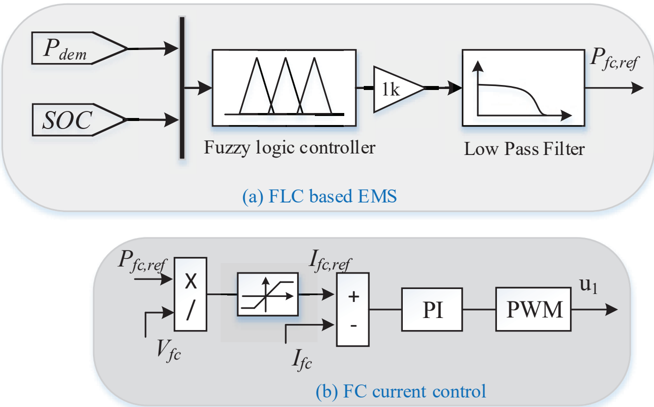

Figure 4. FLC strategy and FC current control

The membership functions of the inputs and output are carried out as in [8-9]. The low pass filter is added to suppress abrupt transitions generated by the fuzzy controller to maintain a high FC lifetime.

IV. RESULTS AND DISCUSSIONS

To verify the proposed EMS, a simplified flight profile is designed with six segments as in Fig. 5: UAV out, climb, accelerate, cruise, and glide descent and UAV in.

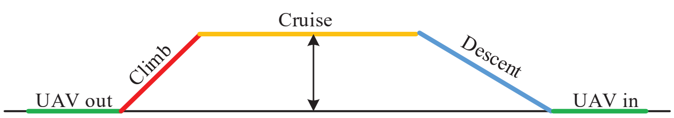

Figure 5. Mission profile of the UAV

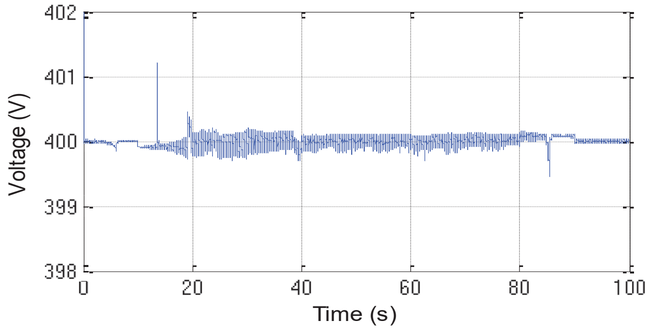

Figure 6. DC bus voltage

The DC bus voltage is kept at its reference value of 400 V by the double PI control loop. Disturbances of ±1 V are observed along the cycle. Therefore, we can conclude that this control and the energy management are sufficient by giving the necessary energy to feed the traction system.

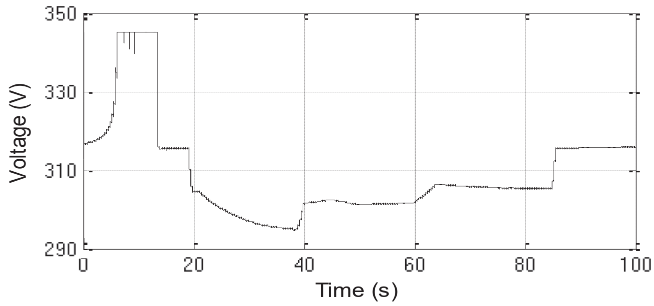

Figure 7. FC voltage

As seen in Fig. 7, the voltage drop is due to the various joule, activation and concentration losses. Note that the greater the power supplied by the FC (Fig. 8), the greater the voltage drop.

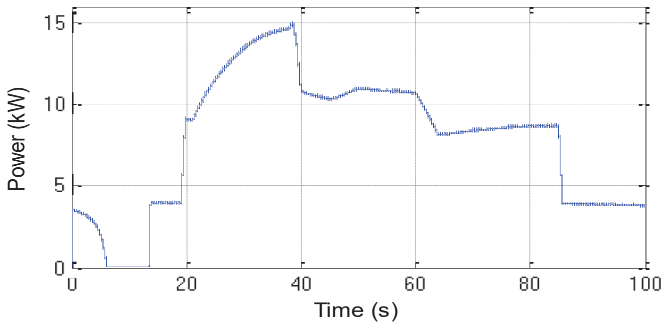

Figure 8. FC Power

The FC is used in the high power range shown in the Fig. 8.

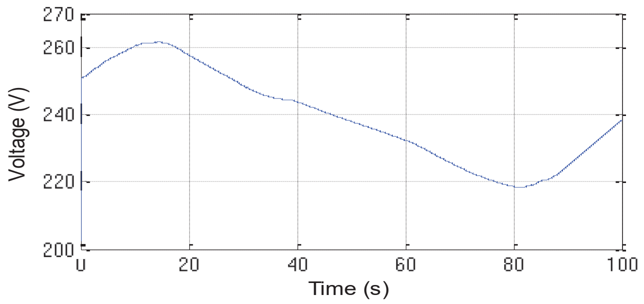

Figure 9. UC voltage

The voltage at the edge of the UC showed in Fig. 9 reflects its state of charge. It should be noted that this voltage must not be too low to guarantee good efficiency of the UC converter.

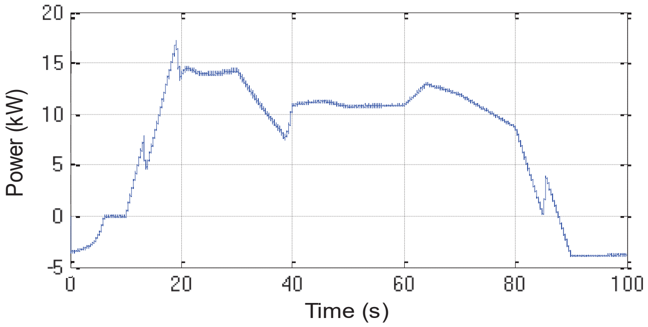

Figure 10. UC Power

Figure 10 shows the UC power, there are power peaks in the power profile

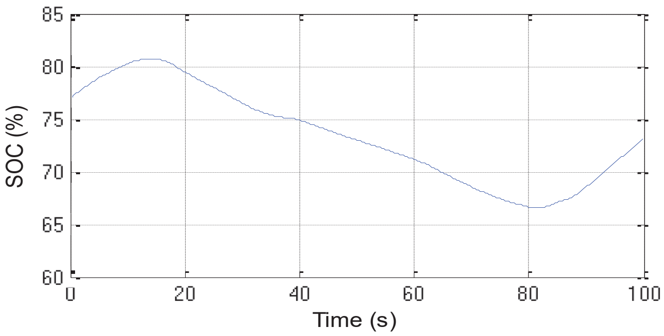

Figure 11. UC state of charge

The UC SOC at the start of the cycle is assumed to be 77% as shown in Fig. 11.

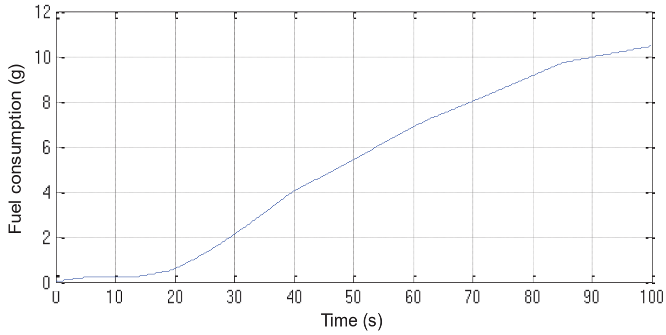

Figure 12. FC fuel consumption

Fig. 12 shows the fuel consumption during the cycle. Note that the variation in fuel consumption is small at the beginning of the cycle because the power consumed by the motor is supplied by the UC, which is initially charged and kept slightly charged by the photovoltaic panels.

Fig. 13 and 14 show the different parameters of the photovoltaic system:

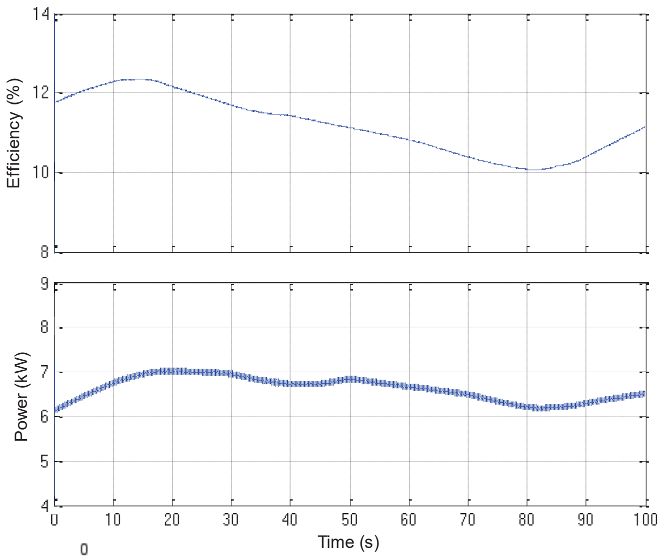

Figure 13. PV efficiency and power

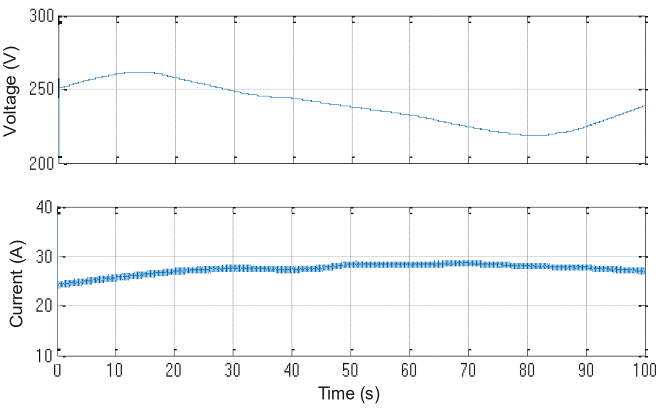

Figure 14. PV voltage and current

The output parameters of the photovoltaic panels are obtained on the assumption that the irradiation has a profile as in the Fig. 15.

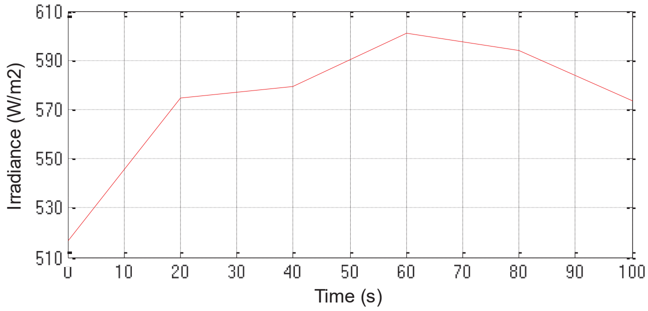

Figure 15. Irradiance received by the PV panels with time

V. Conclusion

In this paper, a fuzzy logic based EMS is proposed to manage the energy flow in an FC/PV/UC UAV. The main objectives of the simulation: firstly, reduce the fuel consumption of the fuel cell system by using it in high efficiency region. Secondly, enhance the endurance of the UAV by using a PV and FC sources. Finally, reduce the stress on the FC system by adding an UC storage system to supply the abrupt power transitions.

References

[1] X. Zhang, L. Liu and G. Xu. "Energy Management Strategy of Hybrid PEMFC-PV-Battery Propulsion System for Low Altitude UAVs," AIAA 2016-5109. *52nd AIAA/SAE/ASEE Joint Propulsion Conference*. July 2016.

[2] J. Sliwinski, A. Gardi, M. Marino, R. Sabatini, "Hybrid-electric propulsion integration in unmanned aircraft", *Energy*, 2017.

[3] D. -J. Lee and Li Wang, "Dynamic and Steady-State Performance of PEM Fuel Cells under Various Loading Conditions," 2007 IEEE Power Engineering Society General Meeting, Tampa, FL, USA, 2007, pp. 1-8,

[4] L. Zhu, J. Han, D. Peng, T. Wang, T. Tang and J. -F. Charpentier, "Fuzzy logic based energy management strategy for a fuel cell/battery/ultra-capacitor hybrid ship," *2014 First International Conference on Green Energy*, Sfax, Tunisia, 2014, pp. 107-112.

[5] G. Ren, J. Wang, C. Chen, H. Wang, "A variable-voltage ultra-capacitor/battery hybrid power source for extended range electric vehicle," *Energy*, vol. 231, 2021, 120837.

[6] C. Zhang, C. Zhang, L. Li, Q. Guo, "Parameter analysis of power system for solar-powered unmanned aerial vehicle," Applied Energy,vol. 295, 117031, 2021.

[7] L. Török, S. D. Sønderskov and S. Munk-Nielsen, "Bidirectional Operation of High Efficiency Isolated DC-DC Converter in Fuel Cell Telecom Back-up Systems," 2018vIEEE International Telecommunications Energy Conference (INTELEC), pp. 1-5.

[8] M. Bai, W. Yang, R. Zhang, M. Kosuda, P. Korba, M. Hovanec, "Fuzzy-based optimal energy management strategy of series hybrid-electric propulsion system for UAVs," *Journal of Energy Storage*, vol. 68, 2023, 107712.

[9] X. Zhang, L. Liu, Y. Dai, T. Lu, "Experimental investigation on the online fuzzy energy management of hybrid fuel cell/battery power system for UAVs," *Int. Journal of Hydrogen Energy*, vol. 43, 2018, pp. 10094-10103.

Closed loop inner current control of Grid Connected MMC based microgrid solar system in dq Frame

1st WIAM HERKAT
dept.Power and Control
university of Boumerdes (UMBB)
Algeria
w.herkat@univ-boumerdes.dz

2nd YASSINE YAKHELEF
dept.Power and Control
university of Boumerdes (UMBB)
Algeria
y.yakhelef@univ-boumerdes.dz

***Abstract*—The microgrid solar system integrates renewable energy sources, such as solar photovoltaic panels, into the grid through an MMC, enabling efficient and reliable power conversion. The inner current control strategy is critical for maintaining the stability and performance of the microgrid under varying operating conditions. In this paper paper presents a comprehensive study on the closed-loop inner current control of a Grid-Connected Modular Multilevel Converter (MMC) based microgrid solar system, employing the dq (direct-quadrature) frame for control reference.it will elaborates on the design and implementation of the closed-loop inner current control system, discussing the selection of control method and appropriate control parameters . The control scheme's effectiveness is evaluated through extensive simulation studies.**

***Index Terms*—Modular multilevel Converter(MMC), PV system grid-connected, current control.**

I. Introduction

The integration of renewable energy sources and the demand for efficient power transmission have led to the widespread adoption of Modular Multilevel Converters (MMCs) in modern power systems. [1] [2] [3]
Modular Multilevel converters offer several advantages, including high modularity and scalability, allowing for easy expansion or modification of the system. Additionally, its ability to tolerate faults within individual submodules enhances the system's reliability. Overall, the MMC circuit has proven to be a versatile and efficient solution for applications such as high-voltage direct current (HVDC) transmission and renewable energy integration. [] Their modular design allows for scalability, ensuring the adaptation to a wide range of power requirement With high efficiency and low harmonic generation, MMCs minimize energy losses during the conversion process, additionally, Their modularity allows for flexible and adaptable control strategies that can be customized to suit different applications and operating conditions [4]

The paper's structure is outlined as follows:in section I we present a concise introduction to the MMC converter,section II focuses on establishing a mathematical model for the MMC,In Section III, we establish a control strategy for inner currents,A simulation is conducted in section IV and performance of the proposed controller is investigated .Finally, the conclusion is provided in section V.

II. MMC Mathematic Model

1) circuit configuration : The MMC circuit is an advanced voltage source converter, which utilizes multiple submodules (SMs) interconnected in a specific configuration. Each submodule consists of a series-connected set of semiconductor switches (typically insulated gate bipolar transistors, IGBTs) and capacitors. These submodules are arranged in arms, often in a symmetrical fashion to ensure balanced operation. The arms are connected in parallel and are controlled independently to achieve the desired output voltage waveform.

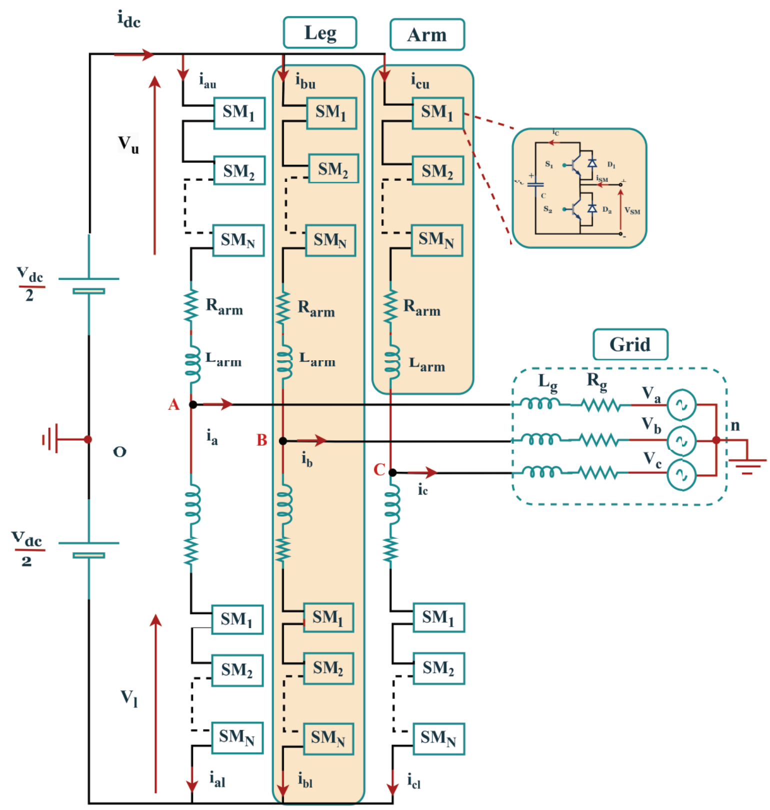

Fig. 1: Circuit diagram for MMC

Each sub module is controlled separately where the individual voltages V_{SM} add up to form a multilevel, nearly sinusoidal staircases waveform [5]
The dynamic equations used for the submodule capacitor voltages are provided by

$$C\frac{V_{SMu}}{dt} = i_{au}S_j \tag{1}$$

$$C\frac{V_{SMl}}{dt} = i_{al}S_j \tag{2}$$

V_{dc}	Dc bus voltage
i_{dc}	DC bus current
i_u	upper arm current
i_l	lower arm current
i_{zj}	AC circulating current
i_{comm}	common mode current
i_{diff}	differential current
i_g	Grid current
i_{oj}	Phase output current
i_{SM}	Submodule current
V_g	Grid voltage
V_c	Capacitor voltage
V_{SM}	Submodule Output Voltage
Vu_j	upper arm voltage of the phase j
Vl_j	lower arm voltage of the phase j
V_{oj}	Inverter output voltage
V_{diff}	differential voltage
L	Arm inductor
R	Arm resistance
Lg	Grid inductor
Rg	Grid resistance
C	Submodule Capacitor

TABLE I: the parameters of MMC

S_1	S_2	V_{SM}	Capacitor
ON	OFF	V_c	Charging
OFF	ON	0	Uncharged

TABLE II: Switching States of SM

where $S_j = 1$ when submodule is ON and $S_j = 0$ when Submodule is OFF Modular Multilevel Converter is mainly composed of N identical submodules per arm that are connected in series. The MMC circuit consists of multiple arms, typically six, for a three-phase system. Each arm is responsible for generating a portion of the output voltage.

Submodules (SMs): Within each arm, multiple submodules are connected in series. The number of SMs per arm can vary based on the desired voltage and power levels. Each submodule contains switching devices, typically Insulated Gate Bipolar Transistors (IGBTs), for controlling current and voltage.

DC Capacitors: Each submodule contains a DC capacitor. These capacitors store and provide energy, ensuring that the output voltage remains stable. [6]
Considering a phase circuit of MMC to simplify the model each arm will be represented by a voltage source in series with the arm inductance ad resistance where,

a specific SM configuration can improve the performance of an MMC in terms of power flow control and fault tolerance, without significantly increasing its cost or complexity. best balance between complexity and functionality can be found in bipolar configurations like the SC-SM and CD SM,though the HB-SM is still an option if negative voltage levels are not required. [7]
circulating current equations [8]

Using Kirchhof voltage law (KVL), the dynamics of the MMC is defined by the following equations:

$$\frac{V_{dc}}{2} - V_{uj} - V_g = (Ri_{uj} + L\frac{di_{uj}}{dt}) + (R_g i_o j + L_g\frac{di_g}{dt}) \quad (3)$$

$$-\frac{V_{dc}}{2} + V_{lj} - V_{oj} = -(Ri_{lj} + L\frac{di_{lj}}{dt}) + (R_g i_o j + L_g\frac{di_g}{dt}) \quad (4)$$

the upper and the lower arm voltages depend on the state of the switches and also the voltage of the capacitors of the modules

$$V_{uj} = \sum_{n=1}^{k} S_{ujk}.V_{cujk} \quad (5)$$

$$V_{lj} = \sum_{n=1}^{k} S_{ljk}.V_{cljk} \quad (6)$$

by defining the phase current i_{oj} and the circulating current i_{zj}, where j refers to the three phases of MMC (a, b, and c)

$$i_{zj} = \frac{i_{uj} + i_{lj}}{2} \quad (7)$$

$$i_{oj} = i_{uj} - i_{lj} \quad (8)$$

The upper and lower arm currents can be expressed by:

$$i_{uj} = i_{zj} + \frac{i_{oj}}{2} \quad (9)$$

$$i_{lj} = i_{zj} - \frac{i_{oj}}{2} \quad (10)$$

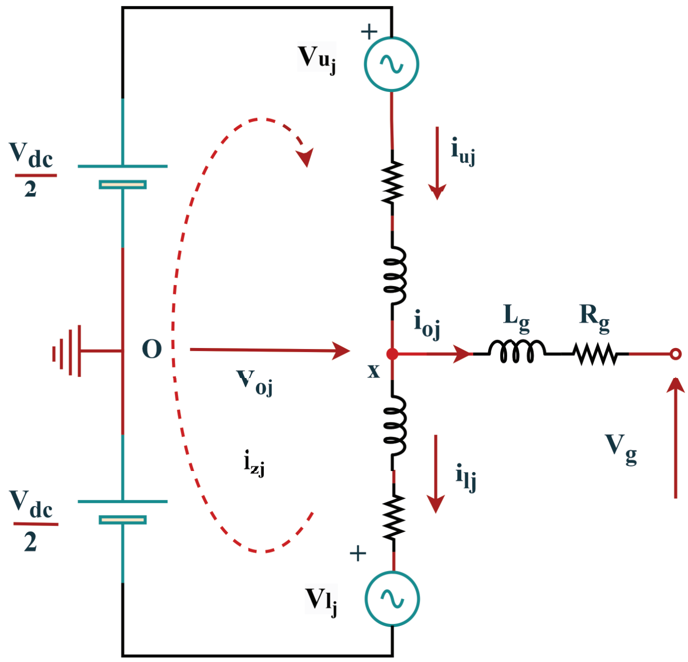

Fig. 2: Single-phase equivalent circuit of the 3Ph MMC

the equations 3 and 4 can be written as follows:

$$V_{oj} = \frac{V_{up} - V_{low}}{2} - \frac{L}{2}\frac{di_{xi}}{dt} - \frac{R}{2}i_{xi} \quad (11)$$

$$2L\frac{di_{zj}}{dt} - 2Ri_{zj} = V_{dc} - (V_{uj} + V_{lj}) \quad (12)$$

$$V_{diff} = \frac{V_u - V_l}{2} \quad (13)$$

In the MMC, the common mode current and differential current are expressed by:

$$i_{comm} = \frac{i_u - i_l}{2} \tag{14}$$

$$i_{diff} = \frac{i_u - i_l}{2} \tag{15}$$

$$i_{uj} = \frac{i_a}{2} + i_{diff} \tag{16}$$

$$i_{lj} = \frac{i_a}{2} - i_{diff} \tag{17}$$

2) MMC model in dq frame: The following system dynamics in dq-frame are obtained by applying the standard abc/dq transformation to (3). [9]

$$L \begin{bmatrix} \frac{di_d}{dt} \\ \frac{di_q}{dt} \end{bmatrix} = \begin{bmatrix} u_d \\ u_q \end{bmatrix} - \begin{bmatrix} R & \omega L \\ \omega L & R \end{bmatrix} \begin{bmatrix} i_d \\ i_q \end{bmatrix} - \begin{bmatrix} e_d \\ e_q \end{bmatrix}$$

where e_d e_q are the grid voltages in dq frame

As indicated in the previous equation, the system dynamics in the dq-frame exhibit significant coupling. To mitigate this coupling, the decoupling control scheme illustrated in Figure 4 is applied in the following manner.

$$\begin{bmatrix} u_d \\ u_q \end{bmatrix} = \begin{bmatrix} -\omega L \\ \omega L \end{bmatrix} \begin{bmatrix} i_d \\ i_q \end{bmatrix} + \begin{bmatrix} e_d \\ e_q \end{bmatrix} + \begin{bmatrix} u_i d \\ u_i q \end{bmatrix}$$

where u_{id} u_{iq} are the control output from the PI controller

III. Overall MMC control

As indicated in equation (20), the system dynamics in the dq-frame exhibit significant coupling. To mitigate this coupling, the decoupling control scheme illustrated in Figure 2 is applied in the following manner. MMC control diagram consists of various

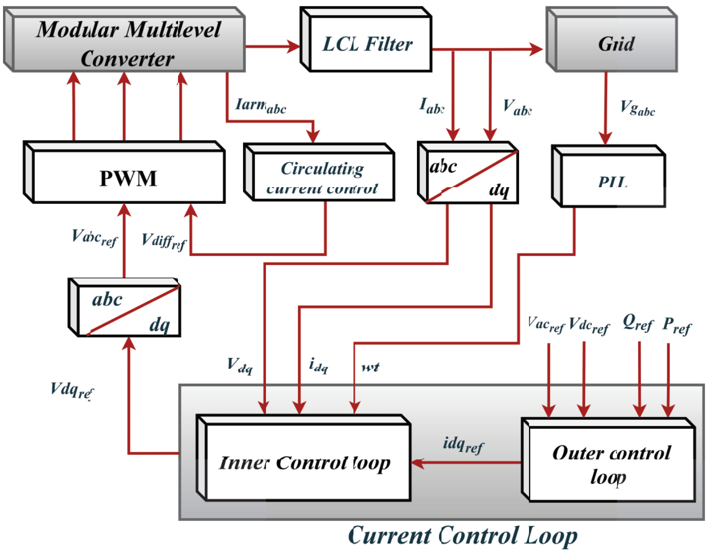

Fig. 3: Control Diagram of MMC

control loops and signal processing elements like filters, d-q axis transformations, and a phase-locked loop (PLL). The main control loops include AC current control and leg current control. [10] .When it comes to inverters with multi-variable control, cascaded current-voltage control is utilized. This control consists of an inner voltage loop and an outer current loop. By introducing multiple feedback variables [11], the controller becomes more flexible and improves the power quality of both the local load voltage and the current exchanged with the grid [12].

the inner control loop generates the reference voltage signal using decoupling current control and voltage feed forward control [13] while The outer control loop sets the desired power exchange between the MMC and the grid. It calculates the reference power values based on grid requirements, system load, or other control objectives. [14] The outer-loop control provides a total of three distinct control modes: active/reactive power control, DC voltage control, and AC voltage control. [15]

The choice of power converter control and modulation techniques for an MMC depends on the specific applications in which it is utilized. To illustrate, solar photovoltaic (PV) systems often make use of sinusoidal pulse width modulation (SPWM) techniques coupled with proportional integral control [16]

The LCL filter plays a crucial role in improving the current quality. It effectively reduces high-frequency harmonics and decreases the ripple caused by switching frequencies in the current waveform [17] Phase-Shifted PWM is a modulation technique that involves generating multiple PWM signals with controlled phase offsets when MMC is operating under unbalanced voltage

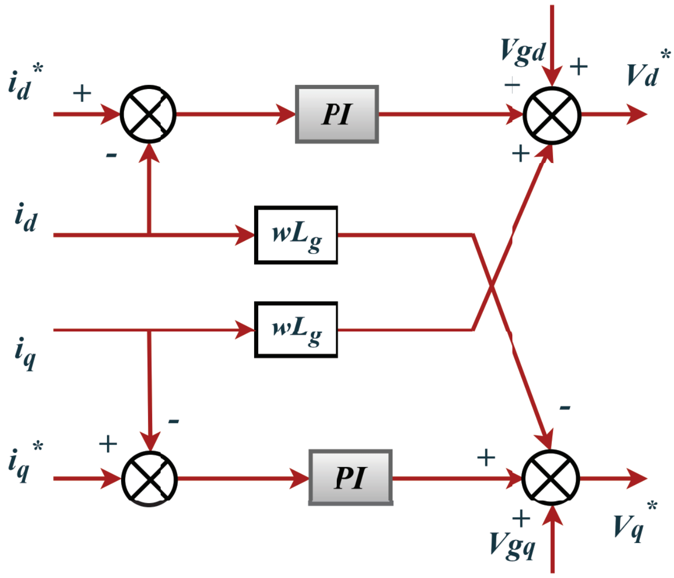

Fig. 4: Inner control loop

conditions, there are additional components, including positive-sequence and zero-sequence circulating currents [18] a dual-vector current controller is proposed to reduce AC-side active power ripple when unbalanced voltages .it also introduces a control approach that accounts for all components of circulating currents under such conditions.

IV. Simulation Results

The proposed control technique aims to regulate the power flow and and control the output current and ensure stability in the three-phase Modular Multilevel converter, Matlab/Simulink software is used to create a three-phase MMC inverter with a resistor-inductor load in order to validate the suggested control scheme.

The diagram of the circulating current in Figure 5 shows that the circulating current is very much like a pure direct current (dc).the circulating current is approaching zero, indicating a balanced condition.In summary, a circulating current plot signifies

a well-controlled and balanced operation, contributing to system stability and efficiency.
As shown in Figure 6 ,before using PI controller the output voltage signal exhibit irregularities and distortions furthermore the absence of precise control mechanisms that lead to deviations from the desired sinusoidal waveform, resulting in higher Total Harmonic Distortion (THD) levels.however after control, lower THD levels are noticed compared to the uncontrolled state, thereby improving the overall quality of the output voltage signal which emphasizes the effectiveness of the controller.
At the same time, Figure 7(a) and (b) show the results obtained by using PI controller ,a more balanced output current is noticed and the waveform looks almost exactly like a smooth, pure sine wave with very little distortion.
The FFT Analysis of the output voltage and output current are illustrated in Figure 8 and Figure 9 respectively ,the introduction of PI control helped in reducing harmonic distortions in the output voltage and current waveform.which demonstrates the effectiveness of the control strategy in improving the power quality of the MMC's outputs.

Parameter	Symbol	Value
Number of submodules	N	4
Switching frequency	F_s	$5000Hz$
Nominal Frequency	f	$50Hz$
Angular frequency -	w	$2*pi*f$
AC System voltage	V_{AC}	$8KV$
Filter inductor	L_g	$0.004H$
Filter capacitor	C_g	$1\mu F$
Submodule capacitance	C	$1000\mu F$
Arm inductance	L_{arm}	$0.004H$
Arm resistance	R_{arm}	$0.1ohm$
Dc bus voltage	V_{dc}	$35.36e+3V$

TABLE III: Simulation parameters of three phase MMC

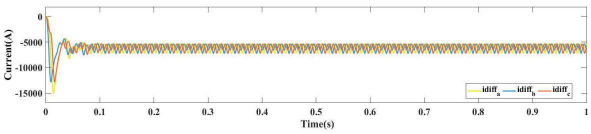

(a) circulating current in MMC

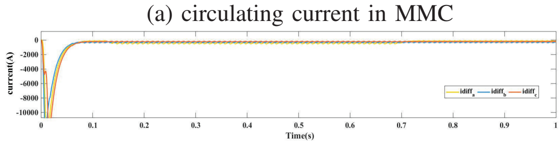

(b) Circulating current using PI controller

Fig. 5: Comparison of Circulating Current: Pre and Post Control

V. Conclusion

Future investigations in the control of Modular Multilevel Converters MMC are likely to focus on several key areas including the development of more sophisticated control algorithms to enhance the performance of MMC, this could involve the use of artificial intelligence, machine learning, and predictive control methods to improve the converter's dynamic response and efficiency furthermore research on how MMC can contribute to grid stability and integration of renewable energy sources

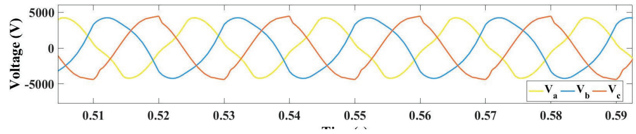

(a) Output voltage with phase shifted PWM

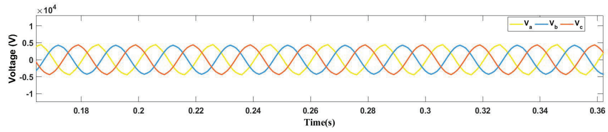

(b) Output voltage after control

Fig. 6: Converter output voltage before and after control

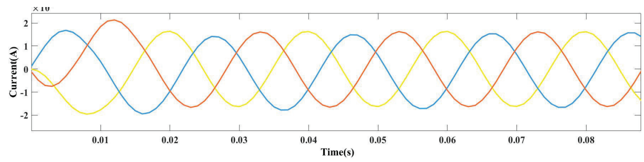

(a) output current

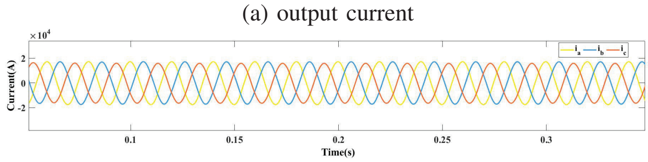

(b) output current using PI controller

Fig. 7: Comparison of output Current: Pre and Post Control

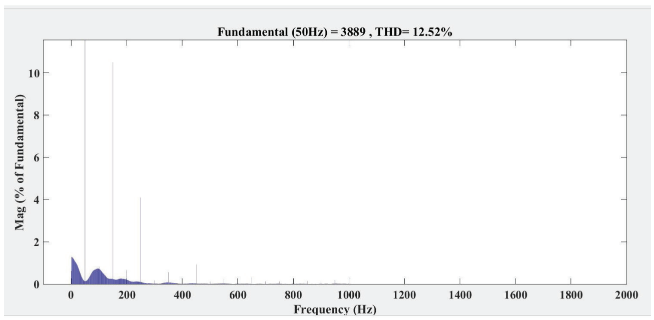

(a) THD of the output voltage

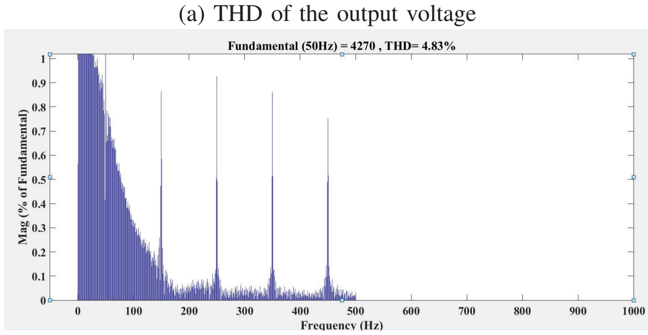

(b) THD of the output voltage using PI controller

Fig. 8: Comparison of output voltage THD Pre and Post Control

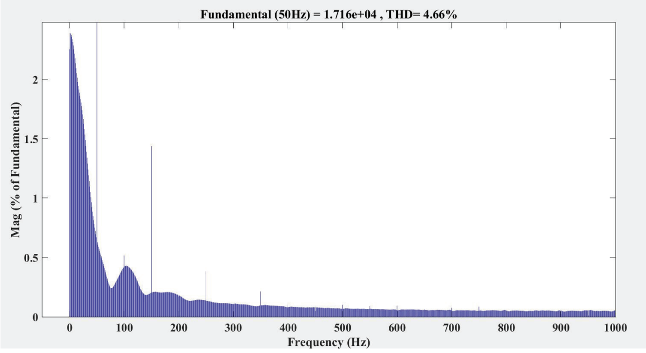

(a) THD of the output current

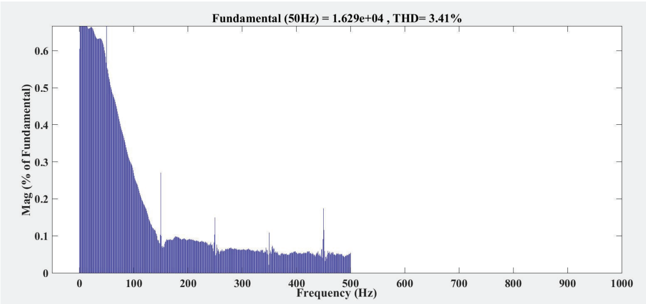

(b) THD of the output current using PI controller

Fig. 9: Comparison FFT analysis of output current Pre and Post Control

REFERENCES

[1] J. Rodriguez, L. G. Franquelo, S. Kouro, J. I. Leon, R. C. Portillo, M. A. M. Prats, and M. A. Perez, "Multilevel converters: An enabling technology for high-power applications," *Proceedings of the IEEE*, vol. 97, no. 11, pp. 1786–1817, 2009.

[2] R. Marquardt, "Modular multilevel converters: State of the art and future progress," *IEEE Power Electronics Magazine*, vol. 5, no. 4, pp. 24–31, 2018.

[3] A. A. Mahmoud, A. A. Hafez, and A. M. Yousef, "Modular multilevel converters for renewable energies interfacing: Comparative review," in *2019 IEEE Conference on Power Electronics and Renewable Energy (CPERE)*. IEEE, 2019, pp. 397–406.

[4] M. Kurtoğlu, F. Eroğlu, A. O. Arslan, and A. M. Vural, "Recent contributions and future prospects of the modular multilevel converters: A comprehensive review," *International Transactions on Electrical Energy Systems*, vol. 29, no. 3, p. e2763, 2019.

[5] U. N. Gnanarathna, A. M. Gole, and R. P. Jayasinghe, "Efficient modeling of modular multilevel hvdc converters (mmc) on electromagnetic transient simulation programs," *IEEE Transactions on power delivery*, vol. 26, no. 1, pp. 316–324, 2010.

[6] L. Harnefors, A. Antonopoulos, S. Norrga, L. Angquist, and H.-P. Nee, "Dynamic analysis of modular multilevel converters," *IEEE Transactions on Industrial Electronics*, vol. 60, no. 7, pp. 2526–2537, 2012.

[7] G. Konstantinou, J. Zhang, S. Ceballos, J. Pou, and V. G. Agelidis, "Comparison and evaluation of sub-module configurations in modular multilevel converters," in *2015 IEEE 11th International Conference on Power Electronics and Drive Systems*. IEEE, 2015, pp. 958–963.

[8] A. Marzoughi, R. Burgos, D. Boroyevich, and Y. Xue, "Steady-state analysis of voltages and currents in modular multilevel converter based on average model," in *2015 IEEE Energy Conversion Congress and Exposition (ECCE)*. IEEE, 2015, pp. 3522–3528.

[9] M. Alqatamin, J. Latham, Z. T. Smith, B. M. Grainger, and M. L. McIntyre, "Current control of a three-phase, grid-connected inverter in the presence of unknown grid parameters without a phase-locked loop," *IEEE Journal of Emerging and Selected Topics in Power Electronics*, vol. 9, no. 3, pp. 3127–3136, 2020.

[10] P. Bordignon, M. Marchesoni, G. Parodi, and L. Vaccaro, "Modular multilevel converter in hvdc systems under fault conditions," in *2013 15th European Conference on Power Electronics and Applications (EPE)*. IEEE, 2013, pp. 1–10.

[11] Q. Liu, T. Caldognetto, and S. Buso, "Review and comparison of grid-tied inverter controllers in microgrids," *IEEE Transactions on Power Electronics*, vol. 35, no. 7, pp. 7624–7639, 2019.

[12] Q.-C. Zhong and T. Hornik, "Cascaded current–voltage control to improve the power quality for a grid-connected inverter with a local load," *IEEE Transactions on Industrial Electronics*, vol. 60, no. 4, pp. 1344–1355, 2012.

[13] X. Zhou, Y. Zhou, Y. Ma, L. Yang, X. Yang, and B. Zhang, "Dc bus voltage control of grid-side converter in permanent magnet synchronous generator based on improved second-order linear active disturbance rejection control," *Energies*, vol. 13, no. 18, p. 4592, 2020.

[14] Y. Zhang, J. Ravishankar, and R. Li, "Modelling and control of modular multi-level converter based hvdc systems using symmetrical components," in *2015 IEEE 15th International Conference on Environment and Electrical Engineering (EEEIC)*. IEEE, 2015, pp. 1910–1915.

[15] T. Yin, Y. Wang, X. Wang, B. Yue, D. Zhao, J. Sun, P. Li, and Y. Liu, "Modeling and analysis of high-frequency mmc impedance considering different control modes and voltage feedforward," *IEEE Access*, vol. 8, pp. 218 575–218 584, 2020.

[16] S. Alotaibi and A. Darwish, "Modular multilevel converters for large-scale grid-connected photovoltaic systems: A review," *Energies*, vol. 14, no. 19, p. 6213, 2021.

[17] M. Liserre, F. Blaabjerg, and S. Hansen, "Design and control of an lcl-filter-based three-phase active rectifier," *IEEE Transactions on industry applications*, vol. 41, no. 5, pp. 1281–1291, 2005.

[18] W.-S. Do, S.-H. Kim, T.-J. Kim, and R.-Y. Kim, "A study of circulating current in mmc based hvdc system under an unbalanced grid condition," in *IECON 2014-40th Annual Conference of the IEEE Industrial Electronics Society*. IEEE, 2014, pp. 4146–4152.

Robustness evaluation of the finitie-control-set model predictive control for DFIG based wind turbine system

Aggoune Amira
Departement of Electrical Engineering
Faculty of Sciences and Technologies
University of Souk Ahras
Souk Ahras, Algeria
amira.agg@hotmail.com

Berrezzek Farid
Departement of Electrical Engineering
Faculty of Sciences and Technologies
University of Souk Ahras
Souk Ahras, Algeria
f.berrezzek@univ-soukahras.dz

Khelil Khaled
Departement of Electrical Engineering
Faculty of Sciences and Technologies
University of Souk Ahras
Souk Ahras, Algeria
khaled.khelil@univ-soukahras.dz

***Abstract*— This paper examines a finite-control-set model predictive control (FCS-MPC) approach for controlling the rotor side converter (RSC) and grid side converter (GSC) within a doubly-fed induction generator (DFIG) based wind power conversion system (WPCS). The primary aim of this research is to assess the FCS-MPC strategy resilience to fluctuations in internal parameters and random wind speeds. Through the utilization of an objective function, this newly introduced strategy determines the optimal vector voltage to be applied to the DFIG power converters at each sampling interval. To evaluate the performance of the FCS-MPC, a computer simulation of a grid-connected 1.5 MW wind turbine is conducted using the MATLAB/SIMULINK environment. The results obtained demonstrate significant robustness, stability, and precision in the control strategy.**

Keywords—finite-control-set model predictive control, rotor side converter, grid side converter, doubly-fed induction generator, wind power conversion system.

I. Introduction

Wind turbines are becoming the most promising renewable energy solution for delivering clean energy to the power grid [1]. The doubly-fed induction generator (DFIG) is the most attractive technology for wind turbine drive because of its primary features, which include four quadrant active and reactive power flow ability, minimal acoustic noise and high efficiency with minimal power converter losses [2], [3]. The generic structure of the DFIG based wind turbine system, as depicted in Fig. 1, consists in connecting the stator coils directly to the power grid and supplying the rotor coils by means of two back-to-back power converters, namely the rotor side converter (RSC) and the grid side converter (GSC) [4]. Generally, the RSC control scheme is implemented in order to enable the wind power conversion system (WPCS) to extract the maximum power from wind energy and to regulate the stator reactive power pursuant to the grid code requirements. While the GSC is regulated to balance the DC-link voltage and to maintain the power factor at unity [5].

Therefore, several control strategies have been discussed in the literature, among them the decoupled vector control associated with conventional PI controllers which permits the independent control of active and reactive power supplied to the grid, however this control method still has poor performance to control nonlinear systems [6]. Rrecently, the finite-control-set model predictive control (FCS-MPC) has been proposed as an efficient control method able to guarantee optimal and reliable control performance to the WPCS [7], [8]. The fundamental idea of FCS-MPC consists of using the dynamical model of the process to predict its future evolution over a finite prediction horizon and output an optimal control action that minimizes an objective function [2]. Hence, the appropriate voltage vector, which minimizes the error between the reference and the predicted value, is applied to the power converters at each sampling period [3].

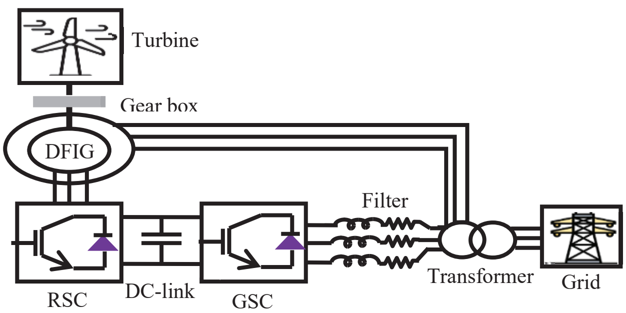

Fig. 1. Overall structure of DFIG based wind turbine system

In this paper, we aim to examine the robustness of the FCS-MPC to internal parameters changes and random wind speed. To ensure efficient power conversion to the DFIG wind turbine system, the introduced control scheme is applied to the control of the RSC and the GSC simultaneously.

The rest of the paper is organized as follows: Mathematical model of the DFIG driven by back-to-back power converter is introduced in Section 2. The FCS-MPC description is the subject of Section 3. Simulation results are given in Section 4. Finally, the conclusion is drawn in Section 5.

II. System modeling

A. DFIG-generator modeling

In the synchronous d-q reference frame, the voltage equations of the DFIG are given as follows [7]:

$$\begin{cases} V_{sd} = R_s i_{sd} + \frac{d\varphi_{sd}}{dt} - \omega_s \varphi_{sq} \\ V_{sq} = R_s i_{sq} + \frac{d\varphi_{sq}}{dt} + \omega_s \varphi_{sd} \\ V_{rd} = R_r i_{rd} + \frac{d\varphi_{rd}}{dt} - \omega_r \varphi_{rq} \\ V_{rq} = R_r i_{rq} + \frac{d\varphi_{rq}}{dt} + \omega_r \varphi_{rd} \end{cases} \tag{1}$$

The flux expressions are given in function of the stator and rotor current as follows [5]:

$$\begin{cases} \varphi_{sd} = L_s i_{sd} + L_m i_{rd} \\ \varphi_{sq} = L_s i_{sq} + L_m i_{rq} \\ \varphi_{rd} = L_r i_{rd} + L_m i_{sd} \\ \varphi_{rq} = L_r i_{rq} + L_m i_{sq} \end{cases} \tag{2}$$

Where $V_{sd,q}, V_{rd,q}$ are the stator and rotor voltages, $\varphi_{sd,q}, \varphi_{rd,q}$ are the stator and rotor fluxes, $i_{sd,q}, i_{rd,q}$ are the stator and rotor currents respectively, R_s, R_r are the stator and rotor resistances, L_s, L_r and L_m are the stator, rotor and mutual inductances respectively, ω_s, ω_r are the stator and rotor angular velocities.

By substituting (2) into (1), the current state representation of the DFIG in the synchronous Park reference frame is written as follows:

$$\frac{d}{dt}\begin{bmatrix} i_{sd} \\ i_{sq} \\ i_{rd} \\ i_{rq} \end{bmatrix} = \begin{bmatrix} \frac{1}{\sigma L_s} & 0 & -\frac{L_m}{\sigma L_s L_r} & 0 \\ 0 & \frac{1}{\sigma L_s} & 0 & -\frac{L_m}{\sigma L_s L_r} \\ -\frac{L_m}{\sigma L_s L_r} & 0 & \frac{1}{\sigma L_r} & 0 \\ 0 & -\frac{L_m}{\sigma L_s L_r} & 0 & \frac{1}{\sigma L_r} \end{bmatrix}$$

$$\begin{bmatrix} -R_s & \omega_s L_s & 0 & \omega_s L_m \\ -\omega_s L_s & -R_s & -\omega_s L_m & 0 \\ 0 & \omega_r L_m & -R_r & \omega_r L_r \\ -\omega_r L_m & 0 & -\omega_r L_r & -R_r \end{bmatrix} \begin{bmatrix} i_{sd} \\ i_{sq} \\ i_{rd} \\ i_{rq} \end{bmatrix} +$$

$$\begin{bmatrix} \frac{1}{\sigma L_s} & 0 & -\frac{L_m}{\sigma L_s L_r} & 0 \\ 0 & \frac{1}{\sigma L_s} & 0 & -\frac{L_m}{\sigma L_s L_r} \\ -\frac{L_m}{\sigma L_s L_r} & 0 & \frac{1}{\sigma L_r} & 0 \\ 0 & -\frac{L_m}{\sigma L_s L_r} & 0 & \frac{1}{\sigma L_r} \end{bmatrix} \begin{bmatrix} V_{sd} \\ V_{sq} \\ V_{rd} \\ V_{rq} \end{bmatrix} \tag{3}$$

Note that $\sigma = 1 - \frac{L_m^2}{L_s L_r}$ is the leakage factor.

The electromagnetic torque of the DFIG is often given by the following expression [4]:

$$C_{em} = \frac{3}{2}\frac{pL_m}{L_s}\left(i_{sq}\varphi_{sd} - i_{sd}\varphi_{sq}\right) \tag{4}$$

The stator active and reactive powers of the DFIG expression can be written as follows [8]:

$$\begin{cases} P_s = \frac{3}{2}\left(V_{sd} i_{sd} + V_{sq} i_{sq}\right) \\ Q_s = \frac{3}{2}\left(V_{sq} i_{sd} - V_{sd} i_{sq}\right) \end{cases} \tag{5}$$

For an ideal grid voltage conditions, the stator flux's amplitude and velocity can be considered constant. Moreover, the stator resistance can be neglected for medium and large wind power generator. Now by aligning the d-axis of the reference frame to the stator flux, the stator voltage expressions can be derived from (1) as follows [2], [8]:

$$V_{sd} = \varphi_{sq} = 0, \; V_{sq} = V_s = \omega_s \varphi_s \tag{6}$$

Consequently, the stator currents can be derived from (2) as follows:

$$\begin{cases} i_{sd} = \frac{\varphi_s}{L_s} - \frac{L_m}{L_s} i_{rd} \\ i_{sq} = -\frac{L_m}{L_s} i_{rq} \end{cases} \tag{7}$$

Finally, the stator active and reactive power can be obtained by substituting (7) and (6) into (5) as follows:

$$\begin{cases} P_s = -\frac{3}{2}\frac{V_s L_m}{L_s} i_{rq} \\ Q_s = -\frac{3}{2}\left(\frac{V_s L_m}{L_s} i_{rd} - \frac{V_s^2}{\omega_s L_s}\right) \end{cases} \tag{8}$$

From (9), it is obvious that the active power is controlled by means of the q-axis rotor current, while the reactive power is controlled using the d-axis rotor current.

B. Power converters modeling

The RSC and GSC considered in this paper are two-level power converters which the expression of the output voltage is defined as [3], [4]:

$$\begin{bmatrix} V_{An}^x \\ V_{Bn}^x \\ V_{Cn}^x \end{bmatrix} = \frac{V_{dc}}{3}\begin{bmatrix} 2 & -1 & -1 \\ -1 & 2 & -1 \\ -1 & -1 & 2 \end{bmatrix}\begin{bmatrix} S_a^x \\ S_b^x \\ S_c^x \end{bmatrix} \tag{9}$$

$x \in \{r, g\}$ with r and g denote the RSC and GSC, respectively. V_{An}, V_{Bn}, V_{Cn} are the output phase voltages, V_{dc} is the DC-link voltage and S_a, S_b, S_c are the converter switching state. Note that for a two-level converter the total number of switching states is equal to eight. Therefore, eight vector voltages can be obtained as illustrated in Fig. 2.

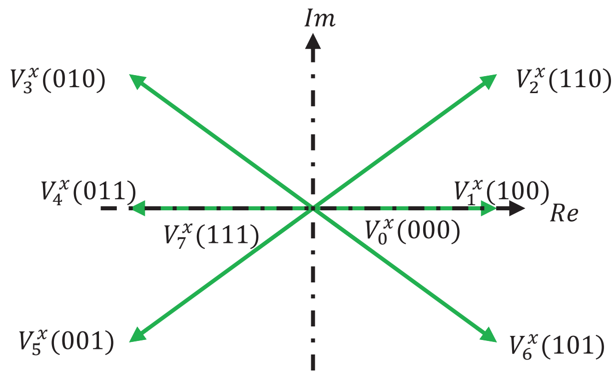

Fig. 2. Possible voltage vectors for two-level conveter

C. Grid filter and DC-link modeling

Fig. 3 shows the equivalent schematic of the GSC of a wind turbine system which is composed of an RL filter and a DC-link capacitor.

At DC-link node, the power flowing through the capacitor is given by (11) [5]:

$$V_{dc} i_{dc} = P_g - P_r \tag{10}$$

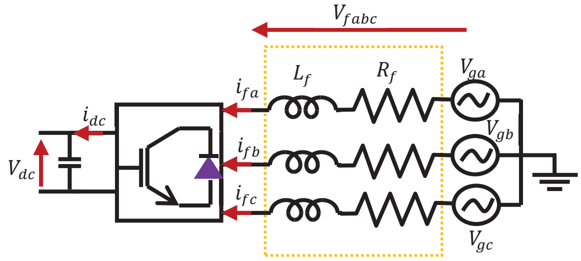

Fig. 3. Equivalent circuit of the GSC

Where P_g is the active power shared with the grid, P_r is the rotor active power and i_{dc} is the capacitor charging current which can be modelled as following:

$$i_{dc} = C\frac{dV_{dc}}{dt} \tag{11}$$

Hence, the DC-link voltage expression can be derived from (10) and (11) as follows [9]:

$$\frac{dV_{dc}}{dt} = \frac{1}{CV_{dc}}\left(P_g - P_r\right) \tag{12}$$

The GSC with an RL filter can be mathematically modelled in Park reference frame as follows [4]:

$$\begin{cases} V_{gd} = R_f i_{fd} + L_f\frac{di_{fd}}{dt} - L_f\omega_s i_{fq} + V_{fd} \\ V_{gq} = R_f i_{fq} + L_f\frac{di_{fq}}{dt} + L_f\omega_s i_{fd} + V_{fq} \end{cases} \tag{13}$$

Where $V_{gd,q}$ denote the grid voltage, $i_{fd,q}$ is the grid current, R_f is the filter resistance and L_f is the filter inductance.

As a result, the current state representation of the GSC can be derived from (14) as follows:

$$\frac{d}{dt}\begin{bmatrix} i_{fd} \\ i_{fq} \end{bmatrix} = \begin{bmatrix} -\frac{R_f}{L_f} & \omega_s \\ -\omega_s & -\frac{R_f}{L_f} \end{bmatrix}\begin{bmatrix} i_{fd} \\ i_{fq} \end{bmatrix} + \begin{bmatrix} \frac{1}{L_f} & 0 \\ 0 & \frac{1}{L_f} \end{bmatrix}\begin{bmatrix} V_d \\ V_q \end{bmatrix} \tag{14}$$

Where: $\begin{cases} V_d = V_{gd} - V_{fd} \\ Vq = V_{gq} - V_{fq} \end{cases}$

The active and reactive powers supplied to the grid can be expressed as follows [5]:

$$\begin{cases} P_g = \frac{3}{2}\left(V_{gd} i_{fd} + V_{gq} i_{fq}\right) \\ Q_g = \frac{3}{2}\left(V_{gq} i_{fd} - V_{gd} i_{fq}\right) \end{cases} \tag{15}$$

Aligning the d-axis of Park reference to the grid voltage we obtain:

$$V_{gd} = V_g,\ V_{gq} = 0 \tag{16}$$

Therefore, the grid active and reactive power expressions are reduced as follows:

$$\begin{cases} P_g = \frac{3}{2} V_{gd} i_{fd} \\ Q_g = -\frac{3}{2} V_{gq} i_{fq} \end{cases} \tag{17}$$

Equation (18) indicates that the grid reactive power control can be achieved by controlling the q-axis current, whereas the active power and the DC-link voltage are regulated by means of the d-axis current.

III. FCS-MPC TECHNIQUE DESCRIPTION

The FCS-MPC is an efficient and reliable control technique that has been regarded as a promising alternative for the control of nonlinear systems in recent years. Based on the dynamical model of the process, predictions of this model are run forward in time and the optimal control input is optimized over a short time of period by minimizing an objective function[2] . Fig. 4 depicts the typical scheme of the FCS-MPC. It is composed of 4 main blocks [10]:

- **References estimation:** This step consists in calculating the desired control values $x^{ref}(k)$ to be imposed to the system. In this study the reference control variables are the system currents that can be defined according to (8) and (17).
- **Extrapolation:** The main purpose of this block is to calculate the future values of the reference-controlled variables $x^{ref}(k+1)$ based on actual and previous sample values $x^{ref}(k)$, $x^{ref}(k-1)$, $x^{ref}(k-2)$… etc. In this paper the 2^{nd} order Lagrange extrapolation is adopted:

$$x^{ref}(k+1) = 3x^{ref}(k) - 3x^{ref}(k-1) + x^{ref}(k-2) \tag{18}$$

- **Predictive model:** In this technique, the dynamic model of the system is explicitly used to predict the future values of the control variables $x(k+1)$. The forward difference Euler method is used to discretise the predictive model as in (19):

$$\frac{dx}{dt} = \frac{x(k+1) - x(k)}{T_s} \tag{19}$$

- **Objective function minimization:** This step evaluates the error between the predicted and the extrapolated control variables as follows:

$$g(k) = \left(x^{ref}(k+1) - x(k+1)\right)^2 \tag{20}$$

The switching state producing the least error is selected to be applied to the static converter during the next sampling period.

A. Current predictive control for the RSC

By discretising the d-q axis rotor current, the predictive model is then described as follows [7]:

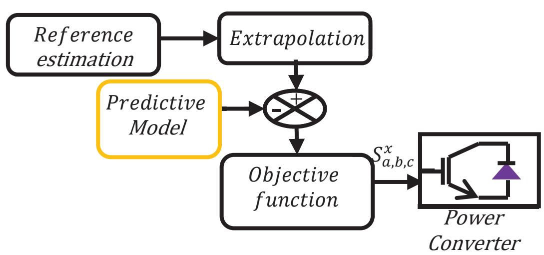

Fig. 4. General structure of the FCS-MPC

$$\begin{bmatrix} i_{rd}(k+1) \\ i_{rq}(k+1) \end{bmatrix} = \begin{bmatrix} T_s\frac{1}{\sigma L_r} & 0 \\ 0 & T_s\frac{1}{\sigma L_r} \end{bmatrix}\begin{bmatrix} V_{rd}(k) \\ V_{rq}(k) \end{bmatrix} + \begin{bmatrix} 1-\frac{T_sR_r}{\sigma L_r} & T_s\left(\frac{\omega_r}{\sigma}-\frac{L_m^2\omega_s}{\sigma L_r L_s}\right) \\ -T_s\left(\frac{\omega_r}{\sigma}-\frac{L_m^2\omega_s}{\sigma L_r L_s}\right) & 1-\frac{T_sR_r}{\sigma L_r} \end{bmatrix}\begin{bmatrix} i_{rd}(k) \\ i_{rq}(k) \end{bmatrix} + \begin{bmatrix} T_s\frac{R_sL_m}{\sigma L_r L_s} & T_s\left(\frac{\omega_r L_m}{\sigma L_r}-\frac{L_m\omega_s}{\sigma L_r}\right) \\ -T_s\left(\frac{\omega_r L_m}{\sigma L_r}-\frac{L_m\omega_s}{\sigma L_r}\right) & T_s\frac{R_sL_m}{\sigma L_r L_s} \end{bmatrix}\begin{bmatrix} i_{sd}(k) \\ i_{sq}(k) \end{bmatrix} + \begin{bmatrix} -T_s\frac{L_m}{\sigma L_r L_s} & 0 \\ 0 & -T_s\frac{L_m}{\sigma L_r L_s} \end{bmatrix}\begin{bmatrix} V_{sd}(k) \\ V_{sq}(k) \end{bmatrix} \quad (21)$$

B. Current predictive control for the GSC

The discret model of the d-q axis grid current can be derived from (14) as follows [4]:

$$\begin{bmatrix} i_{fd}(k+1) \\ i_{fq}(k+1) \end{bmatrix} = \begin{bmatrix} 1-\frac{T_sR_f}{L_f} & \omega_s T_s \\ -\omega_s T_s & 1-\frac{T_sR_f}{L_f} \end{bmatrix}\begin{bmatrix} i_{fd}(k) \\ i_{fq}(k) \end{bmatrix} + \begin{bmatrix} \frac{T_s}{L_f} & 0 \\ 0 & \frac{T_s}{L_f} \end{bmatrix}\begin{bmatrix} V_d(k) \\ V_q(k) \end{bmatrix} \quad (22)$$

C. Objective function definition

In an optimization problem, the evaluation of the performance quality of the controlled system can be achieved by minimizing an objective function. In this context the objective function is used to define the optimal switching state for the next sampling period and select the optimal voltage vector with the minimum error [3], [7]. Generally, the objective function expression is formulated based on the process requirements and the decision variables of the system. The d-q axis rotor currents are used to control the stator reactive and active powers, respectively. While the d-q axis grid currents control is implemented to regulate the DC-link voltage and the grid reactive power respectively. As a result, the objective functions for the RSC and the GSC are written as follows:

$$g(k)_{RSC} = \left(i_{rd}^{ref}(k+1) - i_{rd}(k+1)\right)^2 + \left(i_{rq}^{ref}(k+1) - i_{rq}(k+1)\right)^2 \quad (23)$$

$$g(k)_{GSC} = \left(i_{fd}^{ref}(k+1) - i_{fd}(k+1)\right)^2 + \left(i_{fq}^{ref}(k+1) - i_{fq}(k+1)\right)^2 \quad (24)$$

IV. Results and Discussion

Aiming at evaluating the performance of the introduced FCS-MPC, a computer simulation of a grid-connected 1.5 MW wind turbine system has been carried out using MATLAB/Simulink software. The system parameters are indexed in Table. I. The simulation tests are performed to investigate the decoupling capability and the robustness of the FCS-MPC. Therefore, the following conditions are taken into considerations: a random wind speed profile is applied to the WECS, as depicted in Fig. 5, during the $35s$ of the simulation study. Meanwhile, an increase of 30% and 500% in the nominal values of the mutual inductance (L_m) and the stator/rotor resistances (R_s, R_r) within the ranges of $[0s - 12s]$ and $[12s - 24s]$ respectively, is taken into account. Moreover, the maximum power output of the wind turbine is used as a reference for the stator active power, while the stator reactive set point will vary between $0\ VAR$, $-0.5\ MVAR$ and $0.5\ MVAR$ within the ranges of $[0s - 12s]$, $[12s - 24s]$ and $[24s - 35s]$ respectively. Fig. 7 illustrates the wind turbine system based on DFIG simulation response. The overall control structure is depicted in Fig. 6. The measured DC-link voltage is maintained at its reference value. In addition, the uniqueness of the power factor in the GSC is ensured as validated by maintaining the reactive power of the grid null. The stator active and reactive powers track their imposed references. The d-q axis rotor current evolves into the same form as the stator reactive and the stator active powers and follow their imposed reference determined from (8). From the analysis of the obtained results, we can see that the independent control of active and reactive power is perfectly ensured using the FCS-MPC. Furthermore, the overall stability is well ensured in case of uncertainties and disturbances. However, we can see that the system response time is slightly influenced by the variation of the mutual inductance. It can be concluded that the control objectives of both the RSC and GSC are fulfilled and the FCS-MPC shows high robustness and can be considered as a very promising alternative for the control of the DFIG based wind turbine system.

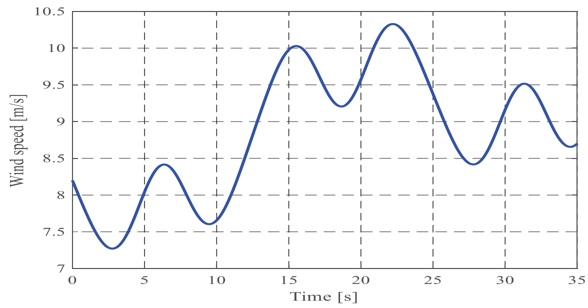

Fig. 5. Adopted wind speed profile

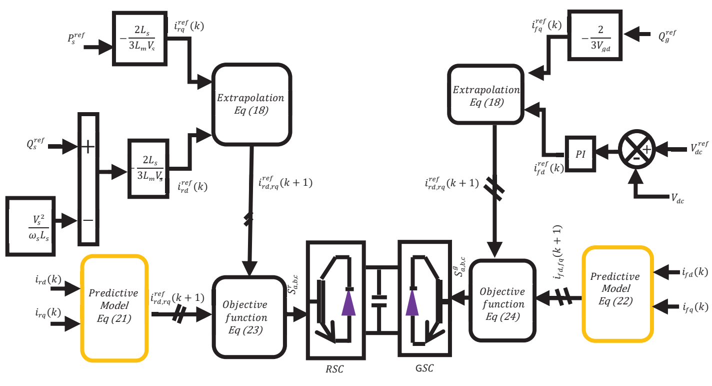

Fig. 6. Overall control structure

V. Conclusion

This paper delves into the control of a wind turbine system centered around a doubly-fed induction generator (DFIG), employing finite-control-set model predictive control (FCS-MPC) to overcome the challenges posed by fluctuating wind speeds and alterations in system parameters. The primary aim is to govern both the rotor side converter (RSC) and the grid

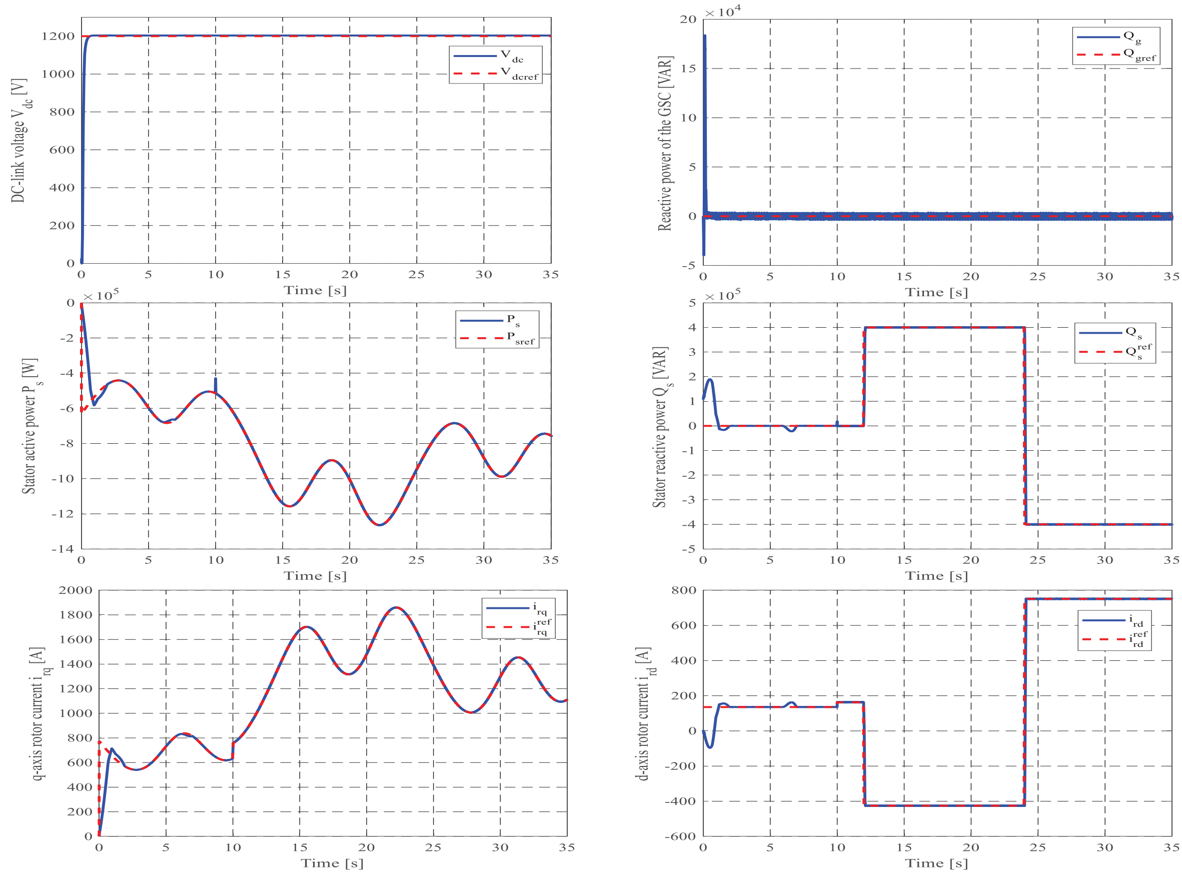

Fig. 7. DFIG based wind turbine system simulation results

TABLE I. PARAMETERS OF THE GRID-CONNECTED DFIG

Parameter	Value/Unit	Parameter	Value/Unit
Nominal Power	1.5 MW	Rotor resistance	0.021 Ω
Stator inductance	0.0137 H	System inertia	1000 kg.m^3
Rotor inductance	0.0135 H	Viscous friction	0.024 N.m.s/rad
Mutual inductance	0.0135 H	Blade radius	35.25 m
Stator resistance	0.012 Ω	Gear box gain	70
Filter resistance	0.002 Ω	Filter inductance	0.005 H

side converter (GSC) of the DFIG. The devised control strategy is constructed based on the system mathematical model and is refined through the minimization of an objective function, which selects the most appropriate voltage vector for application at each sampling time. The simulation results obtained under conditions involving random wind speed variations and changes in DFIG parameters underscore the noteworthy attributes of FCS-MPC, including its heightened stability, precision, and robustness. Furthermore, these outcomes validate the effectiveness of employing FCS-MPC for the decoupling control of active and reactive power in the system.

REFERENCES

[1] Y. Zhang and J. Jiao, "Model Predictive Rotor Current Control for Doubly Fed Induction Generators under Unbalanced Grid Voltages," *Proc. - 2018 IEEE Int. Power Electron. Appl. Conf. Expo. PEAC 2018*, pp. 1–5, 2018.

[2] Z. K. Nagy and R. D. Braatz, "Nonlinear Model Predictive Control for Batch Processes," *Control Handb. Second Ed.*, pp. 15-1-15–30, 2018.

[3] P. Kou, D. Liang, J. Li, L. Gao, and Q. Ze, "Finite-Control-Set Model Predictive Control for DFIG Wind Turbines," *IEEE Trans. Autom. Sci. Eng.*, vol. 15, no. 3, pp. 1004–1013, 2018.

[4] H. El Alami *et al.*, "Robust Finite Control-Set Model Predictive Control for Power Quality Enhancement of a Wind System Based on the DFIG Generator," *Energies*, vol. 16, no. 3, 2023.

[5] G. S. Kaloi, J. Wang, and M. H. Baloch, "Active and reactive power control of the doubly fed induction generator based on wind energy conversion system," *Energy Reports*, vol. 2, pp. 194–200, 2016.

[6] B. Q. Van Ngo, P. Rodriguez-Ayerbe, and S. Olaru, "Model Predictive Direct Power Control for doubly fed induction generator based wind turbines with three-level neutral-point clamped inverter," *IECON Proc. (Industrial Electron. Conf.*, pp. 3476–3481, 2016.

[7] G. F. Gontijo, T. C. Tricarico, B. W. Franca, L. F. Da Silva, E. L. Van Emmerik, and M. Aredes, "Robust Model Predictive Rotor Current Control of a DFIG Connected to a Distorted and Unbalanced Grid Driven by a Direct Matrix Converter," *IEEE Trans. Sustain. Energy*, vol. 10, no. 3, pp. 1380–1392, 2019.

[8] T. A. Nguyen *et al.*, "An efficient model predictive control based on Lyapunov function for doubly fed induction generator fed by a T-type inverter," *Electr. Eng.*, vol. 103, no. 1, pp. 663–676, 2021.

[9] D. Zouheyr, B. Lotfi, L. Thierry, and B. Abdelmadjid, "Grid Side Inverter Control for a Grid Connected Synchronous Generator Based Wind Turbine Experimental Emulator," *Eur. J. Electr. Eng.*, vol. 23, no. 1, pp. 1–7, 2021.

[10] V. Yaramasu and B. Wu, *Model Predictive Control of Wind Energy Conversion Systems*. 2016.

Energy performance of phase change materials integrated into brick wall for cooling load management in residential buildings on a sunny day in Bechar, Algeria

Allam Bachir.
Smart Structures Laboratory (SSL), University of Ain Témouchent-Belhadj Bouchaib,
Ain Témouchent, Algeria
bachir.allam@univ-temouchent.edu.dz

Nehari Taieb.
Smart Structures Laboratory (SSL), University of Ain Témouchent-Belhadj Bouchaib,
Ain Témouchent, Algeria

Zehouani Assala.
Smart Structures Laboratory (SSL), University of Ain Témouchent-Belhadj Bouchaib,
Ain Témouchent, Algeria

Hadjadj Mohammed.
Smart Structures Laboratory (SSL), University of Ain Témouchent-Belhadj Bouchaib,
Ain Témouchent, Algeria

Abstract— **Achieving zero-energy buildings relies on optimizing the building envelope's energy efficiency and utilizing renewable energy sources. Within the energy sector, the building industry stands as a significant consumer, accounting for approximately 30% of total energy consumption, primarily attributed to space cooling needs. For this propos this paper presents a numerical study on the heat transfer characteristics of a porous brick filled with phase change materials (PCMs) in typical days of July 2021 in Bechar city (Algeria). In the thermal model presented in this study, the PCM is filled in the square cavities of the bricks. The 2D-numerical model was carried out using Ansys Fluent software, based on the finite volume analysis and the enthalpy porosity-based method. To assess the efficacy of incorporating PCM into building bricks, a comparative analysis was conducted between two different cases - the normal bricks and bricks with PCM filled in the square cavities. Furthermore, the study was conducted with four different PCMs. The findings revealed that using PCM in building bricks stabilizes and reduces indoor temperature fluctuation. When utilizing Capric acid as a PCM, the lowest recorded maximum temperature reached was 27.8°C. This resulted in a notable decrease of 34% in peak indoor heat flux, with a corresponding shift in timing by 2.5 hours.**

Keywords – Solar energy storage; Energy consumption; Building brick; phase change materials; Thermal comfort

I. INTRODUCTION

The continual rise in the cost of fossil fuels and their decreasing availability, combined with requirements to reduce carbon emissions, reveal the necessity for more rational and efficient energy use. Buildings are great energy consumers: they are responsible for 36% of energy consumption in worldwide[1]. The heat gains and losses in buildings are addressed by the building envelope. Reduced building energy consumption in air conditioning is becoming increasingly significant as energy conservation and CO_2 emission reduction become more essential. Therefore, decreasing the high-energy consumption in buildings by incorporating passive design strategies or peak load shifting and reduction is essential[2]. Integrating phase change material (PCM) into the building envelope is a powerful way to reduce energy consumption. PCM can absorb and release a large amount of energy under a smaller volume and temperature changes to reduce indoor temperature fluctuations and building energy consumption. PCM is a promising option to improve energy efficiency and protect the environment[3]. Therefore, researchers focused on the integration of PCM in building envelopes. Many recent kinds of research focused on finding a suitable PCM for building envelopes using the most appropriate integration method and dimensions. They carried out how to effectively integrate PCMs within the building walls, roofs, and floors using an experimental or numerical method.

Different methods for integrating phase change materials into building envelopes are developed[4]

- Direct incorporation of PCM by mixing it with building materials.
- Direct impregnation of liquid PCM into porous construction components. This technique is based on dipping construction materials in liquid PCM.
- The PCM is encapsulated before being integrated into building components.
- Form-stable composite PCM: This technique is based on maintaining the optimum amount of PCM in supporting materials.

Whatever method is used to integrate PCM into building materials, the dynamic thermal performance of the building envelope is strongly influenced[5].

Fired clay brick is a widely used material for wall construction in many countries around the world. The attractive features of brick that make it more popular in the construction industry are its availability, durability, good mechanical properties and ease of installation. It is recognized that the integration of PCM is simple for building bricks with a prevailing openings or cavities[6]. Various authors conducted an experimental or numerical investigation for the thermal performance of building brick containing PCM [5], [7]–[16]. The results in kinds of the literature demonstrated that incorporating PCM into building brick could considerably reduce the thermal load compared to traditional brick and thermal comfort could be achieved. Consequently, the energy consumption in buildings would be minimized significantly.

In this context, the main objective of this study is to examine the benefits of integrating PCM into brick cavities. A conventional brick (without PCM) is considered as a reference for the comparison results, and the natural convection inside the liquid PCM is considered in the mathematical model. Firstly,

the influence of the PCM thermal-physio proprieties on the thermal performance of the brick is analyzed, so as to obtain the appropriate PCM in hot climate Finally, the thermal regulation performance of brick with four different PCMs is comprehensively evaluated. The conclusion of this study is helpful to reveal the influence of phase change materials on the thermal inertial of the brick, so as to achieve the heat transfer effect by designing new building brick model.

II. PHYSICAL MODEL AND VALIDATION

Fig. 1 shows the detailed dimensions of the brick used in the analysis. This configuration was used to investigate the performance of brick with three squares cavities filled with different PCMs. the analysis was conducted to compare the behavior of the brick filled with PCM and traditional brick.

.

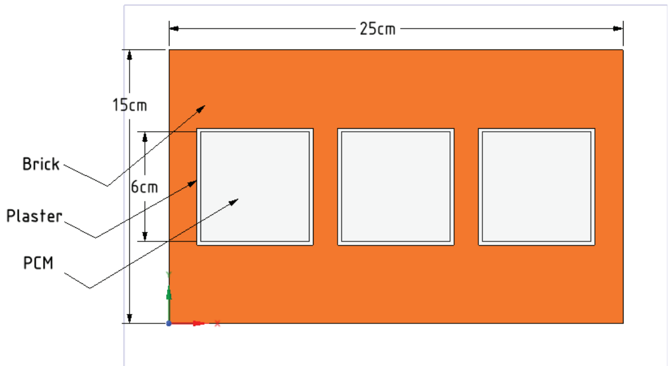

Fig. 1. Detailed dimensions of the brick integrated with PCM used in analysis.

To model the heat transfer and the phase change processes (solidification and melting) through the building bricks incorporate with PCM, the following simplifying assumptions are adopted.

- The properties of bricks are temperature independent.
- The heat capacity and thermal conductivity of the PCM vary as piecewise linear.
- The adiabatic wall assumption is adopted for the right and left sides of the bricks
- The motion of PCM in a liquid state is incompressible, Newtonian and laminar.

Two-dimensional convection and conduction modes of heat transfer have been considered in the melted PCM. With the foregoing assumptions, the mathematical model of this problem can be performed using the following equations:

$$\frac{\partial T}{\partial t} = \frac{\partial}{\partial x}\left(\frac{\lambda_{brick}}{\rho_{brick} C_{P,brick}} \frac{\partial T}{\partial x}\right) + \frac{\partial}{\partial y}\left(\frac{\lambda_{brick}}{\rho_{brick} C_{P,brick}} \frac{\partial T}{\partial y}\right) \quad (1)$$

For PCM region:

$$\frac{\partial(\rho_{PCM} h_{PCM})}{\partial t} = \frac{\partial}{\partial x}\left(\lambda_{PCM} \frac{\partial T}{\partial x}\right) + \frac{\partial}{\partial y}\left(\lambda_{PCM} \frac{\partial T}{\partial y}\right) \quad (2)$$

Where f is the value of liquid fraction and $L_{f_{PCM}}$ is the latent heat of PCM. The value of latent heat is zero when material is solid (f =0) and L when material is liquid (f =1).

$$f = \begin{cases} f = 0, \ T_{PCM} < T_{solidus}, \\ \dfrac{T_{PCM} - T_{solidus}}{T_{liquidus} - T_{solidus}}, \quad T_{liquidus} < T_{PCM} < T_{solidus}, \\ f = 0, \ T_{PCM} > T_{liquidus}, \end{cases} \quad (3)$$

A. *Boundary and initial conditions*

In this study, transient boundary conditions were used, where the outdoor weather conditions change with time (Fig. 2). The indoor air temperature was assumed to be constant at 25 °C throughout the simulation. This temperature was also taken as the initial condition for the entire system. Moreover, convection heat transfer was assumed over the indoor and outdoor wall with constant convective heat transfer coefficient of h_i =5 W/m^2 K and h_o =20 W/m^2 K [10].Thermo-physical properties of the brick and PCM are illustrated in Tables 1.

$$-\lambda_{brick} \frac{\partial T}{\partial x}\Big|_{y=0} = h_i \,(T_{indoor} - T_{brick}) \quad (4)$$

$$-\lambda_{brick} \frac{\partial T}{\partial x}\Big|_{y=H} = h_o \,(T_{sa} - T_{brick}) \quad (5)$$

where h_i and h_o are the inner and outdoor convective heat transfer coefficient and T_{brick} is the brick surface temperature. The present numerical study was carried out using Ansys Fluent software. The physical model is based on the finite-volume method and an enthalpy porosity formulation is adopted to model the phase change process. The domain is discretized in the form of an unstructured grid and subdivided on 82560 elements. A time step of (1 s) was found sufficient to provide accurate results. The grid size and the time step were selected after careful analysis of the autonomy of the results to these parameters. The convergence is verified at each time step, with the convergence criterion of 10^{-7} for all variables.

A. *Model validation*

This study used the enthalpy proposed method to simulate the behaviour of a PCM integrated into three squares cavities of the brick. Results of this model was validated against the numerical results obtained from Mahdaoui [10] Fig. 3 shows the comparison between the predicted indoor surface temperature with the same as obtained in [10] for the case of brick with PCM mass (16%). Based on the obtained results it is evident that a good agreement has been obtained during this comparison. The maximum relative deviation between the present study and the numerical results in [10] is around 1.2%.

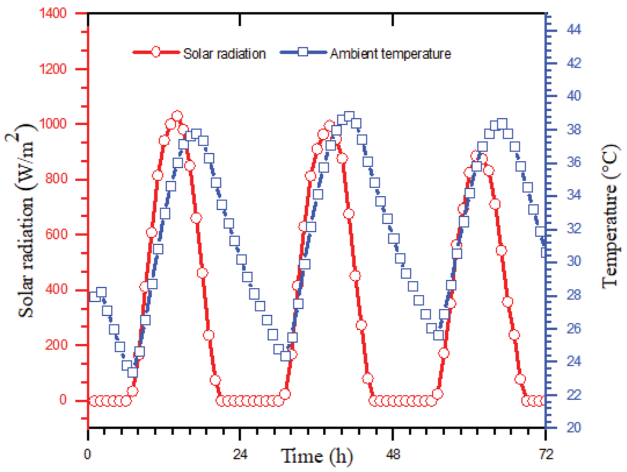

Fig. 2. Variation of solar radiation and ambient temperature for Bechar city.

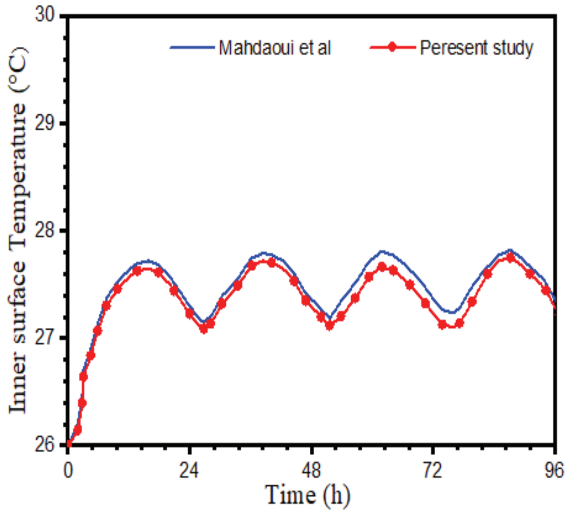

Fig. 3. Model validation with[10].

Table 1. Thermo-physical properties of the brick PCM [17][18][19].

Material	RT-42	n-Eicosane	Capric acid	RT-24	brick
Density, kg/m^3	885 (s) 820 (l)	885 (s) 778 (l)	1018 (s) 888 (l)	900 (s) 760 (l)	664
Specific heat capacity, J/(kg. k)	1800(s) 2400 (l)	2010 (l) 2040 (s)	1900 (s) 2400 (l)	2100(s) 2100(l)	741
Thermal conductivity	0.2	0.15	0.372 (s) 0.153 (l)	0.21	0.207
Viscosity, (Pa.s)	0.02534	0.00355	0.002664	0.0254	-
Thermal expansion coefficient, (1/k)	0.001	0.001	0.001	0.001	-
Latent heat,(kJ/kg)	141.6	241	152.7	144	-
Solidus temperature, (°C)	39	36	31	22	-
Liquidus temperature, (°C)	43	38	33	25	-

Note: *s* and l respectively represent the solid state and liquid state

III. RESULTS AND DISCUSSION

A. Effect of PCM type

Four different PCMs, n-Eicosane, Capric acid, RT-24 and RT-42, integrate into a building brick, are investigated. First, integrating PCM to the brick enhances the thermal properties of building materials by modifying the thermal storage ability of the wall materials and decreasing and shifting the peak load on the building. This can be observed in Fig.4, which plots the transition variation of the inner surface temperature using the four different PCMs. When PCM is used, the inner surface temperature significantly decreased. This decrease is much pronounced in the case of using PCM with a melting point close to the thermal comfort temperature. This decrease is caused by two reasons. The first reason is the added thermal resistance due to the existence of the PCM with low thermal conductivity of 0.15 W/m K. The second reason is due to the energy storage in the PCM cavity during the melting which prevent some heat to transfer through the brick structure. In more detail, the inner peak surface temperature decreased from 34 °C in the case of brick without PCM to around 28°C, 30 °C, and 31 °C for the brick containing Capric acid RT-42, and RT-24, PCMs, respectively.

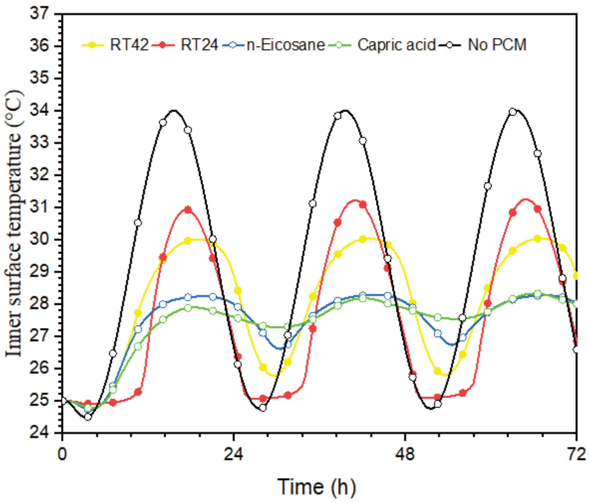

Fig. 4 Influence of integration of four PCMs on the inner surface temperature of brick

To better clarify the result is Fig. 4, the mass fraction of the PCM integrated in brick is presented in the Fig.4 shows liquid fraction versus time (three cycles) for the four PCMs. It is noticed that due to the lower melting temperature of RT-24, it completely melts. Also, can be seen, the molten fraction exceeded 60% for the capric acid, while it was less than 30% for the PCMs RT42 and n n-Eicosane.

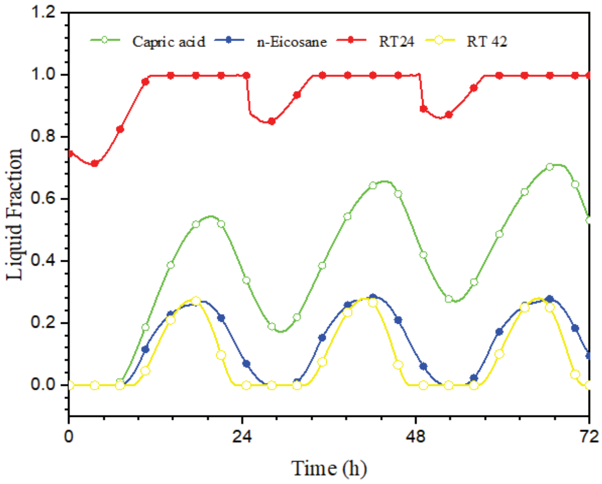

Fig.4 Variations of the liquid fraction of four PCMs

So, it's obvious that the higher the molten fraction, the higher was the thermal energy absorbed / released by PCM.

Fig. 6 represents the contour of the temperature variation for the building brick over the daytime of 3 July 2021 with PCM. It can be seen from the Fig. 7 that the contour lines are parallel to the horizontal wall of bricks near the top side and bottom side and start distorted near the PCM container. It is due to the thermo-physical properties of PCM. Furthermore, because the internal natural convection of PCM during melting is considered in this study, the temperature of the top part of PCM container is always higher than the bottom part, as indicated by the temperature contours. The melted PCM has a lower density as compared to solid, therefore due to bouncy effect the melted PCM moves upwards in the square cavity and solid moves downside. By this way, the lower part of the building bricks is at a lower temperature as compared to the upper part of the brick which can be seen from Fig.5.

The above results demonstrated that the PCM type significantly impact the dynamic thermal behavior of the brick wall. In conclusion, the capric acid is the most suitable PCM that leads to the best thermal efficiency of brick walls subjected to the external climatic conditions of the hot region. The energy efficiency of brick integrated with four different types of PCM is depicted in Fig.6. On a typical summer day, the energy consumption was calculated by adding the instantaneous heat flux gain. Meanwhile, the energy-saving rate of brick with PCM was calculated using traditional brick as a baseline. According to Fig.6, the energy consumption of brick with RT-24 and RT-42 is the highest, with energy-saving rates of 45.79% and 35.54%, respectively. In terms of energy efficiency, brick integrated with n-Eicosane ranks second with a 54.94% energy-saving rate. However, capric acid integrated into brick outperforms it by saving approximately 61.8% of energy. The results suggest that the type of phase change material (PCM) has a significant influence on the dynamic thermal behavior of brick walls. Consequently, capric acid proves to be the most effective PCM for enhancing the thermal performance of brick walls in hot external climates.

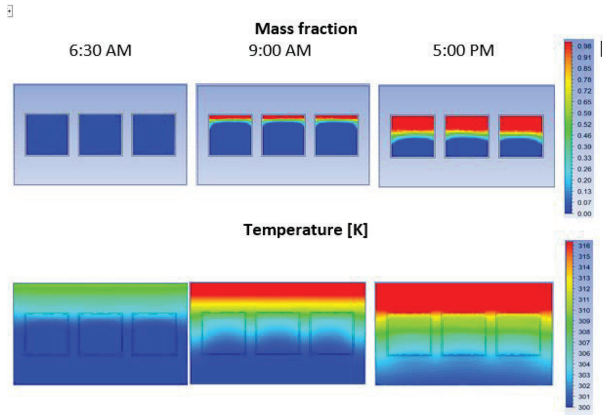

Fig. 5. Temperature variation and mass fraction of building brick with PCM at different time interval: (a) 6:30 AM, (b) 9:00AM, (c) 5:00 PM.

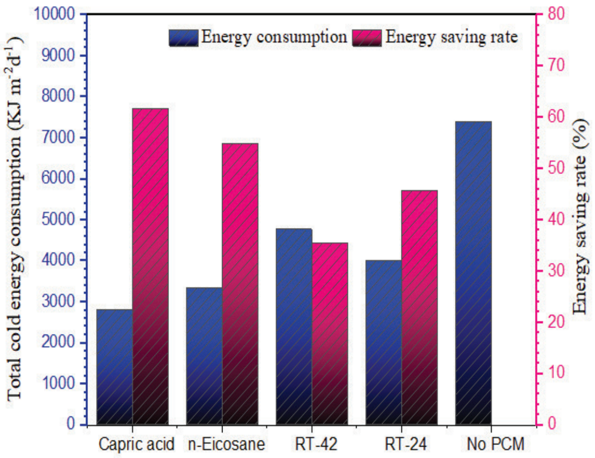

Fig.6. Influence of four PCMs on energy efficiency on July 2, 2021

III. CONCLUSION

The thermal behavior of using bricks filled with different PCMs was investigated as a method for reducing the heat gain in buildings during the day. Weather data in a hot climate is used in the analyses. A paramedic study is conducted to assess the effect of different PCMs integration. Through the comparative analysis of the inner surface temperature of traditional brick and brick integrated with PCM, it is concluded that Capric acid is the more effective PCM as compared to the n Eicosone, RT-24, and RT-42 for the considered ambient conditions. In general, incorporating PCM into the brick improves the storage capacity and insulation power of this building element. This is demonstrated by a significant reduction in the amplitude and a significant phase shift of the thermal wave as it crosses the brick wall with PCM. Moreover, it provides interesting passive temperature regulation, improves internal comfort, and thus contributes to reduce energy consumption of air conditioning systems in buildings.

IV. Acknowledgment

The authors thank everyone who helped us during the experimentation and writing process.

References

[1] G. Diarce, Á. Campos-Celador, K. Martin, A. Urresti, A. García-Romero, and J. M. Sala, "A comparative study of the CFD modeling of a ventilated active façade including phase change materials," Appl. Energy, vol. 126, pp. 307–317, 2014, doi: 10.1016/j.apenergy.2014.03.080.

[2] I. Nardi, E. Lucchi, T. de Rubeis, and D. Ambrosini, "Quantification of heat energy losses through the building envelope: A state-of-the-art analysis with critical and comprehensive review on infrared thermography," Build. Environ., vol. 146, pp. 190–205, 2018, doi: 10.1016/j.buildenv.2018.09.050.

[3] Y. Huang, S. Yang, M. Aadmi, Y. Wang, M. Karkri, and Z. Zhang, "Numerical analysis on phase change progress and thermal performance of different roofs integrated with phase change material (PCM) in Moroccan semi-arid and Mediterranean climates," Build. Simul., 2022, doi: 10.1007/s12273-022-0922-z.

[4] K. Faraj, M. Khaled, J. Faraj, F. Hachem, and C. Castelain, "A review on phase change materials for thermal energy storage in buildings: Heating and hybrid applications," J. Energy Storage, vol. 33, 2021, doi: 10.1016/j.est.2020.101913.

[5] Y. Chihab, R. Bouferra, M. Garoum, and M. Essaleh, "Thermal inertia and energy efficiency enhancements of hollow clay bricks integrated with phase change materials," J. Build. Eng., vol. 53, no. March, p. 104569, 2022, doi: 10.1016/j.jobe.2022.104569.

[6] C. Gentilini, E. Franzoni, G. Graziani, and S. Bandini, "Mechanical properties of fired-clay brick masonry models in moist and dry conditions," Key Eng. Mater., vol. 624, pp. 307–312, 2015, doi: 10.4028/www.scientific.net/KEM.624.307.

[7] B. Jamal, M. Boukendil, L. El moutaouakil, A. Abdelbaki, and Z. Zrikem, "Numerical investigation of combined heat transfer through hollow brick walls," Eur. Phys. J. Plus, vol. 135, no. 10, 2020, doi: 10.1140/epjp/s13360-020-00840-8.

[8] Y. Gao et al., "Thermal behavior analysis of hollow bricks filled with phase-change material (PCM)," J. Build. Eng., vol. 31, no. December 2019, p. 101447, 2020, doi: 10.1016/j.jobe.2020.101447.

[9] Y. Hamidi, M. Malha, and A. Bah, "Analysis of the thermal behavior of hollow bricks walls filled with PCM: Effect of PCM location," Energy Reports, vol. 7, no. May, pp. 105–115, 2021, doi: 10.1016/j.egyr.2021.08.108.

[10] M. Mahdaoui et al., "Building bricks with phase change material (PCM): Thermal performances," Constr. Build. Mater., vol. 269, no. xxxx, p. 121315, 2021, doi: 10.1016/j.conbuildmat.2020.121315.

[11] M. R. Elmarghany, A. Radwan, M. A. Shouman, A. A. Khater, M. S. Salem, and O. Abdelrehim, "Year-long energy analysis of building brick filled with phase change materials," J. Energy Storage, vol. 50, no. January, p. 104605, 2022, doi: 10.1016/j.est.2022.104605.

[12] B. Lamrani, K. Johannes, and F. Kuznik, "Phase change materials integrated into building walls: An updated review," Renew. Sustain. Energy Rev., vol. 140, no. January, 2021, doi: 10.1016/j.rser.2021.110751.

[13] A. C. Rai, "Energy performance of phase change materials integrated into brick masonry walls for cooling load management in residential buildings," Build. Environ., vol. 199, no. April, p. 107930, 2021, doi: 10.1016/j.buildenv.2021.107930.

[14] A. Bouchair, "Steady state theoretical model of fired clay hollow bricks for enhanced external wall thermal insulation," Build. Environ., vol. 43, no. 10, pp. 1603–1618, 2008, doi: 10.1016/j.buildenv.2007.10.005.

[15] Y. Hamidi, Z. Aketouane, M. Malha, D. Bruneau, A. Bah, and R. Goiffon, "Integrating PCM into hollow brick walls: Toward energy conservation in Mediterranean regions," Energy Build., vol. 248, p. 111214, 2021, doi: 10.1016/j.enbuild.2021.111214.

[16] C. Jia, X. Geng, F. Liu, and Y. Gao, "Thermal behavior improvement of hollow sintered bricks integrated with both thermal insulation material (TIM) and Phase-Change Material (PCM)," Case Stud. Therm. Eng., vol. 25, no. March, p. 100938, 2021, doi: 10.1016/j.csite.2021.100938.

[17] X. Xie, W. Zhang, X. Luan, W. Gao, X. Geng, and Y. Xue, "Thermal performance enhancement of hollow brick by

agricultural wastes," Case Stud. Constr. Mater., vol. 16, no. March, p. e01047, 2022, doi: 10.1016/j.cscm.2022.e01047.

[18] S. Hamdaoui, A. Bouchikhi, M. Azouggagh, M. Akour, A. Ait Msaad, and M. Mahdaoui, "Building hollow clay bricks embedding phase change material: Thermal behavior analysis under hot climate," Sol. Energy, vol. 237, no. March, pp. 122–134, 2022, doi: 10.1016/j.solener.2022.03.073.

[19] N. Hichem, S. Noureddine, S. Nadia, and D. Djamila, "Experimental and numerical study of a usual brick filled with PCM to improve the thermal inertia of buildings," Energy Procedia, vol. 36, pp. 766–775, 2013, doi: 10.1016/j.egypro.2013.07.089.

Improving Efficiency and Reliability in Wireless Energy Transfer Systems via Electromagnetic Analysis

Nadir Benalia
University of ziane Achour
LAADI Laboratory
Djelfa, Algeria
nadir.benalia@univ-djelfa.dz

Idriss Benlaloui, IEEE Member
University of Batna2,
LSPIE Laboratory,
Batna, Algeria
i.benlaloui@univ-batna2.dz

Rachad Moumni
University of ziane Achour
LAADI Laboratory
Djelfa, Algeria
rmoumni1@gmail.com

Kouider Laroussi
University of ziane Achour
LAADI Laboratory
Djelfa, Algeria
kouider.laroussi@univ-djelfa.dz

Tarek Boutabba
University of Khenchela
, El-Hamma, Algeria,
LSPIE Laboratory, Batna2, Algeria
boutabba_tarek@yahoo.fr

Amor Fezzani
Unité de Recherche Appliquée en Energies Renouvelables
Centre de Développement des Energies Renouvelables
Ghardaia 47133, Algeria
amorfezzani@yahoo.fr

Abstract—**This paper leads to the examination of circular and rectangular models and their influence on the efficiency of wireless power transfer (WPT) systems. The study utilizes ANSYS Maxwell 3D simulation software to analyze the magnetic vector and field of these models. The investigation involves the exploration of different vertical (Z) gap distances and horizontal (Y) spacing. By leveraging ANSYS Maxwell, we gain the ability to visualize, analyze, and optimize electromagnetic fields, leading to a comprehensive understanding of the WPT system.**

Keywords- Wireless power transfer Inductive; Circular coil; rectangular coil; electromagnetic fields,* ANSYS *Maxwel.

I. Introduction

Electric vehicles (EVs) have emerged as an attractive alternative to traditional fossil fuel-powered vehicles, offering the potential to reduce CO2 emissions, improve fuel efficiency, and minimize air pollution and environmental degradation [1-2]. Moreover, EVs generally incur lower operating costs due to reduced fuel and maintenance expenses compared to their fossil fuel counterparts. The absence of vibration and noise associated with internal combustion engines also contributes to a quieter and more comfortable driving experience for EV users. The adoption of electric vehicles holds significant benefits for both the environment and individual consumers [3-4].

In recent years, there has been a growing interest in wireless charging, a groundbreaking technology that allows for the transmission of electrical energy between two coils without the necessity of physical wires. Inductive coupling wireless charging, based on the principle of induction, utilizes electromagnetic fields to wirelessly transfer energy between two closely positioned coils. However, there are limitations to wireless power transmission (WPT), particularly in terms of the range and fast charging requirements of battery electrical storage technology [5].

Researchers have sought to enhance the effectiveness of wireless charging systems through the use of different coil forms. Circular and rectangular shapes are commonly employed in charging stations due to their ease of implementation [6-12]. Analyzing the electromagnetic properties of these coils, which consist of separate transmitter and reception coils, involves considering mutual induction and self-induction effects, which affect the coupling coefficient—a crucial factor in this analysis.

Recent designs have explored circular coupling and other shapes to improve power transfer efficiency, presenting more complex calculations. Finite element analysis, such as the use of ANSYS Maxwell software, proves valuable in overcoming these challenges.

This study focuses on investigating a circular spiral design to enhance inductive charging supply, taking into account both horizontal and vertical alignment concerning the distance. The analysis includes evaluating the inductance and mutual inductance characteristics, as well as the magnetic induction effects, to predict an appropriate shielding system.

The structure of this research is as follows: The principle of wireless power transfer, including a description and analysis of the circular spiral and rectangular coil models using ANSYS Maxwell, is discussed to assess the effectiveness of the proposed system. Subsequently, simulation results are presented, followed by concluding remarks.

II. PRINCIPLE OF WIRELESS POWER TRANSFER

As shown in figure 1, wireless energy transmission uses a transformer-like system with two separate coils for energy transfer through magnetic coupling, inducing voltage and current in the receiving coil from the transmitting coil's alternating voltage. This enables wireless power transfer to a load.

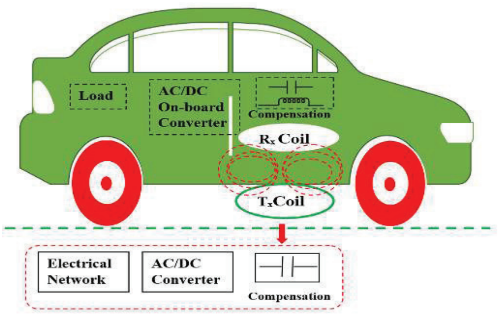

Figure 1. Wireless charging system for EVs [1].

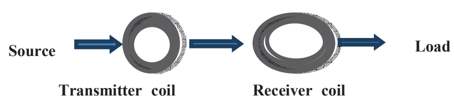

Figure 2. Diagram of the principle of wireless energy transfer

III. MODEL OF WIRELESS ENERGY TRANSFER SYSTEM

Figure 2 depicts the equivalent circuit utilized for computing the geometric parameters of the coil and evaluating the efficiency of wireless energy transfer.

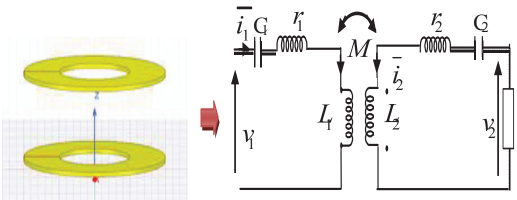

Figure 3. Equivalent wireless charging circuit

r1, r2 : The resistance of the primary and secondary coils.
L1, L2 : The self-inductance of the primary and secondary coils.
M : The mutual inductance between the primary and secondary coils.

$$\begin{pmatrix} v_1 \\ v_2 \end{pmatrix} = \begin{pmatrix} Z_{11} & Z_{12} \\ Z_{21} & Z_{22} \end{pmatrix} \begin{pmatrix} i_1 \\ i_2 \end{pmatrix} \tag{1}$$

$$v_1 = L_1 \frac{di_1}{dt} + M \frac{di_2}{dt} + r_1 \cdot i_1 + v_{C1} \tag{2}$$

$$v_2 = -L_2 \frac{di_2}{dt} + M \frac{di_1}{dt} - r_2 \cdot i_2 - v_{C2} \tag{3}$$

$$v_1 = r_1 \cdot i_1 + \frac{1}{jC_1 w} i_1 + jwL_1 i_1 - jwM i_2 \tag{4}$$

$$v_2 = -r_2 \cdot i_2 - \frac{1}{jC_2 w} i_2 + jwM i_1 - jwL_2 i_2 \tag{5}$$

IV. A PRESENTATION OF THE ANALYSING SYSTEM

A. Geometry parameter:

The importance of mutual inductance in the wireless power transfer (WPT) system cannot be understated, as it is significantly influenced by the design of the magnetic coupler. To validate the rationality of selecting either rectangular or circular type magnetic couplers, Ansoft Maxwell simulation was performed, and the results are presented in Fig. 4, Table 1, and Table 2.

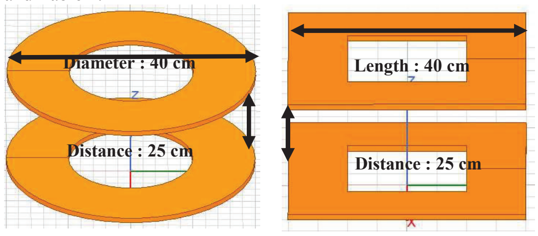

Figure 4. Geometrics of both circular coils and rectangular coils by an Ansys-Maxwell software design

TABLE I. . GEOMETRIC PARAMETERS OF CIRCULAR AND RECTANGULAR COILS

Paramètres	**Circular**		**Rectangular**	
A	**25 cm**	**Air gap**	**25 cm**	**Air gap**
Wire type		**Copper**		**Copper**
Hc	**1 cm**	**Coil Thickness**	**1 cm**	**Coil Thickness**
Dist	**20 cm**	**Coil outer**	**40 cm**	**The length of the outer side**
Wc	**10 cm**	**Coil inside radius**	**10 cm**	**The length of the inner side of the coil**
A	**25 cm**	**Air gap**	**25 cm**	**Air gap**

To elucidate the arrangement, the system comprises of two identical coils - one functioning as a transmitter and the other as a receiver. The dissimilarity lies in the current flow through each coil, leading to a modification in the electrical parameters. Detailed values of these parameters can be referenced from Table II.

TABLE II. ELECTRICAL PARAMETERS FOR THE TWO COILS: CIRCULAR AND RECTANGULAR

Symbol	Quality	Value
N_1	Number of primary coil turns	**10**
N_2	Number of secondary coil turns	**10**
I_1	Primary coil current	**10 (A)**

V. SIMULATION RESULTS AND DISCUSSION

A. Study of the Circular model

A.1 Vertical misalignment

Figure 5 illustrates the magnetic field distribution for two circular coils with similar properties. Each coil possesses an outer radius of 20 cm, an inner radius of 10 cm, and a thickness of 1 cm. Both coils are separated by a distance of 25 cm in the Z direction and have a current of 10 (A) amperes passing through them. Notably, the magnetic induction (B) near the coils, close to the current source, exhibits its highest intensity.

In the study model, it is assumed that the medium, which is air, possesses a magnetic permeability equal to 1. The impact of this assumption on the mutual inductance and coupling coefficient is presented in figures 6. These figures demonstrate that as the distance between the two coils increases and the magnetic permeability decreases, the amount of energy transferred between the coils decreases correspondingly.

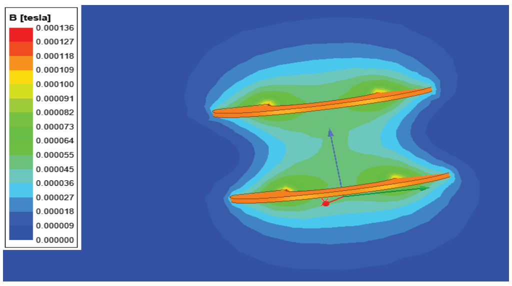

Figure 5. Distribution of the magnetic field lines at a distance of 25 cm

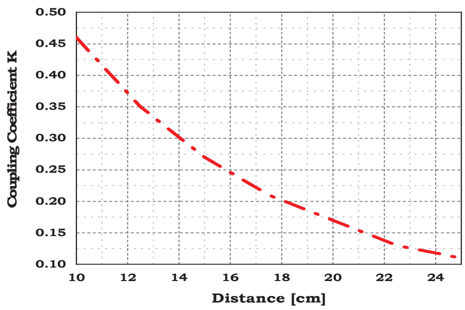

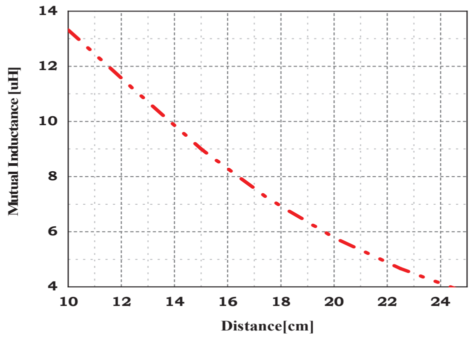

Figure 6. (a) Coupling coefficient; (b) Mutual inductance, under variation of vertical misalignment d=10 cm to 25 cm

A.2 Horizontal misalignment

In Figure 7, it can be observed that a magnetic field is present in the surrounding space of the two coils. This magnetic field weakens as the distance between the coils increases. Consequently, efficient wireless energy transfer occurs through strong magnetic field coupling without the need for physical contact.

The results obtained from the tests indicate that when the coils are horizontally aligned, the coupling coefficient and mutual induction exhibit changes in a parabolic pattern. As the misalignment between the coils increases, both the coupling coefficient and mutual inductance decrease. The maximum values of the coupling coefficient and mutual inductance are achieved when the coils have zero misalignment and are in phase (X = 0 cm). Figure 8 illustrates that the magnetic coefficients are most effective when the two coils are in close proximity to each other.

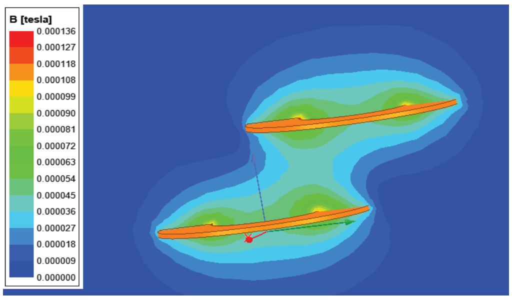

Figure 7. Distribution of the magnetic field lines at a distance of 25 cm and alignment along (Y) -20cm to +20cm

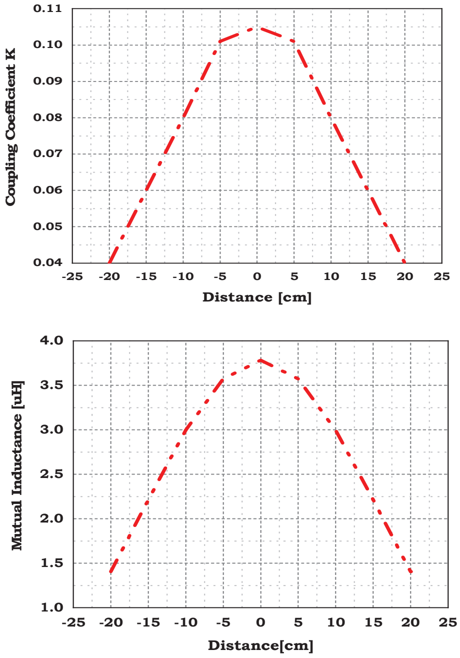

Figure 8. Coupling coefficient (a) and variation of the mutual inductance (b) from horizontal misalignment (rectangular mode) d=-20 cm to 20 cm

B. Study of the rectangular model :

B.1 Vertical misalignment

The given interpretation discusses the concept of wireless energy transfer through magnetic fields between two coils. It explains that the magnetic field exists in the surrounding space of the coils and weakens as the distance between them increases. The efficient transfer of energy is achieved through strong magnetic field coupling without physical contact.
Furthermore, the interpretation mentions that the study model considers the medium, which is air, to have a magnetic permeability of 1. It highlights the impact of this assumption on mutual inductance and coupling coefficient, illustrated in figures 10. These figures demonstrate that as the distance between the coils increases and the magnetic permeability decreases, the amount of energy transferred between the coils decreases as well.

B.2 Horizontal misalignment

In Figure 11, it can be observed that a magnetic field is present in the surrounding space of the two coils. This magnetic field weakens as the distance between the coils increases. Consequently, the most efficient way to transfer energy wirelessly is through strong magnetic field coupling, eliminating the need for physical contact.

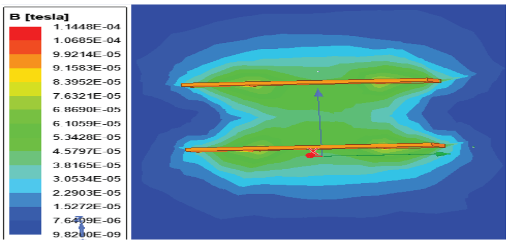

Figure 9. Distribution of the magnetic field lines at a distance of 25 cm

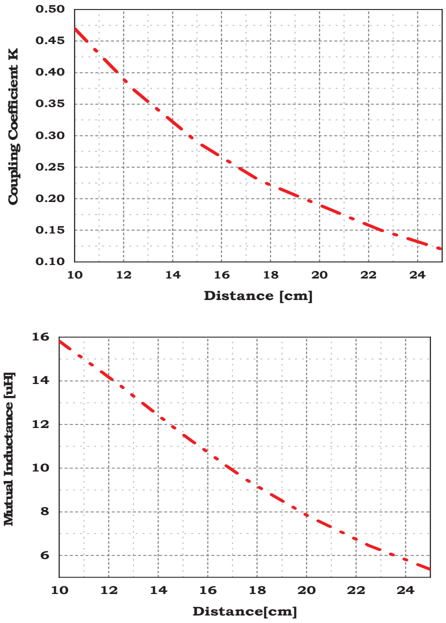

Figure 10. (a) Coupling coefficient; (b) Mutual inductance, under variation of vertical misalignment d=10 cm to 25 cm.

The results obtained from the experiments show that when the coils are horizontally aligned, there are parabolic changes in the coupling coefficient and mutual induction. As the misalignment between the coils increases, both the mutual inductance and coupling coefficient decrease. When there is zero misalignment, and the two coils are perfectly in phase (X = 0 cm), the coupling coefficient and mutual inductance reach their maximum values. Therefore, the magnetic coefficients are most effective when the two coils are positioned close to each other, as depicted in Figure 12.

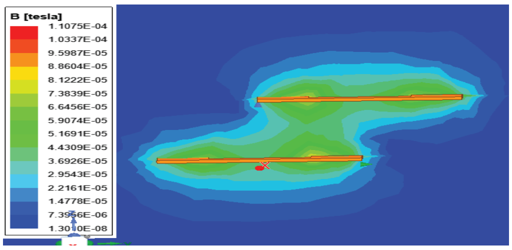

Figure 11. Distribution of the magnetic field lines at a distance of 25 cm and alignment along Y -20cm to +20 cm

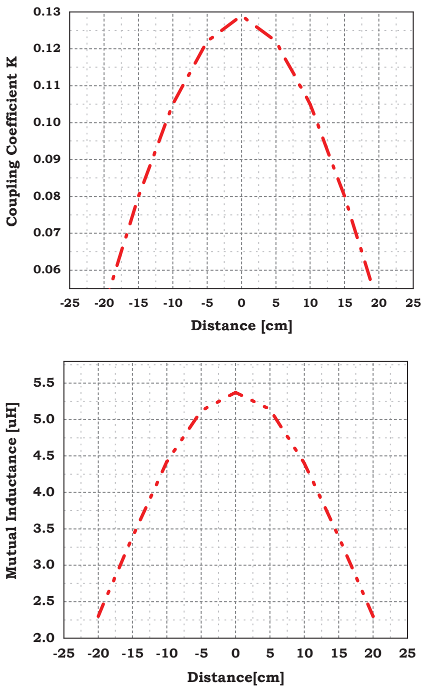

Figure 12. Coupling coefficient (a) and variation of the mutual inductance (b) from horizontal misalignment (rectangular mode) d=-20 cm to 20 cm

VI. Conclusion

In this paper, we conducted an electromagnetic analysis of wireless energy transfer for Electric Vehicle (EV) systems. Our research focused on investigating the effects of the air gap and horizontal spacing between coils on the system. The results of our study indicate that as the air gap and horizontal spacing increase, both the mutual inductances and coupling coefficient decrease. From these findings, we can infer that the efficiency of power transfer is significantly influenced by the distance between the transmitter and receiver coils. To address this magnetic issue, numerical methods are required, but they can be time-consuming. To optimize efficiency, we utilized the ANSYS Maxwell software, which provided an effective solution. For accuracy and precise control over the quantitative results, we employed a mesh grid, with particular attention to the air gap region.

References

[1] Benalia, N.; Laroussi, K.; Benlaloui, I.; Kouzou, A.; Bensaleh, A.; abdrhman, M.; Kannel, R.; Optimized Power Pads for Charging ElectricVehiclesBased on a New Rectangular Spiral Shape Design.Sustainability 2023, 15(2), 1230.
https://doi.org/10.3390/su15021230

[2] Benlaloui, I.;Benalia, N.; Laroussi, K.; Power Pad using New Rectangular Spiral Shape Design for Charging Electric Vehicles Conference: 2022 2nd International Conference on Advanced Electrical Engineering (ICAEE)
https:doi/10.1109/ICAEE53772.2022.9962118

[3] Lassioui, A.; Fadil, H.E.; Belhaj, F.Z.; Rachid, A. Battery Charger for Electric Vehicles Based ICPT and CPT-A State of the Art. In Proceedings of the 2018 Renewable Energies, Power Systems Green Inclusive Economy (REPS-GIE), Casablanca, Morocco,23–24 April 2018; pp. 1–6.

[4] Lassioui, A.; Fadil, H.E.; Belhaj, F.Z.; Rachid, A. Battery Charger for Electric Vehicles Based ICPT and CPT-A State of the Art. In Proceedings of the 2018 Renewable Energies, Power Systems Green Inclusive Economy (REPS-GIE), Casablanca, Morocco,23–24 April 2018; pp. 1–6.

[5] Daniel Ongayo and Moin Hanif, Member, IEEE"Comparison Of Circular And Rectangular Coil Transformer" Conference Paper · November 2015.
https:doi/10.1109/COBEP.2015.7420222

[6] Kadem, K.; Bensetti, M.; LeBihan, Y.; Labouré, E.; Debbou, M.Optimal Coupler Topology forDynamicWireless Power Transfer forElectric Vehicle. Energies 2021, 14,3983. https://doi.org/10.3390/

[7] Ahmed A.S. Mohameda,b,Ahmed A. Shaiera, Hamid Metwallya, Sameh I. Selema A comprehensive overview of inductive Pad in electric vehicles,stationaryCharging.https://doi.org/10.1016/j.apenergy.2020.114584

[8] Yang Yang Jinlong Cui and Xin Cui 2Design and Analysis of Magnetic Coilsfor Optimizing the Coupling Coeffcient inan ElectricVehicleWireless Power Transfer System,Energies 2020, 13, 4143; https:doi:10.3390/en13164143.

[9] Ahmad, A., Alam, M.S., Chabaan, R., and Mohamed, A., "Comparative Analysis of Power Pad for Wireless Charging of ElectricVehicles," SAE Technical Paper 2019-01-0865, 2019.
https:doi/10.4271/2019-01-0865.

[10] Heqi Xu , Chunfang Wang , Dongwei Xia and Yunrui Liu, Design of Magnetic Coupler for Wireless Power Transfer,Energies 2019, 12, 3000; https:doi/10.3390/en12153000.

[11] Benalia, N.; Laroussi, K. :Benlaloui, I; Improvement of the Magnetic Coupler design for Wireless Inductive Power Transfer ,The 5th International Conferenceonn Power Electronics and their Applications (ICPEA) ,29-31 March 2022 , Ha'il ,KSA.https://doi.org/10.1109/ICPEA51060.2022.9791150

[12] Bentalhik, I.; Lassioui,A.; El fadil, H.; Bouanou, T.; Rachi, A.; El idrisi, Z.; Hamed, A.; Analysis, Design and Realization of a Wireless Power Transfer Charger for Electric Vehicles: Theoretical Approach and Experimental Results *World Electr. Veh. J.* 2022, *13*(7), 121.
https://doi.org/10.3390/wevj13070121

Integrated On-Chip Inductor Design for Photovoltaic DC-DC Converter

Mokhtaria Derkaoui[1]*, Yamina Benhadda[2]

[1]*LARATIC Laboratory, National Higher School of Telecommunications & ICT of Oran, Algeria*
[2]*LEPA Laboratory, University of Sciences and Technology of Oran, Algeria*
*mokhtaria.derkaoui@ensttic.dz

Abstract—The research of this work concerns the study of an integrated on-chip inductor with a circular topology. The topology of the inductor is chosen for its ability to deliver better performance and high inductance value. The inductor is situated in DC-DC Boost converter connected to a photovoltaic module. The paper presents the integrated inductor geometrical and electrical dimensioning. The equivalent electrical circuit of the integrated inductor with different layers is defined. Heat equation was utilized by using finite elements method to demonstrate the temperature distribution, the temperature gradient, the enthalpy, the total heat source and total heat flow in the integrated spiral planar inductor. The simulation of the DC-DC Boost converter with PV panel is validated using the equivalent electrical circuit of the integrated circular inductor to show its performances. The study combines theoretical analysis, modeling and simulation techniques to evaluate the performance and effectiveness of the circular on-chip inductor topology. The results obtained provide valuable insights into the design and operation of the integrated inductor based PV system.

Keywords—DC-DC Converter; Inductor; Integration; On-Chip; Photovoltaic.

I. Introduction

Electric power generated by a photovoltaic system is influenced by solar radiation and temperature variations [1-2]. The maximum power produced by photovoltaic (PV) module is delivered to the load by adjusting the voltage through a DC-DC converter [3-4]. DC-DC converters play a crucial role in these systems by simplifying the conversion and distribution of power [5-7]. This miniaturization of converters has pushed towards developing distributed architectures and embedded systems for on-chip systems containing several components [8-9]. Therefore, the integration of the passive components of these converters becomes an inevitable solution in order to reduce sizes and cost [10-11]. On-chip integrated spiral planar inductors remove several inconveniences, at recent years [12-14]. The aim of this paper is to address the challenges in PV systems containing a DC-DC converter with an integrated on-chip inductor. We propose a comprehensive study on the topology of the circular spiral planar inductor integrated in a DC-DC Boost converter, which offers improved performance and a high inductance value. The model presented in this study includes geometric and electric characteristics to develop analytical equations for the inductor topology. Besides, we focus on implementing a PV system for the DC-DC converter, which integrates the proposed circular inductor. This control strategy aims to operate the PV panel at its maximum power point, optimizing the overall energy conversion efficiency of the system. The performance of the integrated on-chip inductor in the converter is validated using specialized software. The simulations allow us to evaluate the effectiveness and efficiency of the designed integrated inductor in the DC-DC Boost converter and its application in photovoltaic systems.

II. DC-DC Converter for Photovoltaic Systems

Photovoltaic energy is considered one of the most important renewable energy sources for the production of electricity, it can supply a DC-DC converter to enable the power transfer to the load. For a photovoltaic generator to operate in optimal conditions, it must be equipped with an adaptation quadrupole. This adaptation is achieved by automatically searching for the maximum power point (PPM) of the PV generator and this when the system is placed in an environment where the weather conditions (sunshine, temperature) and load are stable [3-5]. This quadrupole can be a DC-DC converter depending on the application. The opposing problem is the design and realization of a control that converges the PV system to the optimal conditions independent of weather and load variations [6-7]. The opposing problem is the design and implementation of a control system that converts the PV system to optimum conditions regardless of weather variations and load. The block diagram of a typical photovoltaic system is illustrated in Fig.1.

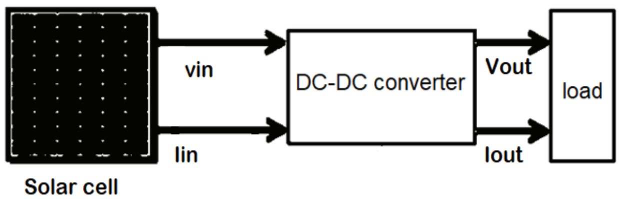

Fig.1. Photovoltaic system block diagram

For ideal DC-DC converters, both the input and output power are equal (1).

$$V_{in} \cdot I_{in} = V_{out} \cdot I_{out} \tag{1}$$

In this work, DC-DC Boost converter (Fig.2) was chosen to be used in a PV system due to its simplicity of implementation and high efficiency.

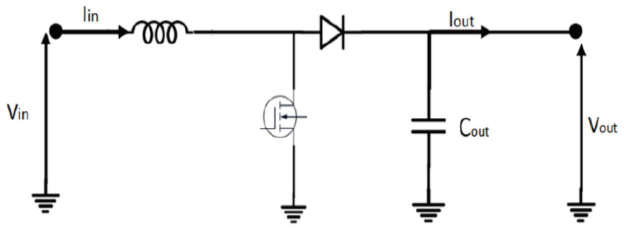

Fig.2. DC-DC Boost Converter electrical diagram

A) Photovoltaic Module

The PV generator (SP75) panel consists of several elementary photovoltaic cells. The equivalent circuit of the photovoltaic cell (Fig.3) includes a current source connected in parallel with a diode, a shunt and a series resistors [2] [5]. The technical characteristics of the PV panel are determined in Table 1.

Table 1. PV panel technical characteristics

Maximum working voltage	5.5 V
Maximum current	0,6 A
Maximum power	3 W
Minimum working voltage	5 V
Maximum power tolerance	15%
Working temperature	-45°C to +85 °C

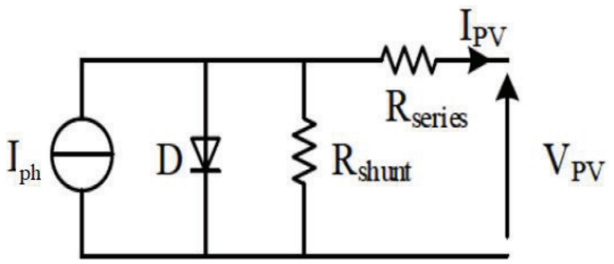

Fig.3. Equivalent circuit of PV cell

The generated current by the cell I_{PV} is given by (2) [3- 4].

$$I_{PV} = I_{ph} - I_{sat} \cdot \left(e^{\frac{q \cdot (V_{PV} + I_{PV} \cdot R_{series})}{n \cdot K \cdot T_c}} - 1 \right) - \frac{V_{PV} + (I_{PV} \cdot R_{series})}{R_{shunt}} \quad (2)$$

I_{sat}: junction saturation current

K: Boltzmann constant

T_c: cell temperature

q : electron charge

n: ideality factor of the junction

Photocurrent of the cell I_{ph} depends on the solar irradiation level and the working temperature is given by (3).

$$I_{ph} = I_{sc} + K_i \cdot (T_c - T_r) \cdot \frac{I_r}{1000} \quad (3)$$

I_{sc}: short circuit current of the cell at standard test conditions (STC)

K_i: cell short circuit current/temperature coefficient (A/K)

T_c, T_r: cell working and reference temperature at standard test conditions (STC)

I_r: irradiance covering cell surface (W/m²)

B) DC-DC Boost Converter Design

As shown in Fig.4, DC-DC Boost converter consists of PV voltage source, inductor L, capacitor C, load resistor R and also both transistor and diode operating as switches. Our research in this paper is to reduce the size of the DC–DC Boost converter and preserve its performances in order to integrate it in the photovoltaic module. The reduction of the size needs to reduce the size of the inductor.

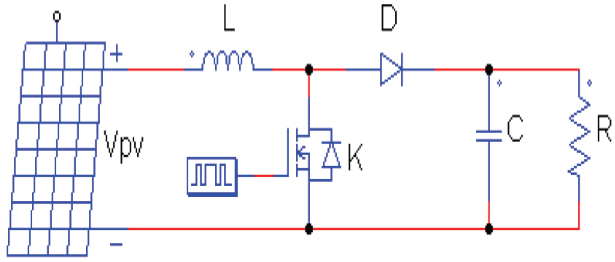

Fig.4. PV panel integrated with DC–DC Boost converter

The converter is considered as the starting point of the integrated inductor design. For that, we have chosen the following specifications:

- Input voltage: V_{PV} = 5 Volts
- Output voltage: V_{out} = 17 volts
- Output power: P_{out} = 3W
- Operating frequency: f = 6 MHz

The link between the input and output voltage (4) and current (5) is related to the duty cycle α, where its maximum is around 70%.

$$V_{out} = \frac{V_{PV}}{1-\alpha} \quad (4)$$

$$I_{out} = (1-\alpha) \cdot I_{PV} \quad (5)$$

The average output current I_{out} is given by (6).

$$I_{out} = \frac{P_{out}}{V_{out}} \quad (6)$$

The average current flowing through the inductor ΔI_L is given by (7), it determines the peak amplitude of current and it never drops to zero.

$$\Delta I_L = I_{Lmax} - I_{Lmin} = \frac{V_{out}}{V_{PV}} \cdot (\alpha \cdot I_{out}) \quad (7)$$

The inductance L is given by (8).

$$L = \frac{\alpha \cdot (1-\alpha) \cdot V_{out}}{\Delta I_L \cdot f} \quad (8)$$

The capacitance C of DC-DC Boost converter is given by (9) for an output voltage ripple ΔV_{out} equal to 10 % of the output voltage.

$$C = \frac{\alpha \cdot I_{out}}{\Delta V_{out} \cdot f} \quad (9)$$

The load resistance of the DC-DC Boost converter is given by (10).

$$R = \frac{V_{out}}{I_{out}} \quad (10)$$

C) Integrated Inductor Topology

The integrated inductor consists of a circular planar spiral coil in copper (Cu). The on-chip coil is superimposed on NiZn ferrite layer and isolated from there by SiO_2 silicon dioxide layer. All these different layers are superimposed on silicon layer (Si), which serves as a substrate (Fig.5).

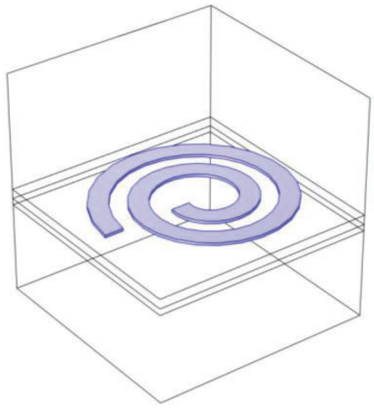

Fig.5. Circular on-chip inductor 3D view

The required NiZn ferrite volume for the energy storage is given by (11) [12].

$$Vol = \frac{W_{indu}}{W_{vmax}} \quad (11)$$

W_{indu} and W_{vmax} represent the total magnetic stored energy (12) and the maximum volume density of energy (13).

$$W_{indu} = \frac{1}{2} \cdot L \cdot I_{out}^2 \quad (12)$$

$$W_{vmax} = \frac{B_{max}^2}{2 \cdot \mu_0 \cdot \mu_{rNiZn}} \quad (13)$$

B_{max}= 0.3 T

μ_{rNiZn}= 1500

Therefore, 0.889 mm^3 of NiZn is necessary to store 0.021 µJ of energy in the inductor.

The integrated circular planar spiral inductor is characterized by geometrical parameters (Table 2), the angles are limited to multiples of 45 degrees.

Table 2. Geometrical parameter values

Geometrical parameters	Values
Outer diameter d_{out}	5 mm
Inner diameter d_{in}	3 mm
Turns number n	2
Coil thickness t	50 µm
Coil width w	100 µm
Coil total length l_t	10 mm
Coil spacing s	0.3 mm

The equivalent electrical circuit extracted from Fig.5.a determines the electrical behavior of the integrated planar inductor. Different structures have been proposed for the integrated inductors, however the most successful design is illustrated in Fig.6, which has been widely studied [12-14]. The circuit contains different electrical parameters that define each material layer. They are calculated by (14-19).

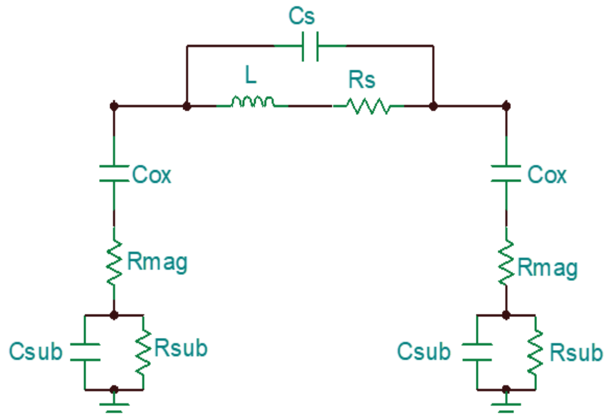

Fig.6. Lumped elements equivalent electrical circuit

$$Rs = \rho_{cu} \cdot \frac{lt}{w \cdot t} \quad (14)$$

$$R_{mag} = 2 \cdot \rho_{NiZn} \cdot \frac{t_{mag}}{w \cdot lt} \quad (15)$$

$$R_{sub} = 2 \cdot \rho_{Si} \cdot \frac{t_{Sub}}{w \cdot lt} \quad (16)$$

$$C_{sub} = \frac{1}{2} \cdot \varepsilon_0 \cdot \varepsilon_{rSi} \cdot \frac{w \cdot lt}{t_{sub}} \quad (17)$$

$$C_{ox} = \frac{1}{2} \cdot \varepsilon_0 \varepsilon_{rSiO2} \cdot \frac{w \cdot lt}{t_{ox}} \quad (18)$$

$$C_s = \frac{1}{2} \cdot \varepsilon_0 \varepsilon_{rair} \cdot \frac{t \cdot lt}{s} \quad (19)$$

III. Inductor Thermal Behaviour

Fig.7 shows the 3D extremely fine mesh of the integrated circular inductor with all different layers.

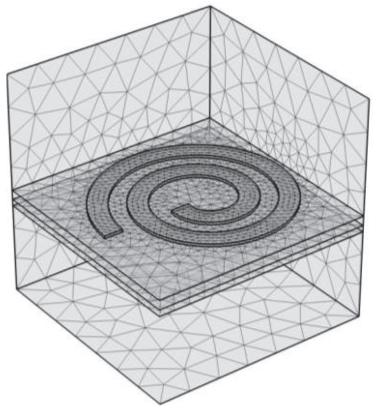

Fig.7. Mesh of the circular inductor with different layers

By solving heat equation [13][15], we visualize the temperature, the temperature gradient, the enthalpy, the total heat source and the total heat flow on the integrated circular planar inductor. We notice that the temperature value achieves 39 °C, the temperature gradient is around 0.5 10^5 K/m in the borders, the enthalpy is about 1.2 10^4 J/Kg and the total heat source generated by Joule effect achieves 7.81 10^8 W/m^3 in the spiral inductor and the total heat flow attains 0.8 10^5 W/m^2.

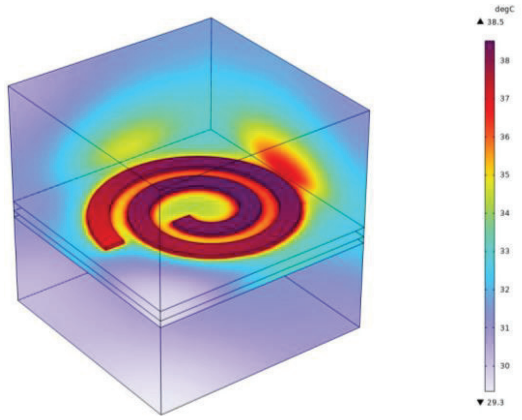

(a)

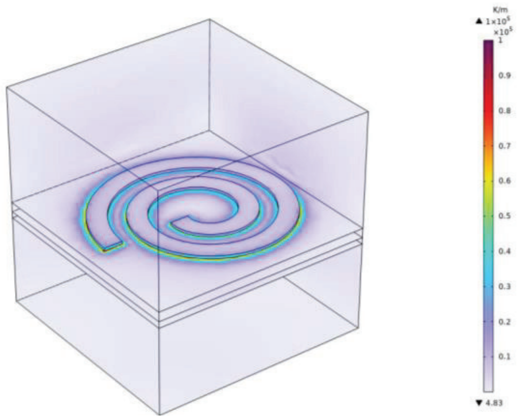

(b)

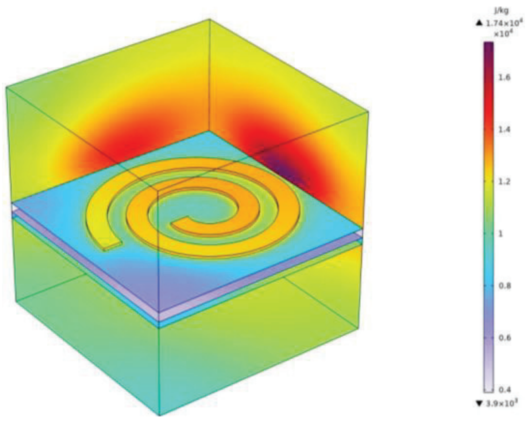

(c)

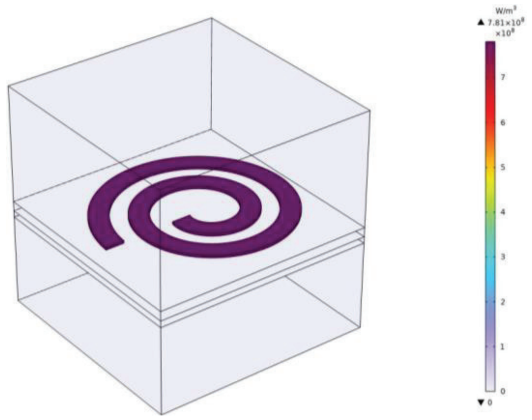

(d)

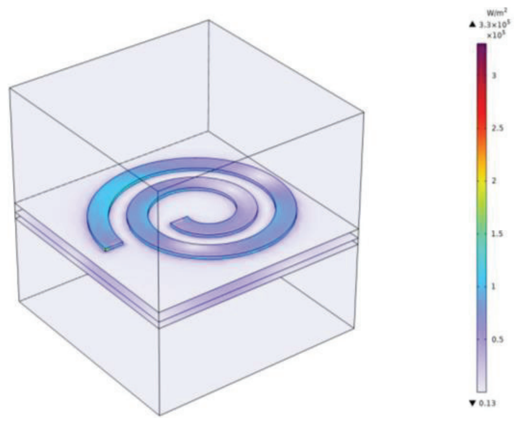

(e)

Fig.8. (a) Temperature distribution, (b) Temperature gradient, (c) Enthalpy, (d) Total heat source, (e) Total heat flow

IV. Simulation of DC-DC Boost Converter for Photovoltaic Applications

Fig.9 shows the circuit diagram of the DC-DC Boost converter containing the PV panel as a thermal energy source converted to electricity and the equivalent electrical circuit of the integrated inductor.

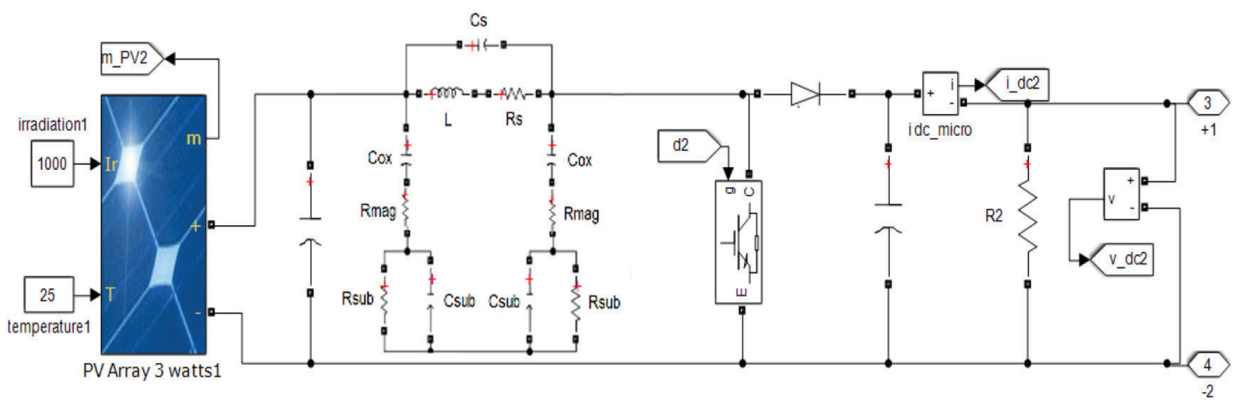

Fig.9. Photovoltaic system using DC-DC Boost converter with integrated on-chip inductor

Simulated results of the DC-DC Boost converter at a switching frequency of 6 MHz are presented in Fig.10. We notice that the converter displays a continuous output signals with a transient mode during the initial microseconds. The output current is approximately 0.17 A indicating a stable and continued transfer of power to the load. The output voltage also achieves 17 V. The current across the inductor is about 0.40 A. The obtained values are close to the DC-DC Boost converter specifications. In Fig.11 the maximum photovoltaic current achieves 0.6 A and the power is about 2.9 Watt for a voltage of 3.8 V. In Fig.12 the increase of the irradiation allows to increase the current and the power in the photovoltaic panel. These results show that the integrated on-chip planar inductor works well. Hence, we can confirm that the geometrical and electrical dimensions are well defined.

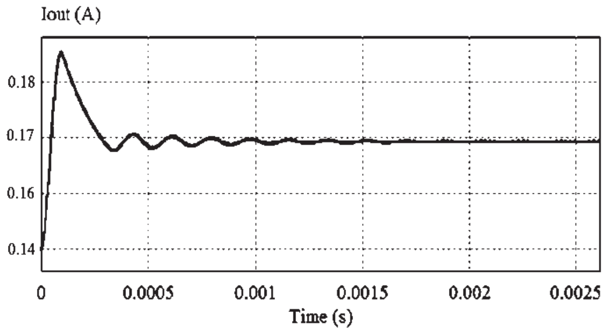

(a)

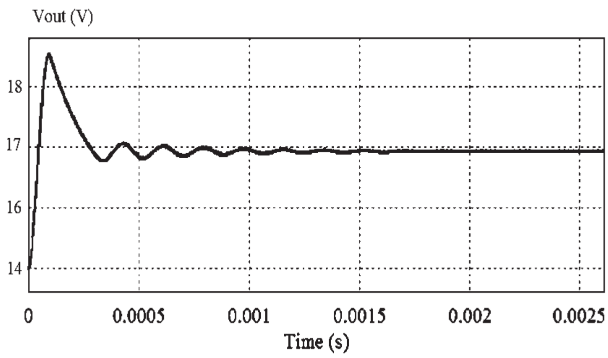

(b)

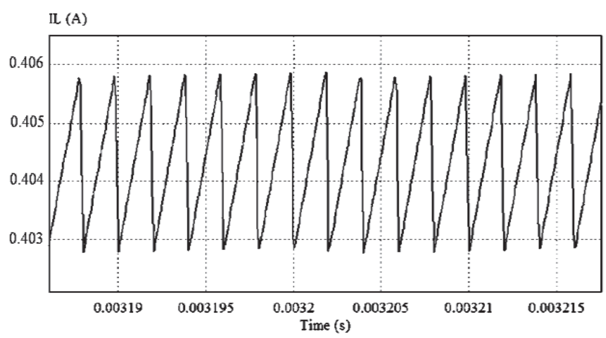

(c)

Fig.10. Output waveforms with 1000 W/m² irradiation and 25°C temperature: (a) Current I_{out}, (b) Voltage V_{out}, (c) Inductance current I_L

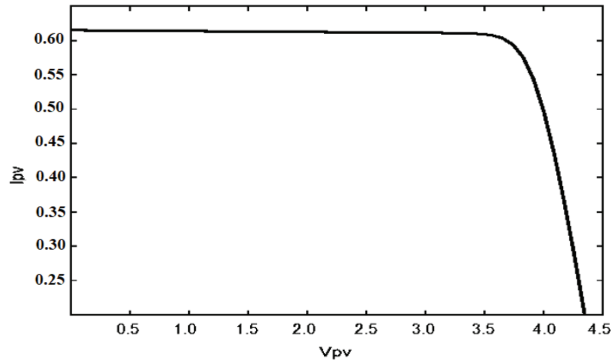

(a)

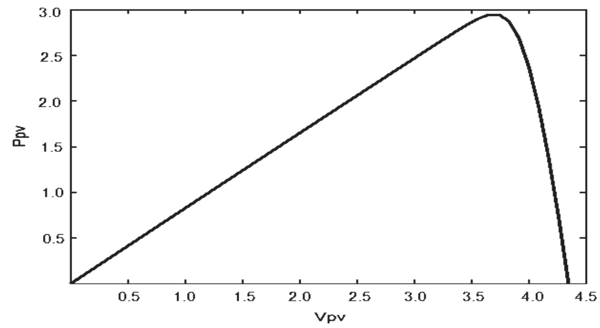

(b)

Fig. 11. (a) I-V and (b) P-V Characteristics of Solar Cell

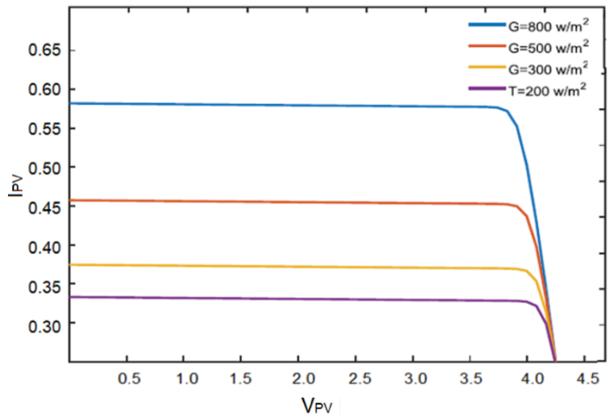

(a)

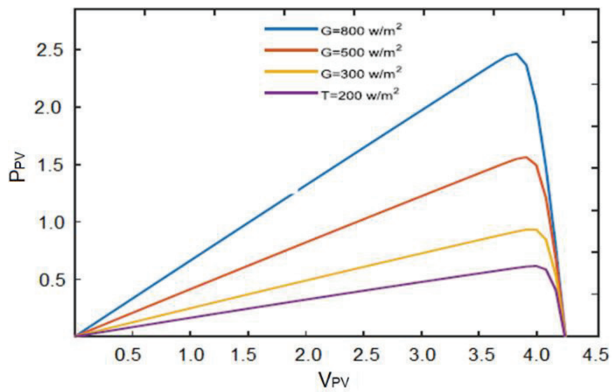

(b)

Fig.12. (a) I-V and (b) P-V characteristics at different irradiation level with 25°C

V. Conclusion

In this paper, we have presented the dimensioning, the modeling and the simulation of the circular on-chip planar inductor integrated in DC-DC Boost converter using for PV system. Simulations were established to evaluate the photovoltaic panel behaviour. The simulations were conducted under a temperature of 25°C and constant irradiation of 1 kW/m². We have extracted geometrical and electrical parameters of the integrated circular planar inductor basing on the specifications of DC-DC Boost converter. By using a software simulation, we have extracted converter output voltage and current waveforms. The results obtained in this work serve as a valuable reference for the inductor integration into photovoltaic applications. The circular on-chip planar inductor was found appropriate for operating the DC-DC Boost converter combined with photovoltaic generator. We conclude that the results of dimensioning in this work are interesting indeed.

References

[1] O. Ibrahim, N. Z. Yahaya, Matlab/Simulink Model of Solar PV Array with Perturb and Observe MPPT for Maximising PV Array Efficiency, 2015 IEEE.

[2] R. Gladwin Antony, *et al*, "Design of Solar Charging Case for Mobile Phones," Journal of Physics: Conference Series (International Conference on Physics and Energy), vol. 2040, 2021.

[3] J. J. Khanam, S. Y. Foo, Modeling of a photovoltaic array in MATLAB simulink and maximum power point tracking using neural network, Electrical & Electronic Technology Open Access Journal, vol. 2, no. 2, 2018.

[4] K. V. G. Raghavendra, *et al*, "A Comprehensive Review of DC–DC Converter Topologies and Modulation Strategies with Recent Advances in Solar Photovoltaic Systems," electronics, vol. 31, n. 9, p 1- 41, 2020.

[5] S. Saravanan, N.R. Babu, "A modified high step-up non-isolated DC–DC converter for PV application," Journal of Applied Research and Technology, vol. 15, n.3, p 242–247, 2017.

[6] N. Belhaouas, M.S. Ait Cheikh, A. Malek, C. Larbes, Matlab-Simulink of photovoltaic system based on a two-diode model simulator with shaded solar cells, Revue des Energies Renouvelables, vol. 16, no.1, pp 65 – 73, 2013.

[7] G. Pratapsinh Parmar and D. Urvashi Patel, "A Review on DC-DC converters for Photovoltaic system," IJIREEICE, vol. 3, no. 12, pp. 143– 146, Dec. 2015.

[8] Zaghba, A. Borni, A. Bouchakour, N. Terki, Buck-boost converter system modelling and incremental inductance algorithm for photovoltaic system via Matlab/Simulink, Revue des Energies Renouvelables SIENR'14 Ghardaïa (2014) , pp 63 – 70.

[9] M. R. Benzidane, *et al*, "Miniaturization and Optimization of a DC–DC Boost Converter for Photovoltaic Application by Designing an Integrated Dual-Layer Inductor Model," Transactions on Electrical and Electronic Materials, vol. 23, p 462–475, 2022.

[10] Derkaoui M, Benhadda Y, Hamid A, Temmar A. (2021) Design and modeling of circular planar inductor and transformer in monolithic technology for RF systems. J Electr Eng Technol 16:1481–1493.

[11] Aldoumani, M.; Yuce, B.; Zhu, D. Using the Variable Geometry in a Planar Inductor for an Optimised Performance. Electronics 2021, 10, 721.

[12] Derkaoui, M.; Benhadda Y.; Chaabene G.; Spiteri P.; "On-Chip GaN Planar Transformer Design for Highly Integrated RF Systems", Journal of Circuits, Systems and Computers, Vol. 32, No. 09, 2350149 (2023).

[13] Benhadda, Y., Derkaoui, M., Mendaz, K., Kharbouch, H., Spiteri, P. "Design for Integrated Planar Spiral Inductor for MEMS", Periodica Polytechnica Electrical Engineering and Computer Science, (2023).

[14] M. H. Bechir, *et al*, "Planar inductor equivalent circuit model taking into account magnetic permeability, loss tangent, skin and proximity effects versus frequency,"Analog integrated circuits and signal processing, vol.88, n.1, p 105–113, 2016.

[15] K. Górecki, J. Zaręebski, "Investigations on the influence of selected factors on thermal parameters of impulse-transformers". Inf. MIDEM-J. Microelectron. Electron. Compon. Mater. 2017, 47, 3–13

Fractional and Integer Orders PI Controllers Application to Wind Power Systems

Frikh Mohamed Lamine
Dept of Electrical Engineering
university of badji mokhtar
Annaba, Algeria
frikhlamine@yahoo.fr

***Abstract*—Wind power plants are known to have nonlinear dynamics and carry many uncertainties as parameter uncertainties and unknown nonlinear disturbances. So, it is a challenging task to design a robust controller for this system. This paper proposes a robust fractional-order proportional integral (FOPI) controller for maximum power point tracking (MPPT) control of permanent magnet synchronous generator (PMSG)-based wind energy conversion system. A comparison with the integer order proportional integral (IOPI) controller has been handled under the same number of parameters design and tuning constraints. This may guarantee the robustness to the loop gain variations of the designed controllers and the desired control performance. Comparison of the two controllers via the simulation tests show that, the IOPI controller designed cannot always be stabilizer to reach flat-phase constraint while FOPI controller designed is always stabilizing.**

Keywords—PMSG, MPPT, FOPI, TSR, Fractional calculus.

I. INTRODUCTION

Today wind power is quickly growing renewable energy source because it is clean, suitable, and safe for some applications, with comparatively initial low costs [1]-[2]. Based on the type of the wind turbine and generator utilized, variable speed wind turbines (VSWTs) equipped with permanent magnet synchronous generators (PMSGs) have many advantages compared to fixed speed wind turbines (FSWTs). The VSWT is more efficient than the FSWT because it offer optimized wind energy conversion, less mechanical stress, operation at the maximum power point (MPP) for wide range, and raise captured wind energy. Moreover, PMSGs are commonly used in VSWTs due to their reliability, simple structure, high torque density, and high degree of reliability because a gearbox is not required [2].

Control strategy in MPPT techniques is an important factor to extract maximum power from variable speed systems through controlling generator speed which is closely related to the wind speed. There are numerous literature works discussing the different techniques of maximum power point tracking [3]. The most widely used three MPPT methods are tip speed ratio (TSR), perturb and observe (P&O) and power feedback.

(PSF) methods [4]. The TSR method will be adopted in this work for its simple algorithm and fast response [2]

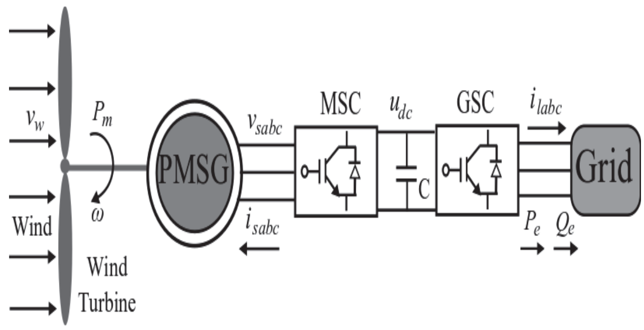

Fig. 1 Variable speed wind turbine system.

The structure (VSWT) system based on a (PMSG) is shown in Fig. 1. It consists of two power converters. One controls the speed of the wind turbine, while the other one care about shaping of the currents injected to the grid [5].

Lately, fractional calculus has been regarded as a powerful tool for modeling and control in different applications as control of power electronic converters, heat diffusion, viscoelastic phenomena, and distributed parameter systems [6]. Development of control systems for the wind turbines based- PMSG, is an essential issue. Field oriented control using classical integer order proportional integral IOPI controller is largely applied for the control of the wind turbines based-PMSG. Yet, the design of a controller for this system have many challenges, for instance, many uncertainties and nonlinear dynamics [7]. When the system to be controlled is characterized by uncertainties and nonlinearities, the performance of the IOPI control method degrades. To ameliorate the system performance, robust control based on fractional-order proportional integral FOPI controller is proposed in the present work.

The paper is organized as follows. The wind turbine system and the PMSG models are detailed in section II. The control strategy is presented in section III. Simulation results are given in section IV. Conclusion is given at the end.

II. System Modeling

A. Wind Turbine Modeling

The mechanical power and torque P_m, T_m are described as follows [5]:

$$P_m = \frac{1}{2} C_p(\lambda, \beta) \rho \pi R^2 v_w^3 \quad (1)$$

$$T_m = \frac{1}{2} C_p(\lambda, \beta) \rho \pi R^3 \frac{v_w^2}{\lambda} \quad (2)$$

$$C_p(\lambda, \beta) = 0.5176\left(\frac{116}{\lambda_i} - 0.4\beta - 5\right) e^{\frac{-21}{\lambda_i}} + 0.0068\lambda \quad (3)$$

$$\frac{1}{\lambda_i} = \frac{1}{\lambda + 0.08\beta} - \frac{0.035}{\beta^3 + 1} \quad (4)$$

$$\lambda = \frac{\omega R}{v_w} \quad (5)$$

Where v_w is the wind speed, R is the blade radius, ρ is the air density, C_p is power coefficient, which is function of pitch angle β and tip speed ratio λ, *ω* is the rotor angular speed, P_m is power of wind turbine. Fig. 2 show The relation among power coefficient and tip speed ratio.

When the values of β=0° and λ= λ_{opt}=8.1, C_p has optimum value C_{opt}=0.48, the optimal rotor angular speed is provided as reference to the controller and given by:

$$\omega_{opt} = \frac{\lambda_{opt} v_w}{R} \quad (6)$$

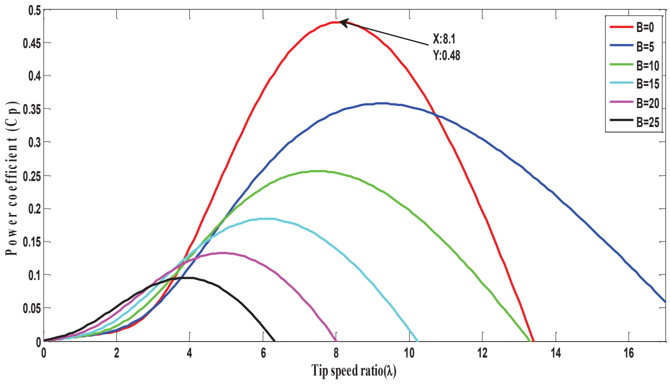

Fig. 2 The C_p curve.

B. PMSG Model

The stator voltage equations for PMSG may be represented in the dq-axes as below [8] :

$$\begin{cases} u_d = L_d \dfrac{di_d}{dt} + R_s i_d - \omega_e L_q i_q \\ u_q = L_q \dfrac{di_q}{dt} + R_s i_q - \omega_e L_d i_d + \omega_e \psi_f \end{cases} \quad (7)$$

where u_d, u_q and i_d, i_q are the stator voltages and currents of the dq components, respectively. The parameters R_s, ψ_f, ω_e, are the stator windings resistance, the flux permanent magnetic and the electrical speed, respectively. The parameters L_d, L_q are the stator windings inductance of the dq components, here L_d=L_q=L. The electromagnetic torque T_e of PMSG is given below:

$$T_e = 1.5 P \psi_f i_q \quad (8)$$

P known as pair of poles.

The dynamical rotation model of wind turbine is described as:

$$J \frac{d\omega_m}{dt} T_m - B\omega_m - T_e \quad (9)$$

where ω_m represent rotational speed. B and J are the friction factor and inertia moment, respectively.

With the aim of controlling the PMSG, field orientation control (FOC) has been applied. The scheme of control system shown in Fig. 3 is composed of two control loops. The inner loops adjust the stator current dq components to track the reference currents i_d^* i_q^* whereas the outer loop adjust the generator speed [9].

According to the maximum power point operation, the optimal speed is calculated and taken as an entry point to the speed loop ω_{opt}, generates in turn the reference of i_q^* (current of quadrature). The outputs of the current loops are the inputs of generator converter's (u_d, u_q) [5].

Due to the relative rapid of the dynamics of electrical systems compared with dynamics of mechanical systems, the inner loops are not critical. So, classical proportional integral controllers can be utilized to adjust the PMSG's current. However, the speed loop's is critical because their dynamic is slow and, in addition, the mechanical system is nonlinear. Two controllers are tested to regulate the speed loop; a classical IOPI controller and a Fractional FOPI controller.

The simplified first-order transfer functions of electrical and mechanical plants given by:

$$M(s) = \frac{1}{Ls + R_s} \quad (10)$$

$$F(s) = \frac{1}{Js + B} \quad (11)$$

III. Control System

A. Fractional Order Controller

Fractional calculus generalizes the conventional integration and differentiation to the non-integer order operator ${}_aD_t^{\alpha}$, where a and t are the boundary of the operation and α ϵ R. The fractional operator has the following form:[7]

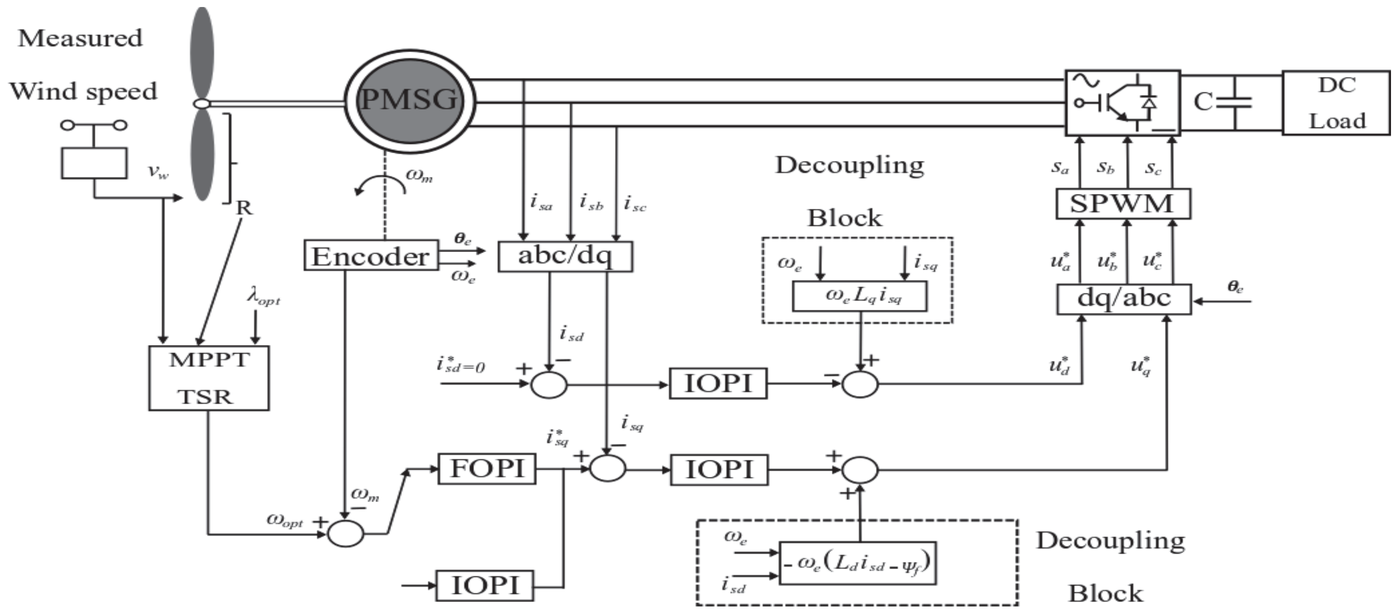

Fig. 3 PMSG control system based on FOC

$$ {}_aD_t^{\alpha} = \begin{cases} \dfrac{d^{\alpha}}{dt^{\alpha}} & \alpha > 0 \\ 1 & \alpha = 0 \\ \int_a^t (d\tau)^{\alpha} & \alpha < 0 \end{cases} \tag{12} $$

The Riemann–Liouville definition is [10]-[11]:

$$ {}_aD_t^{-\alpha} f(t) = \frac{1}{\Gamma(\alpha)} \int_a^t (t-\tau)^{\alpha-1} f(\tau)\, d\tau \tag{13} $$

$$ {}_aD_t^{-\alpha} f(t) = \frac{1}{\Gamma(n-\alpha)} \frac{d^n}{dt^n} \left[\int_a^t \frac{f(\tau)}{(t-\tau)^{\alpha-n+1}} d\tau \right] \tag{14} $$

with

$$ \Gamma(x) = \int_0^{\infty} y^{x-1} e^{-y} dy \tag{15} $$

In this work, α (the fractional order identifying number) is supposed to fulfills the restriction $0 < \alpha \le 2$. As well, it's supposed that a=0. The utilized convention is as follow : ${}_0D_t^{-\alpha} \equiv D_t^{-\alpha}$.

In this paper, the frequency approximation of Oustaloup [12] is used. The approximating transfer function proposed by Oustaloup is:

$$ s^{\alpha} = Z \prod_{n=-N}^{N} \frac{s + \omega_n'}{s + \omega_n}, \quad \alpha \in \Re^{+} \tag{16} $$

with

$$ \omega_n' = \omega_b \left(\frac{\omega_h}{\omega_b} \right)^{\frac{n+N+\frac{1}{2}(1-\alpha)}{2N+1}} \tag{17} $$

$$ \omega_n = \omega_b \left(\frac{\omega_h}{\omega_b} \right)^{\frac{n+N+\frac{1}{2}(1+\alpha)}{2N+1}} \tag{18} $$

$$ Z = \left(\frac{\omega_h}{\omega_b} \right)^{-\frac{\alpha}{2}} \prod_{n=-N}^{N} \frac{\omega_n}{\omega_n'} \tag{19} $$

The used differential equation in temporal domain of the fractional FOPI controller, has the following form:

$$ u(t) = K_p \left(e(t) + K_i D_t^{-\alpha} e(t) \right) \tag{20} $$

where $\alpha < 2$, K_p and K_i are the proportional and integral constants of the controller, respectively. With α=1 in (20), a traditional PI controller is gotten. Therefore, utilizing Laplace transform, the transfer functions of the used fractional FOPI and classical IOPI controllers are as follows:

$$ C(s) = K_p \left(1 + \frac{K_i}{s^{\alpha}} \right) \tag{21} $$

$$ E(s) = K_p \left(1 + \frac{K_i}{s} \right) \tag{22} $$

B. Design Constraints

Suppose the crossover frequency of the gain is ω_c with a phase margin ϕ_m. To ensure the system robustness and stability , three tuning constraints are proposed [11]:

(i) The constraint of the phase margin

$$ Arg\left[G(j\omega_c)\right] = Arg\left[C(j\omega_c)F(j\omega_c)\right] = -\pi + \phi_m \tag{23} $$

(ii) Crossover frequency constraint of the gain

$$\left|G(j\omega_c)\right| dB = \left|C(j\omega_c)F(j\omega_c)\right| dB = 0 \tag{24}$$

(iii) The system Robustness to variation in the gain requires that the derivative of phase with respect to the frequency is zero equal. Hence, the plotted phase of Bode is flat on the gain crossover frequency. This signify that the overshoot values of the response are almost the same and the robustness of the system is achieved.

$$\left(\frac{d\left(Arg\left|G(j\omega)\right|\right)}{d\omega}\right)_{\omega=\omega_c} = 0 \tag{25}$$

C. FO-PI Controller Design strategy applied to Wind Turbine Speed Control

As mentioned previously, the currents of PMSG can be adjusted by using classical PI controllers (electrical plant). Also, a classical integer order IOPI controller and a fractional order FOPI controller are tested to regulate the wind turbine speed (mechanical plant).

The open-loop G(s) of the wind turbine speed after applying the FOPI controller is:

$$G(s) = C(s)F(s) = K_p\left(1+\frac{K_i}{s^\alpha}\right)\left(\frac{1}{Js+B}\right) \tag{26}$$

We can get the frequency response from the open loop of G(s) as follows:

$$G(j\omega) = KK_p\left(1+\frac{K_i}{(j\omega)^\alpha}\right)\left(\frac{1}{1+T(j\omega)}\right) \tag{27}$$

with $K=\frac{1}{B}$, and $T=\frac{J}{B}$

As stated in constraint (i)

$$Arg\left|G(\omega_c)\right| = -\arctan\frac{K_i\omega_c^{-\alpha}\sin\left(\alpha\frac{\pi}{2}\right)}{1+K_i\omega_c^{-\alpha}\sin\left(\alpha\frac{\pi}{2}\right)} - \arctan(T\omega_c) \tag{28}$$

$$= -\pi + \phi_m$$

From (28) it can be established a relation among Ki and α as:

$$K_i = \frac{-\tan\left[\arctan(T\omega_c)+\phi_m\right]}{\omega_c^{-\alpha}\sin\left(\alpha\frac{\pi}{2}\right)+\omega_c^{-\alpha}\cos\left(\alpha\frac{\pi}{2}\right)\tan\left[\arctan(T\omega_c)+\phi_m\right]} \tag{29}$$

When Constraint (iii) which is related to robustness to loop gain variations in the plant

$$\left(\frac{d\left(Arrg\left|G(j\omega)\right|\right)}{d\omega}\right)_{\omega=\omega_c} = \frac{K_i\alpha\omega_c^{\alpha-1}\sin\left(\alpha\frac{\pi}{2}\right)}{\omega_c^{2\alpha}+2K_i\omega_c^{\alpha}\cos\left(\alpha\frac{\pi}{2}\right)+K_i^2}$$

$$-\frac{T}{1+(T\omega_c)^2} = 0 \tag{30}$$

Likewise, we can establish another equation about K_i from (30) as follows:

$$K_i = \frac{-\sigma \pm \sqrt{\sigma^2 - 4C^2\omega_c^{-2\alpha}}}{2C\omega_c^{-2\alpha}} \tag{31}$$

where:

$$C = \frac{T}{1+(T\omega_c)^2} \tag{32}$$

$$\sigma = 2C\omega_c^{-\alpha}\cos\left(\alpha\frac{\pi}{2}\right) - \alpha\omega_c^{-\alpha-1}\sin\left(\alpha\frac{\pi}{2}\right) \tag{33}$$

The K_p equation can be established as stated in Constraint (ii)

$$\left(\frac{K_pK\sqrt{\left[1+K_i\omega_c^{-\alpha}\cos\left(\alpha\frac{\pi}{2}\right)\right]^2+\left[K_i\omega_c^{-\alpha}\sin\left(\alpha\frac{\pi}{2}\right)\right]^2}}{\sqrt{T^2+(\omega_c)^2}}\right) = 1 \tag{34}$$

Obviously, based on equations (29), (31) and (34), α, Ki and Kp can be determined graphically. The summarized procedure to tune the parameters Ki, α and K_p is:

(1) Given $\omega_c = 10(\text{rad/s})$, $\phi_m = 60°$.

(2) According to (29), plot curve 1, K_i with respect.to α, and according to (31), plot curve 2, K_i with respect.to α. The two curves are shown in Fig. 4.

(3) From the point of intersection on the above two curves, get the values of K_i and α, K_i=121.4, α=0.341.

(4) Calculate the K_p from (34), K_p=0.355.

After that, the proposed FOPI controller can be given as follow:

$$C(s) = 0.355\left(1+\frac{121.4}{s^{0.341}}\right) \tag{35}$$

if $\alpha > 0$, the fractional controller presents null steady-state error. But in the current study $\alpha \ll$ ($\alpha = 0.341$) which makes the integer controller output converges toward its final faster than the fractional controller. To avoid this issue, the fractional integrator must be implemented as:

$\frac{1}{s^{0.341}} = \frac{1}{s} s^{1-0.341}$, in order to guarantee the impact of the $\frac{1}{s}$ [13].

For the considered plant, fractional order FOPI controller is designed. Fig. 5 show the Bode diagrams of G(s). Obviously the phase is flat at $\omega_c = 10(\text{rad/s})$ and the constraints mentioned above are fulfilled. This signifies that the system is more robust to gain changes. But the constraints are not fulfilled at the same time for classical integer order IOPI controller (K_i=5.81, K_p=17.29) with the same set of the designed method.

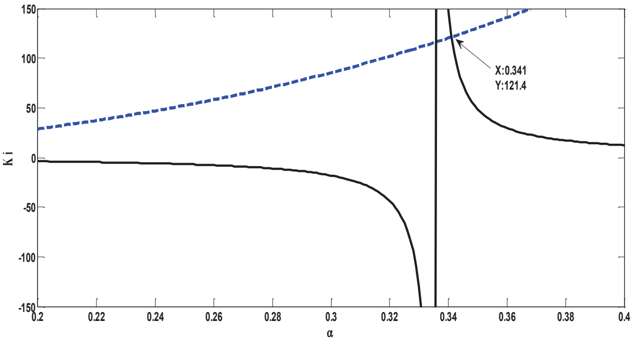

Fig. 4 Finding K_i and α graphically.

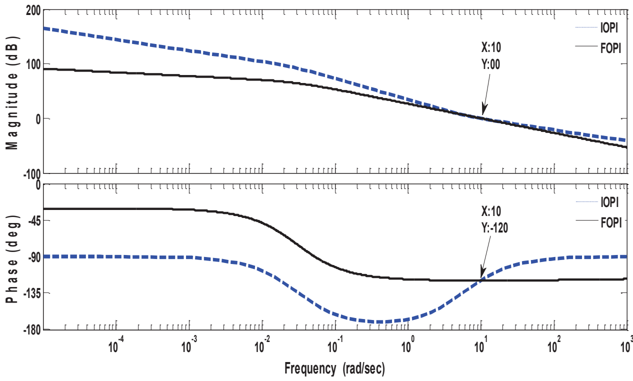

Fig. 5 Bode plot of G(s).

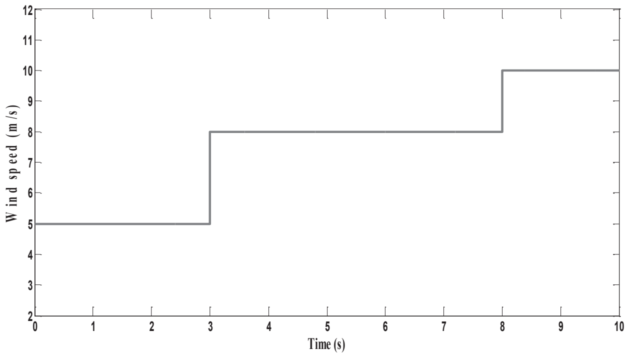

Fig. 6 Wind speed profile.

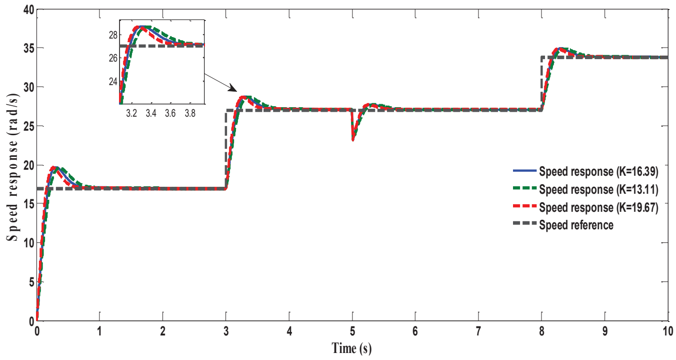

Fig. 7 Speed responses with disturbance utilizing FOPI when considering loop gain variation.

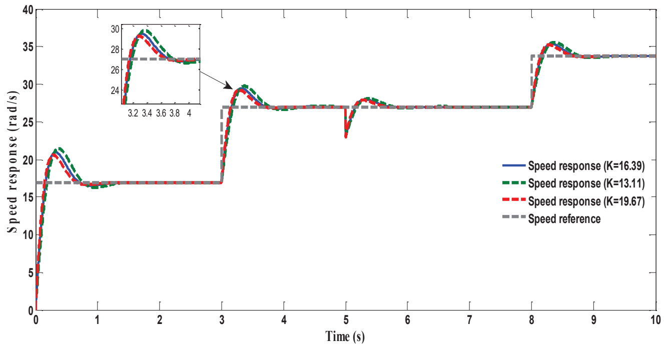

Fig. 8 Speed responses with disturbance utilizing IOPI when considering loop gain variation.

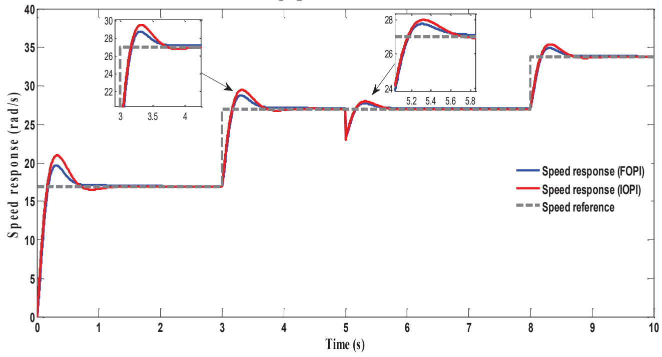

Fig. 9 Speed response and disturbance rejection comparison.

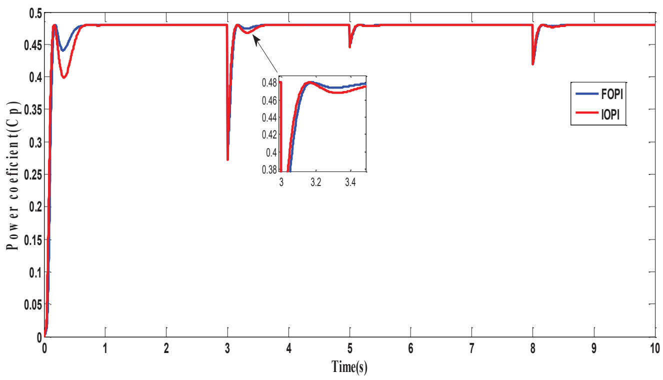

Fig. 10 Power coefficient variation.

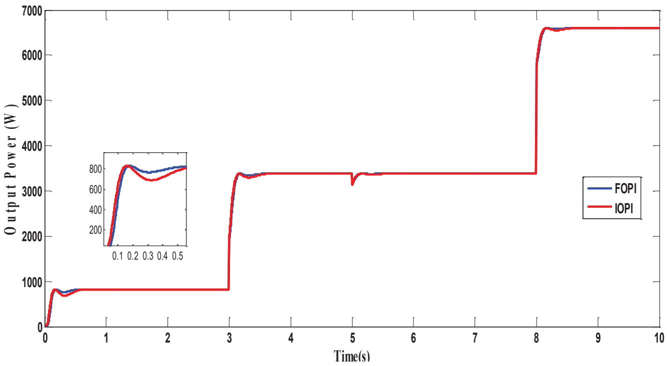

Fig. 11 Output power variation.

IV. Simulation Results

The tuning procedures above for the controller is illustrated and simulated on MATLAB/Simulink.

The parameters used for simulation study are as follows: PMSG and wind turbine: R_s=1.5Ω/ L_d=L_q=0.0058mH/ ψ_f=0.314Wb / J=2N.m/ B=0.061N.m.s/rad / R=2.4m/ ρ=1.52Kg/m^3.

The utilized profile of wind speed is illustrated in Fig. 6.

Fig. 7 shows the plotted speed responses with disturbance utilizing the FOPI controller, the plant gain K varying from 13.11 to 19.67(±20% changes from the chosen value 16.39). The disturbance is chosen to be a step of amplitude -4 at t=5s. In Fig. 8 utilizing the classical IOPI controller, the responses of speed and disturbance are plotted with the plant gain K varying from 13.11 to 19.67(±20% changes from the chosen value 16.39).

From Figs. 7 and 8, the designed factional order FOPI controller work effectively in this paper. The overshoots of the speed and disturbance responses under gain changes remain almost constant, i.e. the iso-damping property is displayed while, with the classical integer order IOPI controller, the overshoots are variable, which means the system using the fractional FOPI controller is more robust than the classical IOPI controller to loop gain variations.

Obviously from Fig. 9, the overshoot of the speed response and disturbance with the proposed factional order FOPI controller is smaller than that of the speed response and disturbance with the classical integer order IOPI controller. Fig.10 and 11 give power coefficient and output power responses respectively. The IAE performance indexes are 5.406 and 5.758 for the FOPI and IOPI respectively. Thus, we can see that the factional FOPI controller surpass the classical integer IOPI controller.

V. Conclusion

In this paper, a fractional FOPI controller with a simple and practical design method is proposed to regulate the generator speed. The fairness issue in comparing with the classical integer order proportional integral IOPI controller has been handled under the same number of parameters design and tuning constraints. From the simulation results, the designed fractional FOPI controller can enhance the control performance for the closed-loop wind turbine system and attain convenient dynamic performance and robustness when compared with the classical IOPI controller.

Acknowledgment

Frikh Mohamed Lamine would like to thank the Badji Mokhtar University of Algeria for the support.

References

[1] S. Li, T. A. Haskew, R. P. Swatloski, and W. Gathings, “Optimal and direct-current vector control of direct-driven PMSG wind turbines,” *IEEE Trans. Power Electron.*, vol. 27, no. 5, pp. 2335–2337, 2012.

[2] R. I. Putri, M. Pujiantara, A. Priyadi, T. Ise, and M. H. Purnomo, “Maximum power extraction improvement using sensorless controller based on adaptive perturb and observe algorithm for PMSG wind turbine application,” *IET Electr. Power Appl.*, vol. 12, no. 4, pp. 455–462, 2018.

[3] N. Fazli and J. Siahbalaee, “Direct torque control of a wind energy conversion system with permanent magnet synchronous generator and matrix converter,” *8th Power Electron. Drive Syst. Technol. Conf. PEDSTC 2017*, no. Pedstc, pp. 166–171, 2017.

[4] I. Yazici and E. K. Yaylaci, “Maximum power point tracking for the permanent magnet synchronous generator-based WECS by using the discrete-time integral sliding mode controller with a chattering-free reaching law,” *IET Power Electron.*, vol. 10, no. 13, pp. 1751–1758, 2017.

[5] J. Zaragoza, C. S. Staines, A. Arias, J. Pou, E. Robles, and S. Ceballos, “Comparison of speed control strategies for maximum power tracking in a wind energy conversion system,” *Proc. Mediterr. Electrotech. Conf. - MELECON*, pp. 961–966, 2010.

[6] S. Ghasemi, A. Tabesh, and J. Askari-Marnani, “Application of Fractional Calculus Theory to Robust Controller Design for Wind Turbine Generators,” *IEEE Trans. Energy Convers.*, vol. 29, no. 3, pp. 780–787, Sep. 2014.

[7] S. Ebrahimkhani, “Robust fractional order sliding mode control of doubly-fed induction generator (DFIG)-based wind turbines,” *ISA Trans.*, vol. 63, pp. 343–354, 2016.

[8] S. Li and J. Li, “Output Predictor-Based Active Disturbance Rejection Control for a Wind Energy Conversion System with PMSG,” *IEEE Access*, vol. 5, no. c, pp. 5205–5214, 2017.

[9] P. Gajewski and K. Pieńkowski, “Advanced control of direct-driven PMSG generator in wind turbine system,” *Arch. Electr. Eng.*, vol. 65, no. 4, pp. 643–656, 2016.

[10] Y. Tang, X. Zhang, D. Zhang, G. Zhao, and X. Guan, “Fractional order sliding mode controller design for antilock braking systems,” *Neurocomputing*, vol. 111, pp. 122–130, 2013.

[11] I. Attoui and A. Omeiri, “Modeling, control and fault diagnosis of an isolated wind energy conversion system with a self-excited induction generator subject to electrical faults,” *Energy Convers. Manag.*, vol. 82, pp. 11–26, Jun. 2014.

[12] A. Oustaloup, F. Levron, B. Mathieu, and F. M. Nanot, “Frequency-band complex noninteger differentiator: Characterization and synthesis,” *IEEE Trans. Circuits Syst. I Fundam. Theory Appl.*, vol. 47, no. 1, pp. 25–39, 2000.

[13] C. A. Monje, A. J. Calderon, B. M. Vinagre, Y. Chen, and V. Feliu, “On fractional PI λ controllers: Some tuning rules for robustness to plant uncertainties,” *Nonlinear Dyn.*, vol. 38, no. 1–4, pp. 369–381, 2004.

Neural Input Output Linearization Control of DFIG based Wind Turbine

Mendaz kheira
Department electrical engineering,
faculty of science and technology
University Ain Temouchent
IRECOM laboratory Sidi Bel Abbes,
Algeria
kheira.mendaz@univ-temouchent.edu.dz

Benhadda Yamina
Department of electrical engineering,
Mohamed Boudiaf University,
Oran
Algeria
benhadda_yamina@yahoo.fr

Flitti Mohamed
Department electrical engineering,
faculty of science and technology
University Ain Temouchent
ICEPS laboratory Sidi Bel Abbes,
Algeria
mohamed.flitti@univ-temouchent.edu.dz

***Abstract*— this paper presents dynamic modeling and control of Doubly Fed Induction Generator (DFIG) based on wind turbine systems, where the stator of DFIG is directly connected to the grid and a PWM inverter fed the rotor. The stator active and reactive powers control of the DFIG is based on the combination of intelligent technique and nonlinear control presented by Neural Input Output linearization active and reactive power control of DFIG. Numerical simulations using MATLAB-SIMULINK shown clearly the robustness of the proposed control.**

Keywords—DFIG, IOLC, robustness, nonlinear control.

I. INTRODUCTION

Wind turbines are heavily used due to their variable speed characteristics and thus influence on system dynamics. However, the imbalance of wind energy greatly affects the energy conversion, and this problem can be overcome by using a doubly-fed induction generator (DFIG) [1]- [3]. Doubly-fed wound-rotor induction motors with vector control are very attractive for high power variable speed drive and power generation applications. DFIG is used in a variety of wind energy conversion systems. The machine has proven its efficiency due to properties such as robustness, cost and simplicity. It has several advantages, including variable speed operation.

The input-output linearization control is an analytical design approach that aims to reduce the original nonlinear problem to a simpler linear control problem. The nonlinear control system is designed using a two-step procedure.

Firstly, a nonlinear process model synthesizes a nonlinear state feedback controller that linearizes the map between a newly manipulated input and the controlled output. In the second step, a linear pole placement controller is designed for the feedback linearized system

The neural network (ANN) is widely used as a universal approximates in nonlinear mapping and uncertain nonlinear control problems. Artificial neural control is very powerful tool capable of achieving very good results in the control of complex systems. It is preferred to use neural networks (ANN) for control when requirements for precision are high and system is not identified precisely or its parameters are changing [7]-[8].

This article discus about the control of stator active and reactive powers by using combination of tow control wish are intelligent control (artificial neural network) used for controlling active and reactive power and Input Output linearization controller used for controlling the rotor current of DFIG connected directly to the grid by the stator side and fed by PWM inverter.

II. MODELING OF THE WIND TURBINE

The aerodynamic power P_{tur} captured by the wind turbine is given by [1] – [5]:

$$P_{tur} = 12\ C_p(\lambda,\beta)\ \rho\ \ S\, v^3 \tag{1}$$

Where: ρ is the air density ($1.25\ kg/m^3$); S is wind turbine blades swept area in the wind (m^2) ; R is the turbine radius (m) ; v is wind speed(m/s) ; β blade pitch angle (°) and λ is the tip-speed ratio defined by :

$$\lambda = \frac{\Omega_{tur}\, R}{v} \tag{2}$$

C_p is the power coefficient of wind is treated in bibliographies for a wind of 4KW [3]- [4] by:

$$C_p(\lambda,\beta) = \big(0.5 - 0.0167\ (\beta - 2)\big)\sin\left[\frac{\pi.(\lambda+0.1)}{10-0.3.\beta}\right] - 0.00184.(\lambda-3).(\beta-2). \tag{3}$$

The characteristics of the wind will determine the amount of energy that can actually be extracted from the wind farm [1].

The wind speed will be modeled in deterministic form by a sum of several harmonics:

$$V_v = 8 + 0.2\, sin(0.1047\ t) + 2\, sin(0.2665\, t) + 0.2\, sin(3.6645\, t). \quad (4)$$

Expression of the aerodynamic torque is given by [2]:

$$\mathrm{T_{tur}} = \mathrm{P_{tur}}\, \Omega_{\mathrm{tur}} = \frac{\pi}{2\,\lambda}\, \rho\, R^3\, Cp(\lambda, \beta). \quad (5)$$

The gearbox is the connection between the turbine and the generator modeled by [5]-[6]:

$$\mathrm{T_{mec}} = \mathrm{T_{tur}} G. \quad (6)$$

$$\Omega_{\mathrm{mec}} = G\, \Omega_{\mathrm{tur}}. \quad (7)$$

Where: $\mathrm{T_{mec}}$ is mechanical torque, Ω_{tur}, Ω_{mec} are the turbine and generator speed, and G is the gearbox ratio.
The equation of system dynamics, can be written as [5]:

$$J\frac{d\Omega_{\mathrm{mec}}}{dt} + f\, \Omega_{\mathrm{mec}} = \mathrm{T_{mec}} - \mathrm{T_{em}}. \quad (8)$$

Where: f is the viscous friction coefficient, $\mathrm{T_{em}}$ is the electromagnetic torque of the generator.
$C_p(\lambda, \beta)$ illustrated in Figure. 1, in our case $C_p opt = 0.48$ is obtained for $\beta = 0$ and $\lambda = \lambda_{opt} = 8$.

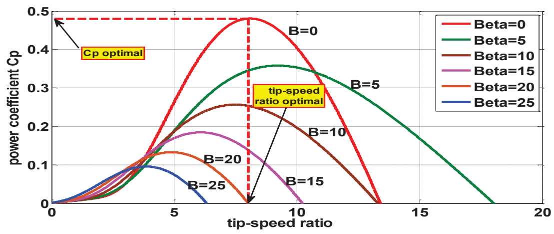

Fig.1 Power Coefficient variation against λ and β.

III. MODELING OF DOUBLY FED INDUCTION GENERATOR

We present in preferred way the dynamics electrical model of the DFIG-generator in a synchronous reference frame (d, q) rotating at an angular speed of ω_s . The basic equations used to model the DFIG generators in the rotating d–q reference frame are written as: [4]- [5].

$$\begin{cases} \mathrm{V_{sd}} = \mathrm{R_s}\, \mathrm{I_{sd}} + \frac{d\varphi_{sd}}{dt} - \omega_s\varphi_{sq} \\ \mathrm{V_{sq}} = \mathrm{R_s}\, \mathrm{I_{sq}} + \frac{d\varphi_{sq}}{dt} + \omega_s\varphi_{sd} \\ \mathrm{V_{rd}} = \mathrm{R_r}\, \mathrm{I_{rd}} + \frac{d\varphi_{rd}}{dt} - (\omega_s - \omega_r)\varphi_{rq} \\ \mathrm{V_{rq}} = \mathrm{R_r}\, \mathrm{I_{rq}} + \frac{d\varphi_{rq}}{dt} + (\omega_s - \omega_r)\varphi_{rd} \end{cases}. \quad (9)$$

The stator and rotor flux are expressed by [4]-[5]:

$$\begin{cases} \varphi_{sd} = \mathrm{L_s}\, \mathrm{I_{sd}} + \mathrm{M}\, \mathrm{I_{rd}} \\ \varphi_{sq} = \mathrm{L_s}\, \mathrm{I_{sq}} + \mathrm{M}\, \mathrm{I_{rq}} \\ \varphi_{rd} = \mathrm{L_r}\, \mathrm{I_{rd}} + \mathrm{M}\, \mathrm{I_{sd}} \\ \varphi_{rq} = \mathrm{L_r}\, \mathrm{I_{rq}} + \mathrm{M}\, \mathrm{I_{sq}} \end{cases}. \quad (10)$$

Where: $\mathrm{R_s}$, $\mathrm{R_r}$, L_s and L_r are respectively the resistance and inductance of the stator and the rotor ; M is the mutual inductance, $\mathrm{I_{sd}}$, $\mathrm{I_{sq}}$, $\mathrm{I_{rd}}$, $\mathrm{I_{rq}}$ represent the d and q components of the stator and rotor currents ; ω_s is the stator angular frequency ($\omega_r = \omega_s - P\, \Omega_{mec}$); ω_r is rotor angular frequency, and P number of pole pairs.

Equation (11) represents the expression of electromagnetic torque [2]-[4]:

$$\mathrm{T_{em}} = \mathrm{P}\frac{\mathrm{M}}{\mathrm{L_s}}(\varphi_{sd}\, \mathrm{I_{rq}} - \varphi_{sq}\, \mathrm{I_{sd}}). \quad (11)$$

Expression of active and reactive power:

$$\begin{cases} P_s = \mathrm{V_{sd}}\ \mathrm{I_{sd}} + \mathrm{V_{sq}}\ \mathrm{I_{sq}} \\ Q_s = \mathrm{V_{sq}}\ \mathrm{I_{sq}} - \mathrm{V_{sd}}\ \mathrm{I_{sd}} \end{cases}. \quad (12)$$

$$\begin{cases} P_r = \mathrm{V_{rd}}\ \mathrm{I_{rd}} + \mathrm{V_{rq}}\ \mathrm{I_{rq}} \\ Q_r = \mathrm{V_{rq}}\ \mathrm{I_{rq}} - \mathrm{V_{rd}}\ \mathrm{I_{rd}} \end{cases}. \quad (13)$$

Expression of stator active and reactive power:

$$\begin{cases} P_s = \mathrm{V_{sd}}(\frac{\varphi_{rd} - L_r\, I_{rd}}{L_m}) + \mathrm{V_{sq}}(\frac{\varphi_{rq} - L_r\, I_{rq}}{L_m}) \\ Q_s = \mathrm{V_{sq}}(\frac{\varphi_{rq} - L_r\, I_{rq}}{L_m}) - \mathrm{V_{sd}}\ (\frac{\varphi_{rd} - L_r\, I_{rd}}{L_m}) \end{cases}. \quad (14)$$

$$\begin{cases} P_s = \mathrm{V_{sd}}\frac{\varphi_{rd}}{L_m} - V_{sd}\frac{L_r\, I_{rd}}{L_m} + \mathrm{V_{sq}}\frac{\varphi_{rq}}{L_m} - V_{sq}\frac{L_r\, I_{rq}}{L_m} \\ Q_s = \mathrm{V_{sq}}\frac{\varphi_{rq}}{L_m} - V_{sq}\frac{L_r\, I_{rq}}{L_m} - \mathrm{V_{sd}}\frac{\varphi_{rd}}{L_m} + V_{sd}\frac{L_r\, I_{rd}}{L_m} \end{cases}. \quad (15)$$

IV. INPUT OUTPUT LINEARIZATION CONTROL (IOLC)

The model of DFIG according to the rotor components is represented by the following equations [6].

$$\begin{cases} \frac{dI_{rd}}{dt} = -a_1\, \mathrm{I_{rd}} + \omega_s \mathrm{I_{rq}} + a_2\varphi_{rd} - a_3\omega_r\varphi_{rq} + a_4\mathrm{V_{sd}} + a_3 V_{rd} \\ \frac{dI_{rq}}{dt} = -\omega_s\, I_{rd} - a_1 I_{rq} + a_2\varphi_{rd} - a_3\omega_r\varphi_{rq} + a_4 V_{sq} + a_3 V_{rq} \\ \frac{d\varphi_{rd}}{dt} = -\mathrm{R_r}\, \mathrm{I_{rd}} + (\omega_s - \omega_r)\varphi_{rq} + V_{rd} \\ \frac{d\varphi_{rq}}{dt} = -\mathrm{R_r}\, \mathrm{I_{rq}} - (\omega_s - \omega_r)\varphi_{rd} + V_{rq} \end{cases} \quad (16)$$

Where

$$\begin{cases} a_1 = \left(\frac{1}{\sigma\, T_r} + \frac{1}{\sigma\, T_s}\right),\ a_2 = \frac{1}{\sigma\, T_s L_r},\ a_3 = \frac{1}{\sigma\, L_r},\ a_4 = \frac{1-\sigma}{\sigma\, L_m} \\ \sigma = 1 - \frac{L_m^2}{L_s\, L_r},\ T_r = \frac{R_r}{L_r},\ T_s = \frac{R_s}{L_s} \end{cases}.$$

σ is the dispersion coefficient.
The electromechanical dynamic equation is given by:

$$\frac{d\omega_r}{dt} = \frac{P^2}{J}\left(\varphi_{rq} I_{rd} - \varphi_{rd} I_{rq}\right) + \frac{P}{J}\left(C_{vis} + C_G\right) \quad (15)$$

Where P is the number of pole pairs ; J is the inertia of the shaft, C_G is the torque on the generator .All frictions on this shaft are included in C_{vis}.
We put :
$(\mathrm{I_{rd}}, I_{rq}, \varphi_{rd}, \varphi_{rq}, \omega_r) = (x_1, x_2, x_3, x_4, x_5)$
The system is written in the form :

$$\frac{dx}{dt} = f(x) + g(x)\, U \quad (16)$$

Where :

$$f(x) = \begin{cases} \frac{dx_1}{dt} = f_1(x) + a_3 V_{rd} \\ \frac{dx_2}{dt} = f_2(x) + a_3 V_{rq} \\ \frac{dx_3}{dt} = f_3(x) + V_{rd} \\ \frac{dx_4}{dt} = f_4(x) + V_{rq} \\ \frac{dx_5}{dt} = f_5(x) \end{cases} \quad (17)$$

$$U = [V_{rd} \quad V_{rq}]^T;\ g(x) = \begin{bmatrix} a_3 & 0 & 1 & 0 & 0 \\ 0 & a_3 & 0 & 1 & 0 \end{bmatrix}^T \quad (18)$$

The choice of outputs is according to the objectives of control. The active power is chosen as the first output while the reactive power is chosen as the second output.

$$\mathbf{y}(x) = \begin{bmatrix} h_1(x) \\ h_2(x) \end{bmatrix} = \begin{bmatrix} I_{rd} \\ I_{rq} \end{bmatrix}. \quad (19)$$

The time derivative of the system output $h_1(x)$ can be expressed as:

$$y_1 = h_1(x) = I_{rd} \quad (20)$$

$$\frac{\mathbf{dy_1}}{\mathbf{dt}} = \frac{\mathbf{dh_1(x)}}{\mathbf{dt}} = \frac{\mathbf{d}\boldsymbol{I_{rd}}}{\mathbf{dt}} \quad (21)$$

$$\frac{dI_{rd}}{dt} = L_f h_1(x) + L_{g1} h_1(x) V_{rd} + L_{g2} h_1(x) V_{rq} \quad (22)$$

$$\frac{dI_{rd}}{dt} = \frac{\boldsymbol{dI_{rd}}}{\boldsymbol{dt}} = -a_1 I_{rd} + \omega_s I_{rq} + a_2 \varphi_{rd} - a_3 \omega_r \varphi_{rq} + a_4 V_{sd} + a_3 V_{rd} \quad (23)$$

The degree of $h_1(x)$ is $r_1 = 1$.

The time derivative of the system output $h_2(x)$ can be expressed as:

$$y_2 = h_2(x) = I_{rq} \quad (24)$$

$$\frac{dy_2}{dt} = L_f h_1(x) + L_{g1} h_1(x) V_{rd} + L_{g2} h_1(x) V_{rq} \quad (25)$$

$$\frac{dy_2}{dt} = -\omega_s I_{rd} - a_1 I_{rq} + a_2 \varphi_{rd} - a_3 \omega_r \varphi_{rq} + a_4 V_{sq} + a_3 V_{rq} \quad (26)$$

The degree of $h_2(x)$ is $r_2 = 1$.

The global relative degree is lower than the order n of the system $r = r_1 + r_2 = 2 < n < 4$.

The relation between the input (V_{rd}, V_{rq}) and the output (y_1, y_2) is given by equation (27):

$$\begin{bmatrix} \frac{dy_1}{dt} \\ \frac{\mathbf{dy_2}}{dt} \end{bmatrix} = A(x) + D(x) \begin{bmatrix} V_{rd} \\ V_{rq} \end{bmatrix}. \quad (27)$$

$$A(x) = \begin{bmatrix} L_f h_1(x) \\ L_f h_2(x) \end{bmatrix}. \quad (28)$$

$$L_f h_1(x) = -a_1 I_{rd} + \omega_s I_{rq} + a_2 \varphi_{rd} - a_3 \omega_r \varphi_{rq} + a_4 V_{sd} \quad (29)$$

$$L_f h_2(x) = -\omega_s I_{rd} - a_1 I_{rq} + a_2 \varphi_{rd} - a_3 \omega_r \varphi_{rq} + a_4 V_{sq} \quad (30)$$

$$D(x) = \begin{bmatrix} L_{g1} L_f h_1 & L_{g2} L_f h_1 \\ L_{g1} L_f h_2 & L_{g2} L_f h_2 \end{bmatrix}. \quad (31)$$

$$D(x) = \begin{bmatrix} a_3 & 1 \\ 1 & a_3 \end{bmatrix}. \quad (32)$$

The nonlinear feedback provide to the system a linear comportment input/output:

$$\begin{bmatrix} \frac{dy_1}{dt} \\ \frac{dy_2}{dt} \end{bmatrix} = \begin{bmatrix} V_1 \\ V_2 \end{bmatrix}. \quad (33)$$

$$\begin{bmatrix} V_{rd} \\ V_{rq} \end{bmatrix} = D^{-1}(x) \begin{bmatrix} V_1 - L_f h_1(x) \\ V_2 - L_f h_2(x) \end{bmatrix}. \quad (34)$$

The internal inputs (V_1, V_2) are definite: [7]-[8]

$$V_1 = \frac{dh_1(x)}{dt} = \frac{\boldsymbol{dI_{rd}}}{\boldsymbol{dt}} \quad (35)$$

$$V_2 = \frac{dh_2(x)}{dt} = \frac{\boldsymbol{d\,I_{rq}}}{\boldsymbol{dt}} \quad (36)$$

$$V_1 = \frac{de_1}{dt} + K_1 e_1 \quad (37)$$

$$V_2 = \frac{de_2}{dt} + K_2 e. \quad (38)$$

The error of the track is given by flowing equation:

$$\frac{de_1}{dt} + K_1 e_1 = 0 \quad (39)$$

$$\frac{de_2}{dt} + K_2 e = 0 \quad (40)$$

$$e_1 = \boldsymbol{I_{rd_{ref}}} - \boldsymbol{I_{rd}} \quad (41)$$

$$e_2 = Q\, I_{rq_{ref}} - I_{rq} \quad (42)$$

$$\begin{bmatrix} V_{rd} \\ V_{rq} \end{bmatrix} = D^{-1}(x) \begin{bmatrix} \left(\frac{\boldsymbol{dI_{rdref}}}{dt} - \frac{\boldsymbol{dI_{rd}}}{dt}\right) + K_1 (\boldsymbol{I_{rdref}} - \boldsymbol{I_{rd}}) - L_f h_1(x) \\ \left(\frac{\boldsymbol{d\,I_{rqref}}}{dt} - \frac{\boldsymbol{d\,I_{rq}}}{dt}\right) + K_2 (\boldsymbol{I_{rqref}} - \boldsymbol{I_{rq}}) - L_f h_2(x) \end{bmatrix} \quad (43)$$

Where:

The coefficients K_1, K_2 are choosing to satisfy asymptotic stability and excellent tracking [6].

$$\left(\frac{\boldsymbol{dI_{rdref}}}{dt} - \frac{\boldsymbol{dI_{rd}}}{dt}\right) + K_1 (\boldsymbol{I_{rdref}} - \boldsymbol{I_{rd}}) = 0 \quad (44)$$

$$\left(\frac{\boldsymbol{d\,I_{rqref}}}{dt} - \frac{\boldsymbol{d\,I_{rq}}}{dt}\right) + K_2 (\boldsymbol{I_{rqref}} - \boldsymbol{I_{rq}}) = 0 \quad (45)$$

Where:

$$\frac{\boldsymbol{dI_{rdref}}}{dt} = 0, \frac{\boldsymbol{d\,I_{rqref}}}{dt} = 0$$

$$\frac{\boldsymbol{dI_{rd}}}{dt} + K_1 \boldsymbol{I_{rd}} = K_1 \boldsymbol{I_{rdref}} \quad (46)$$

$$\frac{\boldsymbol{d\,I_{rq}}}{dt} + K_2\ \boldsymbol{I_{rq}} = K_2\ \boldsymbol{I_{rqref}} \quad (47)$$

From equation (49) and equation (50) the current and flux transfer function given by flowing equation:

$$\frac{\boldsymbol{I_{rd}}}{\boldsymbol{I_{rdref}}} = \frac{1}{1 + \frac{1}{K_1} p} \quad (51)$$

$$\frac{\boldsymbol{I_{rq}}}{\boldsymbol{I_{rqref}}} = \frac{1}{1 + \frac{1}{K_2} p} \quad (52)$$

In closed loops, the current transfer functions have first-order dynamics

$$FT_1 = \frac{K}{1+T\,p} \tag{53}$$

From equation (51) and equation (53) and with identification:

$$T = \frac{1}{K_1} \Rightarrow K_1 = \frac{1}{T} = \frac{3}{T_r} \tag{54}$$

With: $T_r = 3\,T(\pm 5\%)$

Where: T_r : response time, T: time constant

$$T_r = \frac{1}{\varepsilon\,\omega_{n1}} \tag{55}$$

$$T = \frac{T_r}{3} = \frac{1}{3\varepsilon\,\omega_{n1}} \tag{56}$$

$$K_1 = 3\varepsilon\,\omega_{n1} \tag{57}$$

With: $\omega_{n1} = 50[\frac{rd}{s}]$

From equation (52) and equation (53) and with identification:

$$T = \frac{1}{K_2} \Rightarrow K_2 = \frac{1}{T} = \frac{3}{T_r} \tag{54}$$

With: $T_r = 3\,T(\pm 5\%)$

Where: T_r : response time, T: time constant

$$T_r = \frac{1}{\varepsilon\,\omega_{n2}} \tag{55}$$

$$T = \frac{T_r}{3} = \frac{1}{3\varepsilon\,\omega_{n2}} \tag{56}$$

$$K_2 = 3\varepsilon\,\omega_{n2} \tag{57}$$

With: $\omega_{n2} = 60[\frac{rd}{s}]$

V. ARTIFICIAL NEURAL NETWORK ACTIVE AND REACTIVE POWER CONTROLLER

The Artificial Neural Network (ANN) is widely used in many fields of technology application and scientific research. This technique can be used in cases of difficult problems that cannot be describe by precise mathematical approaches where they are very complicated to manipulated [7]-[8].

The architecture of Neural Network, It is a network with two layers : layer1 is the hidden layer and layer2 is output layer. that the Artificial Neural Networks are a Multilayer Perceptron networks (MLP) with a structure of (2-5-1), The inputs are the measured and reference active and reactive power (P_s, Q_s and P_{sref}, Q_{sref}) and the outpout is the courant I_{rd} and I_{rq} .

The Fig1 shows the combination between tow control wish are inputs output linearization control and neural network for the given system, inputs output linearization control is used to regulate the current I_{rd} and I_{rq} ; we should have two outputs (V_{rd}, V_{rq}) for input-output decoupling. Concerning the neural network is used to control active power P_s and reactive power Q_s.

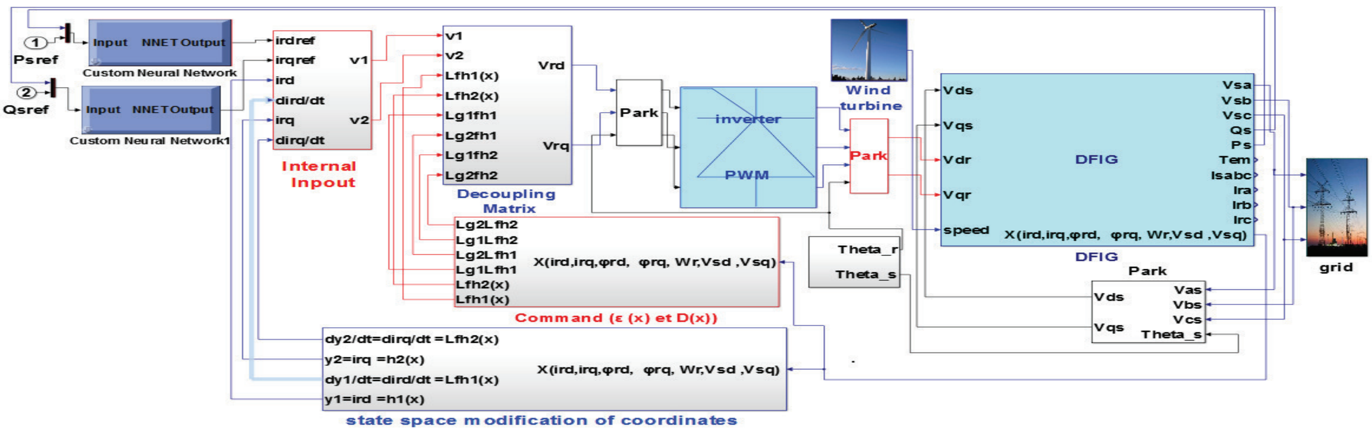

Fig.1 Neural Input Output linearization stotor active and reactive power controller of DFIG.

VI. RESULT AND DISCUSE

The simulation study has been carried out using MATLAB environment. The simulation results show the application of Neural Input Output linearization stator active reactive power control of the DFIG.

According to the simulation results shown in Fig. 2, the NIOLC shows that the amplitudes of the ripples of the stator active power are smaller and occur in a shorter period in comparison with the ripples obtained for the Input Output linearization stator active reactive power command (IOLC).

The proposed NIOLC control ensures the best optimal power tracking performance and the reduction of ripple of stator active power compared IOLC.

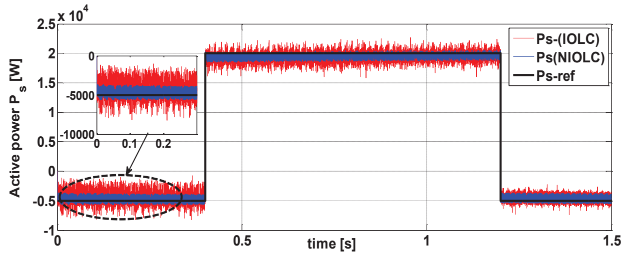

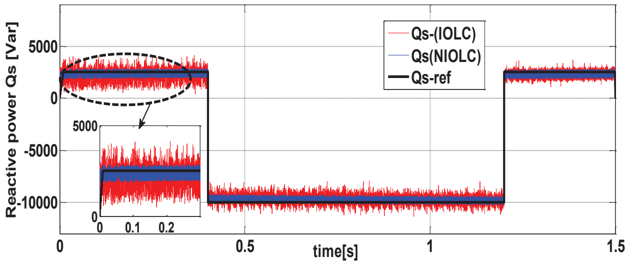

Fig.2 Stator active and reactive power of DFIG responses.

The Fig.3 shows the rotor currents generated by the wind turbine-doubly fed induction generator system with application of Neural Input Output linearization stator active and rective power contoller (NIOLC) and Input Output linearization stator active and rective power contoller (IOLC) . We can observe that the phase rotor currents given by NIOLC have almost sinusoidal shape compared to IOLC.

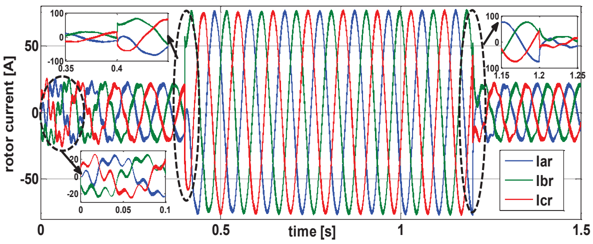

(a) NIOLC

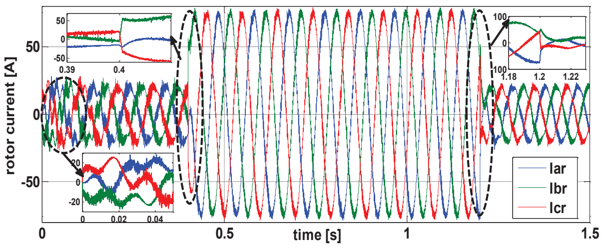

(b) IOLC

Fig.4 Rotor current of DFIG response of NIOLC and IOLC.

In Fig.5 we can observe the phase stator currents have almost sinusoidal shape with application Neural Input Output linearization stator active and rective power contoller compared to Input output linearization controller. We can see in this figure the pssage between operating modes, which are zoomed in this figure indicating 50 Hz frequency.

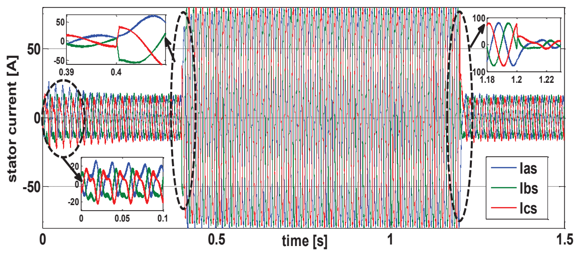

(a) NIOLC

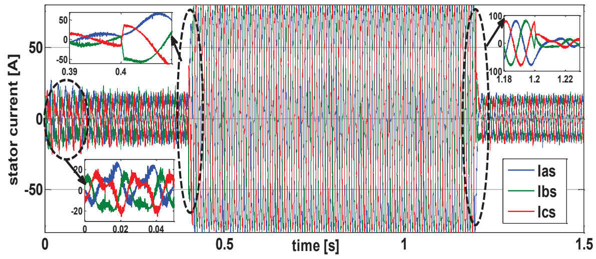

(b) IOLC

Fig.5 Stator current of DFIG response of NIOLC and IOLC.

VII. CONCLUSION

The aim of this paper is to study a system which converts wind energy into electrical energy. In this paper, we represented the use of Input Output linearization command to control the stator active and reactive power of the DFIG injected in the grid.

This study show the performance given by Neural Input Output Linearization used to control the stator active and reactive power of the DFIG; we can see this performance in the respect of the stator active and reactive power of the change of their reference and the passage between operating modes observed in current signals.

REFERENCES

[1]. E. Bounadja, A. Djahbar,Z. Boudjema, "Variable structure control of a doubly fed induction generator for wind energy conversion systems", Energy Procedia,vol. 50, N^{0} . 11, pp. 999 – 1007, 2014.

[2]. Y. Ibrahim, S. Abdelhafid, W. Patrice, "Direct Power Control of Wind Turbine Based on Doubly Fed Induction Generator", European Journal of Electrical Engineering, vol. 21, N^{0} . 5, pp. 458–464, 2019.

[3]. B. Saïd, A. Hafedh, E. Ahmed, C.N. Mohamed, "Comparative study of three types of controllers for DFIG in wind energy conversion system", Protection and Control of Modern Power Systems, vol. 3, N^{0} . 21, pp 1-12, 2018.

[4]. S. K. Ghulam, W. Jie, B. Mazhar Hussain, "Active and reactive power control of the doubly fed induction generator based on wind energy conversion system", Energy Reports, vol. 2, pp 194-200, 2016.

[5]. A. N. J. Almakki, A. A. Mazalov, "Improved DFIG DFTC by Using A Fractional-Order Super Twisting Algorithms In Wind Power Application", Modern Transportation Systems and Technologies, vol. 7, N^{0} . 3, pp 1197-1210, 2020.

[6]. Y. Fetene, D. Shibeshi, "Fractional Order Sliding Mode Speed Control of Feedback Linearized Induction Motor", Power Electronics and Drives. 5(41), pp. 109-122, 2020.

[7]. R. Raveendra, V. C. Veera Reddy, J. M. V. CHandra. , "Speed control induction motor drive using artificial neural networks-Levenberg-Marquardt bakpropagation algorithm", International Journal of Applied Engineering Research, vol 13, No 1, pp. 80-85, 2018.

[8]. K. Rahul, G. Prerna, "Neural network applications in electrical drives-trends in control, estimation, diagnostics, and construction", Energies, vol 16, No 11, pp. 1-25, 2023.

The 1st National Conference on Green Energy (NCGE' 2023)
December 02, 2023, Boumerdes, Algeria.

Integrating Photovoltaic Panels into Electric Drive Motors for Environmentally-Friendly Electric Vehicles

FEZAZI Omar
ICEPS Laboratory (Intelligent Control & Electrical Power Systems)
Djillali Liabes University, Sidi Bel-Abbes, Algeria
fezaziomarfz@gmail.com

Ayad Ahmed Nour El Islam
Kasdi merbah university
Ouargla , Algeria
ayadnourislam@yahoo.fr

Abstract— **The transition to clean and renewable energy sources has become a critical focus in addressing the global challenge of reducing greenhouse gas emissions and combating climate change. In this study, the powering of electric vehicles with solar panels integrated into an electric drive motor system is examined. By employing photovoltaic technology to capture solar energy, the aim is to reduce our dependency on fossil fuels and the emissions associated with them. The performance and viability of this integration are examined using simulation techniques with MATLAB SimPower Systems. The behavior of the combined photovoltaic-electric motor system is modeled and analyzed under various operating conditions, evaluating energy efficiency. Results from simulations are used to determine how the photovoltaic panel integration will affect the entire system performance, including power production, efficiency, and electric vehicle range. The potential benefits of integrating photovoltaic panels into electric drive motor systems for reducing greenhouse gas emissions and achieving sustainable transportation are demonstrated through MATLAB SimPower Systems simulation. The study's conclusions boost the use of renewable energy in the transportation industry, advancing efforts to identify cleaner and more sustainable energy sources on a worldwide scale.**

Keywords- Green Energy, Renewable Energy; photovoltaic panel, electric vehicles; Drive system

I. INTRODUCTION

Interest in sustainable transportation options has increased as a result of the pressing need to address environmental issues such as greenhouse gas emissions and climate change [1], [2]. Among these, electric vehicles (EVs) have become a potential technology to decrease emissions, improve air quality, and minimize dependency on fossil fuels. Increasing EV autonomy and maximizing battery power utilization are essential goals in order to make EVs more practical and interesting [3], [4].

This study focuses on the integration of photovoltaic (PV) panels into electric drive motors to develop an efficient drive system that optimizes battery power usage and employs solar energy to charge the battery. The objective is to extend the autonomy of electric vehicles while encouraging the use of sustainable energy sources and reducing the environmental impact [1], [5].

The integration of PV panels into the electric drive motor system represents an innovative approach to extend EV autonomy and reduce dependency on conventional charging methods. By using clean and renewable solar energy, the EV battery can be charged, thereby reducing carbon emissions and promoting sustainable transportation.

The study uses simulation methods with MATLAB SimPower Systems to simulate and analyze the behavior of the combined PV-electric motor system in order to meet these goals. Important factors, including the battery's state of charge, the motor's current and voltage, and the power produced by the solar panels, are assessed under a variety of operating circumstances. These findings shed important light on the possible advantages of PV panel integration and how it affects total EV performance.

Matlab SimPower System is used because it provides a powerful and realistic simulation environment that closely mirrors real-world conditions [6]. This advanced tool proves invaluable for modeling and testing complex systems, making it an ideal choice for analyzing and evaluating the proposed PV-integrated drive system for electric vehicles. This research contributes to the growing knowledge of sustainable transportation, focusing on the importance of optimizing battery usage and utilizing solar energy to drive the EV industry forward. By enhancing EV autonomy through efficient drive systems and renewable energy integration.

II. EV DRIVE SYSTEM

The electrical drive system of electric vehicles (EVs) involves several crucial conversion steps, as shown in Fig 1. It includes two DC/DC converters, along with an AC/DC or DC/DC converter, all of which play vital roles in regulating power flow between the battery and the electric machines [7].

As a direct current (DC) power source, the battery provides current at a particular voltage. Power must be processed through a power converter device in order to guarantee that it is delivered to the battery at the proper voltage. Similar processing is required to ensure that the electric machine obtains the maximum amount of power necessary for effective vehicle propulsion.

An additional DC converter, known as the Maximum Power Point Tracking (MPPT) converter [8], [9], is responsible for integrating solar energy from the PV panels. This converter is connected to the main DC converter in the electrical drive system. It optimizes the power powered by the PV panels by tracking the maximum power point (MPP)[7].

The type of electric equipment in use and the intended maximum power supply are the two main criteria that affect how precisely power converters perform. High-power, quick-acting semiconductor components serve as high-speed switches in these converters. Different switching states change the input voltage and current through capacitive and inductive components, producing an output voltage and current that differs from the input voltage and current.

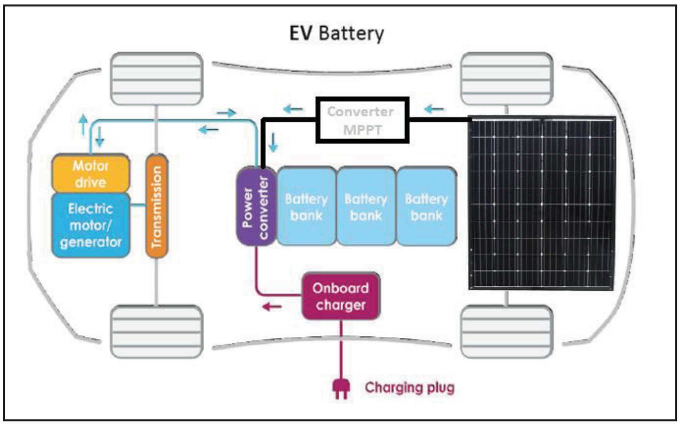

Figure 1. EV drive system [3], [10]

III. Power Electronics Component Layout In A Battery Electric Vehicle (BEV)

Fig 2 [3], [10] resume the typical configuration of power electronics components in a Battery Electric Vehicle (BEV). A DC/DC auxiliary converter provides power for the vehicle's internal equipment, typically at 12V for current vehicles, but possibly can reach 48V for future vehicles. A DC motor is chosen for this application to propel the BEV, and the mechanical transmission often relies on fixed gearing and a differential. However, various BEV configurations are possible, depending on cost and performance constraints [5]

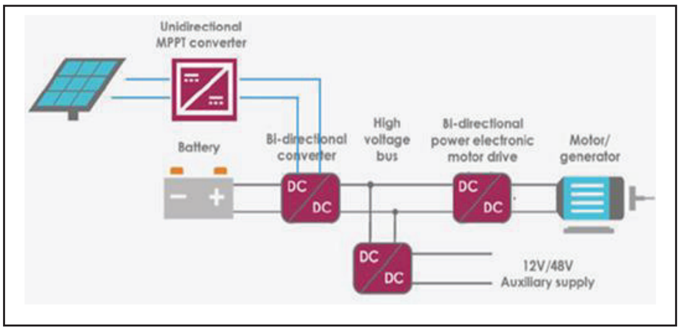

Figure 2. Power electronics component layout in a battery electric vehicle (BEV)

The MPPT converter uses a 130-watt photovoltaic (PV) power supply and runs at 17/48V in the boost converter mode. Most EVs use a step-up (boost converter) and a step-down (buck converter) as part of their power processing DC/DC converter. This is due to the fact that the battery voltage is often lower than the high-voltage bus voltage. The converter functions in buck (step-down) mode when recovering kinetic energy, bringing the voltage from the high-voltage bus down to a level that is safe for the battery. The converter operates in boost mode when the car is moving, controlling the DC voltage to produce a higher level of voltage for the electric motor [7].

IV. DC Motor Choice

The DC motor (DCM) was chosen for the electric vehicle (EV) drive system due to its ease of use, low cost, and wide application in other electromechanical systems that need to move. Vehicles, industrial tools, and robotic manipulators are just a few of the areas where DC motors are used [11], [12].

One of the main advantages of using DC motors in EVs is their simple structure, making them easy to manufacture and maintain. The straightforward construction contributes to cost-effectiveness, which is crucial for the mass production of electric vehicles and for making them more accessible to consumers [11], [12].

Additionally, shown in Fig 3 the torque and speed of DC motors naturally decouple. This translates into increased control and flexibility when operating the EV because the torque and rotational speed of the motor are relatively independent of one another. Due to the control system's inherent decoupling, it is simpler to regulate and improve the performance of the motor.

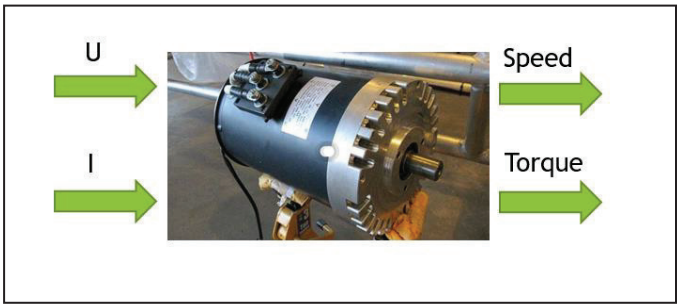

Figure 3. Natural decoupling DC motor characteristic

V. PV Integration Simulation

It is discussed utilizing Matlab simpower system how the PV integration into the driving system is simulated. The electrical properties and dynamic behavior of the system were captured during the initial simulation of the PV-integrated drive system using MATLAB SimPower Systems. The components of the PV panel, battery system, motor, and power electronics were incorporated in the simulation model. Figure 4 represents the first part of the simulation in this part the Drive system for the EV is built, the system consists of a 5 HP, 1750 RPM DC motor powered by a 48 V $(SOC = 80\ \%)$ battery through a Buck-boost chopper (DC-DC converter). The purpose is to observe the behavior of speed, torque, current, and battery charge level [4], [13] Drive system first part EV SimPower Systems Matlab model

Fig 4 illustrates the schematic representation of the first part system, which incorporates a four-quadrant chopper into the existing setup. This integration aims to enhance the performance and control capabilities of the (EV) drive system.

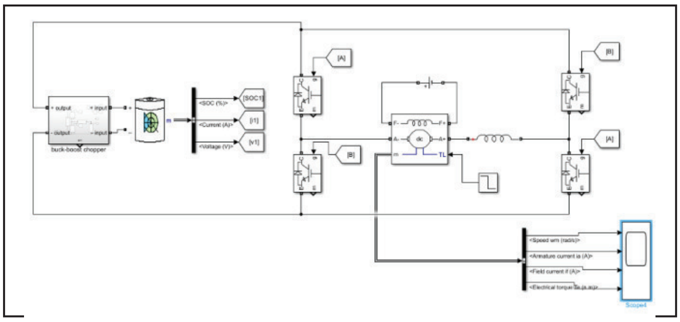

Figure 4. Drive system first part EV SimPower Systems Matlab model

The first chopper is used in the initial step to stabilize the DC bus voltage. This part makes sure that the system receives a consistent and dependable supply of power. The first chopper contributes to the stability and effectiveness of the overall system by controlling the voltage.

The additional element added to the second system, the four-quadrant chopper, takes over management of the voltage needed to drive the motor. It functions throughout the entire voltage-current plane, allowing for bidirectional power flow and regenerative braking. This advanced control capability provides greater flexibility and efficiency in managing the motor's performance and energy consumption.

This method offers superior voltage regulation and increased motor performance by combining the stabilizing function of the first chopper with the precise control of the four-quadrant chopper. The entire effectiveness, dependability, and responsiveness of the EV drive system are enhanced by this integration.

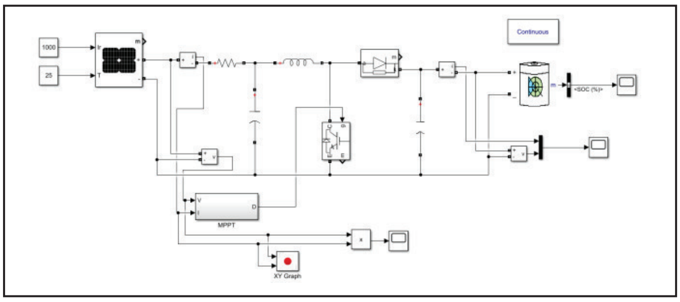

Figure 5. PV Integration SimPower Systems Matlab model

Fig 5 represents the integration of the PV panel into our system. The integration is achieved through a Boost chopper that ensures Maximum Power Point Tracking (MPPT). The PV panel used in the integration has a power rating of 130 W, with an open-circuit voltage (VOC) of 21.7 V and a short-circuit current (ISC) of 8.4 A.

VI. RÉSULTATS AND INTERPRÉTATION

Based on the results of the next simulation Fig 6 that represent the speed response of the second system, several observations can be made. In the time interval 0<t<3s, the motor gradually starts its operation. Initially, it is at rest, and then the acceleration of the motor causes the speed to increase rapidly, reaching 100 rad/s at t=0.2s. The speed remains stable until t=1s, after which it increases rapidly until t=1.2s, and then stabilizes again. At t=2s, the motor's speed increases rapidly until t=2.2s and remains constant until t=3s.

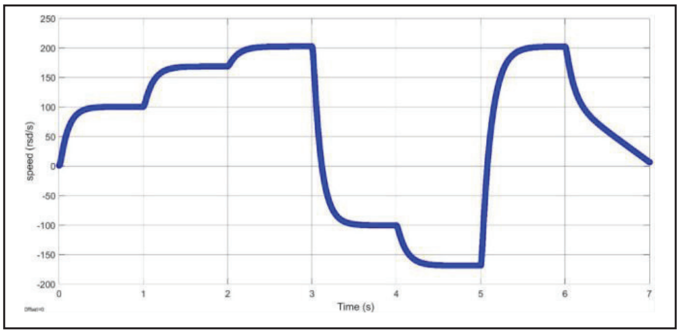

Figure 6. Speed Response (rad/s)

The second phase occurs between 3<t<5s, during which the motor rotates in the opposite direction. The motor's speed becomes negative, reaching -100 rad/s at t=3.3s, and remains constant until t=4s. Between 4s and 4.25s, the speed decreases further, reaching -160 rad/s. From 4.25s to 5s, the motor's speed remains constant at this negative value.The third phase begins, and the motor starts driving again. The acceleration increases between 5s and 5.3s, reaching a value of 200 rad/s. The breaking then remains constant until 6s. Finally, the motor decelerates until it reaches a speed of 5 rad/s at t=7s.

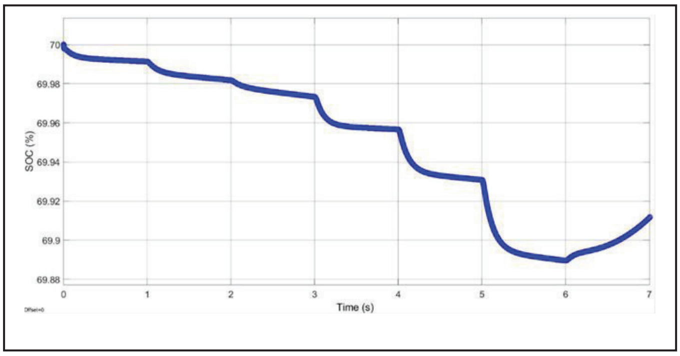

Figure 7. SOC response (%) drive and regenerative modes

Fig 7 represents the SOC response of the second system. During the first phase, which corresponds to the driving phase, the initial battery autonomy is at 70%. At t=0s, the battery level decreases slightly to 69.9%. From t=1s to t=2s, the battery level continues to decrease, reaching 69.98%. Between 2s and 3s, the battery discharge continues, resulting in a level of 69.97%. From 3s to 4s, the battery level decreases further to 69.959%. Between 4s and 5s, the battery level continues to decrease, reaching 69.93%. Finally, between 5s and 6s, the battery level decreases again, reaching 69.89%. In the second phase, corresponding to the braking phase, between 6s and 7s, the battery level starts to increase, reaching 69.91%.

Fig 8 shows the responses of the current and the torque, between t=0 and t=1s, both the current and torque increase rapidly, reaching their maximum values of 10.2A and 10.2N•m, respectively, at t=0.1s. Subsequently, they both decelerate, reaching 0A and 0N•m at t=1s. From 1s to 2s, the current and torque exhibit similar patterns, maintaining their respective values. Between 2s and 3s, they continue to follow the same patterns, but with a decreased maximum value of 7A for the current and 7N•m for the torque.

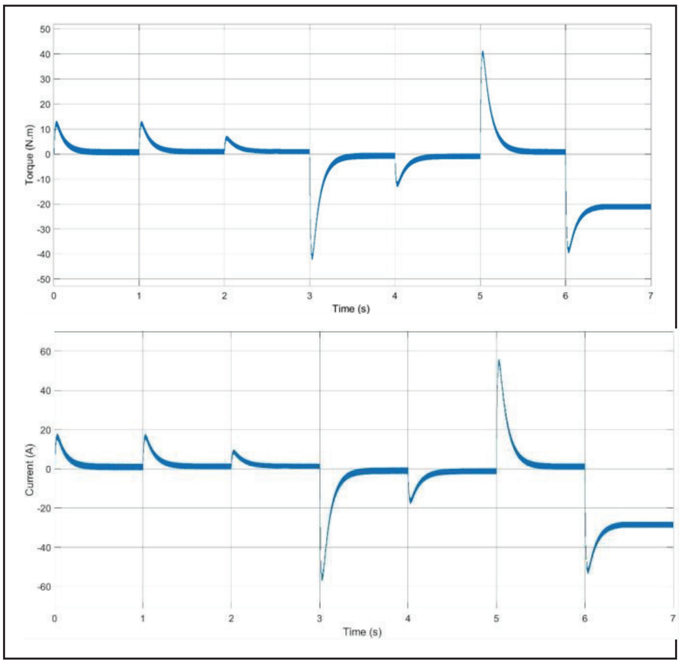

Figure 8. Torque (N.m) and current responses (A)

During the next phase, from 3s to 4s, the current and torque exhibit distinct behaviors. The current rapidly decreases to -41A at t=3.1s, indicating a reverse flow of energy. Similarly, the torque decreases rapidly to -41N•m. Afterward, they both gradually increase, reaching 0A and 0N•m at t=4s,

Between 4s and 5s, the current and torque repeat their previous patterns, but with an increased minimum value of -11A for the current and -11N•m for the torque. Between 5s and 6s, both the current and torque increase, reaching their respective maximum values of 41A and 41N•m at t=5.1s. They then decrease, returning to 0A and 0N•m at t=6s. Finally, from 6s to 7s, the current and torque exhibit a similar pattern as in the previous phase, with the current decreasing to -39A at t=6.1s and the torque decreasing to -39N•m. They both subsequently increase to -20A and -20N•m at t=7s.

During the time interval between 0 and 3s, both the current and torque are positive, indicating the driving phase where energy flows from the battery to the motor. From 3s to 5s, both the current and torque become negative, representing the regenerative braking phase, where energy is returned from the motor back to the battery. Between 5s and 6s, both the current and torque return to being positive, indicating the driving phase once again. Finally, from 6s to 7s, both the current and torque are negative, signifying the regenerative braking phase.

Fig 9 illustrates the characteristics of the I-V output curve of the solar panel. From the graph, it can be observed that the solar panel operates more efficiently around the maximum power point (Vmp and Imp). By operating at this point, the solar panel can achieve maximum power generation and optimize its performance.

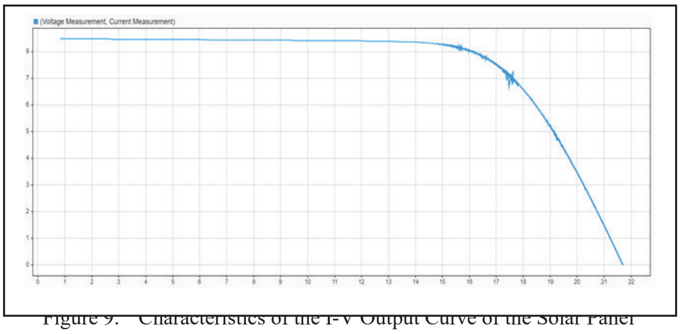

Figure 9. Characteristics of the I-V Output Curve of the Solar Panel

Fig 10 represents the PV power output at the initial instant, the power output is observed to be zero. However, as time progresses, the power rapidly increases, reaching a peak value of 130W. This represents the maximum power that the PV system can deliver. Subsequently, the power output stabilizes and remains constant.

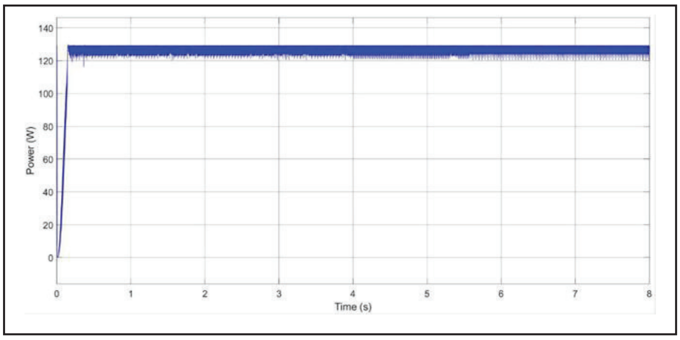

Figure 10. Response of PV Output Power (W)

This observation indicates that the PV system effectively harnesses the maximum power available from the PV panel. The rapid increase in power output showcases the system's ability to utilize the available solar energy efficiently and convert it into electrical power. Once the maximum power point is reached, the system operates at its optimal performance, ensuring the continuous and stable generation of power.

Understanding the initial power response and the utilization of the maximum power of the PV system provides valuable insights into the system's efficiency and capability to extract the maximum energy from the PV panel. This knowledge aids in the design and optimization of PV systems for enhanced power generation and utilization.

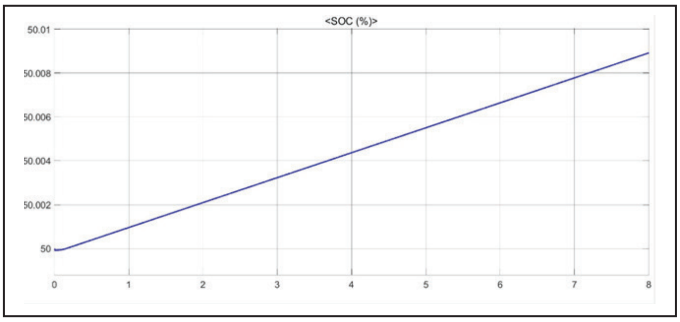

Figure 11. SOC state of charge response (%) PV integration

Fig 11 focuses on the behavior of battery charging in a PV-integrated drive system. The initial battery charge at t=0 is set to 50%, and the charging process is analyzed as the motor is driven and the solar panel starts supplying power.

Initially, after the motor is driven, the stat of charge of the battery is 50%. However, as the solar panel begins generating electricity, it gradually charges the battery. Over a period of 8 seconds (t=8s), the battery charge level increases to 50.0095%.

This observation highlights the effectiveness of the PV integration in charging the battery. The gradual increase in the battery charge demonstrates the ability of the solar panel to harness solar energy and convert it into electrical energy, thereby replenishing the battery's charge. This behavior exemplifies the energy-saving and sustainable features of the PV-integrated drive system.

Understanding the battery charging behavior in a PV-integrated drive system provides valuable insights into the system's efficiency and the role of solar energy in extending the vehicle's autonomy. Such knowledge contributes to the optimization of PV-integrated drive systems and promotes the adoption of renewable energy sources in electric vehicles.

CONCLUSION

The integration of photovoltaic (PV) panels in the electric drive system of (EVs) was stayed, with a focus on improving the autonomy and charging efficiency. Through MATLAB SimPower Systems, the performance and viability of this integration, as well as its potential impact on power production, efficiency, and electric vehicle range, were assessed.

The findings of the simulation provided important new perspectives on the behavior and efficiency of the system. The PV panels' effective power generation and efficient use of solar energy were proven, with operation centered on the maximum power point. A second renewable energy source was made accessible to the electric drive system by adding PV panels, lowering dependency on the primary battery and advancing environmentally friendly transportation.

The PV-integrated drive system's battery charging behavior and the solar panel's I-V output curve's properties were examined. An increased driving range for the EV was made possible by the effective conversion of solar energy into electrical power and the progressive charging of the battery.

The choice of a DC motor in the drive system was justified due to its simple structure, cost-effectiveness, and natural decoupling between torque and speed. Analysis of the motor's performance during driving and regenerative braking phases revealed efficient energy flow and utilization.

In order to ensure optimal performance and power consumption, power converters were included into the drive system. This allowed for effective power regulation and processing between the batteries, electric machines, and PVs.

In general, it was determined that integrating PV panels into EVs' electric drive systems was advantageous. It is recommended that renewable energy sources be used in the transportation sector. This will help reduce greenhouse gas emissions, improve air quality, and progress environmentally friendly transportation on a global scale.

This study offered useful details for the design and improvement of PV-integrated electric drive systems, supporting the use of renewable energy sources for cleaner and more sustainable transportation.

REFERENCES

[1] M. J. Riezenman, “Electric Vehicles,” *IEEE Spectr.*, vol. 29, no. 11, pp. 18–21, 1992, doi: 10.1109/6.166491.

[2] O. Schwedes and M. Keichel, *The Electric Car*. Springer Fachmedien Wiesbaden, 2021. doi: 10.1007/978-3-658-29760-2.

[3] F. Omar, *Electric vehicle*. Sidi Bel Abbes: djillali liabes university, 2020.

[4] O. FEZAZI, Ahmed Nour El Islam AYAD, and SEYF EDDINE BECHEKIR, “Validation of a SimPower System Simulation for a Buck-Boost Chopper in the Drive System of an Electric Vehicle using RT LAB,” *1. Int. SELÇUK Sci. Res. Congr.*, 2023.

[5] H. K. Omar FEZAZI., BAAHMED DJELLOUL., “Integration of Photovoltaic Panels in Electric Drive Motors for Sustainable Electric Vehicle Operation,” *Le 1er Séminaire Natl. sur les pollutions environnementales le développement durable*.

[6] F. Omar, A. A. N. el Islam, F. Omar, and A. A. N. el Islam, “Association Induction Motors to Converters,” in *Induction Motors - Recent Advances, New Perspectives and Applications*, IntechOpen, 2023. doi: 10.5772/INTECHOPEN.1001574.

[7] V. V. Korolev, I. V. Vasin, and Y. A. Gapchenko, “Energy-Efficient Car Electric Drive System,” *Proc. 2020 IEEE Conf. Russ. Young Res. Electr. Electron. Eng. EIConRus 2020*, pp. 690–692, Jan. 2020, doi: 10.1109/EICONRUS49466.2020.9039405.

[8] H. S. Lee and J. J. Yun, “Advanced MPPT Algorithm for Distributed Photovoltaic Systems,” *Energies 2019, Vol. 12, Page 3576*, vol. 12, no. 18, p. 3576, Sep. 2019, doi: 10.3390/EN12183576.

[9] S. A. Mohamed, · Montaser, and A. El Sattar, “A comparative study of P&O and INC maximum power point tracking techniques for grid-connected PV systems,” *SN Appl. Sci.*, vol. 1, 2019, doi: 10.1007/s42452-018-0134-4.

[10] “Electric Cars: Technology | edX.” https://www.edx.org/course/electric-cars-technology (accessed Nov. 08, 2022).

[11] F. Omar, H. Habib, N. Ahmed, and A. Sid, “Adaptive control of DC motor without identification of parameters,” *Facta Univ. - Ser. Electron. Energ.*, vol. 35, no. 3, pp. 301–312, 2022, doi: 10.2298/FUEE2203301O.

[12] F. Omar, A. Haddj, E. Mrabet, I. Belkraouane, and Y. Djeriri, “Journal Europé en des Systèmes Automatisés,” *J. Eur. des Systèmes Autom.*, vol. 54, no. 6, pp. 897–902, 2021.

[13] Omar FEZAZI and B. DJELLOUL., “Validation of a PV-Integrated Drive System for Electric Vehicles Using MATLAB SimPower Systems and RT LAB,” in *1. INTERNATIONAL SELÇUK SCIENTIFIC RESEARCH CONGRESS*, 2023.

The 1st National Conference on Green Energy (NCGE' 2023)
December 02, 2023, Boumerdes, Algeria.

Design and Implementation of Field-Oriented Control (FOC) in Wind Energy Conversion Systems Based on DFIGs Using Back-to-Back Converters

Itouchene Hichem[1*], Amrane Fayssal[2], Boudries Zoubir[3], Issaadi Idris[4]

[1] Laboratory of industrial Technology and Information (LII), Faculty of Technology University of Bejaia, Algeria
hichem.itouchene@univ-bejaia.dz

[2] LAS Research Laboratory Department of Electrical Engineering, University of Setif 1, Setif, Algeria
Amrane_fayssal@univ-setif.dz

[3] Laboratory of industrial Technology and Information (LII), aculty of Technology University of Bejaia, Algeria
zboudries@yahoo.fr

[4] LAS Research Laboratory Department of Electrical Engineering, University of Setif 1, Setif, Algeria
idris.issaadi@univ-setif.dz

Abstract— **This paper presents a comprehensive modeling and study of Field-Oriented Control (FOC), a prominent control strategy in Wind Energy Conversion Systems (WECS). The aim of applying this control is to separate the active and reactive powers generated by the Doubly Fed Induction Generator (DFIG) Using Back-to-Back Converters, contributing to efficient power generation from wind resources. Furthermore, a detailed analysis of simulation results is conducted, focusing on providing solutions and techniques to enhance system performance, enabling more reliable and efficient wind energy conversion.**

Keywords- DFIG, WECS, FOC, Back-to-Back converters.

I. Introduction

In recent times, there has been a growing emphasis on the wind power industry. There are numerous strong reasons for integrating wind energy more extensively into our electrical systems. A fundamental aspect is that wind power is not only environmentally conscious and sustainable but also presents the advantage of having minimal operational expenses [1-2].

The most recent advancements in wind turbine technology involve operating at variable speeds. This strategy improves energy efficiency, reduces mechanical strain, and elevates the overall performance of the generated electrical power. In opposition to fixed-speed wind turbines, these models frequently employ a DFIG [1-3].

The Doubly Fed Induction Generator (DFIG) has the ability to maintain a consistent voltage and frequency, even when there are changes in rotor speed, which makes it well-suited for fluctuating wind energy conditions. By incorporating a bidirectional AC-AC (back-to-back) converter within the rotor circuit, the operational speed range can extend beyond the synchronous speed. This enables power generation from both the stator and the rotor. An important advantage is that the capacity of the rotor converter can be a fraction of the overall output power, determined by permissible sub- and super-synchronous speed ranges [2-4]. Figure 1 illustrates the strategy of integrating a back-to-back power electronic converter into a wind power system based on the DFIG.

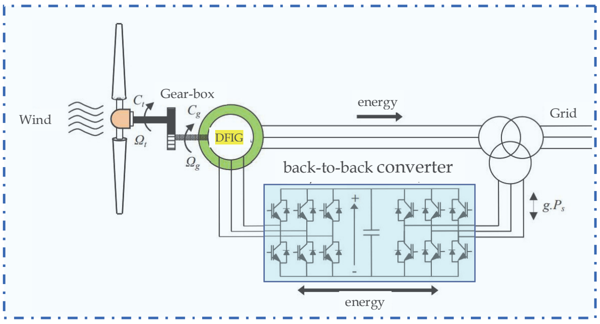

Fig 1. Wind energy conversion based on DFIG configuration.

Traditional control approaches for DFIG wind turbine systems involve stator flux-oriented control (FOC) and stator voltage-oriented control (VOC) [5]. These methods decouple the rotor current into active and reactive components, allowing manipulation of active and reactive power by indirectly controlling input currents. Research has explored employing PI controllers in conjunction with FOC, utilizing disparities in active and reactive power to establish reference currents sent to the inverter. Additionally, a cascade PI control strategy for generating a rotor voltage was proposed by [6-7]. Consequently, the uncomplicated design of conventional PI controllers establishes them as the primary selection for control techniques in power systems, owing to their simplicity [5].

II. Model of Turbine

The input power of the wind turbine usually is:

$$P_v = \frac{1}{2}[\rho.\pi.R^2.v^3] \qquad 1$$

With:
ρ=1.225 $kg.m^{-3}$: air density, R: radius of turbine, V: wind speed (m/s).
The wind turbine's mechanical power output is:

$$P_{aero} = C_p.P_v = \frac{1}{2}.C_p(\lambda;\beta).\rho.\pi.R^2.v^3 \qquad 2$$

$$\lambda = \frac{\Omega_t . R}{V}$$

$$C_{aero} = \frac{P_{aero}}{\Omega_{turbine}} = \frac{C_p(\lambda;\beta).\rho.\pi.R^2.v^3}{2 \cdot \Omega_{turbine}} \qquad 3$$

Where: C_p represents power coefficient; λ: relative speed; (β): pitch angle (deg); Ω_t: turbine speed (rd/s);
C_pCan be described as:

$$C_p(\lambda, \beta) = 0.5176 * \left(\frac{\left[\frac{116}{\lambda_i}\right] -}{0.4\,\beta - 5} \right) e^{-[21/\lambda_i]} + 0.0068\,\lambda) \qquad 4$$

Where:

$$\lambda_i = \left(\frac{116}{\lambda + 0.08\beta} - \frac{1160.035}{\beta^3 + 1} \right)^{-1}$$

The maximum value of C_p (C_p _max = 0.5483) is attained when the blade pitch angle (β) is set to 0° and the tip speed ratio (λ_obt) is set to 6.4, as demonstrated in Figure 2.

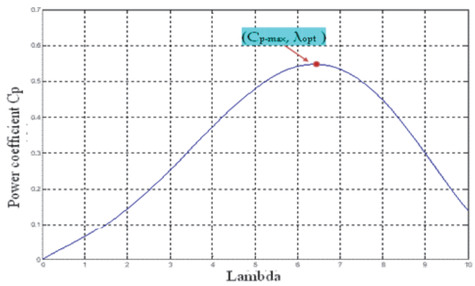

Fig 2. Power coefficient variation Cp against tip speed ratio λ.

Notably, this point corresponds to the maximum power point tracking (MPPT) condition, as reported in reference [8].

The turbine is normally connected to the generator shaft through a gearbox, which has a speed gain G chosen to place the generator shaft speed within a desired speed margin. Neglecting transmission losses, the turbine's torque and speed are related to the generator side by [9].

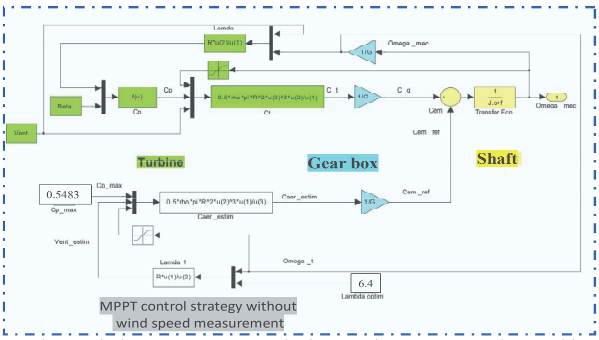

Fig 3. Wind Power System Employing Maximum Power Point Tracking (MPPT) Regulation

$$T_g = \frac{T_t}{G} \qquad 5$$

$$\Omega_t = \frac{\Omega_{mec}}{G} \qquad 6$$

$$T_g = T_{em} + J\frac{d\Omega_{mec}}{dt} + f_r \Omega_{mec} \qquad 7$$

III. Modeling of DFIG

The DFIG's electrical equations are written as follows [3– 10].

$$\begin{aligned} V_{sd} &= R_s\, I_{sd} + \frac{d\,\emptyset_{sd}}{dt} - \omega_s\, \emptyset_{sq} \\ V_{sq} &= R_s\, I_{sq} + \frac{d\,\emptyset_{sq}}{dt} + \omega_s\, \emptyset_{sd} \\ V_{rd} &= R_r\, I_{rd} + \frac{d\,\emptyset_{rd}}{dt} - \omega_r\, \emptyset_{rq} \\ V_{rq} &= R_r\, I_{rq} + \frac{d\,\emptyset_{rq}}{dt} + \omega_r\, \emptyset_{rd} \end{aligned} \qquad 8$$

With:

$$\emptyset_{sd} = L_s\, I_{sd} + L_m\, I_{rd}\,; \quad \emptyset_{sq} = L_s\, I_{sq} + L_m\, I_{rq}$$

$$\emptyset_{rd} = L_r\, I_{rd} + L_m\, I_{sd}; \quad \emptyset_{rq} = L_r\, I_{rq} + L_m\, I_{sq}$$

Electromagnetic torque:

$$T_{em} = \frac{3}{2} P * \frac{L_m}{L_s} (\emptyset_{sq} I_{rd} - \emptyset_{sd} I_{rq}) \qquad 9$$

$$\boldsymbol{T_t = T_{em} + J\frac{d\Omega_r}{dt} + f_r \Omega_r} \qquad 10$$

The stator active and reactive powers:

$$\begin{aligned} \boldsymbol{P_s} &\boldsymbol{= (3/2)[V_{sd}\, I_{sd} + V_{sq}\, I_{sq}]} \\ Q_s &= (3/2)[V_{sq}\, I_{sd} - V_{sd}\, I_{sq}] \end{aligned} \qquad 11$$

IV. Control Design

In this work, we demonstrate the application of Field-Oriented Control (FOC) to the Rotor-Side Converter (RSC). Below is the design for this control.

The rotor-side converter is controlled in a synchronously rotating d-q axis frame, with the d-axis oriented along the stator flux vector position. The effect of the stator resistance can be neglected, and the stator flux can be held constant as the stator is connected to the grid. Consequently [10]:

$$\emptyset_{sq} = 0\,, \quad \emptyset_{sd} = \emptyset_s \qquad 12$$

If the resistances of the phases are neglected, we can express the stator voltage:

$$V_{sd} = 0\,;\ V_{sq} = V_s = \omega_s \emptyset_s \qquad 13$$

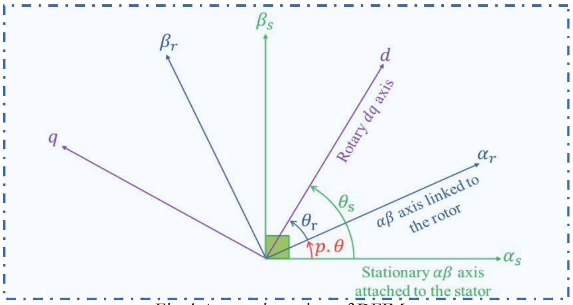

Fig.4 Axes orientation of DFIM.

In this case, the torque is given by:

$$T_{em} = -\frac{3}{2} P \frac{L_m}{L_s} (\emptyset_{sd} * I_{rq}) \quad 14$$

After applying the conditions found in equation (10), we obtain the rotor flux and stator current equations as follows.

$$\emptyset_{sd} = \emptyset_s = L_s * I_{sd} + L_m * I_{rd}$$
$$\emptyset_{sq} = \mathbf{0} = \boldsymbol{L_s * I_{sq} + L_m * I_{rq}} \quad 15$$

$$I_{sq} = -\frac{\mathrm{L_m}}{\mathrm{L_s}} * \mathrm{I_{rq}} \quad 16$$

$$I_{sq} = -\frac{\mathrm{L_m}}{\mathrm{L_s}} * \mathrm{I_{rq}}$$

The rotor voltages can be expressed according to the rotor currents as follows:

$$V_{rd} = R_r I_{rd} - g\omega_s \left| L_r - \frac{L_m^2}{L_s} \right| I_{rq}$$
$$V_{rq} = R_r I_{rq} + g\omega_s \left| L_r - \frac{L_m^2}{L_s} \right| I_{rd} + g\frac{L_m V_s}{L_s} \quad 17$$

Based on the equations provided above, we can create a simplified schematic diagram of the Field-Oriented Control (FOC) strategy for Doubly Fed Induction Generator (DFIG), as illustrated in Figure 4.

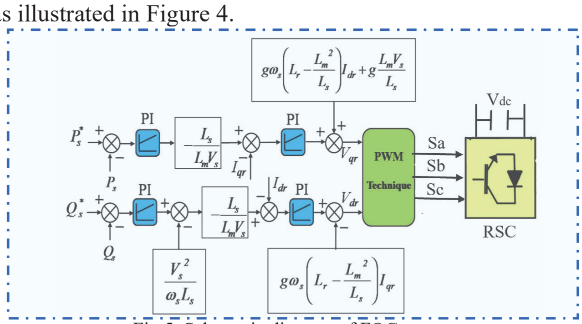

Fig 5. Schematic diagram of FOC strategy

IIV. Simulation Result

In this section, we will showcase simulation results within the MATLAB Simulink environment. The focus is on the implementation of Field-Oriented Control (FOC) applied to the rotor-side Converter (RSC) of a Doubly-Fed Induction Generator (DFIG) under two distinct scenarios: constant wind speed and varying wind speed.

The parameters for the wind turbine and DFIG are detailed as follows:

- DFIG Parameter: Pn=1.5Mw, P=2, Rs= 0.012Ω, Rr=0.021 Ω, Ls= 0.0137 Ω, Lr=0.0136 Ω, Lm=0.0135 Ω, Vdc=1200 volt
- Turbine Parameter: Np=3, R=35.25m, G=90, fv=0.0024, J=1000Kg.m^2

The resulting curve depicting the response of the DC bus voltage is displayed below.

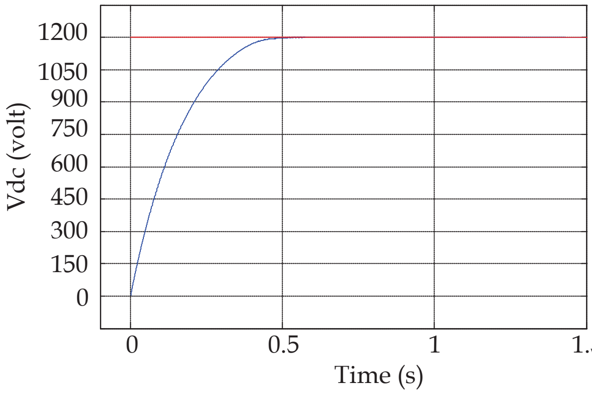

Figure 6. DC bus voltage output curve

A. *Variable Wind Speed*

During this test, we introduce varying wind speeds throughout the simulation duration while maintaining nominal conditions. The reactive power reference remains at zero to achieve a unit power factor on the stator side of the Doubly-Fed Induction Generator (DFIG). The reference for active power is established using the Maximum Power Point Tracking (MPPT) strategy. The simulation results for the Field-Oriented Control (FOC) of the DFIG are depicted in Figure 6.

Through the simulation results, we observe that:

The active and reactive powers consistently track their set references, regardless of fluctuations in wind speed. Furthermore, the power factor attains unity when reactive powers reach zero.

The generator's electromagnetic torque varies in alignment with the turbine's torque, which directly correlates with wind speed. Likewise, the stator current experiences fluctuations in accordance with changes in wind conditions, mirroring shifts in power.

The stator currents are directly proportional to the active power, while the rotor current illustrates a transition from sub-synchronous mode (where slip > 0 ➔ resulting in rotor speed < synchronous speed) to super-synchronous mode (where slip < 0 ➔ leading to rotor speed > synchronous speed) in the Doubly-Fed Induction Generator (DFIG), depicted in Figure 6.

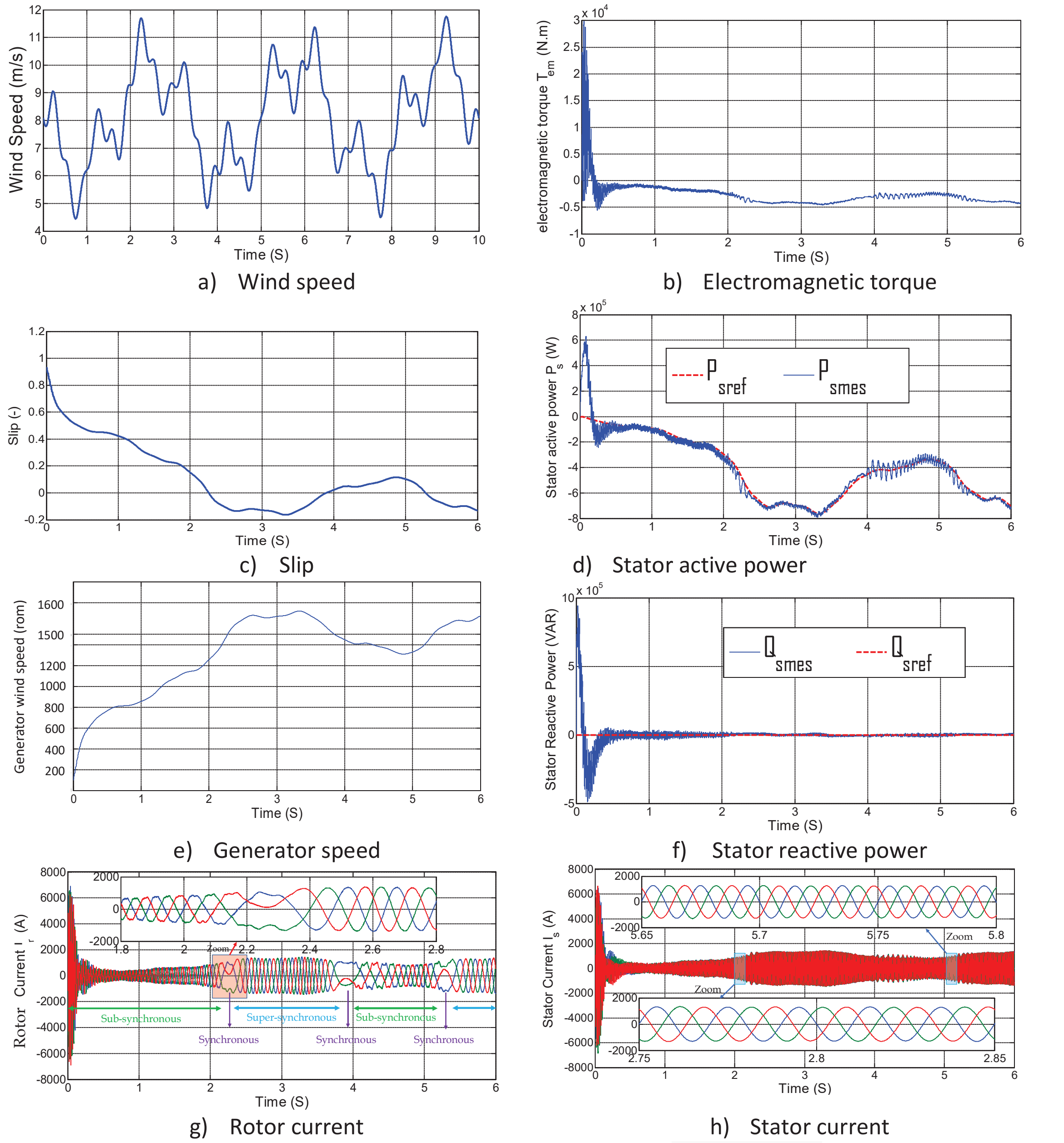

Fig 7. Simulation results of the IFOC applied to the DFIG under varying wind speeds.

Using the same conditions as in the previous test, but with a consistent wind speed of 11 m/s, the subsequent simulation outcomes are acquired

Based on the results of this test and upon comparison with the findings from the previous test, a clear observation emerges: the active and reactive powers meticulously follow their designated references.

Additionally, it is worth noting that both the stator and rotor currents display a quasi-sinusoidal behavior.

This conformity underscores the effectiveness of the control strategy in maintaining stable and desirable operational parameters within the system.

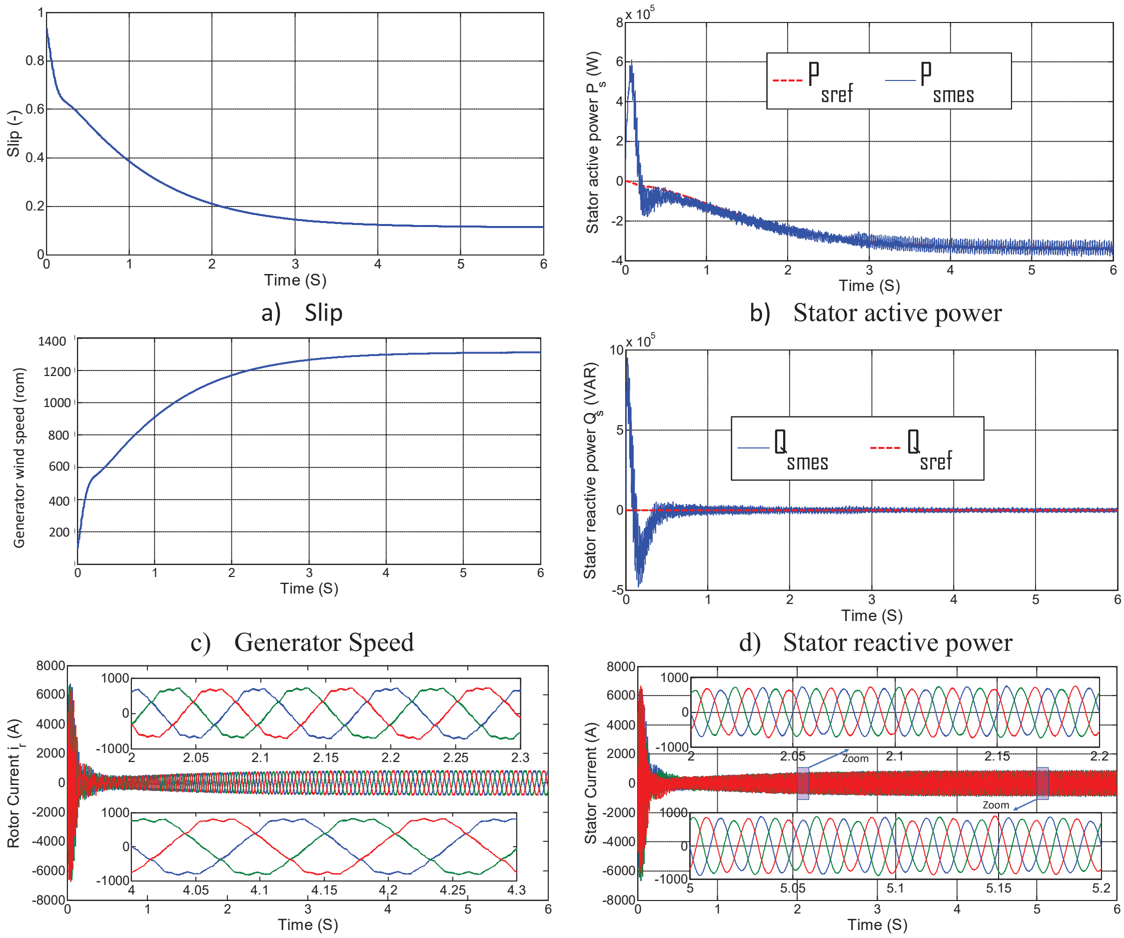

a) Slip b) Stator active power

c) Generator Speed d) Stator reactive power

e) Rotor current f) Stator current

Fig 8. Simulation results of the IFOC applied to the DFIG under constant wind speed.

CONCLUSION

This study successfully presented the design and implementation of Field-Oriented Control (FOC) within wind energy conversion systems that rely on DFIGs. Simulation results in the MATLAB/SIMULINK environment confirm the effectiveness of the proposed approach in enhancing the performance and efficiency of the WECS based on DFIGs. This is achieved through precise control of active and reactive power components, as well as the separation of transient and reactive forces under different wind conditions. This work not only advances the understanding of FOC's applicability in WECS but also provides valuable insights for future research endeavors and practical implementations in the renewable energy sector. With the continued rise in demand for clean and efficient energy solutions.

ACKNOWLEDGMENT

I would like to thank all the individuals who have supported and encouraged me during this research endeavor, I also wish to extend my heartfelt appreciation to the dedicated researchers who have lent their time, expertise, and intellect to contribute to this work. Their expertise and collaboration have enriched the study, and I am grateful for their valuable insights and ideas.

Once again, thank you for your support, your collaboration, and your commitment to the advancement of knowledge.

REFERENCES

[1] Thongam JS, Ouhrouche M (2014) MPPT control methods in wind energy conversion systems. http://www.intechopen.com. Last access 22 Oct 2014.

[2] Basem E. Elnaghi, Fathy A. Elkader, Mohamed M. Ismail, Ahmed E. Kalas `` Adaptation of PI controller used with combination of perturbation and observation method and feedback method for DFIG``, Electr Eng, pp: 1047–1058, 2017, https://doi.org/10.1007/s00202-017-0565-8.

[3] H. Mesai Ahmed, A. Bentaallah, Y. Djeriri, A. Mahmoudi`` Comparative study between pi and fuzzy pi controllers for DFIG integrated in variable speed wind turbine``, International Journal of Energetica (IJECA), ISSN: 2543-3717 Volume 4. Issue 2. 2019.

[4] R. Pena, Jon C Clare, ``A doubly fed induction generator using back-to-back PWM converters supplying an isolated load from a variable speed wind turbine``, Article in IEE Proceedings - Electric Power Applications · Vol. I43. No. 5, September 1996

[5] Y. Djeriri, A. Meroufel, A. Massoum, and Z. Boudjema, `` A comparative study between field oriented control strategy and direct power control strategy for DFIG``, Article in Journal of Electrical Engineering · June 2014

[6] Y. Zhou, P. Bauer, J.A. Ferreira, and J. Pierik, "Control of DFIG Under Unsymmetrical Voltage Dip", IEEE Power Electronics Specialists Conference, 2007, pp. 933-938.

[7] A. Tapia, G. Tapia, J. X. Ostolaza, and J. R. Sáenz, "Modeling and control of a wind turbine driven doubly fed induction generator", IEEE Trans. on Energy Conversion, June 2003, pp. 194–204. 6. G. Tapia, A. Tapia, and J. X. Ostolaza", Journal of Electrical Engineering, Vol-14,iss-2, pp-9, 2014

[8] Fayssal Amrane, Azeddine Chaiba, Bruno Francois, and Badreddine Babes, ``Experimental Design of Stand-alone Field Oriented Control for WECS in Variable Speed DFIG- based on Hysteresis Current Controller``, 15-th International conference on electricalmachine, pp. 304-308, 2017

[9] D. Aouzellag, K. Ghedamsi, E.M. Berkouk, ``Network power flux control of a wind generator``, Renewable Energy, Vol. 34, pp. 615-622, 2009.

[10] S.Mensou, A.Essadki, I.Minka, N.Tamou, B.B.Idrissi," Backstepping Controller for a Variable Wind Speed Energy Conversion System Based on a DFIG",978-1-5386-8/17/$31.00 2017 IEEE.

Analysis and Simulation of Conventional Sliding Mode Control for Wind Turbines based on a Doubly Fed Induction Generators

Itouchene Hichem[1*], Amrane Fayssal[2], Boudries Zoubir[3], Abdoune Kaddour[4]

[1*] Laboratory of industrial Technology and Information (LII), Faculty of Technology University of Bejaia, Algeria
hichem.itouchene@univ-bejaia.dz
[2] LAS Research Laboratory Department of Electrical Engineering, University of Setif 1, Setif, Algeria
Amrane_fayssal@univ-setif.dz
[3] Laboratory of industrial Technology and Information (LII), faculty of Technology University of Bejaia, Algeria
zboudries@yahoo.fr
[4] Laboratoire de Maitrise des Energies Renouvelables, Faculté de Technologie, Université de Bejaia, Bejaia,Algeria
kaddour_abdoune@yahoo.fr

Abstract— **In this work, we study a wind energy conversion system (WECS) based on a Doubly Fed Induction Generator (DFIG), using conventional sliding mode control (C-SMC) to separate active and reactive power. To confirm the robustness of the proposed control, we show simulation results using the MATLAB Simulink environment.**

Keywords- C-SMC; robustness; Wind Energy; Wind Turbine; DFIG

I. INTRODUCTION

Wind energy is a significant and growing renewable source with the potential for further growth in the future [1]. An unprecedented global challenge is being launched today in the field of energy resources. In this context, ongoing research and development efforts are aimed at improving wind turbines' efficiency, reliability, and cost-effectiveness, addressing environmental concerns, and integrating wind energy into existing power grids [2].

Over the last two decades, wind turbine sizes have undergone significant development, ranging from 20 kW to 2 MW, and ongoing efforts are focused on designing even larger wind turbines. Additionally, numerous innovative concepts have been formulated and subjected to testing [3]. This era of growth and experimentation coincides with the increasing utilization of the doubly fed induction generator (DFIG) in wind power generation [4]. This choice is attributed to the DFIG's distinct advantages [5], characterized by the direct connection of the stator DFIG winding to the grid and the connection of its rotor winding to the grid via a variable frequency converter [6-7], as depicted in Figure 1.

However, the application of linear control strategies encountered challenges in managing the complexity of variable speed wind turbine (VSWT) systems. These systems, characterized by their intricate nonlinearity, strong coupling characteristics, and uncertainties in both aerodynamics and electrical components, necessitated the exploration of various nonlinear control approaches for VSWTs [8].

Amidst these challenges, a notable approach emerged in the form of sliding mode control. This method was proposed to address the need for high-performance and more effective regulation of the active and reactive power generated by the DFIG [4]

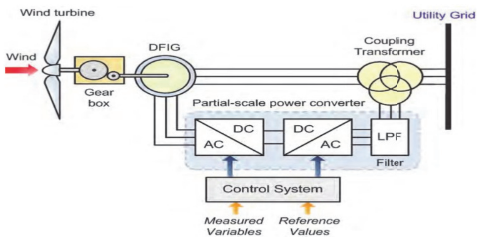

Fig 1. Schematic diagram of a single DFIG based wind turbine.

II. MODELLING OF THE DFIG

The DFIG's electrical equations are written as follows [4–9].

$$\begin{aligned} V_{sd} &= R_s I_{sd} + \frac{d\,\emptyset_{sd}}{dt} - \omega_s \emptyset_{sq} \\ V_{sq} &= R_s I_{sq} + \frac{d\,\emptyset_{sq}}{dt} + \omega_s \emptyset_{sd} \\ V_{rd} &= R_r I_{rd} + \frac{d\,\emptyset_{rd}}{dt} - \omega_r \emptyset_{rq} \\ V_{rq} &= R_r I_{rq} + \frac{d\,\emptyset_{rq}}{dt} + \omega_r \emptyset_{rd} \end{aligned} \quad (1)$$

With:

$$\begin{aligned} \emptyset_{sd} &= L_s I_{sd} + M I_{rd} \\ \emptyset_{sq} &= L_s I_{sq} + M I_{rq} \\ \emptyset_{rd} &= L_r I_{rd} + M I_{sd} \\ \emptyset_{rq} &= L_r I_{rq} + M I_{sq} \end{aligned} \quad (2)$$

Electromagnetic torque:

$$T_{em} = PM\,(I_{rd} I_{sq} - I_{rq} I_{sd}) \quad (3)$$

and its associated motion equation is:

$$T_{em} = T_r + J\frac{d\Omega_r}{dt} \quad 4$$

The state model can then be written as:

$$[\dot{X}] = [A].[X] + [B].[U] \quad 5$$

With:

$$[X] = \; [I_{sd}\; I_{sq}\; I_{rd}\; I_{rq}\;]^t$$

$$[U] = [V_{sd}\; V_{sq}\; V_{rd}\; V_{rq}\;]^t$$

Where:

$$[A] = \begin{bmatrix} -a_1 & a\omega + \omega_s & a_3 & a_5\omega \\ -a\omega - \omega_s & -a_1 & -a_5\omega & a_3 \\ a_4 & -a_6\omega & -a_2 & -\frac{\omega}{\sigma} + \omega_s \\ a_6\omega & a_4 & \frac{\omega}{\sigma} - \omega_s & -a_2 \end{bmatrix}$$

$$[B] = \begin{bmatrix} b_1 & 0 & -b_3 & 0 \\ 0 & b_1 & 0 & -b_3 \\ -b_3 & 0 & b_2 & 0 \\ 0 & -b_3 & 0 & b_2 \end{bmatrix}$$

$$\alpha = \frac{1-\sigma}{\sigma};\; a_1 = \frac{R_s}{\sigma\, L_s};\; a_2 = \frac{R_r}{\sigma\, L_r};\; a_3 = \frac{R_r\, M}{\sigma\, L_s\, L_r};$$

$$a_4 = \frac{R_s\, M}{\sigma\, L_s\, L_r};\; a_5 = \frac{M}{\sigma\, L_s};\; a_{36} = \frac{M}{\sigma\, L_r}$$

III. FIELD ORIENTED CONTROL OF DFIG

The rotor-side converter is controlled in a synchronously rotating d-q axis frame, with the d-axis oriented along the stator flux vector position. The effect of the stator resistance can be neglected, and the stator flux can be held constant as the stator is connected to the grid. Consequently [4-5]:

$$\emptyset_{sq} = 0\,, \quad \emptyset_{sd} = \emptyset_s \quad 6$$

If the resistances of the phases are neglected, we can express the stator voltage:

$$V_{sd} = 0\,;\; V_{sq} = V_s = \omega_s \emptyset_s \quad 7$$

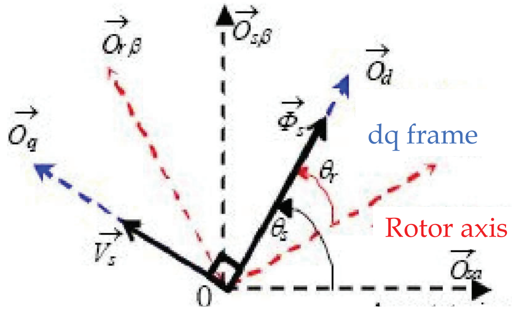

Fig 2. Stator and rotor flux vectors in the synchronous d-q Frame.

We implement an uncoupled power control system, where the transversal component I_{rq} of the rotor current controls the active power. The reactive power is controlled by the direct component I_{rd}.

$$P_s = -\frac{M}{L_s} V_s\, I_{rq}$$

$$Q_s = \left[\frac{V_s}{L_s\, \omega_s} - \frac{M}{L_s}\right] V_s\, I_{rd} \quad 8$$

The arrangement of the equations gives the expressions of the voltages according to the rotor currents:

$$I_{rd} = -\frac{1}{\sigma\, T_r} i_{rd} + g\omega_s i_{rq} + \frac{1}{\sigma\, L_r} V_{rd}$$

$$I_{rd} = -\frac{1}{\sigma}\left(\frac{1}{T_r} + \frac{M^2}{L_s\, T_s\, L_r}\right) I_{rq} - g\omega_s i_{rd} + \frac{1}{\sigma\, L_r} V_{rq} \quad 9$$

Where:

$$T_r = \frac{L_r}{R_r};\quad T_s = \frac{L_s}{R_s}\,;\sigma = 1 - \frac{M^2}{L_s L_r}$$

IV. ROBUST CONTROL DESIGN

Sliding mode control is a nonlinear control technique that focuses on robustness and stability by guiding the system state along a predefined sliding surface [4-10].

The relationship defining the sliding surface corresponds to the error between the measured and reference quadrature rotor current is given by this relation:

$$e(I_{rq}) = I_{rq}^{ref} - I_{rq}$$

$$e(I_{rd}) = I_{rd}^{ref} - I_{rd} \quad 10$$

For n=1, the speed control manifold equation can be obtained:

$$\dot{e}(I_{rq}) = \dot{I}_{rq}^{ref} - \dot{I}_{rq}$$

$$\dot{e}(I_{rd}) = \dot{I}_{rd}^{ref} - \dot{I}_{rd} \quad 11$$

Substituting the expression of I_{rd} and I_{rq} in equation (11), we obtain:

$$\dot{e}(I_{rq}) = i_{rq}^{ref} - \left|\frac{1}{\sigma}\left(\frac{1}{T_r}+\frac{M^2}{L_s\, T_s\, L_r}\right)I_{rq} - g\omega_s i_{rd} + \frac{1}{\sigma\, L_r}V_{rq}\right| \qquad 12$$

$$\dot{e}(I_{rd}) = i_{rd}^{ref} - \left[-\frac{1}{\sigma\, T_r}i_{rd} + g\omega_s i_{rq} + \frac{1}{\sigma\, L_r}V_{rd}\right]$$

We take:

$$V_{rq} = V_{rq}^{eq} + V_{rq}^{n} \qquad 13$$

$$V_{rq} = V_{rd}^{eq} + V_{rd}^{n}$$

In permanent regime, we have:

$$e(I_{rq}) = 0, \dot{e}(I_{rq}) = 0, V_{rq}^{n} = 0 \qquad 14$$

$$e(I_{rd}) = 0, \dot{e}(I_{rd}) = 0, V_{rd}^{n} = 0$$

Where:

$$V_{rq}^{eq} = \left(i_{rq}^{ref} + \frac{1}{\sigma}\left(\frac{1}{T_r}+\frac{M^2}{L_s\, T_s\, L_r}\right)I_{rq} + g\omega_s i_{rd}\right)\sigma\, L_r \qquad 15$$

$$V_{rd}^{eq} = \left(i_{rd}^{ref} + \frac{1}{\sigma\, T_r}i_{rd} - g\omega_s i_{rq}\right)\sigma\, L_r$$

The correction factor can be expressed as follows:

$$V_{rq}^{n} = K_{V_{rq}} sign\left(e(I_{rq})\right) \qquad 16$$

$$V_{rq}^{n} = K_{V_{rd}} sign(e(I_{rd}))$$

$K_{V_{rq}}$ *and* $K_{V_{rq}}$ *is* Positive constant.

Using the equations provided earlier, we can design a control diagram using the MATLAB Simulink software, as shown in the following figure.

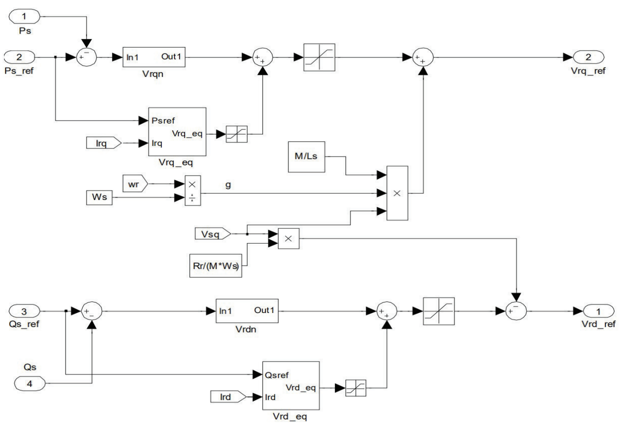

Fig 3- Block simulation of MATLAB Simulink for C-SMC

V. Prepare Your Paper Before Styling

The wind energy conversion system, based on a 1.5MW Doubly Fed Induction Generator (DFIG), is simulated using the MATLAB software. The parameters for both the turbine and DFIG are indicated in the following:

- DFIG Parameter: Pn=1.5Mw, P=2, Rs= 0.012Ω, Rr=0.021 Ω, Ls= 0.0137 Ω, Lr=0.0136 Ω, Lm=0.0135 Ω, Vdc=1200 volt
- Turbine Parameter: Np=3, R=35.25m, G=90, fv=0.0024, J=1000Kg.m^2

A. *Case 1: Reference tracking test*

Wind turbines operate under a constant wind speed and rated conditions, with different references assigned to both active and reactive powers. This is done to verify whether they are accurately tracking their references or not. Figure 4 illustrates the simulation results using the MATLAB software.

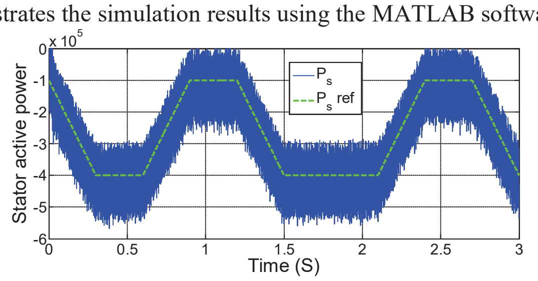

a) Stator active power

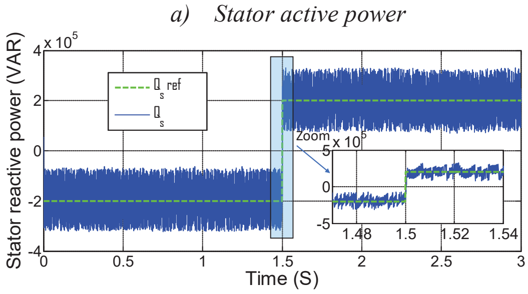

b) Stator reactive power

Fig 4. Simulation results of the CSMC applied to the DFIG (Reference tracking test)

Figure 4 presents the stator active and reactive power and its reference characteristics versus time. From the simulation results, we observe that the stator active and reactive powers closely follow their references, indicating the effectiveness of the proposed control and its capability to separate the active and reactive powers of the DFIG.

B. *Case 2: Robustness test*

In this test, we varied the parameters of the DFIG model by decreasing the stator inductance Ls by 10% from its rated value. The figure 5 illustrates the simulation results of the applied sliding mode control on the DFIG driven by wind turbines.

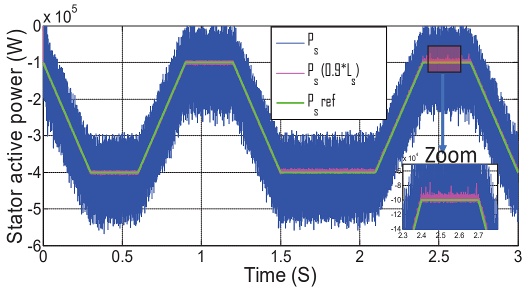

a) Stator active power

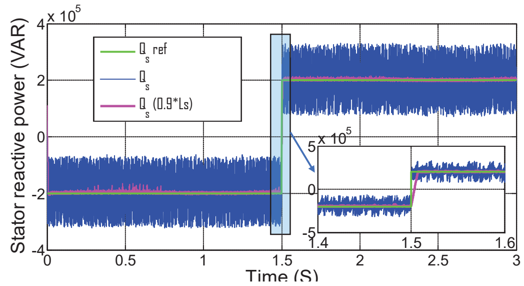

b) Stator reactive power

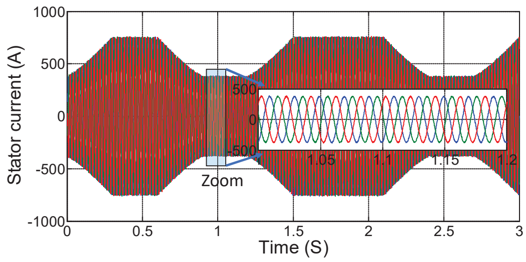

c) Stator current

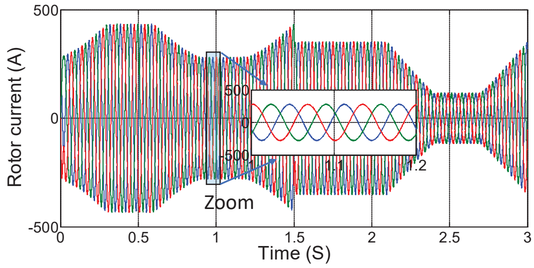

d) Rotor current

Fig 5. Simulation results of the CSMC applied to the DFIG (Robustness test)

Based on the simulation results of the robustness test presented above and their comparison with the outcomes of the reference tracking test, the effectiveness of the proposed sliding mode control (C-SMC) is confirmed. This is demonstrated by its accurate tracking of the specified references for active and reactive power. Moreover, both the stator and rotor currents display quasi-sinusoidal behavior. By analyzing the simulation results, we can deduce some characteristics of sliding mode control:

- Utilizes a sliding surface to enforce desired dynamics and regulate the system by making the system trajectory slide along this surface.
- Prone to chattering, which is high-frequency oscillation around the sliding surface due to discontinuous control actions.
- Exhibits robustness against parameter variations, external disturbances, and modeling inaccuracies due to its inherent control mechanism.
- Requires the state trajectory to converge towards the sliding surface, leading to reduced tracking error and improved control performance.

VI. Conclusion

In this research paper, we presented a study on applying sliding mode control to a wind energy system utilizing a doubly-fed induction generator (DFIG). Simulation results affirm the control's high dynamic performance and robustness, despite variations in DFIG parameters. However, this studied strategy posed the chattering phenomenon which is high-frequency oscillation around the sliding surface due to discontinuous control actions. Therefore, To address this issue and achieve better results, we recommend the implementation of alternative nonlinear control techniques such as backstepping, Model Reference Adaptive Control (MRAC), Model Reference Adaptive System (MRAS), and input-output linearizing control.

Acknowledgment

I would like to thank all the individuals who have supported and encouraged me during this research endeavor, I also wish to extend my heartfelt appreciation to the dedicated researchers who have lent their time, expertise, and intellect to contribute to this work. Their expertise and collaboration have enriched the study, and I am grateful for their valuable insights and ideas. Once again, thank you for your support, your collaboration, and your commitment to the advancement of knowledge.

References

[1] Brice Beltran, Tarek Ahmed-Ali, and Mohamed El Hachemi Benbouzid, ``High-Order Sliding-Mode Control of Variable-Speed Wind Turbines``, IEEE TRANSACTIONS ON INDUSTRIAL ELECTRONICS, VOL. 56, NO. 9, PP : 3314-3321, 2009.

[2] R. Mahroug, M. Matallah, and S. Abudura, "Modeling of wind turbine based on dual DFIG generators", International Journal of Power Electronics and Drive Systems (IJPEDS) Vol. 13, No. 2, pp. 1170-1185, June 2022.

[3] Y. Amirat, M. E. H. Benbouzid, B. Bensaker, R. Wamkeue, and H. Mangel, "The state of the art of generators for wind energy conversion systems," in Proc. ICEM, Crete Island, Greece, Sep. 2006.

[4] Youcef Bekakra, and Djilani Ben Attous, `` Direct control of doubly fed induction generator fed by PWM converter with a variable structure control based on a sliding mode control``, Int J Syst Assur Eng Manag Vol.5, No.3, PP:213–218, 2014, DOI 10.1007/s13198-013-0147-8

[5] Youcef Bekakra and Djilani Ben Attous, `` Sliding Mode Controls of Active and Reactive Power of a DFIG with MPPT for Variable Speed

Wind Energy Conversion``, Australian Journal of Basic and Applied Sciences, Vol.5, No.12, PP.2274-2286, 2011.

[6] Youcef Bekakra, Djilani Ben attous, ``Active and Reactive Power Control of a DFIG with MPPT for Variable Speed Wind Energy Conversion using Sliding Mode Control``, World Academy of Science, Engineering and Technology International Journal of Electrical and Computer Engineering Vol:5, No:12, 2011.

[7] Hernán De Battista, Student Member, IEEE, Ricardo J. Mantz, and Carlos F. Christiansen, ``Dynamical Sliding Mode Power Control of Wind Driven Induction Generators``, Article in IEEE Transactions on Energy Conversion · January 2001.

[8] O. Oualah, D. Kerdoun, A. Boumassata,`` Super-twisting sliding mode control for brushless doubly-fed reluctance generator based on wind energy conversion system``, Electrical Engineering & Electromechanics, 2023, No. 2, PP:86-92, https://doi.org/10.20998/2074-272X.2023.2.13

[9] S.Mensou, A.Essadki, I.Minka, N.Tamou, B.B.Idrissi,” Backstepping Controller for a Variable Wind Speed Energy Conversion System Based on a DFIG”,Vol.978, No.1, 2017.

[10] Y Djeriri , H Mesai Ahmed, `` Robust nonlinear control of wind turbine driven doubly fed induction generators``, Heritage and Sustainable Development, Vol. 2, No. 1, pp.17-29, 2020, https://doi.org/10.37868/hsd.v2i1.28

The 1st National Conference on Green Energy (NCGE'2023)
December 02, 2023, Boumerdes, Algeria.

Optimal Tuning of Fractional Order PID Controller Applied to Renewable Energy Systems: A Review

KAMEL Hocine
Institute of Electrical and Electronic Engineering
University of M'hamed Bougara-Boumerdes
Boumerdes, Algeria
h.kamel@univ-boumerdes.dz

YAKHELEF Yassine
Faculty of Technology
University of M'hamed Bougara-Boumerdes
Boumerdes, Algeria
y.yakhelef@univ-boumerdes.dz

***Abstract*—This review provides a succinct exploration of Fractional Order PID control, encompassing its fundamentals, fractional calculus backdrop, controller formulation, and the use of metaheuristic methods for parameter optimization. Concrete instances of application are showcased to elucidate the practical implementation of each optimization algorithm, thereby maximizing the utility derived from the obtained findings.**

***Index Terms*—FOPID Controller, Parametric Optimization, Metaheuristics , Evolutionary Algorithms.**

I. Introduction

The inception of applying fractional-order controllers in the control of dynamic systems can be attributed to the pioneering efforts of A. Oustaloup who is renowned for his formulation and advancement of the CRONE (Commande Robuste d'Ordre Non Entier, signifying Non-integer-order Robust Control) controller, which marked a significant milestone in this realm of control theory [1]. In 1994, the inaugural documentation of a fractional PID controller was disseminated by I. Podlubny. Indeed, the use of such a controller turns out to be an appropriate methodology to control fractional order systems [1]. The fractional-order PID controller (FOPID) is a generalization of the integer-order PID. In addition to the parameters of the latter, the FOPID contains two other parameters to be autotuned, which implies complexity when designing this controller. In this paper, we deal with metaheuristics techniques as a means of optimizing these parameters.

The paper is organized as follows. Section II gives a description of the Integer Order PID controller. Section III covers the basics of fractional calculus and introduces the $PI^{\lambda}D^{\mu}$ controller. Section IV delves into defining metaheuristics algorithms and their classification, subsequently providing different examples of their applications. Finally, conclusion and perspective are given in Section V.

II. Integer order PID controller

As shown in [2], based on suerveys, the PID controller is the most used in industry. This latter, is requested for its simplicity of tuning parameters, good control performance and excellent robustness to uncertainties [3]. The PID controller takes different forms depending on the situation where it will be used [4]. Each structure is composed of the three parts : Proportional part, integral part, and derivative part. By adding them, we obtain the PID control law u(t) as follows [3]:

$$u(t) = \overbrace{k_c e(t)}^{Proportional\,action} + \overbrace{\frac{k_c}{\tau_i}\int_0^t e(k)dk}^{Integral\,action} + \overbrace{k_c \tau_d \frac{de(t)}{dt}}^{Derivative\,action} \tag{1}$$

where $e(t)$ is the system error and the constants $k_c, \tau_i, and \tau_d$ are the proportional gain, the integral time, and the derivative time constant respectively. A typical PID based feedback control system is shown in the block diagram of Fig. 1.

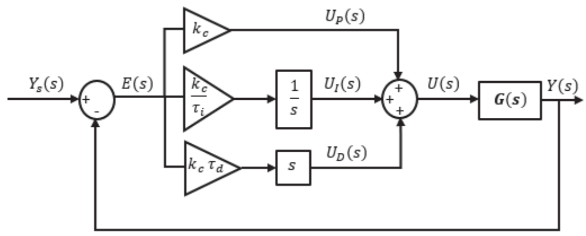

Fig. 1. PID closed loop system.

III. Fractional Order PID Controller

Although PID controllers are very effective in the industrial environnement, their simple structure makes them more suitable for pure first and second order systems, while this is not the case with industrial installations where the processes are more complex because are higher order and may have other characteristics such as time delay and non-linearity, which make it more difficult to correct them with an integer order PID controller [5].

With the development of fractional calculus, the fractional order PID (FOPID) controller was introduced. It makes it easier and more efficient to control nonlinear systems, eliminate the problem of steady state error, and reject disturbances for more complex systems in various fields [6].

A. Fractional Calculus

Fractional calculus is an extension of integration and differentiation to the basic operator of non-integer order denoted

${}_{t_0}D_t^{\alpha}$ and defined as [7] :

$$ {}_{t_0}D_t^{\alpha} = \begin{cases} \frac{d^\alpha}{dt^\alpha} & if \quad \alpha > 0 \\ 1 & if \quad \alpha = 0 \\ \int_{t_0}^{t} (dt)^{-\alpha} & if \quad \alpha < 0 \end{cases} \tag{2} $$

where $t, t_0 \in \mathbb{R}$ represent the independent variable with respect to which the operator is applied and its initial value respectively, and $\alpha \in \mathbb{R}$ is its order. Indeed, several definitions of fractional derivative exist in the leterature. The most frequent definitons have been used in the references [7]–[10].

1) Grünwald-Letnikoff definition: The Grünwald-Letnikoff derivative is obtained by extending the integer order derivative to a non-integer order α. For a very small discretization step, we obtain :

$$ {}_{t_0}D_t^{\alpha} x(t) = \frac{\sum_{l=0}^{\left[\frac{t-t_0}{h}\right]} (-1)^l \begin{pmatrix} \alpha \\ l \end{pmatrix} x(t-lh)}{h^\alpha} \tag{3} $$

$$ {}_{t}D_{t_0}^{\alpha} x(t) = \frac{\sum_{l=0}^{\left[\frac{t-t_0}{h}\right]} (-1)^l \begin{pmatrix} \alpha \\ l \end{pmatrix} x(t+lh)}{h^\alpha} \tag{4} $$

where $\left[\dfrac{t-t_0}{h}\right]$ represents the integer part of $\dfrac{t-t_0}{h}$.

2) Riemann-Liouville definition: The Riemann-Liouville fractional derivative is defined as follows :

$$ {}_{t_0}D_t^{\alpha} x(t) = \begin{cases} \dfrac{1}{\Gamma(-\alpha)} \int_{t_0}^{t} (t-\tau)^{-\alpha-1} x(\tau) d\tau & if \quad \alpha \in \mathbb{R}^- \\ x(t) & if \quad \alpha = 0 \\ \dfrac{d^{[\alpha]}}{dt^{[\alpha]}} {}_{t_0}D_t^{\alpha-[\alpha]} x(t) & if \quad \alpha \in \mathbb{R}^+ \end{cases} \tag{5} $$

$$ {}_{t}D_{t_0}^{\alpha} x(t) = \begin{cases} \dfrac{1}{\Gamma(-\alpha)} \int_{t}^{t_0} (\tau-t)^{-\alpha-1} x(\tau) d\tau & if \quad \alpha \in \mathbb{R}^- \\ x(t) & if \quad \alpha = 0 \\ (-1)^{[\alpha]} \dfrac{d^{[\alpha]}}{dt^{[\alpha]}} {}_{t}D_{t_0}^{\alpha-[\alpha]} x(t) & if \quad \alpha \in \mathbb{R}^+ \end{cases} \tag{6} $$

where $[\alpha]$ represents the integer part of α .

3) Caputo definition: The Caputo definition is defined as follows :

$$ {}_{t_0}D_t^{\alpha} x(t) = \begin{cases} \dfrac{1}{\Gamma(-\alpha)} \int_{t_0}^{t} (t-\tau)^{-\alpha-1} x(\tau) d\tau & if \quad \alpha \in \mathbb{R}^- \\ x(t) & if \quad \alpha = 0 \\ {}_{t_0}D_t^{\alpha-[\alpha]} \dfrac{d^{[\alpha]}}{dt^{[\alpha]}} x(t) & if \quad \alpha \in \mathbb{R}^+ \end{cases} \tag{7} $$

$$ {}_{t}D_{t_0}^{\alpha} x(t) = \begin{cases} \dfrac{1}{\Gamma(-\alpha)} \int_{t}^{t_0} (\tau-t)^{-\alpha-1} x(\tau) d\tau & if \quad \alpha \in \mathbb{R}^- \\ x(t) & if \quad \alpha = 0 \\ (-1)^{[\alpha]} {}_{t}D_{t_0}^{\alpha-[\alpha]} \dfrac{d^{[\alpha]}}{dt^{[\alpha]}} x(t) & if \quad \alpha \in \mathbb{R}^+ \end{cases} \tag{8} $$

By analyzing the three definitions, we notice that the fractional derivative of a function $x(t)$ at a moment t depends on the history of $x(t)$. It is said that the operator ${}_{t_0}D_t^{\alpha}$ has a memory effect.

B. $PI^{\lambda}D^{\mu}$ Controller

The fractional order PID controller, with the incorporation of fractional calculus, is an extension of the ordinary PID controller described by equation (1). The $PI^{\lambda}D^{\mu}$ Controller's law can be written in the form of an integro-differential equation as follows [8]:

$$ u(t) = K_P e(t) + K_I D_t^{-\lambda} e(t) + K_D D_t^{\mu} e(t) \tag{9} $$

where $K_P, K_I, and K_D$ are the coefficients of the proportional, integral, and derivative terms of the controller, respectively.

By applying the following two properties of the Laplace transform of a derivative and an integral of order $\alpha \in \mathbb{R}^+$ of any function $x(t)$

$$ L\{D_t^{\alpha} x(t)\} = s^{\alpha} X(s) \tag{10} $$

$$ L\{D_t^{-\alpha} x(t)\} = s^{-\alpha} X(s) \tag{11} $$

on equation (9), we obtain :

$$ U(s) = K_P E(s) + K_I s^{-\lambda} E(s) + K_D s^{\mu} E(s) \tag{12} $$

Using FOPID controller, a typical structure of feedback control system is shown in Fig. 2.

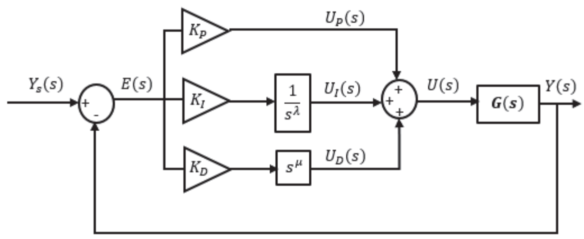

Fig. 2. FOPID closed loop system.

IV. Parameters optimization methods of FOPID controller

Following the appearance of the fundamental concepts of autotuning control design in the 1950s, it was K. J. Aström and Hägglund who introduced the use of a relay feedback test as a key method for auto-tuning in 1970. Since the result of this study, the auto-tuner can identify one point on the process' Nyquist curve, as the usual limit cycle oscillations caused by the process dynamics seen in process control are often persistent [11]. In the case of the fractional order PID controller FOPID, in addition to the adjustment of the proportional K_P, derivative K_D and integral K_I constants, two other parameters are adjusted : the fractional order of both the integral part λ and the derivative part μ. The ideal during the autotuning of these parameters is to find an optimal solution (values) to better meet the requirements of the specifications (cost, time robustness...etc). Therefore, in order to achieve that in real time, for more complex control systems, several metaheuristic techniques are proposed. The notion of "metaheuristic" can be clarified by intervening the definitions of the terms relating to it. These definitions are given by wang as follows [12]:

- Heuristic : " A heuristic is a reasoning methodology in problem solving that enables a solution to a problem is derived by trial-and-error and/or rule of thumb ".
- Metaheuristic : " A metaheuristic is a generic or higher-level heuristics that is more general in problem solving ".
- Metaheuristic computing : " is an adaptive and/or autonomous methodology for computing that applies general heuristic rules, algorithms, and processes in solving a category of computational problems ".

These three definitions are simplified with the following large definition of El-Ghazali Talbi [13]: " Metaheuristics are a branch of optimization in computer science and applied mathematics that are related to algorithms and computational complexity theory ".

When these techniques are used to autotune the parameters of an FOPID controller, we will then face an optimization problem that can be considered as follows [14]:

$$Min\overrightarrow{f}(\overrightarrow{k}) = \left[f_1(\overrightarrow{k}), f_2(\overrightarrow{k}), .., f_i(\overrightarrow{k})\right] \tag{13}$$

$$s.t: \quad g_j(\overrightarrow{k}) \leq 0 \tag{14}$$

where $\overrightarrow{k} = [K_P, K_I, \lambda, K_d, \mu]$ is the vector of FOPID parameters, $\overrightarrow{f}(\overrightarrow{k})$ is the objective function, and $g_j(\overrightarrow{k})$ are the constraints functions.

Metaheuristic algorithms can be classified in different ways according to their characteristics. The most important are succinctly outlined in [15] and illustrated in Fig. 3.

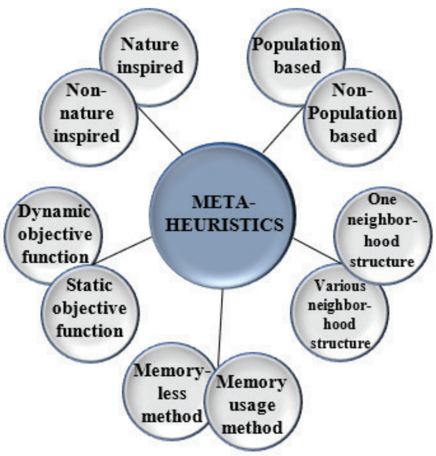

Fig. 3. Classification of metaheuristic algorithms.

Sometimes, it is not easy to classify an algorithm according to the criteria shown in Fig. 3, especially with the appearance of several more developed and even hybrid algorithms. Hence, another way of classification is introduced as shown in [16], [17]. This new classification is divided into six categories : Evolutionary Algorithms (EA) (Exemple: Genetic Algorithm (GA)), Local Search Algorithms (LSA) (Exemple: Simulated Annealing algorithm (SA)), Swarm Intelligence based Algorithms (SIA) (Exemple: Particle Swarm Optimization (PSO)), Physical based Algorithms (PA) (Exemple: Gravitational Search Algorithm (GSA)), Chemical based Algorithms (CA) (Exemple: Gases Brownian Motion Optimization (GBMO)), and Human based Algorithms (HA) (Exemple: Teaching Learning Based Optimization (TLBO)).

Some examples of application of these cited algorithms are given in TABLE I.

V. Conclusion

In this paper, the fractional order PID controller was introduced. By using optimization methods, the FOPID controller has been very useful and effective in controlling different types of systems compared to the ordinary PID. However, many metaheuristic methods are being developed and even hybridized to achieve more satisfactory results. To remedy this, the use of artificial intelligence is recommended.

References

[1] P. Shah, S. Agashe, "Review of fractional PID controller," Mechatronics, vol. 38, pp. 29–41, 2016.

[2] C. -C. Yu, Autotuning of PID Controllers: A Relay Feedback Approach, London: Springer Science & Business Media, 2006.

[3] S. W. Sung, J. Lee, and I.-B. Lee, Process Identification and PID Control. Singapore: John Wiley & Sons, 2009.

[4] K. Bingi, R. Ibrahim, M. N. Karsiti, S. M. Hassan, and V. R. Harindran, "A comparative Study of 2DOF PID and 2DOF fractional order PID controllers on a class of unstable systems," Archives of Control Sciences, vol. 28, no. 4, pp. 635–682, 2018.

[5] A.Visioli, "Tuning of PID controllers with fuzzy logic," IEE Proceedings-Control Theory and Applications, vol. 148, no. 1, pp. 1–8, 2001.

[6] S. Sondhi and Y. V. Hote, "Fractional Order Controller and its Applications: A Review," Proc. of AsiaMIC, Phuket, 2012.

[7] R. Caponetto, G. Dongola, L. Fortuna, and I. Petráš, Fractional Order Systems: Modeling and Control Applications, Singapore: World Scientific, 2010.

[8] C. A. Monje, Y. Q. Chen, B. M. Vinagre, D. Xue, and V. Feliu, Fractional-order Systems and Controls: Fundamentals and Applications, London: Springer Science & Business Media, 2010.

[9] D. Valério and J. S. d. Costa, An Introduction to Fractional Control, London: The Institution of Engineering and Technology, 2013.

[10] I. Pan and S. Das, Intelligent Fractional Order Systems and Control: An Introduction, Heidelberg: Springer, 2013.

[11] C. A. Monje, B. M. Vinagre, V. Feliu, and Y. Q. Chen, "On Auto-tuning of Fractional Order PIλDμ Controllers," IFAC Proceedings Volumes, vol. 39, no. 11, pp. 34–39, 2006.

[12] Y. Wang, "A Sociopsychological Perspective on Collective Intelligence in Metaheuristic Computing," International Journal of Applied Metaheuristic Computing (IJAMC), vol. 1, no. 1, pp. 110–128, 2010.

[13] E.-G. Talbi, Metaheuristics: from design to implementation, New Jersey: John Wiley & Sons, 2009.

[14] M. Nasir, M. Saloumi, and A. B. Nassif, "Review of Various Metaheuristics Techniques for Tuning Parameters of PID/FOPID Controllers," in ITM Web of Conferences, 2022.

[15] C. Blum and A. Roli, "Metaheuristics in combinatorial optimization: Overview and conceptual comparison," ACM Computing Surveys, vol. 35, no. 3, p. 268–308, 2003.

[16] R. A. Zitar, M. A. Al-Betar, M. A. Awadallah, I. A. Doush, and K. Assaleh, "An intensive and comprehensive overview of JAYA algorithm, its versions and applications," Archives of Computational Methods in Engineering, vol. 29, no. 2, pp. 763–792, 2022.

TABLE I

EXAMPLES OF APPLICATION OF THE SIX CATEGORIES OF METAHEURISTICS ALGORITHM.

Category	Example of Algorithm	Application of the Algorithm	Year	Ref.number
EA	GA	Implementation of Fractional Order PID Controller for an AVR System	2016	[18]
		Fractional Order PID Control of Hybrid Power System with Renewable Generation	2019	[19]
		Optimal Control of Smart Nano-Grid	2020	[20]
		Load-following control of a nuclear reactor	2021	[21]
LSA	SA	Control of a field-controlled DC servo motor	2017	[22]
		Control of a Heavy Duty Gas Turbine Plant	2018	[23]
SIA	PSO	Control of DC motor system	2015	[24]
		Control of five bar linkage robot	2015	[25]
		Control of smart nano grid	2020	[20]
		Control of wind turbine	2020	[26]
PA	GSA	Control of MagLev System	2015	[27]
		Control of a pumped storage unit	2017	[28]
		Control of inverted pendulum system	2022	[29]
CA	GBMO	Load–frequency control	2016	[30]
		Control of vibration mitigation of seismic-excited structures	2018	[31]
HA	TLBO	Control of Multivariable Systems	2019	[32]
		Control of a two-area hydrothermal power system	2019	[33]
		Control of Grid-Connected PV Systems	2020	[34]

[17] S. Mirjalili, ”SCA: a sine cosine algorithm for solving optimization problems,” Knowledge-based systems, vol. 96, pp. 120–133, 2016.

[18] A. G.Suri babu and B.T.Chiranjeevi, ” Implementation of fractional order PID controller for an AVR system using GA and ACO optimization techniques,” in IFAC-PapersOnLine, 2016.

[19] M. Regad, M. Helaimi, R. Taleb, H. A. Gabbar, and A. M. Othman, ”Fractional order PID control of hybrid power system with renewable generation using genetic algorithm,” in 2019 IEEE 7th International Conference on Smart Energy Grid Engineering (SEGE), 2019.

[20] S. Yousaf, A. Mughees, M. G. Khan, A. A. Amin, M. Adnan, ”A comparative analysis of various controller techniques for optimal control of smart nano-grid using GA and PSO algorithms,” in IEEE Access, 2020.

[21] M. Rafiei, G.R. Ansarifar, K. Hadad, and M. Mohammadi, ”Load-following control of a nuclear reactor using optimized FOPID controller based on the two-point fractional neutron kinetics model considering reactivity feedback effects,” Progress in Nuclear Energy, vol. 141, p. 103936, 2021.

[22] P. Kumar, Sh. Chatterjee, D. Shah, U. K. Saha, and Sa. Chatterjee, ”On comparison of tuning method of FOPID controller for controlling field controlled DC servo motor,” Cogent Engineering, vol. 4, no. 1, p. 1357875, 2017.

[23] A. Shumitha, S. Prasaanth, K. Suthesh, S. Balamurugan, and K. R. M. Vijaya Chandrakala, ”Simulated Annealing Based Fractional Order PID Controller for a Heavy Duty Gas Turbine Plant,” in 2018 3rd IEEE International Conference on Recent Trends in Electronics, Information & Communication Technology (RTEICT), 2018.

[24] W. Lin and Z. Chongquan, ”Design of optimal fractional-order PID controllers using particle swarm optimization algorithm for DC motor system,” in 2015 IEEE Advanced Information Technology, Electronic and Automation Control Conference (IAEAC), 2015.

[25] M. P. Aghababa, ”Optimal design of fractional-order PID controller for five bar linkage robot using a new particle swarm optimization algorithm.,” Soft Computing, vol. 20, no. 10, pp. 4055–4067, 2015.

[26] A. Mukhtar, P. M. Tiwari, H. P. Singh, ”Performance Improvement of Wind Turbine Control using Fractional Order PID Controller with PSO Optimized gains.,” in 2020 International Conference on Advances in Computing, Communication & Materials (ICACCM), 2020.

[27] P. Roy, M. Borah, L. Majhi, N. Singh, ”Design and implementation of FOPID controllers by PSO, GSA and PSOGSA for MagLev system,” in 2015 International Symposium on Advanced Computing and Communication (ISACC), 2015.

[28] C. Li, N. Zhang, X. Lai, J. Zhou, Y. Xu, ”Design of a fractional-order PID controller for a pumped storage unit using a gravitational search algorithm based on the Cauchy and Gaussian mutation,” Information Sciences, vol. 396, pp. 162–181, 2017.

[29] D. Biswas, K. D. Sharma, G. Sarkar, ”GSA Based FOPID Controller Tuning in NSOF Domain for a Class of Nonlinear Systems,” in International Conference on Computational Intelligence in Communications and Business Analytics, 2022.

[30] A. Zamani, S. M. Barakati, S. Yousofi-Darmian, ”Design of a fractional order PID controller using GBMO algorithm for load–frequency control with governor saturation consideration,” ISA transactions, vol. 64, pp. 56–66, 2016.

[31] S. Etedali, A. A. Zamani, S. Tavakoli, ”A GBMO-based PIλDμ controller for vibration mitigation of seismic-excited structures,” Automation in Construction, vol. 87, pp. 1–12, 2018.

[32] J. Bhookya, R. Kumar Jatoth, ”Fractional order PID controller design for multivariable systems using TLBO,” Chemical Product and Process Modeling, vol. 15, no. 2, p. 20190061, 2019.

[33] T. S. Gorripotu, H. Samalla, C. Jagan Mohana Rao, A. T. Azar, D. Pelusi, ”TLBO algorithm optimized fractional-order PID controller for AGC of interconnected power system,” in Soft Computing in Data Analytics: Proceedings of International Conference on SCDA 2018, 2019.

[34] A. Badis, M. H. Boujmil, ”Cascade Control Based on TLBO-FOPID for Grid-Connected PV Systems,” in Proceedings of the 8th International Conference on Sciences of Electronics, Technologies of Information and Telecommunications (SETIT'18), 2020.

The 1st National Conference on Green Energy (NCGE' 2023)
December 02, 2023, Boumerdes, Algeria.

Study of optimal fuzzy MPPT controller of a photovoltaic system

[1]Chettah Chouaib
Department of Petrochemical, August 20th; 1955 University of Skikda, Algeria.
Hyperfrequency and Semiconductor Laboratory, Brothers Mentouri University of Constantine, Algeria.
c.chettah@univ-skikda.dz & chettah_chouaib@yahoo.fr

[2]Mouatsi Abdelmalek
Department of Electrical systems engineering, M'hamed Bougara University of Boumerdes, Algeria.
abdelmalek.mouatsi@yahoo.fr

[3]Chettah Khaled
Department of Physics, Brothers Mentouri University of Constantine, Algeria.
Mechanics Research Center (CRM), Brothers Mentouri University of Constantine, Algeria.
khaledphys25@gmail.com

Abstract—**The output power of a photovoltaic generator depends on a few parameters among which are the intensity of the solar radiation, the temperature of the cells, etc. Due to the characteristics highly nonlinear electrical properties of photovoltaic cells and their associations, the efficiency of photovoltaic systems (PV) can be improved by solutions based on Maximum power point tracker (MPPT) methods. There are MPPT techniques commonly used conventional methods, namely the Perturbation and Observation (P&O) method, and advanced techniques, such as fuzzy MPPT. This comparative study between these different MPPT techniques to analyze, simulate, and evaluate the overall PV power system under varying operating conditions. To do this the mathematical models of the components of the system PV have been developed. The simulation results proved in general that the performance of the fuzzy MPPT controller is well better than those of the P&O MPPT controller.**

Keywords-PV;MPPT; P&O; styling; fuzzy logic

I. Introduction

In recent years, the production of electricity from photovoltaic conversion has increased remarkably in the world. Photovoltaic (PV) solar energy has been growing rapidly for several years because it is an inexhaustible source that does not pollute the environment. Photovoltaics can play an important role in converting light into electricity. A photovoltaic system must be equipped with an adaptation quadrupole to operate under optimal conditions. This adaptation is carried out by automatically seeking the generator's maximum power point (PPM) [1-2]. This quadrupole can be a DC-DC converter. The problem is to design and implement a control that makes the photovoltaic system converge towards optimal operating points, independent of climatic variations and the load.

The purpose of this study is to optimize the power of the PV system; it consists of the analysis of the output of the GPV to extract the maximum power delivered whatever the conditions of temperature and illuminance [3-5].

The study was completed by a comparative study with a test of robustness between the so-called conventional methods, namely the Perturbation-Observation (P&O) method and that based on the Fuzzy approach.

II. Material and Methods

The MPPT control: This is an electronic assembly at the level of the regulator, allowing the maximum energy to be obtained from a photovoltaic solar installation. It principle of the control is to vary the duty cycle D automatically until the optimal value is obtained so as to maximize the power of the panel, thus whatever the weather conditions T and G, the control of the converter places the system at the maximum function point (Vmpp, Impp) [6].

MPPT maximum power point tracking method: Much research has been developed on the different algorithms of MPP maximum power point tracking. Taking into account the variables of the system parameters and/or climatic changes.

This tracking problem has been the subject of several research to this day. Several methods have also been developed and used.

The observation & Observation method (P&O): The P&O algorithm consists of modifying the operating point of the PV module, by increasing or decreasing the duty cycle of a DC-DC converter, and measuring the output power before and after the disturbance. If the power increases, the algorithm perturbs the system in the same direction. Otherwise, the system is disturbed in the opposite direction. As the name suggests, this method works by perturbing the system and observing the impact on the power at the output of the GPV.

The algorithm can be represented mathematically by the expression:

$$V(K) = V(K-1) + \Delta V.sign\left(\left.\frac{dP}{dV}\right|_{V=V_{n-1}}\right) \quad (1)$$

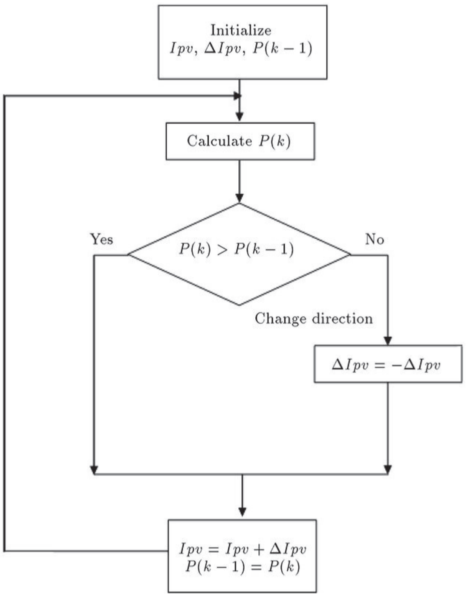

Figure 1. Flowchart of the PO method

Fuzzy logic: Fuzzy logic control has been used in MPPT maximum power point tracking systems, this control offers the advantage of being a robust and relatively simple control to develop and it does not require exact knowledge of the model to be regulated. The general structure of a fuzzy system:

- Fuzzifier.
- Fuzzy Rule base.
- Fuzzy inference system.
- Defuzzifier.

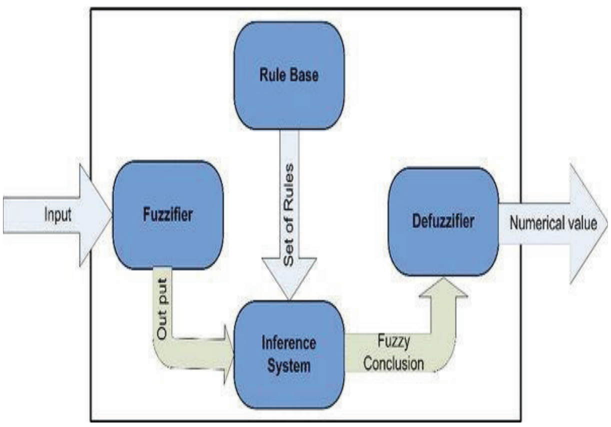

Figure 2. General structure of a system based on fuzzy logic

To test the operation of the algorithms modeled previously, the MPPT control block for the photovoltaic system has been inserted, the control inputs are the current and the voltage of the panel, the output represents the step of the duty cycle which generates the modulation signal PWM.

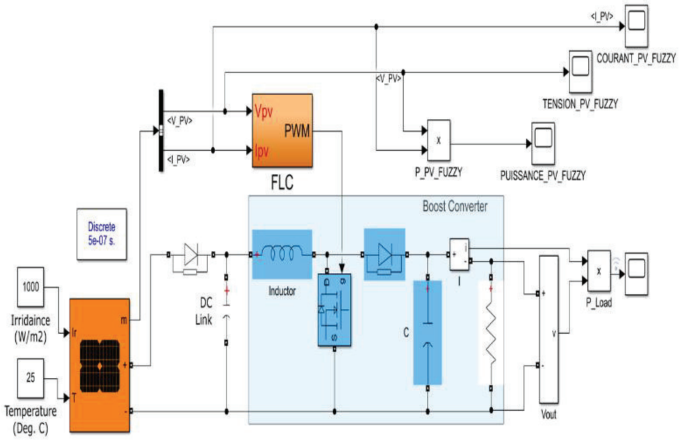

Figure 3. MATLAB SIMULLINK schematic of a PV System with fuzzy control

III. Results and Discussion

Different output results of PV array and load, for different irradiance values, were obtained by simulating fuzzy MPPT and P&O controllers. These results confirm the proper functioning of the controller (P&O). The P&O controller has a fast response time.

Maximum point tracking with fuzzy MPPT controller has minimum voltage and power ripple rate against different variations, power losses are less in the transient state, and it is robust to different voltage variations, atmospheric conditions.

We tested the operation of the studied system under a fixed temperature at 25°C and a variable irradiance (1000W\m², 800W\m², 400W\m², and 1000W/m²); we obtain variations shown in the following Figures 6&7.

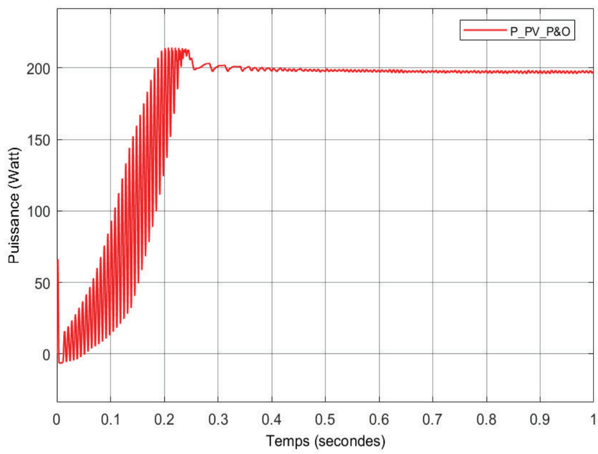

Figure 4. GPV output power (MPPT P&O)

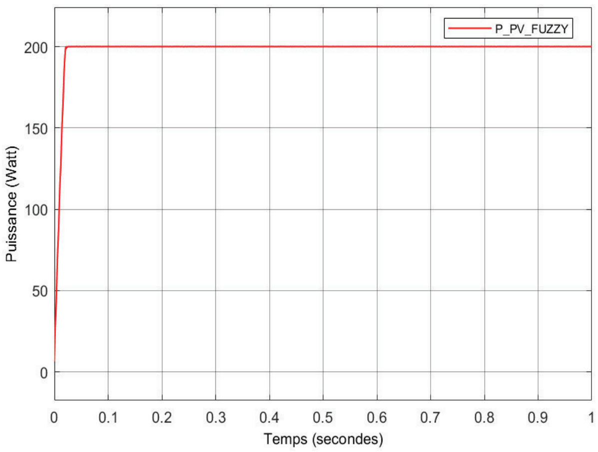

Figure 5. GPV output power with fuzzy logic

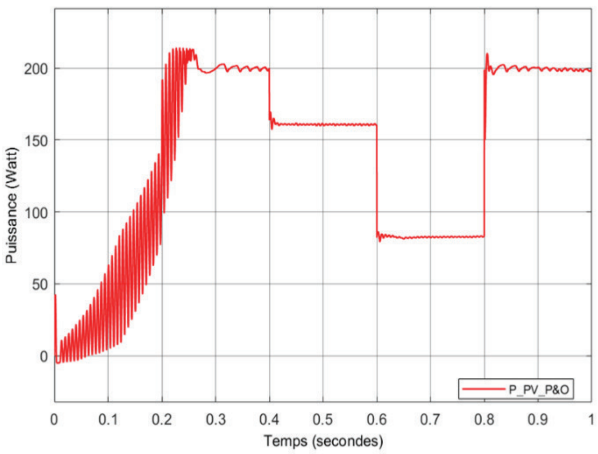

Figure 6. Output power of the GPV for different variations of irradiance (P&O)

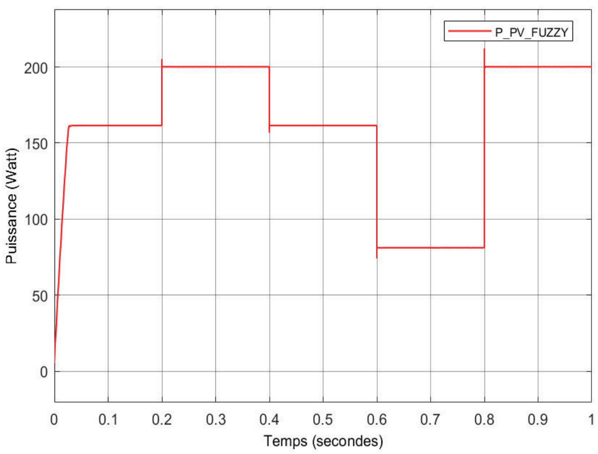

Figure 7. GPV output power for different irradiace (FLC)

Different output results of PV array and load, for different irradiance values, were obtained by simulating fuzzy MPPT and P&O controllers. These results confirm the proper functioning of the controller (P&O). The P&O controller has a fast response time.

Maximum point tracking with fuzzy MPPT controller has minimum voltage and power ripple rate against different variations, power losses are less in the transient state, and it is robust to different voltage variations, atmospheric conditions.

After the simulation with changes in sunshine, we now move on to the comparison between the two controls studied, this comparison is illustrated in Fig. 8.

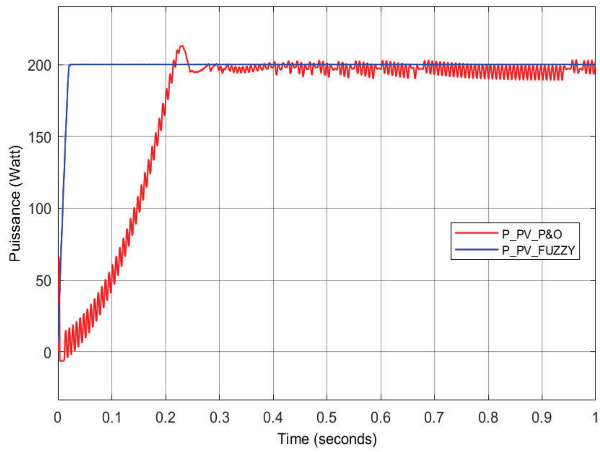

Figure 8. GPV output power with fuzzy logic control and P&O

According to the previous figure, we can clearly see the advantages of the MPPT command based on fuzzy logic, the fuzzy MPPT command (in blue) is robust and has greater speed in terms of rethink time, and greater precision. , therefore a very low error in steady state, compared to the MPPT P&O command. From this fact it can be concluded that the logic-based MPPT command is more advantageous than the MPPT P&O command, considering its speed and accuracy.

IV. Conclusion

The simulations carried out by the use of the techniques P&O, fuzzy logic under various meteorological conditions made it possible to say that the results obtained by the controller fuzzy MPPT are better than that of the controller P&O MPPT, from the point of view of robustness vis-à-vis the changes in meteorological parameters. The load power follows the power of the GPV well whatever the variations of the meteorological parameters for the two controllers.

The P&O method, although efficient in terms of MPP tracking, exhibits power losses due to the oscillation of the operating point of the system around its optimal position and a long transient state.

References

[1] Solar Power Solutions : The DIY Guide to Catch the Sun: From Grid-Tie to Off-Grid, Energy Nest, 2020.

[2] S. Deambi, Photovoltaic System Design: Procedures, Tools and Applications, CRC Press, 2016.

[3] N. Travis, Solar Power: The beginner's guide on how to design and install a photovoltaic system for your home, cars, vans and boats, 2019.

[4] T.M. Razykov, et al., “Solar photovoltaic electricity: Current status and future prospects," Solar energy, vol. 85, no 8, pp. 1580-1608, 2011.

[5] W. Xiao, Photovoltaic power system : modelling, design and control, John Wiley & Sons, 2017.

[6] P. Ganvir and R.Shaha., "Grid Connected Solar Photovoltaic Array with MPPT MATLAB Simulation, " International Journal of Trend in Scientific Research and Development (IJTSRD), vol. 3 , no. 84, 2019.

Two-Mass Wind Turbine Speed Control Using Computational Tuning Strategies

Frikh Mohamed Lamine
Dept: of Electrical Engineering
University of Badji Mokhtar
Annaba, Algeria
frikhlamine@yahoo.fr

Abstract— **Due to its inherent benefits, the complicated nonlinear wind turbine system is frequently modeled as a two-mass system. On the other hand, the stress caused by wind turbulence and excessive overshoot can be reduced by utilizing an effective speed control strategy. PID controller emerge as suitable option to control the speed of a two-mass wind turbine system. In this study, computational tuning strategies are used to tune the parameters of the PID controllers (k_p, k_i, k_d): Particle Swarm Optimization (PSO), Flower Pollination (FPA) and artificial bee colony optimization (ABC). The results show the higher performance of the Artificial Bee Colony (ABC-PID) controller design strategy when compared with the other two computational tuning strategies in terms of multiple performance evaluation indices under various wind speed operating conditions.**

Keywords— Two-mass wind turbine system, Computational tuning strategies, Artificial bee colony optimization.

I. Introduction

The increasing population expansion associated with higher rates of electricity consumption resulted in higher risk of depletion of natural resources which resulted in an increasing interest for renewable energy generation systems [1]. Moreover, renewable energies have the advantage of being free from greenhouse gases pollution, higher reliability, and wide accessibility. Nowadays, wind energy is considered as the most interesting and rapidly growing source of electricity among the different renewable energy sources [2].

The dynamics of the wind turbine is commonly modeled as a two-mass system. In addition, the flexibility of the wind turbine is integrated in the two mass model as the modes are present. Stress in wind turbines is caused by some of the factors such as wind fluctuations and high overshoot. Because the axis of the wind turbine and generator are coupled with two shafts through gearbox, the speed fluctuations will transfer to the generator. This shows the importance of the speed control of two-mass wind turbines in reducing rotor speed fluctuations and high overshoot.

Because of its simple structure and robust performance in a wide range of operating conditions the Proportional-Integral-Derivative (PID) controller, has been widely implemented in industrial installations. Unfortunately, it has been a hard task to tune properly the gains of PID controllers due to the complex behavior of the industrial installations. For such reasons, heuristic approaches have been proposed for the purpose of tuning the parameters of PID controllers.

Particle Swarm Optimization (PSO) algorithm has been implemented in [3] to search for the optimal values of the PID controller for a nonlinear hydraulic system. A PI-PD cascade controller designed to control an interconnected four areas thermal system has been tuned using a Flower Pollination algorithm (FPA) in [4],. The Artificial Bee Colony (ABC) based optimization method proposed in [5] has been applied in [6] to optimize the PID controller parameter of the AVR system.

In this study, PID controller is used to control the speed of a two-mass wind turbine. the controller is tuned using computational tuning strategies.

The paper is organized as follows: the next section gives a description of the studied two-mass wind turbine system. In Section 3, the speed control problem is presented. The computational based PID controller design strategy is given in Section 4. In Section 5, simulation results of the studied methods implementation are presented, with comparative study and discussions. Conclusions are given at the end.

II. Descreption of The Wind Turbine System

A. Dynamic Wind Turbine Modeling

The wind turbine's mechanical output power and torque are determined by.

$$P_t = \frac{1}{2}\rho\pi R^2 C_p(\lambda,\beta)\upsilon^3 \tag{1}$$

$$C_p(\lambda,\beta) = 0.5176\left(\frac{116}{\lambda_i} - 0.4\beta - 5\right)e^{-\frac{21}{\lambda_i}} + 0.0068\lambda \tag{2}$$

$$\frac{1}{\lambda_i} = \frac{1}{\lambda + 0.08\beta} - \frac{0.035}{\beta^3 + 1} \tag{3}$$

$$\lambda = \frac{\omega_t R}{\upsilon} \tag{4}$$

$$T_t = \frac{P_t}{\omega_t} = \frac{\rho\pi R^3\upsilon^2 C_p(\lambda,\beta)}{2\lambda} \tag{5}$$

where the air density, wind speed, and blade radius are represented by, ρ, v, and R, respectively. The power coefficient, C_p, depends on the blade pitch β and tip speed ratio λ. With ω_t is the rotor's angular speed.

B. Mechanical Drive Train Model

Commonly, a two-mass model of the wind turbine's dynamics is shown in Fig. 1 and represented by:

$$J_t \frac{d\omega_t}{dt} = T_t - T_{ls} - K_t \omega_t \quad (6)$$

$$T_{ls} = K_{ls}(\theta_t - \theta_{ls}) + B_{ls}(\omega_t - \omega_{ls}) \quad (7)$$

$$J_g \frac{d\omega_g}{dt} = T_{hs} - T_{em} - K_g \omega_g \quad (8)$$

where J_t, K_t, K_{ls} and B_{ls} are the turbine's side inertia, the turbine's external damping, low speed shaft stiffness and damping coefficients, respectively, T_{em}, T_{ls} and T_{hs} are the the electromagnetic torque, the low and high speed shaft torques, respectively.

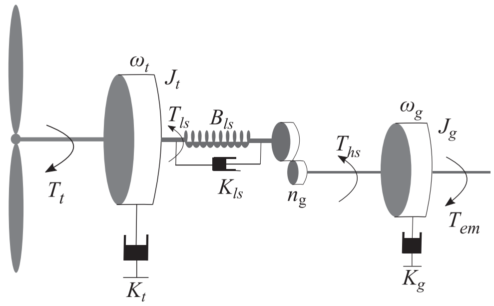

Fig. 1. Two-mass mechanical drive train.

III. Speed Control of Two-Mass Wind Turbine

The mechanical power should be maximized when the wind speed is below its rated value. In Fig. 2, the coefficient curve $C_p(\lambda, \beta)$ is shown. It demonstrates that C_p has a maximum value of $C_{pmax}(\lambda_{opt}, \beta_{opt})$ $=Copt$=0.48 for an ideal pitch angle of βopt =0° and a tip speed ratio of λ_{opt}=8.1. This value corresponds to the turbine's optimal operating point, ω_{opt} and maximum power production achieved.

The most widely utilized PID controller's transfer function is given by:

$$C(s) = \frac{U(s)}{E(s)} = k_p + \frac{k_i}{s} + k_d \frac{s}{T_f s + 1} \quad (9)$$

where k_p, k_i and k_d are the proportional, integral and derivative gains, respectively. s is the Laplace variable. T_f is the derivative term filter parameter.

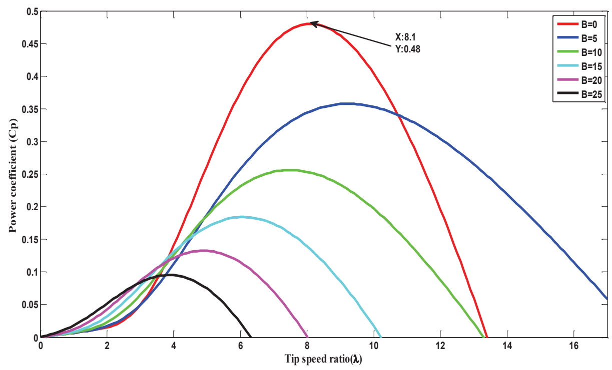

Fig. 2. The C_p plot.

The transfer function of the controlled system is required in order to determine the controller parameters k_p, k_i, and k_d. The transfer function of the wind turbine two-mass system is calculated in the following form from the block diagram illustrated in Fig. 3 and obtained from (6-8).

$$G_t(s) = \frac{\omega_t(s)}{T_t(s)} = \frac{n_g^2 J_g s^2 + B_{ls} s + K_{ls}}{n_g^2 J_t J_g s^3 + B_{ls}(J_t + n_g^2 J_g)s^2 + K_{ls}(J_t + n_g^2 J_g)s} \quad (10)$$

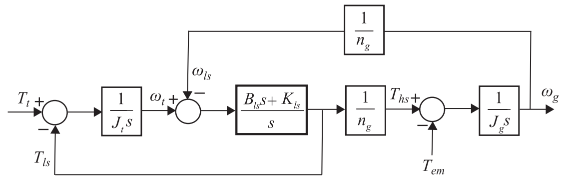

Fig. 3. Two-mass wind turbine system block diagram.

IV. Controller Design Utilizing Computational Intelligence Methods

Computational intelligence strategies (CI) contain swarm intelligence computation and evolutionary computational strategies such as Particle Swarm Optimization (PSO), Flower Pollination algorithm (FPA) and Artificial Bee Colony (ABC). The error between the reference and the measured output variable is used to create a fitness function when applying computational intelligence strategies to tune the PID controller. Then, depending on the optimization method employed, the optimization algorithms adjust the controller's parameters as shown in Fig.4.

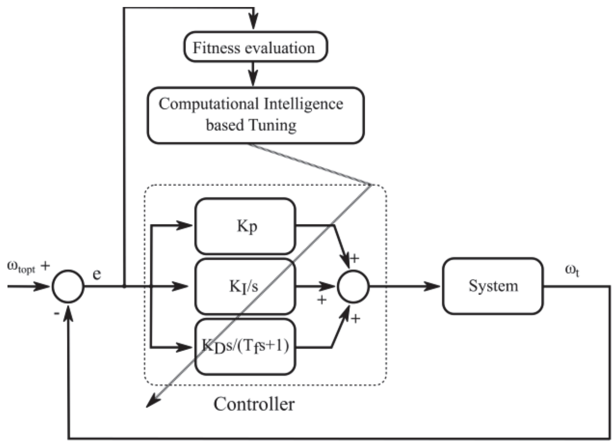

Fig. 4. PID controller parameters tuning utilizing computational intelligence methods.

Only the artificial bee colony algorithm is detailed in this paper.

A. Artificial Bee Colony Algorithm

Three types of bees make up the artificial bee colony in the ABC algorithm: employees, observers, and scouts. An employed bee is a bee that goes to a food source after visiting one independently before waiting on the dance surface to decide which food source to choose. A scout bee is one that searches randomly. The basic steps to tune the parameters of the PID controller based on ABC algorithm are given as:

- Initialize.
- Repeat.
  - Put the employed bees on the food sources in the memory.
  - Put the onlooker bees on the food sources in the memory.

- Send the scouts to the search region to look for new food sources.
- Until (requirements are fulfilled).

The main steps to tune the parameters of the PID controller based on PSO and FPA are detailed in [3] and [4].

B. Fitness Evaluation

The choice of the objective function that is used to evaluate each agent's fitness is main step for evaluating computational intelligence algorithms. In order to minimize the error signal between the measured output and the reference, Integral of Time multiplied by the Squared Error (ITSE) is used.

V. Results And Discussion

The parameters utilized for system simulation are listed in Table I. The dynamic behavior of the two-mass system is simulated under several wind speed profiles, including base and step change wind (Fig. 5(a)), and gust wind (Fig. 5(b)). To select the controller parameters that give the optimum performance, the computational intelligence-based controller design strategies have been tested and compared.

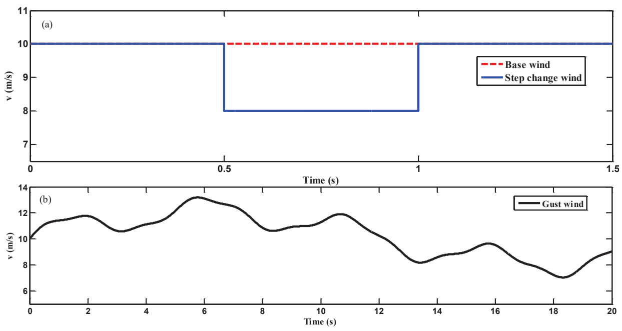

Fig. 5. Wind speed profile.

Fig. 6 shows the responses of the two-mass wind turbine system in the case of base wind speed. Table 2 illustrates the optimized controller parameters, the closed loop response performance in terms of settling time, rise time and overshoot, as well as the performance of the optimization strategies in terms of ITSE objective function and calculation time.

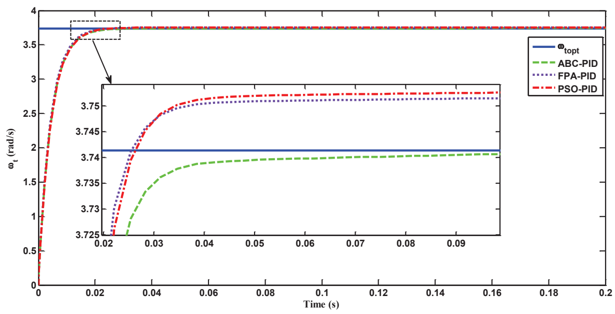

Fig. 6. Response of the wind turbine's speed to base wind profile.

The computational intelligence-based controller design strategies show close values in the closed loop performances. The Artificial Bee Colony PID Controller design strategy (ABC-PID) is more desirable, based to the optimization algorithm's results, both in terms of the ITSE objective function and in terms of calculation time.

From Fig. 7 and 8. The results show that the ABC-PID controller has a reduced tracking error than the other CI strategies.

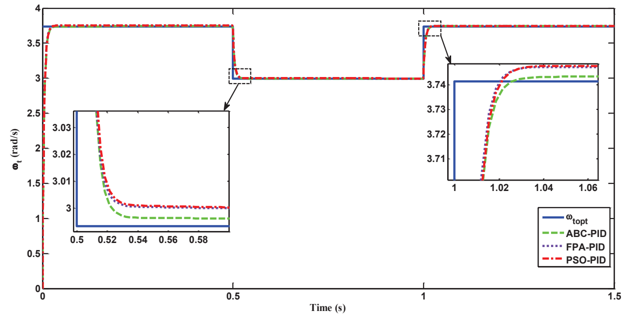

Fig. 7. Response of the wind turbine's speed to step changes in wind speed.

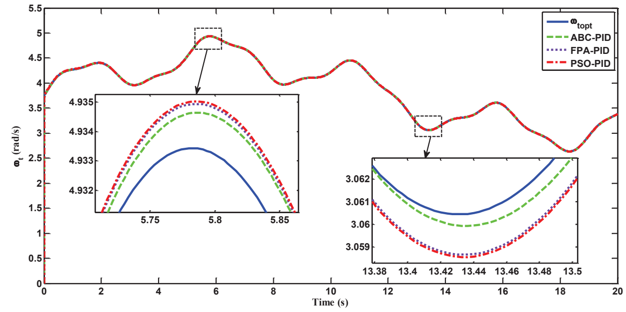

Fig. 8. Response of the wind turbine's speed to gust wind speed.

TABLE I. Two-Mass Wind Turbine System Parameters

Parameters	Value
Air density	$\rho = 1.29$ kg/m^2
Turbine radius	$R = 21.65$m
Gearbox ratio	$n_g = 43.165$
Turbine inertia	J_t =3.25*105kg.m^2
Generator inertia	J_g =34.4kg.m^2
Turbine external damping coefficient	K_t =0
Generator external damping coefficient	K_g =0
Shaft stiffness coefficient	K_{ls} =2.691*105Nm/rad
Shaft damping coefficient	B_{ls} =9500Nm/rad/s

TABLE II. PID Controller Parameters Obtained With Various Tuning Methods

Parameter	PSO-PID	FPA-PID	ABC-PID
k_p	9.561e7	10e7	9.7062e7
k_i	9.975e7	10e7	2.552e7
k_d	9.907e2	10e2	83.8214
settling time t_s(s)	0.0132	0.0127	0.0134
Overshoot M_p (%)	0.2228	0.2056	0.0488
Rise time t_r (s)	7.5e-3	7.1e-3	7.4e-3
Objective function	6.31e-6	5.777e-6	5.196e-6
Calculation time	164.46	170.35	3.40

VI. Conclusion

A tuning parameters of the integer PID controller design based on computational intelligence algorithms applied to control the speed of a two-mass wind turbine system. Better transient performance is made possible by designing a speed control strategy for the wind turbine that minimizes the impacts of wind turbulence and high overshoot. simulation results utilizing different wind profiles demonstrate the superior performance of the PID controller based on ABC tuning algorithm in terms of convergence time and performance index value when compared with the other computational intelligence tuning strategies.

REFERENCES

[1] M. L. Frikh, F. Soltani, N. Bensiali, N. Boutasseta, and N. Fergani, "Fractional order PID controller design for wind turbine systems using analytical and computational tuning approaches," *Comput. Electr. Eng.*, vol. 95, no. June 2020, p. 107410, 2021.

[2] M. Nasiri, J. Milimonfared, and S. H. Fathi, "Modeling, analysis and comparison of TSR and OTC methods for MPPT and power smoothing in permanent magnet synchronous generator-based wind turbines," *Energy Convers. Manag.*, vol. 86, pp. 892–900, Oct. 2014.

[3] Y. Ye, C.-B. Yin, Y. Gong, and J. Zhou, "Position control of nonlinear hydraulic system using an improved PSO based PID controller," *Mech. Syst. Signal Process.*, vol. 83, pp. 241–259, Jan. 2017.

[4] P. Dash, L. C. Saikia, and N. Sinha, "Flower Pollination Algorithm Optimized PI-PD Cascade Controller in Automatic Generation Control of a Multi-area Power System," *Int. J. Electr. Power Energy Syst.*, vol. 82, pp. 19–28, 2016.

[5] D. Karaboga and B. Basturk, "A powerful and efficient algorithm for numerical function optimization: artificial bee colony (ABC) algorithm," *J. Glob. Optim.*, vol. 39, no. 3, pp. 459–471, Oct. 2007.

[6] H. Gozde and M. C. Taplamacioglu, "Comparative performance analysis of artificial bee colony algorithm for automatic voltage regulator (AVR) system," *J. Franklin Inst.*, vol. 348, no. 8, pp. 1927–1946, Oct. 2011.

Assessment of hybrid bidirectional deep learning models for short term global horizontal irradiance forecasting

Louiza Ait Mouloud, Aissa Kheldoun, Oussama Merabet
Laboratory of Signals & Systems,
Institute of Electrical and Electronic Engineering,
University M'hamed Bougara,
Boumerdes 35000, Algeria
l.aitmouloud@univ-boumerdes.dz
aissa.kheldoun@univ-boumerdes.dz
o.merabet@univ-boumerdes.dz

Hamza Belmadani
Electronics Department, SET Laboratory organization,
Faculty of Technology
Blida 1 University
Blida, Algeria
belmadanihamza@etu.univ-blida.dz

Abstract—**The integration of renewable energy sources, such as solar energy, into power systems is crucial for enhancing their environmental sustainability. However, the intermittency of solar irradiance poses operational and control challenges. To address this issue, global horizontal irradiance (GHI) can be forecasted. This paper proposes a hybrid deep learning-based forecasting method, namely the Convolutional Neural Network and Bidirectional Long Short Term Memory (CNN-BiLSTM), and compares it with three other hybrid models: the Convolutional Neural Network Long Short Term Memory (CNN-LSTM), the Convolutional Neural Network Gated Recurrent Unit (CNN-GRU), and the Convolutional Neural Network Bidirectional Gated Recurrent Unit (CNN-BiGRU). The comparison focuses on the annual forecasting of GHI over a 1-hour horizon in Alice Springs, Australia, and the accuracy of the models is evaluated using four metrics: root mean squared error (RMSE), mean absolute error (MAE), coefficient of determination (R^2), and(nRMSE) normalized root mean square. The results demonstrate that the proposed model outperforms significantly the other models.**

Keywords—Global Horizontal Irradiance, Deep Learning, Short-term Forecasting, Hybrid Deep Learning Models.

I. INTRODUCTION

The need to combat pollution and climate change has led to a shift towards cleaner energy sources, with solar energy being a promising alternative[1]. However, its variability makes it difficult to integrate into power systems[2]. To address this issue, researchers are working on forecasting solar irradiance using different time horizons, including ultra-short-term, short-term, medium-term, and long-term[2]. Machine learning techniques such as artificial neural networks (ANNs) and deep learning methods like long short-term memory (LSTM) and gated recurrent units (GRUs) have enabled more advanced methods for solar irradiance forecasting [3]. The paper [4]conducted three experiments using the Phoenix and Arizona dataset to predict one hour ahead of solar irradiance using Gated Recurrent Unit (GRU). Hybrid models, which combine multiple methods, have been shown to yield more accurate results than standalone models. Singla et al [5] combined a bidirectional long short-term memory (BiLSTM) with a wavelet transform method (WT) to forecast 24h ahead global horizontal irradiance and found that their proposed model outperformed other models. Another paper [6] proposed a deep learning method; convolutional long short term memory (CLSTM) for half-hourly, daily, and monthly global solar radiation prediction and found that their method outperformed other standalone methods. Moreover the study conducted by [7] proposed BiGRU along with the ARIMA model as well as the naive decomposition processes in a novel way to forecast solar irradiance and found that their hybrid BiGRU-ARIMA outperformed standalone models in the case of short-term intervals of one hour. This paper introduces a hybrid method, CNN-BiLSTM, for forecasting Global Horizontal Irradiance and compares it with other powerful hybrid methods based on CNN-LSTM, CNN-GRU, and CNN-BiGRU. The forecasting is performed on an hourly basis for annual data and the results are analyzed using the Taylor diagram and four different metrics to assess the accuracy of the suggested methods. The key contributions of this paper include the application of a bidirectional hybrid deep learning-based method for forecasting solar irradiance in Alice Springs, Australia. The performance of the suggested hybrid model is evaluated using the Taylor diagram and different evaluation metrics, and a comparison with benchmark models shows that the suggested method outperforms all of them.

II. THEORICAL BACKROUND

CNN-BiLSTM model is proposed in this study to perform short-term (1-hour) global horizontal forecasts is composed of two main neural network models, CNN and BiLSTM. The CNN architecture is employed to extract spatial features while the BiLSTM is a combination of two LSTMs. The first one works on training the network in the forward direction to extract information from the future state. The second work in a backward direction, so it obtains information from the past state. Thereby, bidirectional neural networks are more consistent with reality [8]and are employed mainly to model temporal features. This paper uses a one-dimensional convolution layer with a Relu activation function, 64 filters, and a kernel size of 2 plus a max-pooling layer with a pool size of 2. Additionally, a bidirectional LSTM layer is added with 50 filters and the Relu activation function and finally, a dense layer is used to predict the global horizontal irradiance value.

III. SITE LOCATION AND DATASET

Desert Knowledge Australia (DKA) Solar Center is a demonstration facility for different PV technologies in Alice Springs, Australia. The climate is arid with 300 days of sunshine, generating an average of 420,000 kWh annually. The data used in this study is from the DKA Solar Center website and consists of historical global horizontal irradiance collected from different sensors.

IV. FORECASTING PROCESS

The proposed forecasting process shown in figure 1 consists of collecting two years of data from Alice Springs, Australia. The data is preprocessed and then fed into the deep learning models. The predictions performed by the proposed models are evaluated using four different metrics MAE, RMSE, R^2 and nRMSE.

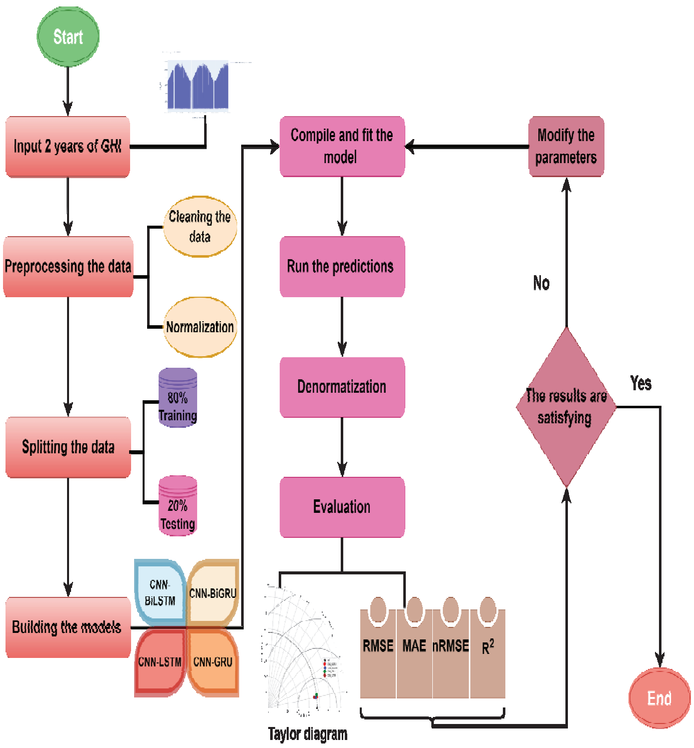

Fig.1. Flowchart of the proposed forecasting process

A. Data aquisition

In the present study, the global Horizontal irradiance data of the Alice Spring station is used. The obtained dataset is acquired over two years period (July 1, 2019 to January 20, 2022) with 5 minutes resolution. The data has been resampled in python to 1 h resolution with 22438 samples. Few of them are missing values due to short-term network or minor system outage as mentioned in DKA solar center website.

B. Data preprocessing

Preprocessing the raw data is a very crucial step for obtaining satisfying forecasting results. In our study, the preprocessing consists of cleaning the dataset from missing and impossible values generated by sensors. Using python build-in methods bfill (= backward fill) and ffill (= forward fill) that replace the missing values with the next and previous valid values respectively. Afterwards, for an easier and more stable learning process, feature scaling or normalization is based on the Min-Max Scaler method to get all of the data between the range [0, 1]. The latter method is described by the following expression:

$$x_{scaled} = \frac{x - x_{min}}{x_{max} - x_{min}} \quad (1)$$

C. Data splitting

The data is split manually into 80% training and 20% testing, a common choice adopted by most researchers.

D. Emplementation

The hybrid model was built using the Keras library as described in the above section and then compiled using a common regression metric, mean absolute error (MAE), and adaptive moment estimation (ADAM). After that, the model is fitted using a moderate number of epochs (30) to avoid high computation and training time. Moreover, for a smooth learning curve batch size of 128 is employed irrespective of the dataset size and the number of samples. Finally, evaluate the testing data set and run the predictions. Since deep learning models are stochastic meaning that it uses randomness in learning, the results of the prediction differ each time we train the model. Therefore, we run the predictions ten times and compute the average of the results.

E. Performance matrices

In this study, common evaluation metrics are used to test the model's performance. These metrics are MAE (Mean Absolute Error), RMSE (Root Mean Square Error), R^2 (coefficient of determination), and nRMSE (normalized root mean square).

$$RMSE = \sqrt{\frac{1}{m}\sum_{i=0}^{m}(y_i - \hat{y}_i)^2} \quad (2)$$

$$MAE = \frac{1}{m}\sum_{i=0}^{m}|y_i - \hat{y}_i| \quad (3)$$

$$R^2 = 1 - \frac{\sum_i(\hat{y}_i - y_i)^2}{\sum_i(y_i - \bar{y}_i)^2} \quad (4)$$

$$nRMSE = \frac{RMSE}{\sum_{i=0}^{m} y_i} \quad (5)$$

Where:

y_i is the forecast value,

$\hat{y}_i$ is the true value

$\bar{y}_i$ is the mean of output.

V. RESULTS AND DISCUSSION

Figures 2, 3 and 4 show the forecasting results of CNN-BiLSTM, Taylor's diagram evaluating the four models and the bar plots of the four metrics for the performance assessment, respectively. From table 1 and metrics are shown in figure 3, it is notable that the CNN-BiLSTM model outperforms all the considered models as it has the lowest annual RMSE (54.2138 W/m^2), MAE (28.3697 W/m^2), nRMSE (0.0447), and the highest R^2 (0.9786). Followed by CNN-LSTM, then CNN-BiGRU, And finally, CNN-GRU which has shown the worst performance with the annual RMSE (68.0781 W/m^2), MAE(42.6681 W/m^2), and R^2 (0.9677). One can notice that the performances of both CNN-LSTM and CNN-BiLSTM models are similar and this can be explained by the fact that both structures are almost the same except that CNN bidirectional LSTM consists of two LSTMs instead of one LSTM as in the case of CNN mono-directional LSTM. It is also worth mentioning that both CNN–BiLSTM and CNN–LSTM demonstrated considerably better and more stable performance than other models in annual error measurements. From Figure 1 it can be seen that the CNN-BiLSTM model produces the best annual forecasts as the actual and the predicted results are almost identical. The Taylor diagram that is shown in figure 2 demonstrates the latter outcomes. The said diagram uses three different statistics: coefficient of correlation, centered root-mean-square difference, and the amplitude of their variations (represented by their standard deviation notably, valuating the four hybrid models). It is notable that all the models are close to the reference or the observed point. However, CNN BiLSTM seems the closest to the reference point, making it the best model with a coefficient of correlation R=0.9903. Even though comparison of the investigated models was somehow difficult due their good prediction. Nevertheless, based on the obtained metrics, the CNN BiLSTM hybrid model seems to be the best contender compared to the others regarding the one-hour ahead forecasting based on the annual data.

Table 1: The error measurements (MAE, RMSE, nRMSE and, R^2) for the four different models on annual forecasting.

Metrics	CNN-LSTM	CNN-GRU	CNN-BiGRU	**Proposed**
MAE (w/m^2)	28.8998	42.6681	29.3724	**28.3697**
RMSE(w/m^2)	54.6260	68.0781	56.2739	**54.2138**
R^2	0.9785	0.9677	0.9778	**0.9786**
nRMSE	0.0511	0.0567	0.0510	**0.0447**

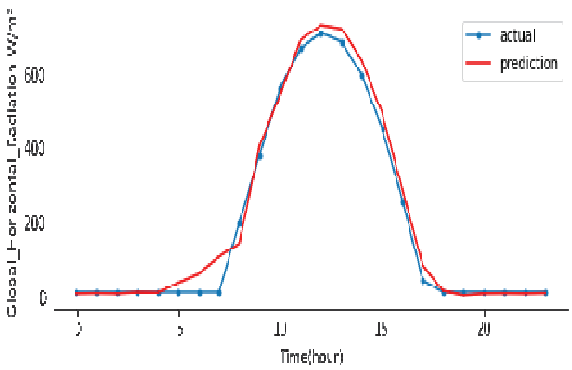

Fig .2. The actual and predicted GHI with CNN-BiLSTM

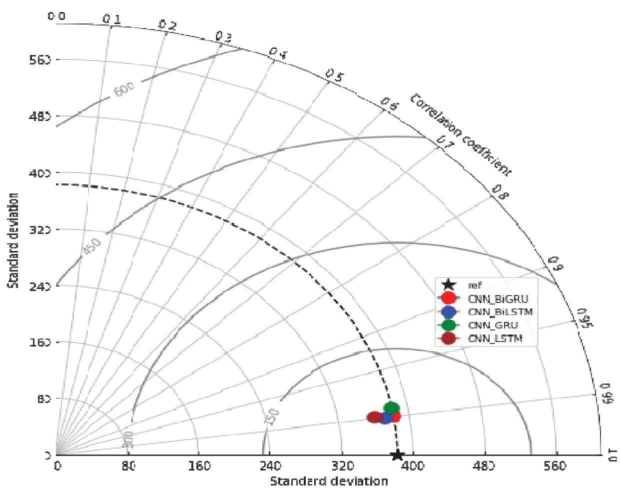

Fig.3. Taylor diagram for the annual GHI forecasting

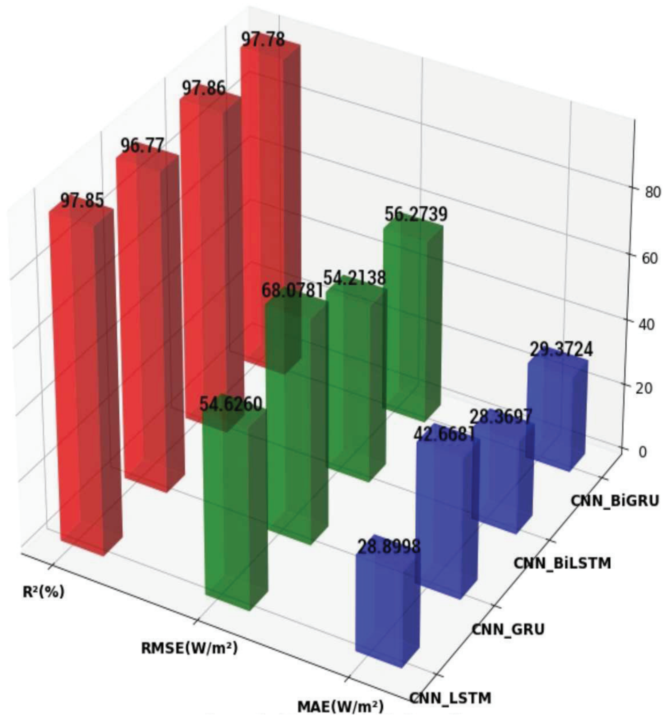

Fig.4. Bar plot in 3D of obtained metrics for the four models being applied for the annual GHI forecasting

VI. COMPARAISON WITH PREVIOUS WORK

For purpose of comparison with previous work, the use of common metrics is not feasible. In fact, different databases are used for the development of forecasting models. Therefore, in the present paper, the method of evaluation proposed by Mohammadi et al. in their work [9] is adopted. To this, the normalized Root Mean Squared Error is employed. This latter is independent of the data type and size and reflects only the features related to the prediction model. The method ranges the nRMSE to classify the level of the forecasting precision as shown in Table 2.

Table 2 Model performance with respect to nRMSE

nRMSE	Model Precision
>0.10	Excellent
0.10-0.20	Good
0.20-0.30	Fair
<0.30	Poor

From Table 3 it can be noticed that our results significantly outperform other papers 'results holding the least nRMSE (0.0447) for annual forecasting achieved with CNN-BiLSTM. Furthermore, table 2 demonstrates the excellent precision of the proposed models for annual GHI forecasting with nRMSE less than 0.1.

Table 3 Annual forecasting performance of CNN-BiLSTM compared to the benchmark models in terms of nRMSE

Authors	Regions	Annual
Gao et al [10]	Los Angeles Denver Hawaii's Big Island. Tamanrasset	0. 1310 0. 2069 0.1927 0. 1587
Blaid et al [11]	Ghardaı¨a, Algeria	0.1300
Alzahrani et al [12]	Canada	0.086
Cyril Voyant [13]	Marseille, France	0.137
Emre Akarslan [14]	Turkey	0.3129
Proposed CNN-BiLSTM	Alice Springs, Australia	**0.0447**

VII. CONCLUSION

Forecasting solar irradiance is challenging due to its nonlinearity and intermittency. In this work, a hybrid deep learning model, CNN-BiLSTM, is introduced and implemented to forecast hourly global horizontal irradiance on an annual basis. The major novelty of this paper is the use of stronger bidirectional deep learning hybrid models and comparing their results with other hybrid models. The proposed models are accurate and cost-effective, as only a GHI sensor is required to create the data. Further work could include the use of optimization algorithms for determining optimal hyperparameters and extending the present work to multivariate data to further improve the accuracy of global horizontal irradiance predictions. The robustness of the irradiance prediction can also be reached by evaluating the proposed models for different databases.

Acknowledgment

The authors would like to acknowledge the financial support of the Directorate General for Scientific Research and Technological Development (DG-RSDT), Algeria.

REFERENCES

1. Bendiek, P., et al., *Solar irradiance forecasting using a data-driven algorithm and contextual optimisation.* Applied Sciences, 2021. **12**(1): p. 134.
2. El-Amarty, N., et al., *A comprehensive review of solar irradiation estimation and forecasting using artificial neural networks: data, models and trends.* Environmental Science Pollution Research 2023. **30**(3): p. 5407-5439.

3. Rahimi, N., et al., *A Comprehensive Review on Ensemble Solar Power Forecasting Algorithms.* Journal of Electrical Engineering Technology 2023. **18**(2): p. 719-733.
4. Rajagukguk, R.A., R.A. Ramadhan, and H.-J.J.E. Lee, *A review on deep learning models for forecasting time series data of solar irradiance and photovoltaic power.* Energies, 2020. **13**(24): p. 6623.
5. Singla, P., M. Duhan, and S.J.E.S.I. Saroha, *An ensemble method to forecast 24-h ahead solar irradiance using wavelet decomposition and BiLSTM deep learning network.* Earth Science Informatics, 2022. **15**(1): p. 291-306.
6. Ghimire, S., et al., *Deep solar radiation forecasting with convolutional neural network and long short-term memory network algorithms.* Applied Energy, 2019. **253**: p. 113541.
7. Jaihuni, M., et al., *A partially amended hybrid bi-GRU—ARIMA model (PAHM) for predicting solar irradiance in short and very-short terms.* Energies, 2020. **13**(2): p. 435.
8. Zhu, Q., et al., *A hybrid VMD–BiGRU model for rubber futures time series forecasting.* Applied Soft Computing, 2019. **84**: p. 105739.
9. Mohammadi, K., et al., *Support vector regression based prediction of global solar radiation on a horizontal surface.* 2015. **91**: p. 433-441.
10. Gao, B., et al., *Hourly forecasting of solar irradiance based on CEEMDAN and multi-strategy CNN-LSTM neural networks.* Renewable Energy, 2020. **162**: p. 1665-1683.
11. Belaid, S., A.J.E.C. Mellit, and Management, *Prediction of daily and mean monthly global solar radiation using support vector machine in an arid climate.* Energy Conversion, 2016. **118**: p. 105-118.
12. Alzahrani, A., et al., *Solar irradiance forecasting using deep neural networks.* Procedia Computer Science 2017. **114**: p. 304-313.
13. Voyant, C., et al., *Hybrid methodology for hourly global radiation forecasting in Mediterranean area.* Renewable Energy, 2013. **53**: p. 1-11.
14. Akarslan, E., F.O. Hocaoglu, and R.J.R.E. Edizkan, *Novel short term solar irradiance forecasting models.* Renewable Energy, 2018. **123**: p. 58-66.

Direct reactive power control of DFIG with fixed switching frequency for grid-connected wind turbine

Oualid Djoudi
Laboratoire de Technologie Industrielle et de l'Information (LTII), Faculté de Technologie, Université de Bejaia, 06000 Bejaia, Algérie

Sofia Lalouni Belaid
Laboratoire de Technologie Industrielle et de l'Information (LTII), Faculté de Technologie, Université de Bejaia, 06000 Bejaia, Algérie

Salah Tamalouzt
Laboratoire de Technologie Industrielle et de l'Information (LTII), Faculté de Technologie, Université de Bejaia, 06000 Bejaia, Algérie

Abstract— **This paper presents an improved direct reactive power control (DRPC) strategy based on the space vector modulation (SVM) technique applied to a two-level voltage inverter feeding the rotor of a doubly fed induction generator (DFIG) driven by a variable speed wind turbine (WT). Reactive power is controlled by acting on the rotor flux magnitude. Thanks to the fixed switching frequency approach of SVM, the proposed SVM-DRPC technique enables control with better performance, namely the reduction of machine ripples, often encountered with conventional DRPC control. Simulation results obtained with the proposed SVM-DRPC control show satisfactory improvements over the switching table-based DRPC control (ST-DRPC). This improvement can be seen in the ripple reduction in torque and stator reactive power.**

Keywords-component; doubly fed induction generator; direct reactive power control; space vector modulation; variable speed wind turbine

I. INTRODUCTION

The most widely used renewable energy source is wind power, due to its high availability and advanced operating technology. Today, grid-connected wind energy conversion systems more frequently use the doubly fed induction generator (DFIG). Thanks to the ability to control the DFIG via the rotor windings, it can operate over a wide speed range. In addition, the power available in the rotor is a fraction of the stator power. This is an advantage when using a small converter to control the DFIG [1].

However, due to its non-linear nature, its high dynamics and the variation of its parameters during operation, the DFIG is more difficult to control. The torque and flux of this machine must be managed by more advanced control algorithms to overcome these limitations. Several studies have been carried out to control the DFIG in a grid-connected wind turbine system [2]-[5], [6]. Field oriented control (FOC) is the most widely cited strategy for controlling the WT-DFIG. While decoupling the electromagnetic torque from the rotor flux, optimum turbine efficiency can be achieved by controlling the DFIG mechanical speed. This control technique provides a finer response in steady-state operation thanks to the presence of an internal loop for the current. Nevertheless, control performance is affected by parametric variation [2].

Direct torque control (DTC) is one of the algorithms proposed for controlling DFIG-based wind turbines, and was introduced in 1985 by Takahashi. Due to its simpler implementation, improved transient response and low dependence on machine parameters, this control outperforms the FOC strategy [3]. However, flux and torque ripples are the main problem with traditional DTC. This is due to the variable switching frequency of hysteresis controllers. Several works have been proposed to improve the performance of DTC control applied to the WT-DFIG, while maintaining its advantages: simplicity of implementation and independence from parametric variations. [4] proposes a DTC applied to a multi-level converter, in order to benefit from the high degree of freedom in selecting the appropriate voltage vector. In [5], the classical DTC switching table and hysteresis controllers have been replaced by a fuzzy controller. Both techniques presented in [4] and [5] reduce steady-state flux and torque ripples. However, the switching frequency is constantly variable.

Space vector modulation (SVM) is a technique that offers the possibility of adjusting the switching frequency. Integrating the SVM technique into DTC control overcomes the ripple phenomenon by imposing a constant switching frequency [6]. SVM-DTC was applied to the DFIG by [7]. Flux and torque ripples have been reduced with a fixed switching frequency. However, power flow control by the grid side converter (GSC) is neglected. Furthermore, the advantage of controlling stator reactive power has not been exploited. The aim of this paper is to demonstrate the improved performance of SVM-DTC while controlling stator reactive power and power flow between the rotor and the grid. MATLAB/Simulink software is used to simulate the proposed control system in order to test theoretical assumptions.

II. WT-DFIG MODELING

The mathematical model of the DFIG expressed in the d-q synchronous reference is described by the following equations.

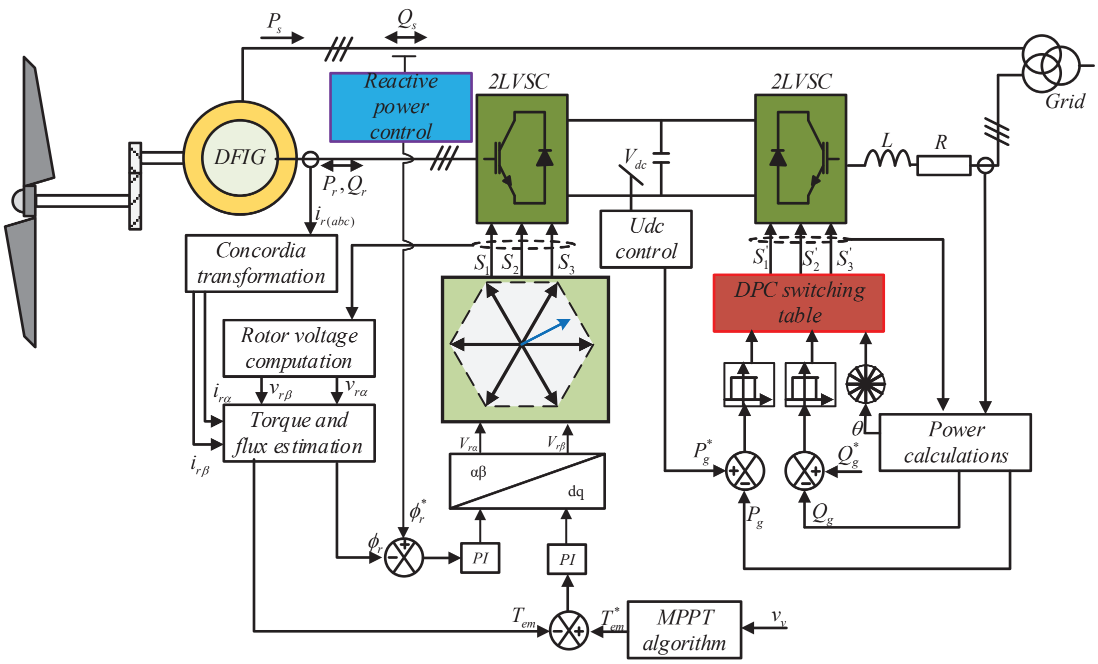

Fig. 1. Global diagram of proposed control scheme.

$$\begin{cases} V_{sd} = R_s i_{sd} + \dfrac{d\varphi_{sd}}{dt} - \omega_s \varphi_{sq} \\ V_{sq} = R_s i_{sq} + \dfrac{d\varphi_{sq}}{dt} + \omega_s \varphi_{sd} \\ V_{rd} = R_r i_{rd} + \dfrac{d\varphi_{rd}}{dt} - \omega_r \varphi_{rq} \\ V_{rq} = R_r i_{rq} + \dfrac{d\varphi_{rq}}{dt} + \omega_r \varphi_{rd} \end{cases} \tag{1}$$

Where, V_{sd} , V_{sq} , V_{rd} and V_{rq} are respectively the stator and rotor voltages in the d-q frame; i_{sd} , i_{sq} , i_{rd} and i_{rq} are respectively the stator and rotor currents in the d-q frame; R_s and R_r are the phase resistance of the stator and rotor, respectively; ω_s and ω_r are the stator and rotor current pulses, respectively.

The magnetic fluxes of the DFIG are defined as follows:

$$\begin{cases} \varphi_{sd} = L_s i_{sd} + M i_{rd} \\ \varphi_{sq} = L_s i_{sq} + M i_{rq} \\ \varphi_{rd} = L_r i_{rd} + M i_{sd} \\ \varphi_{rq} = L_r i_{rq} + M i_{sq} \end{cases} \tag{2}$$

Where, φ_{sd} , φ_{sq} , φ_{rd} and φ_{rq} are respectively the stator and rotor fluxes in the d-q frame; L_s , L_r and M are respectively the stator and rotor inductances and the mutual inductance.

The mechanical torque at the wind turbine shaft is given by Eq. 3.

Identify applicable sponsor/s here. If no sponsors, delete this text box. (sponsors)

$$T_m = \frac{\pi}{2\lambda} \cdot \frac{C_p(\lambda, \beta).\rho.R^3.v_v^2}{G} \tag{3}$$

Where, ρ air density, R rotor radius, G the multiplier gain and v_v wind speed. C_p : represents the power coefficient, a function of the speed ratio λ and blade pitch angle β .

Electromagnetic torque can be written as a function of rotor current and flux, as indicated in the following expression:

$$T_{em} = P(\varphi_{rd} i_{rq} - \varphi_{rq} i_{rd}) \tag{4}$$

III. Design of SVM-DRPC

The block diagram of the proposed control is shown in Fig. 1. The outputs of the two PI controllers for the control variables design the reference voltage vector (amplitude/angle) in the stationary αβ frame (Fig. 2). To generate the reference voltage vector at the converter output, the SVM technique allocates a fair application time for the two adjacent vectors. An application time is allocated to the zero-voltage vector to complete the sampling period. As a result, a fixed switching frequency is obtained. The application times of the adjacent vectors and the zero vector are given by the following equations.

$$T_k = \frac{\sqrt{3}.T_s.V_r^*}{U_{dc}} \sin\left(\frac{k}{3}\pi - \theta\right) \tag{5}$$

$$T_{k+1} = \frac{\sqrt{3}.T_s.V_r^*}{U_{dc}} \sin\left(\theta - \frac{k-1}{3}\pi\right) \tag{6}$$

Where, T_k and T_{k+1} respectively represent the duration of the first and second adjacent vectors and T_0 represents the duration of the zero-vector.

$$T_0 = T_s - T_k - T_{k+1} \tag{7}$$

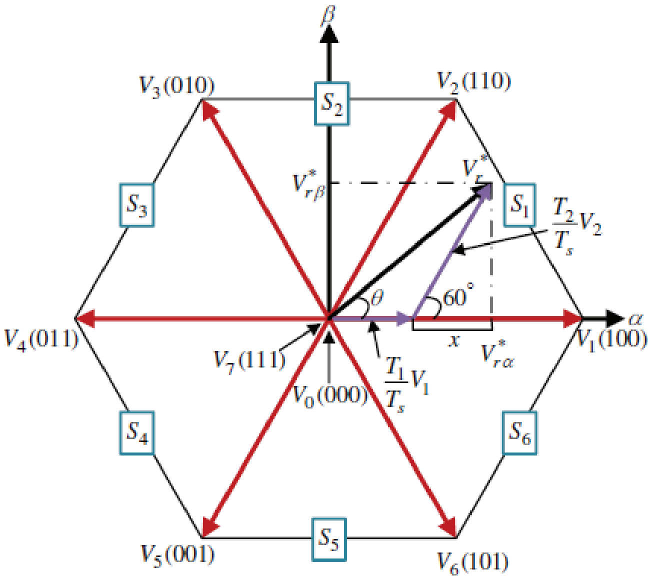

Fig. 2. Projection of reference voltage vector.

IV. Grid Side Converter (CCR) Control

The GSC is the intermediary between the rotor side converter (RSC) and the grid. Its main task is to transport active and reactive power between these two elements. One of the most commonly used controls in recent years is direct power control (DPC). It does not require the Park transform and PWM modulation block. To control the active and reactive power transmitted by the GSC, you simply need to know the instantaneous values of the powers and the position of the voltage vector applied to the GSC. Based on these three parameters, a switching table is constructed for direct selection of the appropriate voltage vector.

Active/reactive power can be determined from GSC voltage and current according to the following equation.

$$\begin{cases} P_g = V_{G\alpha} i_\alpha^{'} + V_{G\beta} i_\beta^{'} \\ Q_g = V_{G\alpha} i_\beta^{'} - V_{G\beta} i_\alpha^{'} \end{cases} \tag{8}$$

To better locate the position of the GSC voltage vector, the fixed frame is divided into 12 sectors. The following equation is used to obtain the position of the GSC voltage vector.

$$(n-2)\frac{\pi}{6} \le \theta_n \le (n-1)\frac{\pi}{6}\ ;\ n = 1, 2, .., 12 \tag{9}$$

The selection of the appropriate voltage vector by the DPC control is made by applying the rules in Table 1. Where 1 represents the hysteresis controller output, when the error is greater than the positive level of the hysteresis band, and 0 when the error is less than the negative level of the hysteresis band. The schematic diagram of DPC control of GSC is shown in Fig. 1.

V. Simulation Results

A simulation is run on MATLAB/Simulink to test the proposed control technique. Fig. 3 shows the wind speed profile. The evolution of electromagnetic torque, stator reactive power and reactive power at the point of common coupling (PCC) are illustrated in Figs. 4, 5 and 6 respectively. Simulation results for torque, stator reactive power and PCC reactive power obtained using the SVM-DRPC technique show satisfactory improvements over conventional ST-DRPC control. Considerable ripple reduction is achieved.

The evolution of the three rotor phases current is shown in Fig. 7. Fig. 8 shows the evolution of the power coefficient of the WT. Operation with optimum extraction of wind power is ensured. The DC bus voltage and reactive power at GSC are shown in Figs. 9 and 10 respectively. The dc bus voltage follows its reference despite the variation in DFIG speed, while operation with a unity power factor is obtained on the rotor side when the reactive power is set to zero at GSC. Figs. 11 and 12 show, respectively, the harmonic spectrum of the stator current for the ST-DRPC control and the proposed SVM-DRPC technique. The total harmonic distortion (THD) is lower with SVM-DRPC than with ST-DRPC. The improvement in stator current shape is around 55%.

Table I. DPC switching table for GSC control

H_P	H_Q	***Sectors***											
		N_1	N_2	N_3	N_4	N_5	N_6	N_7	N_8	N_9	N_{10}	N_{11}	N_{12}
0	1	V_6	V_1	V_1	V_2	V_2	V_3	V_3	V_4	V_4	V_5	V_5	V_6
	0	V_1	V_2	V_2	V_3	V_3	V_4	V_4	V_5	V_5	V_6	V_6	V_1
1	1	V_7	V_7	V_0	V_0	V_7	V_7	V_0	V_0	V_7	V_7	V_0	V_0
	0	V_6	V_7	V_1	V_0	V_2	V_7	V_3	V_0	V_4	V_7	V_5	V_0

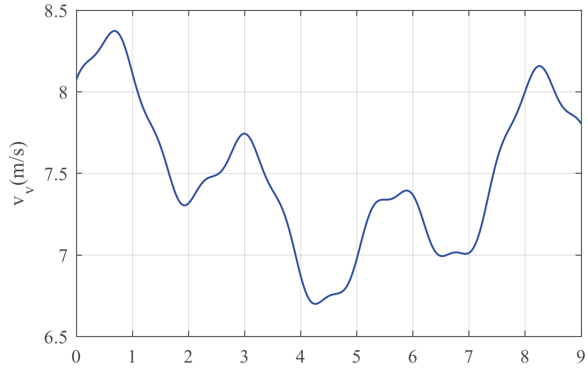

Fig. 3. Wind speed profile.

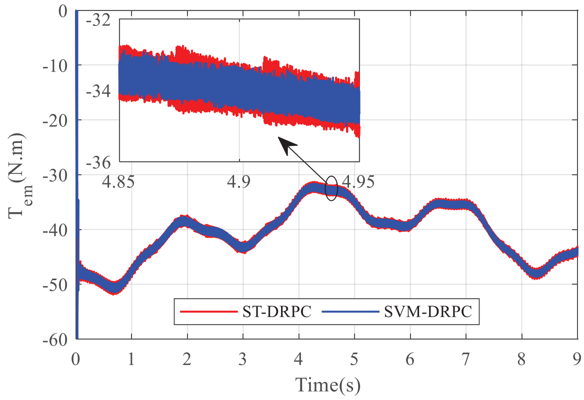

Fig. 4. Evolution of electromagnetic torque with zoom.

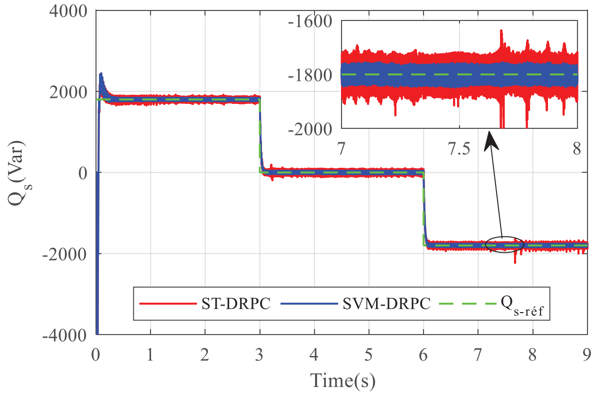

Fig. 5. Stator reactive power curve with zoom.

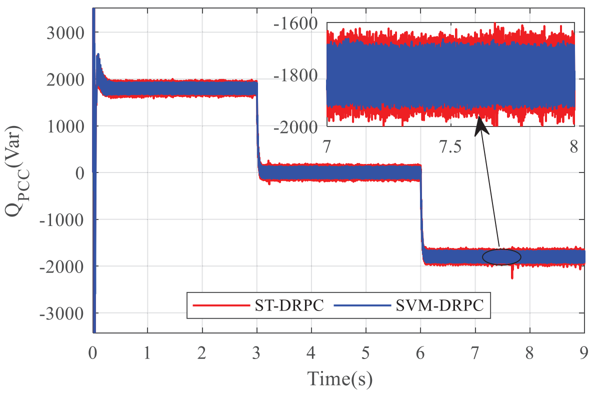

Fig. 6. Reactive power curve at the point of common coupling (PCC), with zoom.

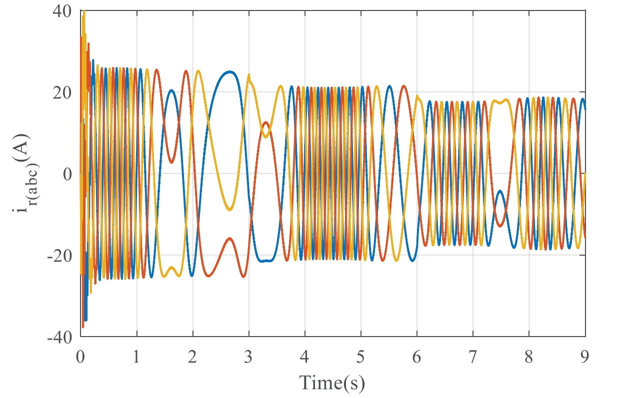

Fig. 7. Rotor current evolution.

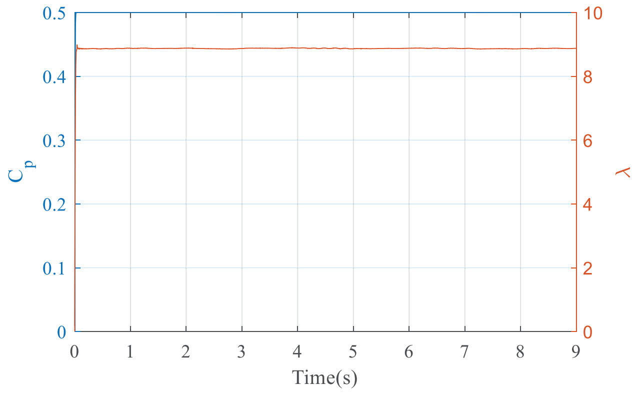

Fig. 8. Power coefficient and speed ratio of WT.

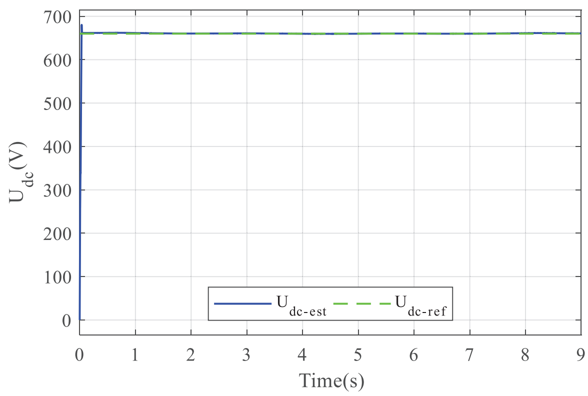

Fig. 9. DC bus voltage curve.

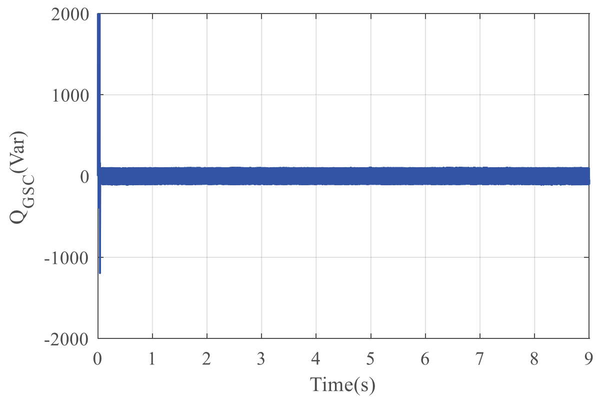

Fig. 10. Reactive power curve at the GSC.

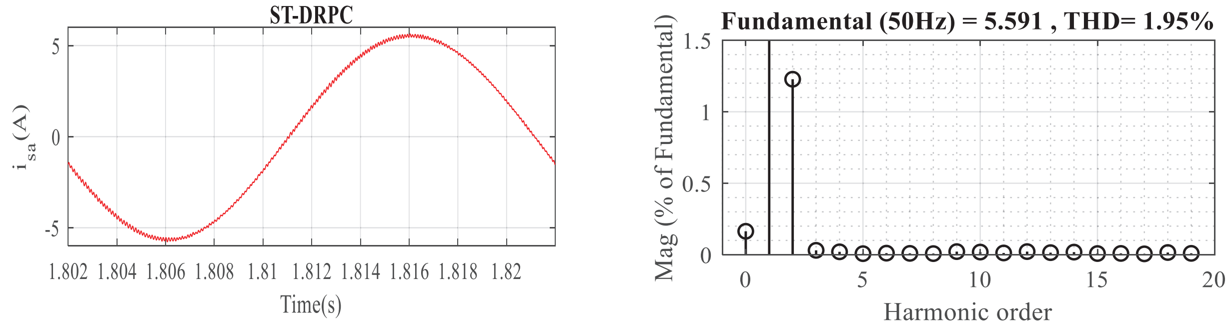

Fig. 11. Spectral analysis of the stator current obtained with the ST-DRPC.

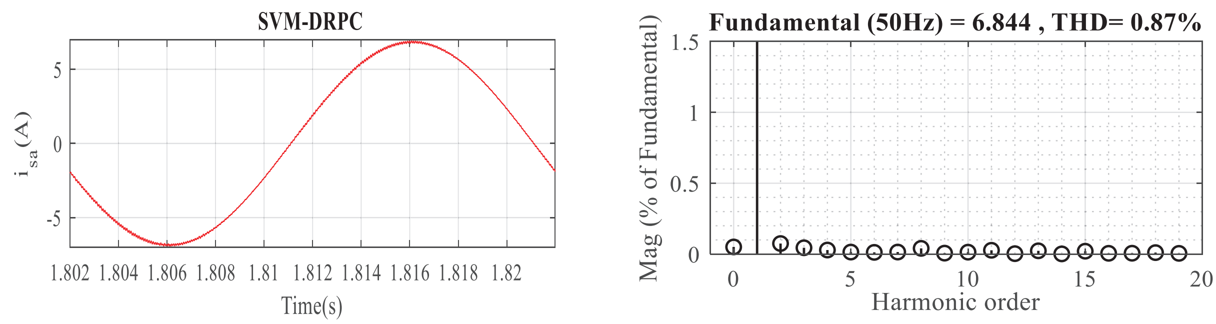

Fig. 12. Spectral analysis of the stator current obtained with the SVM-DRPC.

I. CONCLUSION

In this work, an improved SVM-DRPC control is applied to the WT-DFIG drive. The main objective is to reduce the ripples that occur in electromagnetic torque and rotor flux with ST-DRPC. Simulation results show improved performance, a significant reduction in electromagnetic torque ripples and stator reactive power when the DRPC drive is equipped with the SVM modulation technique. In addition, the DC bus voltage follows its reference perfectly during the simulation.

REFERENCES

[1] S.Kouadria, E.Berkouk, Y.Messlem, M.Denaï,''Improved control strategy of DFIG-based wind turbine using direct torque and direct power control techniques,'' Journal of Renewable and Sustainble Energy. 10(4), 2018.

[2] N. El Ouanjili, A. Derouich, A. Ghzizal, M. Taoussi, Y. El Mourabit, Mezioui, K., Bossoufi, B. ''Direct torque control of doubly fed induction motor using three-level NPC inverter'', Protection and control of Modern Power System, 4(17), 2019.

[3] S.Tamalouzt, N.Benyahia, T.Rekioua, D.Rekioua, R.Abdessamed ''Performances analysis of WT-DFIG with PV and fuel cell hybrid power sources system associated with hydrogen storage hybrid energy system,'' International Journal of Hydrogen Energy. In press, 43(45), pp.21006-21021, 2016.

[4] S. Tamalouzt, '' Performances of direct reactive power control technique applied to three-level inverter under random behavior of wind speed'', Rev. Roum. Sci. Techn.– Électrotechn. et Énerg, 64(1), pp. 33–38, 2019.

[5] O. Djoudi, S. Lalouni Belaid and S.Tamalouzt, "Multilevel Converter and Fuzzy Logic Solutions for Improving Direct Control Accuracy of DFIG-based Wind Energy System", Periodica Polytechnica Electrical Engineering and Computer Science, 67(2), pp. 136–148, 2023.

[6] A.Ammar, A.Bourek, A.Benakcha, '' Nonlinear SVM-DTC for induction motor drive using input-output feedback linearization and high order sliding mode control,'' ISA transactions, pp.428-442, 2017.

[7] R. Gupta, G. Dynamina, '' Matlab simulation of DTC-SVM of double fed induction generator for wind energy system '', In: Innovation in Power and Advanced Computing Technologies (i-PACT), Vellore, India, 2017.

Power Tracking Optimization of Conventional MPPTs using Artificial Neural Network Hybrid algorithm

Bentrad Moutaz Bellah
Electrical Department ,LGEB
Mohamed Khider university
Annaba, Algeria
moutazbellah.bentrad@univ-biskra.dz

Bahi Tahar
Electrical Department ,LASA
Badji Mokhtar university
Annaba, Algeria
tbahi@hotmail.fr

Boulassel Adel
Electrical Department ,LAM2SIN
Badji Mokhtar university
Annaba, Algeria
adel.boulassel@univ-annaba.org

Abstract— **This research conducts a comparison between conventional Maximum Power Point Tracking techniques, specifically Incremental Conductance and Perturb and Observe, and a new hybrid strategy that utilizes Artificial Neural Networks. The hybrid algorithm combines the strengths of Incremental Conductance, Perturb and Observe, and Artificial Neural Networks by leveraging historical data to dynamically fine-tune control parameters. The primarily aim of this study is to showcase the hybrid approach's superiority through various scenarios of solar conditions. It showcases rapid responsiveness to shifts in solar conditions, enhancements in power quality and tracking precision, sustained stability, and a noteworthy increase in power extraction when contrasted with established techniques. The next phase involves real-time simulations using representative solar energy systems. Performance indicators are assessed across diverse scenarios, covering quick fluctuations in irradiance and transient circumstances. Outcomes affirm that the hybrid MPPT approach driven by Artificial Neural Networks surpasses the performance of traditional methods from various perspectives. The central goal is to ascertain the most fitting hybrid MPPT technique by evaluating crucial performance benchmarks, encompassing response time, power quality, tracking precision, stability, and power yield.**

Keywords —Renewable energy, , Hybrid ,Conventional MPPT, Neural network, Solar Conditions.

I. Introduction

Solar energy has emerged as a viable and sustainable source of electricity generation, with photovoltaic (PV) systems playing a crucial role in harnessing this abundant renewable resource. PV systems utilize solar panels equipped with photovoltaic cells to convert sunlight directly into electrical energy. It is an attractive alternative to conventional sources of electricity for many reasons: it is safe, silent, and non-polluting, renewable, highly modular in that their capacity can be increased incrementally to match with gradual load growth, and reliable with minimal failure rates and projected service lifetimes of 20 to 30 years [1, 2]. It requires no special training to operate; it contains no moving parts; it is extremely reliable and virtually maintenance free; and it can be installed almost anywhere. The intensity of the sunlight that reaches the earth varies with time of the day, season, location, and the weather conditions.

Apart from harvesting the resource and decreasing the dependency on fossil fuel because they are limited, one must understand the consequences of using fossil fuels. Burning of fossil fuels for energy has an adverse effect on the environment. It releases CO_2 into the atmosphere which is responsible for the greenhouse effect. Further, it also causes the ozone layer to be depleted. These mentioned phenomena can cause several events to occur such as acid rain, air pollution, land pollution because of excavating operations, etc…3].

Solar energy is the most abundant form of energy available to us. It is approximated that 10000 TW worth of solar energy is incident on earth's surface in a day ,according to a report, the world energy consumption in 2015 was 17.4 TW altogether .There has been a minimal increase in the energy consumption every year, approximately 1-1.5% annual growth. The world's total energy consumption is expected to grow by 56% by the year 2040 .Comparing current consumption, projected growth in two decades, and the amount of solar radiation received in an hour we can just imagine the potential solar energy holds. The total energy consumed is not small fraction of what we receive in an hour [4].

Solar cells are made up of semiconductor materials, such as silicon, which is used to produce electricity. The electricity is conducted as a stream of tiny particles called electrons and the stream is called electric current. A typical solar cell has two layers of silicon, which is n-type at the top and p-type at the bottom. When sunlight strikes the solar cell, the electrons are absorbed by silicon, they flow between n and p-layers to produce electric current and the current leaves the cell through the metal contact. The electricity generated is of AC type [5].

The most widely used algorithms are perturb and observe (P&O) [6,7] and incremental conductance (InC) [8]. However, they may suffer from certain limitations, including slow tracking speed, sensitivity to partial shading, and oscillations around the MPP.

In our previous research under 'Power Management of a Solar System using Hybrid Maximum Power Point Tracking Algorithm' name, the Inc technique has been enhanced through using ANN algorithm and then combine both techniques to benefit from both advantages that they acquire in the aim of extracting the maximum amount of power and enhance its quality .

'Power Management of a solar system using adaptive Hybrid algorithm based on Artificial Neural Network and P&O' is another research that holds the same objective through enhancing the performance of P&O technique.

In this work , both results from the previous works will be studied and compared to extract information regarding response time , power quality, tracking ability , stability, and the amount of extracted power from the photovoltaic generator, in the aim of choosing the best MPPT with the best performance under various solar conditions.

II. MODDELISATION

The studied system is composed of photovoltaic panels and a capacitor at the input of the boost converter with a "tracker" of the maximum power point (MPPT), a DC input capacitor, of an inductive filter, and the non-linear load.

A. Photovoltaic generator

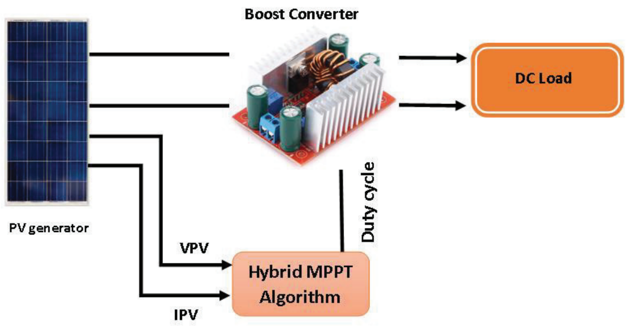

Fig. 1. Hybrid MPPT implimentation in PV generator

1) Photovoltaic model

The equivalent circuit of a photovoltaic (PV) cell is shown in Fig. 2. The current source I_{ph}represents the cell photocurrent. R_{sh} and R_s are the intrinsic shunt and series resistances of the cell, respectively. Usually, the value of R_{sh} is very large and that of R_s is very small, hence they may be neglected to simplify the analysis [9].

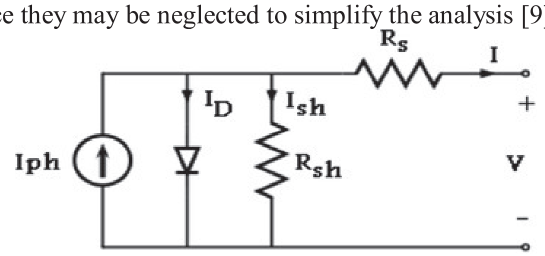

Fig. 2. PV cell equivalent circuit

$$I_{ph} = [I_{sc} + \frac{K_i}{T-298}] \times \frac{I_r}{1000} \quad (1)$$

Here, I_{ph}: photo-current (A); Isc: short circuit current (A) ; K_i : short-circuit current of cell at 25 °C and 1000 W/m^2 ; T: operating temperature (K); I_r : solar irradiation (W/m^2). Module reverse saturation current I_{rs}:

$$I_{rs} = I_{sc}/(e^{\frac{qVOC}{NSknT}} - 1) \quad (2)$$

Here, q= 1.6 × 10−19C: electron load; V_{oc} : open circuit voltage (V); N_s: number of cells connected in series; n: the ideality factor of the diode; k: Boltzmann's constant, = 1.3805 × 10−23 J/K.

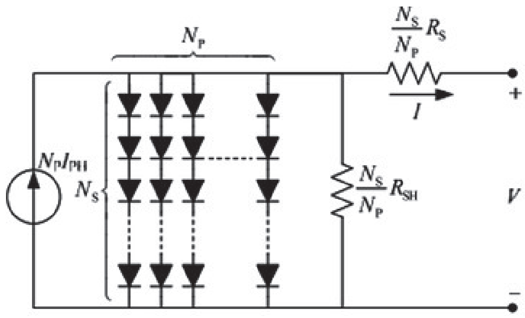

Fig. 3. Equivalent circuit of solar array

For the photovoltaic generator we chose the following profile for the temperature and the irradiation :

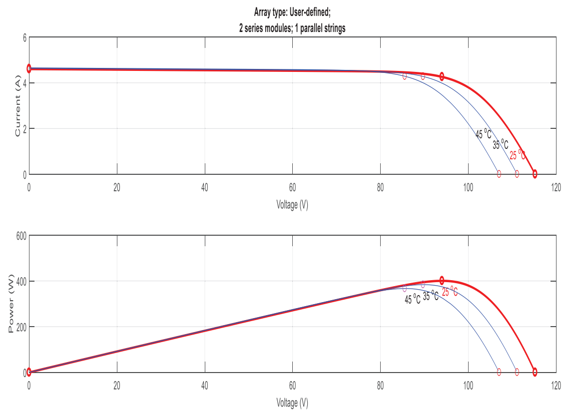

Fig. 4. I-V and P-V characteristics at 1000 W/m^2 and variable temperature of a user defined Module

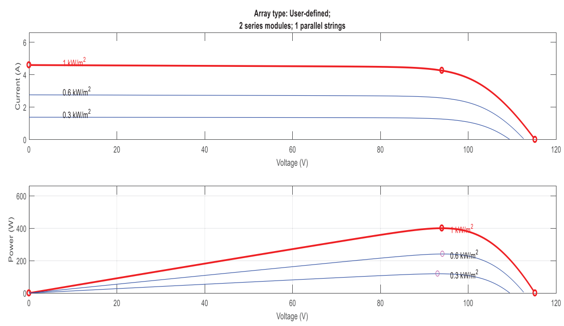

Fig. 5. I-V and P-V characteristics at 25°C and variable irradiance of a user defined Module

TABLE I. PARAMETER OF THE PV MODULE.

Parameter	Value
Cells per module	60
Maximum power	200.22(W)
Open circuit voltage (Voc)	57.6(V)
Short-circuit current (Isc)	4.6(A)
Voltage at maximum power point (Vmp)	47(V)

Current at maximum power point (Imp	4.26(A)
Light-generated current (IL)	4.6092(A)
Diode saturation current (I0)	1.2872e-10(A)
Diode ideality factor	1.5395
Shunt resistance (Rsh)	412.7019(ohms)
Series resistance (Rs)	0.82756(ohms)

B. Boost Converter

A boost converter is a device that converts a DC voltage into another DC voltage of higher value. This type of converter can be used as a load source adapter when the load needs a higher voltage than the PV generator. It is essentially composed of an inductance (L), a capacitor (C), a switch (K) which can take two states 1 and 0 (like IGBT or MOSFET) and a diode (D) [10].,the theoretical transfer function of the boost converter is:

$$\frac{Vout}{Vin} = \frac{1}{1-\alpha} \quad (3)$$

Where, is α is the duty cycle ; V_{out} : output voltage and V_{in} is input voltage.

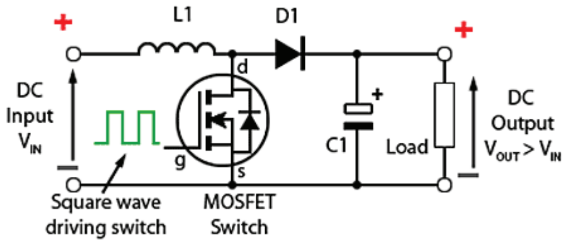

Fig. 6. Boost converter circuit

C. Maximum Power Point Tracking

There are many MPPT algorithm which can be used for implementation via Incremental conductance method, constantvoltage method, Fuzzy logic based method etc. different MPPT algorithms are briefed about their features and limitations as follows [11] .

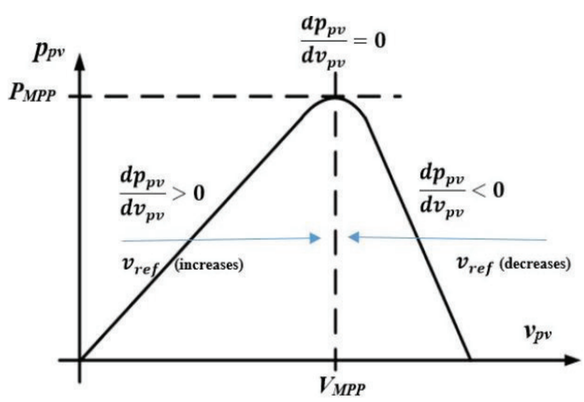

Fig. 7. Maximum power point of a PV array

1) incremental conductance algorithm

The incremental conductance algorithm depends on the slope of the P–V curve, which is affected by the solar irradiation level and load resistance. As the algorithm uses the current and voltage of the PV module in the calculation, the effect of solar irradiation and load changes on the current and voltage of the PV module must be considered in the algorithm[12].

TABLE II. CHANGES IN PV VOLTAGE AND CURRENT DURING CHANGES IN SOLAR IRRADIATION AND LOAD RESISTANCE

		dv	dI
Solar	Increase	Increase	/
Irradiation	Decrease	Decrease	/
Load	Increase	Increase	Decrease
Resistance	Decrease	Decrease	Increase

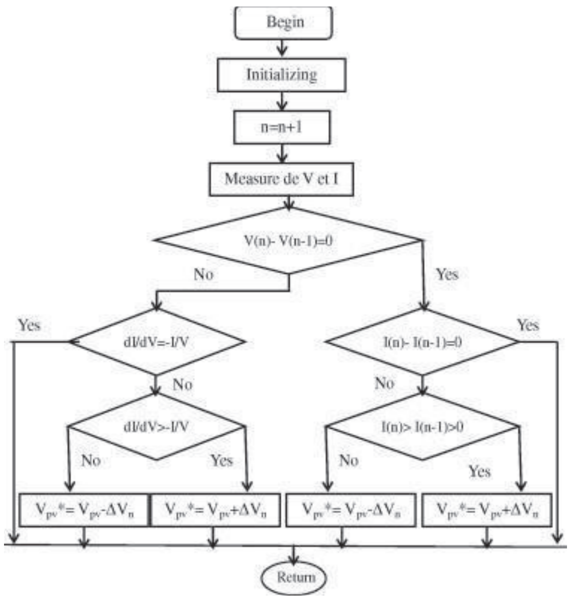

Fig. 8. Incremental conductance Mppt algorithm organizational chart

2) Perturb and observe

It operates by perturbing the system by increasing or decreasing the panel operating voltage and observing the impact of this change on the panel output power [13].

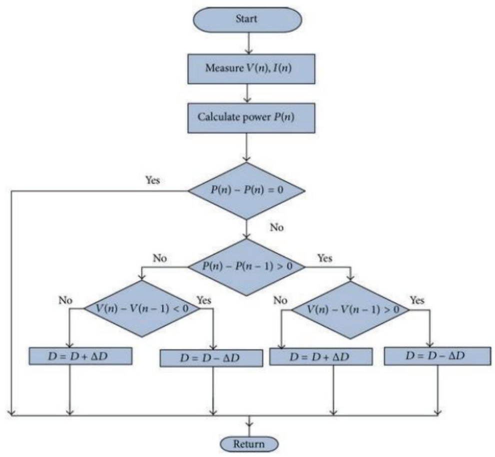

Fig. 9. Perturb&observe Mppt organizational chart

D. ANN algorithm

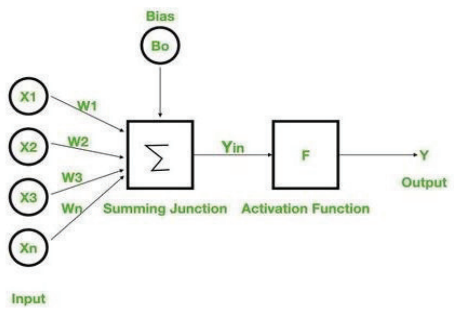

Fig. 10. Neural network structure

The suggested neural network uses historical data containig Ipv , Vpv as inputs and the duty cycle that controls the closing duration of the Mosfet embedded in the PWM which also controls the boost converter to generate maximized power in the output, our ANN uses Backpropagation technique and contains one hidden layer , the latter contains 10 hidden neurones , and each learning process passess by thousand epochs to optimize the performance of the ANN and reduce the resulted error using mean square error (MSE) technique.

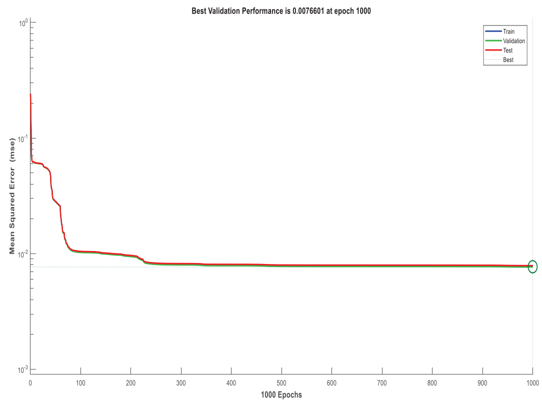

Fig. 11. MSE performance curve

III. RESULTS AND DISCUSSION

The simulation process passes through two major steps : the first one will be dedicated for implimenting the ANN based on the historicl data gathered from the INC technique and another ANN based on P&O and compare the results with the ones gathered from the INC,P&O algorithms , and the second phase will combine both techniques and monitoring the behaviour of the hybridation on the generated output power , it is worth to mention that the simulation process will pass through different solar conditions as follows :

In the first scenario, we maintain a constant temperature of 25 °C and vary the irradiation levels at 300, 600, and 1000 W/m². We monitor and record the generated power of the PV array and the connected load for each irradiation level.

In the second scenario, we keep the irradiation level constant at 1000 W/m² and vary the temperature levels at 25, 35, and 45°C. Similarly, we observe and record the generated power for both the PV array and the load at each temperature level. This analysis allows us to explore how changes in temperature impact the overall performance of the PV system and how it affects the load.

The obtained results are as follows:

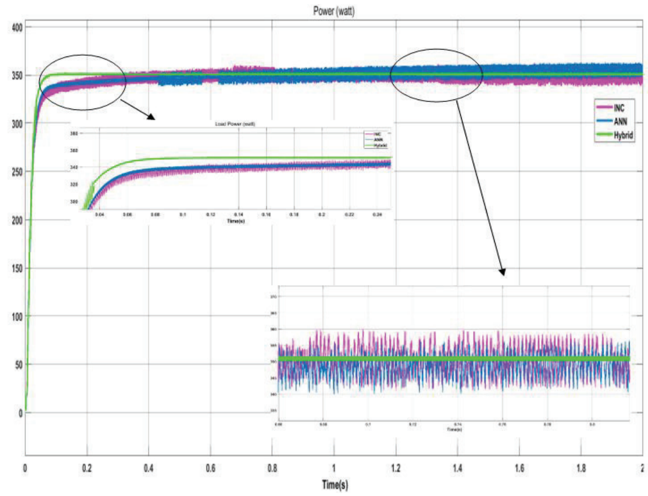

Fig. 12. Output load power using INC,ANN,Hybrid in standard solar conditions

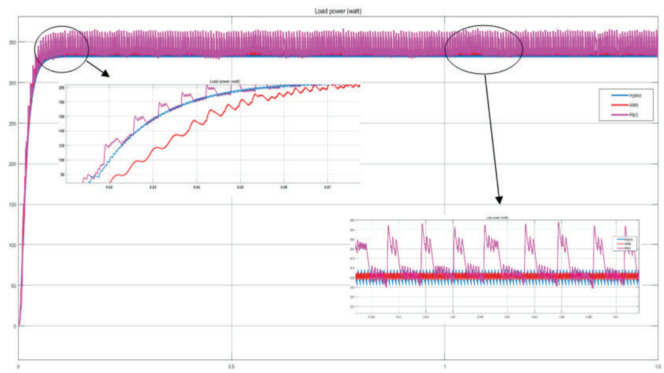

Fig. 13. Output load power using P&O,ANN,Hybrid in standard solar conditions

1st scenario:

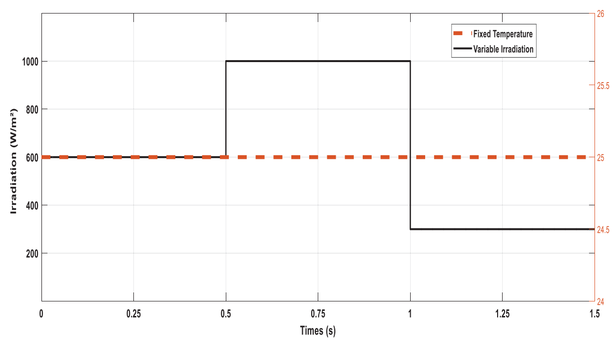

Fig. 14. Temperature and irradiation profile

Incrimental conductance :

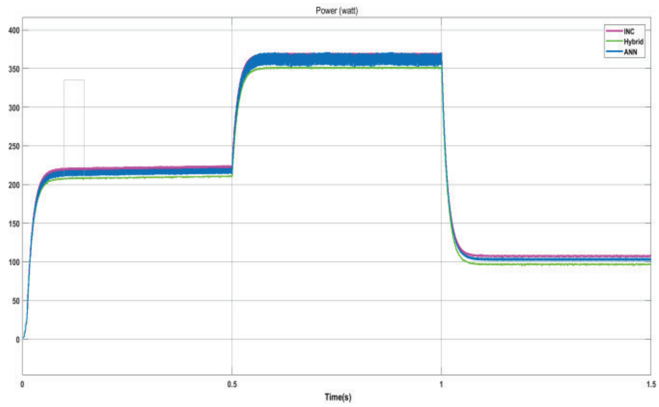

Fig. 15. Output load power using INC,ANN,Hybrid in under variable irradiation conditions

Perturb and Observe MPPT :

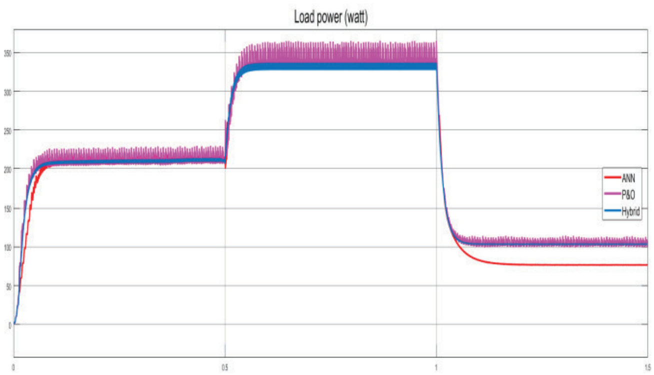

Fig. 16. Output load power using P&O,ANN,Hybrid in under variable irradiation conditions

2nd Scenario :

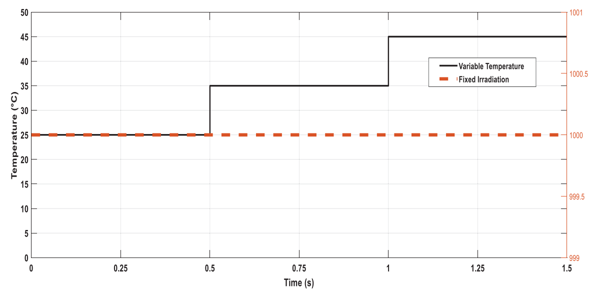

Fig. 17. Temperature and irradiation profile

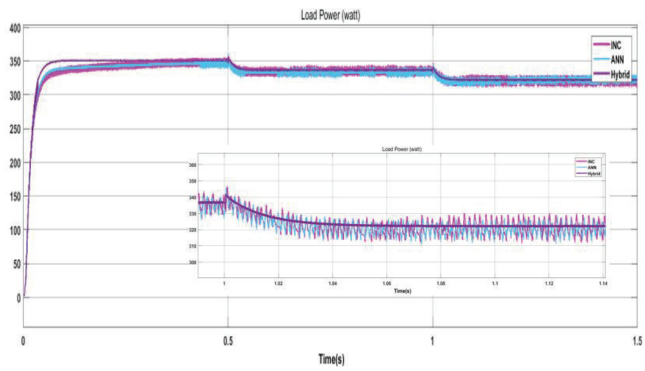

Fig. 18. Load power under ANN,INC and Hybrid MPPT during variable temperature conditions.

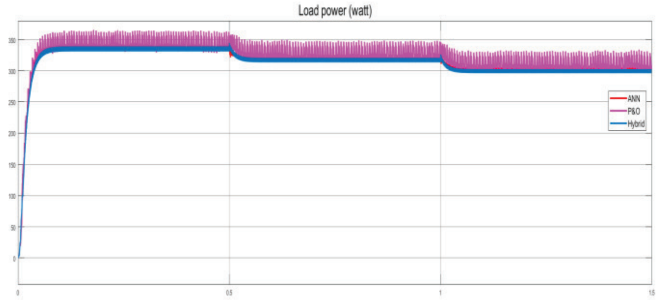

Fig. 19. Output power under ANN,P&O and Hybrid MPPT during variable temperature conditions.

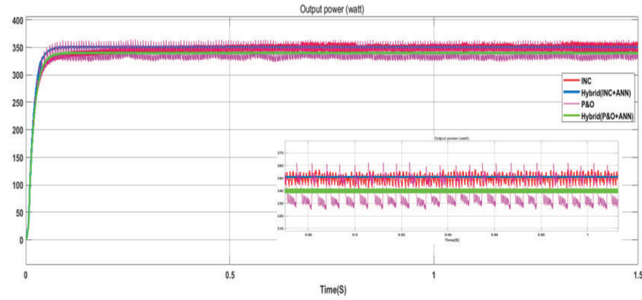

Fig. 20. MPPTs Comparison

TABLE III. MPPT PERFORMANCE TABLE

MPPT Algorithm	Effeciency (%)	Response time(s)
Inc	87.37	0.38
ANN	87.12	0.48
Hybrid (INC+ANN)	87.75	0.066
P&O	86.51	0.068
ANN	83.75	0.08
Hybrid(P&O+ANN)	83.62	0.074

MPPT Algorithm	Tracking	Power quality	Stability	Power extraction	Response time
Inc	X	X	X	✓	X
ANN	X	X	✓	X	X
Hybrid (INC+ANN)	✓	✓	✓	✓	✓
P&O	X	X	X	✓	✓
ANN	X	✓	✓	X	X
Hybrid(P&O+ANN)	✓	✓	✓	X	✓

IV. CONCLUSION

the optimized hybrid algorithm driven by INC emerges as the clear winner, surpassing other techniques in terms of stability, response time, power extraction, and power quality. Its capacity to seamlessly integrate historical data with real-time adaptability contributes to its impressive performance across these vital dimensions. As renewable energy systems demand greater efficiency, the INC-based hybrid algorithm presents itself as a promising solution to elevate photovoltaic system performance to new heights.

REFERENCES

[1] R. W. Ritchie, Using Sunlight for Your Own Solar Electricity: Build Your Own System, Become Independent of the Grid, Domestic Photo Voltaics: Ritchie Unlimited Publications, 1999.

[2] D. G. F. Sonnenenergie, Planning and installing photovoltaic systems: a guide for installers, architects and engineers: Earthscan, 2007.

[3] Richardson, L. (2017, May 14). Solar electricity vs. fossil fuels: how do they compare? Retrieved from Energsage: https://news.energysage.com/solar-energy-vs-fossil-fuels/

[4] Ayaz A. Khamisani, Design Methodology of Off-Grid PV Solar Powered System (A Case Study of Solar Powered Bus Shelter) https://www.eiu.edu/energy/Design%20Methodology%20of%20Off-Grid%20PV%20Solar%20Powered%20System_5_1_2018.pdf

[5] U.S Energy Information Administration. (2013, July 25). EIA projects world energy consumption will increase 56% by 2040. Retrieved from Today in Energy: https://www.eia.gov/todayinenergy/detail.php?id=12251

[6] N. Femia, G. Petrone, G. Spagnuolo, and M. Vitelli, "Optimization of Perturb and Observe Maximum Power Point Tracking Method," IEEE Trans. Aerospace .Electro systems ,vol. 20, no. 4, pp. 963–973, 2005.

[7] N. Femia, G. Petrone, G. Spagnuolo, and M. Vitelli, "Predictive & Adaptive MPPT Perturb and Observe Method," IEEE Trans. Aerospace. .Electro, vol. 43, no. 3, 2007.

[8] A. Safari and S. Mekhilef, "Simulation and Hardware Implementation of Incremental Conductance MPPT With Direct Control Method Using Cuk Converter," IEEE Trans. Indus. Electron vol. 58, no. 4, pp. 1154–1161, 2011.

[9] Xuan Hieu Nguyen, Minh Phuong Nguyen "Mathematical modeling of photovoltaic cell/module/arrays with tags in Matlab/Simulink" Nguyen and Nguyen Environ Syst Res (2015) 4:24

[10] ZIAT Soheir Ibtissem , MEDJAHED nour el houda " Modélisation et simulation d'un système photovoltaïque commandé par la commande MPPT (P&O)" Centre Universitaire Belhadj Bouchaib d'Ain-Temouchent pp. 34, 2019/2020.

[11] Marcelo Gradella Villalva, Jonas Rafael Gazoli, Ernesto Ruppert Filho,"Analysis and simulation of the P&O MPPT algorithm using alinearized PV array model", Industrial Electronics, 2009. IECON '09. 35th Annual Conference of IEEE.

[12] Liqun Shang, Hangchen Guo & Weiwei Zhu, An improved MPPT control strategy based on incremental conductance algorithm,

[13] J. Ahmed, and Z. Salam, " An improved perturb and observe P&O maximum power point tracking (MPPT) algorithm for higher efficiency,"Applied Energy, vol. 150, pp. 97–108, 2015.

Enhancing PV System Maximum Power Point Tracking (MPPT) with KGMO and Fast Terminal Sliding Mode-GWO

Salah Anis Krim[1], Fateh Krim[2], Hamza Afghoul[3]
[1,2,3]Laboratory of Power Electronics and Industrial Control
University of Setif 1. 19000 Setif, Algeria
[1]krimsalahanis@gmail.com, [2]krim_f@ieee.org, [3]hamza.afghoul@gmail.com

Abstract— **A comparative examination of the three MPPT algorithms used for Partial Shading Conditions, Artificial Neuronal Network (ANN) MPPT, Kinetic Gas Molecules Optimization (KGMO) MPPT and Fast Terminal Sliding Mode (FTSM-GWO) MPPT, under consistent shading circumstances, is provided in this contribution. A smart method is to use FTSM and Grey Wolf Optimization (GWO) algorithms under partly shadowed situations on a global MPP. This work now plans to include a GWO methodology that successfully sets the efficient FTSM controller parameters such that the global maximum PV device power point is monitored under partial shade. In the MATLAB setting and test performance, it is programmed for the suggested methodology of changing shade patterns dynamically. The findings have been assessed and compared with ANN, KGMO and FTSM algorithms. Unlike the others, the methodology of monitoring the global MPP in a less accurate way has been found. These methods are also evaluated and contrasted in a PV array under various partial shadowing circumstances. The superiority of FTSM-GWO controller over ANN and KGMO controllers in terms of rapidity, accuracy and stability has been clearly demonstrated.**

Keywords-PV; MPPT; FTSM; GWO; KGMO

I. Introduction

Several approaches are being utilised to maximise the energy from solar cells [1-3]. To improve the efficiency of the nanowire CdS/CdTe solar cell, Dang et al. [4] used a 10 nm thick molybdenum oxide transparent layer. However, single and multiple axis solar trackers are also employed to improve solar insolation gathering [5-11]. Particle Swarm Optimization (PSO)[12] is one of the most used MPPT methods. Motahhir et al.[13] examine MPPT based on PV panel and power converter parameters.It is important that the P&O method has low implementation costs. This method can effectively handle both steady and dynamic environmental variables such as temperature and sun radiation[14]. Alik et al.[15] also employ this approach due of its cheap cost, simplicity, and accuracy. Moshksar et al.[16] suggested a novel MPPT algorithm to increase the installation's performance. Ramos-Hernanz et al.[17] examine three variants of the algorithm P&O in simulation and real life. Others employ the IC MPPT control method, which accurately monitors PV module temperature and follows MPP without oscillations [5].According to Chen et al.[18-20], the IC control method enhances P&O behaviour. They developed a novel IC controller based on fuzzy logic with direct control to overcome the limitations of the traditional control algorithm IC. On the other hand, Ramos-Hernanz et al. Rezk et al. [21] compare four MPPTs: P&O, IC, Hill Climbing (HC), and Fuzzy Logic Controller (FLC).The methods utilised by Cortajarena et al. [22] are HC, P&O, and SMC. Chaieb et al. [23]suggested a novel MPPT-based approach that is both simple and effective. The suggested technique combines the Simplifed Accelerated Particle Swarm Optimization (SAPSO) algorithm with the conventional HC algorithm. The most common approaches are P&O and IC, concludes Li [24]. The P&O approach works effectively when the sun irradiation and temperature are stable. A simple analogue circuit or microprocessor can construct a low-cost P&O controller. However, this approach is slow to monitor the MPP and the output power oscillates around it. The IC approach outperforms the P&O algorithm but is more difficult to implement. Due of their simplicity, P&O and IC control algorithms are used by Bayod-Rujula et al [25]. In certain cases, like as fast changes in irradiance or partial shadowing of the installation, these algorithms are inefficient. Li et al. [26] introduced an MPPT control strategy using Variable Climate Parameters (VWP) that can monitor the MPP more rapidly and compares this novel algorithm to the P&O algorithms and the fuzzy control approach. However, Jamal et al. [27] compared FTSMC to P&O and the traditional SMC algorithm. Controlling the MPPT in partial shade is one of the primary issues in PV systems. According to Mohapatra et al. [28], the choice of MPPT control method relies on the application, hardware availability, cost, convergence time, accuracy, and system dependability. Hadji et al. [29] compared a Genetic Method control algorithm to P&O and IC. Unlike Yatimi et al. [30], who compare P&O with SMC, Ramos-Hernanz et al. [31, 32] proposed a novel SMC-based control method. The algorithm's performance was simulated and compared to actual testing. The simulated findings matched the experimental results well. MPPT may also use fuzzy logic based controllers [33, 34]. In this research, time delay voltages and currents are used. The link between variables is established or learned using fuzzy logic rules. Shahid et al. [5] suggested an incremental conductance based indoor PV system method. The research used a temperature controller to transmit the focused light and solar PV panel temperatures to Standard Test Conditions (STC). A MPPT based on variable step sized incremental conductance algorithm was added to the load side to provide higher power quality. This is the maximum power point of the PV panel, which is identified using a search algorithm. Recently, MPPT algorithms for outdoor solar PV systems have been proposed and implemented [35–38]. The effect of temperature on MPP of solar panels was explored by Yadav et al. [39] and Zahedi [40]. The band gap of the semiconductor material narrows as the PV material's temperature rises, providing electrons greater energy. The decreased band gap increases the carrier and thereby reduces carrier mobility. They recombine on the opposite electrode. Recombination causes saturation current. To test the effect of open circuit voltage on solar cell temperature, Takur et al. Temperature increases with high light concentration in low concentration PV systems, as shown by Yadav et al. [41]. Yadav et al. [42] studied the effect of temperature on solar cell open circuit voltage and MPP at various temperatures.

Therefore, this article presents a comparative analysis using MPPT algorithms with ANN, KGMO and FTSM algorithms. The findings of a computer simulation (MatLab/Simulink) are used to compare the proficiency of the PV system in two separate study: I a standard PV array with uniform solar irradiation simulation . The PV system operates in two separate hardware prototype of PV array operating in two scenarios for partial shading. The paper is structured accordingly; Section 2 defines the PV interface and the interleaved modeling. The MPPT methods are shown in section 3, and the simulation results in section 4. In addition, there is also a presentation on the effectiveness of the MPPT algorithms and the comparative analysis. Finally, Section 5 deals with the conclusions.

II. PROPOSED SYSTEM MODELLING

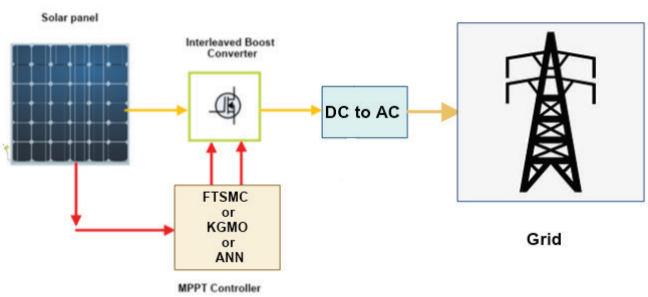

Figure 1. Block diagram of proposed system

A. PV modeling

The imposed PV cell is presented in this article Figure 2, as the current source with an anti-parallel series-related diode and parallel resistance. The circuit description and complete mathematical modeling are described in detail in [20].

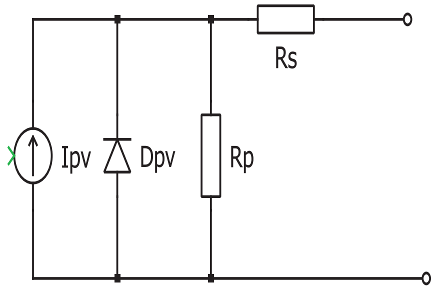

Figure 2. PV model

B. Modified Interleaved Boost Converter

The circuit configuration of the interlocking boost converter as seen in Figure 3 is to maximise the power processing capacity and to operate solar systems at maximum capacity. Interlinked topology step-up converters are working for 180-degree binary branches from each other. Typically each procedure works in the same way as the standard boost converter described above. The current increases in inductor 2, whenever two switches are turned on. At this time diode 2, which is energy-saving induction source 2, has been turned off, so that the output voltages are higher than the input voltage. If two switches are switched off, the two-diode connects and provides the capacitor with energy and load, and the two ramps with a path downstream current depending on the difference between the source and the load voltage. Apply a transition to complete the same case loop one-half of a switching time later. Due to an efficient improvement in the switching frequency, the interleaved boost converter offers a low winging strength at the input level, thereby minimizing output and input condenser filters that are comparatively high if a traditional boost transformer is used [11]. Additionally, the transfer and division of the current between the two arms leads to better stability, minimising major power losses (I^2R). Moreover, the changing of the input current between both weapons reduces dramatically power losses by shifting and dividing them (I^2R). In addition, the converter puts low stress on the passive and active components because of the existing partitions, which increase power process capacity[12][13][14][15]. In the other hand, with the connected boost converter, the sum of pology components that can lead to higher costs is improved.

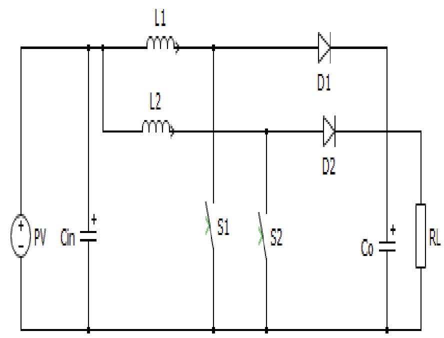

Figure 3. Modified Interleaved boost converter

III. MAXIMUM POWER POINT TRACKING

To harvest maximum power from the PV panel a charge controller with MPPT capability is proposed in this paper. The two broad categories of MPPT techniques are the indirect techniques and direct techniques. Indirect techniques include the fixed voltage, open circuit voltage and short circuit current methods. In this kind of tracking, simple assumption and periodic estimation of the MPPT are made with easy measurements. For example, the fixed voltage technique only adjusts the operating voltage of the solar PV module at different seasons with the assumption of higher MPP voltages in winter and lower MPP voltages in summer at the same irradiation level. This method is not accurate because of the changing of irradiation and temperature level within the same season.

$$V_{MMP} = k.V_{oc} \quad (1)$$

Another most common indirect MPPT technique is the open circuit voltage (OV) method. In this method, it is assumed that k is a constant and its value for crystalline silicon is usually to be around 0.7 to 0.8. This technique is simple and is easier to implement compared to other techniques. However the constant k is just an approximation Leading to reduced efficiency, and each time the system needs to find the new open circuit voltage (Vout) when the illumination condition changes. To find the new open circuit voltage, each time the load connected to the PV module must be disconnected causing power loss. Direct MPPT methods measure the current and voltage or power and thus are more accurate and have faster response than the indirect methods. Perturb and observe (P&O) is one of the direct MPPT techniques, which is used here with some modifications.

Typically, P&O method is used for tracking the MPP. In this technique, a minor perturbation is introduced to, cause the power variation of the PV module. The PV output power is periodically measured and compared with the previous power. If the output power increases, the same process is continued otherwise perturbation is reversed. In this algorithm perturbation is provided to the PV module or the array voltage. The PV module voltage is increased or decreased to check whether the power is increased or decreased. When an increase in voltage leads to an increase in power, this means the operating point of the PV module is on the left of the MPP [26]. Hence further perturbation is required towards the right to reach MPP. Conversely, if an increase in voltage leads to a decrease in power, this means the operating point of the PV module is on the right of the MPP and hence further perturbation towards the left is required to reach MPP. The flow chart of the adopted FTSM algorithm for the charge controller is given in Fig. 5. When the MPPT charge controller is connected between the PV module and battery, it measures the PV and battery voltages. After measuring the battery voltage, it determines whether the battery is fully charged or not. If the battery is fully charged (12.6 V) at the battery terminal) it stops charging to prevent battery over charging. If the battery is not fully charged, it starts charging by activating the DC/DC converter. The microcontroller will then calculate the existing power Pnew at the output by measuring the voltage and current, and compare this calculated power to the previous measured power Pold. If Pnew is greater than Pold, the PWM duty cycle is increased to extract maximum power from the PV panel. If Pnew is less than Pold, the duty cycle is reduced to ensure the system to move back to the previous maximum power. This MPPT algorithm is simple, easy to implement, and low cost with high accuracy [26–28].

IV. PROPOSED TECHNIQUES

A. Fast Terminal Sliding Mode Controllers

The strategy of FTSM switches involves the tuning of a set of unknown parameter α_k ,β_k, γ_k and λ_k as shown in Figure 4. The assortment of these operative bounds is a hard and time-consuming problem. Since the iterative trials-errors procedures become ineffective, such a tuning problem is formulated as a constrained optimization program as follows: (25)

$$Minimize\ f_i(k,t)$$
$$k = (\alpha_i, \beta_i, \gamma_i, \lambda_i,)^T$$
$$Subject\ to: \quad g_1(k,t) = \delta_z - \delta_z^{max} \leq 0;\ g_2(k,t) = \delta_\emptyset - \delta_{z\emptyset}^{max} \leq 0; g_3(k,t) = \delta_\theta - \delta_\theta^{max} \leq 0\ ;\ g_4(k,t) = \delta z - \delta zmax \leq 0 \quad (11)$$

$$k_1(t) = V_{PV}(t)\ , k_2(t) = I_{PV}(t)\ ,$$
$$k_3(t) = V_b(t)\ ,\ \ k_{ref}(t) = V_{ref}(t) \quad (12)$$

and the structure (12) becomes

$$\dot{k}_1 = \frac{(-k_2 + I_{PV})}{S_1} \quad (13)$$

$$\dot{k}_2 = f_1(k) + g_1(k)d(t) \quad (14)$$

$$\dot{k}_2 = f_2(k) + g_2(k)d(t \quad (15)$$

where $k = [k_1 \quad k_2 \quad k_3]^T \quad (16)$

$$f_{1(k)} = \frac{k_1}{M} - \frac{R_s}{L\left(1+\frac{R_s}{R}\right)}k_2 + \frac{1}{L}\left(\frac{R_s}{(R+R_s)} - 1\right)k_3 - \frac{V_D}{L}$$

(17)

$$g_{1(k)} = -\frac{R_s}{L\left(1+\frac{R_s}{R}\right)}k_2 + \frac{1}{L}\left(\frac{R_s}{(R+R_s)} - 1\right)k_3 + \frac{V_D}{L} \quad (18)$$

$$f_{2(k)} = \frac{1}{S_2\left(1+\frac{R_s}{R}\right)}k_2 - \frac{1}{S_2(R+R_s)}k_3 \quad (19)$$

$$g_{2(k)} = \frac{1}{S_2\left(R+\frac{R_s}{R}\right)}k_2 \quad (20)$$

B. KGMO-Based MPPT Algorithm

The basic principle of the Kinetic gas molecule optimization (KGMO) algorithm was suggested with the laws of gas molecules.

The molecular kinetic concept of idyllic gases is described as follows:

1. A gas consists of a group of particles that are transportable in a conventional. Motion of gas particles is based on Newton's law.
2. Particles within a gas are sockets and do not inhabit any volume.
3. The bump of particles is flexible; hence, no energy is increased or vanished throughout the bump.

4. There are no attractive or repulsive forces that exist among the particles.

5. The avg KE of a particle. velocity of particle is updated and position of particle is updated.

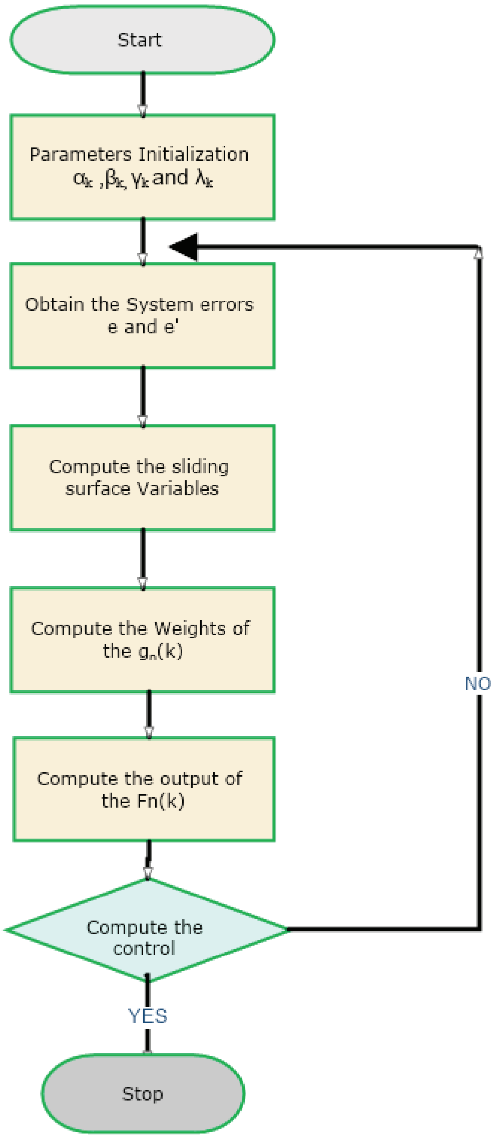

Figure 4.. Flow chart of FTSM controller.

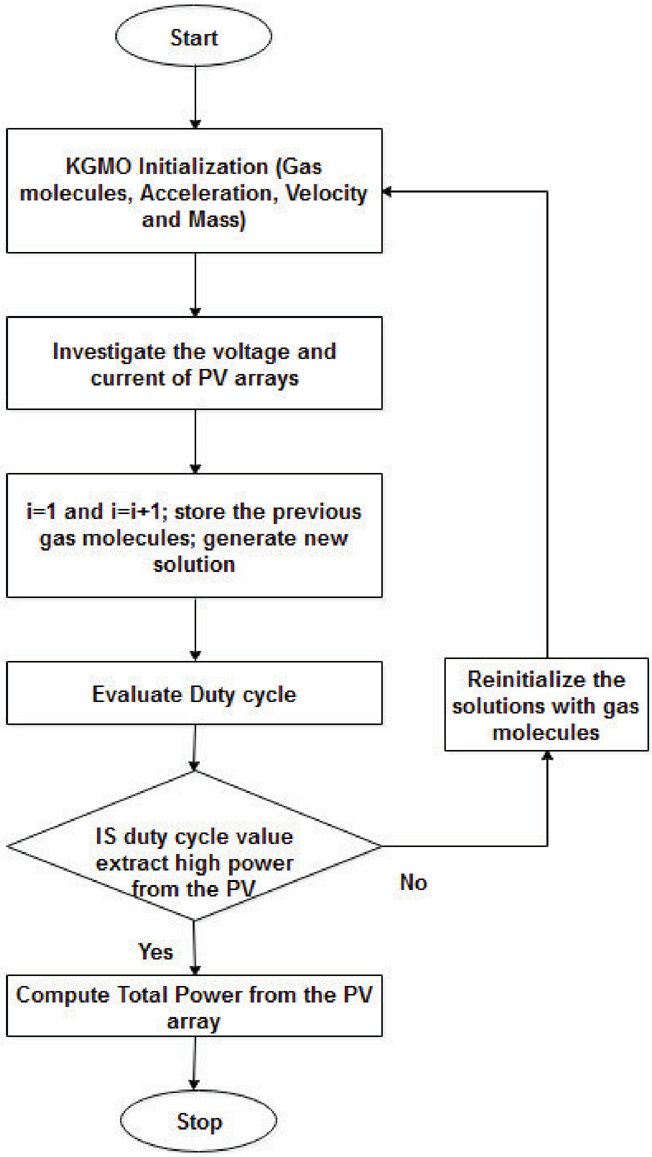

Figure 5. Flow chart of KGMO controller

This segment outlines the kinetic optimization development with gas molecules. The gas particles move within the vessel till they meet at the part of the vessel which has the least temperature and kinetic energy (KE). Gas particles interact with each other based on low intermolecular electric forces, where the electric force is the outcome of progressive and adverse loads in the particles. In this method, each gas particle and the agent have four features: position, KE, speed and mass. The kinetics of every gas particle determines the speed and location of the gas molecule. In this method, the gas particles discover the whole research space and achieve the lowest temperature. The flowchart of KGMO algorithm is represented in Figure 5.

V. SIMULATION OUTCOMES

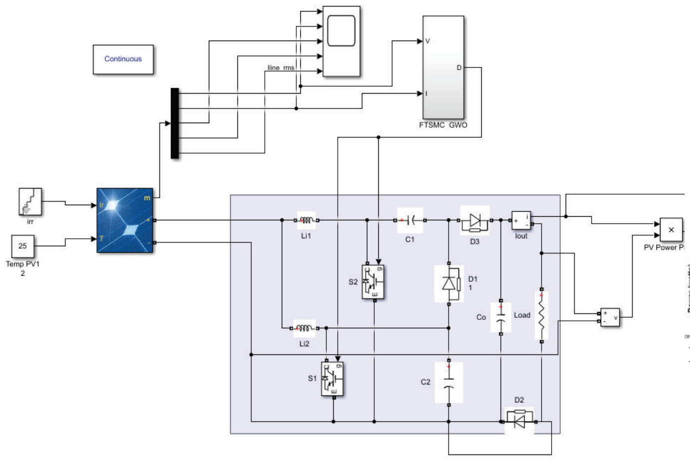

Figure 6. Simulink model diagram of the proposed system

The efficiencies were determined according to the measured input and output power. Figure 7 represents the results for a conventional controller. As shown in Figures 8 to 10, compared to the conventional charge controller, the developed MPPT charge controllers significantly improve efficiency for each of the test time. These results prove that maximum power is harvested from the PV module by using the MPPT charge controller. When the battery is fully charged (12.6 V), the MPPT charge controller still provide low current (5 mA) to avoid self-discharge of the battery. Hence, the overall efficiency is improved by using the FTSM- GWO MPPT charge controller. These results are also depicted in Figs. 9.

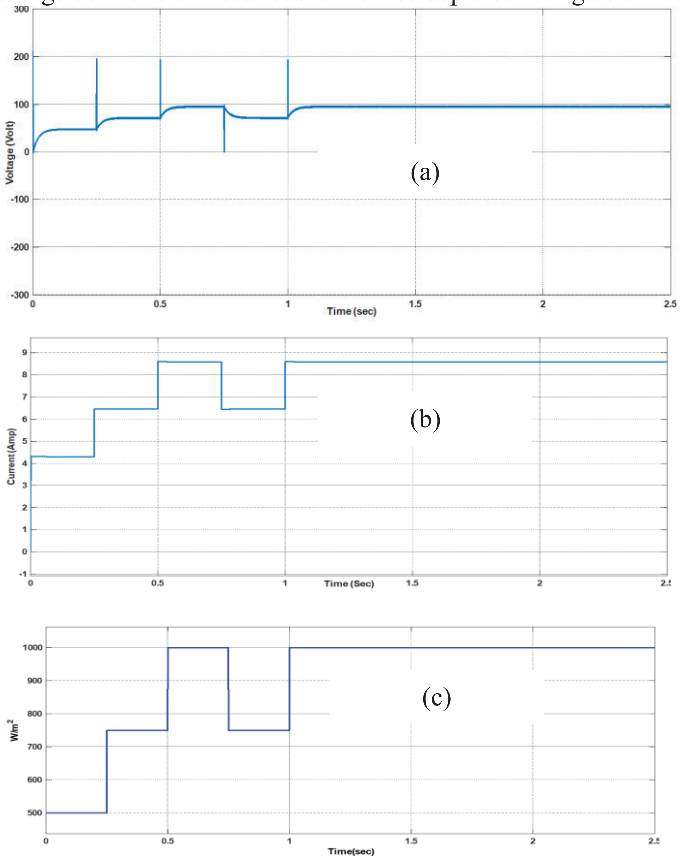

Figure 7. Input variables (a) Input Voltage (b) Input current (c) Irradiation

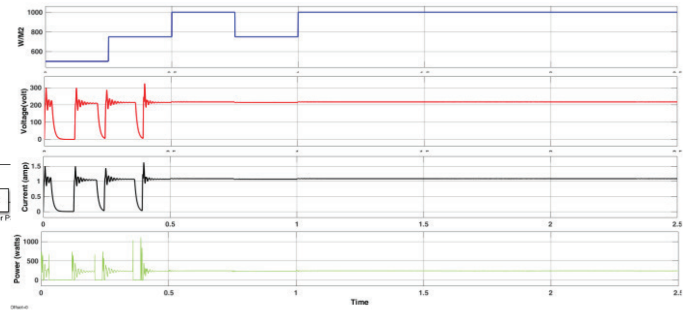

Figure 8. ANN based MPPT Output Power, Output Voltage, Output Current (V_{in}=100, I_{in}=8.6, D=0.5 and V_{out} =217 and I_{out}=1.08, P_{out}=234)

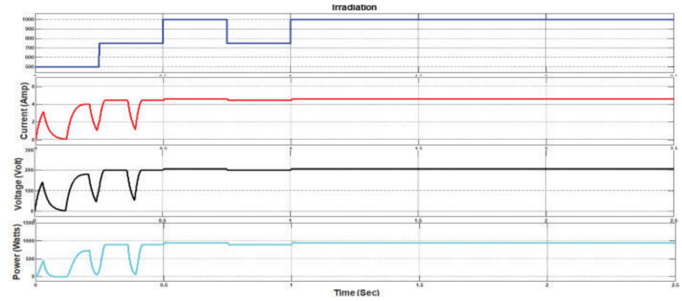

Figure 9. KGMO based MPPT Output Power, Output Voltage, Output Current (V_{in}=100, I_{in}=8.6, D=0.5 and V_{out} =200 and I_{out}=4.3, P_{out}=860)

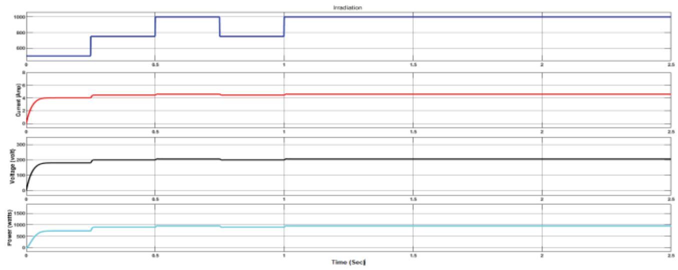

Figure 10. FTSMC-GWO based MPPT Output Power, Output Voltage, Output Current (V_{in}=100, I_{in}=8.6, D=0.5 and V_{out} =200 and I_{out}=4.8, P_{out}=960)

CONCLUSION

In this work, MPPT controllers based on KGMO and FTSM-GWO are constructed in order to extract the maximum amount of power possible from a PV module. The results of the simulation show that the FTSM approach has a short response time during transients and a low power oscillation during steady states. This was demonstrated as one of the benefits of using the technique. In addition to this, it is able to quickly follow rapid changes in the amount of solar irradiation and has a little power oscillation when the amount of solar irradiation is changing slowly. In other words, it is rather impressive. As a direct consequence of this, in contrast to the ANN, and KGMO algorithms, this approach is not only more rapid but also more accurate. In summary, the performance of the multilayer FTSM controller is satisfactory in terms of identifying and monitoring the MPP in environments in which the weather is in a state of continual flux. The future work will consider the experimental validation of the obtained results.

REFERENCES

[1]. A. A. Kulaksiz and R. Akkaya, "A genetic algorithm optimized ANN-based MPPT algorithm for a stand-alone PV system with induction motor drive". Sol. Energy 86, 2020, pp. 2366–2375..

[2] J. Manuel Lopez-Guede, E. Zulueta, U. Fernandez-Gamiz, and F. Oterino, "Systematic modeling of photovoltaic modules based on artifcial neural networks". Int J Hydrogen Energy 41, 2016, pp. 12672–12687.

[3]. H. Shahid. et al. « Design and modeling of an optical band gap matched temperature controlled indoor concentrated light transmission system for photovoltaic energy production." Optik 176, 2020, pp.502–511.

[4]. H. Dang and V.P. Singh "Nanowire CdS-CdTe solar cells with molybdenum oxide as contact." Sci. Rep. 5, 2015, pp. 48-59.

[5. H. Shahid et al." Implementation of the novel temperature controller and incremental conductance MPPT algorithm for indoor photovoltaic system". Sol. Energy 163, 2018, pp. 235–242 .

[6]. R. I. Putri, S. Wibowo and M. Rifai, " Maximum power point tracking for photovoltaic using incremental conductance method". 2nd International Conference on Sustainable Energy Engineering and Application ,Icseea 2014 Sustainable Energy for Green Mobility 68, 2014, pp. 22–30.

[7]. K.K.Kumar, R. Bhaskar and H. Koti, "Implementation of MPPT algorithm for solar photovoltaic cell by comparing short-circuit method and incremental conductance method." 7th International Conference Interdisciplinarity in Engineering (Inter-Eng 2013) 12, 2014, pp. 705–715.

[8]. M. Kamran et al. "Implementation of improved Perturb & Observe MPPT technique with confned search space for standalone photovoltaic system." J. King Saud Univ. Eng. Sci. 2021, pp. 212-219.

[9]. E. K. Anto, J.A Asumadu and P. Y. Okyere, "PID Control for Improving P&O-MPPT Performance of a Grid-Connected Solar PV System With Ziegler-Nichols Tuning Method." Proceedings of the 2016 Ieee 11th Conference on Industrial Electronics and Applications (Iciea), 2016, pp. 1847–1852.

[10]. M.A.Sahnoun, H.M R. galde, J. Carmona and J. Gomand, "Maximum power point tracking using P&O control optimized by a neural network approach: a good compromise between accuracy and complexity." Mediterranean Green Energy Forum 2013: Proceedings of an International Conference Mgef-13 42, 2013, pp. 650–659.

[11]. A. Faizal, R. Sutoyo, A. Mulyono and F. Yendra "Design maximum power point tracking (MPPT) on photovoltaic panels using fuzzy logic method". Am. J. Eng. Appl. Sci. 9, 2016, pp.789–797 .

[12.] M. Mao et al.," A two-stage particle swarm optimization algorithm for MPPT of partially shaded PV arrays." Int. J. Green Energy 14, 2017, pp.694–702 .

[13] S. Motahhir, A. El Hammoumi and A. El Ghzizal, "The most used MPPT algorithms: review and the suitable low-cost embedded board for each algorithm". J. Clean. Prod. 246, 2020, pp. 83-94.

[14] V.K. Devi, K. Premkumar, A.B. Beevi and S. Ramaiyer, "A modifed Perturb & Observe MPPT technique to tackle steady state and rapidly varying atmospheric conditions." Sol. Energy 157, 2017, pp. 419–426.

[15] R. Alik and A. Jusoh. "An enhanced P&O checking algorithm MPPT for high tracking efficiency of partially shaded PV module." Sol. Energy 163, 2018, pp. 570–580.

[16] E. Moshksar and T. Ghanbari, "A model-based algorithm for maximum power point tracking of PV systems using exact analytical solution of single-diode equivalent model." Sol. Energy 162, 2018, pp. 117–131.

[17] J.A .Ramos-Hernanz,. et al. "Study of the behavior of the Perturbation and Observation algorithm for MPPT" ,International Conference on Technical and Physical Problems of Electrical Engineering, 2016.

[18] Y. Chen, Z. Lai and R. Liang, "A novel auto-scaling variable step-size MPPT method for a PV system". Sol. Energy 102, 2014, pp. 247–256..

[19] T. Radjai, , L.Rahmani, S. Mekhilef and J.P. Gaubert," Implementation of a modifed incremental conductance MPPT algorithm with direct control based on a fuzzy duty cycle change estimator using dSPACE". Sol. Energy 110, 2020, pp. 325–337.

[20] J.A amos-Hernanz et al., "Study of the behavior of the Incremental Conductance algorithm for MPPT." 2016 8th International Conference on Electronics, Computers and Artifcial Intelligence (Ecai)., 2016.

[21] H. Rezk, and A. M. Eltamaly, "A comprehensive comparison of different MPPT techniques for photovoltaic systems". Sol. Energy 112, 2020, pp. 1–11.

[22] J.A ortajarena, O. Barambones, P. Alkorta,and J. De Marcos, " Sliding mode control of grid-tied single-phase inverter in a photovoltaic MPPT application." Sol. Energy 155, 2020, pp. 793–804.

[23] H. Chaieb and A. Sakly. "A novel MPPT method for photovoltaic application under partial shaded conditions". Sol. Energy 159, 2018, 291–299

[24]S. Li, " A MPPT control strategy with variable weather parameter and no DC/DC converter for photovoltaic systems." Sol. Energy 108, 2020, pp. 117–125.

[25] A. Bayod-Rujula and J. Cebollero-Abian, "A novel MPPT method for PV systems with irradiance measurement." Sol. Energy 109, 2020, pp. 95–104

[26] S. Li, H. Liao, H. Yuan, Q. Ai and K.A. Chen "MPPT strategy with variable weather parameters through analyzing the effect of the DC/DC converter to the MPP of PV system." Sol. Energy 144, 2017, pp. 175–184.

[27] J. El Khazane and E. H. Tissir, "Achievement of MPPT by fnite time convergence sliding mode control for photovoltaic pumping system." Sol. Energy 166, 2018, pp. 13–20.

[28] A. Mohapatra,, B. Nayak, P. Das and K.B. Mohanty. "A review on MPPT techniques of PV system under partial shading condition." Renew. Sustain. Energy Rev. 80, 2020, pp. 854–867.

[29]S. Hadji, J.P Gaubert and F. Krim, "Teoretical and experimental analysis of genetic algorithms based MPPT for PV systems". in International Conference on Technologies and Materials for Renewable Energy, Environment and Sustainability-Tmrees15 74, 2018, pp.772–787.

[30] H. Yatimi and E. Aroudam, "MPPT algorithms based modeling and control for photovoltaic system under variable climatic conditions". in 11th International Conference Interdisciplinarity in Engineering, Inter-Eng 2017 22, pp. 757–764.

[31] J. Ramos-Hernanz, J. Manuel Lopez-Guede, O. Barambones, E. Zulueta and U. Fernandez-Gamiz, "Novel control algorithm for MPPT with boost converters in photovoltaic systems." Int J Hydrogen Energy 42, 2017, pp.17831–17855 .

[32] J.A. Ramos-Hernanz. et al. "Sliding mode real-time control of photovoltaic systems using neural estimators. " Int. J. Photoenergy, 2018, pp. 521-527.

[33] T.H. Kwan and X. Wu " Maximum power point tracking using a variable antecedent fuzzy logic controller." Sol. Energy 137, 2016, 189–200..

[34] Y. Chen, Y. Jhang and R. Liang "A fuzzy-logic based auto-scaling variable step-size MPPT method for PV systems." Sol. Energy 126, 2020, pp. 53–63.

[35] L. El Bahir, and T. Hassboun, "Accurate Maximum power point tracking algorithm based on a photovoltaic device model. " Int. J. Photoenergy, 2021, pp. 569-581.

[36] M. A. Farahat and M. A. Enany and Nasr, A. "Assessment of maximum power point tracking techniques for photovoltaic system applications." J. Renew. Sustain. Energy 7, 2015, 042702 .

[37] Y. Hong, et al., "maximum power point tracking for a distributed PV system under rapidly changing environmental conditions." IEEE Trans. Power Electron. 30, 2020, pp. 4209–4218.

[38] A P. Bhatnagar and B.R.K. Nema, "Conventional and global maximum power point tracking techniques in photovoltaic applications: a review." J. Renew. Sustain. Energy 5, 2013, 032701.

[39.] P. Yadav, Tripathi, M. Lokhande, and M Kumar, M. "Estimation of steady state and dynamic parameters of low concentration photovoltaic system." Solar Energy Mater. Solar Cells 112, 2020, pp. 65–72.

[40] A. Zahedi, "Review of modelling details in relation to low-concentration solar concentrating photovoltaic". Renew. Sustain. Energy Rev. 15, 2011, pp. 1609–1614..

[41] A. K. Takur, G. Wantz, G. Garcia-Belmonte, J. Bisquert and L. Hirsch "Temperature dependence of open-circuit voltage and recombination processes in polymer-fullerene based solar cells." Solar Energy Mater. Solar Cells 95, 2020, pp. 2131–2135 .

[42] A. S. Yadav, R. K. Pachauri, and Y. K. Chauhan. "Comprehensive investigation of PV arrays with puzzle shade dispersion for improved performance". Sol. Energy 129, 2020, pp. 256–285..

An adaptive microgrid protection coordination scheme based on dual settings DOCRs

Merabet Oussama, Kheldoun Aissa, Bouchahdane Mohamed, Ait Mouloud Louiza
Laboratory of Signals & Systems
Institute of Electrical and Electronic Engineering
University M'hamed Bougara
boumerdes, Algeria
o.merabet@univ-boumerdes.dz
aissa.kheldoun@univ-boumerdes.dz
m.bouchahdane@univ-boumerdes.dz
l.aitmouloud@univ-boumerdes.dz

Belmadani Hamza, Hattabi Intissar
Electronics Department, SET Laboratory
Faculty of Technology
Blida 1 University
Blida, Algeria
belmadanihamza@etu.univ-blida.dz
hattabi_intissar@univ-blida.dz

Abstract— **The microgrid idea might be a viable answer to the rising demand problem. Protection coordination concerns are seen as a barrier for microgrid operation in both islanded and grid-connected modes. The goal of this research is to provide an optimum coordination mechanism for relay configurations in a distribution system. The proposed technique employs dual setting directional overcurrent relays (DS-DOCRs) where the protective relays can work in grid connected and islanded modes of operation and have two separate relay settings. The presented approach is used to test the distribution element of the IEEE 14-bus test system. An optimization algorithm was utilized to calculate the optimal settings using MATLAB, while the power system assessments are performed in DIgSILENT. The test results demonstrate the advantages of the suggested strategy. The coordination optimization problem (COP) using dual settings numerical relays shows that the miscoordination does not occur in both modes of operation when utilizing the suggested technique.**

Keywords: Dual settings relay; optimal coordination; DOCR; optimization algorithm; distribution system.

I. Introduction

Due to their low-cost, green energy generation and minimal maintenance, renewable energy source-based DGs (RES-DGs) such as wind turbine Generator (WTG) and Photovoltaic (PV) have been widely integrated in the distribution network (DN). Therefore, several challenges, notably impacting the traditional protection systems. The dynamic and intermittent nature of these energy sources can potentially disrupt protective relay coordination, thus necessitating adaptive protection strategies. One of the most important microgrid protection components is the direction overcurrent relay (DOCR). TDS and PS are the two types of independent variables in a relay coordination system. Several optimization strategies are presented in order to determine DOCRs optimal settings. Depending on the decision variables, the optimal coordination of overcurrent relays was achieved using linear programming, nonlinear programing or (MINLP) techniques [1]. Only TDS is handled in linear programming, while PS is fixed. The ideal TDS value is found using linear programming (LP) approaches such as root tree optimization (RTO) [2] , genetic algorithm (GA) [3], and so on. Moreover, many optimization techniques have been adopted from numerous studies to handle the coordination optimization problem (COP). The modified firefly algorithm (MFA) was utilized to deal with relay coordination in [4], another work based on the modified African vultures optimizer was presented in [5], Biodiversity Based Optimization, Harris hawk Optimization, Hybrid Whale Optimization, New-rooted Tree Algorithm, gravitational search algorithm (GSA), Gorilla troops optimizer and teaching learning based optimization (TLBO) are some of the numerous researches that have been done to find the best and minimum relay operating time [6]. Several coordination approaches for conventional and dual setting DOCR have been presented using the aforementioned techniques. Because conventional DOCR functions in a single mode of operation, there is only one setting that DOCR uses for both main and backup operations. Whereas, dual setting DOCR can operate independently for both grid connected and islanded mode of operation. In [7], a strategy for the microgrid is adopted and validated in both islanded and grid-connected modes. In [8], the dual setting approach is used to deal with the power distribution system topology, and the transient stability of the associated DGs is taken into account. In reference [9], a comparison of traditional optimization coordination and various optimization techniques in the situation of complex networks was presented. In this work, the IEEE 14-bus test system distribution network, as a meshed distribution system, was chosen to evaluate the suggested research advantages.

An adaptive protection scheme is proposed. The suggested protective strategy based on DS-DOCRs is simulated in two different modes of operations (grid connected and islanded modes). The load flow and short circuit simulations are done in DIgSILENT, and the given optimization issue is handled using an optimization algorithm in the MATLAB environment. The derived optimal DOCR parameters and tripping time are compared to existing techniques.

The innovations and efficacy of this work are highlighted based on the speed of the MG protection system. Section II of this essay will cover the problem formulation. Section III offers proposed method, the optimization technique and the protection scheme used where section IV deals with the test system that is under study, section V discuss the obtained results using the proposed method and section VI concludes.

II. Problem formulation

One of the consequences of an electrical network breakdown is a fast increase in fault current to dangerous levels. The purpose of optimal DOCR coordination is to find the parameters (PS, TDS) that decrease the operation time of the protective relays. Primary relays in the distribution network ensure appropriate fault clearing to prevent equipment connected to the system from malfunctioning. These issues are resolved by improving the plug and clock dial settings. The target function in this work is the total of the operating times of all primary relays responding to line faults. The relay time current characteristics for DOCRs are shown as follows:

$$T_{i,j} = A_i \frac{TDS_i}{\left[\left(\frac{I_{scj}}{PS_i}\right)^{B_i} - 1\right]} \tag{1}$$

Where A and B are constants that vary depending on the kind of overcurrent relay (OCR). These OCRs are typically set to 0.14 and 0.02 respectively, where i is the relay identification and j is the fault site identifier. The terms Iscij and Ipi denote the relay fault current and pickup current, respectively [10]. Each DOCR has a single set of settings for both primary and backup operations. The optimization goal is to reduce the timings of all primary relays while preserving protection coordination conditions. The objective function is therefore expressed as in Eq.(2):

$$\text{Minimize, } T_{op} = \sum_{i=1}^{m} W\, T_{pri} \tag{2}$$

Depending on the variable settings, the goal function is subject to additional Constraints. Because the relay must allow the system to function correctly even in a minor overload scenario, the plug setting should be more than the maximum expected load via the relays.

Furthermore, the plug setting should be smaller than the least fault current detectable by the related relay. In every other scenario, the relay is immune to that fault. Furthermore, PS and TDS must be within the range of each relay. PS and TDS bounds of the ith relay can be represented as in (3) and (4) to meet these requirements.

$$TDS_{min} \leq TDS \leq TDS_{max} \tag{3}$$

$$PS_{min} \leq PS \leq PS_{max} \tag{4}$$

Where TDS and PS are the time dial settings and plug settings, according to [9], the TDS and PS parameters are in the range of [0.05, 1.1] and [1.1, 2.5] respectively. Furthermore, it has been previously stated that the backup relay should not run before the primary relay in order to provide dependable protection. As a result, the coordination time interval (CTI) requirement is:

$$T_{bc} - T_{pr} \geq CTI \tag{5}$$

Where T_{pr} and T_{bc} are the primary and backup relays operating times respectively and CTI stands for the time coordination interval between relays that is in the range of [0.2, 0.3] for the numerical relays and [0.3, 0.4] for the electromechanical relays.

III. Proposed method

A. Optimization algorithm

PSO is an algorithm based on population dynamics that uses a population of individuals to investigate promising search space regions. In this instance, the population is referred to as a swarm, and its members are referred to as particles. Each particle moves with a variable velocity throughout the search space and remembers the best spot it has ever come across. The global variation of PSO communicates to all particles the best position ever reached by all members of the swarm. The general ideas of the PSO method are mentioned in [11].

B. The adaptive protection scheme

In this paper, a novel adaptive protection method is developed to deal with the relays coordination problem. The proposed method operates in two different modes of operation (grid connected and islanded mode). The proposed scheme was designed to deal with the protective relay coordination problem, the numerical relays were used in this work with their ability to carry different group of settings for different power systems configuration.

In Fig 1 the protection technique is displayed, the load flow and short circuit analysis are calculated using DIgSILENT software with both grid connected and islanded scenarios and the optimization process was done in MATLAB R2018a on a Windows 10, 64-bit platform with an 8 GB RAM Core i5 PC.

The proposed approach uses the Particle swarm optimization algorithm. The relays group of settings are selected and applied in the numerical relays then reactivated with each change of the system configuration.

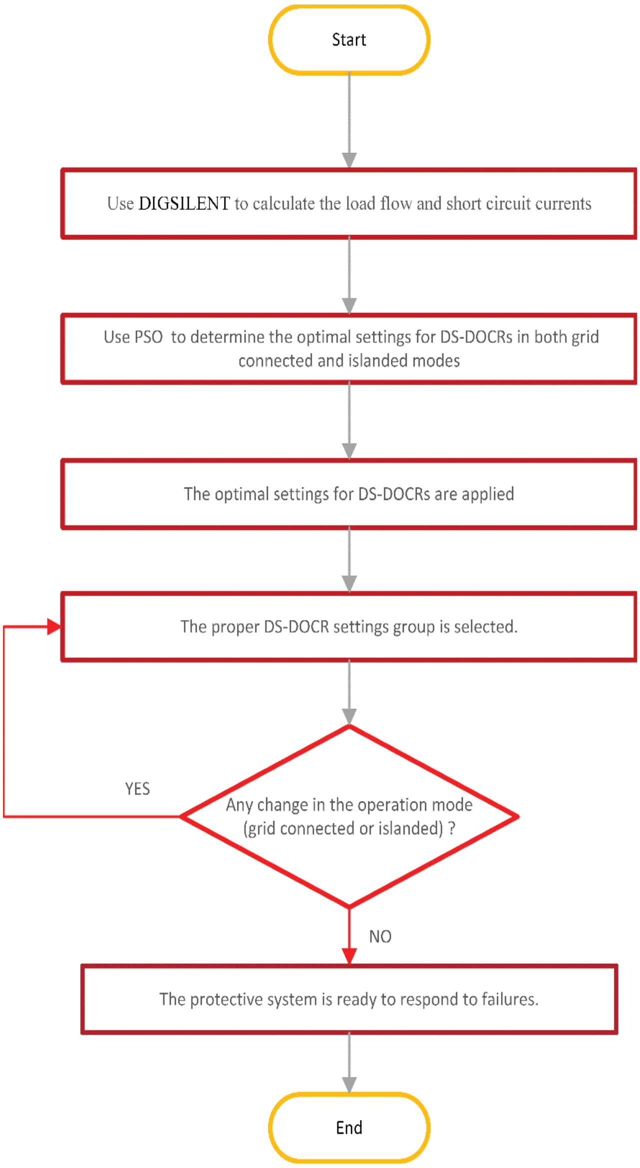

Figure 1. The adaptive protection scheme

IV. Test system under study

In this study, the proposed DSDOCR-based protection system is tested on the distribution network of the IEEE 14-Bus test system. Fig.2 depicts the selected system's single line diagram (SLD). The IEEE 14-bus system is connected to the grid through two 132 kV/33 kV transformers (T1 and T2). Furthermore, this system has seven buses, 16 protection relays and three DG units, each with a capacity of 20 MVA, are linked to this network. The rest of the system's data are in [12]. The created approach will be tested in two different scenarios:

Scenario 1: Grid connected mode (the system shown in Fig.2).

Scenario 2: islanded mode of operation (the system under study is disconnected from the main grid from transformer 1 and transformer 2. This results in the distribution system becoming an island microgrid).

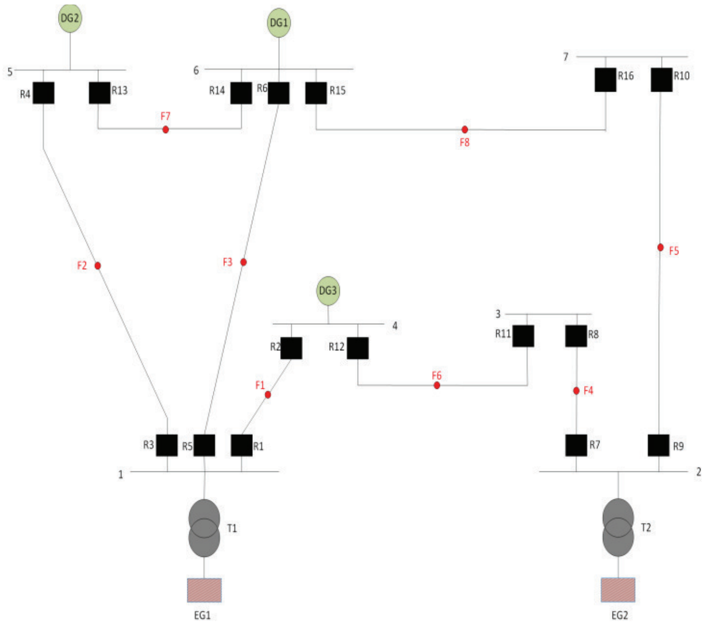

Figure 2. IEEE 14 bus distribution system.

V. Results and discussion

This section discusses the optimal relay settings and total operating time for failures at middle points F1 - F8 in two different operating modes. For comparative analysis and assessment, the dual-setting design technique is used on the IEEE 14 bus distribution test system illustrated in Fig. 2. The following settings for both design methodologies are examined in grid-connected and islanded modes of operation. Table 1 and table 2 shows the short circuit currents of the first and second scenarios respectively. The data were calculated using DIgSILENT software, the optimization process was done using PSO algorithm and the findings are summarized in table 3 and 4 for the grid connected and islanded mode respectively, where all relays settings (TDS and PS settings) and the overall operating time of all primary relays are displayed. The validation of the results is shown in figure 3 and figure 4 where the coordination time interval between the operating times of the primary and backup relays is shown. The CTI is kept in a range of [0.2, 0.3], so it is clear that the protection coordination scheme is working properly, no miscoordination between the relays and with minimum operating times for both grid connected and islanded modes.

Table 1: Short circuit current values in the main scenario (scenario1).

Fault location	Short-circuit currents (A)					
	Primary Relays		1st back-up relay		2nd back-up relay	
F1	R1	6021	R4	965	R6	1566
	R2	3815	R11	2166		
F2	R3	5462	R2	1696	R6	593
	R4	3033	R14	1450		
F3	R5	6477	R2	2012	R4	483
	R6	4080	R13	1046	R16	1275
F4	R7	5902	R10	1392		
	R8	3206	R12	3206		
F5	R9	4878	R8	1574		
	R10	2278	R15	2278		
F6	R11	3886	R7	3886		
	R12	4617	R1	3050		
F7	R13	3446	R3	1819		
	R14	4707	R5	2196	R16	1094
F8	R15	4479	R5	2312	R13	1026
	R16	2417	R9	2417		

Table 2: Short circuit current values in scenario2.

Fault location	Short-circuit currents (A)					
	Primary Relays		1st back-up relay		2nd back-up relay	
F1	R1	2707	R4	1142	R6	1566
	R2	2148	R11	295		
F2	R3	2432	R2	1313	R6	1122
	R4	2337	R14	602		
F3	R5	2288	R2	1357	R4	936
	R6	2876	R13	753	R16	260
F4	R7	1211	R10	1211		
	R8	2426	R12	2426		
F5	R9	1756	R8	1756		
	R10	1663	R15	1663		
F6	R11	894	R7	894		
	R12	3262	R1	1530		
F7	R13	2303	R3	497		
	R14	2664	R5	587	R16	329
F8	R15	3039	R5	770	R13	815
	R16	974	R9	974		

Table 3. Relay settings and operation times for grid connected 14-bus distribution system.

Relay	TDS	PS	Relay	TDS	PS
1	0.0593	2.6197	9	0.0967	5
2	0.2798	1.2746	10	0.4137	0.2091
3	0.2733	5	11	1.1	0.1
4	0.2310	1.7667	12	0.2669	3.5336
5	0.1353	4.9984	13	0.7383	2.0821
6	0.0205	3.7644	14	0.2685	5
7	0.1654	3.1630	15	0.7170	0.7864
8	0.5487	0.1	16	0.5661	0.1041
OF(s)	11.4638				

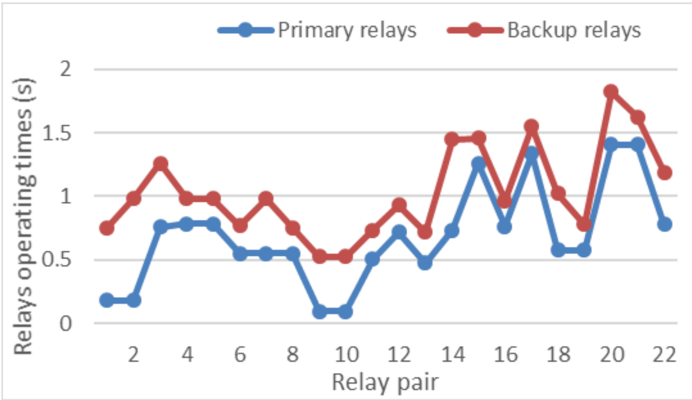

Fig. 3. Relays coordination time interval (CTI) for the grid connected 14-bus distribution system.

Table 4. Relay settings and operation times for islanded 14-bus distribution system.

Relay	TDS	PS	Relay	TDS	PS
1	0.1119	2.4051	9	0.1620	1.8897
2	0.1581	0.5371	10	0.2698	1.0520
3	0.2916	1.2506	11	0.1856	0.8421
4	0.2152	0.7837	12	0.4601	0.9890
5	0.1161	1.5850	13	0.1845	3.9728
6	0.1265	1.1487	14	0.2170	2.0986
7	0.2483	0.6902	15	0.1285	2.1839
8	0.5214	0.3924	16	0.1886	0.6820
OF(s)	9.8872				

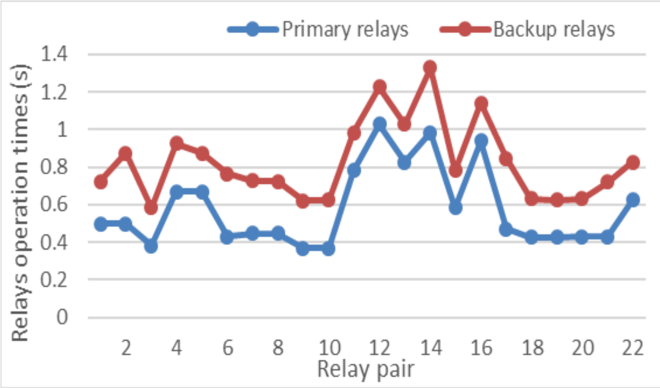

Figure 4. Relays coordination time interval (CTI) for the islanded 14-bus distribution system.

IV. Conclusion

According to the literature study, MG's protection optimization based on grid connected and islanded modes of operation has gotten less attention. The purpose of this study was to fill the identified knowledge gap. The dual setting DOCRs have presented a modified optimal protection system. After rigorous examinations on the distribution section of the IEEE 14-bus test system with two different scenarios (grid connected and islanded modes), the DIGSILENT software was used to determine the load flow and short circuit analysis where the optimal settings were calculated using the particle swarm optimization algorithm in the MATLAB environment. The test findings underlined the efficiency of the given technique. The test results indicated that the created protection mechanism is faster, with no mis-coordination for various network topologies, including grid connected and islanded modes of operation. Furthermore, the suggested technique may be enhanced in future research efforts and may be implemented in more complicated power networks.

References

[1] Noghabi, A.S., H.R. Mashhadi, and J.J.I.T.o.P.D. Sadeh, Optimal coordination of directional overcurrent relays considering different network topologies using interval linear programming. IEEE Transactions on Power Delivery, 2010. **25**(3): p. 1348-1354.

[2] Urdaneta, A., et al., *Presolve analysis and interior point solutions of the linear programming coordination problem of directional overcurrent relays.* International Journal of Electrical Power & Energy Systems, 2001. **23**(8): p. 819-825.

[3] Idarraga-Ospina, G., et al., *Directional overcurrent relay coordination by means of genetic algorithms of Chu–Beasley.* IEEJ Transactions on Electrical and Electronic Engineering, 2018. **13**(4): p. 522-528.

[4] Khurshaid, T., et al., Improved firefly algorithm for the optimal coordination of directional overcurrent relays. IEEE Access, 2019. **7**: p. 78503-78514.

[5] Korashy, A., et al., *Optimal coordination of distance relays and non-standard characteristics for directional overcurrent relays using a modified African vultures optimization algorithm.* IET Generation, Transmission & Distribution, 2023.

[6] Oussama, M., et al. An optimal coordination of directional overcurrent relays using a Gorilla troops optimizer. in 2023 International Conference on Advances in Electronics, Control and Communication Systems (ICAECCS). 2023. IEEE.

[7] Beder, H., et al., *A new communication-free dual setting protection coordination of microgrid.* IEEE Transactions on Power Delivery, 2020. **36**(4): p. 2446-2458.

[8] Yazdaninejadi, A., et al., *Dual-setting directional overcurrent relays for protecting automated distribution networks.* IEEE Transactions on Industrial Informatics, 2018. **15**(2): p. 730-740.

[9] Merabet, O., et al., *Optimal coordination of directional overcurrent relays in complex networks using the Elite marine predators algorithm.* Electric Power Systems Research, 2023. **221**: p. 109446.

[10] Sadeghi, S., H. Hashemi-Dezaki, and A.M.J.E.P.S.R. Entekhabi-Nooshabadi, *Optimized protection coordination of smart grids considering N-1 contingency based on reliability-oriented probability of various topologies.* Electric Power Systems Research, 2022. **213**: p. 108737.

[11] *CHOUDHARY, Pankaj Kumar et DAS, Dushmanta Kumar. Optimal coordination of over-current relay using particle swarm optimization (pso) algorithm. In : 2020 IEEE Applied Signal Processing Conference (ASPCON). IEEE, 2020. p. 308-312.*

[12] Ataee-Kachoee, A., H. Hashemi-Dezaki, and A.J.E.P.S.R. Ketabi, Optimized adaptive protection coordination of microgrids by dual-setting directional overcurrent relays considering different topologies based on limited independent relays' setting groups. Electric Power Systems Research, 2023. **214**: p. 108879.

Implementation of an artificial neural network MPPT method based on Perturb&Observe algorithm for Photovoltaic system

Meryem Lagoune
Electrical Engineering Department
Automatic Laboratory of Setif-LAS, Setif, Algeria
meryemagon964@gmail.com

Samia Latreche
Electrical Engineering Department
Automatic Laboratory of Setif-LAS, Setif, Algeria
ksamia2002@yahoo.fr

Badreddine Babes
Research Center In Industrial Technologies CRTI
P.O. box 64, Cheraga 16014, Algiers, Algeria
elect_babes@yahoo.fr

Mabrouk Khemliche
Electrical Engineering Department
Automatic Laboratory of Setif-LAS, Setif, Algeria
mabroukkhemliche@univ-setif.dz

Abstract—In this paper, an artificial neural network (ANN) maximum power point tracking (MPPT) method is presented. It is accurate and quick to find and track the maximum power point (MPP) in photovoltaic (PV) applications, stable in the presence of slowly changing solar irradiance, and fast and accurate in rapidly changing solar irradiance. The MPPT control system's other components, including PV modules and DC/DC boost converters, are simulated under Matlab/Simulink, and their results under rapidly and slowly varying solar irradiance are also compared. ANN and P&O MPPT algorithms are also tested. According to the results of the simulation, the ANN technique responds much faster and with greater accuracy to rapid changes in solar irradiation. Additionally, this approach operates under gradual or continuous chaAdditionally, this approach operates under gradual or continuous changes with less power oscillation.

Keywords: PV System, MPPT Controller, Perturb&Observe algorithm, Simscape, Artificial neural network (ANN), SCG algorithm

I. INTRODUCTION

Renewable energy sources have become quite important. Since PV systems are not linear, unique techniques are needed to harvest the most power possible. The PV module's nonlinear I/V curve features a unique maximum power point. Electronic converters are employed at this step to function. Maximum Power Point Tracking (MPPT) approaches are algorithms used to manage these power electronic converters. The literature has a variety of original algorithms, each with unique benefits and downsides. [1].

Artificial neural networks (ANN) are capable of imitating the behavior of human biological neural networks. ANN is frequently employed in nonlinear systems to describe complicated interactions between inputs and outputs. Additional connections between inputs and ANN nonlinear systems' outputs. It also has inputs, at least one hidden layer, and one output layer, and is also known as a parallel distributed information processing structure.

These layers are made up of linked processing units known as neurons. A technique known as "backpropagation" is used to determine the contribution of each neuron's mistake after processing a batch of input. The gradient descent optimization approach frequently employs backpropagation to modify the weight of neurons by determining the gradient of the loss function. The term "backpropagation error" is another name for this method. This is a result of the error's calculation at output and subsequent propagation via the network layers [2].

SYSTEM MODELLING AND SIMULATION

The main component of the PV cell is a p-n junction created in a thin semiconductor wafer. Through the photovoltaic effect, solar energy is immediately transformed into electricity. A PV cell's electrical properties are non-linear and strongly influenced by temperature and sun irradiation. [2], [3], [6]. The single-diode model is the most researched and used in this study due to its simplicity and accuracy. An analogous circuit, like the one in Figure 1, with a photocurrent source connected in series with a diode, a shunt resistance Rsh, and a series resistance Rs may be used to electrically represent the PV cell in this model.

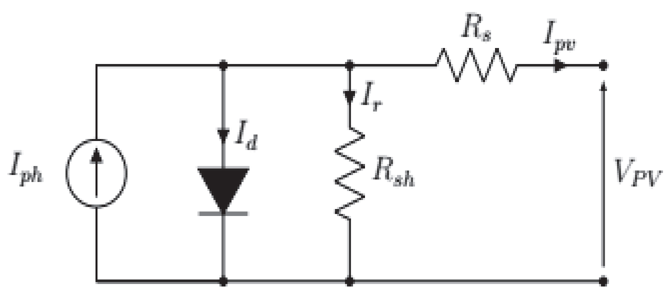

Figure 1: Equivalent circuit of a PV cell

$$I_{pv} = I_{ph} - I_d - I_r = I_{ph} - I_0 \left(e^{\frac{V_{pv}+R_s I_{pv}}{nV_t}} - 1 \right) - \frac{V_{pv} + R_s I_{pv}}{R_{sh}} \quad (1)$$

- I_{pv} : is the cell output current.
- I_{ph} : represents the light-produced current in the cell.
- I_d : is modelled using Shockley formula.
- I_r : is derived current by the shunt resistance.
- I_0 : is reverse saturation current of the diode.
- V_{pv} : is cell output voltage.
- R_s : is cell series parasitic resistance.
- R_{sh} : is cell shunt parasitic resistance.
- V_t : is the thermal voltage.
- n : is diode ideality factor.
- K : is Boltzmann constant $1.3806503\text{x}10^{-23}$J/K
- q : is elementary charge $1.60217646\text{x}10^{-19}$C
- T : is cell temperature in Kelvin degree.

$$V_t = \frac{KT}{q} \quad (2)$$

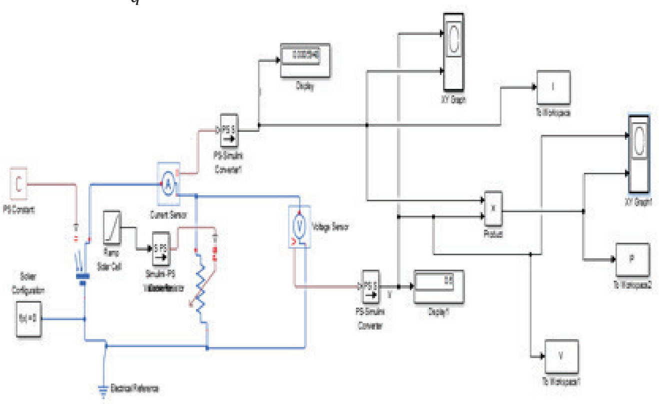

Figure 2: Simulation of PV cell in Matlab Simulink tool with Simscape library

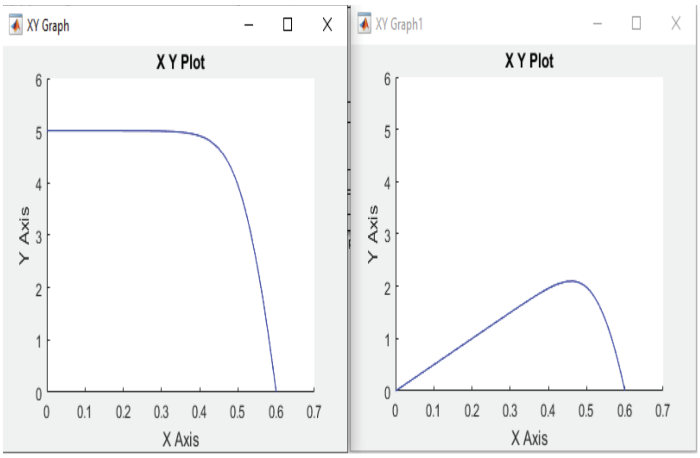

Figure 3: I/V characteristics, P/V characteristics of the selected PV

II. MPPT CONTROL FOR PV SYSTEM

With an appropriate control algorithm, the MPPT unit is a power conversion system that enables getting the most power possible out of a PV array. By adjusting the current pulled from the PV array or the voltage across it to provide operating at or close to the MPP, the supplied power may be maximized. For improving the energy usage efficiency of the PV arrays, many MPPT Algorithms with varying degrees of complexity, accuracy, efficiency, and implementation difficulties have been developed [3], [7].

III.1 PERTURB AND OBSERVE ALGORITHM

The P&O-MPPT method is typically used because of its inexpensive cost, straightforward structure, and modest measured parameters [4],[8]. Figure 4 provides the P&O stages.

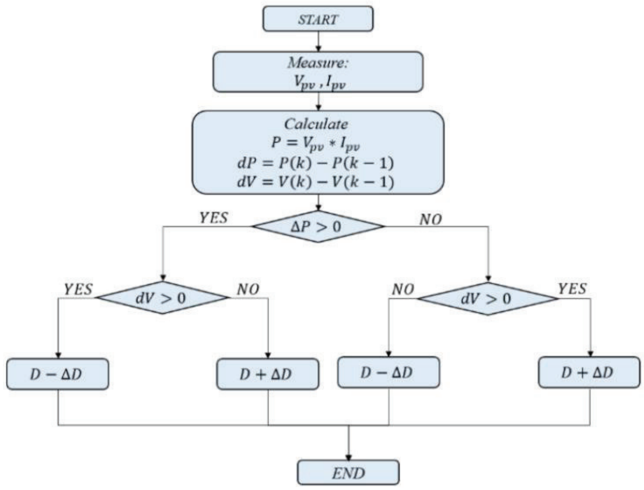

Figure 4: Perturb and Observe (P&O) algorithm

III.2 NEURAL NETWORK-BASED MPPT TECHNIQUE

The MPP of our 60W PV array is tracked here using a neural network. In our study, the neural network is trained using Matlab and the Levenberg-Marquardt method. Using the Levenberg-Marquardt approach, nonlinear least squares issues may be resolved quickly and precisely. We chose to train the neural network using the Levenberg Marquardt method as the temperature and irradiance effects are very nonlinear in generating the output power and voltage. We build the neural network-based MPPT for a PV array in the manner shown in the following phases [9], [12], and [14].

III.2.1 Testing the network

Ten of the acquired data points are utilized as test points after the neural network's training is complete. Test points have the purpose of assessing the designed ANN's performance following the completion of its training. then the mistake is feedback
to train the neural network further. Using the Matlab net toolbox displayed in Figure 5 [10], the network is trained [11],[13].

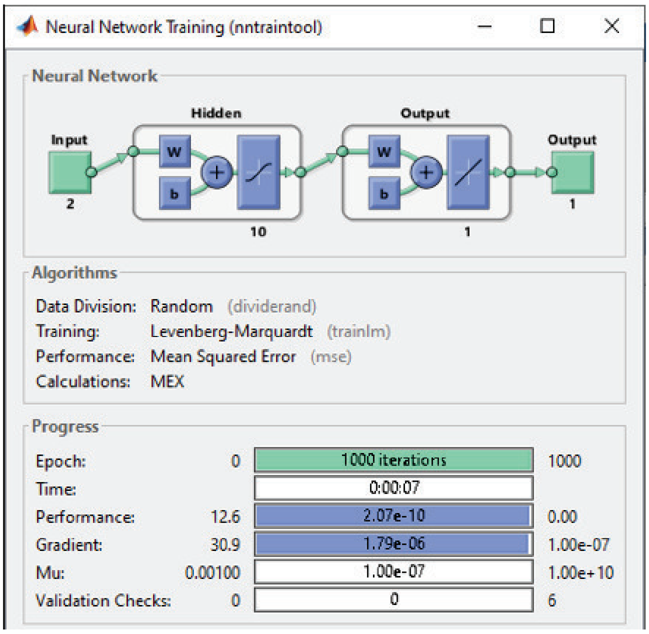

Figure 5: ANN training with Matlab net toolbox

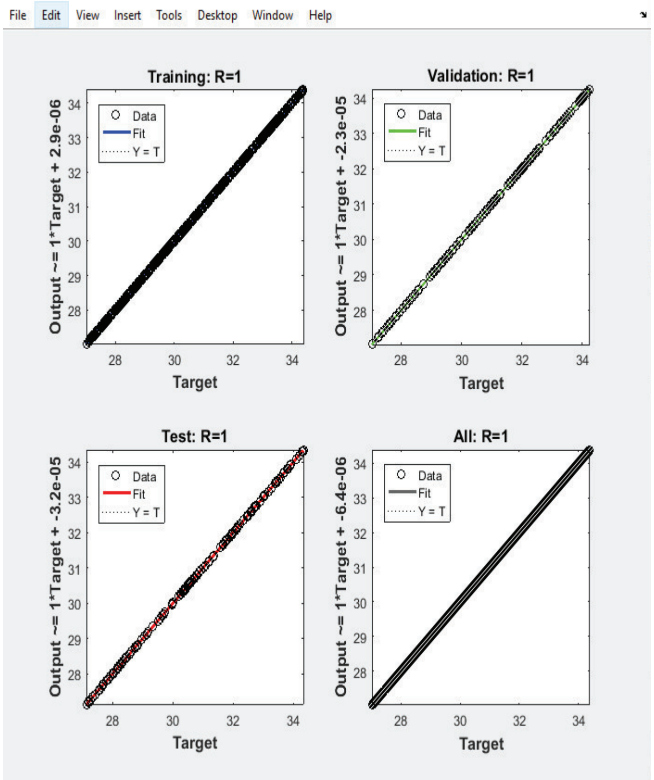

Figure 6: Regression plot for SCG algorithm

III. SIMULATIONS OF PROPOSED SYSTEM

Using Matlab/Simulink software and accounting for variations in solar irradiation, MPPT approaches based on P&O, ANN, and the suggested controller were reviewed, and compared, and simulations were run to test the dynamic behavior of the chosen PV system.

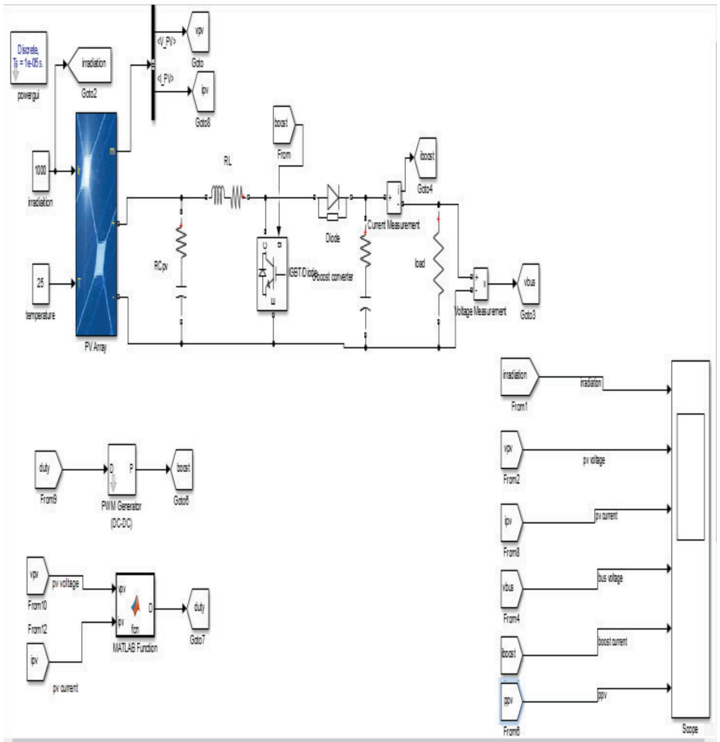

Figure 7: PV System with Power Converter P&O - MPPT Control

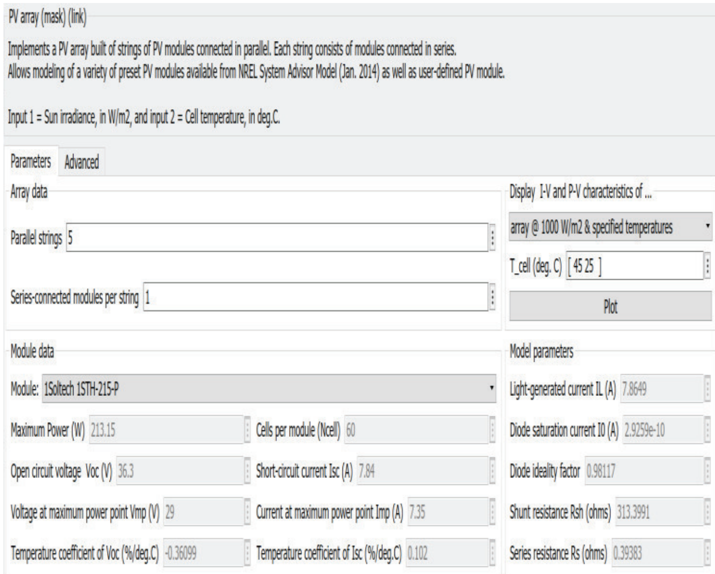

Figure 8: PV module parameters

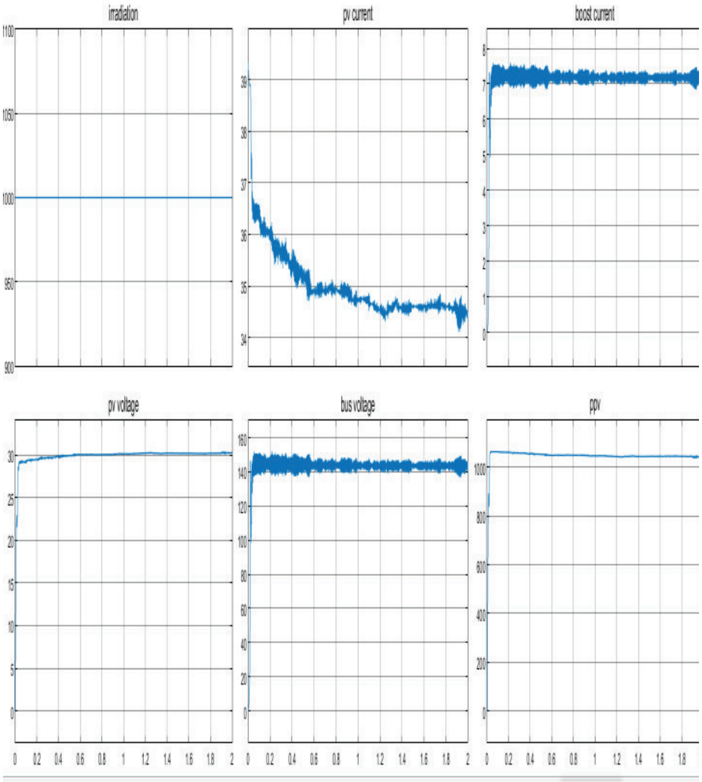

Figure 9: System with Power Converter and ANN MPPT Control

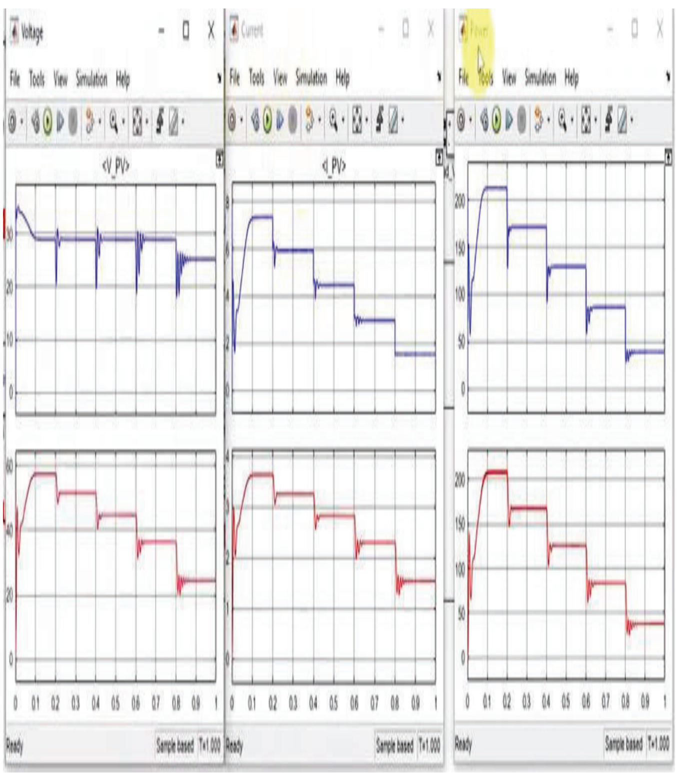

Figure 10: PV module parameters

Using Matlab/Simulink software and accounting for variations in solar irradiation, MPPT approaches based on P&O, ANN, and the suggested controller were reviewed, and compared, and simulations were run to test the dynamic behavior of the chosen PV system.

PV module simulations (1 Soltech 1STH-215-p) are performed using the P&O PMMT control-based model that has been provided. The PV system's inputs include temperature and irradiance, while the outputs of the DC/DC Boost Converter—voltage, current, and actual power—are also inputs to the RLC Load.

Simulated results from the constructed control system were validated using the SIMSCAPE module of MATLAB. The MPPT algorithm sets the duty cycle appropriately since the MOSFET is regulated by PWM and managed by the MPPT controller. The switching frequency is tuned to the duty cycle D of the used DC/DC converter.

Using a neural network, we can use Fig. 7 to determine the outputs from the PV module (1 Soltech 1STH215-p).

IV. CONCLUSION

This paper's simulation findings for the ANN and P&O approaches demonstrate that, in the situation of rapidly changing solar irradiation, the ANN method is particularly quick and accurate in locating and tracking the MPP. Additionally, using this approach, the maximum power point under gradually increasing solar irradiation may be extracted. On the other hand, the P&O approach fails to follow the MPP when irradiance varies quickly over a short period. Additionally, this approach has significant long-term power loss due to high MPP oscillation under slowly changing solar irradiation.

References

[1] Villalva, M.G., Gazoli, J.R., Filho, E.R., 2009. A comprehensive approach to modeling and simulation of photovoltaic arrays. IEEE Trans. Power Electron. 24, 1198– 1208.

[2] Kassis, A.,Saad, M., 2010. Analysis of multi-crystalline silicon solar cells at low illumination levels using a modified two-diode model. Solar Energy Materials and Solar Cells 94, 2108–2112

[3] Esram, T., Chapman, P.L., 2007. Comparison of photovoltaic array maximum power point tracking techniques. IEEE Trans. Energy Conver. 22, 439–449

[4] Karami, N.,Moubayed, N.,Outbib, R., 2017. General review and classification of different MPPT Techniques. Renew. Sustain. Energy Rev. 68, 1–18.

[5] Ahmed, J., & Salam, Z. (2016). A modified P&O maximum power point tracking method with reduced steady-state oscillation and improved tracking efficiency. IEEE Transactions on Sustainable Energy, 7(4), 1506-1515.

[6] S. Latreche, A. E. Badoud, and M. Khemliche, "Implementation of MPPT algorithm and supervision of shading on photovoltaic module," Engineering, Technology and Applied Science Research, vol. 8, no. 6, pp. 3541–3544, Dec. 2018, doi: 10.48084/etasr.2354

[7] F. Bait, S. Latreche, and M. Khemliche, "Simulation of different faults in photovoltaic installation," in 2022 19th IEEE International Multi-Conference on Systems, Signals and Devices, SSD 2022, May 2022, pp. 1130–1138, doi: 10.1109/SSD54932.2022.9955851.

[8] S. Latreche, A. Khenfer, and M. Khemliche, "Sensors placement for the faults detection and isolation based on bridge linked configuration of photovoltaic array," Electrical Engineering and Electromechanics, vol. 2022, no. 5, pp. 41–46, Sep. 2022, doi: 10.20998/2074-272X.2022.5.07

[9] Y. Lahiouel, S. Latreche, and H. Afghoul, “Experimental realization using a dSP ACE card of the PI control for an active power filter,” in 2022 19th IEEE International Multi-Conference on Systems, Signals and Devices, SSD 2022, May 2022, pp.53–57, doi: 10.1109/SSD54932.2022.9955690

[10] H. E. Amara, S. Latreche, M. A. Sid, and M. Khemliche, “Sliding mode observer and event triggering mechanism co-design,” Engineering, Technology and Applied Science Research, vol. 10, no. 2, pp. 5487–5491, Apr. 2020, doi: 10.48084/etasr.3285

[11] Lahiouel Y., Latreche S., Khemliche M., Boulemzaoud L. Photovoltaic fault diagnosis algorithm using fuzzy logic controller based on calculating distortion ratio of values. Electrical Engineering Electromechanics, 2023, no.4, pp. 40-46. doi:https://doi.org/10.20998/2074-272X.2023.4.06

[12] M. Negnevitsky, Artificial intelligence, 2nd ed.2005, pp. 1–415

[13] R. Ramaprabha and B. L. Mathur, “Intelligent controller based maximum power point tracking for solar PV system,” International Journal of Computer Applications, vol. 12, no. 10, pp. 37–42, Dec. 2011

[14] J. Xu, A. Shen, C. Yang, W. Rao, and X. Yang, “ANN based on IncCond algorithm for MPP tracker,” in Sixth International Conference on Bio-Inspired Computing: Theories and Applications, 2011, vol. 3, pp. 129–134

Partial Shading Detection Using Neural Network Methods

Aicha Moulay (Author)
Smart Grids and Renewable Energies Laboratory
University Tahri Mohammed of Béchar.
Béchar, Algeria
aichamoulay03@gmail.com

Tarak Benslimane
Laboratoire de Génie Electrique, Department of Electrical Engineering, Faculty of Technology
University of M'sila
Msila, Algeria
bens082002@yahoo.fr

Othmane Aabdelkhalek
Smart Grids and Renewable Energies Laboratory
University Tahri Mohammed of Béchar
Bechar, Algeria
Othmane_elec@yahoo.fr

Abstract—**This paper introduces an intelligent methodology for detecting and classifying partial shading states in photovoltaic systems using neural networks. The approach involves a three-layered artificial neural network that relies on four distinct datasets (Irradiance, Temperature, Voltage and Current of photovoltaic array). The proposed method is characterized by its simplicity and efficiency in identifying and categorizing partial shading scenarios alongside normal operating conditions. These outcomes are achieved through simulation within the Matlab/Simulink environment.**

Keywords-Solar Panel; Shading; neural network; Detection;

I. INTRODUCTION

Renewable energy derives from natural sources, including wind, solar power, water, biomass, and geothermal energy, and it enjoys the advantage of being continuously replenished. These energy sources are notably more reliable than fossil fuels, primarily because they are consistently accessible and have a minimal environmental impact. [1]

Shading is a common phenomenon that affects the performance of a PV array when it encounters various obstructions, such as passing clouds, tufts of shade, advancing buildings, dirt, debris, bird droppings, varying terrain, and more. Partial shading on a PV array results in a decrease in its power output. In the case of a PV module, shading not only reduces power generation but can also lead to hot spots and damage to the individual solar cells. [2]

II. PHOTOVOLTAIC SYSTEM MODELING:

A. PV cell

A Photovoltaic (PV) cell is a device that converts sunlight or incident light into direct current (DC) based electricity.[2]

B. PV Module

The electrical characteristics of the photovoltaic module used under standard conditions STC (Temperature Module =25°C, Solar Irradiance=1000W/m^2) are shown in **Table.1**

Table. 1. PV Module Specifications

Parameters	Values
Maximum Power (Pmax)	30 W
Voltage at Pmax (Vmpp)	17.80 V
Current at Pmax (Impp)	1.666A
Open circuit voltage (Voc)	22.2 V
Short circuit current (Isc)	1.801 A
Temperature coefficient of Voc	-0.34 V/°C
Temperature coefficient of Isc	0.0037mA\C
NOCT	45 ± 2°C
Operating Temperature	25 ^{0}C

C. The P-V and I-V characteristics of the pv module under STC conditions:

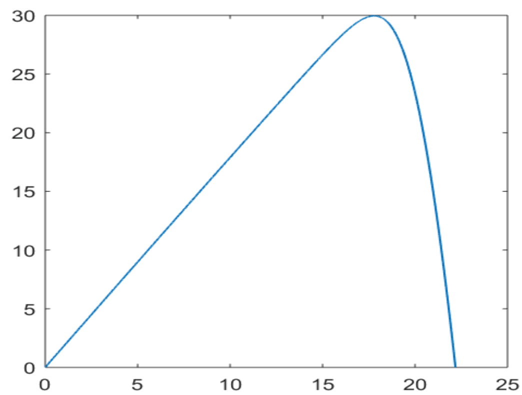

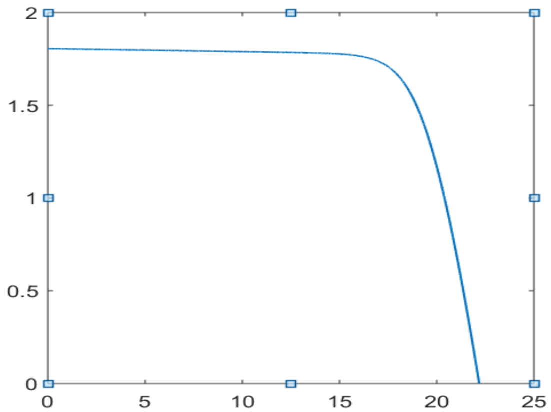

Figure. 1. P-V and I_V characteristics of PV module under STC conditions

The proposed PV array system consists of two strings arranged in parallel, each string contain three modules joined in series. In solar panels, bypass diodes are connected "parallel" to a photovoltaic cell or panel to shunt current around it, whereas blocking diodes are connected "series" to the PV panels to prevent current from flowing back into them. Figure. 2 below describes the proposed panels with bypass and blocking diodes.

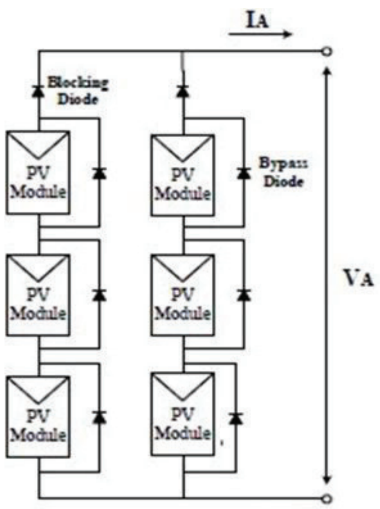

Figure.2. Block diagram of PV panels

D. PV system modeling :

The schematic of a grid connected PV system is shown in Figure. 3. It consist of the PV array, DC-DC converter which is driven by MPPT(Maximum Power Point Tracking) controller and the charge load.

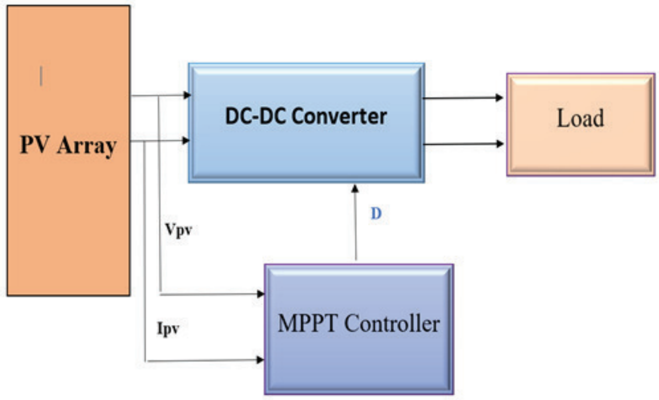

Figure.3 Block diagram of PV stand-alone PV system

MPPT algorithm has been designed to continuously adjusts the duty cycle of the converter in order to extract maximum available power. At MPP (Rin=RMPP), the duty cycle of the converter is calculated as [3] described un equation (1)

$$D_{MPP} = 1 - \sqrt{\frac{R_{MPP}}{R_L}} \qquad (1)$$

The parameters of boost converter are calculated using [3]–[5] and the result values are described in table below:

Table. 2 Boost converter components parameters

parameters	Values
Inductor	2mH
Input Capacitance	212μF
Output Capacitance	24 μF
Switching frequency	10KHz
Duty Cycle	0.67

III. PARTIAL SHADING EFFECTS :

A solar photovoltaic (PV) system comprises multiple PV modules interconnected in both parallel and series configurations. The total power output of a PV array is the sum of the power generated by each individual solar module. In modern applications, grid-connected PV arrays are frequently installed on building exteriors, rooftops, or within urban environments, where the likelihood of encountering partial shading events is elevated. When specific solar cells are shaded or receive insufficient solar radiation, this can result in a decrease in the overall power output as it dissipates the energy generated by the unaffected solar cells[6].

In this study, we examine three distinct cases of partial shading: the first involves the shading of one module, the second involves the shading of two modules, and the last case pertains to the shading of four out of six modules. Figure.4 describes the resultant I-V and P-V curves of 3 different cases in partial shading fault in addition to normal case where all modules are under STC conditions.

- case 1: All modules are in STC conditions.
- case 2: One of the modules is partially shaded in normal conditions.
- case 3: Two modules are under shade.
- case 4: Four modules are under shade.

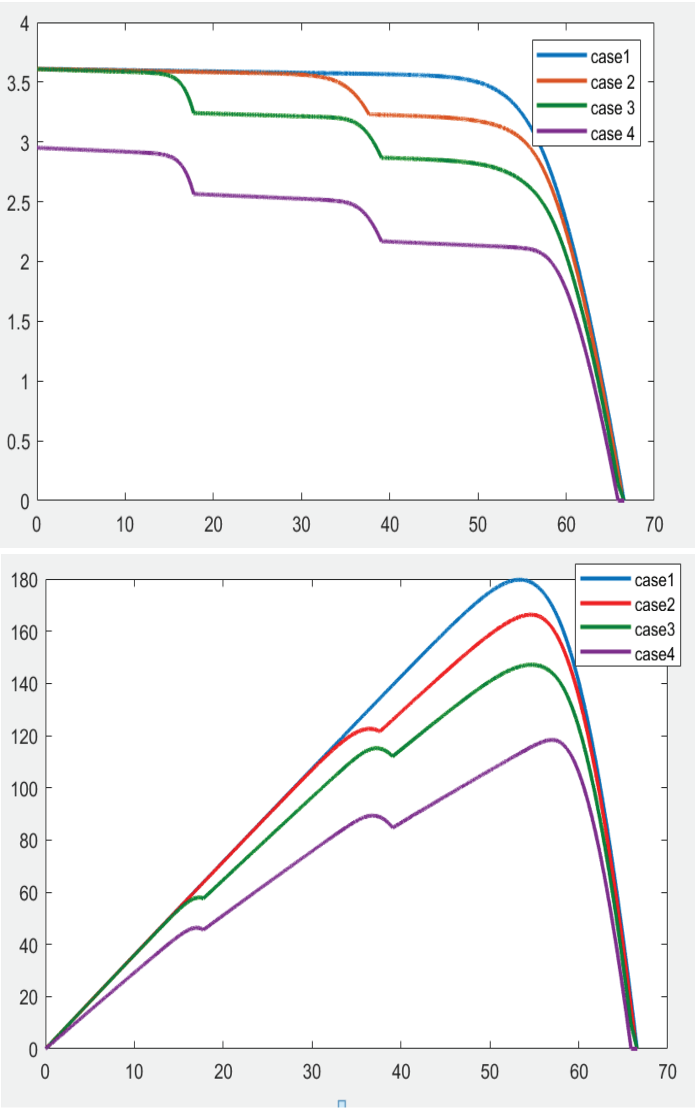

Figure.4 I-V and P-V characteristics of PV array under different faults

IV. METHODOLOGIES AND RESULTS :

A. *Artificial neural networks(ANNs)*

Artificial neural networks (ANNs) are complex computational models inspired by the complex processes of the human brain. In an ANN, multiple interconnected nodes, known as neurons, communicate through weighted connections[7]. These networks are commonly employed in various applications, including image processing and data classification.

One of the central functions of a neural network is to master the comprehension of complex nonlinear function mappings. This is achieved through a combination of sequential training methods and self-adaptive mechanisms. It's important to emphasize that ANNs diverge from traditional mathematical problem-solving approaches. Instead of offering precise solutions, they provide approximations based on the inherent characteristics of the input data [7]and [8].
Furthermore, neural network applications possess the remarkable capability to distill simplicity from intricate natural systems with exceptional accuracy. This is achieved by utilizing a substantial number of input variables[9]. The flexibility and adaptability of ANNs make them valuable tools in addressing a wide range of real-world problems, contributing to advancements in fields like artificial intelligence, pattern recognition, and predictive modeling.

The multilayer perceptron (MLP) is a type of feed-forward neural network. It consists of three essential layers: an input layer, a hidden layer, and an output layer. The input layer receives the input signal to be processed, while the output layer performs functions such as classification and prediction. The MLP employs a connected network structure that includes an infinite series of hidden layers positioned between the input and output layers. Data travels in a unidirectional manner, moving from the input layer to the output layer, akin to the feed-forward network architecture. To train all the nodes within the MLP, the backpropagation learning technique is employed[10].
Figure.5 illustrates a simple multi-layer perceptron.

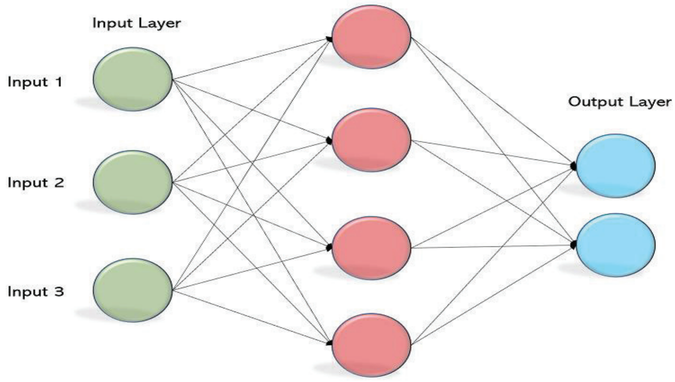

Figure.5 A three-input two-output multi-layer perceptron ANN

B. *Methodology used*

A simple feedforward multilayer perceptron (MLP) is chosen, consisting of four input neurons aligned with the network. We've employed pattern recognition neural networks alongside the Levenberg-Marquardt algorithm, recognized as the most effective algorithm after evaluating various alternatives. This algorithm is utilized to update the network's biases and weights, with the goal of minimizing the error between the target values and the neural network's output. The output layer accounts for four distinct output scenarios, encompassing one normal case and three partial shading scenarios. Figure.6 illustrates the ANN model used in this study.

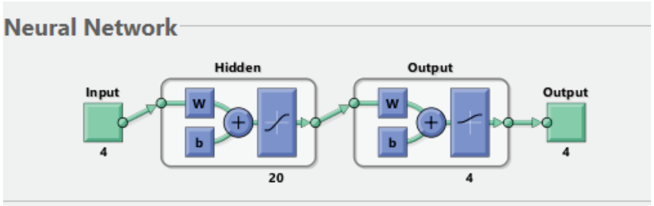

Figure.6 The neural network model

In this study, 192000 points are used as a result of simulating the system in MATLAB/Simulink where each data point consists of solar irradiance, ambient temperature, voltage array, current array. which serve as inputs for the network's hidden layer. This hidden layer comprises 20 neurons and utilizes a tangential sigmoid activation function, yielding outputs within the range of -1 to 1.

C. *Results and discussion*

Using Matlab, we perform automatic learning for the chosen ANN model until we obtain a very small mean square error (MSE) with a smaller gradient value. Figure.7 describes the MSE value obtained after 25 iterations.

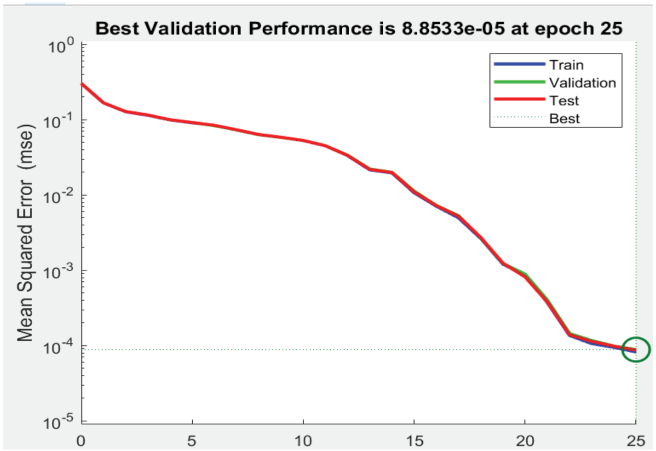

Figure.7 The mean square error

Figure.8 shows the confusion matrix of the proposed ANN Obtained after performing classification which shows the best results.

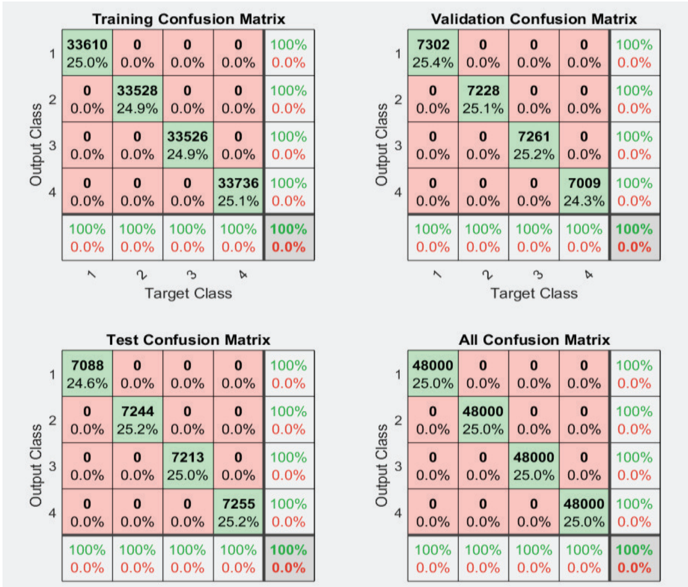

Figure8. Confusion matrix for the ANN model

The obtained results show that this methodology has good performance in detecting and classifying normal or shading states. The employed ANN has proven its effectiveness in classifying all studied cases, with a performance that reaches 100%.

I. CONCLUSION :

The paper presents a method based on artificial neural networks (ANN) for detecting and classifying shading states in PV systems. Based on the results obtained from simulations, it can be concluded that this methodology is both effective and reliable. Therefore, this ANN topology can be further developed to address various types of faults, including electrical faults such as line-to-line faults, open circuits, and short-circuit faults, as well as boost converter faults. This approach holds promise for real-world experimental applications.

References

[1] M. Sabbaghpur Arani and M. A. Hejazi, "The comprehensive study of electrical faults in PV arrays," *J. Electr. Comput. Eng.*, vol. 2016, 2016, doi: 10.1155/2016/8712960.

[2] A. Djalab, N. Bessous, M. M. Rezaoui, and I. Merzouk, "Study of the Effects of Partial Shading on PV Array," *Proc. - Int. Conf. Commun. Electr. Eng. ICCEE 2018*, pp. 6–10, 2019, doi: 10.1109/CCEE.2018.8634512.

[3] N. Hashim, Z. Salam, D. Johari, and N. F. Nik Ismail, "DC-DC Boost Converter Design for Fast and Accurate MPPT Algorithms in Stand-Alone

Photovoltaic System," *Int. J. Power Electron. Drive Syst.*, vol. 9, no. 3, p. 1038, 2018, doi: 10.11591/ijpeds.v9.i3.pp1038-1050.
[4] B. M. Ahmed and N. F. Farman ALhialy, "Optimum Efficiency of PV Panel Using Genetic Algorithms to Touch Proximate Zero Energy House (NZEH)," *Civ. Eng. J.*, vol. 5, no. 8, pp. 1832–1840, 2019, doi: 10.28991/cej-2019-03091375.
[5] S. Motahhir, A. El Ghzizal, S. Sebti, and A. Derouich, "Modeling of Photovoltaic System with Modified Incremental Conductance Algorithm for Fast Changes of Irradiance," *Int. J. Photoenergy*, vol. 2018, 2018, doi: 10.1155/2018/3286479.
[6] P. Mundra, A. Arya, and S. K. Gawre, "Partial Shading Condition on PV Array: Causes, Effects and Shading Mitigation using DSMPPT," *Int. J. Eng. Adv. Technol.*, vol. 9, no. 3, pp. 1134–1139, 2020, doi: 10.35940/ijeat.c4714.029320.
[7] A. D. Dongare, R. R. Kharde, and A. D. Kachare, "Introduction to Artificial Neural Network (ANN) Methods," *Int. J. Eng. Innov. Technol.*, vol. 2, no. 1, pp. 189–194, 2012, [Online]. Available: https://citeseerx.ist.psu.edu/viewdoc/download?doi=10.1.1.1082.1323&rep=rep1&type=pdf.
[8] M. A. Zdiri, B. Bouzidi, O. Kahouli, and H. H. Abdallah, "Fault Detection Method for Boost Converters in Solar PV Systems," *19th Int. Conf. Sci. Tech. Autom. Control Comput. Eng. STA 2019*, pp. 237–242, 2019, doi: 10.1109/STA.2019.8717239.
[9] O. I. Abiodun, A. Jantan, A. E. Omolara, K. V. Dada, N. A. E. Mohamed, and H. Arshad, "State-of-the-art in artificial neural network applications: A survey," *Heliyon*, vol. 4, no. 11, p. e00938, 2018, doi: 10.1016/j.heliyon.2018.e00938.
[10] S. Abinaya and M. K. K. Devi, "Enhancing crop productivity through autoencoder-based disease detection and context-aware remedy recommendation system," *Appl. Mach. Learn. Agric.*, pp. 239–262, Jan. 2022, doi: 10.1016/B978-0-323-90550-3.00014-X.

Comparative Study Between Three Types of Controllers (PI,SMC,BS) For MPPT Of Wind Turbine

Fatima Zohra Belaimeche
Intelligent Control and Electrical Power Systems Laboratory, Faculty of Electrical Engineering, Djillali Liabes University
Sidi Bel Abbes,Algeria
belaimechefatima90@yahoo.com

Abstract— **In this paper, a comparative study between three types of controllers PI classic,sliding mode and backstepping controllers is proposed to maximize the power extraction of a variable speed wind turbine. This algorithm works in the partial load region. It has been used to control the wind turbine speed so that it reaches the desired value which corresponds to the maximum power point. Complete simulation of the MPPT system validates the efficiency of the proposed backstepping control law. Compared to the conventional PI controller usually used and sliding mode, the backstepping control allows to exhibit excellent transient response during large range of operating conditions.**

Keywords—MPPT;PI;SMC;BS;WECS.

I. Introduction

Recently, pollutants in the air are progressing in correlation with the increasing consumption of energy. The ever-increasing demand for conventional energy sources like coal, natural gas and crude oil is driving society towards the research and development of alternative environmental friendly energy sources [1].

Wind energy power generation is the most important form of the utilization of wind energy. The maximum extraction of power from a renewable energy source mainly depends on the strength of the source as well as on the operating point of the energy conversion system [2].

The most classical approach used in our work consists in controlling the speed of rotation by a PI controller. In order to cancel the static error and reduce the response time while maintaining the stability of the system, a proportional integral controller is used; the classical PI controller may not give satisfactory performance against variations parameters [3].

The sliding mode control (SMC) strategy has been widely used for robust control of nonlinear systems. Sliding mode control, based on the theory of variable structure systems (VSS), has attracted a lot of research on control systems for the last two decades [2].

It achieves robust control by adding a discontinuous control signal across the sliding surface, satisfying the sliding condition. However, this type of control has an essential disadvantage, which is the chattering problem caused by the discontinuous control action [4].

The paper is structured as follow: In first place,a model of wind turbine will be presented, then the proportional integral (PI), Sliding mode (SMC), Backstepping (BS) control strategies applied for MPPT to maximize the power during the wind energy conversion are developed.The systems performances were simulated and compared using Matlab/Simulink environment. Simulation results show the effectiveness of the proposed control strategies compared to the PI one, regarding reference tracking and sensibility to high variations of wind speed.

II. Wind Turbine Modeling

A. Model wind turbine

Wind turbines convert the kinetic energy present in the wind into mechanical energy by means of producing torque.

The wind power developed by the turbine is given by the equation (1)[7].

$$P_t = \frac{1}{2} C_p(\lambda) \rho \pi R^2 V^3 \quad (1)$$

Where ρ is the air density, R is the radius of the swept area of the turbine rotor, cp is the power coefficient that is function of the tip-speed ratio λ for a fixed blade pitch angle, ω_{win} is the wind speed. The tip speed ratio is defined as:

$$\lambda = \frac{\Omega_t R}{V} \quad (2)$$

The power coefficient can be expressed by the following expression:

$$C_P = f(\lambda, \beta) = C_1 \left(\frac{c_2}{\lambda_i} - C_3 \beta - C_4 \right) exp\left(\frac{-C_5}{\lambda_i} \right) + C_6 \lambda \quad (3)$$

With

$$\frac{1}{\lambda_i} = \frac{1}{\lambda + 0.08\beta} - \frac{0.035}{\beta^3 + 1}$$

And

$C_1 = 0.5176$; $C_2 = 116$; $C_3 = 0.4$; $C_4 = 0.5176$; $C_5 = 0.5176$; $C_6 = 0.0068$

The expression of the torque of the turbine

$$C_t = \frac{1}{2} C_m(\lambda,\beta)\rho\pi R^3 V_1^2 \quad (4)$$

The torque coefficient C_m is defined by:

$$C_m = \frac{C_p}{\lambda} \quad (5)$$

From figure 1, the maximum values of Cp is achieved for the curve associated to $\boldsymbol{\beta}=0^\circ$.

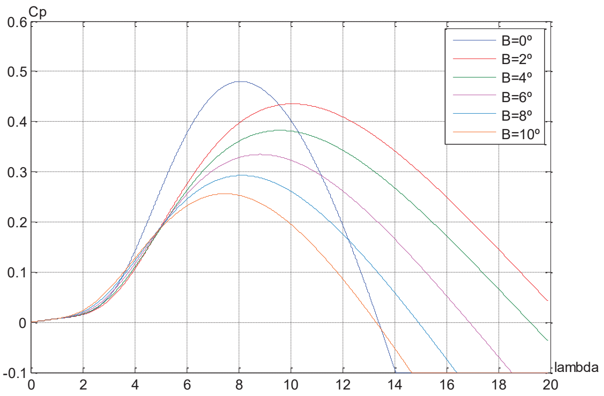

Fig. 1. Power coefficient curves.

From this curve, the maximum value of power coefficient Cp is (C_{pmax}=0.48) which corresponds for an optimal tip-speed ratio ($\boldsymbol{\lambda}_{opt}$=8.1). We take note that the blades orientation angle is fixed $\boldsymbol{\lambda}$ = 0.

III. Maximum Power Point Tracking Technique Design

In order to realize the MPPT control, it is necessary to estimate the reference speed of the generator [5]. To do that, we use the Eq.5, the speed reference $\boldsymbol{\Omega}g^*$ can be given by:

$$\Omega_g^* = \frac{\lambda_{opt} v G}{R} \quad (5)$$

A. Control by PI classic :

The PI regulator must be designed to stabilize the speed control transient state with a zero steady state error by a tuning judicious of its parameters k_p and loop, and improve the dynamics of the controlled system during k_i.

A simplified block diagram of the speed control is shown in figure 2.

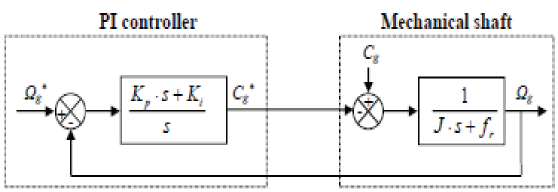

Fig. 2. Block diagram of control loop with PI regulator

We can write the closed loop transfer function in the following mathematical form (6)

$$\frac{\Omega_g}{\Omega_g^*} = \frac{K_p.s+K_i}{J.s^2+(f_r+K_p)s+K_i} \quad (6)$$

To lower the effect of the disturbance (C_{mec}), we interest to choose a high value for the gain K_p. The other gain is chosen so as to have a 2nd order transfer function, having a natural pulsation and a damping coefficient, determined as follows:

$$\begin{cases} \omega_n = \sqrt{\frac{K_i}{J}} \\ \xi = \frac{f_r+K_p}{J.2\omega_n} \end{cases} \quad (7)$$

So, to impose a response time and a damping factor, we find:

$$\begin{cases} K_i = \omega_n^2.J \\ K_p = 2\xi\omega_n J - f_r \end{cases} \quad (8)$$

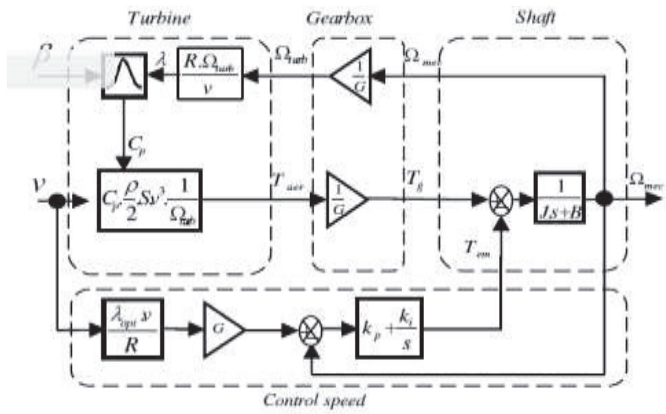

Fig. 3. Bloc diagram of speed control.

B. Sliding mode control

Sliding mode control is one of the effective nonlinear robust control approaches since it provides system dynamics with an invariance property to uncertainties once the system dynamics are controlled in the sliding mode [8-9]. The main feature of Sliding mode controller (SMC) is that it only needs to drive the error to a switching surface [6]:

To design a sliding mode speed control, we consider the system of equations (9):

$$\frac{d\Omega}{dt} = \frac{1}{J}(C_m - C_{em} - \omega f_r) \quad (9)$$

The relative degree of the surface is equal to one to be able to appear the C_{em} command in its derivative of the speed(r=1).

The sliding surface is defined by:

$$S(\Omega) = \Omega^* - \Omega \quad (10)$$

We consider the following Lyapunov function

$$V(S(\Omega)) = \frac{1}{2}S(\Omega)^2 \quad (11)$$

The derivative of Lyapunov's candidate function:

$$\dot{V}(S(\Omega)) = S(\Omega).\dot{S}(\Omega) \quad (12)$$

With

$$\dot{S}(\Omega) = \dot{\Omega}^* - \dot{\Omega} \quad (13)$$

Substituting (9) in the last equation (13) we get

$$\dot{S}(\Omega) = \dot{\Omega}^* + \frac{1}{J}(C_{em} + \omega f_r - C_m) \quad (14)$$

By replacing the expression of Cem by the equivalent and discontinue control (C_{emeq} +C_{emn}) in the previous equation, we find:

$$\dot{S}(\Omega) = \dot{\Omega}^* + \frac{1}{J}((C_{emeq} + C_{emn}) + \omega f_r - C_m) \quad (15)$$

During the sliding mode and in steady state we have:

$S(\boldsymbol{\Omega})=0$, $\dot{S}(\Omega) = 0$ and $C_{emn}=0$, where we get from the expression of the equivalent command C_{emeq} :

$$C_{emeq} = -J\dot{\Omega}^* - \omega f_r + C_m \quad (16)$$

By replacing the expression (16) in (15) we obtain:

$$\dot{S}(\Omega) = \frac{1}{J}(C_{emn}) \quad (17)$$

To ensure the convergence of the Lyapunov function, we need to set:

$$C_{emn} = -K sign(S(\Omega)) \quad (18)$$

With K positive constant

C. Control by Backstepping

To design a velocity backstepping control, we consider the system of equations (19):

$$\frac{d\Omega}{dt} = \frac{1}{J}(C_m - C_{em} - \omega f_r) \quad (19)$$

The speed error can be given by:

$$S(\Omega) = \Omega^* - \Omega \quad (20)$$

Considering V as a Lyapunov candidate function:

$$V(e) = \frac{1}{2}e(\Omega)^2 \quad (21)$$

The derivative of (21) is given by:

$$\dot{V}(e(\Omega)) = e(\Omega).\dot{e}(\Omega) \quad (22)$$

With

$$\dot{e}(\Omega) = \dot{\Omega}^* - \dot{\Omega} \quad (23)$$

Substituting (19) in the last equation we get:

$$\dot{e}(\Omega) = \dot{\Omega}^* + \frac{1}{J}(C_{em} + \omega f_r - C_m) \quad (24)$$

Replacing (24) in (22), we obtain:

$$\dot{V}(e) = e(\Omega).(\dot{\Omega}^* + \frac{1}{J}(C_{em} + \omega f_r - C_m)) \quad (25)$$

The stabilizing of backstepping control law for speed is defined by:

$$C_{em} = -J\dot{\Omega}^* - \omega f_r + C_m - K_1 e(\Omega) \quad (26)$$

Where K_1 is a positive constant

To ensure the convergence of the Lyapunov candidate function, replacing expression (26) in (25) gives:

$$\dot{V}(e) = e(\Omega).\dot{e}(\Omega) = -K_1 e(\Omega)^2 < 0 \quad (27)$$

IV. Simulation Results And Discussion

This control structure is simulated by considering the wind profile figure 4. We show the results obtained for MPPT control strategies used.

The results obtained for the various simulation tests carried out, for a wind turbine, a gearbox and the generator shaft, to extract the maximum MPPT power with the proposed control techniques by the following regulators:

- proportional and integral (PI).
- sliding mode(MG).
- backstepping(Bs).

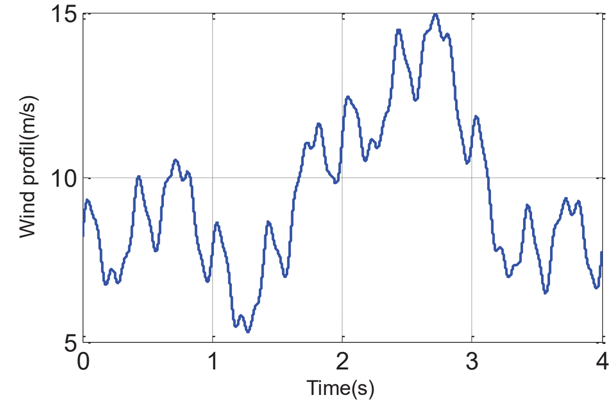

Fig. 4. Variable wind speed profil

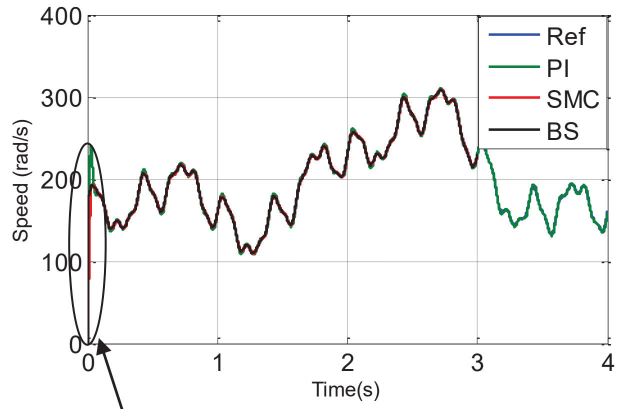

(a)

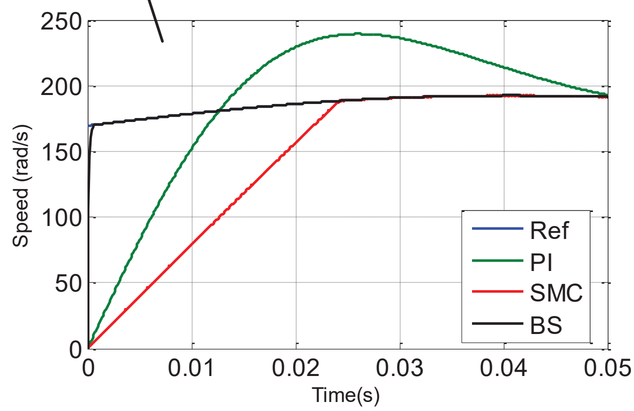

(b)

Fig. 5. (a) Speed of three controllers

(b) Speed with zoom

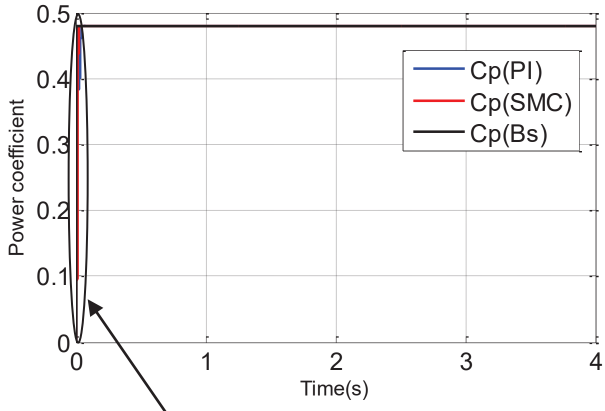

(a)

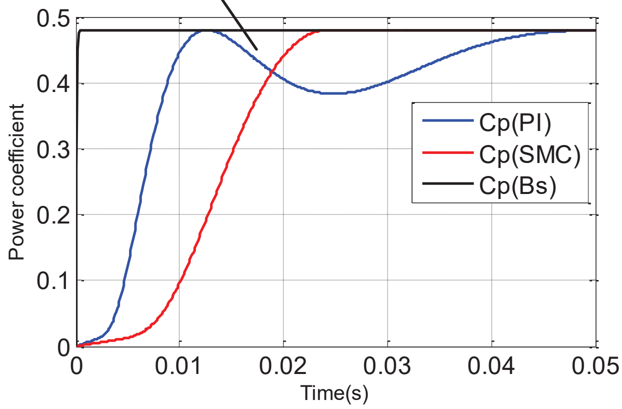

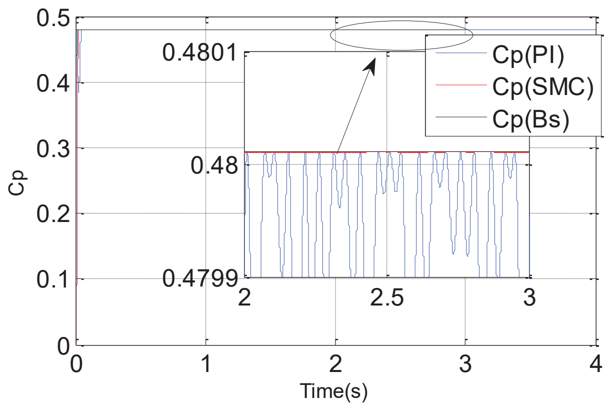

(b)

Fig. 6. (a) Power cefficient of three controllers

(b) Power cefficient with zoom

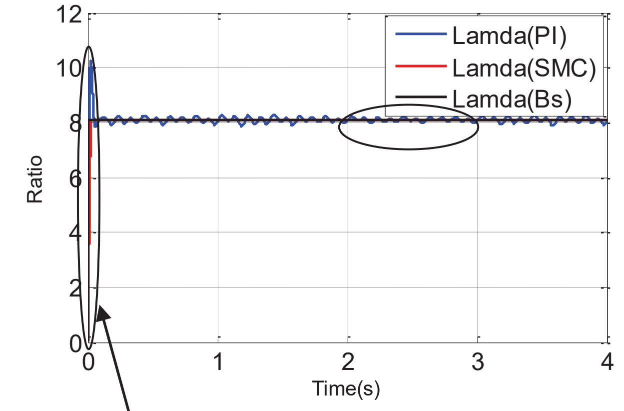

(a)

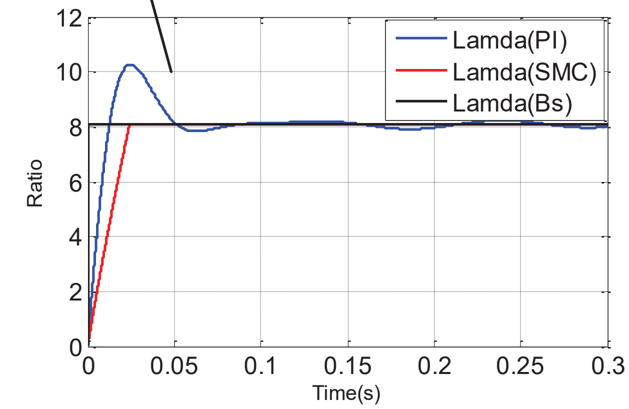

(b)

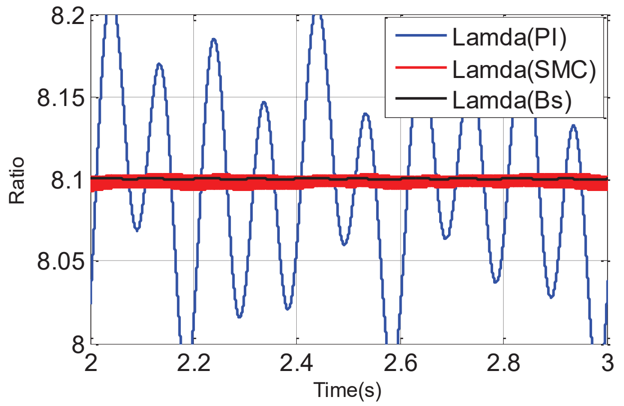

(c)

Fig. 7. (a) Tip speed ratio of three controllers

(b) ,(c)Tip speed Ratio with zoom

Through this first we will evaluate the performance of the three control strategies (PI, SMC, and BS) of the turbine. Also, we compare the responses of three types of controllers applied to the turbine. The simulation results in figure 5, shows a good set followed generator speed, a slight overshoot for a PI controller; unlike for a backstepping and sliding mode controllers shows a good set followed the reference of generator speed without overshoot and faster response time.

Figure 6 presents the evolution of power coefficient of the three control strategies(PI,SMC,BS) of the turbine, it reaches the optimal value (λ_max=8.1) in the three cases with faster response time for the backstepping controller compared to PI and sliding mode controllers.

Figure 7 present a good reference tracking for tip speed ratio, and transient performances with specific overshoot for PI. However, it is also observed that SMC generates undesirable chattering due to its discontinuous termVn which affect the performances of the system, BS's results present better tracking performances of tip speed compared to PI and SMC. The proposed BS succeeded to overcome the problem of undesirable chattering whilst preserving the features of SMC.

V. Conclusion

This paper proposed a comparative study between three types of controllers for maximum power point tracking (MPPT) control strategy using propotional integrator ,sliding mode and backstepping control . First, the modeling of the wind turbine is introduced, thereafter a control strategy using PI first, sliding mode and backstopping are shown.

Simulation results show the performance of the controllers. It's clear that the disadvantage of sliding mode is chattering phenomenon that generates the harmonics and helps to stress the mechanical part, while . All this leads us to think of other improvements such as moving to a backstepping control to eliminate the chattering phenomenon.

APPENDIX

TABLE I. Wind energy conversion system parameters

Name and symbols of parameters	Rated Value
Blade radius,R	35.25m
Number of blades	3
Gearbox ratio, *G*	90
Total moment of inertia, *J*	1000 kg.m^2
Viscous friction coefficient, *fr*	0.0024N/m
Nominal wind speed, *v*	12.15 m/s

References

[1] M.Loucif, "Maximum Power Point Tracking Based on Backstepping Control of Wind Turbine," Electrotehnica, Electronica, Automatica,vol. 104 62, Nr. 3,(2014).

[2] Y. Djeriri, "Lyapunov-Based Robust Power Controllers for a Doubly Fed Induction Generator," Iranian Journal of Electrical and Electronic Engineering 04,551–558,(2020).

[3] F.Z.Belaimeche,A,Bentaallah,S.Massoum,W.Patrice, "A comparative Study Between The Simplified Input/Output Linearizing Control With Fuzzy PI and Classic PI For DFIG In Wind Turbines", Elektrotehniški Vestnik Journal of Electrical Engineering and Computer Science Volume85,No. 4 (2018).

[4] Z. Boudjema, A.Meroufel, E. Bounadja, Y.Djeriri,: "Nonlinear control of a doubly fed induction generator supplied by a matrix converter for

wind energy conversion systems, Journal of Electrical Engineering", Vol. 13, No. 4, pp. 60-68, 2013.

[5] S.Sabiri, N. Machkour, N. Rabbah, M. Nahid, and E. Kheddioui, "Command of a doubly fed induction generator with a backstepping controller for a wind turbine application," International Review of Automatic Control, Vol. 10, No. 1, pp. 56–62, 2017.

[6] S. Boubzizi , H. Abid, A. El hajjaji and M.Chaabane,: "Comparative study of three types of controllers for DFIG in wind energy conversion system," Protection and Control of Modern Power Systems ,(2018).

[7] K. Anusha, S. Siva prasad, " An Enhanced Pitch Control Using Fuzzy Logic For Stability Improvement In DFIG Based Wind Energy Systems ".IJISET-International Journal of Innovative Science, Engineering & Technology, Vol. 2 Issue 10, ISSN 2348 – 7968. October 2015.

[8] R.J.Wai, J.M. Chang, " Implementation of robust waveletneural-network sliding-mode control for induction servo motor drive". IEEE Transactions on Industrial Electronics, vol.50, no.6, pp. 1317-1334,2008.

[9] As tromK.J., Wittenmark B, "Adaptive Control". New York, Addison-Wesley,1995.

Controle of PV system by fuzzy logic based on MPPT using P&O and IncCond algrithms

Khoukha Bouguerra
Electrical Engineering Department,
Automatic Laboratory of Setif-LAS
Ferhat Abbas Setif 1 University-UFAS, Setif, Algeria
khaoukha.bouguerra@yahoo.com

Samia Latreche
Electrical Engineering Department
Automatic Laboratory of Sétif-LAS
Ferhat Abbas Sétif 1University-UFAS, Setif, Algeria
ksamia2002@yahoo.fr

Faiçal Kharchouche
Electrical Engineering Department,
DAC HR Laboratory, Setif
Ferhat Abbas Setif 1 University, Setif, Algeria
faical.kharchouche@univ-setif.dz

Mabrouk Khemliche
Electrical Engineering Department,
Automatic Laboratory of Sétif-LAS
Ferhat Abbas Sétif 1 University-UFAS, Setif, Algeria
mabroukkhemliche@univ-setif.dz

Abstract—**The objective of this work is the use of fuzzy logic control (FLC) based on Perturb & Observe algorithm (P&O) to track the maximum power point (MPPT). The MPPT control is a complex issue, because in the one hand the PV panel will always suffer from the rapid external disturbances due to the variation in weather conditions. On the other hand the PV system could suffer from some internal disturbances such as load variation which remains the design of an appropriate maximum power point tracking (MPPT) controller so difficult [1]. Several techniques have for searching the MPP of photovoltaic systems such as perturb and observe (P&O), the incremental conductance (IncCond) [2] and the hill climbing [3]. These approaches vary in complexity, time response, implementation cost, accuracy and other aspects. But they can, however, fail to achieve MPP under rapidly changing atmospheric conditions. The second one was such as fuzzy logic controller (FLC) [4]. Fuzzy logic controllers have been very successfully applied to many industrial applications over the past few decades [5]. The application of human thinking and natural language in FLC, made it to use in almost all sectors of science and industry [6]. Fuzzy logic-based MPPT tracker have exposed very excellent performances under changing irradiance and temperature conditions without any knowledge of PV generator model. The simulation results presented in this paper, obtained using the Matlab/Simulink environment, show the efficiency and good performance of the proposed system.**

Keywords - PV system faults; P&O algorithm, IncCond algorithm; FLC control; MPPT tracking.

I. INTRODUCYION

Energy now serves as a crucial building block for the social and economic development of any nation. Due to the lack of enough resources from traditional energy sources like fossil and nuclear fuels, the need for energy is one of the biggest problems contemporary living faces on a daily basis without a solution [7]. Despite air pollution and other issues, fossil fuels like natural gas and oil are crucial for the generation of energy [8]. In addition to raising the earth's temperature owing to the concentration of carbon dioxide, air pollution causes smog and acid rain. Additionally, nuclear energy is complicated, pricey, and its fuel is extremely hazardous, necessitating equipment with very high security and measures [9–10].

Helium is created when hydrogen undergoes a self-regulating process in the sun, releasing massive quantities of energy into the atmosphere. This energy is more than enough to meet our requirements, so it must be used to ensure a brighter future and a safer planet without relying on increasingly limited conventional energy. Due to their grid compatibility and effective application in residential and commercial locations during the last decade, solar power plants linked to the grid have gained more attention [11]. There are PV power plants on land or offshore that float at the water's surface [12]. Additional benefits of solar energy are its lack of pollution, ease of installation in any place, quiet operation, and low maintenance requirements for maintaining the Integrity of the Specifications.

The only direct converter that can convert solar energy into electrical energy using PV panels is the photovoltaic generator GPV [5], which provides the opportunity to generate power directly from a renewable and easily accessible resource. In terms of an energy source that is consistent with the limitations of local and global surroundings (complete shading or partial solar panel owing to clouds, trees, dust, snow, shadows from leaves, buildings), their advances consequently represent a significant challenge. Photovoltaic systems can be used in a wide range of stand-alone and grid-connected configurations. Water pumping, air conditioning, lighting, photovoltaic power plants, military applications, space field, and hybrid systems are just a few of the uses for solar energy.

Photovoltaic (PV) energy is one of the most important energy sources since it is clean and inexhaustible. It is important to operate PV energy conversion systems in the maximum power point (MPP) to maximize the output energy of PV arrays. MPPT control is necessary to extract maximum power from the PV arrays. A large number of techniques have been proposed for tracking the maximum power point [13], the classic analyzed methods, the incremental conductance (IncCond), perturb and observe (P&O). Unconventional methods have been also used in literature such as sliding mode controller (SMC) [7] and fuzzy logic controller (FLC). It has an excellent performances and the immunity to disturbances techniques are easily implemented and have been widely. PV systems need special control techniques to ensure the taking out of the utmost available power. Otherwise, the system may not be sustainable. This paper presents a comparison of different MPPT methods P&O and FLC.

II. PV SYSTEM MODELLING AND SIMULATION

II.1 PV SYSTEM DESCRIPTION

A photovoltaic system has four building blocks (Fig.1). The first block represents the energy source (a solar panel), the second a static DC-DC converter, the third the load, and the fourth the control system. The static converter's primary function is to match the panel's impedance so that it can produce the most energy [5].

The operating point of solar panels can fluctuate because environmental factors can have a big impact on them [14]. In order to increase output power and boost PV efficiency, several control techniques must be used. Both the P&O and IncCond approaches are iterative, simple to construct, and able of adapting to changes in climatic circumstances, but they also have certain inherent uncertainties, such as the power value at MPP and the existence of large oscillations.

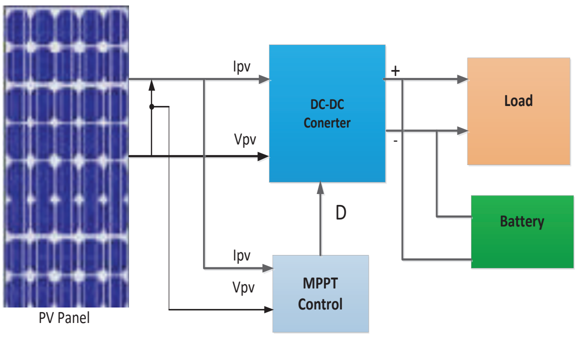

Fig.1 Photovoltaic system structure

II.2 GPV MODELLING

Due to its high efficiency and performance in case of external changes, FLC technology has become one of the most widely used controllers in renewable energy systems [15]. In addition, this technique allows for tracking maximum power in partial shade conditions compared to other calculation methods from one diode electrical circuit of cell (Fig.2).

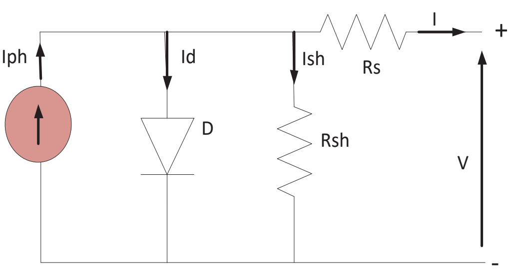

Fig.2 Electrical circuit of PV cell

$$I = I_{ph} - I_0 \cdot \left[\exp\left(\frac{q.(V + I.R_S)}{n.K.N_s.T}\right) - 1 \right] - I_{sh} \tag{1}$$

$$I_{ph} = I_{sc} + K_i.(T - 298).\frac{G}{1000} \tag{2}$$

$$I_0 = I_{rs}.\left(\frac{T}{T_n}\right)^3.\exp\left[\frac{q.E_{g0}.\left(\frac{1}{T_n} - \frac{1}{T}\right)}{n.K}\right] \tag{3}$$

$$I_{rs} = \frac{I_{sc}}{\exp\left(\frac{qV_{oc}}{n.K.N_P.T}\right) - 1} \tag{4}$$

where I_{ph} and I_{sc} are respectively the Photo-current and the short-circuit current, K_i = 0.0032 is the short-circuit current of cell at 25°C, T is the operating temperature, T_n = 298°K represents the normal temperature, G is the solar irradiance in W/m^2, q = 1.6 10^{-19} is the electron charge, V_{oc} is the open-circuit voltage, n=1.3 represents the ideality factor of the diode, K is the Boltzmann's constant (J/°K), $E_{g0}=1.1eV$ is the band gap energy of the semiconductor, N_s is the number of cells connected in series, N_p is the number of cells connected in parallel, R_s and R_p are respectively series and parallel resistances.

II.3 PV MODULE SIMULATION

The dedicated studied system for this work is simulated under a Matlab/Simulink environment. It is composed by (N_sxN_p) PV modules. Each module produces a maximum power of 40W at 21.8V. The electrical characteristics of each PV module under standard test conditions are shown in table 1. The system is also composed of a DC-DC boost converter equipped with perturb and observe (P&O) MPPT. The simulation is done for a constant irradiance 1000W/m^2 and constant temperature 25°C. The simulated P/V and I/V curves are shown respectively in Fig.3 and Fig.4.

TABLE I. ELECTRICAL CHARACTERISTICS OF THE PV MODULE

Rated power P_{mp}	40w
Voltage at maximum power (V_{mp})	18.24 V
Current at maximum power (I_{mp})	2.20 A
Open-circuit Voltage (V_{oc})	21.8 V
Short-circuit Voltage (I_{sc})	2.35 A

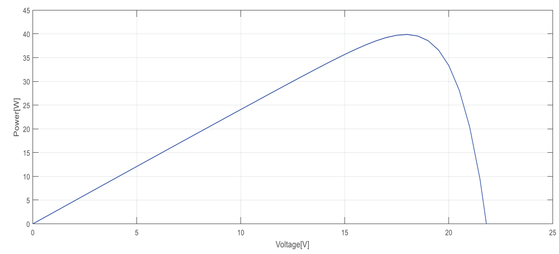

Fig.3. P/V characteristic

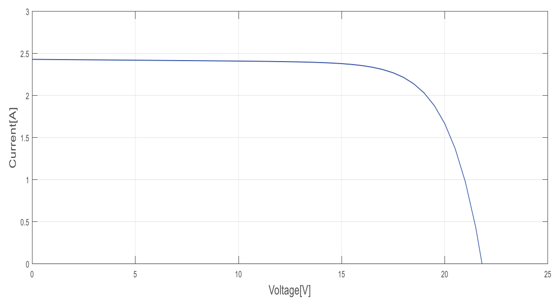

Fig.4. I/V characteristic

II.4. Power Conversion Structure

The synthesis of the MPPT control of a photovoltaic system the scheme in Fig. 5 represents a system consisting of a GPV and a DC/DC converter. The role of this converter (in the framework of the PV) is to the adaptation between the source (GPV) and the charge for a maximum power transfer [16]. There are several types of DC/DC converters that prove to be used in the PV system according to the planned installation; elevator converter, lowering converter, and the elevator-lowering converter. The maximum power point varies proportionally with the variation of irradiance and temperature. Several methods are used to track this, the basic principle of which is to change the cyclic ratio of DC/DC converter which varies the output voltage and thus the power produced [17].

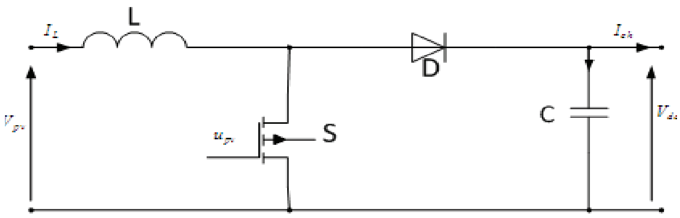

Fig.5. DC-DC boost converter

$$V_{pv} = L\frac{dI_L}{dt} + V_{dc}\left(1-u_{pv}\right)$$

$$\left(1-u_{pv}\right)I_L = C\frac{dV_{dc}}{dt} + I_{ch} \qquad (5)$$

III. MPPT Methods

Maximizing PV power is still a difficult task [6]. The effectiveness of the photovoltaic system is significantly impacted by the technology used to monitor the PPM maximum power point. The power of a PV generator can be maximized in a variety of ways. The most often employed ones are fuzziness of logic, incrimination of induction, perturbation, and observation. These approaches differ in a number of areas, including convergence speed, system stability, simplicity (Fig.6).

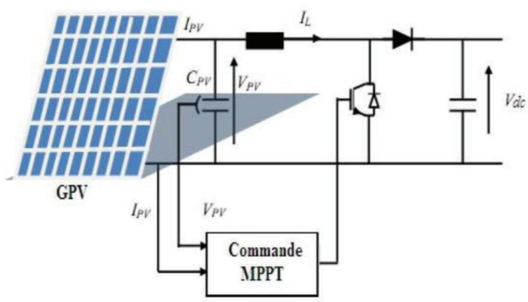

Fig.6. Synthesis of MPPT control of a photovoltaic generator

III.1. Perturb and Observe Algorithm

This approach is based on the idea that modest variations in the PV system's voltage V_{PV} from its starting value can have a significant impact on the converter's cyclic ratio [18]. The power derivative with respect to voltage is equal to zero at the MPP.

$$\frac{dP}{dV} = 0 \qquad P = V * I \qquad (6)$$

P&O algorithm is one of the most extensively utilized MPPT strategies because it is so simple to apply. This approach is based on perturbing the photovoltaic system by altering the duty cycle and then evaluating the impact on the PV generator's output power. If the perturbation results in a rise in output power, the operating point has shifted toward the maximum power and the subsequent perturbation will be made in the same direction. However, the new perturbation is created in the opposite direction if the output power drops. It suffers from the lack of speed and adaptability which is necessary for tracking the fast transients under varying environmental conditions, it has sever power oscillations in permanent mode and a slow erroneous convergence to MPP in the event of a sudden shift in irradiance, which leads to system power losses. Fig.7 shows the P&O algorithm diagram[19].

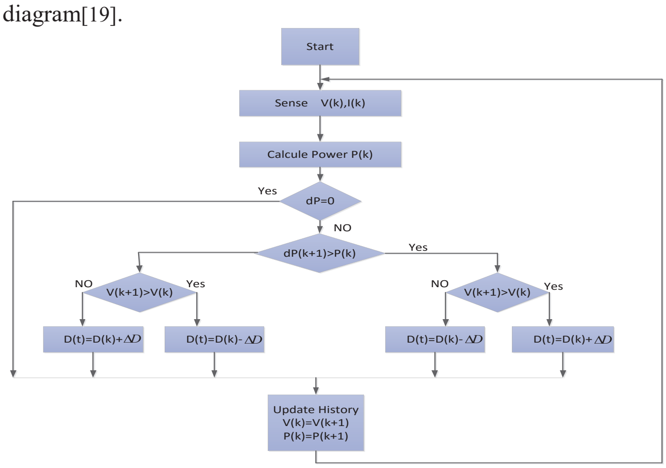

Fig.7. P&O Algorithm

III.2. Incremental Conductance (IncCond)

This approach, as implied by its name, is based on an understanding of the fluctuation in the solar generator's conductivity and its location in relation to the maximum point of operation.

$$\begin{cases} dI/dV = -I/V & if \quad \mathrm{P} = MPP \\ dI/dV \succ -I/V & if \quad \mathrm{P\ is\ on\ the\ left\ of}\ MPP \\ dI/dV \prec -I/V & if \quad \mathrm{P\ is\ on\ the\ right\ of}\ MPP \end{cases} \qquad (7)$$

III.3. Fuzzy Controller Synthesis

The maximum power supplied by the photovoltaic panel is not always stable and fixed in the same operating point; it varies with the weather conditions, such as solar irradiance, shadow, and temperature. The use of control techniques to maximize output power and improve PV efficiency is necessary. Both the P&O and IncCond methods are iterative, simple to develop, and respond to variations in weather conditions, however, they include certain imprecisions, such as the power value at MPP, and the presence of significant fluctuations [14].

The FLC technique has grown to be one of the most popular controllers in renewable energy systems because of its high efficiency and performance in the face of external changes [15]. In contrast to other computation techniques, this method also enables tracking of maximum power during conditions of partial shadow.

Fig.8 provides a general breakdown of the blurring controller's architecture. The error (e) and its derivative (de), which are the two inputs for this controller, have through three steps of information processing: fuzzification, défuzzification, and inference to produce the output (du). The following is a summary of each block's function.

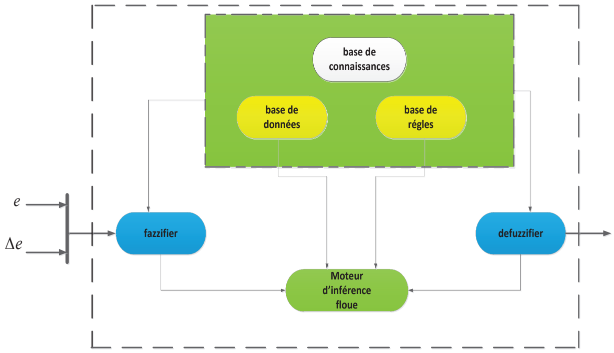

Fig. 8. Fuzzy regulator synthesis block scheme

In our situation, the power and voltage derivatives dP_{PV} and dV_{PV} as shown in Fig.9, along with the error and the variation of the error, are the inputs of the blur regulator.

$$e_{pv}(k) = \frac{P_{pv}(k) - P_{pv}(k-1)}{V_{pv}(k) - V_{pv}(k-1)} \quad de_{pv}(k) = e_{pv}(k) - e_{pv}(k-1) \tag{8}$$

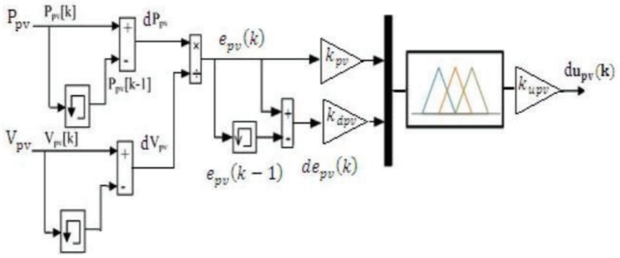

Fig.9. General diagram of a fuzzy MPPT controller

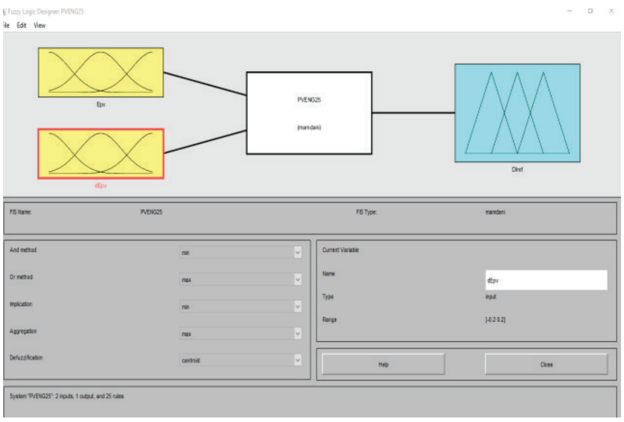

Fig.10. The blur controller's language variables

The blur controller's language variables are described as follows: The association between inputs and outputs is (PB: Positive Big, PS: Positive Small, Z: Zero, NS: Negative Small, NB: Negate Big).

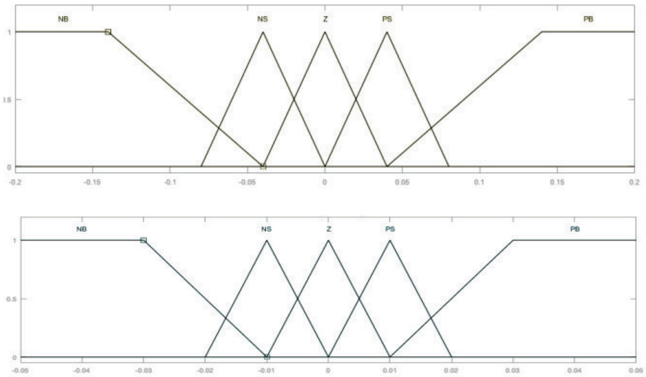

Fig.11. Membership Function of (e_{PV}, de_{PV})

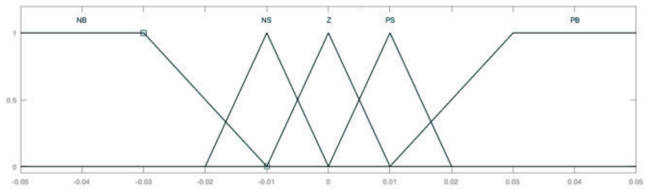

Fig.12. Membership Function of du_{PV}

du_{pv}	NB	NS	Z	PS	PB
NB	PB	PB	PB	Z	Z
NS	PB	PB	PS	Z	NS
Z	PB	PS	Z	NS	NB
PS	PS	Z	NS	NB	NB
PB	Z	NS	NB	Z	NB

IV. SIMULATIONS OF PROPOSED SYSTEM

To test the dynamic behaviour of the selected PV system, MPPT techniques based on P&O, on fuzzy logic controle, and on the proposed controller were simulated, evaluated, and compared using Matlab/Simulink software, taking into consideration the variation in solar irradiance and temperature .

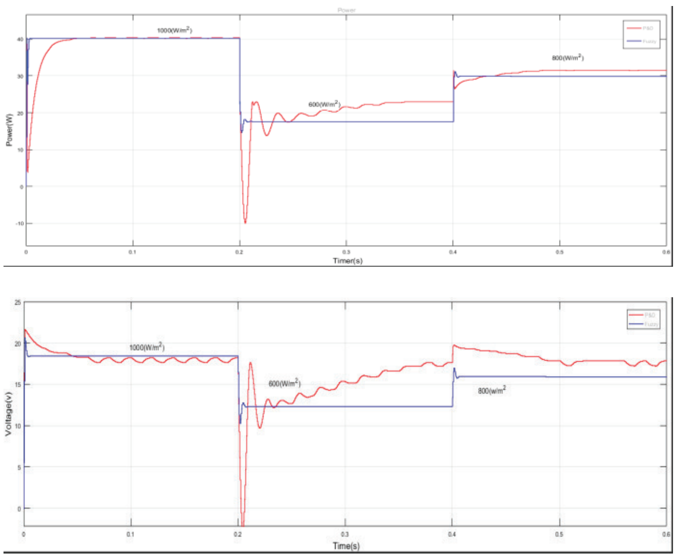

Fig.13.PV panel output power and voltage under varying irradiance

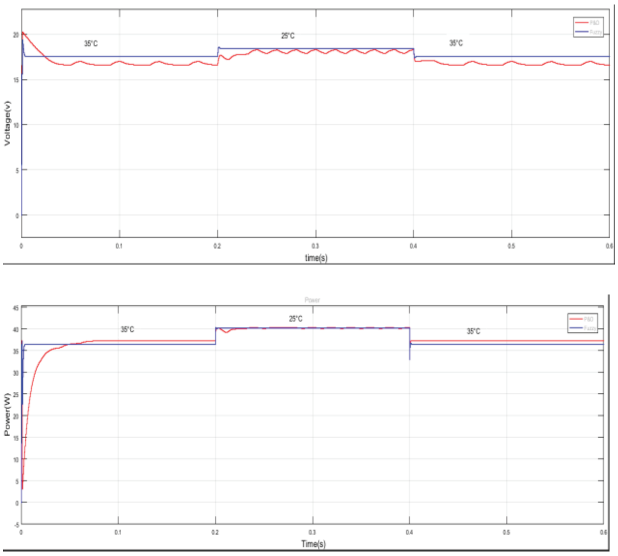

Fig.14.PV panel output power and voltage under varying temperature

V. CONCLUSION

The results show that all techniques introduced here are able to track the MPP with different time but we note that the system with the fuzzy logic control FLC reaches steady state of both irradiance steps much faster compared to the other tracking strategies while the P&O method is slow under rapidly irradiance changing. We note also here that the proposed FLC provides quickly moving of the operating point toward the MPP which reduce the power losses due to search process. Fig.14 and Fig.15 illustrate the power and voltage responses of PV system under rapid temperature variation and varying irradiance levels in order to verify the robustness of proposed technique. The obtained results show a good robustness of the FLC technique. It takes less time to track accurately and maintains the output power at MPP all time. From the above results, it can be clearly seen that the FLC technique and exhibits good performance compared to classical P&O.

For solar systems to function better, various MPPT control mechanisms are investigated and developed in this work. According to the simulation results, the FLC controller offers good performance and exhibits extremely strong dynamics in comparison to other tactics when lighting changes, allowing it to better pursue the maximum power point with lower power losses.

REFERENCES

[1] S. Latreche, A. Khenfer, and M. Khemliche, "Sensors placement for the faults detection and isolation based on bridge linked configuration of photovoltaic array", *Electrical Engineering and Electromechanics*, Journal vol.2022, no. 5, pp. 41–46, Sep. 2022, doi: https://doi.org/10.20998/2074-272X.2022.5.07

[2] Y. Lahiouel, S. Latreche, M. Khemliche, L. Boulemzaoud, Photovoltaic fault diagnosis algorithm using fuzzy logic controller basedon calculating distortion ratio of values. Electrical Engineering & Electromechanics, 2023, no. 4, pp. 40-46. doi: https://doi.org/10.20998/2074-272X.2023.4.06

[3] F. Liu, Y. Kang, Y.,Zhang, & S. Duan, (2008, June). Comparison of P&O and hill climbing MPPT methods for grid-connected PV converter. In Industrial Electronics and Applications, 2008. ICIEA 2008. 3rd IEEE Conference on (pp. 804-807). IEEE.

[4] M. Derri, M. Bouzi, I. Lagrat, & Y. Baba, (2014, December).Maximum Power Point Tracking using Fuzzy Logic Controller for Stand Alone photovoltaic System. In International Journal of Engineering Research and Technology (Vol. 3, No. 11 (November-2014)). ESRSA Publications

[5] C. Vincenzo et al. "An intelligent flying system for automatic detection of faults in photovoltaic plants." Journal of Ambient Intelligence and Humanized Computing, 11. 5 (2020): 2027-2040.

[6] Y. Zhu, J. Fei, Adaptive Global Fast Terminal Sliding Mode Control of Grid connected Photovoltaic System Using Fuzzy Neural Network Approach, IEEE Access,vol.5, pp.9476–9484, 2017

[7] A. Djalab, A. Teta, M. M. Rezaoui, M. Boudiaf, "Analysis of MPPT Methods: P & O, INC and Fuzzy Logic (CLF) for a PV System", 2019.

[8] L. Zhihua, W. Yuanzhang, Z. Diqing, and W. Chunhua. "An Intelligent using a stable single input fuzzy logic controller. Renewable and Sustainable Energy Reviews, 49, 907-920.

[9] M. Khemliche, S. Djeriou, S. Latreche. "Diagnostic de défauts dans le système photovoltaïque par les réseaux de neurones artificiels ". Revue des Énergies Renouvelables, SIENR'12 Ghardaïa. Vol, pp. 331-343, 2012.

[10] A.M. Hassan et al. "Real time fault detection in photovoltaic systems.", Energy Procedia, 111 (2017): 914-923.

[11] J. Gosumbonggot and G. Fujita, Partial Shading Detection and Global Maximum Power Point Tracking Algorithm for Photovoltaic with the Variation of Irradiation and Temperature, Energies, vol.12, no. 202, pp.1- 22, 2019..

[12] M. Dhimish, & G. Badran, Photovoltaic Hot-Spots Fault Detection Algorithm Using Fuzzy Systems. IEEE Transactions on Device and Materials Reliability, 2019 ,vol. 19, no. 4, pp. 671-679. doi: https://doi.org/10.1109/TDMR.2019.2944793

[13] M.A. Moussa, A. Derrouazin, M. Latroch, M. Aillerie, A hybrid renewable energy production system using a smart controller based on fuzzy logic. Electrical Engineering & Electromechanics, 2022, no. 3 pp.46-50, . doi: https://doi.org/10.20998/2074-272X.2022.3.07

[14] F. Bait, S. Latreche, and M. Khemliche, "Simulation of different faults in photovoltaic installation," in *2022 19th IEEE International Multi-Conference on Systems, Signals and Devices, SSD 2022*, May 2022, pp. 1130–1138, doi: 10.1109/SSD54932.2022.9955851

[15] Z. Bouguerra and A. Benfdila, Comparative Study of Individual and Hybrid Renewable Energy Systems (Photovoltaic, Wind Energy and Hybridization).Controlled by Fuzzy Logic Control, Journal of Engineering Science and Technology Review, vol. 14, no.5, pp.180–186,2021.

[16] S. Latreche, A. E. Badoud, and M. Khemliche, "Implementation of MPPT algorithm and supervision of shading on photovoltaic module," *Engineering, Technology and Applied Science Research*, vol. 8, no. 6, pp. 3541–3544, Dec. 2018, https://doi.org/doi: 10.48084/etasr.2354.

[17] M. Derri, , Bouzi, M., Lagrat, I., & Baba, Y. (2014, December). Maximum Power Point Tracking using Fuzzy Logic Controller for Stand-Alone photovoltaic System. In International Journal of Engineering Research and Technology, Vol. 3, No. 11, November 2014. ESRSA Publications.

[18] H. E. Amara, S. Latreche, M. A. Sid, and M. Khemliche, "Sliding mode observer and event triggering mechanism co-design,"*Engineering Technology and Applied Science Research*, vol. 10, no. 11 pp. 5487–5491 Apr. 2020, doi: 10.48084/etasr.3285.

[19] C..C., Chu, & C.L. Chen, (2009). Robust maximum power point tracking method for photovoltaic cells: A sliding mode control approach. Solar Energy Journal, 83(8), 1370-1378.

Intelligent Maximum Power Point Tracking of Photovoltaic Solar Systems using Fuzzy Logic control

Amel Smaili
LABSET
USDB University
Blida Algiers, Algeria
smailiamel775@gmail.com

El Ghalia Boudissa
LABSET
USDB University
Blida Algiers, Algeria
boudissaelg@yahoo.fr

M'hamed Bounekhla
LABSET
USDB University
Blida Algiers, Algeria
bounekhla.mhamed@yahoo.fr

Abstract—**In order to meet the global demand for energy, solar power has been introduced as a renewable, environmentally-friendly source of electricity. It converts solar energy into electricity via solar panels, whose power output varies with environmental conditions, temperature and irradiation. Due to the high cost of photovoltaic electricity, we need to convert the maximum amount of available solar energy by operating the photovoltaic system at its maximum power point MPP. In this paper, a fuzzy logic-based control approach is suggested to track the MPP. The fuzzy logic based maximum power point tracking MPPT method revolves around a configuration that contains 4 principal components: the PV system, the load, the Sepic Converter serving as a matching stage between the PV system and the load, and the MPPT controller. A simulation was conducted in MATLAB Simulink with 1Soltech 1STH-215-P Module; the obtained results were satisfactory and show that the fuzzy logic approach is effective in tracking the maximum power point under different environmental conditions.**

Keywords-solar energy; Maximum power point tracking MPPT; Fuzzy Logic Control; PV system; Temprature; Irradiance; Sepic Converter;

I. INTRODUCTION

The Global demand for energy is rising significantly, due to population growth and industrial development. However, non-renewable energies - fossil fuels – are common across the world, although they pose a number of problems, including heavy pollution of the ecosystem and the fact that they are exhaustible and limited, so that at some stage they may no longer be able to meet the world's energy needs. Hence, the global shift is occurring towards renewable energies [1].

Of all the renewable energy resources, our attention turns to solar power due to its nature as a renewable and environmentally friendly electricity source. Moreover, solar power is scalable and operates through a technology that directly converts solar energy into electricity using photovoltaic (PV) panels. The latter's efficiency depends on the environmental conditions and the chosen load [2].

From an economic perspective, fully utilizing the reachable output of the solar panels is of crucial importance, thus the PV system should be operated at its maximum power point in any environmental conditions.

Several conventional algorithms have been introduced to ensure that the PV system operates at its maximum power point [3]-[4]. Among these, the perturb and observe (P&O) algorithm which is the simplest and the most basic one to implement. Nevertheless, it will work properly in stable, slowly changing environmental conditions, whereas, it will experience extended tracking delays for the Maximum Power Point Tracking when conditions change rapidly [5].

In this paper, we suggest a fuzzy logic-based control approach in order to optimize the power output of PV panels, intending to overcome the drawbacks presented by conventional algorithms, as well as increasing the overall performance of the photovoltaic solar panels under changeable environmental conditions.

II. SYSTEM MODELING AND ANALYSIS

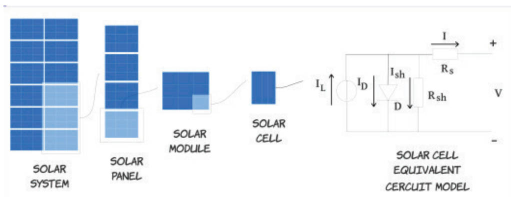

Figure 1. From solar system to solar cell equivalent circuit model.

The solar system consists of several photovoltaic PV panels connected together either in parallel or in series configurations forming a PV array as shown in Figure 1. The Single Diode Model of the PV module equation is defined by (1) [6]-[7]:

$$I = I_L - I_o\left(e^{\frac{q(V+R_sI)}{AkT}} - 1\right) - \frac{V + R_sI}{R_{sh}} \quad (1)$$

With, "I" is the PV output current, "I_L" indicates the photo-generated current, "I_O" represents the saturation current, "V" is the output voltage, R_s and R_{sh} refer, respectively, to the series and shunt resistance.

Note that T is the absolute temperature, q refers to the electron charge $(q = 1.60217646 \times 10^{-19} C)$, k is the Boltzmann constant$\left(K = 1.38065 \times 10^{-23}\, {}^{J}/_{K}\right)$, A denotes diode ideality factor. [6]-[7].

In order to clearly observe the effect of temperature and irradiation on the operating point of the PV cell, we simulate in Matlab a "1Soltech 1STH-215-P" PV module whose characteristics are presented in Table I.

The panel reaches its peak operational performance when the temperature is maintained at 25°C, coupled with an irradiance of 1000W/m². So, we will establish one of these factors as a reference while altering the other to observe its influence.

TABLE I. 1SOLTECH 1STH-215-P PV MODULE CHARACTERISTICS

1Soltech 1STH-215-P Module	
Parameter	**Value**
Maximum power (W)	213.15
Open circuit voltage Voc (V)	36.3
Voltage at maximum power point Vmp (V)	29
Current at maximum power point Imp (A)	7.35
Short-circuit current Isc (A)	7.84

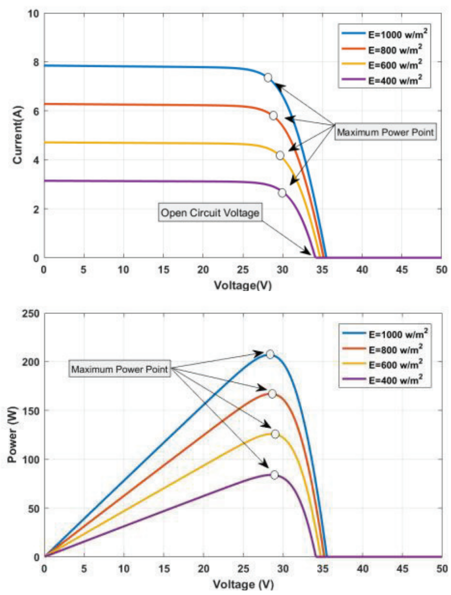

Figure 2. Current, voltage and power characteristics of PV panel under fixed temperature and different solar irradiance.

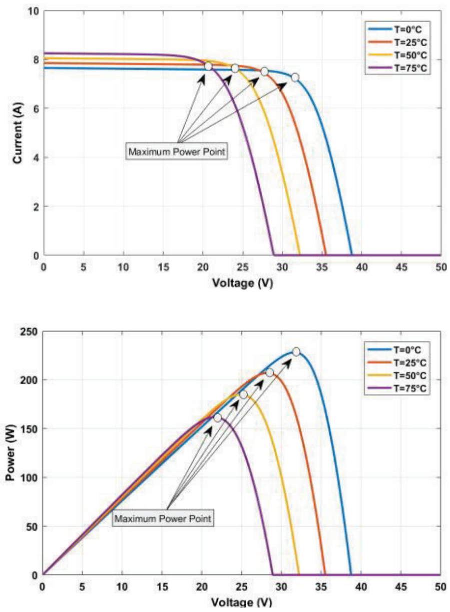

Figure 3. Current, voltage and power characteristics of PV panel under fixed irradiance and different temperature.

The power output of the PV panel increases with an increase of irradiation; however, the maximum power point remains relatively consistent, hovering at around 80% of the open circuit voltage [7] as shown in Figure 2.

Figure 3 reveals that unlike irradiance, the relationship between the temperature and the power is an inverse correlation, the maximum point in this case is not fairly stable and might occur at varying voltages.

III. FUZZY LOGIC BASED MPPT DESIGN

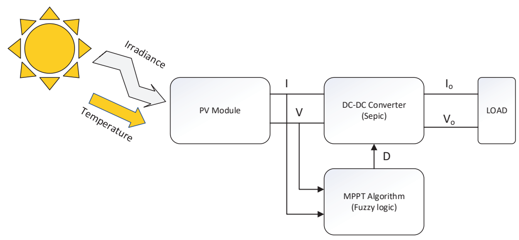

Figure 4. PV system block diagram.

According to the Voltage-Power characteristics it is clear that's one singular voltage value aligns with the maximum power point, which in turn means one specific resistance value [8].

So, in order to achieve the MPP, the impedance seen by PV panel must be matched to the load resistance, this explains the incorporation of the matching stage-a DC-DC converter- between the PV module and the load as shown in Figure 4.

To control the converter, we'll use a Fuzzy logic MPPT algorithm to monitor the duty cycle D and find its most suitable value that guarantees the matching between the two impedances in any environmental conditions.

A. The basic components of a fuzzy logic Control

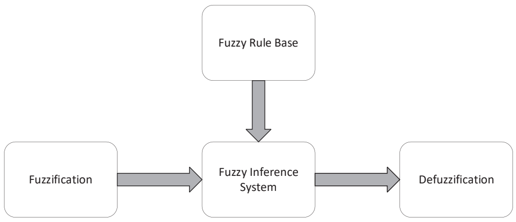

Figure 5. Structure of fuzzy logic controller.

The fuzzy logic controller consists of 3 principal components which are fuzzification, fuzzy inference rules and defuzzification.

1) Fuzzification: Before starting the first step of fuzzy control, it's imperative to define the inputs and outputs to be fuzzified. In our case, the error (E) and the variation of error (DE) are our inputs while the variation of the duty cycle D is the output of our fuzzy controller.

$$E = \frac{\Delta P}{\Delta V} = \frac{P(n)\text{-}P(n\text{-}1)}{V(n)\text{-}V(n\text{-}1)} \quad (2)$$

$$\Delta E = E(n)\text{-}E(n\text{-}1) \quad (3)$$

In order to calculate the E and DE, at the instant sampling "n" as shown in (2) and (3) [6]. We continuously measure the current I and voltage V of the photovoltaic module and then we calculate the power as in (4).

$$P=V.I \quad (4)$$

After identifying the system's inputs and the outputs, we represented them with membership functions by using Mamdani method as in Figures 6.

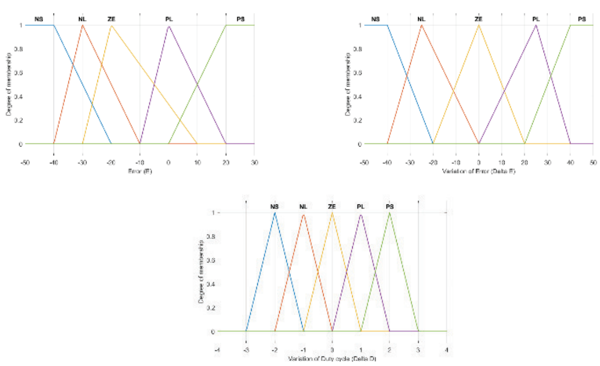

Figure 6. Inputs and output memberships functions.

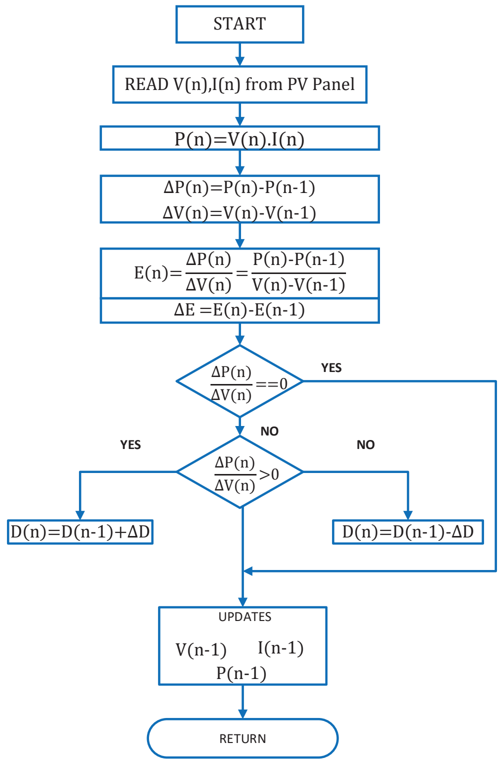

Figure 7. MPPT algorithm.

2) Fuzzy inference rules: The purpose of this step is to set up rules that link outputs to inputs, based on observations of inputs and outputs.

Within our research, we used a table inference of 25 rules "Table II [9]" that has the purpose of increasing or decreasing the duty cycle according to the actual point's position in relation to the maximum power point [6].

3) Defuzzification: This operation is the inverse of fuzzification, so it aims to convert the linguistic output to numerical output by using a fuzzy centroid method, which calculates the centroid subsequent to rules aggregation.

To implement the fuzzy MPPT control we used the algorithm depicted in figure 7.

TABLE II. INFERENCE RULES

E/ΔE	NS	NL	ZE	PL	PS
NS	PS	PS	PL	PS	PS
NL	PS	PL	PL	PL	PS
ZE	NL	NL	ZE	PL	PL
PL	NS	NL	NL	NL	NS
PS	NS	NS	NL	NS	NS

IV. Results and Discussion

In this section we will present the results of simulation carried out using MATLAB, Simulink, utilizing “1Soltech 1STH-215-P” PV module.

The Figure 8 provides an overview of the general Simulink model of the PV system which contains a PV array, the Sepic converter and the fuzzy logic block. Figure 8 gives an in-depth exposition of the fuzzy logic block constituent elements.

The Results of simulation under ideal environmental conditions 25°C and 1000 W/m² are presented in Figure 9.

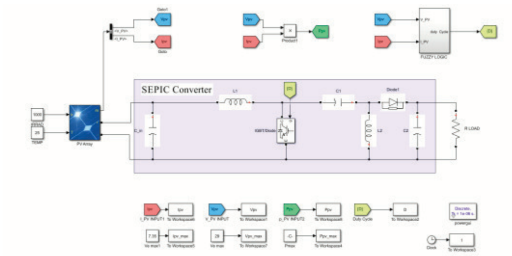

Figure 8. Simulink model of PV System.

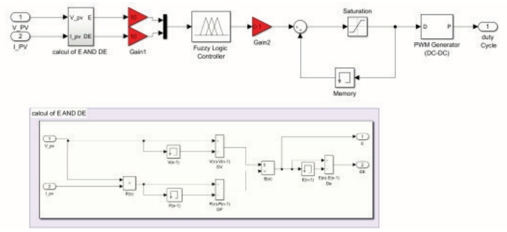

Figure 9. Fuzzy MPPT algorithm block.

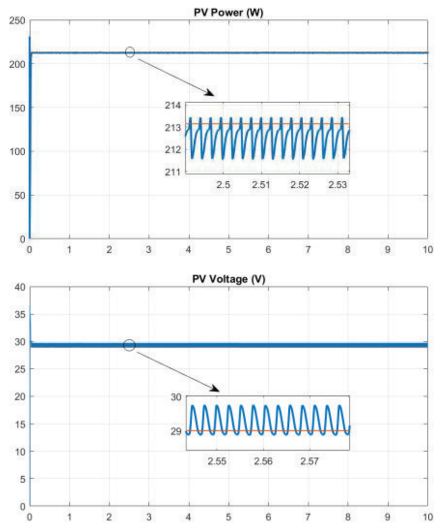

Figure 10. Fuzzy MPPT Power and Voltage response.

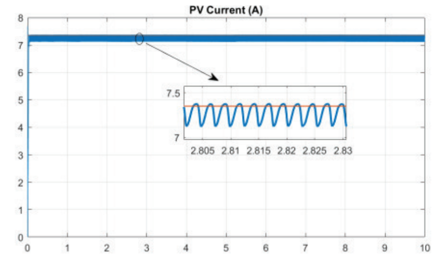

Figure 11. Fuzzy MPPT Current Response.

In order to clearly see the effectiveness of the fuzzy MPPT approach in achieving its objective of tracking the maximum power point across different environmental conditions, we perform two simulations within MATLAB Simulink:

- Variable solar irradiance: We examine different solar irradiation levels (1000 W/m², 800 W/m², 600 W/m²) while maintaining a constant temperature of 25°C.
- Variable temperature: we study different degrees of temperature (25°C, 50°C, 75°C) at a fixed solar irradiance 1000 W/m².

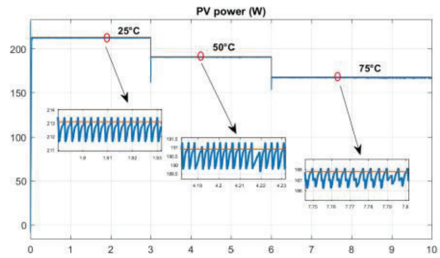

Figure 12. Fuzzy MPPT power response under variable temperature and fixed irradiation.

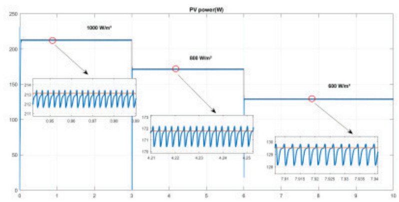

Figure 13. Fuzzy MPPT power response under variable irradiation and fixed temperature.

Figure 12 and Figure 13, clearly show that the Fuzzy MPPT method has an excellent response time. This method detects rapidly the change in environmental conditions and then adjust the system operating point, so that the system works at the MPP.

The results highlight the ability of the Fuzzy MPPT method to track the maximum power point, once the MPP is found, the method maintains a consistent oscillation around this point ensuring the system's operation point doesn't deviate from the MPP.

V. CONCLUSION

Solar energy is one of the most widely used renewable energies in the world. This energy is directly converted into electricity by solar panels. Environmental changes, temperature and irradiation, affect the operating point of the PV system that's why many algorithms have been developed to ensure that the PV system work at its maximum power point. In this article, we present a Fuzzy MPPT approach that was carried out in MATLAB Simulink using the "1Soltech 1STH-215-P" PV module. The results show that the FUZZY MPPT approach is effective in tracking the maximum power point.

VI. REFERENCES

[1] Kannan Nadarajah, Vakeesan Divagar. Solar energy for future world: - A review. Renewable and Sustainable Energy Reviews, 2016.

[2] Mohsen Taherbaneh A. H. Rezaie, H. Ghafoorifard, K. Rahimi,and M. B. Menhaj. International Journal of Photoenergy, Maximizing Output Power of a Solar Panel via Combination of Sun Tracking and Maximum Power Point Tracking by Fuzzy Controllers,2010.

[3] XIE Wei, HUI Jing. 2010 International Conference on Digital Manufacturing & Automation, MPPT for PV System Based on A Novel Fuzzy Control Strategy, 2010.

[4] Pallavee Bhatnagar, R.K. Nema. Renewable and Sustainable Energy Reviews, Maximum power point tracking control techniques: State-of-the-art in photovoltaic applications,2013.

[5] D. Sera et T. Kerekes, R. Teodorescu, and F. Blaabjerg. IEEE ISIE 2006, Improved MPPT method for rapidly changing environmental conditions, 2006.

[6] Ahmad Saudi Samosir Herri Gusmedi, Sri Purwiyanti, Endah Komalasari, International Journal of Electrical and Computer Engineering (IJECE), Modeling and Simulation of Fuzzy Logic based Maximum Power Point Tracking (MPPT) for PV Application ,2018.

[7] Ekrem Kandemir, Numan S. Cetin, Selim Borekci. PERIODICALS OF ENGINEERING AND NATURAL SCIENCES, A Comparison of Perturb & Observe and Fuzzy-Logic Based MPPT Methods for Uniform Environment Conditions 2017.

[8] Ranganai T. Moyo, Pavel Y. Tabakov, and Sibusiso Moyo. Southern African Solar Energy Conference (SASEC 2019), THE EFFICACY OF THE MAXIMUM POWER TRANSFER THEOREM IN IMPROVING THE EFFICIENCY OF PHOTOVOLTAIC MODULES: A REVIEW, 2020.

[9] Sid-ali Blaifi, Samir Moulahoum, Bilal Taghezouit, Abdelhakim Saim. Renewable Energy, An enhanced dynamic modeling of PV module using LevenbergMarquardt algorithm, 2019.

Development of a smart controller for a stand-alone photovoltaic system with Battery State of Health monitoring

Elouahab Bouguenna
Division Energie Solaire Photovoltaïque
Centre de Développement des Energies Renouvelables, CDER
16340 Bouzareah, Algiers, Algeria
a.bouguenna@cder.dz

Walid Merrouche
Division Energie Solaire Photovoltaïque
Centre de Développement des Energies Renouvelables, CDER
16340 Bouzareah, Algiers, Algeria
w.merrouche@cder.dz

Bilal Taghezouit
Division Energie Solaire Photovoltaïque
Centre de Développement des Energies Renouvelables, CDER
16340 Bouzareah, Algiers, Algeria
b.taghezouit@cder.dz

Abstract*— Ensuring the safe operation and extended lifespan of batteries hinges on the criticality of monitoring their state of health (SOH). The primary challenge associated with the model-based approach to monitoring battery state lies in the precision of parameter measurements. This paper proposes a development of a smart controller for stand-alone photovoltaic (PV) systems, with improvement of a previous SOH model to reflect the battery aging state by monitoring the working zone and temperature. Hence, the proposed controller is designed to optimize the PV system performance by continuously monitoring the battery SOH and regulating the charging and discharging of the battery accordingly. The system consists of a microcontroller unit (MCU) PIC18F45K22, which is included in the EasyPIC board, programmed by the MicroC IDE application, based on the C language, and sensors to capture the battery parameters such as voltage, current and temperature and the LCD to see it currently, after we put the microcontroller in the controller board. Therefore, the performance of the proposed system is evaluated through simulations by PROTEUS software and experiments, and the results demonstrate that the smart controller can improve the efficiency and reliability of the stand-alone PV system while extending the life of the battery. The proposed system has the potential to significantly enhance the feasibility and adoption of stand-alone PV systems for off-grid applications.

Keywords*— Stand-alone Photovoltaic systems, Solar controller, Solar Battery, State of health, Battery working zone and temperature tracking.

I. Introduction

The global electricity consumption over the past decades has demonstrated a robust correlation with the advancement of industries, transportation, and communication technologies. Presently, a substantial portion of electricity generation relies on non-renewable sources like coal, natural gas, oil, and uranium. Unfortunately, these resources possess an exceptionally gradual regeneration rate within the context of human timeframes. Consequently, there exists a foreseeable risk of these resources being depleted in the medium to short term.

Amid the gradual exhaustion of fossil energy reserves, economic upheavals triggered by escalating oil prices, and occurrences of nuclear plant disasters like the incidents at Three Mile Island (USA, 1979) and Chernobyl (USSR, 1986), the global populace's enthusiasm for renewable energy sources has continued to surge. This growing interest has already outpaced the available supply, contributing to significant volatility in global oil prices, as illustrated, for instance, by substantial fluctuations [1].

A variety of renewable energy sources exists, encompassing hydroelectric, geothermal, wind, biomass, and photovoltaic energy. Among these, photovoltaic energy stands out prominently. Benefiting from its favorable geographical positioning, Algeria boasts a significant solar potential, particularly pronounced in the southern regions of the country. Undoubtedly, solar energy holds paramount importance in Algeria's energy landscape, with its availability varying substantially across seasons. In winter, solar radiation hovers around 4 kW/m2/day, while in the peak of summer, it can surge to an impressive 8.5 kW/m2/day [2].

An emerging trajectory within power electronics is the advancement towards renewable energy systems incorporating distributed generation. The imperative of environmental preservation is a pivotal driver that has catalyzed the pursuit of novel avenues for harnessing electrical energy. It's the synergy of technological breakthroughs and evolving regulatory landscapes that has spurred heightened enthusiasm for renewable energy production. This momentum is propelled by the persistent global escalation in energy requirements, consequently elevating the significance of renewable sources, which have now assumed a pivotal role in both cogeneration and energy distribution.

Owing to the non-linear behaviors of photovoltaic systems, the task of effectively controlling them using conventional regulators becomes intricate. These standard approaches necessitate numerous simplifications and system linearizations, which, in turn, often diverge from the intricate realities of the actual system dynamics. In the realm of stand-alone photovoltaic (PV) systems (i.e., not grid-connected) batteries serve as pivotal components for storing surplus energy and supplying power during periods of inadequate sunlight. However, these batteries are susceptible to issues like overcharging, deep discharges, temperature fluctuations, and current drifts. Consequently, the integration of a regulator becomes imperative to safeguard their operation. The significance of a charge controller in such stand-alone PV system is undisputed, demanding meticulous execution to balance the demands of cost, simplicity, and reliability [3].

The primary focus of this work revolves around elevating the performance of photovoltaic systems through the innovation of a solar controller. This controller serves a multifaceted purpose: gauging battery terminal parameters such as temperature, current, and voltage to ascertain the battery's health status, and refining the regulation threshold values by compensating for temperature fluctuations. The solar controller assumes the role of continuous monitor over the battery's condition, ensuring protection against overcharging and over-discharging. Achieving this involves dynamically adjusting the current through the DC-DC converter, an integral component of the regulator's power board. Simultaneously, the controller manages the MOSFET transistor during discharge, strategically allowing or halting the load's operation. This is particularly crucial in scenarios of deep discharge or extreme cold conditions, amplifying the battery's lifespan through judicious control to counteract potential damage.

This study aims to realize instantaneous measurements of battery terminal parameters (current, voltage, and temperature) through sensor technology. Nonetheless, it's important to note that the state of health (SOH) isn't directly ascertainable via sensors. To bridge this gap, a control circuit was meticulously constructed within the Proteus software environment. This circuit simulated the measurement of battery parameters and the monitoring of battery SOH. This simulation was facilitated by a virtual microcontroller programmed with MicroC assembler, leveraging the Working Zone and Temperature Tracking (WZTT) methodology [4]. Subsequently, the program code was generated and deployed into a physical microcontroller embedded within the control circuit. This real-world implementation enabled the real-time measurement and continuous tracking of the battery's state of health.

The remaining of this paper is organized as follows: An overview of different components including in our PV system with battery SOH monitoring with the working zone and temperature tracking model are presented in section2. The methodology, followed by the results obtained from the experimental study and discussion, are demonstrated in section 3. Finally, the conclusions of the work are presented in section 4.

II. MATERIALS AND METHODS

II.1 Battery SOH *monitoring system*

In this section, we will outline the process and the essential components involved in creating the State of Health (SOH) monitoring system integrated into a solar regulator. The primary objective is to enhance the efficiency of a standalone Photovoltaic system (PVS) by continually assessing the health of the battery using the WZTT model. This information, along with real-time measurements of current, temperature, voltage, and SOH, is then exhibited on an LCD screen.

Illustrated in Figure 1 is the solar controller within an standalone PVS designed for battery charging purposes. The charge controller consists of two main parts: the control unit, which incorporates the SOH monitoring system, and the power unit represented by the DC-DC converter. The control unit monitors the power unit of the regulator through the Pulse Width Modulation (PWM) signal.

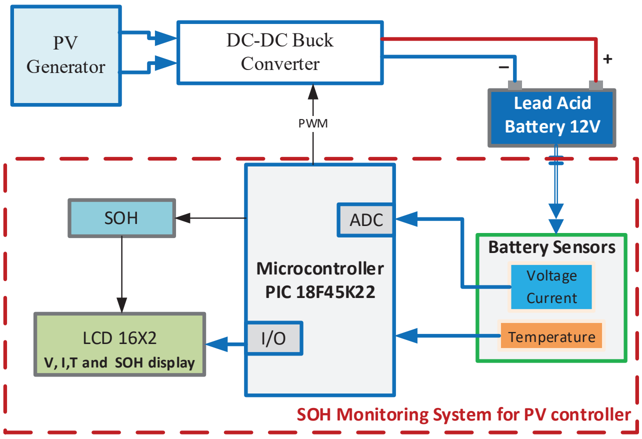

Figure 1: Block diagram of the battery SoH monitoring system for a PV controller.

This paper's primary focus revolves around the SOH monitoring system, which is predominantly comprised of:

A. Microcontroller PIC18F45K22

The famous PIC18F45K22 microcontroller from MICROCHIP is used given the performance it offers. It is a component like a microprocessor that has an analog-to-digital converter ADC, which can be programmed by a software called MikroC PRO for PIC based on C language, so that it automatically executes commands (machine code). Therefore, a PIC microcontroller can operate autonomously after programming.

EasyPIC v7 Development Board, is used to program the 18F45K22 PIC microcontroller and test the general PIC working. The EasyPic development board, part of the MikroElektronika family, stands as an innovative platform designed to support Microchip's array of DIP (Dual Inline Package) microcontrollers [5]. This exceptional board boasts a comprehensive array of peripherals that align seamlessly with the product's purpose. Moreover, it presents a multitude of expansion possibilities, facilitating limitless potential for customization, and ensures effortless interfacing for unparalleled user convenience.

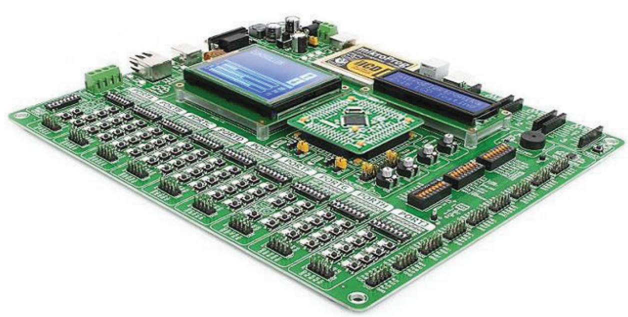

Figure 2 : Easypicv7 development board.

B. LCD display

LCD displays efficiently retrieve real-time data from the microcontroller, meticulously presenting it in a specific sequence: the initial line showcases the battery voltage and temperature, while the subsequent line divulges the battery current and SOH (State of Health).

C. Sensors

a) *Current Sensor ACS712*: operates on the principle of Hall Effect, wherein the flow of current generates a magnetic field that is subsequently transformed into a voltage signal. It is specially designed for use with microcontrollers such as PIC and Arduino. This sensor is known by its offset voltage which is equal to 2.5V for zero current intensity and the general relation of the input current in the microcontroller is given by the equation1 as fellows:

$$I = (V - 2.5)/S \tag{1}$$

Where S is the sensitivity (S=*66mV/A* for ACS712-30A).

b) *Digital Temperature Sensor DS18B20*: functions via a streamlined 1-wire interface mechanism. Its capabilities encompass temperature measurement spanning from -55 to 128°C, ensuring a commendable accuracy of ±0.5°C for temperatures lying between -10 to 85°C. For consistent and reliable operation, the sensor requires a power supply ranging from 3V to 5.5V. The distinctive advantage of this communication approach lies in its efficiency, utilizing only a single microcontroller pin [5].

c) *Voltage Sensor*: functions as a voltage divider, featuring a pairing of two resistances - 3 KΩ and 1 KΩ. This arrangement effectively divides the incoming voltage into four equal parts, resulting in a reduction to a quarter of its original value.

II.2 Battery SOH monitoring model

A. overview of recent SOH estimation methods

Accurate Battery State of Health (SOH) information is an effective tool to give an indication of the battery's expected performance and useful life, as well as the time remaining until the next replacement. Therefore, the integration of SOH estimation function in new Battery Management Systems (BMS) and software tools has become a burning research topic.

Regarding SOH estimation methods, three approaches are mainly used: a coulomb counting method [6], an OCV (Open Circuit Voltage) method [6] and a Kalman filter method [7]. These methods can be applied to all battery systems, especially HEV (Hybrid Electric Vehicles), EV (electric vehicles) and PVS (Photovoltaic System).

Other methods for estimating SOH are presented in various publications such as electrochemical impedance spectroscopy (EIS) [8], least square (LS) and fuzzy logic (FL) [6], machine learning approach (ML) [9], and some popular intelligent methods like incremental capacity (IC) and wavelet neural networks with genetic algorithm (GA-WNN) [10] have been validated for SOH prediction.

The battery SOH estimation methods cited above are methods known for their implementation complexity and difficult mathematical computation that overcome the problems associated with inaccurate SOH estimates found in the aged state of the battery. It has been found that simple techniques such as OCV or Coulomb counting methods require significantly less measurement and computational resources than complex model-based approaches, including filter and observer-based methods.

B. Working Zone and Temperature Tracking WZTT method

In this study, we have worked for the development of a straightforward, non-destructive, and readily applicable approach within our Photovoltaic (PV) system. The objective of this endeavor is to enhance the functionality of the PV system while simultaneously establishing a mechanism for the ongoing monitoring and assessment of our solar battery's aging process, before its replacement. This novel method represents a refined iteration of a preceding model, building upon its foundations [11], To depict the progressive aging of the battery, we introduce a novel approach that hinges on the monitoring of operational conditions and temperature. This marks a noteworthy stride towards offering a simple, easily implementable, dynamic, and non-destructive gauge of the battery's State of Health (SOH). Our method achieves this by a comprehensive revamping of the SOH equation, incorporating pivotal battery characteristics. A prominent enhancement is the integration of the battery life parameter into the calculation of the zone factor. This strategic augmentation empowers users to seamlessly adapt the model to diverse solar battery variants, drawing exclusively from the data sheet information.

The efficacy of our innovation is underscored by the derivation of model parameters through real-world measurements, culminating in a remarkable reduction in the error associated with battery SOH estimation. This approach strikes a harmonious balance between simplicity and precision, encapsulating a method that effectively estimates SOH with a noteworthy degree of accuracy.

The essence of this method can be summarized into a concise three-step process. Initially, a diverse range of data produced by the battery during its operation, including voltage, current, and temperature, is collected. Subsequently, a tabulated correlation is established, mapping the aging speed coefficients for the working zone health factor (n_{WZ}) and the temperature health factor (n_T) to each specific data type. These coefficients are then computed in real-time for every instance. Finally, the collected aging speed coefficients are integrated and employed to determine the battery's aging state.

The aging speed coefficient pertaining to the working zone (n_{WZ}) is intrinsically linked to the designated lifespan of individual batteries (as detailed in Table 1). For instance, a battery designed to last 2 years necessitates a higher aging rate than one designed for a 10-year lifecycle.

The Arrhenius law [12] and [13], affirms that for every 10°C increase in temperature the lead acid battery life is halved (and decreases by a fifth for Li-ion battery). There is a proportionality and exponential temperature behavior, so the temperature health factor (n_T) should have an exponential form.

The enhanced state of health model is as follows:

$$SOH(t) = SOH_0 - \int_0^t (n_T n_{WZ}) dt \tag{2}$$

Where, SOH_0 represents the initial SOH value calculated just before the launch of the battery SOH program.

In practical systems, the SOH_0 doesn't invariably equate to 100%; its value is contingent upon the initial measured capacity, denoted as C_i. In this context, SOH_0 is defined as the percentage representation of the initial capacity (C_i) in relation to the battery's nominal capacity (C_d), which is provided by the manufacturer.

$$SOH_0 = \frac{C_i}{C_d} \times 100\% \tag{3}$$

The elevated temperatures significantly affect the SOH of batteries. High temperatures accelerate the degradation of active materials and there by hasten the loss of permanent capacity (shortening the lifespan). Actually, all batteries achieve optimum cycle life if operated at 20°C or below.

The temperature health factor (n_T) represents the SOH degradation related to the battery temperature fluctuations. According to the Arrhenius law, the temperature aging speed coefficient is combined with other degradation factors through multiplication. The n_T coefficient is precisely defined within an exponential expression as follows:

$$n_T = 2^{\frac{T-T_{ref}}{\alpha}} \tag{4}$$

Where T is the measured temperature in °C, T_{ref} is the reference temperature and α is the rise in temperature that results in the battery SOH rate reducing by half. According to [12-13] α is equal to 10°C

n_{WZ} is the factor of SOH degradation related to the battery working zone.

TABLE 1: ENHANCED WORKING ZONE PARAMETER n_{wz}.

Working zone	n_{wz} (s^{-1})
Zone1 : Safe Charge or discharge zone	$n_{wz1} = \frac{6.34\times10^{-9}}{l_d}$
Zone2 : Overcharge or deep-discharge zone	$n_{wz2} = x_1 \times n_{wz1}$
Zone3 : Saturation or exhaustion zone	$n_{wz3} = x_2 \times n_{wz1}$

As depicted in Figure 3, there exist three distinct working zones that depend on the battery voltage, which are:

- Safe zone (indicated in green): designates the secure charging and discharging region. Positioned between the overdischarge threshold voltage (Vod) and the overcharge threshold voltage (Vg), this zone is characterized by a working zone factor equivalent to the low aging speed coefficient n_{WZ1}.

- Dangerous zone (indicated in orange): it is the overcharge zone and the overdischarge zone. The working zone factor is equal to n_{WZ2}. Considering the dangerous effect of overcharging and overdischarging processes on the battery health, n_{WZ2} must be greater than n_{WZ1}.

- Exhaustion zone (indicated in red): it is the saturation zone (where the battery charging voltage is higher than Vs) and the exhaustion zone (where the battery discharging voltage is lower than Vex). The working zone factor is equal to n_{WZ3} and it must be greater than n_{WZ2}as the saturation and exhaustion zones are the most dangerous zones and significantly affect the battery SOH.

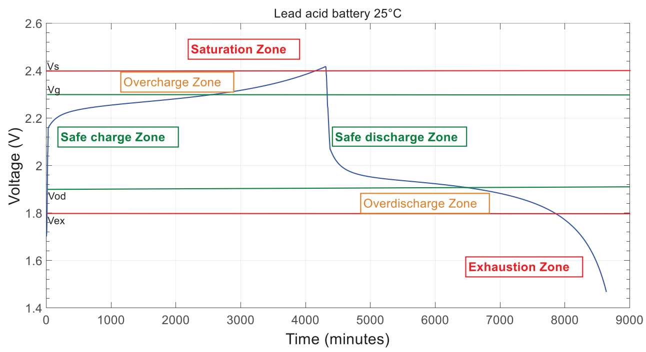

Figure 3: Working zone of the battery.

SOH degradation is accelerated in zones 2 and 3 because of the gravity of degradation mechanisms, particularly sulfation in discharge and corrosion in charge of Lead-Acid batteries. The working zone thresholds of the battery output voltage are listed in table 2. Table 1 shows the modified values of the working zone parameter n_{WZ} in the three working zone. The n_{WZ1} base equation is the slope of SOH degradation from 100% to 80% during the design lifetime *ld* given by the battery manufacturer. Typically, manufacturers give the battery lifetime in years, for safe working zones at the reference temperature Tref (20 or 25°C) to a specified SOH minimum threshold (commonly 80%). By applying the "trial-and-error" method based on the experimental data, it is found that the model parameter n_{WZ2} is nearly thirty times (x_1 = 30) greater than n_{WZ1}, and n_{WZ3} is twenty times greater than n_{WZ2} and thus six hundred times than n_{WZ1} (x_2 = 600).

TABLE 2: WORKING ZONE THRESHOLDS OF BATTERY OUTPUT VOLTAGE AT 25◦C.

Working zone	***State***	***Zone conditions***
Saturation zone	Charge I > 0	$V_{bat} > V_s$ V_s=2.4V per Cell V_s is the saturation threshold voltage
Overcharge zone		$V_g \le V_{bat} \le V_s$ V_g=2.3V per Cell V_g is the overcharge threshold voltage
Safe charge zone		$V_{bat} < V_g$
Safe discharge zone	Discharge I < 0	$V_{bat} > V_{od}$ V_{od}=1.9 V per Cell V_{od} is the over discharge threshold voltage
Deep-discharge zone		$V_{ex} \le V_{bat} \le V_{od}$ V_{ex}=1.8V per Cell V_{ex} is the exhaustion threshold voltage
Exhaustion zone		$V_{bat} < V_{ex}$

III. RESULTS AND DISCUSSION

We present the modelling, simulation and tests on the development board of the various measurements and calculations of the battery parameters programmed on the PIC18F45K22 microcontroller.

The program is written in assembly language using a comprehensive 'MikroC' development tool designed specifically for PIC microcontrollers. The simulation of our electronic circuit is made on the Proteus software, we can implement this program in a simulated PIC. The EasyPicv7 development board was used to implement and test the program using a real PIC.

In this section we will present the tests results by simulation in Proteus software, where figure 4 illustrates the control circuit with which we can subsequently generate the hexadecimal code in the real microcontroller to show measurements and monitoring of the battery SOH.

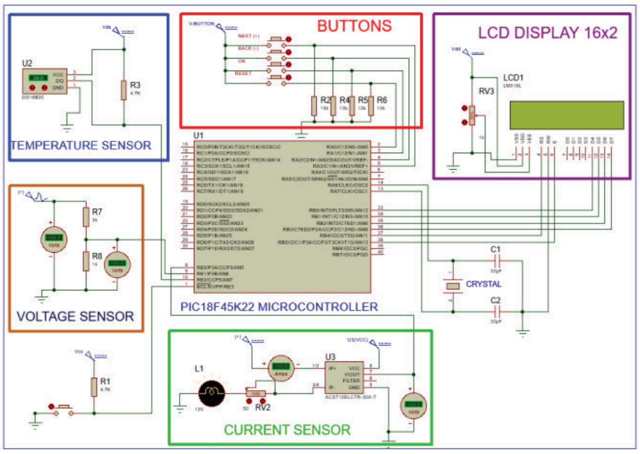

Figure 4: Battrey SoH monitoring control circuit

The MikroC code implemented in the PIC microcontroller is shown in the following flowchart:

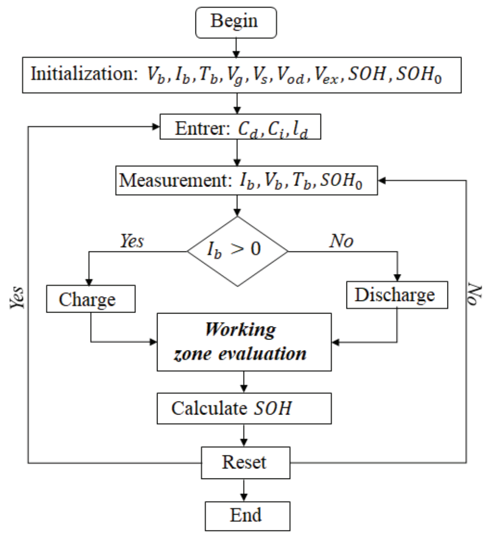

Figure 5: Main flow chart for monitoring battery parameters and SoH

The current, voltage and temperature measurements are displayed on the LCD screen, which can be varied once we vary the values by the sensors, which is very practical and these parameters are changeable in reality so they require monitoring and follow-up thanks to our control circuit. The monitoring of these parameters is important because they have a great influence on the lifetime of batteries in order to follow their state of health. Simulation and tests are shown in Figure 6.

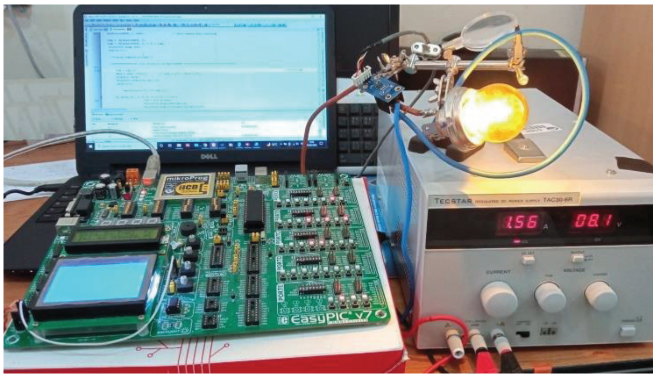

Figure 6: Simulation and tests

Using the push buttons, the values of both measured and nominal capacitances are validated, which will be saved in the microcontroller EEPROM in order to calculate the initial state of health SOH_0. Another parameter that must be introduced is the design lifetime, which is included in the working zone health factor equation (figure 7). Following the variation of the battery voltage in charging and discharging along the three operating zones, as well as the change in temperature, the calculation of SOH is continuously for each new instantaneous measurement, and will be displayed on the LCD display.

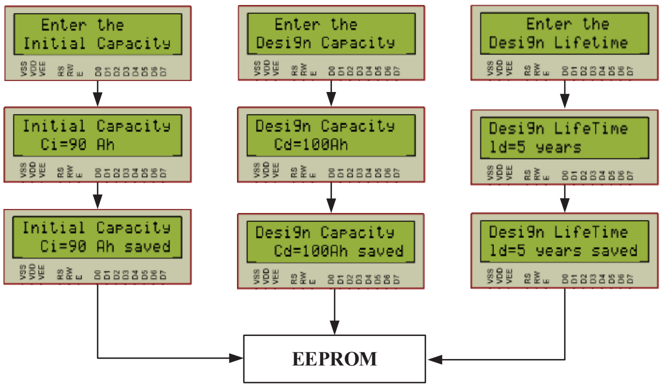

Figure 7: Saving data to EEPROM

For C_i=90Ah, C_d=100Ah and l_d=5 years, we obtain SOH_0=90% in a reference temperature Tref=25°C, and the continuous calculation of the state of health (SOH) in the different zones of battery operation is shown in figure 8 with display of all information of each zone.

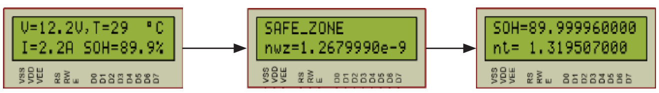

(a) SAFE ZONE

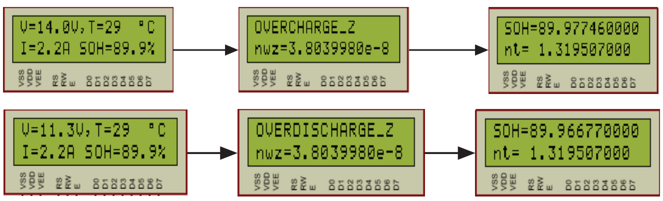

(b) OVERCHARGE AND OVER-DISCHARGE ZONE

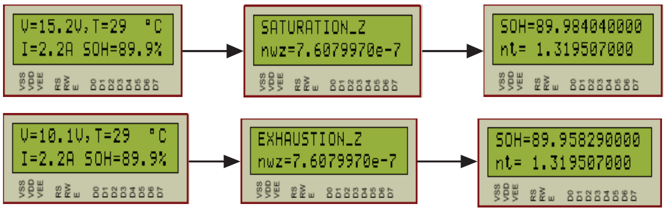

(c) SATURATION AND EXHAUSTION ZONE

Figure 8 LCD Display at different working zones

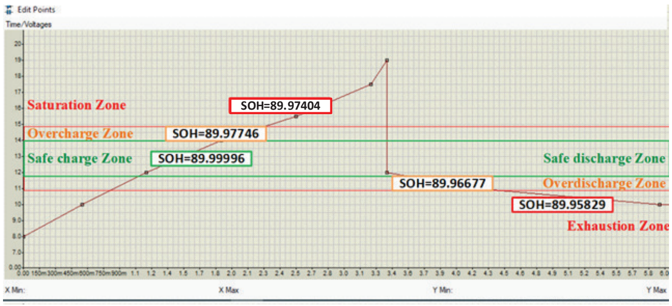

Figure 9: Battery state of health (SoH) monitoring by the WZTT method.

Battery parameter measurements and simulation results are displayed on the LCD screen, from the continuous real-time calculation of the battery state of health (SOH), using the WZTT model in each operating zone. The working zone and temperature health factors are calculated to reduce SOH estimation error. The decrease of the battery state of health, which depends on these two factors in saturation zone in charge and exhaustion zone in discharge, is faster than that of other zones. Therefore, the safe zone is considered an adequate zone to protect the battery from degradation.

CONCLUSION

In this paper, the study aimed to measure dynamic parameters such as battery voltage, current, and temperature, and to develop a robust model to estimate and continuously monitor the State of Health (SOH) of the battery in real-time. The proposed WZTT estimation model offers a pragmatic solution for integrating into photovoltaic (PV) systems, which can enhance system performance by leveraging crucial information provided by the battery manufacturer (i.e., nominal capacity and design lifetime).

The universal applicability of the model responds to diverse battery types, and the implementation process is simplified by incorporating the manufacturer data into the model's mathematical framework.

The integration of battery parameter measurements into the LCD facilitates real-time monitoring of the corresponding SOH, providing insights into the battery's working domain, health indicators, and encompassing both charging and discharging scenarios. The simulation outcomes, validated through both Proteus software and the EasyPic development board, illustrate a commendable balance between simplicity and precision.

The model's applicability transcends the confines of this study, finding pertinence within battery management systems (BMS). Its impact is particularly profound within lead-acid battery-based devices, while concurrently influencing solar regulator control circuits, especially in off-grid scenarios. These implementations serve a dual purpose – monitoring the battery's lifespan and instituting safeguards against detrimental conditions like overcharging, deep discharging (i.e., saturation zone and exhaustion zone respectively), as well as fluctuations in temperature and current.

In the realm of future research, advanced AI and machine learning could revolutionize battery management by utilizing real-time data for heightened accuracy in State of Health (SOH) estimations and adaptable model development. Additionally, the versatile WZTT model has the potential to optimize extensive energy networks through cross-system integration, accommodating diverse renewable sources and storage systems for elevated overall performance. As sustainability gains prominence, expanding the model's capacities becomes imperative, encompassing assessments of battery impact beyond SOH.

ACKNOWLEDGMENT

This work was supported from the Centre de Développement des Energies Renouvelables (CDER), Direction Générale de la Recherche Scientifique et du Développement Technologique (DGRSDT).

DECLARATION

- The authors declare that they have no known financial or non-financial competing interests in any material discussed in this paper.
- The authors declare that this article has not been published before and is not in the process of being published in any other journal.
- The authors confirmed that the paper was free of plagiarism.

REFERENCES

[1] S. Bri, M. Elalami, and A. Nakheli, "Conception of the Solar Regulator for Renewable Energy," *Smart Grid Renew. Energy*, vol. 03, no. 03, pp. 207–213, 2012, doi: 10.4236/sgre.2012.33029.

[2] S. Z. A. Dib, "Réalisation d ' un régulateur solaire à base de microcontrôleur pour le contrôle de l ' état de charge et la protection des accumulateurs," *Rev. des Energies Renouvelables*, vol. 12, pp. 137–147, 2009.

[3] L. Messikh, S. Chikhi, and F. C. T. Chergui, "Mise au point d ' un régulateur de charge / décharge de batterie avec seuils adaptatifs de tension pour les applications photovoltaïques," *Revue*, vol. 11, pp. 281–290, 2008.

[4] W. Merrouche *et al.*, "Improved model and simulation tool for dynamic SOH estimation and life prediction of batteries used in PV systems," *Simul. Model. Pract. Theory*, vol. 119, p. 102590, Sep. 2022, doi: 10.1016/j.simpat.2022.102590.

[5] MikroElektronika, *EasyPIC V7 User Manual*. 2012.

[6] K. Saqli, H. Bouchareb, M. Oudghiri, and N. K. M'sirdi, "An overview of state of charge(Soc) and state of health(soh) estimation methods of li-ion batteries," *Int. Conf. Integr. Model. Anal. Appl. Control Autom.*, no. c, pp. 99–104, 2019.

[7] M. Murnane and A. Ghazel, "A Closer Look at State of Charge (SOC) and State of Health (SOH) Estimation Techniques for Batteries," *Analog devices*, 2017.

[8] E. Riviere, "Détermination in-situ de l ' état de santé de batteries lithium-ion pour un véhicule électrique," *Nature*, 2017.

[9] C. Vidal, P. Malysz, P. Kollmeyer, and A. Emadi, “Machine Learning Applied to Electrified Vehicle Battery State of Charge and State of Health Estimation: State-of-the-Art,” *IEEE Access*, vol. 8, pp. 52796–52814, 2020, doi: 10.1109/ACCESS.2020.2980961.

[10] C. Chang, Q. Wang, J. Jiang, and T. Wu, “Lithium-ion battery state of health estimation using the incremental capacity and wavelet neural networks with genetic algorithm,” *J. Energy Storage*, vol. 38, no. January, p. 102570, 2021, doi: 10.1016/j.est.2021.102570.

[11] D. Guasch and S. Silvestre, “Photovoltaic Applications,” vol. 206, no. November 2001, pp. 193–206, 2003, doi: 10.1002/pip.480.

[12] J. Bizouard, V. Schneider, and M. Boost, “A Battery Node for Power Plant Monitoring Systems,” pp. 607–616.

[13] M. Ecker *et al.*, “Development of a lifetime prediction model for lithium-ion batteries based on extended accelerated aging test data,” *J. Power Sources*, vol. 215, pp. 248–257, 2012, doi: 10.1016/j.jpowsour.2012.05.012.

The 1st National Conference on Green Energy (NCGE'2023)
December 02, 2023, Boumerdes, Algeria.

Kernel Principal Components Analysis Improvement Based on Variogram Data Selection for Fault Detection

1st Mohammed Tahar Habib KAIB
Signals and Systems Laboratory,
University M'Hamed Bougara,
Boumerdes, Algeria.
m.kaib@univ-boumerdes.dz

2nd Abdelhalim LOUIFI
Signals and Systems Laboratory,
University M'Hamed Bougara,
Boumerdes, Algeria.
a.louifi@univ-boumerdes.dz,

3rd Yassine YAKHELEF
L.A.I.G. Laboratory,
University M'hamed Bougara of,
Boumerdes, Algeria.
y.yakhelef@univ-boumerdes.dz,

4th Abdelmalek KOUADRI
Signals and Systems Laboratory,
University M'Hamed Bougara,
Boumerdes, Algeria.

5th Abderazak BENSMAIL
Signals and Systems Laboratory,
University M'Hamed Bougara,
Boumerdes, Algeria.

6th Mohamed Faouzi HARKAT
Electronics Department, Faculty of Engineering,
University Badji Mokhtar,
Annaba, Algeria

***Abstract*—Kernel Principal Component Analysis (KPCA) is a widely used Fault detection and diagnosis (FDD) technique because of its simplicity and flexibility. For a good FDD model, KPCA requires extensive training data, on the other hand, if this data is too large then it may affect the performance of the model. Reduced KPCA (RKPCA) is an alternative for KPCA to overcome this problem with adequate FDD performances. RKPCA algorithms reduce the size of the training data before building the ordinary KPCA model. The proposed reduction technique selects only the non-correlated samples to form a reduced matrix that contains only non-correlated observations. The proposed algorithm is applied to simulated faults in photovoltaic farms and then it is compared to the conventional KPCA algorithm. The proposed algorithm led to satisfying overall performances as anticipated.**

***Index Terms*—Fault Detection, Kernel Principal Component Analysis, Principal Component Analysis, Reduced Kernel Principal Component Analysis, Photovoltaic Farms.**

I. Introduction

Data-driven fault detection and diagnosis (FDD) techniques require a large amount of data collected from different sensors placed through all the monitored plants to build an FDD model. Many techniques were proposed but the widely used one is Principal Component Analysis (PCA) and its alternative for non-linear systems Kernel Principal Component Analysis (KPCA) [1]. PCA reduces the number of variables by the mapping from input space to a lower dimension space that contains the majority of the original data variability with a set of linearly independent vectors as the basis of this space [2], [3]. KPCA was proposed by Scholkopf et al. [4], it applies PCA in a higher dimensional feature space, and the mapping from input space to this space is accomplished via kernel trick [4]. Unfortunately, for large training data sets KPCA needs more computational time than ordinary PCA and more storage space for the model and it can also become disadvantageous in terms of performance compared to other FDD techniques [1], [4], [5]. To overcome this KPCA's drawback, Reduced KPCA (RKPCA) algorithms were proposed. RKPCA minimizes the size of the training data by reducing the number of observations and at the same time, they preserve most of the original data information [6].

For the monitoring indices, The Hotelling (T^2), the Prediction Square Error (Q), and the combined index (φ) are used and they are evaluated using different metrics such as False Alarm Rate (FAR), Missed Detection Rate (MDR), and Detection Time Delay (DTD).

The proposed algorithm is based on the RKPCA technique, the retained observations (samples) are selected using variogram of the training data set which is proposed in [7]. The main idea of the proposed algorithm is to improve the performance of KPCA by omitting similar and correlated observations from the training data. The main contribution of this paper is to enhance KPCA's FDD performances using a reduced data set with a reliable and effective data reduction method. The proposed algorithm was tested and compared to KPCA algorithm using a simulated data set of photovoltaic farms obtained from [8].

This paper is organized as the following: Section I General introduction, section II gives a literature review of KPCA for FDD, section III introduces the proposed algorithm, section IV gives a brief description of the processes used in this paper, section V shows results and gives discussion about them, and section VI gives a general conclusion.

II. Literature Review

Let $\tilde{X}_{n\times m}$ be the zero mean and unit variance matrix of the training data matrix X, where n is the number of observations and m is the number of variables. ϕ is the mapping from input space R^m to higher dimensional feature space F.

$$\phi : R^m \longrightarrow F, \tilde{x}_i \longrightarrow \phi\left(\tilde{x}_i\right) \tag{1}$$

$\tilde{x_i}$ is i^{th} row vector from $\tilde{X}$. The matrix of features and that of its corresponding covariance are respectively given by

$$\Phi = \left[\phi\left(\bar{x}_1\right)\phi\left(\bar{x}_2\right)\ldots\phi\left(\bar{x}_n\right)\right]^T \tag{2}$$

$$\Sigma_\phi = \frac{1}{n}\sum\nolimits_{i=1}^{n}\phi\left(\bar{x}_i\right)\phi(\bar{x}_i)^T \tag{3}$$

Positive eigenvalue λ_k and its corresponding eigenvector v_k are computed as:

$$\Sigma_\phi v_k = \lambda_k v_k \tag{4}$$

$$v_k = \sum\nolimits_{i=1}^{n}\alpha_{ki}\phi\left(\bar{x}_i\right) \quad k = 1\cdots n \tag{5}$$

The kernel function is defined as

$$\kappa(\bar{x}_i, \bar{x}_j) = \phi(\bar{x}_i)^T\phi\left(\bar{x}_j\right) \tag{6}$$

After the mapping and some algebraic manipulations, the eigenvalue problem to be solved is presented in (7) (matrix notation):

$$K\delta_k = \lambda_k n\delta_k \tag{7}$$

To perform the kernel trick stated in [4], a kernel function that satisfies Mercer's theorem is used instead of mapping ϕ. The one used in this paper is known as the Radial Basis Function (RBF).

$$\kappa\left(\bar{x}_i, \bar{x}_j\right) = \exp\left[-\frac{\left\|\bar{x}_i - \bar{x}_j\right\|^2}{2\varsigma^2}\right] \qquad i = 1\cdots n, j = 1\cdots n \tag{8}$$

The hyperparameter ς^2 is selected as the following $\varsigma^2 = rm\sigma^2$ [**?**], where r is empirically obtained and m is the number of variables and σ^2 is the variance of the training data. Relevant principal components are selected using the CPV technique as stated in [7]. For fault detection purposes, T^2, Q, and φ indices are used. They are given as the following, respectively.

$$T^2 = \kappa(\bar{x})^T\hat{P}_\phi\hat{\Lambda}_\phi^{-1}\hat{P}_\phi^T\kappa\left(\bar{x}\right) \tag{9}$$

$$Q = \kappa\left(\bar{x}, \bar{x}\right) - \kappa(\bar{x})^T\hat{P}_\phi\hat{\Lambda}_\phi^{-1}P_\phi^T\kappa\left(\bar{x}\right) \tag{10}$$

$$\varphi = \frac{T^2}{T_\alpha} + \frac{Q}{Q_\alpha} \tag{11}$$

where $\hat{P}_\phi$ and $\hat{\Lambda}_\phi$ are the principal eigenvectors and their corresponding eigenvalues of K.
Their limits are given in [7]. A fault is detected if the value of one of the previous indices exceeds its corresponding established control limit.

III. Proposed Algorithm

For some applications, If the proposed algorithm in [7] is directly applied to this data set the reduced matrix will be the same as the original matrix because the selected lag is small (less than $\frac{n}{2}$). The proposed algorithm in this paper is slightly modified from the original algorithm presented in [7]. The selected lag must be greater than $n/2$. As mentioned in [7], variogram quantifies spatial correlation and characterizes spatial continuity. Using the normalized matrix $\tilde{X}_{N\times m}$, the empirical variogram is then given by equation (12).

$$\gamma_j\left(h\right) = \frac{1}{2N\left(h\right)}\sum\nolimits_{i=1}^{n-h}\left(\tilde{x}_{(i+h)j} - \tilde{x}_{ij}\right)^2 \tag{12}$$

$i = 1\cdots n-h, h = 1\cdots n-1$, and $N\left(h\right)$ is the number of pairs that are separated by the lag h. and the total variogram is given by:

$$\gamma\left(h\right) = \frac{1}{m}\sum\nolimits_{j=1}^{m}\gamma_j\left(h\right) \tag{13}$$

Around the sill there is no correlation between observations that are separated by the given lag [9]. Algorithm 1 represents the reduction method of [7], where w is the distance to the sill of the variogram, the proposed algorithm in this paper selects only lags that are greater than $n/2$ because once a lag that is less or equal to $n/2$ is selected then the reduced matrix is the same as the original one. Besides, algorithm 2 shows the entire RKPCA algorithm.

Algorithm 1 Data Reduction

procedure REDUCE($\tilde{X}_{n\times m}, w$)
  for <$h \leftarrow$ `1 to` $n-1$> **do**
    $N\left(h\right) = n - h$
    $V = \left[\tilde{X}_{(1:n-h)\times m} - \tilde{X}_{(h+1:n)\times m}\right]^T$
    $.\left[\tilde{X}_{(1:n-h)\times m} - \tilde{X}_{(h+1:n)\times m}\right]$
    $\widehat{\gamma}\left(h\right) = \frac{1}{2N(h)}V$
    $\gamma\left(h\right) = mean(\widehat{\gamma}\left(h\right))$ {each row mean}
  for <$h \leftarrow$ `1 to` $n-1$> **do**
    if $\gamma\left(h\right) \geq sill - w || \gamma\left(h\right) \leq sill + w$ **then**
      $s = h$
    b *is the smallest lag that is greater than* $\frac{n}{2}$
    $\tilde{X}_{r\times m} = \begin{bmatrix}\tilde{X}_{(1:n-b)\times m}\\ \tilde{X}_{(b+1:n)\times m}\end{bmatrix}$
    return $\tilde{X}_{r\times m}$ $\{r < N\}$

False Alarm Rate (FAR), Missed Alarm Rate (MDR), and Detection Time Delay (DTD) are respectively given by

$$FAR = \frac{N_{NF}}{N_N} \tag{14}$$

where N_{NF} is the number of normal samples that exceeds control limit, and N_N is the total number of normal samples.

$$MDR = \frac{N_{FN}}{N_F} \tag{15}$$

Algorithm 2 Proposed RKPCA

Training Part:
1. Normalize $X_{n\times m}$
2. Use algorithm 1 that reduces $X_{n\times m}$ to$\tilde{X}_{r\times m}$
3. Compute $X_{r\times m}$ using mean and standard deviation of $X_{n\times m}$
4. Normalize $X_{r\times m}$
5. Apply KPCA on reduced normalized data
6. Compute fault detection statistics and their corresponding upper control limits
Testing Part:
1. Normalize testing data using the mean and standard deviation of the reduced matrix
2. Build test Kernel matrix
3. Compute different statistics and compare them to their limits
4. make a decision if there is a fault or not

where N_{FN} is the number of faulty samples that are under the control limit, and N_F is the total number of faulty samples.

$$DTD = t_d - t_o \tag{16}$$

where t_d and t_o are the detection time and occurrence time of a fault, respectively.

For comparison and evaluation of the proposed algorithm and other ones, the following cost function is used:

$$J_s = \alpha_1 FAR_s + \alpha_2 MDR_s + \alpha_3 \left(1 - e^{-\tau DTD_s}\right) \tag{17}$$

where $\tau = 0.1$ in this case. The J_s is the cost function value for each monitoring index, and the total cost function value which is given by J is the mean of the cost function of the three monitoring indices.

$$J = mean\left(J_{T^2},\ J_Q,\ J_\varphi\right) \tag{18}$$

IV. Process Description

A simulated 250-kW PV power plant was utilized to create training and testing data sets of PV fault cases. Three fault types and normal operation (free-of-fault state) are defined. The default sets are as follows. From the figure presented in the Appendix section of [8], the fault cases F1, F2, and F3 describe a string fault (tested on string 1), string-to-ground fault (tested on string 1), and string-to-string fault (tested between strings 1 and 2), respectively. Training and testing datasets were built. The training dataset included 600 instances, each with 30 features and one column for classes or categories. The training fault-free data has 100 observations. The first fault is a string fault, the second one is a string-to-ground fault, and the third one is a string-to-string fault. The testing dataset contained 50 instances. Measurements were taken in the period from 0.1 s to 0.3 s, with transient time from 0.1 s to 0.2 s, and faults occurring from 0.2 s to 0.3 s [8]. Each faulty data set contains 35 non-faulty samples and 25 faulty samples used to test and evaluate the proposed algorithm. For further understanding of the system read [8].

TABLE I
Comparison Between Different Algorithms Based on Different Monitoring Indices and Metrics.

Indices	Faults	T^2			Q			φ		
Metrics		FAR	MDR	DTD	FAR	MDR	DTD	FAR	MDR	DTD
KPCA	F 1	0.00	0.04	1	0.00	0.00	1	0.09	0.00	1
	F 2	0.03	0.00	1	0.00	0.00	1	0.20	0.00	1
	F 3	0.06	0.96	23	0.03	0.28	2	0.20	0.08	1
Proposed algorithm	F 1	0.00	0.04	1	0.00	0.00	1	0.09	0.00	1
	F 2	0.06	0.00	1	0.03	0.00	1	0.20	0.00	1
	F 3	0.06	0.96	23	0.03	0.24	1	0.11	0.12	1

TABLE II
Comparison Based on Cost Function J

Method	Size	CPV	PCs	J
KPCA	100	99	8	0.42
Proposed Algorithm	80	99	8	**0.39**

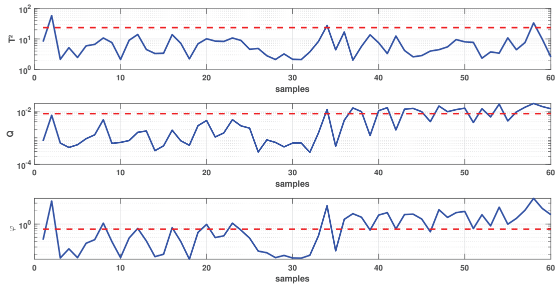

Fig. 1. 3^{rd} Fault Detection using KPCA.

V. Results and Discution

The reduction part of the proposed algorithm has successfully reduced the number of observations from 100 samples to only 80 samples which is reduced by 20% from the total number of samples. The proposed algorithm reduces the number of observations and also gives a good monitoring performance compared to the KPCA algorithm in terms of overall monitoring. To illustrate the monitoring performance of the proposed algorithm, table I presents the monitoring metrics for each monitoring index for different types of faults, The proposed algorithm has given promising results and it has outperformed the conventional KPCA algorithm for the third fault and it has the same performances for the other two faults. This performance was a result of omitting the correlated samples from the training data set.

From table II, the overall performance based on J (equation 18) has been enhanced using the proposed algorithm with the same number of Principal components which is 8.

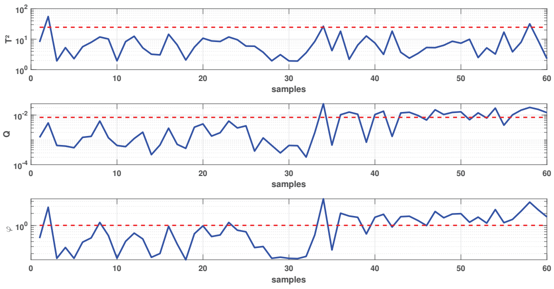

Fig. 2. 3^{rd} Fault Detection using Proposed Algorithm.

As it can be seen from both figures, the KPCA and the proposed algorithm have failed to detect the fault based on the T^2 monitoring index. For the Q index both KPCA and the proposed algorithm have slightly performed better than the T^2 index. In the end, for the combined index the proposed algorithm has slightly performed better than KPCA. For the other two faults, both algorithms have successfully detected the fault.

VI. Conclusion

This paper presents a slightly modified reduction method based on the variogram for the RKPCA algorithm in order to enhance the monitoring performances. The proposed algorithm uses variogram (i.e. spatial continuity) in order to retain a set of uncorrelated observations from the original data. The proposed algorithm is applied to simulated photovoltaic farms and it is compared to the KPCA algorithm, the proposed algorithm has the best performances compared to it.

References

[1] Bencheikh, F., Harkat, M., Kouadri, A. & Bensmail, A. New reduced kernel PCA for fault detection and diagnosis in cement rotary kiln. *Chemometrics And Intelligent Laboratory Systems*. **204** pp. 104091 (2020)

[2] Iannucci, L. Chemometrics for Data Interpretation: Application of Principal Components Analysis (PCA) to Multivariate Spectroscopic Measurements. *IEEE Instrumentation Measurement Magazine*. **24**, 42-48 (2021)

[3] Zhang, X. & Ren, X. Two dimensional principal component analysis based independent component analysis for face recognition. *2011 International Conference On Multimedia Technology*. pp. 934-936 (2011)

[4] Schölkopf, B., Smola, A. & Müller, K. Nonlinear component analysis as a kernel eigenvalue problem. *Neural Computation*. **10**, 1299-1319 (1998)

[5] Chin, T. & Suter, D. Incremental kernel principal component analysis. *IEEE Transactions On Image Processing*. **16**, 1662-1674 (2007)

[6] Dhibi, K., Fezai, R., Bouzrara, K., Mansouri, M., Kouadri, A. & Harkat, M. Machine learning based multiscale reduced kernel pca for nonlinear process monitoring. *2020 17th International Multi-Conference On Systems, Signals Devices (SSD)*. pp. 302-307 (2020)

[7] Kaib, M., Kouadri, A., Harkat, M. & Bensmail, A. RKPCA-based approach for fault detection in large scale systems using variogram method. *Chemometrics And Intelligent Laboratory Systems*. pp. 104558 (2022), https://www.sciencedirect.com/science/article/pii/S0169743922000697

[8] Sherif S. M. Ghoneim, N. Fault Detection Algorithms for Achieving Service Continuity in Photovoltaic Farms. *Intelligent Automation Soft Computing*. **30**, 467-479 (2021), http://www.techscience.com/iasc/v30n2/44023

[9] Armstrong, M. & Armstrong, M. The Variogram. *Basic Linear Geostatistics*. pp. 25-46 (1998)

The 1st National Conference on Green Energy (NCGE' 2023)
December 02, 2023, Boumerdes, Algeria.

A Maximum Power Point Tracking Technique of Photovoltaic System Based on the Synergetic Control method

MAHGOUN MOHAMED SEDDIK
Electrical Engineering Department
University of Ferhat Abbas Setif 1
Setif, Algeria
mahgounm@yahoo.fr

***Abstract*— A novel non-linear power point tracking method of photovoltaic system (PV) based on synergetic control strategy is proposed in this paper. This technique uses a synergetic control strategy to achieve the maximum power point tracking (MPPT). The PV system consists mainly of a solar array, DC/DC boost converter, MPPT controller, and an output load. A DC/DC boost converter is introduced in the content of this work as an interface between a photovoltaic array and a resistive load. Synergetic control is easy to implement, synergetic controller is used for boost converter to achieve the maximum power output. The stability of the closed-loop system is guaranteed using Lyapunov's method .To show the robustness and validity of this approach a mathematical model is presented and simulated using Matlab /SIMULINK under different atmospheric conditions (under environmental changes solar radiation and PV cell temperature). The results show satisfactory performance of the proposed approach.**

Keywords*— *Photovoltaic system; Synergetic control; Sliding Mode Control; Lyaponov Stability; Boost converter; Maximum power point tracking.

I. INTRODUCTION

Increase in human population in the world has elevated the power demand. In order to satisfy the power demand, fossil based energy source alone was utilized but, this has lead to pollution. Hence, the increase power demand can be met out using renewable energy sources [1].Wind and solar power generation is two of the most promising renewable power generation technologies. Photovoltaic source is becoming more and more used as a renewable source since it offers several advantages such as incurring no fuel, not being polluting and no emitting noise. According to 2022 data, as shown in Figure 1, the global PV capacity has grown from 70 GW in 2011 to 942 GW in 2021, and the annual addition has maintained a steady growth over the last few years [02].

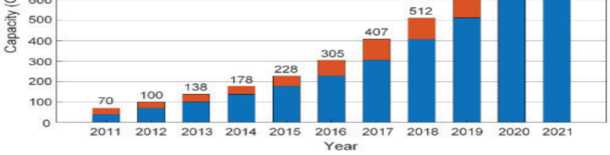

Fig.1. Global PV capacity and annual additions.

The photovoltaic module represents the fundamental power conversion unit of PV system, the fact that the output characteristic depends on the solar radiation and the cell temperature. In order to get the maximum of power from solar panels and enhance the PV system's efficiency, the selection of a maximum power point tracker (MPPT) algorithm is necessary. A large number of MPPT control algorithms have been developed for several years which drive the PV array to the peak of the power against environment changes. Each MPPT technique has its own advantages and disadvantages. These control techniques could be classified into two categories namely the conventional methods and intelligent methods. Among conventional MPPT mentioned in the literature, perturbation and observation (P&O), incremental conductance (IC) and the hill climbing (HC), are the most widely used since they are simple and easy to implement. The P&O algorithm consists of disturbing the PV output voltage and observing the PV output power to determine the peak power direction [3]. The IC method compares between the instantaneous conductance (I/V) of PV array and the incremental conductance (dI/dV) to track MPP [4]. The HC technique locates the MPP by relating changes in the power output to changes in duty ratio of the converter. Mathematically, the MPP is achieved when dP/dD is forced to be zero, where D represent the duty ratio [5]. However, these techniques have some disadvantages. The major of them is the power oscillation around MPP and the confusion in the direction of tracking caused by rapidly changing in atmospheric conditions [6]. To solve these problems many solutions have been reported in literature. To get better performance to the PV system, intelligent control techniques are proposed over the past years such as fuzzy logic controller [07], artificial neural-network [08] and meta-heuristic techniques which are used for the global search under partial shading conditions like genetic algorithm (GA) [09], particle swarm optimization (PSO) [10], artificial bee colony (ABC) [11] and ant colony optimization (ACO) [12]. Despite of their effectiveness, these techniques are more complex and require huge knowledge in the design of the control system. Sliding mode control has been considered as one of the most powerful control techniques, this is due to the simplicity of its implementation and robustness compared to uncertainties of the system and external disturbances. Unfortunately, this type of controller suffers from a major disadvantage, that is, the phenomenon of chattering. So in this paper and in order to eliminate this phenomenon, a novel non-linear control algorithm based on a synergetic controller is proposed. This theory has initially been successfully applied in power electronics control, in battery charging system, then recently in control of the epidemic system and in the control of wind turbine system [13]. This paper proposes a new strategy based on synergetic control theory to track the MPP for stand-alone photovoltaic system under different atmospheric conditions. The main goal of the proposed MPPT controller is to ensure the system stability at the maximum power, good robustness and fast dynamic response simultaneously. The design of the synergetic MPPT controller is explained and mathematically described in the paper. The developed MPPT controller was tested in simulation using Matlab/Simulink.

II. PHOTOVOLTAIC SYSTEM DESCRIPTION

The configuration of the proposed system consists of PV array, a DC–DC boost converter, a resistive load and a nonlinear MPPT controller as shown in Figure2.

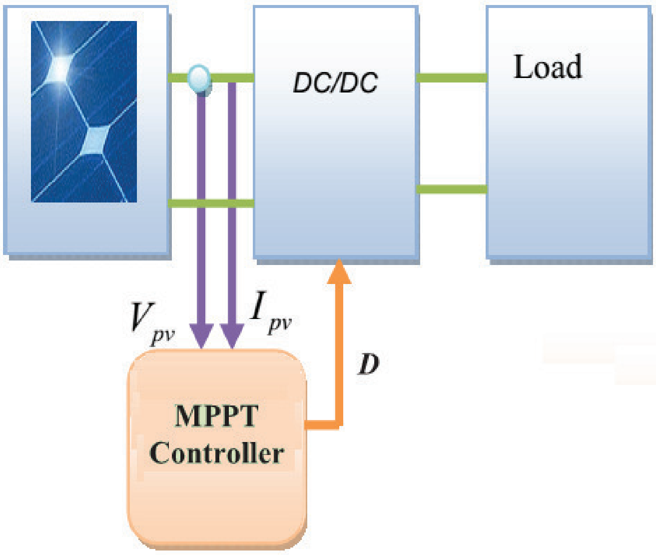

Fig.2. Block diagram of the photovoltaic system.

A. Photovoltaic panel modeling

A photovoltaic cell is often presented as an electric current generator whose behavior is equivalent to a current source shunted by a diode. The diode is formed by a p–n junction. The physical phenomena at the level of the cell have been studied by incorporating two series and parallel intrinsic resistors Rs and Rp into the model level, as shown in Figure 3.

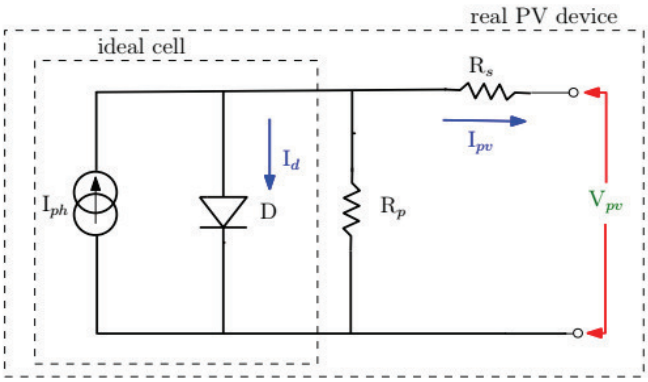

Fig 3.Equivalent circuit of a photovoltaic cell.

Therefore, the process of modeling the solar cell can be represented through Equations (1)–(3) in terms of the photocurrent I_{ph}, the current I_d via the diode, and the leakage current I_{sh} [14]. Furthermore, electrical proprieties of the cell differs somewhat from those of a diode. Therefore, I_d is represented using the Shockley equation, as shown below [15]:

$$I_d = I_s\left[\exp\left(\frac{V_{pv}+R_sI_{pv}}{nV_{Th}}\right)-1\right] \tag{1}$$

The leakage current caused by the shunt resistance R_p is as follows:

$$I_{sh} = \frac{V_{pv}+R_sI_{pv}}{R_p} \tag{2}$$

The net current I_{pv} supplied by the cell can be stated in the following way:

$$I_{pv} = I_{ph} - I_s\left[\exp\left(\frac{V_{pv}+R_sI_{pv}}{nV_{Th}}\right)-1\right]-\frac{V_{pv}+R_sI_{pv}}{R_p} \tag{3}$$

Thus, replacing I_d and I_{ph} by their expressions in the above governing equation allows it to be written as follows:

$$I_{pv} = I_{ph} - I_s\left[\exp\left(\frac{V_{pv}+R_sI_{pv}}{nV_{Th}}\right)-1\right]-\frac{V_{pv}+R_sI_{pv}}{R_p} \tag{4}$$

With:

$$V_{Th} = \frac{KT}{q} \tag{5}$$

I_{ph} : The net produced current;

I_d : The diode current;

I_{sh} : The photocurrent in shunt;

I_s : the saturation current of the diode;

q : The electron charge (q = 1.6 × 10-19 C);

R_s : the cell intrinsic series resistance;

R_p : The cell intrinsic shunt or parallel resistance;

n : the diode ideality factor which is between 1 and 2;

K : The Boltzmann constant (k = 1.38 × 10-23 J/K);

T : the temperature of the junction during its operation (K).

A photovoltaic generator consists of a set of elementary photovoltaic cells connected in series and/or in parallel. Therefore, the following equation describes the current delivered by the PV panel as a function of the number of cells in series N_s and parallel N_p [16]:

$$I_{pv} = N_p.I_{ph} - N_p.I_s\left[\exp\left(\frac{V_{pv}+R_sI_{pv}}{n.K.T.N_s}\right)-1\right]-N_p.q.\left(\frac{V_{pv}+R_sI_{pv}}{N_s.R_p}\right) \tag{06}$$

This equation shows clearly that the generated power of the PV module is strongly influenced by irradiance and temperature. So, it is necessary to study how these two climatic parameters will affect at the characteristics of the cell by drawing the curve of current (Ipv) versus voltage (Vpv) for various irradiations at constant temperature (Figure4), and for different temperatures at constant irradiance (Figure5).

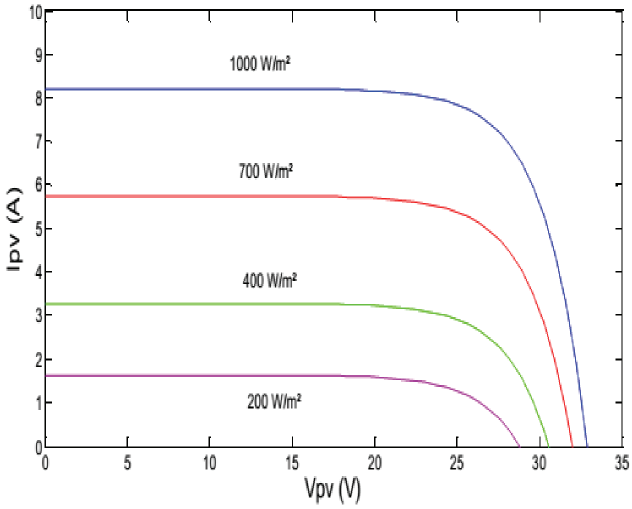

Fig.4. PV characteristic under different irradiances levels (temperature =25°C).

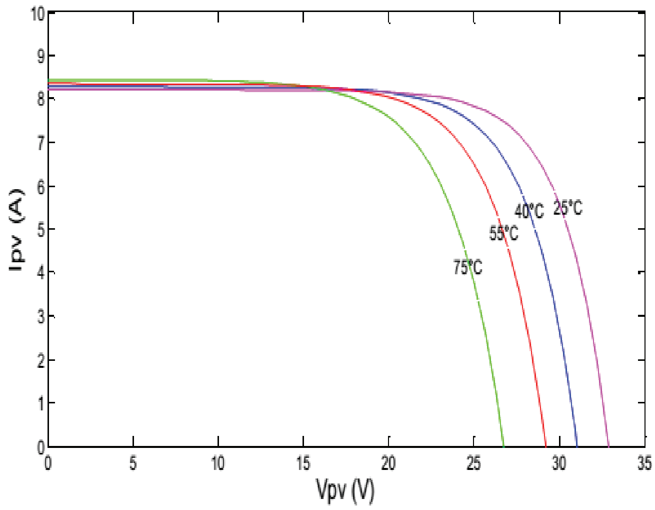

Fig 5. PV characteristic under different temperatures (irradiance = 1000 W/m²).

B. DC–DC boost converter modeling

The converter is used to regulate the PV module output voltage Vpv in order to extract as much power as possible from the PV module. Referring to Ref. [13], the dynamics of the boost converter is given by Eq. (07):

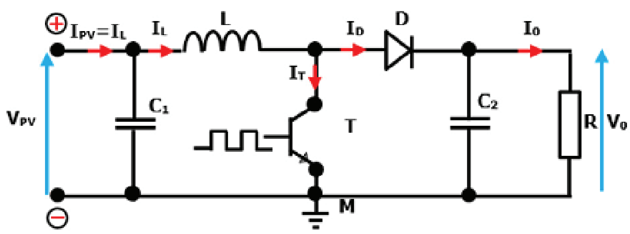

Fig 6. Boost converter model.

$$\begin{aligned} \frac{di_L}{dt} &= \frac{V_{pv}}{L} - (1-D)\frac{V_o}{L} \\ \frac{dV_o}{dt} &= \frac{V_o}{RC_2} - (1-D)\frac{i_L}{C_1} \end{aligned} \tag{7}$$

III. DESIGN OF SYNERGETIC MODE MPPT CONTROLLER

A. Synergetic control theory

Synergetic control is a state space approach for the design of control for complex highly connected nonlinear systems [17]. It forces the system state variables to evolve on a designer chosen invariant manifold enabling for desired performance to be achieved despite uncertainties and disturbances without damaging chattering inherent to the sliding mode technique. Let us consider the system to be controlled is described by a non-linear differential equation of this form:

$$\frac{dx}{dt} = \mathrm{f}(\mathrm{x}, D, \mathrm{t}) \tag{8}$$

Where x represents the system state vector, Dthe control input vector and f a continuous differentiable nonlinear function.

Synergetic synthesis begins with the definition of the macro-variable based on the equations of the state space. For the macro-variable, it can be expressed as follows:

$$\psi = \psi(\mathrm{x}, \mathrm{t}) \tag{9}$$

The objective of the synergetic controller is to operate the controlled system on the manifold for which the macro-variable is null ψ=0.

The expected dynamic evolution of the macro-variable is given as a function of:

$$\mathrm{T}\dot{\psi} + \psi = 0 \quad T \succ 0 \tag{10}$$

Where the derivative of the total macro-variable is noted by $\dot{\psi}$, and T is a parameter design which designates the convergence rate from the closed loop system to the manifold that is to be specified by ψ=0.

Finally, the control law (evolution in time of the control output) is synthesized according to equation (10) and the dynamic model of the system.

B. Synergetic MPPT controller design

The output power of solar array can be expressed as $P_{pv} = I_{pv}V_{pv}$ .By selecting the manifold as $\frac{dP_{pv}}{dI_{pv}} = 0$, it is guaranteed that the system state will hit the manifold and produce maximum power output persistently.

$$\psi(\mathrm{x}, \mathrm{t}) = \frac{dP_{pv}}{dI_{pv}} \tag{11}$$

Hence, the manifold is defined as:

$$\psi = \frac{dP_{pv}}{dI_{pv}} = \frac{dI_{pv}V_{pv}}{dI_{pv}} = V_{pv} + I_{pv}\frac{dV_{pv}}{dI_{pv}} = 0 \tag{12}$$

Differentiating the macro-variable along Equation (08) leads to Equation (13):

$$\frac{d\psi}{dt}=\left(\frac{d\psi}{dx}\right)\left(\frac{dx}{dt}\right) \tag{13}$$

By applying Equation (13) we find:

$$\frac{d\psi}{dt}=\left(\frac{d\psi}{dI_{pv}}\right)\left(\frac{dI_{pv}}{dt}\right) \tag{14}$$

Compensating Equation (14) in Equation (10) give us:

$$T\left[\left(\frac{d\psi}{dI_{pv}}\right)\left(\frac{dI_{pv}}{dt}\right)\right]+\psi=0 \tag{15}$$

Where:

$$\begin{aligned}\frac{d\psi}{dI_{pv}}&=2\frac{dV_{pv}}{dI_{pv}}+I_{pv}\frac{d^2V_{pv}}{dI_{pv}^2}\\ \frac{dI_{pv}}{dt}&=\frac{V_{pv}}{L}-(1-D)\frac{V_{pv}}{L}\end{aligned} \tag{16}$$

The substitution of Equations (16) into the Equation (15) gives the control law equation described in (17):

$$D=1-\frac{V_{pv}}{V_O}-\frac{V_{pv}+I_L\dfrac{dV_{pv}}{dI_L}}{T\dfrac{V_O}{L}\left[2\dfrac{dV_{pv}}{dI_L}+I_L\dfrac{d^2V_{pv}}{dI_L^2}\right]} \tag{17}$$

IV. SIMULATIO RESULTS AND DISCUSSION

To show the effectiveness of the proposed synergetic controller algorithm, the PV system is modeled and simulated using Matlab/Simulink environment. The system specifications used in the simulation are shown in Table1.

TABLEI

Parameter	Value	Parameter	Value
Maximum power (Pmax)	180 W	Capacity C1	1000 µF
Open-circuit voltage (Voc)	45 V	Capacity C2	1000 µF
Short-circuit current (I sc)	5.5 A	Inductance L	1.21 mH
Optimum operating voltage (Vmpp)	36 V	Resistive load R	25Ω
Optimum operating current (I mpp)	5 A	Switching frequency	10 kHz

- **Simulation results at Standard Test Condition: Irr=1000 W/m² and T = 25°C.**

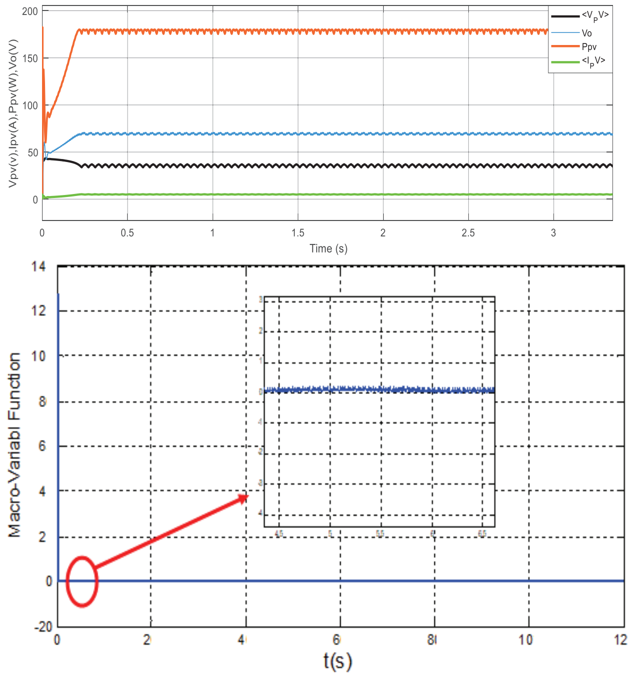

Fig. 7 – Simulation with standard condition: I=1000 W/m², T = 25°C.

- **Simulation results under load variations.**

To show the robustness of the proposed SCMPPT, considering load change i.e the load resistance is abruptly varied from 50 to 100 Ω at 2 sec.

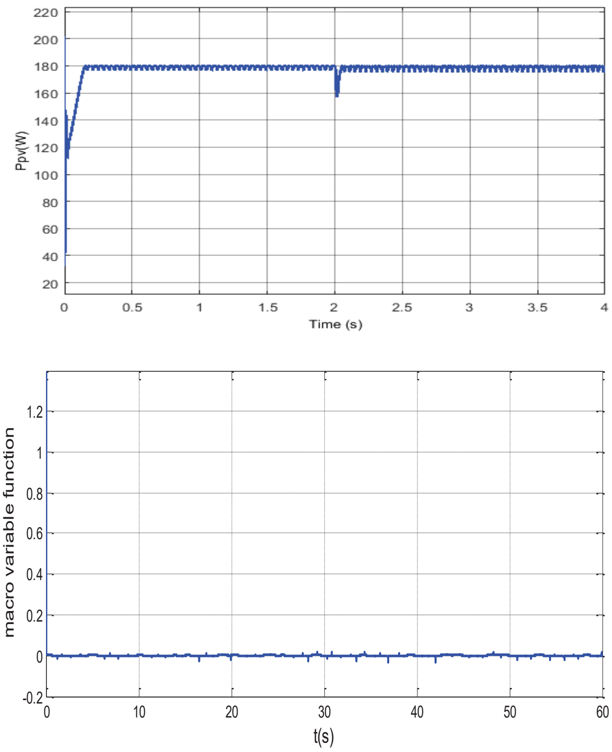

Fig. 8– Simulation under load resistance change.

For all the simulation results above, the synergetic control approach is able to maintain the output at optimum point rapidly a good performance and provide high robustness to the variation of the value of charge.

V. Conclusion

This paper presents a new nonlinear MPPT controller based on the synergetic control theory applied to a stand-alone PV system to extract and maximize the power created from PV system. A DC–DC boost converter is used as an interface between the PV array and the load. For all the simulation results above; the synergetic controller algorithm approach is able to maintain the output at optimum point and provides a good performance. The results also show that the proposed method adapts well to sudden changes in load. As future work, we foresee an experimental implementation of the proposed method in order to better appreciate its behavior in a real way.

References

[1] B.Kumar,P. Seshadri,"Modeling of Battery Management for Standalone PV System",Journal of Physics: Conference Series,RIACT 2021.

[2] U.N. Environment. Renewables 2022 Global Status Report. UNEP-UN Environment Programme. 16 June 2022. Available online:http://www.uneorg/resources/report/renewables-2022-global-status-report .

[3] Kachhiya K, Lokhande M, Patel M (2011) Matlab/simulink model of solar PV module and MPPT algorithm. National Conference on Recent Trends in Engineering and Technology.

[4] Esram, T., Chapman, P.L.: Comparison of Photovoltaic Array Maximum Power Point Tracking Techniques. IEEE Trans. Energy Convers. 22, 439–449 (2007).

[5] Shiqiong, Z., et al.: A novel maximum power point tracking algorithms for stand-alone photovoltaic system. Int. J. Control, Autom. Syst. 8, 1364–1371 (2011).

[6] Gomes de Brito, M.A., et al.: Evaluation of the main MPPT techniques for photovoltaic applications. IEEE Trans. Ind. Electron. 60, 1156–1167 (2013).

[7] Li, X., et al.: A novel beta parameter based fuzzy-logic controller for photovoltaic MPPT application. Renewable Energy 130, 416–427 (2019).

[8] Attia, H.A.: High performance PV system based on artificial neural network MPPT with PI controller for direct current water pump applications, Int. J. Power Electron. Drive Syst. 10, 1329–1338 (2019).

[9] Hadji, S., Gaubert, J.P., Fateh, K.: Theoretical and experimental analysis of genetic algorithms based MPPT for PV systems. Energy Procedia 74, 772–787 (2015).

[10] Li, H., et al.: An overall distribution particle swarm optimization MPPT algorithm for photovoltaic system under partial Shading. IEEE Trans. Ind.Electron. 66, 265–275 (2019).

[11] Salmi, H., et al.: An advanced MPPT based on artificial bee colony algorithm for MPPT photovoltaic system under partial shading condition. Int.J. Power Electron. Drive Syst. 8(2), 647–653 (2017).

[12] Titri, S., et al.: A new MPPT controller based on the Ant colony optimization algorithm for Photovoltaic systems under partial shading conditions. Appl. Soft Comput. 58, 465–479 (2017).

[13] R.Ayat, A.Bouafia,"Experimental validation of synergetic approach based MPPT controller for an autonomous PV system",IET Renew. Power Gener.2021.

[14] Koohi, S.; Rahim, N.A.; Mokhlis, H.; Tyagi, V.V. Photovoltaic electricity generator dynamic modeling methods for smart grid applications: A review. Renew. Sustain. Energy Rev. 2016, 57, 131–172.

[15] S.Mahjoub, C.Alaoui,"Control and Implementation of an Energy Management Strategy for a PV–Wind–Battery Microgrid Based on an Intelligent Prediction Algorithm of Energy Production",Energies 2023, 16, 1883.

[16] Bjaoui, M.; Khiari, B.; Benadli, R.; Memni, M.; Sellami, A. Practical implementation of the backstepping sliding mode controller MPPT for a PV-storage application. Energies 2019, 12, 3539.

[17] M.S. Mahgoun, A.E. Badoud, "New Design And Comparative Study Via Two Techniques For Wind Energy Conversion System",Electrical Engineering & Electromechanics, no, 2021.

Maximum Power Point Tracking of Solar Water Pumping Systems Using Fuzzy Logic Algorithm

Oussama Belaroussi
Department of Electrical and Heat Engineering, Faculty of Power Engineering
Tambov state technical university
Russian Federation, Tambov State.
oussama.belaroussi.47@gmail.com

Abdelkarim Ammar
LSS, Institute of Electrical and Electronic Engineering
University of M'hamed BOUGARA of Boumerdes, Algeria
a.ammar@univ-boumerdes.dz

Ahmed Lechelah
Department of Electrical and Heat Engineering, TSTU
Tambov, Russia Federation.
Lechelah45@gmail.com

Abstract— **In this paper, the Fuzzy Logic Controller (FLC) approach for achieving maximum power point tracking (MPPT) in a solar photovoltaic (PV) array-based water pumping system with an induction motor drive is provided (IMD). The rotor flux orientation vector control (IRFOC) was proposed in this study for operating an induction motor linked to a centrifugal pump. In the same study, FLC-MPPT power detection methods were used to meet the required flow rate and head. This strategy contributes to the effective operation of the pump. MATLAB-Simulink Models were used to model a photovoltaic water pumping system in this study.**

Keywords: FLC; MPPT; DC-DC; Induction motor; PV; FOC

I. INTRODUCTION

The demand for renewable energy is being driven by factors such as the depletion of crude oil sources, extreme weather, and the degradation of the environment. Solar photovoltaic (PV) systems are becoming more popular due to their low cost, high efficiency, scalability, adaptability, and quiet operation. A possible use is the use of photovoltaic (PV) water pump systems, particularly in more rural areas that have limited access to utility electricity. An induction motor is often used to power WP because to the low cost and high frequency of this kind of motor [1][2]. An MPPT is a component of most modern PV pumping systems (MPPT). The PV array is able to function at its maximum power point as a result of this DC–DC converter [3]. Both the perturb and observe and the incremental conductance techniques are very common for MPPT monitoring (MPPT). The most common alternative approach is more difficult to construct than the P&O method. These tactics boost transient responsiveness even when subjected to varying levels of solar insolation. Artificial neural networks are contributing to increased intelligence in this field. Solar photovoltaic (PV) pumping uses direct current (DC) motors to drive centrifugal pumps. These motors run on DC power and are compatible with photovoltaic (PV) solar systems. DC motors are more difficult to maintain and provide less power than AC motors. The commutator and the brushes serve to prevent the motor from becoming submerged. Brushless induction motors are preferred for use in solar water pumps [4]. The PVWPS Advanced Guard may be found in Section I. In Section II, we will talk about the setup of the system. The proposed system's control is broken out in Section III of this document. In Section IV, we provide the findings of the simulation as well as our assessment of how they relate to our optimization contribution. The last section, V, contains the conclusion.

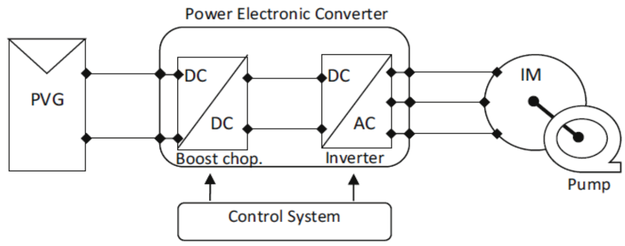

Figure 1. Configuration of solar-powered water pumping system (SWPS)

II. MODELING MATERIALS OF SWPS

Figure 1 depicts the overall layout of the proposed solar photovoltaic array-fed induction motor driven water pumping system that uses a direct current to direct current converter. An array of solar photovoltaic cells, a direct current to direct current converter, a three-phase inverter, an induction motor, and a centrifugal water pump make up the proposed system, from left to right.

A. Photovoltaic Generator

A PVG is a collection of photovoltaic modules that have been connected in series–parallel topologies in order to provide the voltage and power requirements of the association. These requirements include a power converter, an induction motor, and a centrifugal pump. The following current balancing equation may be constructed by considering the appropriate single-diode circuit of the PV module and applying Kirchhoff's current law (KCL) to it [5]:

$$\mathrm{I_{pv}} = \mathrm{I_L} - \mathrm{I_0}\left[\exp\left(\frac{\mathrm{V_{pv}} + \mathrm{R_s I_{pv}}}{\mathrm{V_{th}}}\right) - 1\right] - \frac{(\mathrm{V_{pv}} + \mathrm{R_s I_{pv}})}{\mathrm{R_{sh}}} \quad (1)$$

Where: I_{pv} , R_{sh} and R_s Array output current, PV array equivalent shunt resistance, PV array series resistance, respectively. V_{th} ; symbolizing PV array thermal voltage Eq (2). I_L: Photo-current generated Eq (3), I_0 : PV array reverse saturation current Eq (4), I_{sc} : PV array short circuit current Eq (5).

$$V_{th} = \frac{\left(V_{mp} + R_s I_{mp} - V_{oc}\right)}{\log\left(1 - \frac{I_{mp}}{I_{sc}}\right)} \tag{2}$$

$$I_L = \left(I_{sc} + K_i(T - 298.15)\right)\frac{G}{1000} \tag{3}$$

$$I_0 = \left(I_{sc} - I_{mp}\right)\exp\left(\frac{\left(V_{mp} + R_s I_{mp}\right)}{V_{th}}\right) \tag{4}$$

$$I_{sc} = I_{scR}\frac{G}{G_R}\left[1 + \alpha\left(T_{cel} - T_{celR}\right)\right] \tag{5}$$

B. DC-DC Boost Converter

Boost converters are often used in the process of operating systems at higher voltage levels. The effective running of the system is made easier by a converter that has been thoughtfully constructed. Due to the fact that the boost converter just had one switch, the efficiency with which it was refurbished was extraordinary. Boost converters are helpful in finding the highest power output that a solar PV array is capable of producing [6].

C. Three-phase inverter

It is not possible to power an induction machine with only a boost converter since it modifies and enhances the voltage. In order to interact with the induction machine in a way that is both safe and effective, a photovoltaic system requires an inverter. This allows for the efficient management of energy by converting the direct current output voltage of the transformer to an alternating voltage. VSI is often used. The usage of inverters presently (CSI). In solar energy applications, a balanced three-phase power supply may be achieved with the use of DC-AC converters, specifically three-phase inverters. The functioning is controlled via inverter switches.

D. Induction Motor Dynamic model

Using a space vector notation written in the (d,q) reference frame rotating at synchronous speed $\boldsymbol{\omega_s}$, the IM model is given and described.

Where $\boldsymbol{\theta_s}$ and $\boldsymbol{\theta}$ indicate the position of the (d,q) reference frame and the rotor, respectively.

The electrical equations of the IM may be written as follows [7]:

$$\begin{cases} \frac{dI_{sd}}{dt} = -\lambda I_{sd} + \omega_s I_{sq} + \frac{k_s}{T_s}\varphi_{rd} + \omega k_s \varphi_{rq} + \frac{1}{\sigma L_s}V_{sd} \\ \frac{dI_{sq}}{dt} = -\lambda I_{sq} - \omega_s I_{sd} + \frac{k_s}{T_s}\varphi_{rq} - \omega k_s \varphi_{rd} + \frac{1}{\sigma L_s}V_{sq} \end{cases} \tag{6}$$

$$\begin{cases} \frac{d\varphi_{rd}}{dt} = \frac{M}{T_r}I_{sd} - \frac{1}{T_r}\varphi_{rd} + (\omega_s - \omega)\varphi_{rq} \\ \frac{d\varphi_{rd}}{dt} = \frac{M}{T_r}I_{sq} - \frac{1}{T_r}\varphi_{rq} - (\omega_s - \omega)\varphi_{rd} \end{cases} \tag{7}$$

Where $(\boldsymbol{V_{sd}}, \boldsymbol{V_{sq}})$ and $(\boldsymbol{I_{sd}}, \boldsymbol{I_{sq}})$ represent the voltages and currents of the d-q stator, respectively. $(\boldsymbol{V_{rd}}, \boldsymbol{V_{rq}})$ and $(\boldsymbol{I_{rd}}, \boldsymbol{I_{rq}})$ represent the voltages and currents of the d-q rotors, respectively. $(\boldsymbol{\varphi_{rd}}, \boldsymbol{\varphi_{rq}})$ and $(\boldsymbol{\varphi_{sd}}, \boldsymbol{\varphi_{sq}})$ respectively represent the d-q rotor and stator fluxes. $\boldsymbol{\omega_s}$ and $\boldsymbol{\omega}$ =Ωp represent the synchronous velocity and rotor velocity, respectively. Ts = Ls/Rs and Tr = Lr/Rr are the time constants for the stator and rotor, respectively.

And: $\sigma = 1 - \frac{M^2}{L_s L_r}$; $k_s = \frac{M}{\sigma L_s L_r} = \frac{1-\sigma}{\sigma M}$; $\lambda = \frac{1}{\sigma T_s} + \frac{1-\sigma}{T_r \sigma}$.

The mechanical equations and electromagnetic torque are supplied by:

$$T_e = \frac{pM}{L_r}\left(\varphi_{ds} I_{sq} - \varphi_{sq} I_{ds}\right) \tag{8}$$

$$\frac{d\Omega}{dt} = \left(T_e - T_l - f_r\Omega\right)/J \tag{9}$$

$\boldsymbol{T_l}$ represents the load torque.

E. Water pump

The water pump is the component of the system that is considered to be the most important. The design of it is quite important in order to fulfill the necessary irrigation requirements. There are many different kinds of pumps, each of which has a certain placement and function in the world. In this research, the usage of a centrifugal pump that is powered by an induction motor is suggested. We are able to simulate the features of the pump by:

$$P = \frac{\rho g H Q}{\eta} \tag{10}$$

$$\eta = \frac{Pu}{P} \tag{11}$$

And the torque-speed equation is expressed as follows:

$$T_{pump} = K_1 w^2 + K_2 w Q + K_3 Q^2 \tag{12}$$

$$T_r = A {w_m}^2 \tag{13}$$

$$A = P_n / {w_n}^3 \tag{14}$$

Where: N → the rotational speed shaft of pump given by (rad/s), ρ → volumetric water mass given by (Kg/m^3). Q → the water flow (m^3/s), and H → the height of rise (m), g → the acceleration of gravity (m^2/s). $K_1, K_2, K_3 \rightarrow$ are coefficients given by the manufacturer.

The following is a feed-forward equation for speed calculated from solar power's available power:

$$w_m{}^* = K\sqrt[3]{P_{pv}} \tag{15}$$

Where; P_{pv} is photovoltaic power and K=1/$\sqrt[3]{(A)}$. This feed-forward speed increases the dynamic performance in standalone mode and decreases the system's dependence on the pump's consistent accuracy [8].

III. Control approach of proposed system

A. MPPT control

The MPPT will automatically try to reach maximum power by changing the motor speed in order to meet the increasing demand for PV power. Find out whether the current OP is located to the left or right of the MPP [9]. Because PV pumping systems are so costly, they should almost always be operating in MPPT mode. Because the power of PV modules might vary, it is essential to strike a balance between the load needs and the maximum output [10].

One of the most popular methods for machine learning is called artificial neural networks (ANNs), and it is a computational model that needs input data for training in order to create approximated output results. Artificial Neural Networks are one of the most extensively used machine learning methodologies. The ability of artificial neural networks to accurately replace complex mathematical models is one of the benefits of using these networks. Artificial techniques like as the fuzzy logic controller (FLC) have received a lot of attention [11] due to the fact that they are simple, have a high ability even when given incorrect inputs, do not need a precise mathematical model, and have the potential to solve nonlinearity. The FLC is one of the several MPPT controllers available, and it is consistently regarded as among the most effective.

Triangular membership functions for the fuzzification process were used. For the inputs E, CE and for the output ΔD, 5 membership functions were defined in terms of the following linguistic variables: Negative (NB), Negative Medium (NM), Negative Small (NS), Neutral (ZE), Positive Small (PS), Positive Medium (PM) and Positive Big (PB). The range for the error is (−10 to 10), for the change of error is (−2 to 2) and for the increment in duty cycle is (−1 to 1). Figure 2 shows the membership functions for the inputs and outputs of the controller.

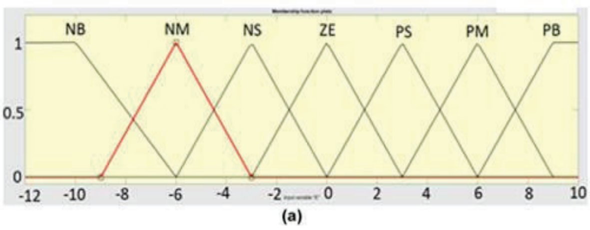

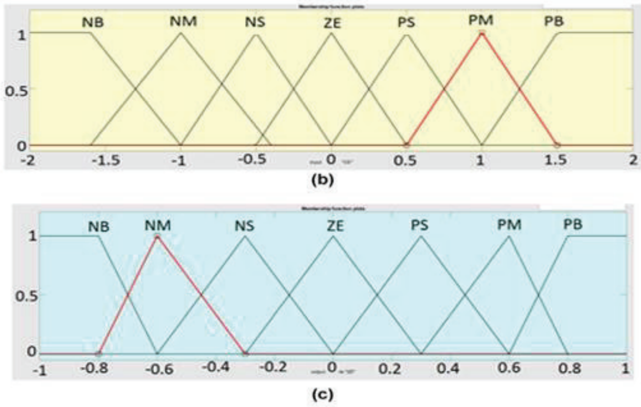

Fig. 2. (a) The input of FLC (Error, E), (b) The input of FLC (Change of error, CE) (c) The output of FLC (Duty, D).

B. Induction motor control

To enhance the induction motor's dynamic performance at a fair cost, a thorough and effective control approach must be implemented. Field Oriented Control, often known as vector control, is a feasible strategy. It is divided into indirect and direct approaches. It may be necessary to orient a rotor, stator, or air-gap flux linkage. For Indirect Field Oriented Control to determine the synchronous speed, slip speed estimation using observed or estimated rotor speed is required. No flux estimate exists inside the system. The synchronous speed for the direct system is determined using the flux angle supplied by the flux estimator or flux sensors. This implementation system details the indirect (rotor) flux-oriented control system with closed-loop speed estimator.

In order to decouple the flux and torque of the induction machine, which is one of the intrinsic features of the DC machine, the FOC is largely dependent on the orientation of the rotating frame such that the axis coincides with the direction of r (as shown in "Fig. 3"). To simplify the control, it is essential to carefully choose the reference. For this, it is assumed that the 'd' axis and the flow axis are aligned; given this condition, we have [12]:

$$\varphi\_rd = \varphi\_r \ ,\varphi\_rq = 0 \tag{16}$$

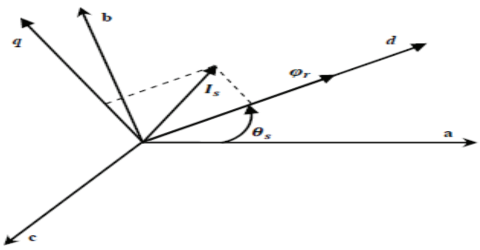

Fig 3. Principle of the vector control

As indicated by Equation, the voltages V_sd and V_sq impact both the currents Isd and Isq and, therefore, the flux and torque (6). In this situation, compensation-based decoupling will be implemented.

These equations may be rewritten from (6):

$$\begin{cases} V_{sd} = V'_{sd} + E_d \\ V_{sq} = V'_{sq} + E_q \end{cases} \tag{17}$$

Where: $\boldsymbol{E_d}$ and $\boldsymbol{E_q}$ are compensation terms.

The resulting equation system is totally decoupled:

$$\begin{cases} V'_{sd} = \sigma L_s \dfrac{dI_{sd}}{dt} + \lambda \sigma L_s I_{sd} \\ V'_{sq} = \sigma L_s \dfrac{dI_{sq}}{dt} + \lambda \sigma L_s I_{sq} \end{cases} \tag{18}$$

In addition, when (8) and (16) are subtracted, the electromagnetic torque equation becomes:

$$C_e = \frac{pM}{L_r} \left(\varphi_r \, I_{sq} \right) \tag{17}$$

And (7) turn into:

$$\begin{cases} \varphi_r = M I_{sd} \\ (\omega_s - \omega) = \dfrac{M}{T_r \varphi_r} I_{sq} \end{cases} \tag{18}$$

This gives:

$$\omega_s = \frac{I_{sq}}{T_r \varphi_r} + \omega \tag{19}$$

Ultimately, we have:

$$\theta_s = \int \frac{I_{sq}}{T_r \varphi_r} + \theta \tag{20}$$

The angle θ_s will be used throughout all conversions.

The expression for the torque as a function of the currents is then:

$$T_e = \frac{pM^2}{L_r} \left(I_{sd} \, I_{sq} \right) \tag{21}$$

And lastly, we have:

$$\begin{cases} \varphi_r = M I_{sd} \\ T_e = \dfrac{pM}{L_r} \left(\varphi_r \, I_{sq} \right) \end{cases} \tag{22}$$

These two equations will be utilized to regulate currents and speeds, making them applicable to vector control.

The overall block diagram of the Indirect FOC for the Induction Motor is seen in Figure 4.

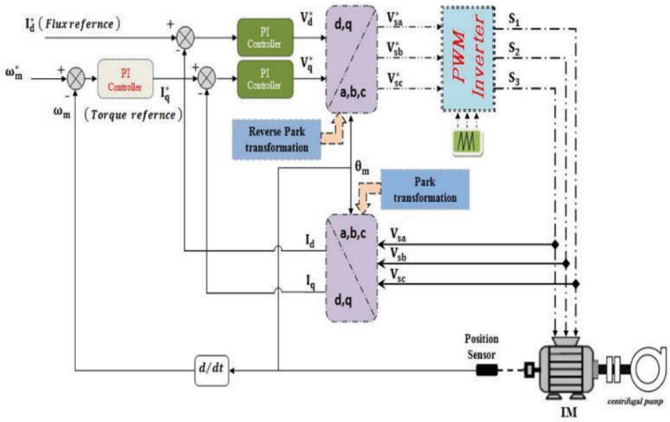

Figure 4. Block Diagram of FOC of Induction Motor feeding a centrifugal pump.

As indicated in Fig. 4, a PI (Proportional Integrator) controller is used to regulate currents; however, the PI controller is not suggested for speed regulation due to its poor performance. In this article, an IP (Integrator - Proportional) controller is employed to compensate the zero that emerges in the closed loop to reduce the overshoot in the speed response.

IV. Simulation Results and Discussions

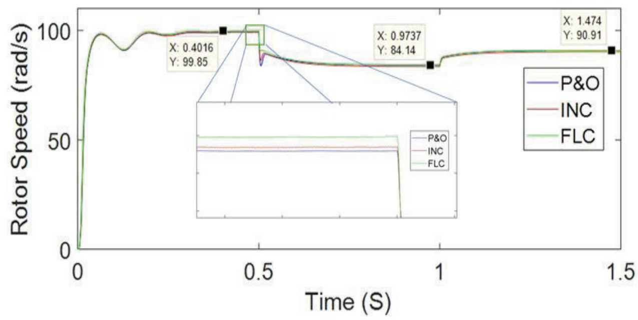

Figure 5. Motor speed under different MPPT Methods

The FLC detects the GMPP (global MPP) of 1065 W, however the P&O (Perturb and Observe) and INC (incremental conductance) cannot swiftly follow the MPP, as shown in Figure 5. This has an instantaneous influence on rotor speed. This study illustrates that the FLC is successful even for difficult optimization issues.

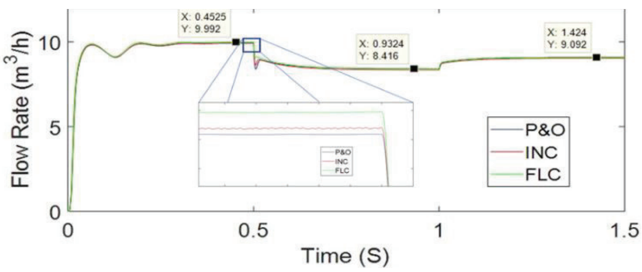

Figure 6. Flow rate affected by different MPPT Methods

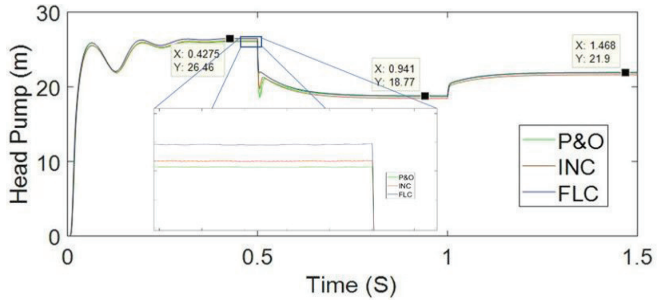

Figure 7. Head pump affected by different MPPT Methods

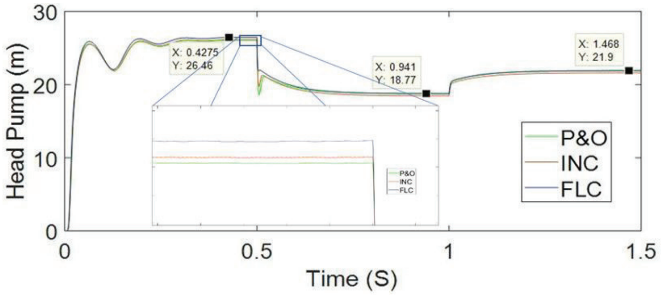

Figure 8. Hydraulic power affected by different MPPT Methods

Figures 6, 7, and 8 illustrate, respectively, the flow rate of the centrifugal pump that was provided by IMD as well as the pump head and the hydraulic power. The intelligent technique, FLC, has a significantly faster response time to reach the MPP than the older ways, P&O and INC, which both have a much longer reaction time. In addition, the FLC technique has a much lower transient length compared to the approaches that came before it. As a consequence of the effect that various MPPT methods have on the pumping system, the findings indicate that the SPWPS (Solar Power Water Pumping System) based on the FLC method has a privileged response in comparison to P & O and INC, and that the response of the FLC almost coincides with the higher DC power under the conditions that have been proposed, whereas the P & O and INC methods do not. As a result, I have provided him with this alternative to pay the cost of feeding more agricultural produce.

V. Conclusion

Improving the tracking efficiency of the PV system is very necessary in order to improve the system's overall efficiency. In order to keep the DC output power and voltage at their optimal levels, the conventional MPPT approaches are applied. These time-honored practices might, to a certain extent, be efficiently replaced or complemented by approaches using artificial intelligence. The goal of this study is to demonstrate how these approaches may assist in extracting the greatest amount of electricity that can be generated by PV arrays for use in a variety of applications, including the charging of electric cars and the provision of water for irrigation.

The findings of the simulations demonstrate that the intelligent procedures, most notably FLC, showed the greatest performance out of all of the methodologies that were examined and tried. It is a fantastic solution that has the greatest steady-state efficiency and response time, as well as the ability to start the system. And the consequences of using DC power have an immediate impact on the efficiency of the pumping system.

Appendix A:

PV Array parameters: Maximum power (Watt-Peak) 249 W ; Short circuit current (ISC) 8.83 A ; Open circuit voltage (VOC) 36.8 V ; Temperature (NOCT) 25 °C ; G = 1000/835/905 W/m^2 (Fixed irradiance) ; Ns = 1 ; Np = 5 .

Converter DC-DC paremeters : Indicator L 1.1478 mh ; Input capacitance Cin 250 uF ; Output capacitance Cout 47 uF ; Frequency 10 KHz.

Appendix B:

Induction motor paremeters : Rs= 6.75 Ω ; Rr =6.21 Ω ; Ls=0.5192 H ; Lr =0.5192 H ; M =0.4957 H ; J =0.0140; Fr= 0.002; P= 2

Centrifugal pump paremeters : The nominal speed 100 rad /s ; The nominal Flow rates 10 m^3/h ; The nominal Head pump 26.5 m ; The nominal Power Hydraulic 720 W .

References

[1] Mohd. Kashif And All. Adaptive Hybrid Generalized Integrator Based Smo For Solar Pv Array Fed Encoderless Pmsm Driven Water Pump. IEEE Transactions On Sustainable Energy 2021, 12(3) , Pp. 1651-1661.

[2] Shrey Verma and all. Solar PV powered water pumping system – A review, Materials Today: Proceedings 2021, 46 (11), pp. 5601–5606.

[3] Said M. A. Ibrahim and all. Comprehensive Design Tool for Sizing Solar Water Pumping System in Egypt. Applied Solar Energy 2020, 56 (1), pp. 18–29.

[4] Utkarsh Sharma and all . Utility-Tied Solar Water Pumping System for Domestic and Agricultural Applications. J. Inst. Eng. India Ser. B 2020, 101(1), pp. 79–91.

[5] Salim Djeriou and all. Efficiency Improvement in Induction Motor-Driven Solar Water Pumping System Using Golden Section Search Algorithm. Arab J Sci Eng 2018, 43, pp. 3199–3211.

[6] Harsha Kukde and all. Solar Powered Brushless DC Motor drive for Water Pumping System. 2017 International Conference on Power and Embedded Drive Control (ICPEDC), Chennai, India, 16-18 March 2017.

[7] Lamyae Et-taaj , Zakaria Boulghasoul , Abdelhadi Elbacha , Abdellah El kharki, “ Robust sensorless Induction Motor control based on Extended Kalman Filter observer “ , 2021 International Congress of Advanced Technology and Engineering (ICOTEN), 04-05 July 2021, Taiz, Yemen.

[8] Utkarsh Sharma and all. Utility-Tied Solar Water Pumping System for Domestic and Agricultural Applications, J. Inst. Eng. India Ser. B 2020, 101(1), pp. 79–91.

[9] Riccardo Antonello and all. Energy-Efficient Autonomous Solar Water-Pumping System for Permanent-Magnet Synchronous Motors. IEEE Transactions on Industrial Electronics 2017, 64 (1), pp. 43 – 51.

[10] Piyush Choudhary and all, Solar powered induction motor-based water pumping system: A review of components, parameters and control methodologies, 2017 4th IEEE Uttar Pradesh Section International Conference on Electrical, Computer and Electronics (UPCON), Mathura, India, 26-28 October 2017.

[11] Belarrousi Oussama., V. F. Kalinin., Amel Terki. “ Effective Fuzzy Logical Control for Photovoltaic System Optimization “ , Вестник ТГТУ, 27(1),pp. 62-72, 2021.

[12] Drive Shaija P J ,Asha Elizabeth Daniel, “ Robust Sliding Mode Control Strategy Applied to IFOC Induction Motor Drive “, 2021 Fourth International Conference on Electrical, Computer and Communication Technologies (ICECCT), Erode, India.

The 1st National Conference on Green Energy (NCGE' 2023)
December 02, 2023, Boumerdes, Algeria.

An Improved Robust of Twisting Sliding Mode Control Based Maximum Power Point Tracking For Solar PV Systems

Nassir DEGHFEL
Automatic Laboratory of Setif
Electrical Engineering Deprtment
University of Sétif 1,
Algria
nassir.deghfel@univ-setif.dz

Abd Essalam BADOUD
Automatic Laboratory of Setif
Electrical Engineering Deprtment
University of Sétif 1,
Algria
badoudabde@univ-setif.dz

***Abstract*—In the past few years, there has been a significant surge in global interest in the recognition of photovoltaic (PV) systems. This is mostly due to its inherent sustainability, endless availability, and ecologically beneficial nature. In order to ensure optimal performance and the extraction of maximum power, the photovoltaic (PV) system necessitates the implementation of a tracking controller. This controller, known as the maximum power point tracking (MPPT) approach, is essential. This paper introduces a novel twisting sliding mode control framework aimed at improving the performance of maximum power point tracking (MPPT). The proposed framework aims to reduce the complexity associated with system management while effectively handling uncertainties and disturbances in both the environment and the photovoltaic (PV) system. In order to assess the effectiveness of the proposed approach in relation to existing techniques, simulations are conducted that take into account the occurrence of rapid and simultaneous fluctuations in irradiance. In addition to comparative analysis with conventional perturb and observe (P&O) and incremental conductance (INC) techniques. The findings indicate that the proposed method exhibits satisfactory performance in terms of its rapid response time, ability to limit power fluctuations, and high tracking efficiency.**

Keywords*—Sliding mode Control, Twisting Algorithm, Boost converter , Photovoltaic Systems, MPPT.

I. INTRODUCTION

In order to ensure a sustainable energy supply, minimize carbon emissions, and decrease reliance on fossil fuels, it is imperative to extensively harness and advocate for the utilization of renewable sources. Photovoltaic (PV) energy stands out as a very effective form of renewable energy due to its notable attributes, including widespread accessibility, straightforward installation process, absence of mechanical components, and uncomplicated maintenance requirements [1]. The efficacy of the PV system is adversely affected by weather conditions, resulting in reduced efficiency and higher costs compared to fossil fuels. The suboptimal efficiency of solar panels, coupled with the fluctuating temperature and radiation levels, has prompted researchers to explore strategies aimed at maximizing the utilization of the generated power [2]. Currently, there is a growing significance placed on the development of maximum power point tracking (MPPT) approaches for optimizing the maximum power point [3]. The primary objective of the Maximum Power Point Tracking (MPPT) technique is to ensure that the voltage (Vpv) and current (Ipv) of the photovoltaic (PV) system consistently operate at the Maximum Power Point (MPP) on the Power-Voltage (P-V) characteristic curve. There are a number of MPPT algorithms available, but the Perturb and Observe (P&O) [4] and Incremental Conductance (IC) [5] methods are the most popular and widely used. Both algorithms have excellent tracking efficiency and can be implemented with minimal effort due to their lack of parameter requirements. These techniques calculate the MPP by tracking the voltage and current fluctuations in real time. In addition, they may determine the necessary values for current, voltage, or duty cycle to carry out the MPPT procedure. Nevertheless, the conventional MPPT approaches have two significant limitations: continuous oscillations around the MPP and the inability to maintain tracking direction when faced with substantial or abrupt changes in solar irradiation [6].

The utilization of non-linear controllers offers a viable option in addressing the inherent nonlinearity of photovoltaic (PV) arrays and power converters. Sliding Mode Control (SMC) is a nonlinear control methodology that is taken from the theoretical framework of Variable Structure System (VSS) theory. The sliding mode control (SMC) algorithm is widely recognized in the field of control theory for its ability to enhance system robustness. Particularly, SMC proves to be a valuable approach. However, the main drawback of conventional SMC algorithm is the chattering phenomenon [7]. In order to address this

problem second order sliding mode control was introduced in literature [8]–[12].
The primary objective of this study is to address the issue of chattering and enhance both the efficiency and robustness of the system. This work employs a Twisting Sliding mode control T-SMC algorithm to address the aforementioned disparity.
The present paper is structured in the following manner: The presentation of the system description can be found in Section 2. In section 3, the proposed algorithm design is shown. Section 4 presents numerical simulations conducted under different climate settings. Ultimately, Section 5 presents several conclusions.

II. SYSTEM DESCRIPTION

The overall efficiency of photovoltaic (PV) systems is often influenced by three primary factors[13]: the conversion efficiency of the PV module, the efficiency of the DC-DC conversion stage, and the effectiveness of the maximum power point tracking (MPPT) technology.
The schematic representation of the cl osed loop system is depicted in Figure 1. It encompasses the electrical circuitry of the solar module, the specifications of which are presented in Table 1. Additionally, the system incorporates the DC-DC converter BOOST and the suggested Maximum Power Point Tracking (MPPT) technique referred to as Second Order Twisting Sliding Mode Control.

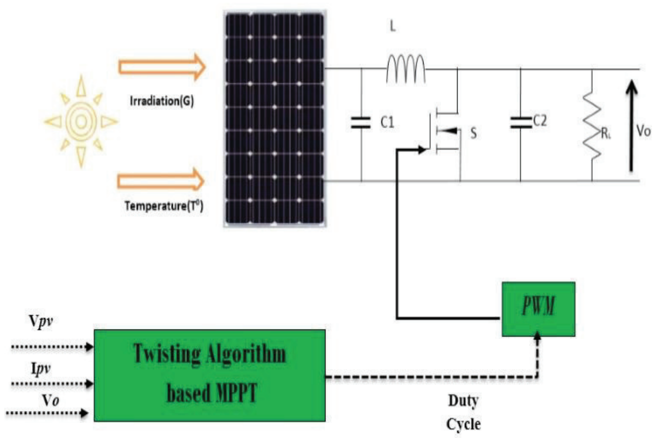

Figure 1. The overall structure of the proposed system

Table I . PV System characteristics

Maximum power (P_{mp})	60 W
Voltage during the open circuit (V_{oc})	21.1 V
Current during the short circuit (I_{sc})	3.8 A
The voltage corresponding to the maximum power (V_{mp})	17.1 V
The Current corresponding to the maximum power (I_{mp})	3.5 A
Input capacitor C_1	100 µF
Output capacitor C_2	100 µF
Inductor L	5 e-3 H

III. MPPT CONTROLLER DESIGN

A second-order sliding mode controller based on a twisting algorithm has been employed to increase power production. In order to reduce chattering phenomenon, the twisting method was devised.
The sliding mode control technique was developed in two stages. The first step is to create a sliding surface on which the DC-DC exhibits the necessary characteristics, while the second is to develop a control rule that will keep the system driven and stable there. In order to ensure that the system states will intersect with the sliding surface and yield the maximum power point (MPP) output, we opt for the sliding surface as specified in reference [14], [15] , which expressed as follow :

$$s(x,t) = 0, \dot{s}(x,t) = 0 \tag{1}$$

$$s(x,t) = \frac{\partial P_{pv}}{\partial V_{pv}} = \frac{I_{pv}}{V_{PV}} + \frac{\partial I_{pv}}{\partial V_{pv}} = 0 \tag{2}$$

The second step is to design the T-SMC control law , which consist of two term are the equivalent control law U_{eq} and the switching control law based T-SMC .
The equivalent control U_{eq} is determined through the solution of the algebraic equation

$$\dot{s} = \left[\frac{dS}{dX}\right]^T \dot{X} = \left[\frac{dS}{dX}\right]^T (h(X)u_{eq} + f(X)) = 0 \tag{3}$$

Where

$$f(X) = \begin{bmatrix} \frac{V_{PV} - V_o}{L} \\ -\frac{V_o}{RC_2} + \frac{I_L}{C_2} \end{bmatrix} \quad \text{and} \quad h(X) = \begin{bmatrix} \frac{V_o}{L} \\ -\frac{I_L}{C_2} \end{bmatrix} \tag{4}$$

Thus, we can obtain

$$U_{eq} = 1 - \frac{V_{PV}}{V_o} \tag{5}$$

The expression of the twisting sliding mode is given by [14]

$$U_{T-SMC} = -\lambda_1 sign(S) - \lambda_2 sign(\dot{S}) \tag{6}$$

The overall control law expressed as

$$U = 1 - \frac{V_{PV}}{V_o} - \lambda_1 sign(S) - \lambda_2 sign(\dot{S}) \tag{7}$$

IV. SIMULATION RESULTS

This section presents a comprehensive assessment of the performance of the proposed T-SMC feedback scheme-based MPPT controller. The performance is assessed by extensive MPPT evaluations and is compared with two other conventional methods, namely incremental conductance (INC) and perturb and observe (P&O), for relative performance analysis. Simulation of the overall system was carried out using MATLAB/Simulink software under a fast-changing irradiance profile, as shown in Figure 2. Figures 3-6 present the responses of PV power, PV voltage, output PV current, and P-V characteristic curves, respectively, using the mentioned MPPT algorithms. It is obvious that the proposed approach provided high dynamic performance, fast response time, easy reach to MPP, high tracking efficiency, and low voltage fluctuations.

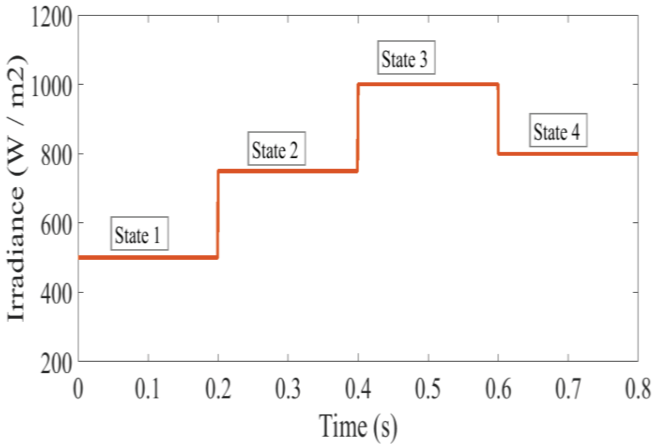

Figure 2. Irradiance profile

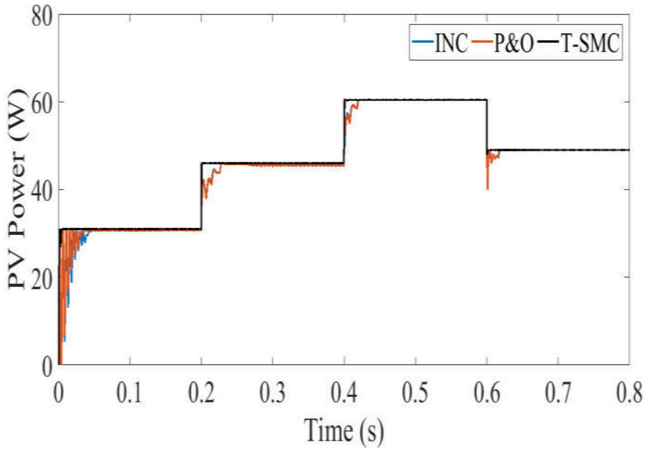

Figure 3. Output PV power extraction using different MPPT methods under variable irradiation

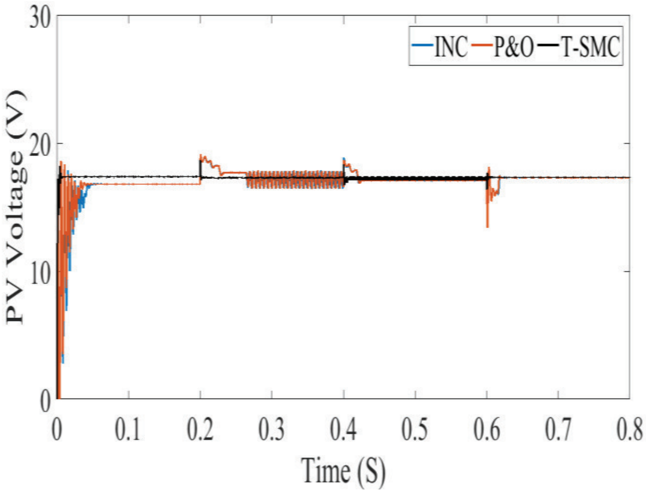

Figure 4. PV array output voltage using different MPPT methods under variable irradiation

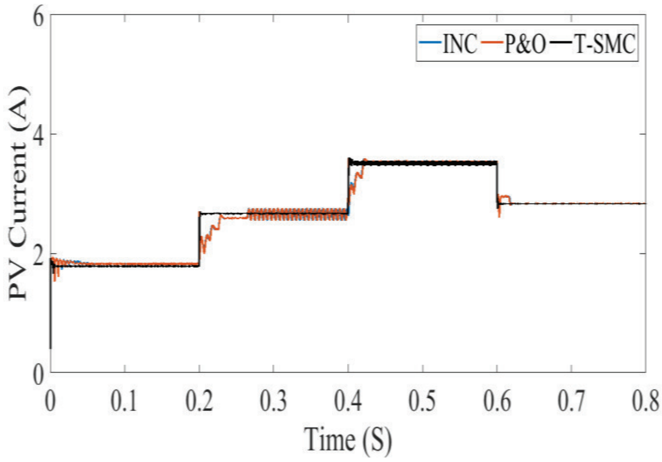

Figure 5. PV array output currrent using different MPPT methods under variable irradiation

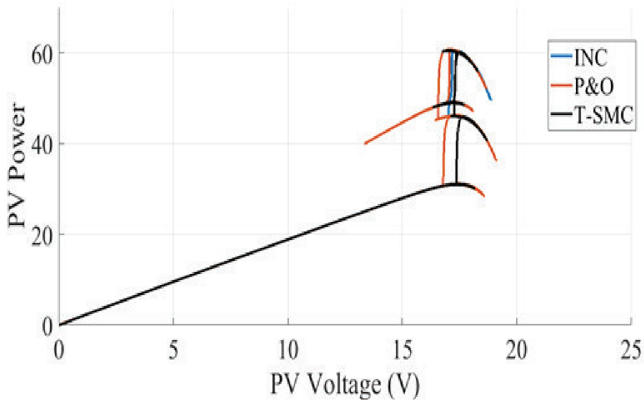

Figure 6. P-V curve using different MPPT methods under variable irradiation

V. Conclusion

This work introduces a T-SMC based MPPT algorithm to address the chattering problem of conventional SMC and enhance the MPP tracking under hard fluctuation atmospheric conditions. In order to validate the viability and efficacy of the suggested approach, MATLAB/Simulink environment was used to carry out the system simulation. Furthermore, a comparative evaluation was conducted to analyze the efficacy of the suggested MPPT approach in comparison to two well recognized MPPT methods, namely Perturb & Observe and Incremental Conductance.

The provided MPPT controller demonstrates strong performance in the face of varying environmental circumstances. The results validate the advantages of the suggested T-SMC in comparison to conventional controllers. Seeing that the power Oscillation, PV voltage ripple, and PV current ripple were almost zero, we can conclude that the proposed T-SMC is able to address the chattering effect in conventional SMC.

References

[1] A. Ali *et al.*, “Investigation of MPPT Techniques under Uniform and Non-Uniform Solar Irradiation Condition-A Retrospection,” *IEEE Access*, vol. 8, pp. 127368–127392, 2020, doi: 10.1109/ACCESS.2020.3007710.

[2] Badoud AE, Ayat Y, Mekhilef S. Development and experimental validation of novel robust MPPT controller based on bond graph and fuzzy logic for PV system under variable weather conditions. Int Trans Electr Energ Syst. 2021;e13091. doi:10.1002/2050-7038.13091

[3] Abd Essalam Badoud, Bertrand Raison and Mabrouk Khemliche, Modeling, simulation and hardware implementation of a bond graph-maximum power point tracker for a photovoltaic panel under partially shaded conditions, Simulation, Vol. 92, Iss. 7, 2016, https://doi.org/10.1177/0037549716646846

[4] D. Sibtain, M. M. Gulzar, K. Shahid, I. Javed, S. Murawwat, and M. M. Hussain, “Stability Analysis and Design of Variable Step-Size P&O Algorithm Based on Fuzzy Robust Tracking of MPPT for Standalone/Grid Connected Power System,” *Sustain.*, vol. 14, no. 15, 2022, doi: 10.3390/su14158986.

[5] M. Alsumiri, “Residual incremental conductance based nonparametric MPPT control for solar photovoltaic energy conversion system,” *Ieee Access*, vol. 7, pp. 87901–87906, 2019.

[6] M. Mao, L. Cui, Q. Zhang, K. Guo, L. Zhou, and H. Huang, “Classification and summarization of solar photovoltaic MPPT techniques: A review based on traditional and intelligent control strategies,” *Energy Reports*, vol. 6, pp. 1312–1327, 2020.

[7] A. Kchaou, A. Naamane, Y. Koubaa, and N. M’sirdi, “Second order sliding mode-based MPPT control for photovoltaic applications,” *Sol. Energy*, vol. 155, pp. 758–769, 2017, doi: 10.1016/j.solener.2017.07.007.

[8] A. Fezzani, N. Bouarroudj, S. Drid, and L. Zaghba, “Robust maximum power point tracking control for photovoltaic system based on second order sliding-mode,” *Int. J. Appl.*, vol. 9, no. 3, pp. 284–296, 2020.

[9] H. Sahraoui, L. Chrifi-Alaoui, S. Drid, and P. Bussy, “Second order sliding mode control of DC-DC converter used in the photovoltaic system according an adaptive MPPT,” *Int. J. Renew. Energy Res.*, vol. 6, no. 2, pp. 375–383, 2016, doi: 10.20508/ijrer.v6i2.3369.g6797.

[10] D. Matouk, F. Abdessemed, O. Gherouat, and Y. Terchi, “Second-order sliding mode for Position and Attitude tracking control of Quadcopter UAV: Super-Twisting Algorithm,” 2020.

[11] R. Khan, L. Khan, S. Ullah, I. Sami, and J. S. Ro, “Backstepping based super-twisting sliding mode mppt control with differential flatness oriented observer design for photovoltaic system,” *Electron.*, vol. 9, no. 9, pp. 1–30, 2020, doi: 10.3390/electronics9091543.

[12] A. K. Podder, N. K. Roy, and H. R. Pota, “MPPT methods for solar PV systems: A critical review based on tracking nature,” *IET Renew. Power Gener.*, vol. 13, no. 10, pp. 1615–1632, 2019, doi: 10.1049/iet-rpg.2018.5946.

[13] M. Mosa, M. B. Shadmand, R. S. Balog, and H. A. Rub, “Efficient maximum power point tracking using model predictive control for photovoltaic systems under dynamic weather condition,” *IET Renew. Power Gener.*, vol. 11, no. 11, pp. 1401–1409, 2017, doi: 10.1049/iet-rpg.2017.0018.

[14] K. Kayisli, “Super twisting sliding mode-type 2 fuzzy MPPT control of solar PV system with parameter optimization under variable irradiance conditions,” *Ain Shams Eng. J.*, vol. 14, no. 1, p. 101950, 2023, doi: 10.1016/j.asej.2022.101950.

[15] K. KAYIŞLI and R. Z. CAGLAYAN, “Twisting Sliding Mode Control based Maximum Power Point Tracking,” *Balk. J. Electr. Comput. Eng.*, vol. 10, no. 4, pp. 356–362, 2022, doi: 10.17694/bajece.1137170.

Standalone Wind Energy Conversion System Control Using New Maximum Power Point Tracking Technique

MAHGOUN Mohamed seddik
Electrical Engineering Department
University of Ferhat Abbas Setif 1
Setif, Algeria
mahgounm@yahoo.fr

Abstract— **A novel control strategy for the operation of a permanent magnet synchronous generator (PMSG) based stand alone variable speed wind turbine is presented in this paper. The direct drive PMSG is connected to the load through a switch mode rectifier. The generator side switch mode rectifier is controlled to achieve maximum power from the wind. The aim of this paper is to optimize the extracted energy from the wind by using a New approach based on the theory of synergetic control in order to achieve a maximum power point tracking (MPPT) of a wind energy conversion system with variable speed and with fixed pitch angle. The closed-loop system stability is guaranteed using Lyapunov's method. Vector control is applied to the Permanent Magnet Synchronous Generator PMSG. Simulation results show that the controllers can extract maximum power and regulate the voltage and frequency. The controller performs very well during dynamic and steady state condition.**

Keywords- Permanent Magnet Synchronous Generator, Wind Energy Conversion System, Maximum Power Point Tracking, Vector Control (CV), switch-mode rectifier, stand alone variable speed wind turbine.

I. Introduction

World energy consumption has experienced a huge increase in recent years, due to massive industrialization which tends to increase more and more, and more precisely in certain geographical areas, particularly in the countries of Asia. Because environmental problems, greenhouse gas emissions, pollutions, and the instability of the prices of these sources in world markets are factors that have prompted industrialized countries to resort to renewable energy to meet their energy needs while at the same time maintaining a margin of economic and environmental safety [1]. Faced in these drawbacks, the use of other types of energy resources is therefore inevitable. An energy is said to be renewable when it comes from sources that nature constantly renews. [2]. Wind power is the fastest generating technology among renewable energy sources. Its use does not cause any release (no greenhouse effect) and does not produce toxic waste [3]. Wind energy is one of the fastest growing renewable energies in the last decade due to the benefits it brings. According to the latest report from the Global Wind Energy Council (GWEC), 2020 was the best year in history for the global wind industry, 2020 saw global new wind power installations surpass 93 GW, a 53% growth compared to 2019, bringing total installed capacity to 743 GW, a growth of 14% compared to 2019 [4]. Variable speed wind turbines unlike fixed speed wind turbines operate over a wide range of wind speeds and draw the maximum power for each of its speeds. Variable speed wind turbines direct-drive based on PMSG have become more attractive in recent years; due to the elimination of gearbox and the benefits of PMSG such as small-size, light-weight, better reliability, high efficiency, less maintenance, and no external magnetization characteristics [6]. Because of these mentioned advantages, PMSG based VS-WECS is also used in this study. Therefore, to extract the maximum power under variations of wind speed, maximum power point tracking (MPPT) strategies play an important role in wind power conversion systems (WECS) because they maximize the power extracted from the wind, and therefore optimize the conversion efficiency [7].

Many types of controllers are implemented for Maximum power point tracking (MPPT) in wind power conversion systems (WECS) such as classical PI controllers [08-09]. However, a classic linear regulator is therefore not suitable for this type of application and it is, therefore, necessary to use more modern and robust regulators. To obtain high performance and better performance, it is necessary to design suitable robust controls, which render the system insensitive to external disturbances and to parametric variations. Among them, the sliding mode control [10-11-12]. This control is characterized by some advantages such as high precession, rapid dynamic response, stability, simplicity of its design, and its implementations. The major drawback of this control is the appearance of the chattering phenomenon which manifests itself in the sliding surfaces. In order to reduce this phenomenon, we propose a new control based on synergetic control [13]. This article proposes a new approach based on Synergetic Control (SC) theory. This theory was introduced by Russian scientists in general terms. The synergistic control has a similar function to sliding mode control (SMC) but the chattering phenomenon is eliminated. The basic idea is to force the system to the desired manifold using continuous controls law [14]. Recent work has shown that this theory has been successfully applied in the field of power electrics control, in which the high level of performance; simplicity of design, and flexibility of the synergetic control have been shown both in simulation and experimentations [12]. In our work, the synergetic controller (SC) is used to design a synergistic speed controller. Simulations results show that the synergetic controller is efficient in speed tracking and extracting optimal power from a wind turbine. But the main objective to eliminate the chattering phenomenon is achieved with synergetic control which confirms the theory.

II. MODELLING OF WIND TURBIN

The wind energy conversion system consists of wind turbines, gearboxes, PMSG and Rectifier, as shown in Figure 1. Wind turbines allow the conversion of kinetic energy into mechanical energy and then into electrical energy with generator (PMSG).

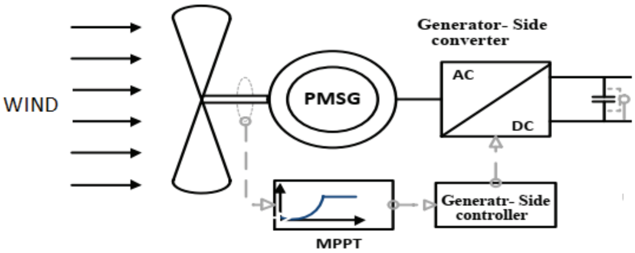

Figure 1. Diagram of the wind turbine.

A. *WIND TURBINE MODELING*

The wind speed V is generally represented by a scalar function which changes over time, in deterministic form by a sum of several harmonics.

$V = f(t)$

(1)

This wind function can be decomposed into an average component, varying slowly, and fluctuations:

$$V = V_0 + \sum_{i=1}^{n} A_i \sin(w_i t + \varphi_i) \qquad (2)$$

V_0 is the mean component; A_i, w_i, φ_i : are respectively the amplitude, the pulsation and the initial phase of each fluctuating spectral component. In Figure (2) is shown an example of a wind profile reconstructed from the spectral characteristic of Vander Hoven and it is this profile that will be applied to the system studied in this article. Its equation is given by:

$$V(t) = 10 + 0.2\sin(0.1047t) + 2\sin(0.2665t) + \sin(1.2930t) + 0.2\sin(3.6645t) \qquad (3)$$

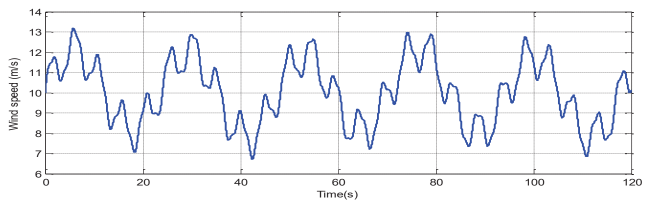

Figure 2. Wind speed profile.

The nonlinear expression for aerodynamic power captured by the wind turbine is given by [15]:

$$P_{aer} = C_p.P_v = \frac{1}{2} C_p(\lambda,\beta).\rho.S.V^3 \qquad (4)$$

ρ is the air density [kg/m^3],V is the wind speed [m/s],

The tip-speed ratio (TSR) λ is calculated by:

$$\lambda = \frac{R.\Omega_{tur}}{V} \qquad (5)$$

R area of rotor blades (m), Ω_{tur} represents the rotational speed of turbine (rd/s), $C_p(\lambda,\beta)$ is the power coefficient wich is a function of both tip speed ratio (TSR) λ and blade pitch angle β (deg). Several numerical approximations exist for $C_p(\lambda,\beta)$. Here the used relation is given by:

$$C_p(\lambda,\beta) = (0.5 - 0.167(\beta-2))\sin\left[\frac{\pi(\lambda+0.1)}{18.5-0.3(\beta-2)}\right] - 0.00184(\lambda-3)(\beta-2) \qquad (6)$$

Fig.3. illustrate the curve of $C_p(\lambda,\beta)$ obtained by equation (6). The maximum value of Cp $(C_p^{\max} = 0.5)$ is for $(\beta = 2)$ degree and for $(\lambda_{opt} = 9.14)$.

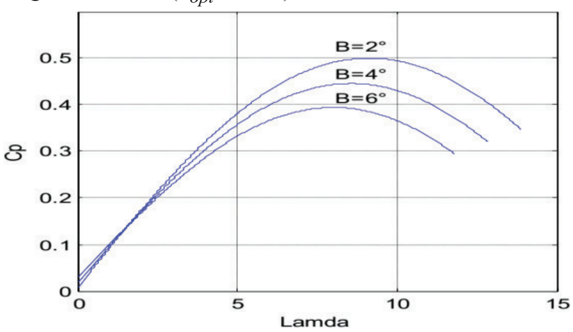

Figure 3. Power coeficient for the wind turbine model.

B. *GEARBOX MODEL*

The function of the gearbox is to convert the mechanical speed of the turbine into the power generation speed, and the pneumatic torque into the gearbox torque according to the following mathematical formula:

$$\begin{cases} T_g = \dfrac{T_{aer}}{G} \\ \Omega_{tur} = \dfrac{\Omega}{G} \\ T_{aer} = \dfrac{P_{aer}}{\Omega_{tur}} \end{cases} \qquad (7)$$

The basic dynamics equations allow to determine the evolution of the mechanical speed based on the total mechanical torque applied to the rotor, which is the sum of all the torques applied to the rotor:

$$J\frac{d\Omega}{dt}=T_g-T_{em}-f.\Omega \qquad (8)$$

Where: T_g : Torque applied on the shaft of the generator; T_{em} : Electromagnetic torque; J: the total moment of inertia, f : The viscous friction coefficient, T_{aer} : is the aerodynamic torque; G : is the gear box ratio,

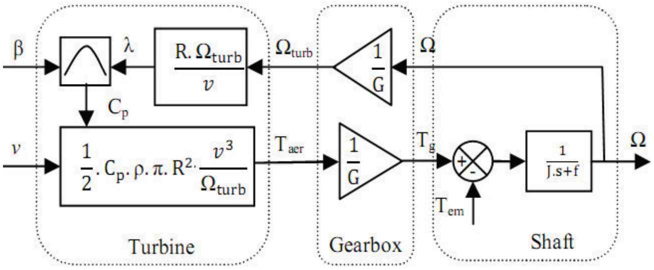

Figure 4. wind turbine model.

C. PMSG Modeling

The Park's transformation is applied to the coordinate model (a; b; c) of the synchronous generator to produce the coordinate model (d; q) of the PMSG. The voltage equations of the direct axis (d) and the orthogonal axis (q) are shown in [12]:

- ***Stator voltages:***

$$\begin{cases} v_d = R_s.i_d + \dfrac{d\phi_d}{dt} - w_e.\phi_q \\ v_q = R_s.i_q + \dfrac{d\phi_q}{dt} + w_e.\phi_d \end{cases} \qquad (9)$$

- ***Stator flux:***

$$\begin{cases} \phi_d = L_d.i_d + \psi_f \\ \phi_q = L_q.I_q \end{cases} \qquad (10)$$

From "(9)" and "(10)" the stator voltages can be written as:

$$\begin{cases} v_d = R_s.i_d + L_d\dfrac{di_d}{dt} - w_e.L_q.i_q \\ v_q = R_s.i_q + L_q\dfrac{di_q}{dt} + w_e.(L_d.i_d + \psi_f) \end{cases} \qquad (11)$$

i_d, i_q : components of stator current in the dq-axes

v_d, v_q : components of stator voltage in the dq-axes,

R_s : stator resistance,

L_d , L_q : d-axis and q-axis inductances,

ψ_f : permanent magnetic flux and

w_e : electrical rotor speed of the generator which is related to the mechanical rotor speed by $w_e = P.\Omega$, where P is the generator number of pole pairs.

The electromagnetic torque of the PMSG is given by:

$$C_{em}=\frac{3}{2}.P.[(L_d-L_q).i_d.i_q+\Psi_f.i_q] \qquad (12)$$

D. MPPT CONTROL STRATEGIES

The objective of MPPT is to optimize the captured wind energy following the optimal speed. To recover as much energy as possible from the wind turbine, we must constantly adapt the mechanical speed of the PMSG to the speed of the wind. The electromagnetic torque drawn from the MPPT control is then applied to the PMSG to ensure that the generator runs at its optimum speed. The figure is shown in Figure 5, illustrating the wind turbine model with MPPT control model:

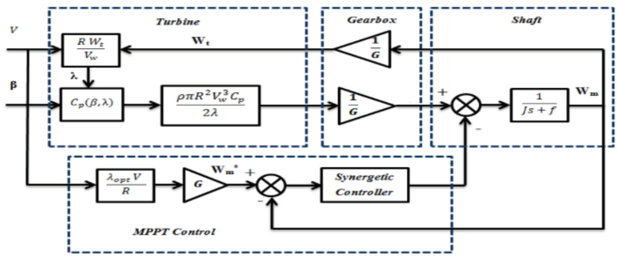

Figure 5. MPPT-synergetic method bloc diagram.

E. VECTOR CONTROL OF PMSG

The conventional method of vector control for the PMSG consists of two current loops. The based-on d-axis is the inner current loop which is the faster. The based-on q-axis is for wind turbine speed or torque control which is the outer loop. The bloc diagram of the speed and currents control system is shown in Fig. 6.

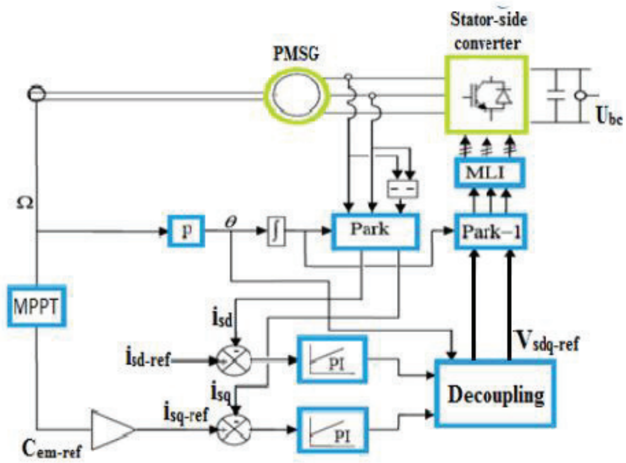

Figure 6. Vector control of PMSG scheme.

F. Modeling of the rectifier

The three-phase rectifier at (PWM) is a static converter AC-DC made up of switching cells generally based on transistors or thyristors. It is made up of three arms present as switches (two switches for each) and which can be controlled in opening and closing. The rectified voltage Vdc is a function of the states of these switches that we consider them ideal in order to facilitate the modeling.

To ensure continuity in currents, each switch is mounted in antiparallel with a recovery diode.

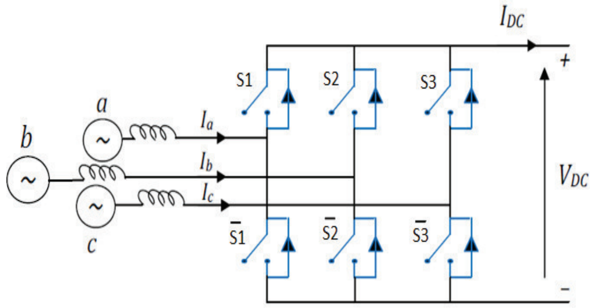

Figure 7. Equivalent diagram of a PWM control rectifier.

The rectifier connection matrix is given by the following matrix equation:

$$\begin{bmatrix} V_a \\ V_b \\ V_c \end{bmatrix} = \frac{V_{dc}}{3} \begin{bmatrix} 2 & -1 & -1 \\ -1 & 2 & -1 \\ -1 & -1 & 2 \end{bmatrix} \begin{bmatrix} S_1 \\ S_2 \\ S_3 \end{bmatrix} \tag{13}$$

$$I_{DC} = S_1.I_a + S_2.I_b + S_3.I_c \tag{14}$$

with:

V_a, V_b, V_c : Reference voltages.

V_{DC} : Rectified voltage.

I_{DC} : Current modulated by the rectifier.

S1, S2, S3: Logic functions corresponding to the state of the switch.

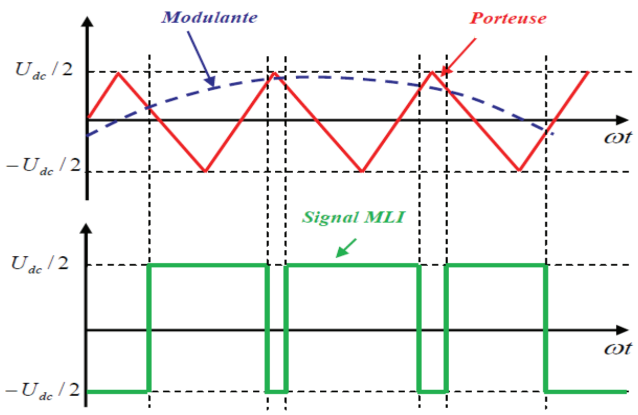

Figure 8. Sinus-triangular PWM control principle.

III. SYNERGETIC CONTROLLER SYNTHESIS

Synergetic control theory was first introduced by Russian researchers in the last few years. Recently this theory has been successfully applied in the field of power electronic controls. The synergistic controller is quite close to the control by sliding mode in the sense where the system is forced to a dynamic chosen by the designer, It differs in the fact that the controller is still continuous. Unlike that used in sliding mode and therefore does not induce any oscillations problem (chattering), major disadvantage of the SMC command.

The system can be represented using the system's state space equations as follows $\dot{x} = f(x,U,t)$ [12]. Where x is the state vector, U is the control input vector and t is time.

Synthesis of a synergetic controller begins by defining a macro-variable, which is a function of the system state variables.

$$\psi = \psi(x,t) \tag{15}$$

The objective of the synergetic controller is to operate the controlled system on the manifold for which the macro-variable is null $\psi = 0$. Macro-variable is chosen by the designer according to the control specifications (e.g. response time).
Second step is to fix the dynamic evolution of macro-variables to the manifold by the following functional equation $T\dot{\psi} + \psi = 0 \qquad T \succ 0$
(16)

Where T is a design parameter describing the speed of convergence to the manifold specified by the macro-variable.

The solution of Equation (16) provides the following function:

$$\psi(t) = \psi_0 . e^{\frac{-t}{T}} \tag{17}$$

In our case and according to Synergetic Control Approach (SCA), we will select the first set of macro-variables as equation (18):

$$\psi = \Omega_{ref} - \Omega \tag{18}$$

This derivative is:

$$\dot{\psi} = \dot{\Omega}_{ref} - \dot{\Omega} \tag{19}$$

Combining these equations (16), (18), and (19), we get the electromagnetic motor torque directly without the PI regulator as the following control law:

$$T_{em-ref} = T_{em} = \frac{J}{T}\left[\frac{Tf}{J}\Omega - \frac{TT_g}{J} + (\Omega_{ref} - \Omega)\right] \tag{20}$$

As we can see the control law depends not only on the state variables of the system but also on the macro-variable and the time constant.

IV. SIMULATIO RESULTS AND DISCUSSION

To evaluate the performance and effectiveness of the proposed method, it is implemented in the MATLAB / SIMULINK software environment. The selected system parameters for wind turbines and PMSG are given in Table (1).

TABLE I.

WT parameters	
Parameters	**Values**
Density of air	1.22 kg/m3
Radius of rotor	3 m
Gear box ratio	G =1
total inertia	16 kg.m2
Total viscous friction coefficient	0.06 N.m/s
Optimal power coefficient	0.5
Optimal tip speed ratio	9.14
Viscous friction coefficient	0.06
PMSG parameters	
Stator resistance	1.4 Ω
d-axis stator inductance Ld	0.0066 H
q-axis stator inductance Lq	0.0058 H
Permanent magnetic flux	0.15 Wb
Number of pole pairs p	17

Figures (9) present the evolution of power coefficient is maintained at its optimum value equal to and there is not a chattering phenomenon, which shows good performance of SC controller to extracting of the maximum power.

Figures (10) show that the speed ratio (TSR) follows its reference very well corresponding to maximum and optimal value (TSR) (λopt=9.14) with adaptation to wind speed without oscillation and overshoot.

Figures (11), display that the turbine rotor speed according to the MPPT each variation of wind speed, the turbine rotor speed stables totally with the theoretical value, and the mechanical speed converges towards the required reference with good dynamics and a good tracking with an adaptation of the wind speed variation. Here chattering phenomenon is eliminated with synergetic control.

Figure (12) shows that the variation of the power produced is adapted to the variation of the mechanical speed of the turbine, and the mechanical speed is adapted to the variation of the wind speed which shows the influence of the variation in mechanical speed in the operation of the wind speed on the power produced.

We note from figure (13) that the currents in the d and q-axis follow their references which confirms the proper functioning of the vector control.

Figure (16) shows the macro variable function and its zoom equal to zero, which shows that the synergetic controller parameters are properly chosen.

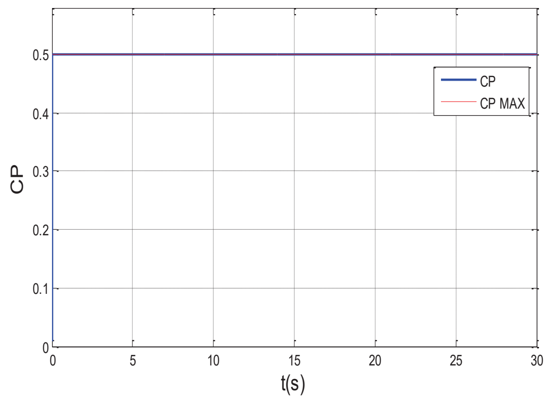

Figure 9. Power coefficient.

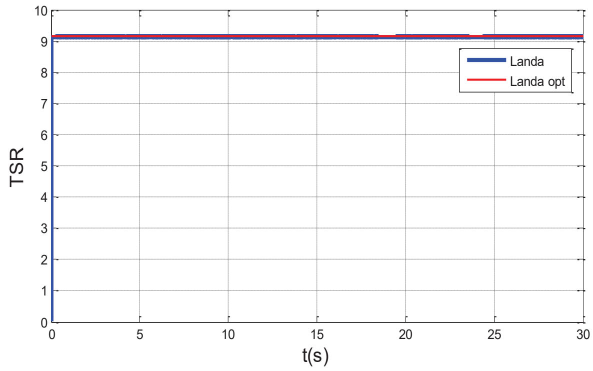

Figure 10. speed ratio (TSR).

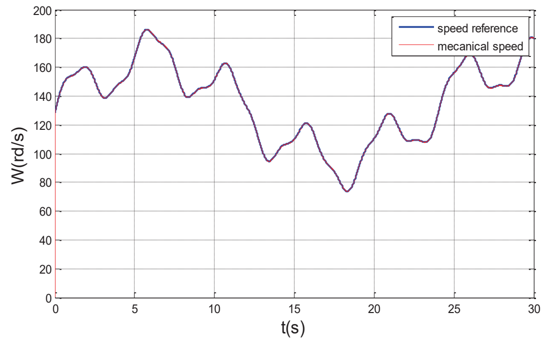

Figure 11. mechanical speed.

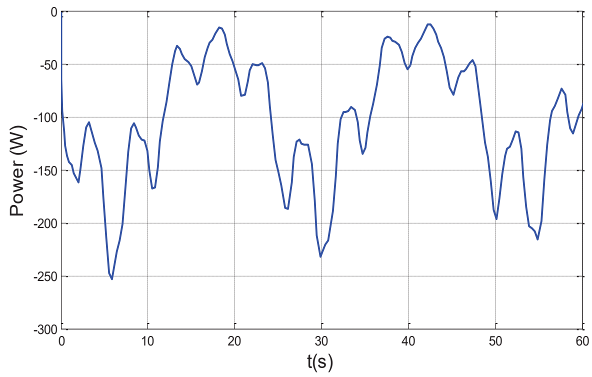

Figure 12. Aerodynamic Power of the turbine..

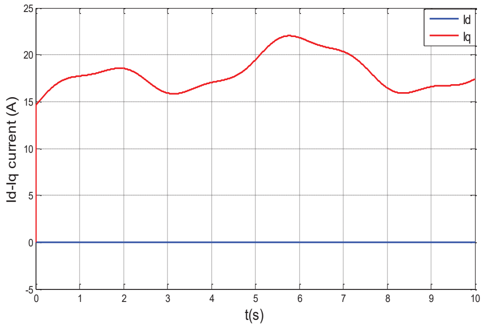

Figure 13. d-q axis current components of PMSG.

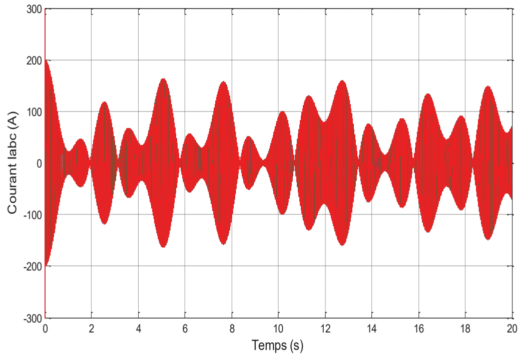

Figure 14. Three-phase currents Iabc at the output of the generator

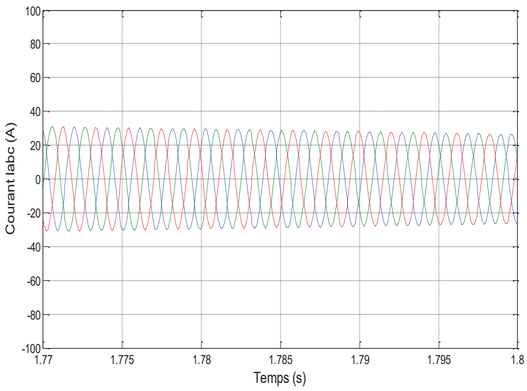

Figure 15. Three-phase currents Zoom

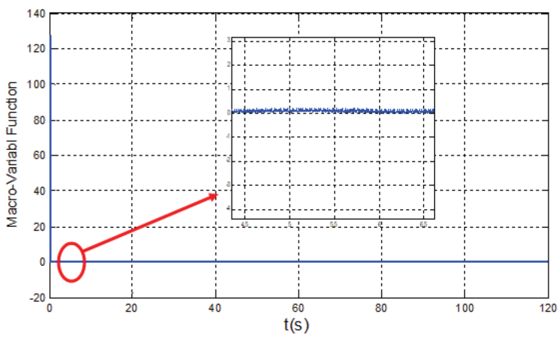

Figure 16. Macro variable function.

V. Conclusion

Control strategy for a stand alone variable speed wind turbine with a PMSG is presented in this paper.We have presented the wind turbine modeling then we have given the PMSG modeling and its vector control for decoupling the direct and quadrature currents. An MPPT control strategy based on synergetic controller (SC) has been proposed to control the VS-WECS based on a PMSG. It has been observed that the wind energy conversion system controlled with a proposed MPPT has good steady state performance and high tracking factor. The power coefficient of the wind turbine is maintained at the optimal value whatever the values of the wind speed.The simulation results demonstrate that the controller works very well and shows very good dynamic and steady state performance.

Acknowledgment (Heading 5)

I would like to thank my supervisor and the whole team of the research laboratory of the automatic university of Setif 1 Algeria.

References

[1] Antar Beddar , Hacene Bouzekri , Experimental enhancement of fuzzy fractional order PI+I controller of grid connected variable speed wind energy conversion system, Energy Conversion and Management 123 (2016) 569–580.

[2] Bekakra, Y., Attous, D.B. Optimal tuning of PI controller using PSO optimization for indirect power control for DFIG based wind turbine with MPPT. Int J Syst Assur Eng Manag 5, 219–229 (2014).

[3] Bouderbala M., Bossoufi B., Lagrioui A., Taoussi M., Aroussi H.A., Ihedrane Y. Direct and indirect vector control of a doubly fed induction generator based in a wind energy conversion system. International Journal of Electrical and Computer Engineering, 2019, vol. 9, no. 3, pp. 1531-1540.

[4] WWEA « GWEC | GLOBAL WIND REPORT 2021», 25 March 2021.

[5] Menezes EJ, Araújo AM, Silva NS. A review on wind turbine control and its associated methods. Journal of Cleaner Production, Vol. 174, 1Iss. 10, pp. 945-953, 2018.

[6] Tiwari R, Padmanaban S, Neelakandan R. Coordinated control strategies for a permanent magnet synchronous generator based wind energy conversion system. Energies, Vol. 10, pp. 1493–1510, 2017.

[7] M.S. MAHGOUN, A.E. BADOUD , “New design and comparative study via two techniques for wind energy conversion system, ” Electrical Engineering & Electromechanics, 2021, no. 3,ISSN 2074-272X.

[8] Liu H, Locment F, Sechilariu M. Experimental analysis of impact of maximum power point tracking methods on energy efficiency for small-scale wind energy conversion system. IET Renew Power Gener. 2017; 11:389–97.

[9] Taner, T. Economic analysis of a wind power plant: A case study for the Cappadocia region. J Mech Sci Technol 32, 1379–1389 (2018).

[10] E. H. Dursun and A. Afsin Kulaksiz, "Maximum Power Extraction from PMSG based VS-WECS by using Variable Step-Size P&O Method," 2019 3rd International Symposium on Multidisciplinary Studies and Innovative Technologies (ISMSIT), Ankara, Turkey, 2019, pp. 1-5, doi: 10.1109/ISMSIT.2019.8932841.

[11] [11] A. Ardjal, M. Bettayeb and R. Mansouri, "Fractional Nonlinear Synergetic Control of Wind Turbine for Maximum Power Point Tracking," 2019 IEEE International Symposium on Signal Processing and Information Technology (ISSPIT), Ajman, United Arab Emirates, 2019, pp. 1-6, doi: 10.1109/ISSPIT47144.2019.9001862.

[12] [12] A. Kolesnikov, G. Veselov, et al., A Synergetic Approach to the Modeling of Power Electronic Systems, the 7th Workshop on

Computers in Power Electronics, COMPEL, pp.259-262, Blacksburg VA, 2000.

[13] [13] K. BEHIH, “Contribution à la commande des systèmes non linéaires incertains et perturbés, ” Thèse de Doctorat, Université de Setif1, 2020.

[14] [14] Souhila Rached Zine(1), Benyounes Mazari(2),Synergistic and Sliding Mode Controls of Wind Energy Conversion System,international Review on Moddeling and Simulation (IREMOS) DOI: https://doi.org/10.15866/iremos.v8i6.8022.

[15] [15] Dursun EH and Kulaksiz AA (2020) MPPT control of PMSG based small-scale wind energy conversion system connected to DC-bus. International Journal of Emerging Electric Power Systems. Epub ahead of print 13 March. DOI: 10.1515/ijeeps2019-0188.

The 1st National Conference on Green Energy (NCGE' 2023)
December 02, 2023, Boumerdes, Algeria.

Photovoltaic Model Parameters Estimation Via the Fully Informed Search Algorithm

Badis Lekouaghet
Division of Welding and Assembly Techniques,
Research Center in Industrial Technologies (CRTI),
P.O.Box 64, Cheraga 16014 Algiers, Algeria
b.lekouaghet@crti.dz

Sid-Ahmed Touil
Department of Electrical Engineering,
University of Jijel,
BP 98 O.A., Jijel 18000, Algeria
sidahmed.touil1@gmail.com

***Abstract*—Effective parameter estimation for photovoltaic (PV) systems holds significant importance for both researchers and industry professionals. The accurate understanding of PV models, achieved through modeling and simulation, plays a pivotal role in optimizing design, control, testing, and forecasting the performance of PV systems. Developing a precise and robust parameter identification method significantly contributes to enhancing the modeling, control, and optimization of photovoltaic systems. In this context, our study introduces a novel metaheuristic algorithm named the Fully Informed Search (FIS) Algorithm. This algorithm is proposed for efficiently identifying the parameters of the single-diode model (SDM). We demonstrate its effectiveness through the application of two distinct case studies within our simulation research. The obtained results affirm the superiority of the proposed algorithm in terms of both stability and accuracy when compared to seven other well-known algorithms.**

***keywords*—Parameters identification; Photovoltaic; meta-heuristic; Fully Informed Search (FIS) Algorithm.**

I. Introduction

Since the end of 2019, the COVID-19's global pandemic has highlighted the energy issue and unbalanced the energy markets, which pushes the researchers to show their agility to build adapted responses and help to construct a solid society ready to face similar issues. COVID-19 has also a considerable affect on the industry. Renewable energy sources (RESs) could protect the humanity in the face of future and current catastrophe due to its preferential access to electricity networks and its lower costs [1]. Consequently, the exploration and harnessing of eco-friendly power sources has emerged as an imperative subject to avoid the crises consequences. Particularly noteworthy, photovoltaic (PV) setups have attained widespread adoption due to its abundant reserves, emission-free nature, and the consistent decrease in costs over successive years, etc. To ensure the effective integration and utilization of PV systems across diverse industrial applications, it becomes critical to have detailed information and rigorous modelling of its basic components. Regrettably, the essential data required to model the fundamental constituent (i.e., solar cell or module) of a complete PV system remains elusive, where almost all manufacturers did not provides the complete necessary information in its data sheets.

Noting that various equivalents circuits model (ECM), including single diode (SDM), double diode (DDM) and triple (TDM), are utilized to study the behaviour of the PV module/array. Among these models, the SDM is consedred to be the easiest one to be implemented, in real application, with the lowest complexity [2]. However, the primary challenge is solving the nonlinear equation offered by the SDM model and identifying its ungiven parameters. Considering the nonlinearity of the model, deterministic methods are streamlined through specific approximations. Recently, optimization algorithms have been broadly studied and have garnered popularity among researchers for solving the parameter estimation problem [3], [4].

One of the first and popular applied meta-heuristic optimization algorithms to extract the unknown PV cell parameters is the particle swarm optimization [5]. Since then, enormous methods have been applied to estimate the SDM and other models parameters. The authors in [6] prove that the introduction of random reselection mechanisms to the PSO, to obtain a hybrid algorithm, gives more robustness and the convergence accuracy against the original algorithm. In Nguyen et al. [7], the PV estimation issue has been addressed using the artificial ecosystem optimization (AEO). This algorithm is based on three mechanisms of ecosystem, first the production which preserves the balance between exploration and exploitation, where the consumption step is applied to examine the search space. Finally, the decomposition mechanism helps to boost the exploitation phase. In [8], the authors proposed a modified Stochastic Fractal Search (MSFS) algorithm to estimate values of PV modules variables for a best modelling. The main modification are applied to the diffusion process and the update processes to enhance the basic algorithm. Ismaeel et al. [9], applied a gradient based optimizer (GBO) to evaluate the unknown PV parameters. Another recent work [10], use a symmetric chaotic (SC) generator to improve the performances of the GBO method. The proposed SC-GBO is examined on different of PV modules, and it outperforms several techniques. In [11] a recent optimization technique, called DOLADE was introduced to tackle the parameters identification problem of solar PV modules. The proposed DOLADE combines the dynamic opposite learning strategy with the differential evolution method to enhance the performance of the JADE algorithm. In Wang et al. [12] the Rao-1 algorithm has been suggested to extract the PV parameters for the DDM. Other variants have been presented to boost the accuracy and effectiveness of Rao-1 algorithm. The authors in [13] exploited the features of using a chaotic map with the basic algorithm to propose a novel version namely LCROA; while the CLRao-1 algorithm [14] introduce three mutually equation based on quantum and Levy flight strategy to improve the standard Rao-1.

While the majority of the methods mentioned above and other algorithms including HHO [15], IGWO [16], RUN [17], GTO [18], CPA [19] and CDO [20] have demonstrated impressive performance in extracting PV parameters, there remains a necessity to create novel optimization algorithms [21], [22]. In this paper, a new metaphor optimization algorithm, based on Rao's algorithms [23], called FIS (fully informed search) Algorithm [24] is presented for estimating the parameters of the SDM for photovoltaic modules.

The rest of this paper is organized as follows. Section II presents the Photovoltaic models and objective function used in this study. The introduced algorithm is presented in Section III. Simulation results are discussed in Section IV. Finally, the conclusion is drawn in Section V.

II. Photovoltaic models and objective function

A. Single diode model

The SDM, which is the most ECM commonly used and the easiest one to be implemented, and the PV module designed with N_s cells linked in a series configuration and/or N_p cells connected in parallel are mathematically expressed by (1) and (2) respectively:

$$I_{pv} = I_L - I_s \left[\exp\left(\frac{q(V_{pv} + I_{pv}R_s)}{nkT} \right) - 1 \right] - \frac{V_{pv} + I_{pv}R_s}{R_p} \quad (1)$$

$$I_{pv} = N_p I_L - N_p I_s \left[\exp\left(\frac{q(V_{pv} + (N_s/N_p)R_s I_{pv})}{nN_s kT} \right) - 1 \right] - \frac{V_{pv} + (N_s/N_p)I_{pv}R_s}{(N_s/N_p)R_p} \quad (2)$$

where

I_{pv} output current

V_{pv} output voltage

I_L photo-generated current

T: cell temperature

k: Boltzman's constant ($1.380653 \times 10^{-23} J/K$),

q: electron's charge ($1.60217646 \times 10^{-19} C$)

n: diode ideality factor,

I_s: reverse saturation current.

R_p: parallel resistance

R_s: series resistance

Note that the previous models comprises five parameters which, have not been provided and should be identified, i.e., n, I_s, I_L, R_s and R_p. The SDM equivalent circuit is as shown in Fig. 1.

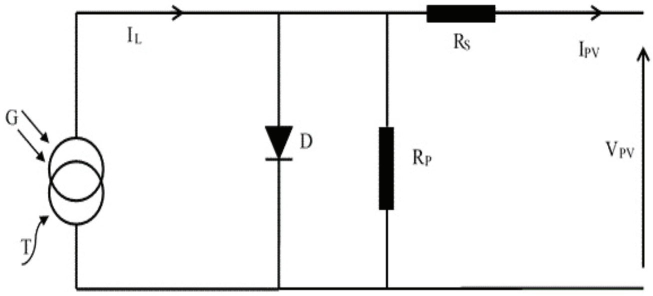

Fig. 1. Equivalents circuits model of SDM.

B. Objective function

Almost all optimization algorithms require and should use an objective function (to be minimized or maximized) during the updating step. In this paper the difference between the computed data (calculated) and the observed data (measured) was established as an objective function. The global difference is calculated by the Root Mean Square Error (RMSE) as follows:

$$RMSE(x) = \sqrt{\frac{1}{M} \sum_{i=1}^{M} f\left(V_{mes},\ I_{mes},\ x\right)^2} \quad (3)$$

where M is the total measured points, f is the error function (Eq. 4), x is the solution vector, I_{mes} and V_{mes} are the measured current and voltage, respectively.

$$f\left(V_{mes},\ I_{mes},\ x\right) = I_L - I_s \left[\exp\left(\tfrac{q(V_{mes} + I_{mes}R_s)}{nkT} \right) - 1 \right] - \tfrac{V_{mes} + I_{mes}R_s}{R_p} - I_{pv}, \quad (4)$$

III. Fully informed search (FIS) algorithm

The FIS is a simple and recent metaphor less algorithm [24] base on another simple algorithm proposed by Rao [23]. Rao algorithms, that do not include any specific or complex parameters, updates the current solutions to converge toward the global solution using three different formula, i.e., (5), (6) and (7) generating respectively three simple algorithm called Rao-1, Rao-2 and Rao-3.

$$Y_{i,j}^{new} = Y_{i,j}^{t} + \rho_{1,j} \times (Y_{b,j}^{t} - Y_{w,j}^{t}) \quad (5)$$

$$\begin{cases} if\ f(Y_i^t) < f(Y_k^t) \\ Y_{i,j}^{new} = Y_{i,j}^{t} + \rho_{1,j} \times (Y_{b,j}^{t} - Y_{w,j}^{t}) + \rho_{2,j} \times (|Y_{i,j}^{t}| - |Y_{k,j}^{t}|) \\ else \\ Y_{i,j}^{new} = Y_{i,j}^{t} + \rho_{1,j} \times (Y_{b,j}^{t} - Y_{w,j}^{t}) + \rho_{2,j} \times (|Y_{k,j}^{t}| - |Y_{i,j}^{t}|) \end{cases} \quad (6)$$

$$\begin{cases} if\ f(Y_i^t) < f(Y_k^t) \\ Y_{i,j}^{new} = Y_{i,j}^t + \rho_{1,j} \times (Y_{b,j}^t - |Y_{w,j}^t|) + \rho_{2,j} \times (|Y_{i,j}^t| - Y_{k,j}^t) \\ else \\ Y_{i,j}^{new} = Y_{i,j}^t + \rho_{1,j} \times (Y_{b,j}^t - |Y_{w,j}^t|) + \rho_{2,j} \times (|Y_{k,j}^t| - Y_{i,j}^t) \end{cases} \quad (7)$$

where $j \in [1 \text{ Dim}]$ is the j^{th} dimension (Dim) of the i^{th} solution (noted by $Y_{i,j}^t$) during the current iteration t. $\rho_{1,j}$ and $\rho_{2,j}$ are two random numbers selected from the interval $[0,\ 1]$. The best, worst and a random solutions are denoted by $Y_{b,j}^t$, $Y_{w,j}^t$ and $Y_{k,j}^t$, respectively. Finally, equation (8) is used to determine the value of the i^{th} solution in the coming iteration.

$$\begin{cases} Y_i^{t+1} = Y_i^{new},\ if\ f(Y_i^{new}) < f(Y_i^t) \\ Y_i^{t+1} = Y_i^t,\ else \end{cases} \quad (8)$$

By keeping the simplicity of the previous techniques, FIS algorithm introduces a new formula to move the current solutions toward the best solution as given in (9). For each iteration, the new introduced variables MY_b^t and MY_w^t are counted using (10) and (11) respectively.

$$Y_{i,j}^{new} = Y_{i,j}^t + \rho_{1,j} \times (MY_{b,j}^t - Y_{i,j}^t) + \rho_{2,j} \times (Y_{i,j}^t - MY_{w,j}^t) \quad (9)$$

$$MY_b^t = \frac{Y_b^t + \sum_{l \in Bi} Y_l^t}{length(Bi) + 1} \quad (10)$$

$$MY_w^t = \frac{Y_w^t + \sum_{l \in Wi} Y_l^t}{length(Wi) + 1} \quad (11)$$

where Wi and Bi are the set of population variables that have a worst and better fitness than the i^{th} variable in iteration t, respectively, and the enumeration of the members in the set is denoted by $length(.)$.

IV. Numerical results

In this particular section, the FIS algorithm is executed within the MATLAB environment to estimate the parameters of SDM. This involves utilizing actual experimental data from two sources: a Poly-solar 320W-72P panel module, and a polycrystalline PV array that consists of three CLS-220P module types, as indicated in the work by Haddad et al [1]. The specific ranges chosen for each variable are illustrated in Tab. I. The outcomes achieved through the implementation of the FIS approach are evaluated against the results of seven alternative algorithms, namely Rao-1 [12], HHO [15], IGWO [16], RUN [17], GTO [18], CPA [19] and CDO method [20]. All these techniques are programmed using a uniform number of iterations (MaxIt) and an identical population size (PopSize) set at 1000 and 30, respectively. Additionally, to ensure reliability in the comparison, each method is executed independently 30 times.

TABLE I
Unknown PV parameters' range for the two studied cases.

	Poly-solar 320W-72P		CLS-220P	
Parameter	Min	Max	Min	Max
I_L $[A]$	0	10	0	10
I_s $[\mu A]$	0	1	0	100
n	1	2	1	2
R_s $[\Omega]$	0	0.1	0	0.1
R_p $[\Omega]$	0	50000	0	50000

A. Case study (i): Poly-solar 320W-72P

First, a thorough examination is conducted for the obtained outcomes from the Poly-solar 320W-72P PV module. Figure 2 illustrates the graphical representation of the I-V characteristics for both the simulated curve, employing the extracted parameters, and the experimental curve. Clearly, the optimized variables, upon integration into the PV model (as outlined in (1)), show a remarkable precision in replicating the real PV characteristic. Table II offers the gained parameters, along with their corresponding RMSE values, comprising both the FIS algorithm and its competing methods. Notably, the lowest RMSE value $(2,5727764 \times 10^{-2})$ with a Std of $6,37109 \times 10^{-4}$ was achieved by the FIS algorithm which confirms the high accuracy and stability of the proposed algorithm.

Furthermore, the convergence graphs of FIS technique in comparison with those of HHO, IGWO, Rao1, RUN, GTO, CPA and CDO are drawn in Fig. 3. Upon observing this graphical representation, the proposed algorithm showcases an accelerated convergence rate towards the the best RMSE with a minimal number of iterations.

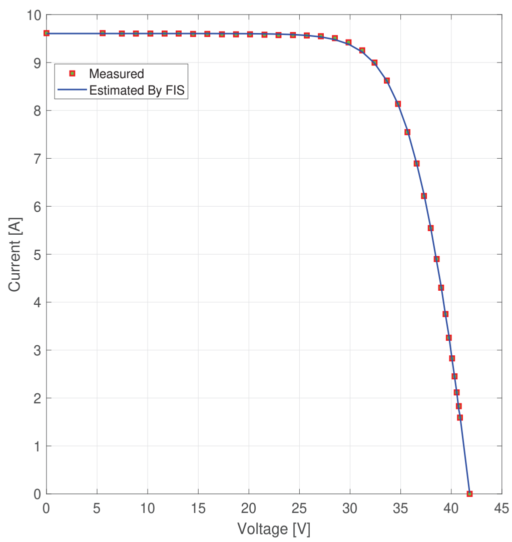

Fig. 2. Experimental and simulated curves for Poly-solar 320W-72P module.

B. Case study (ii): CLS-220P module

The results derived from the analysis of a photovoltaic (PV) array (three CLS-220P polycrystalline modules), constitute the

TABLE II
ESTIMATED PARAMETERS OF POLY-SOLAR 320W-72P AT THE BEST RMSE

Parameters	I_L $[A]$	I_s $[A]$	n	R_s $[\Omega]$	R_p $[\Omega]$	$RMSE$	Std
FISA	9,60508	1,8298E-07	1,18484	4,5640E-03	20464,28	2,5727764E-02	6,37109E-04
HHO	9,60493	1,8185E-07	1,18442	4,5650E-03	17634,65	2,5730486E-02	2,58656E-02
IGWO	9,60594	1,9314E-07	1,18845	4,5505E-03	38975,06	2,5746217E-02	9,83990E-04
Rao1	9,60478	1,9419E-07	1,18874	4,5373E-03	50000,00	2,5816131E-02	1,04709E-03
RUN	9,60753	1,7996E-07	1,18371	4,5594E-03	100,68	2,5850208E-02	7,53345E-03
GTO	9,58741	2,7469E-07	1,21214	4,3545E-03	20937,45	3,3536324E-02	1,52667E-01
CPA	9,64967	2,8585E-08	1,07361	5,0159E-03	4,68	3,8383140E-02	3,65357E-01
CDO	9,61922	1,0000E-06	1,30979	4,1697E-03	20641,76	6,0737492E-02	5,25619E-02

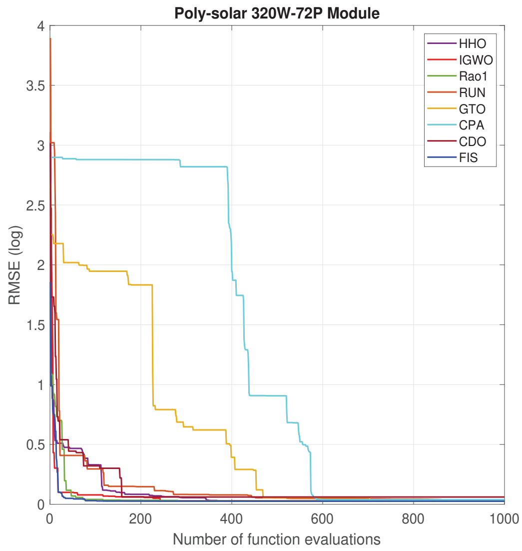

Fig. 3. Convergence graphs for Poly-solar 320W-72P module.

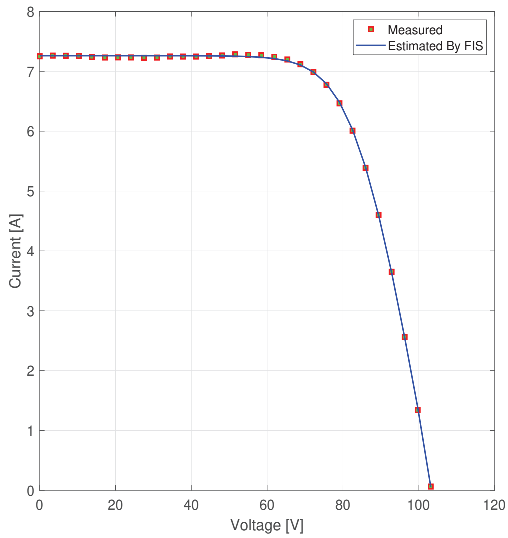

Fig. 4. Experimental and simulated curves for CLS-220P module.

focus of this second case study. In this regard, identified parameters, RMSE and Std attained through the utilization of distinct techniques, including the applied FIS method are tabulated in Tab. III. In the context of this table, it is evident that the best RMSE was acquired by the proposed FIS method, while the least favorable RMSE value was gained by the CDO algorithm. Also, Tab. III shows that the FIS technique proves its superiority in terms of both stability and accuracy when compared to its counterparts. Additionally, the illustrated parameters in this table are used to plot (as depicted in Fig. 4) the I-V curve alongside the actual experimental curve for this case study.

Moreover, a display of the convergence curves produced by various algorithms is presented in Fig. 5. Obviously, This representation further confirms the computational efficiency and precision exhibited by the FIS algorithm.

V. CONCLUSION

The purpose of this paper is to examine the performance of the newly proposed FIS algorithm in estimating the unknown parameters for SDM. The algorithm is built upon Rao's

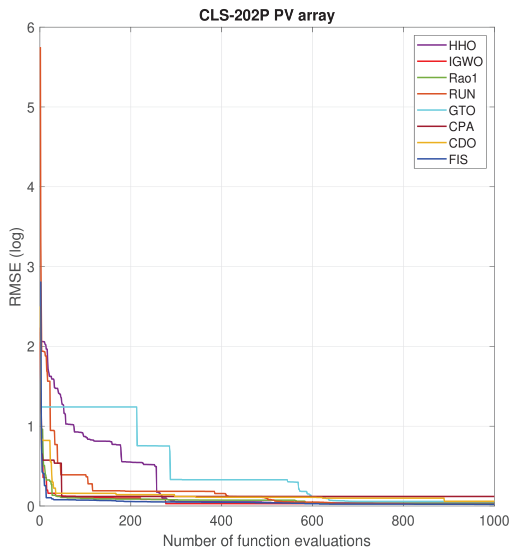

Fig. 5. Convergence graphs for CLS-220P module.

TABLE III
ESTIMATED PARAMETERS OF CLS-220P MODULE AT THE BEST RMSE

Parameters	$I_L\ [A]$	$I_s\ [A]$	n	$R_s\ [\Omega]$	$R_p\ [\Omega]$	$RMSE$	Std
FISA	7,26125	8,8828E-08	1,18003	9,9328E-03	39819,65	2,1078827E-02	3,20551E-03
RUN	7,26277	2,1637E-07	1,24030	9,5564E-03	49998,91	2,3958763E-02	2,25800E-02
IGWO	7,26603	2,1498E-07	1,23987	9,6127E-03	7135,06	2,4761645E-02	8,64107E-03
Rao1	7,25403	2,6397E-07	1,25425	9,5126E-03	32098,25	3,4199762E-02	9,07210E-03
HHO	7,27454	5,8354E-07	1,31585	9,2775E-03	49686,26	3,7871432E-02	1,75464E-02
CPA	7,28469	3,5362E-06	1,47730	8,0784E-03	30708,81	5,7373468E-02	3,87291E-01
GTO	7,23763	1,7703E-06	1,41110	8,4457E-03	35591,81	5,9339053E-02	6,02164E-01
CDO	7,34312	8,8424E-05	1,88946	5,0639E-03	29523,00	1,1939979E-01	2,42783E-02

approach, known for its simplicity and lack of specific or complex parameters. The paper is structured into four sections, encompassing the introduction, ECM of PV cells/modules, the illustration of the proposed method, and its validation using two modules: the Poly-solar 320W-72P panel module, along with a polycrystalline PV array comprising three CLS-220P modules. The accomplished results demonstrate the accuracy of parameters extraction using the FIS algorithm. The used algorithm succeeded in minimizing the fitness function to $2,5727764 \times 10^{-2}$ when applied for the Poly-solar 320W-72P module and it reaches $2,1078827 \times 10^{-2}$ for the CLS-220P PV array. Also, the experiments clearly affirms the superiority of the FIS method over seven recently introduced parameter identification approaches in both accuracy and stability. Besides, with the high matching of I–V characteristic with real data, FIS approach can be used as an efficiency tool for optimizing the PV SDM parameters for various applications such as the MPPT.

REFERENCES

[1] S. Haddad, B. Lekouaghet, M. Benghanem, A. Soukkou, and A. Rabhi, "Parameter estimation of solar modules operating under outdoor operational conditions using artificial hummingbird algorithm," *IEEE Access*, vol. 10, pp. 51 299–51 314, 2022.

[2] M. Benghanem, B. Lekouaghet, S. Haddad, and A. Soukkou, "Optimization of pv cells/modules parameters using a modified quasi-oppositional logistic chaotic rao-1 (QOLCR) algorithm," *Environmental Science and Pollution Research*, vol. 30, no. 15, pp. 44 536–44 552, Jan. 2023.

[3] Z. Gu, G. Xiong, and X. Fu, "Parameter extraction of solar photovoltaic cell and module models with metaheuristic algorithms: A review," *Sustainability*, vol. 15, no. 4, p. 3312, Feb. 2023.

[4] B. Lekouaghet, C. Boubakir, and A. Boukabou, "A new method to represent the i-v and p-v characteristics of different photovoltaic modules," in *2020 6th International Symposium on New and Renewable Energy (SIENR)*. IEEE, Oct. 2021.

[5] M. Ye, X. Wang, and Y. Xu, "Parameter extraction of solar cells using particle swarm optimization," *Journal of Applied Physics*, vol. 105, no. 9, p. 094502, May 2009.

[6] Y. Fan, P. Wang, A. A. Heidari, H. Chen, HamzaTurabieh, and M. Mafarja, "Random reselection particle swarm optimization for optimal design of solar photovoltaic modules," *Energy*, vol. 239, p. 121865, Jan. 2022.

[7] T. T. Nguyen, T. T. Nguyen, and T. N. Tran, "Parameter estimation of photovoltaic cell and module models relied on metaheuristic algorithms including artificial ecosystem optimization," *Neural Computing and Applications*, Mar. 2022.

[8] S. Xu and H. Qiu, "A modified stochastic fractal search algorithm for parameter estimation of solar cells and PV modules," *Energy Reports*, vol. 8, pp. 1853–1866, Nov. 2022.

[9] A. A. K. Ismaeel, E. H. Houssein, D. Oliva, and M. Said, "Gradient-based optimizer for parameter extraction in photovoltaic models," *IEEE Access*, vol. 9, pp. 13 403–13 416, 2021.

[10] M. A. Khelifa, B. Lekouaghet, and A. Boukabou, "Symmetric chaotic gradient-based optimizer algorithm for efficient estimation of PV parameters," *Optik*, p. 168873, Mar. 2022.

[11] J. Zhou, Y. Zhang, Y. Zhang, W.-L. Shang, Z. Yang, and W. Feng, "Parameters identification of photovoltaic models using a differential evolution algorithm based on elite and obsolete dynamic learning," *Applied Energy*, vol. 314, p. 118877, May 2022.

[12] L. Wang, Z. Wang, H. Liang, and C. Huang, "Parameter estimation of photovoltaic cell model with rao-1 algorithm," *Optik*, vol. 210, p. 163846, May 2020.

[13] B. Lekouaghet, A. Boukabou, and C. Boubakir, "Estimation of the photovoltaic cells/modules parameters using an improved rao-based chaotic optimization technique," *Energy Conversion and Management*, vol. 229, p. 113722, Feb. 2021.

[14] A. Farah, A. Belazi, F. Benabdallah, A. Almalaq, M. Chtourou, and M. Abido, "Parameter extraction of photovoltaic models using a comprehensive learning rao-1 algorithm," *Energy Conversion and Management*, vol. 252, p. 115057, Jan. 2022.

[15] A. Sharma, A. Saxena, S. Shekhawat, R. Kumar, and A. Mathur, "Solar cell parameter extraction by using harris hawks optimization algorithm," in *Bio-inspired Neurocomputing*. Springer Singapore, Jul. 2020, pp. 349–379.

[16] A.-E. Ramadan, S. Kamel, T. Khurshaid, S.-R. Oh, and S.-B. Rhee, "Parameter extraction of three diode solar photovoltaic model using improved grey wolf optimizer," *Sustainability*, vol. 13, no. 12, p. 6963, Jun. 2021.

[17] H. Shaban, E. H. Houssein, M. Pérez-Cisneros, D. Oliva, A. Y. Hassan, A. A. K. Ismaeel, D. S. AbdElminaam, S. Deb, and M. Said, "Identification of parameters in photovoltaic models through a runge kutta optimizer," *Mathematics*, vol. 9, no. 18, p. 2313, Sep. 2021.

[18] H. T. Sadeeq and A. M. Abdulazeez, "Giant trevally optimizer (GTO): A novel metaheuristic algorithm for global optimization and challenging engineering problems," *IEEE Access*, vol. 10, pp. 121 615–121 640, 2022.

[19] J. Tu, H. Chen, M. Wang, and A. H. Gandomi, "The colony predation algorithm," *Journal of Bionic Engineering*, vol. 18, no. 3, pp. 674–710, May 2021.

[20] H. A. Shehadeh, "Chernobyl disaster optimizer (CDO): a novel metaheuristic method for global optimization," *Neural Computing and Applications*, vol. 35, no. 15, pp. 10 733–10 749, Feb. 2023.

[21] S. P. Adam, S.-A. N. Alexandropoulos, P. M. Pardalos, and M. N. Vrahatis, "No free lunch theorem: A review," in *Approximation and Optimization*. Springer International Publishing, 2019, pp. 57–82.

[22] B. Lekouaghet, M. A. Khelifa, and A. Boukabou, "Adolescent identity search algorithm for parameter extraction in photovoltaic solar cells and modules," *Journal of Computational Electronics*, vol. 21, no. 4, pp. 859–881, May 2022.

[23] R. V. Rao, "Rao algorithms: Three metaphor-less simple algorithms for solving optimization problems," *International Journal of Industrial Engineering Computations*, pp. 107–130, 2020.

[24] M. Ghasemi, A. Rahimnejad, E. Akbari, R. V. Rao, P. Trojovský, E. Trojovská, and S. A. Gadsden, "A new metaphor-less simple algorithm based on rao algorithms: a fully informed search algorithm (FISA)," *PeerJ Computer Science*, vol. 9, p. e1431, Aug. 2023.